

Center of Excellence for Explosive Detection, Mitigation and Response

A Department of Homeland Security

Center of Excellence

University of Rhode Island (URI);

California Institute of Technology;

Purdue University

New Mexico State University;

University of Illinois

Florida International University

Hebrew University, Jerusalem Israel

Weizmann Institute of Science

Fourth Annual Report Appendices

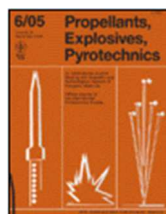
July 2012-September 2013

DHS agreement number: 2008-ST-061-ED0002

Appendices

5.1.1.1 <i>Synthesis and Characterization of Urea Nitrate and Nitro Urea</i> <i>Jimmie Oxley, James Smith</i>	4
5.1.1.2 <i>Characterization and Analysis of Tetranitrate Esters</i> <i>Jimmie Oxley, James Smith</i>	46
5.1.1.3 <i>Factors Influencing Triacetone Triperoxide (TATP) and Diacetone Diperoxide (DADP) Formation: Part I</i> <i>Jimmie Oxley, James Smith</i>	61
5.1.2.1 <i>Role of Metal Ions in the Destruction of TATP: Theoretical Considerations</i> <i>Ronnie Kosloff, Jimmie Oxley, James Smith, and Yehuda Zeiri</i>	99
5.1.2.2 <i>Density-Dependent Liquid Nitromethane decomposition: Molecular Dynamics Simulations on ReaxFF</i> <i>Yehuda Zeiri, Ronnie Kosloff</i>	110
5.1.2.3 <i>Molecular Dynamics Simulations of Weak Detonations</i> <i>Yehuda Zeiri, Ronnie Kosloff</i>	132
5.1.3 <i>Detonation Failure Characterization of Non-Ideal Explosives</i> <i>Steven Son</i>	147
5.1.4 <i>Fast Detection of Triacetone Triperoxide (TATP) from Headspace Using Planar Solid-phase Microextraction (PSPME) Coupled to an IMS Detector</i> <i>James Smith, Jimmie Oxley, Jose Almirall</i>	164
5.1.5 <i>The Adhesion of Particles of Standard Explosives to Model Surfaces</i> <i>Yehuda Zeiri</i>	174
5.2.3 <i>Composites of Carboxylate-capped TiO₂ Nanoparticles and Carbon Black as Chemiresistive Vapor Barriers</i> <i>Nathan Lewis</i>	189
5.2.4 <i>The Kinetics of the Thermal Decomposition of the Chloride Adduct of Ethylene Glycol di-nitrate: An Ion Mobility Spectrometry and <i>ab initio</i> Calculation Study</i> <i>G. Eiceman</i>	195
5.2.5 <i>Solution-based Direct Readout Surface Enhanced Raman Spectroscopic (SERS) Detection of ultra-low Levels of Thiram with Dogbone Shaped Gold Nanoparticles</i> <i>Radha Narayanan</i>	223
5.2.6 <i>Standoff Detection via Single-beam Spectral Notch Filtered Pulses</i> <i>Yaron Silberberg</i>	229

5.3.1 Development of Novel Composite Materials & Structures for Blast Mitigation Arun Shukla	233
5.3.3 Boundary Layer Profile Behind Gaseous Detonation as it Affects Reflected Shock Wave Bifurcation Joseph Shepherd	254
5.3.7 Appendix: Experiments and Analysis of Water-sheet Breakup and Mitigating Potential Under Blast Loading Steven Son	269



Synthesis and Characterization of Urea Nitrate and Nitrourea

Journal:	<i>Propellants, Explosives, Pyrotechnics</i>
Manuscript ID:	Draft
Wiley - Manuscript type:	Full Paper
Keywords:	Urea Nitrate, Nitrourea, Characterization, Spectroscopy, Thermal Analysis

SCHOLARONE™
Manuscripts

view Only

Synthesis and Characterization of Urea Nitrate and Nitrourea

Jimmie C. Oxley^{*a}; James L. Smith^a; Sravanathi Vadlamannati^a; Austin C. Brown^a;
Guang Zhang^a; Devon S. Swanson^a; Jonathan Canino^a

^aUniversity of Rhode Island,
Chemistry Department
51 Lower College Road
Kingston, RI 02881
^{*}joxley@chm.uri.edu

Abstract

Although urea nitrate (UN) has not found use as a legitimate explosive, it has been popular as an improvised explosive. In this paper the dehydration product of UN, nitrourea (NU), is characterized for the purpose of distinguishing the two white solids. Although they both melt around 160°C, all other properties differ markedly (see Table 6) as might be expected from an inorganic salt (UN) and an organic compound (NU).

Keywords: Urea Nitrate, Nitrourea, Characterization, Mass Spectrometry, Infrared Spectrometry, Raman Spectroscopy, Differential Scanning Calorimetry, Thermal Gravimetric Analysis, Nuclear Magnetic Resonance, Solubility, Melting Point, Thermal Decomposition, Synthesis

1 Introduction

Dehydration of ammonium nitrate (AN) salts yields nitramine. Nitramine (eq 1) is relatively unstable compared to nitroguanidine (eq 2) and nitrourea (eq 3). The difficulty in the synthesis of nitrourea (NU, CAS 556-89-8) from urea nitrate (UN, CAS 124-47-0) is providing adequate proof of product. Structures of NU and UN are shown in Figure 1. Both NU and UN are white solids with few physical properties available in the literature. Literature melting points are nearly the same, 158-160°C (UN) and 158°C dec (NU) (Table 1) [1]. Herein we report an extensive physical characterization of NU and contrast it with UN. In addition the two reported routes to the NU product are compared and the decomposition routes of UN proposed.



2 Experimental Section

2.1 Synthesis

NU was synthesized using two different methods, both based on dehydration of UN. In each, the scale of the reaction was designed to make about 1 g of NU. The UN starting material was synthesized by the reaction of nitric acid and urea, as previously reported [2].

2.1.1 Method 1: Using UN and sulfuric acid

Sulfuric acid (7.54g, 0.0769 mol) was poured into a round bottom flask equipped with a football stirrer and cooled to -3.0°C in a salt/ice bath. UN (1.17g, 0.0096 mol) was slowly added, maintaining the temperature between 0 and -3.0°C. The mixture was allowed to stir for 30 minutes keeping the temperature below +3.0 °C; then it was poured over ~10g of ice. The white

precipitate that formed (NU) was collected on filter paper by vacuum filtration. The product was rinsed with three aliquots of cold water, and dried under gentle flow of air. The NU was re-crystallized from glacial acetic acid [1]. Re-crystallized yield was 125 mg, 1.19 mmol, 13%.

2.1.2 Method 2: Using UN, acetic anhydride and acetic acid

Acetic anhydride and glacial acetic acid were purchased from Fisher Scientific. Acetic anhydride (1.40g, 0.0137 mol) was placed in a round bottom flask with a football stirrer and acetic acid (14.0g, 0.233 mol) was added. The mixture was heated to 60°C, and UN (1.40g, 0.0113 mol) was slowly added. The mixture was stirred at 60°C for 15 minutes before removal of heat source. The mixture was allowed to quiescently cool to room temperature. NU was collected on filter paper by vacuum filtration, rinsed with three aliquots of benzene, and oven dried at 40°C. The NU was re-crystallized from glacial acetic acid to yield 670 mg, 6.45 mmol, 67.2% NU [3].

2.2 Densities, Solubility and Melting Points of UN and NU

Ten density determinations for UN and NU products were obtained using a Micromeritics AccuPyc 1340 gas pycnometer. For each determination a sample cup (1.0 mL) was filled to about 75% capacity, weighed, capped, and inserted into the pycnometer. For each sample, ten helium purges and measurements were taken in succession. Arithmetic means and standard deviations of the UN and NU sets were calculated (Table 1).

The solubility of UN and NU in water, ethanol, methanol and acetone are reported in Table 1. Samples of 10-20 mg were weighed into two 10 mL glass vials and capped. Approximate solubility was determined by adding a 1.0 mL and 2.0 mL aliquots into the first and second vial, respectively, and followed by sonication for 5 minutes. Samples were removed and

1
2
3 visually inspected for presence of solid. If solid was still present, an aliquot of 2.0 mL was added
4
5 to each vial and the process repeated until dissolved or 10.0 mL of solvent had been added. If
6
7 the analyte was still not dissolved it was classified “insoluble.” Once approximate solubility was
8
9 obtained, the process was repeated for new samples near the estimated solubility with small
10
11 aliquots of solvent ranging from 0.05 mL – 0.75 mL using 100 μ L and 1.0 mL syringes.
12
13 Arithmetic means and standard deviations (5 replicates) were calculated for the UN and NU sets.
14
15

16
17 Melting points of UN and NU are given in Table 1. Small amounts (~0.5-1.0 mg) of UN
18
19 or NU were loaded into melting point glass capillaries and positioned into a MelTemp melting
20
21 point apparatus. At a setting of 4, samples were observed as they heated. Temperature was
22
23 recorded to the nearest degree as crystals of UN started to melt (range about 3-4°C). The melting
24
25 temperature was taken as the mid-point of the melt range. For NU, decomposition without
26
27 melting was observed. No solid residue was observed after completion of this procedure. The
28
29 decomposition temperature was recorded to the nearest degree. Arithmetic means and standard
30
31 deviations (10 replicates) were calculated for the UN and NU sets.
32
33
34
35
36
37

38 **2.3 Infrared (IR), Raman and Nuclear Magnetic Resonance (NMR) Spectroscopy**

39
40 Fourier Transform Infrared (FTIR) spectra were obtained with Nicolet 6700 FTIR Spectrometer
41
42 employing DTGS TEC detector and KBr beam splitter. Spectral range was 650 to 4000 cm^{-1} at
43
44 resolution of 4.0 cm^{-1} . For attenuated total reflectance (ATR) of solids 22 scans was sufficient.
45
46 An IR gas cell (pathlength 10 cm), with MCT/A detector, was used to monitor decomposition
47
48 gases at 290°C from a transfer line (250°C) connected to a TA Instruments Q5000
49
50 thermogravimetric analyzer (TGA). Raman spectra were obtained on a Bruker Sentera Raman
51
52 Microscope. The microscope module was a Olympus BX51. Excitation source was a 785 nm
53
54
55
56
57
58
59
60

1
2
3 diode laser. A Bruker Advance III nuclear magnetic resonance spectrometer (NMR) was used
4
5 to collect both proton and carbon NMR spectra (^1H at 300 MHz and ^{13}C NMR at 75 MHz). In
6
7 the proton mode 16 scans were collected; carbon mode was run proton decoupled and 512 scans
8
9 were collected.
10

11 12 13 14 **2.4 Gas Chromatography Mass Spectrometry (GC/MS)**

15
16 Gas chromatograph (Agilent model 6890) coupled with mass selective detector (Agilent model
17
18 5793) (GC/MS) was used to characterize the samples. The GC/MS inlet was operated in splitless
19
20 mode with inlet temperature of 125°C and a flow of 11.2mL/min (helium carrier gas). A 15
21
22 meter VF200MS column (J&W) with a 0.25mm inner diameter and a 0.25 μm film thickness was
23
24 operated under a constant flow condition of 1.5mL/min. The oven program had an initial
25
26 temperature of 40°C with a 5 min hold followed by a 20°C/min ramp to 250°C and a post-run at
27
28 310°C for 1 min. The transfer line temperature was 250°C and the mass selective detector
29
30 source and quadrupole temperatures were 230°C and 150°C, respectively. Chemical ionization
31
32 (positive mode) was used with methane as the reagent gas.
33
34
35
36
37
38

39 **2.5 Liquid Chromatography High-Resolution Mass Spectrometry (LCMS)**

40
41 Both UN and NU were analyzed using liquid chromatography/high-resolution mass spectrometry
42
43 (LCMS). The mass spectrometer was operated in both negative and positive ion mode under
44
45 multiple ionization conditions coupled with the HPLC or direct injection into the atmospheric
46
47 pressure chemical ionization (APCI) source via syringe pump. The vaporizer temperature was
48
49 set at 150°C, and capillary was set to 125°C. The discharge current ranged from 5-10 μA , and
50
51 the sheath gas and auxiliary gas were operated at 25 and 10 arbitrary units, respectively, for
52
53 negative mode, and 20 and 0 for positive mode. When directly injected into the ionization
54
55
56
57
58
59
60

1
2
3 source via syringe pump, sample flow rate was $\sim 10 \mu\text{L}/\text{min}$, and the material was dissolved in a
4
5 50:50 methanol-water solution. If adduct formation was desired, 0.25wt% carbon tetrachloride or
6
7 0.23wt% aqueous ammonium acetate was added to the methanol-water mixture. MS resolution
8
9 was set to high (50,000 at 2 Hz), and the maximum injection time was 250 ms.
10
11

14 2.6 Differential Scanning Calorimeter (DSC)

15
16 Analyses were performed using a TA Instruments model Q-100 DSC. Samples were run under
17
18 nitrogen flow (50mL/min), and the system was calibrated against indium (m.p. 156.60°C , H_f
19
20 28.71 J/g). Sample amounts ranged from 0.2 to 0.5mg and were sealed in glass micro-ampoules
21
22 (1.5mm O.D., 0.28mm wall thickness, and 8mm length) [4]. Samples were run in triplicate.
23
24

27 2.7 Thermal Gravimetric Analyzers (TGA)

28
29 The TGA (TA Instruments Q5000) used nitrogen purge gas to constantly sweep the balance (10
30
31 mL/min) and furnace (25 mL/min). Samples (10 mg) were held in open platinum pans (110 μL).
32
33 Runs were performed in duplicate or triplicate, ramping the temperature at $20^\circ\text{C}/\text{minute}$ from
34
35 40°C to 400°C . For some samples decomposition gases were transferred via a heated (250°C)
36
37 transfer line to a Nicolet 6700 FTIR spectrometer.
38
39

42 3.0 Results

45 3.1 Infrared Spectroscopy

46
47 Figure 2 shows the IR spectrum of UN, and Figures 3 and 4 of NU made via methods 1 and 2,
48
49 respectively. Significant differences were not observed between the NU samples. Both UN and
50
51 NU have bands around 1700 cm^{-1} (CO) and in the high and low end of 1300 cm^{-1} (NO), but UN
52
53 is clearly distinguished by the broad band around 2400 cm^{-1} . NU differs from UN between 3400
54
55
56
57
58
59
60

1
2
3 cm^{-1} and 2765 cm^{-1} where at least five bands are resolved. Both the Israeli Police Laboratory [5]
4
5 and a Canadian government laboratory [6] have reported IR of UN. The Canadian facility
6
7 assigned bands at 3402 cm^{-1} (NH_2 asymmetric stretch), 3354 cm^{-1} (NH stretch), 3198 cm^{-1} (NH_2
8
9 symmetric stretch), 1704 cm^{-1} (CO stretch), 1568 cm^{-1} (N-H), 1426 cm^{-1} (C-N), 1298 cm^{-1}
10
11 (NO_3^-). They suggested the peak at 2410 cm^{-1} in UN was OH symmetric stretching from
12
13 hydrogen bonding of adjacent UN molecules, $\text{C}=\text{O}\cdots\text{H}\cdots\text{ONO}_2$. This is consistent with our
14
15 comparison of IR spectra for UN, NU, and urea (Figure 4) where we found this band only in UN.
16
17
18
19

20 21 **3.2 Raman Spectroscopy**

22
23 Raman spectra of UN, NU, U and AN are given in Figure 5. Literature assignments are available
24
25 for the prominent 1043 cm^{-1} and 1057 cm^{-1} lines in AN and UN, respectively. They are due to
26
27 internal symmetric stretching of the NO_3^- anion [7,8]. The 715 cm^{-1} in AN and the 537 cm^{-1} in
28
29 UN may also be due to internal covalent stretches of NO_3^- anion. A C-N symmetric stretching
30
31 mode has been assigned to the 1011 cm^{-1} line in urea and is likely responsible for the 1020 cm^{-1}
32
33 line in UN and possibly the 989 cm^{-1} line in NU. The weak lines in urea at 1625 and 1649 cm^{-1}
34
35 have been assigned to NH_2 deformations. A similar assignment is possible in UN and NU. The
36
37 1540 cm^{-1} line in urea has been assigned to C-O stretching. Raman lines at 1583 cm^{-1} (NU) and
38
39 1574 cm^{-1} (UN) may also result from C-O stretches.
40
41
42
43
44
45

46 47 **3.3 ^1H and ^{13}C NMR Spectroscopy**

48
49 Spectra of NU and UN are shown in Figure 6 In d^6 -acetone NU showed 2 broad peaks--one
50
51 around 12 ppm, assigned to the proton adjacent to nitro group, and one around 7 ppm, assigned
52
53 to the proton attached to the amino group. In contrast, UN showed a single peak at about 8 ppm;
54
55
56
57
58
59
60

1
2
3 indicating hydronium ion exchanges with amino protons and cannot be observed by NMR.
4
5 Proton decoupled ^{13}C NMR in d^6 acetone yields a single peak-at 151 ppm for nitrourea and at
6
7 163 ppm for UN. The latter is higher due to proton-bonding on the oxygen site of the carbonyl
8
9 group.
10

11 12 13 14 **3.4 Gas Chromatography Mass Spectrometry (GC/MS)**

15
16 No attempt was made to analyze UN by GC/MS. NU was analyzed by chemical ionization
17
18 GC/MS in acetonitrile solution. NU, made by methods 1 and 2, as well as crude and
19
20 recrystallized NU, was examined. Spectra are shown in Figure 7. Fragmentation of the early
21
22 peak around 5 minutes indicated nitric acid. The apparent chromatographic peaks of NU were
23
24 very broad and asymmetric with low-mass-weight fragments: 44 (M), 63 (L), 91 (T), 106 (S,
25
26 $\text{NU}+\text{H}^+$) (Figure 7).
27
28
29
30
31

32 **3.5 Liquid Chromatography High-Resolution Mass Spectrometry (LCMS)**

33
34 Negative ion spectra mass spectra for UN and NU (HPLC and direct injection) are given
35
36 in Figure 8. The solvent system was equal portions water and methanol. The solvent system
37
38 was spiked with 0.25 wt% carbon tetrachloride (CCl_4) for adduct formation. Most of the major
39
40 peaks remained the same for NU spectrum whether the sample was introduced via HPLC or
41
42 direct injection. The negative ion spectrum with CCl_4 (Figure 8) provided the best comparison
43
44 of UN and NU. In the negative mode, the principle anionic fragments from NU were $\text{NU} + \text{Cl}^-$
45
46 (139.986), $\text{NU} - \text{H}^+$ (104.010) and nitrate (61.987), and for UN, urea + Cl^- (95.002), 2 urea + Cl^-
47
48 (155.034), nitrate (61.987), and nitric acid + NO_3^- (124.983), the latter two being observed with
49
50 direct injection. In positive mode (Figure 9) the major fragment for both NU and UN was about
51
52 m/z 61.040. For NU this was assigned as cyanic acid complexed with ammonium ion. For UN,
53
54
55
56
57
58
59
60

1
2
3 in addition to 61.040 fragments, m/z 121.072 and 181.104 values suggest that the 61.040 m/z
4
5 fragment be assigned as urea + H^+ ; and the other two fragments as 2x urea + H^+ , and 3x urea +
6
7 H^+ (Table 2).
8
9

10 The direct injection spectra of NU and UN in equal amounts of methanol/water with
11
12 0.23% ammonium acetate for adduct formations are given in Figure 10. In Figure 10a the
13
14 negative ion spectrum of NU has 3 major m/z values (61.003, 61.987, 104.009). Tentative
15
16 assignments are nitramide - H^+ , nitrate, NU - H^+ (See Table 3). The corresponding negative ion
17
18 spectrum of UN (Figure 10b) produced only a nitrate at 61.987 m/z . The positive ion spectra for
19
20 NU and UN in Figure 10c and 10d, respectively, both have a prominent m/z at 61.040 believed
21
22 to be cyanic acid + NH_4^+ in NU and urea + H^+ in UN. Positive and negative ion spectra in
23
24 Figure 11 are direct injections in methanol/water without adduct former for both NU and UN.
25
26 Tentative assignments are given in Tables 2 and 3 for UN and NU respectively.
27
28
29
30
31

32 Mass spectrum of nitrourea changed as the solution aged. In a freshly made
33
34 methanol/water solution, NU - H^+ (104.010) was the largest peak in the negative mode of the MS
35
36 fragmentation pattern. However, when a methanol/water solution of NU is allowed to sit one
37
38 week under ambient conditions all evidence of the NU - H^+ fragment disappears and essentially
39
40 only dicyanic acid - H^+ (85.044) becomes the major peak. This corresponds to the
41
42 decomposition of NU previously reported [9].
43
44
45
46

47 3.6 Differential Scanning Calorimeter (DSC)

48
49 Figure 12 shows thermograms of UN and NU. The thermogram of UN showed a melt near
50
51 162°C and a sharp exotherm immediately thereafter at 167°C. A second broader exotherm was
52
53 observed around 380°C (Table 5). At the completion of each DSC run samples were re-weighed
54
55
56
57
58
59
60

1
2
3 to ensure there had been no leaks from the sealed capillaries. A small amount of white residue
4 was observed in all UN samples. A sharp exotherm for NU was observed at about 162°C. While
5
6 was observed in all UN samples. A sharp exotherm for NU was observed at about 162°C. While
7
8 the DSC of UN showed a melt, the NU did not. The NU energy released, according to DSC, was
9
10 about double the energy of UN (1100 vs. 480 J/g). For NU samples a trace amount of black
11
12 residue remained.
13

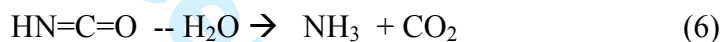
16 3.7 Thermal Gravimetric Analyzer

17
18 There was no discernable difference between the TGA traces of the crude and re-crystallized NU
19
20 or between the NU made by the first or second synthesis methods (Figures 13, 14). The TGA
21
22 traces of UN (Figure 15) and NU (Figures 13, 14) were distinctly different. Weight-loss of both
23
24 UN and NU started at ~140°C; NU exhibited a single weight-loss event (Figures 13, 14), while
25
26 UN experienced three thermal events (Figure 15). The TGA trace of urea (Figure 16) also
27
28 exhibited three thermal events before being completely consumed. FT-IR spectra of the gases
29
30 from decomposition of NU, UN and urea are compared in a stack plot (Figure 17) that also
31
32 includes a mixture of CO₂ and N₂O gas (second spectrum from top). Overlapping spectra of neat
33
34 CO₂ and N₂O gases and a mixture of the two shown in Figure 18 distinguish peaks associated
35
36 with these two gases. Comparison of Figures 17 and 18 suggest that UN decomposition
37
38 produced significant amounts of CO₂ while NU and urea decomposition did not. Further, N₂O
39
40 gas appeared to be present in UN, NU and urea as demonstrated by prominent peak at 2240 cm⁻¹
41
42 and an isolated doublet centered at 1288 cm⁻¹. The 1355 cm⁻¹ peak in Figure 17, adjacent to the
43
44 doublet and only appearing in UN was not assigned. Closer inspection of all three materials
45
46 (Figure 19) reveals another peak centered between the N₂O peak (2240 cm⁻¹) and CO₂ peak
47
48 (2360 cm⁻¹). This peak (2283 cm⁻¹) is assigned to gas phase isocyanic acid, literature value 2269
49
50
51
52
53
54
55
56
57
58
59
60

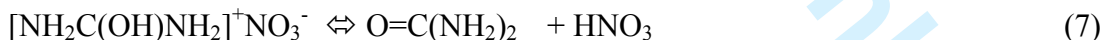
cm⁻¹[10]. Since NU was completely consumed, a suggested mechanism is as shown by equations 4 and 5. Isocyanic acid (HN=C=O) was also observed in the mass spectrum fragmentation pattern of NU (Table 3) and UN (Table 4). The other product nitramide (H₂NNO₂) is believed to decompose via eq. 5.

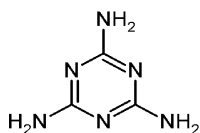
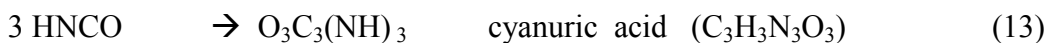


The formation and subsequent hydrolysis of isocyanic acid to ammonia and carbon dioxide has been demonstrated[9]. This hydrolysis had been observed by mass spectrometry in the aging of aqueous methanol solutions of NU via eq. 6.

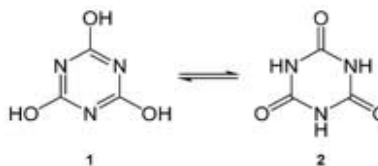


The first weight-loss event for UN (~140°C) only consumed about 40% of the sample (Figure 15). The weight-loss events for NU and UN do not appear to proceed via the same mechanism as their decomposition products are notably different. The decomposition gases of UN exhibit peaks at 2400 and 1350 cm⁻¹ not observed in the spectra of the NU off gases. Formation of urea from UN (eq. 7) and the subsequent reactions of urea (eqs. 8-13) to form melamine, cyanourea, biuret and cyanuric acid results in species which are likely to survive at high temperatures [10].





melamine



cyanuric acid

The IR spectrum corresponding with the weight loss in the NU thermogram is shown in Figure 16. The location of the single weight-loss event for NU and the IR spectrum of its decomposition gases match those observed for urea (see Figure 17). The IR spectrum of urea decomposition gases match those predicted in equation 5. The remaining solid residue was likely one of the products in equations 8-13. Not only is the TGA thermogram of UN more complex than that of NU, but the IR spectra of its decomposition gases also differed. Thus, urea nitrate decomposes via urea (eq. 7) and the decomposition route of urea (eqs. 8-13), while nitrourea decomposes via isocyanic acid and nitramide (eq. 4).

4 Conclusion

UN and NU can be distinguished by a number of their physical properties (Table 6). As expected UN behaves like an ionic compound and decomposes to urea and nitric acid. A difficulty in differentiating between UN and NU has been that they are both white solids with similar melting points.

References

- [1] . A.W. Ingersoll, B.F. Armendt, Nitrourea *Organic Syntheses*, **1925** 5, 85 .
- [2] J.C. Oxley, J.L. Smith, S. Naik, J.S. Moran, Decompositions of Urea and Guanidine Nitrates, *Journal of Energetic Materials*, **2009** 27(1), 17-39.
- [3] C.P. Spaeth, N.J. Woodbury, *Preparation of Nitrourea*. US Patent Feb. 23, 1943.
- [4] L.F. Whiting, M.S. Labean, S.S Eadie, Evaluation of a Capillary Tube Sample Container for Differential Scanning Calorimetry, *Thermochem. Acta* **1988**, 136, 231-245.
- [5] J. Almog, G. Burda, Y. Shloosh, S. Abramovich-Bar, E. Wolf, T. Tamiri, Recovery and Detection of Urea Nitrate in Traces. *J. Forensic Sci.* **2007**, 52(6), 1284-1290.
- [6] S. Desilets. P. Brousseau, D. Chamberland, S. Singh, H. Feng, R. Turcotte, J. Anderson, Degradation Mechanism and the Thermal Stability of Urea Nitrate Below the Melting Point, *Thermochimica Acta* **2011** 521, 176-183.
- [7] L. Nagli, M. Gaft, Y. Fleger, M. Rosenbluh, Absolute Raman cross-sections of some explosives: Trend to UV, *Optical Materials* **2008** 30, 1747-1754.
- [8] K. Akiyama, Y. Morioka, I. Nakagawa, Raman Scattering and Phase Transition of Ammonium Nitrate, *Bull. Chem. Soc. Jpn.* **1981** 54, 1662-1666.
- [9] T.L. Davis, K.C. Blanchard, Dearrangement of Nitrourea and its Application in Synthesis, *J. Am. Chem. Soc.*, **1929**, 51, pp 1790-1801.
- [10] M.S. Lowenthal, R.K. Khanna, M.H. Moore, Infrared Spectrum of Solid Isocyanic Acid (HCNO): Vibrational Assignments and Integrated Band Intensities, *Spectrochimica Acta Part A*, **2002** 58, 73-78.

List of Tables

Table 1. Physical Properties of Urea Nitrate (UN) & Nitrourea (NU)

Table 2. Summary of MS Fragmentation

Table 3. Fragmentation pattern of NU. Assignments with Cl⁻ adduct were supported by additional mass peaks corresponding to the ³⁷Cl⁻ adduct.

Table 4. Fragmentation pattern of UN. Assignments with Cl⁻ adduct were supported by additional mass peaks corresponding to the ³⁷Cl⁻ adduct.

Table 5. DSC Summary of Urea Nitrate & Nitrourea

Table 6. Comparison of UN and NU Physical Properties

TABLE 1

	UN	NU
melting point °C	158-160	153-155 (dec)
density g/cm ³	1.67±0.011	1.73±0.026
solubility mg/mL:		
Water	167.2±0.5	20±2
Ethanol	14.2±0.1	17.2±0.6
Methanol	54.8±0.9	43±8
Acetone	10.4±0.2	41±5

Table 1. Physical Properties of Urea Nitrate (UN) & Nitrourea (NU)

TABLE 2

Solvent & Additive	Size	Nitrourea		Urea Nitrate	
		negative	positive	negative	positive
Liquid Chromatography					
methanol/water CCl ₄	large	NU-H ⁺	isocyanic acid+NH ₄ ⁺	urea+Cl ⁻	urea+H ⁺ 2(urea)+H ⁺
	M-S	NU+Cl ⁻ dicyanic acid-H ⁺ nitramide+Cl ⁻	methyl carbamate+NH ₄ ⁺ methyl carbamate+H ⁺	2(urea)+Cl ⁻ biuret+H ⁺ methylol urea+Cl ⁻	3(urea)+H ⁺ methylol urea+H ⁺ urea+NH ₄ ⁺
methanol CCl ₄	large	NU-H ⁺	isocyanic acid+NH ₄ ⁺	urea+Cl ⁻	urea+H ⁺ 2(urea)+H ⁺
	M-S	NU+Cl ⁻ dicyanic acid-H ⁺ nitramide+Cl ⁻	methyl carbamate+NH ₄ ⁺	2(urea)+Cl ⁻ biuret+H ⁺ methylol urea+Cl ⁻	3(urea)+H ⁺ methylol urea+H ⁺ urea+NH ₄ ⁺
Direct Inject					
methanol/water CCl ₄	large	NU-H ⁺	N/A	NO ₃ ⁻	2(urea)+H ⁺
	M-S	NU+Cl ⁻ nitramide+Cl ⁻ NO ₃ ⁻		HNO ₃ +NO ₃ ⁻	urea+H ⁺ 3(urea)+H ⁺ methylol urea+H ⁺
methanol/water NH ₄ acetate	large	NO ₃ ⁻ NU-H ⁺	isocyanic acid+NH ₄ ⁺	NO ₃ ⁻	urea+H ⁺
	M-S	nitramide-H ⁺			
no additive	large	urea-H ⁺	isocyanic acid+NH ₄ ⁺	NO ₃ ⁻ urea-H ⁺	N/A
	M-S	dicyanic acid-H ⁺ NO ₃ ⁻	urea+NH ₄ ⁺ methyl carbamate+NH ₄ ⁺	Biuret-H ⁺	

Table 2. Summary of HRMS fragmentation

TABLE 3

Additive	Mode	Solvent	Nitrourea											
			Negative					Positive						
			Observed Mass	Assignment	Calculated Mass	Size	# of times	Observed Mass	Assignment	Calculated Mass	Size	# of times		
CCl ₄	LC	Fresh 50-50 MeOH-H ₂ O	85.0050	[Dicyanic acid - H+] ⁻	85.0044	S	3	61.0401	[Isocyanic acid + NH ₄ ⁺] ⁺	61.0396	L	3		
			96.9799	[Nitramide + Cl ⁻] ⁻	96.9810	T	3	76.0395	[Methyl Carbamate + H ⁺] ⁺	76.0393	STM	3		
			104.0090	[Nitrourea - H ⁺] ⁻	104.0102	L	3	93.0659	[Methylcarbamate + NH ₄ ⁺] ⁺	93.0659	MSS	3		
			139.9858	[Nitrourea + Cl ⁻] ⁻	139.9868	M	3							
		Fresh MeOH	85.0050	[Dicyanic acid - H+] ⁻	85.0044	SST	3	61.0401	[Isocyanic acid + NH ₄ ⁺] ⁺	61.0396	L	3		
			96.9799	[Nitramide + Cl ⁻] ⁻	96.9810	T	3	93.0659	[Methylcarbamate + NH ₄ ⁺] ⁺	93.0659	M	3		
			104.0090	[Nitrourea - H ⁺] ⁻	104.0102	L	3							
			139.9858	[Nitrourea + Cl ⁻] ⁻	139.9868	M	3							
		Fresh H ₂ O	85.0050	[Dicyanic acid - H ⁺] ⁻	85.0044	S	3	61.0401	[Isocyanic acid + NH ₄ ⁺] ⁺	61.0396	L	3		
			96.9799	[Nitramide + Cl ⁻] ⁻	96.9810	T	3	93.0659	[Methylcarbamate + NH ₄ ⁺] ⁺	93.0659	S	3		
			104.0090	[Nitrourea - H ⁺] ⁻	104.0102	L	3							
			139.9858	[Nitrourea + Cl ⁻] ⁻	139.9868	M	3							
		Two Day Old 50-50 MeOH-H ₂ O	85.0050	[Dicyanic acid - H ⁺] ⁻	85.0044	S	3	61.0401	[Isocyanic acid + NH ₄ ⁺] ⁺	61.0396	L	3		
			96.9799	[Nitramide + Cl ⁻] ⁻	96.9810	STT	3	76.0395	[Methyl Carbamate + H ⁺] ⁺	76.0393	S	3		
			104.0090	[Nitrourea - H ⁺] ⁻	104.0102	L	3	78.0664	[Urea + NH ₄ ⁺] ⁺	78.0662	S	3		
			139.9858	[Nitrourea + Cl ⁻] ⁻	139.9868	M	3	93.0659	[Methylcarbamate + NH ₄ ⁺] ⁺	93.0659	M	3		
		Two Day Old MeOH	85.0050	[Dicyanic acid - H ⁺] ⁻	85.0044	S	3	61.0401	[Isocyanic acid + NH ₄ ⁺] ⁺	61.0396	L	3		
			96.9799	[Nitramide + Cl ⁻] ⁻	96.9810	T	3	76.0395	[Methyl Carbamate + H ⁺] ⁺	76.0393	MSS	3		
			104.0090	[Nitrourea - H ⁺] ⁻	104.0102	L	3	93.0659	[Methylcarbamate + NH ₄ ⁺] ⁺	93.0659	SSM	3		
			139.9858	[Nitrourea + Cl ⁻] ⁻	139.9868	M	3							
		One Week Old 50-50 MeOH-H ₂ O	85.0050	[Dicyanic acid - H ⁺] ⁻	85.0044	L	3	61.0401	[Isocyanic acid + NH ₄ ⁺] ⁺	61.0396	L	3		
			96.9858	[Nitramide + Cl ⁻] ⁻	96.9810	TST	3	93.0658	[Methylcarbamate + NH ₄ ⁺] ⁺	93.0659	SMM	3		
		Direct Inject	50-50 MeOH-H ₂ O	61.9871	[Nitrate ⁻] ⁻	61.9884	S	5	N/A					
				96.9799	[Nitramide + Cl ⁻] ⁻	96.9810	S	5						
				104.0090	[Nitrourea - H ⁺] ⁻	104.0102	L	5						
				139.9859	[Nitrourea + Cl ⁻] ⁻	139.9868	M	5						
		NH ₄ ⁺ Acetate	Direct Inject	50-50 MeOH-H ₂ O	61.0032	[Nitramide - H ⁺] ⁻	61.0044	TSS	3	61.0401	[Isocyanic acid + NH ₄ ⁺] ⁺	61.0396	LS	2
					61.9871	[Nitrate ⁻] ⁻	61.9884	LLSL	5					
104.0090	[Nitrourea - H ⁺] ⁻				104.0102	LLLML	5							
None	Direct Inject	50-50 MeOH-H ₂ O	59.0127	[Urea - H ⁺] ⁻	59.0251	L	1	61.0401	[Isocyanic acid + NH ₄ ⁺] ⁺	61.0396	L	1		
			61.0000	[Nitramide - H+] ⁻	61.0038	S	1	78.0664	[Urea + NH ₄ ⁺] ⁺	78.0662	S	1		
			74.9951	[Hydroxyurea - H ⁺] ⁻	75.0200	M	1	93.0659	[Methylcarbamate + NH ₄ ⁺] ⁺	93.0659	M	1		
			85.0038	[Dicyanic acid - H+] ⁻	85.0038	S	1	130.06519	[Cyanuric acid + H ⁺] ⁺	130.02527	M	1		
			88.0029	[Nitroso-urea - H ⁺] ⁻	88.0153	S	1							
			96.9858	[Nitramide + Cl ⁻] ⁻	96.9810	S	1							
			104.0150	[Nitrourea - H ⁺] ⁻	104.0102	S	1							

Table 3. Fragmentation pattern of NU. Assignments with Cl⁻ adduct were supported by additional mass peaks corresponding to the ³⁷Cl⁻ adduct.

TABLE 4

Urea Nitrate												
			Negative					Positive				
Additive	Mode	Solvent	Observed Mass	Assignment	Calculated Mass	Size	# of times	Observed Mass	Assignment	Calculated Mass	Size	# of times
CCl ₄	LC	Fresh 50-50 MeOH-H ₂ O	95.0008	[Urea + Cl ⁻] ⁻	95.0018	L	3	61.0401	[Urea + H ⁺] ⁺	61.0396	L	3
			96.9978	[Urea + ³⁷ Cl ⁻] ⁻	96.9988	M	3	78.0665	[Urea + NH ₄ ⁺] ⁺	78.0662	T	3
			102.0299	[Biuret - H ⁺] ⁻	102.0309	T	3	93.0660	[Methylol urea + H ⁺] ⁺	93.0659	S	3
			127.0271	[Ammelide - H ⁺] ⁻	127.0262	STT	3	121.0721	[2xUrea + H ⁺] ⁺	121.0720	L	3
			155.0334	[2xUrea + Cl ⁻] ⁻	155.0341	S	3	181.1045	[3xUrea + H ⁺] ⁺	181.1044	T	3
		95.0008	[Urea + Cl ⁻] ⁻	95.0018	L	3	61.0401	[Urea + H ⁺] ⁺	61.0396	L	3	
		96.9978	[Urea + ³⁷ Cl ⁻] ⁻	96.9988	M	3	93.0659	[Methylol urea + H ⁺] ⁺	93.0659	S	3	
		102.0299	[Biuret - H ⁺] ⁻	102.0309	T	3	78.0664	[Urea + NH ₄ ⁺] ⁺	78.0662	T	3	
		127.0271	[Ammelide - H ⁺] ⁻	127.0262	TTS	3	121.0721	[2xUrea + H ⁺] ⁺	121.0720	L	3	
		155.0334	[2xUrea + Cl ⁻] ⁻	155.0341	S	3	181.1044	[3xUrea + H ⁺] ⁺	181.1044	T	3	
		95.0008	[Urea + Cl ⁻] ⁻	95.0018	L	3	61.0401	[Urea + H ⁺] ⁺	61.0396	L	3	
		96.9978	[Urea + ³⁷ Cl ⁻] ⁻	96.9988	M	3	78.0664	[Urea + NH ₄ ⁺] ⁺	78.0662	T	3	
		102.0299	[Biuret - H ⁺] ⁻	102.0309	TSS	3	93.0659	[Methylol urea + H ⁺] ⁺	93.0659	S	3	
		127.0271	[Ammelide - H ⁺] ⁻	127.0262	S	3	121.0721	[2xUrea + H ⁺] ⁺	121.0720	L	3	
		155.0334	[2xUrea + Cl ⁻] ⁻	155.0341	S	3	181.1044	[3xUrea + H ⁺] ⁺	181.1044	T	3	
	95.0008	[Urea + Cl ⁻] ⁻	95.0018	L	3	61.0401	[Urea + H ⁺] ⁺	61.0396	L	3		
	96.9978	[Urea + ³⁷ Cl ⁻] ⁻	96.9988	M	3	78.0664	[Urea + NH ₄ ⁺] ⁺	78.0662	T	3		
	102.0299	[Biuret - H ⁺] ⁻	102.0309	TSS	3	93.0659	[Methylol urea + H ⁺] ⁺	93.0659	S	3		
	127.0271	[Ammelide - H ⁺] ⁻	127.0262	S	3	121.0721	[2xUrea + H ⁺] ⁺	121.0720	L	3		
	155.0334	[2xUrea + Cl ⁻] ⁻	155.0341	S	3	181.1044	[3xUrea + H ⁺] ⁺	181.1044	T	3		
Direct Inject	50-50 MeOH-H ₂ O	61.9878	[Nitrate ⁻] ⁻	61.9884	L	2	61.0394	[Urea + H ⁺] ⁺	61.0396	SSSL	4	
		124.9829	[Nitric acid + NO ₃ ⁻] ⁻	124.9840	T	4	121.0724	[2xUrea + H ⁺] ⁺	121.0720	L	4	
							130.0652	[Cyanuric Acid + H ⁺] ⁺	130.0253	S	1	
							181.1049	[3xUrea + H ⁺] ⁺	181.1044	S	2	
NH ₄ ⁺ Acetate	Direct Inject	50-50 MeOH-H ₂ O	61.9872	[Nitrate ⁻] ⁻	61.9884	L	1	61.0408	[Urea + H ⁺] ⁺	61.0396	M	2
								62.0435	[Nitromethane + H ⁺] ⁺	62.0237	M	2
								93.0666	[methylol urea + H ⁺] ⁺	93.0659	M	2
None	Direct Inject	50-50 MeOH-H ₂ O	59.0239	[Urea - H ⁺] ⁻	59.0251	MLL	3	N/A				
			61.9871	[Nitrate ⁻] ⁻	61.9884	LST	3					
			89.0403	[Methoxyurea - H ⁺] ⁻	89.0357	SSM	3					

Table 4. Fragmentation pattern of UN. Assignments with Cl⁻ adduct were supported by additional mass peaks corresponding to the ³⁷Cl⁻ adduct.

TABLE 5

UN Ramp Rate (°C/min)	MP (°C)	Max. (°C)	Heat (J/g)	NU Ramp Rate (°C/min)	Max. (°C)	Heat (J/g)
20	163.74	175.79	304.5	20	163.11	1143
20	163.77	174.27	627.3	20	164.15	1077
20	161.15	174.26	415.3	20	161.92	1099
10	159.18	166.7	477.6	20	163.69	887.1
10	159.42	167.12	477.4	20	154.21	1054
10	160.73	167.09	424.9	20	158.71	1113
10	159.51	167.13	399.14	10	152.68	1105
10	158.75	166.55	433.5	10	148.74	1140
				10	148.19	1089
				10	143.67	1045

Table 5. DSC Summary of Urea Nitrate & Nitrourea

TABLE 6

	UN	NU
melting point °C	157-159	153-155
density g/cm ³	1.67±0.011	1.73±0.026
DSC 20°/min dec °C	~160, ~380	~140
DSC J/g	~500, small	1000
TGA dec at °C, % wt loss	160°C, 40%	160°C, 100%
	250°C, 40%	
IR cm ⁻¹	3500, 3200, 2410 broad 1704, 1568, 1426, 1298	3400-2700 mult peaks 1605, 1305
¹ H NMR d ⁶ -acetone ppm	8	7,12
¹³ C NMR d ⁶ -DMSO ppm	163	151
MS negative	nitrate	NU-H ⁺
MS negative with CCl ₄	urea + Cl ⁻ or 2 urea + Cl ⁻	NU + Cl ⁻
MS positive	urea + H ⁺	methyl carbonate+NH ₄ ⁺ cyanic acid+NH ₄ ⁺
solubility mg/mL:		
Water	167.2±0.5	20±2
Ethanol	14.2±0.1	17.2±0.6
Methanol	54.8±0.9	43±8
Acetone	10.4±0.2	41±5

Table 6. Comparison of UN and NU Physical Properties

List of Figures

Figure 1. Chemical Structures of Nitrourea (NU) and Urea Nitrate (UN)

Figure 2. IR spectrum (transmission mode) of recrystallized Urea Nitrate

Figure 3. IR spectrum (transmission mode) of recrystallized Nitrourea using sulfuric acid method 1

Figure 4. IR spectrum (transmission mode) of recrystallized Nitrourea made using acetic anhydride method 2

Figure 5. Raman Spectrum, from top, of UN, Urea, NU, Ammonium Nitrate, respectively. Ammonium nitrate exhibited additional small peak at $\sim 2900\text{ cm}^{-1}$

Figure 6. $^1\text{H-NMR}$ (top) and $^{13}\text{C-NMR}$ (bottom) of Nitrourea(2) and Urea Nitrate(1)

Figure 7. GC/MS chromatograms and spectra with chemical ionization using methane as reagent gas for recrystallized nitrourea synthesized by method 1(left) and method 2 (right)

Figure 8. Negative mode mass spectra of NU and UN in 50-50 MeOH- H_2O with CCl_4 . a) direct inject NU, b) LC NU, c) direct inject UN, d) LC UN

Figure 9. Positive mode mass spectra of NU and UN in 50-50 MeOH- H_2O with CCl_4 . a) LC NU, b) direct inject UN, c) LC UN.

Figure 10. Direct inject mass spectra of NU and UN in 50-50 MeOH- H_2O with ammonium acetate. a) negative mode NU, b) negative mode UN, c) positive mode NU, d) positive mode UN.

Figure 11. Direct inject mass spectra of NU and UN in 50-50 MeOH- H_2O with no additive. a) negative mode NU, b) negative mode UN, c) positive mode NU.

Figure 12. NU CCl_4 Negative Mode a) TIC chromatogram; b) 100-400 amu filter chromatogram

Figure 13. UN CCl_4 Positive Mode a) TIC chromatogram; b) 100-400 amu filter chromatogram

Figure 12. DSC thermograms of nitrourea (top) & urea nitrate (bottom) scanned at $10\text{ }^\circ\text{C/minute}$

Figure 13. TGA trace crude (top) and re-crystallized (bottom) nitrourea

1
2
3 **Figure 14.** TGA Trace Recrystallized Nitrourea synthesized using method 1 (top) &
4 method 2 (bottom). Scan rate 20 °C/min.
5
6

7 **Figure 15.** TGA Trace of Recrystallized Urea Nitrate.
8

9 **Figure 16.** TGA thermogram of urea.
10

11 **Figure 17.** Stacked IR spectra of urea nitrate, CO₂ and N₂O mixture, nitrourea, and urea
12 from top to bottom, respectively. Selected wavenumbers are shown.
13
14

15 **Figure 18.** Overlap IR spectra of CO₂ (—), N₂O (⋯), and a mixture of both (---).
16
17

18 **Figure 19.** Overlap magnified IR spectra of urea nitrate, nitrourea, urea, and a mixture of
19 CO₂ and N₂O.
20
21
22
23
24
25
26
27
28
29
30
31
32
33
34
35
36
37
38
39
40
41
42
43
44
45
46
47
48
49
50
51
52
53
54
55
56
57
58
59
60

FIGURE 1



Figure 1. Chemical Structures of Nitrourea (NU) and Urea Nitrate (UN)

FIGURE 2

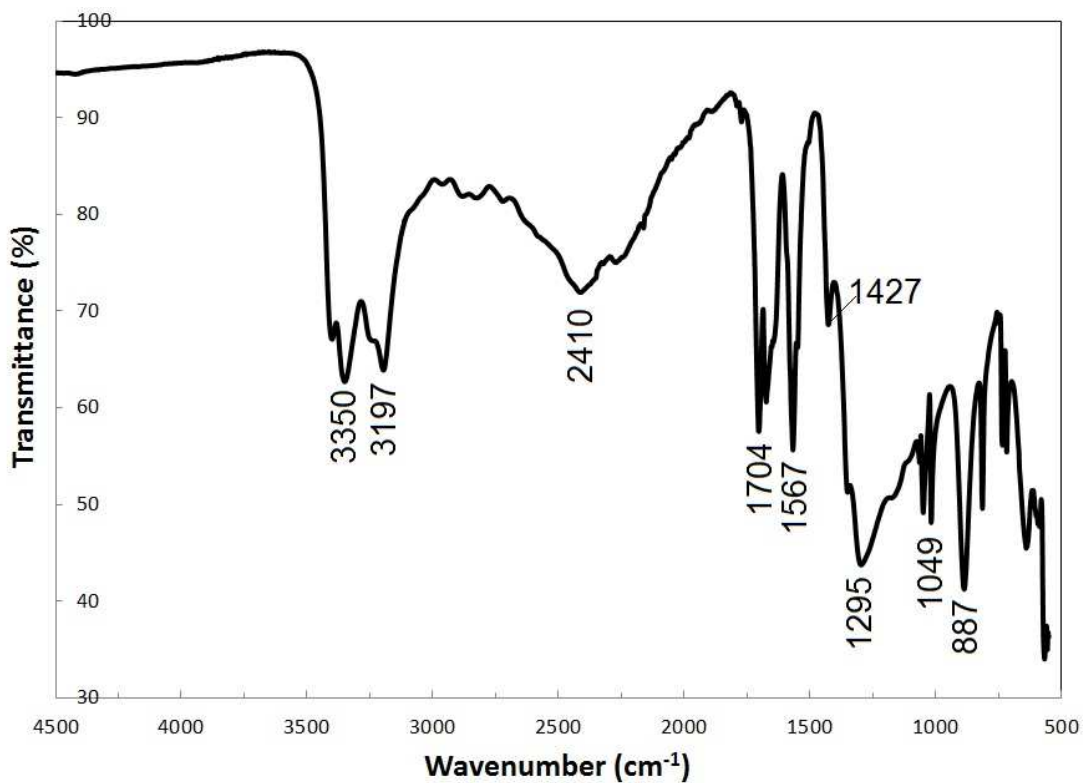


Figure 2. IR spectrum (transmission mode) of recrystallized Urea Nitrate

FIGURE 3

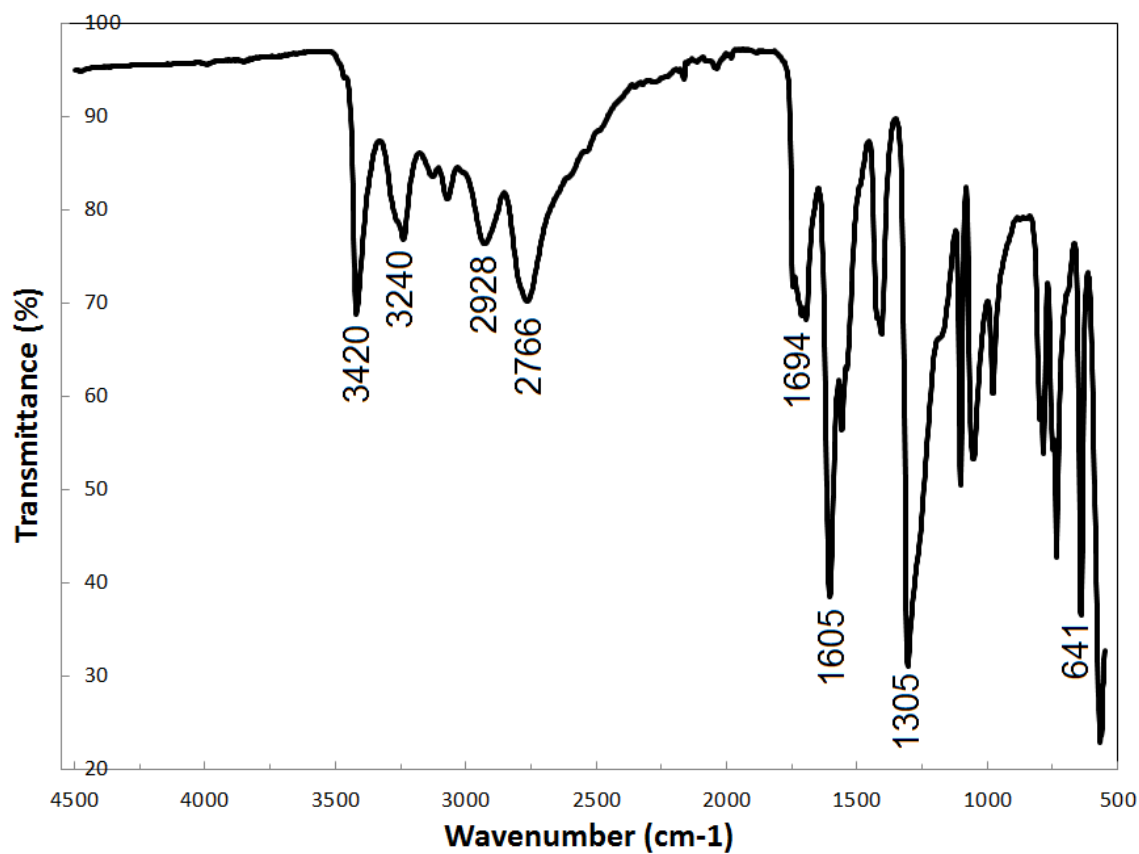


Figure 3. IR spectrum (transmission mode) of recrystallized Nitrourea using sulfuric acid method 1

FIGURE 4

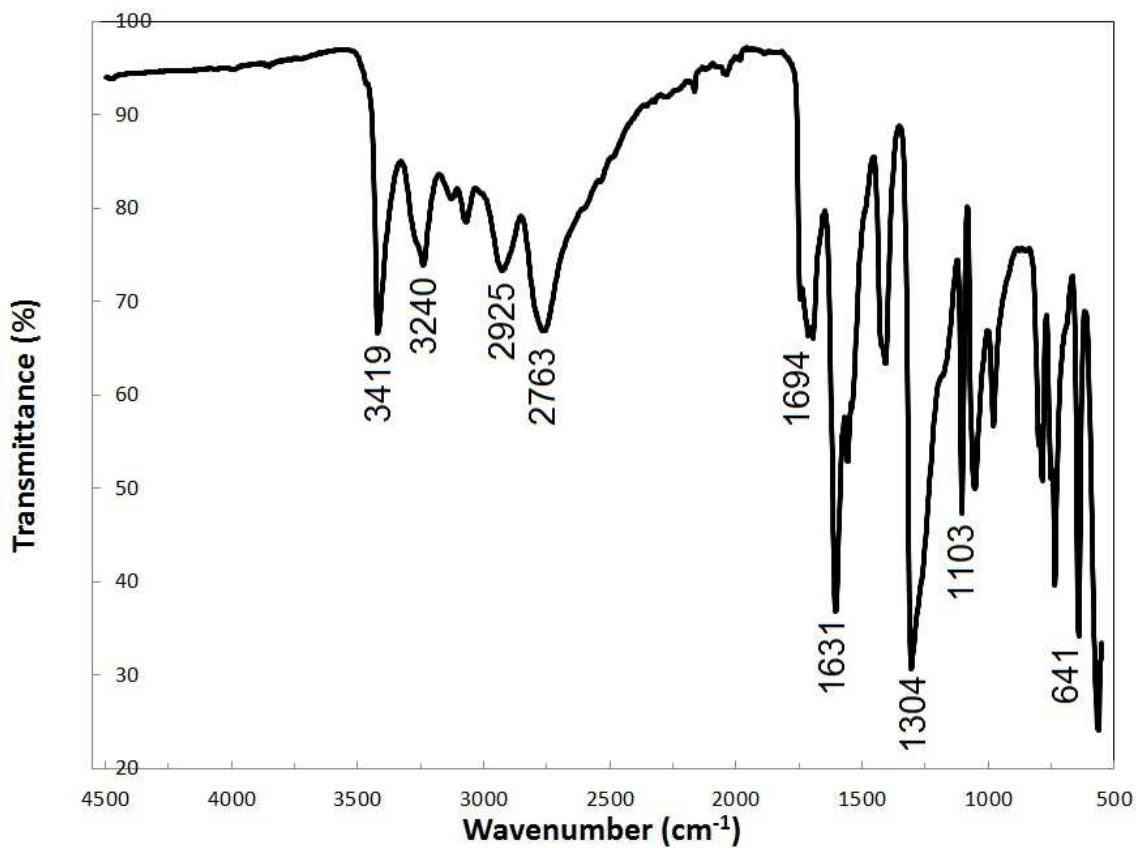


Figure 4. IR spectrum (transmission mode) of recrystallized Nitrourea made using acetic anhydride method 2

FIGURE 5

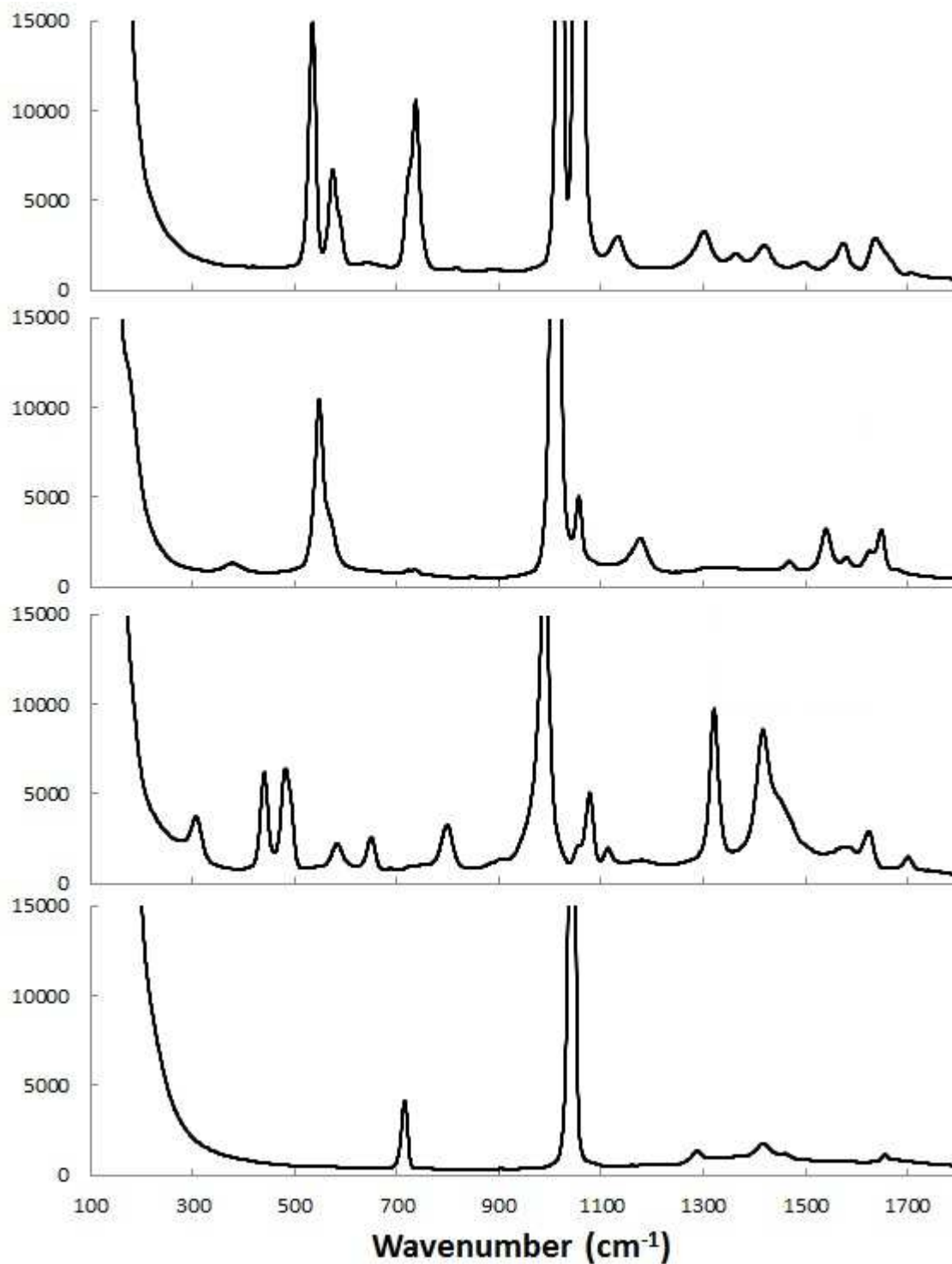


Figure 5. Raman Spectrum, from top, of UN, Urea, NU, Ammonium Nitrate, respectively. Ammonium nitrate exhibited additional small peak at $\sim 2900\text{ cm}^{-1}$.

FIGURE 6

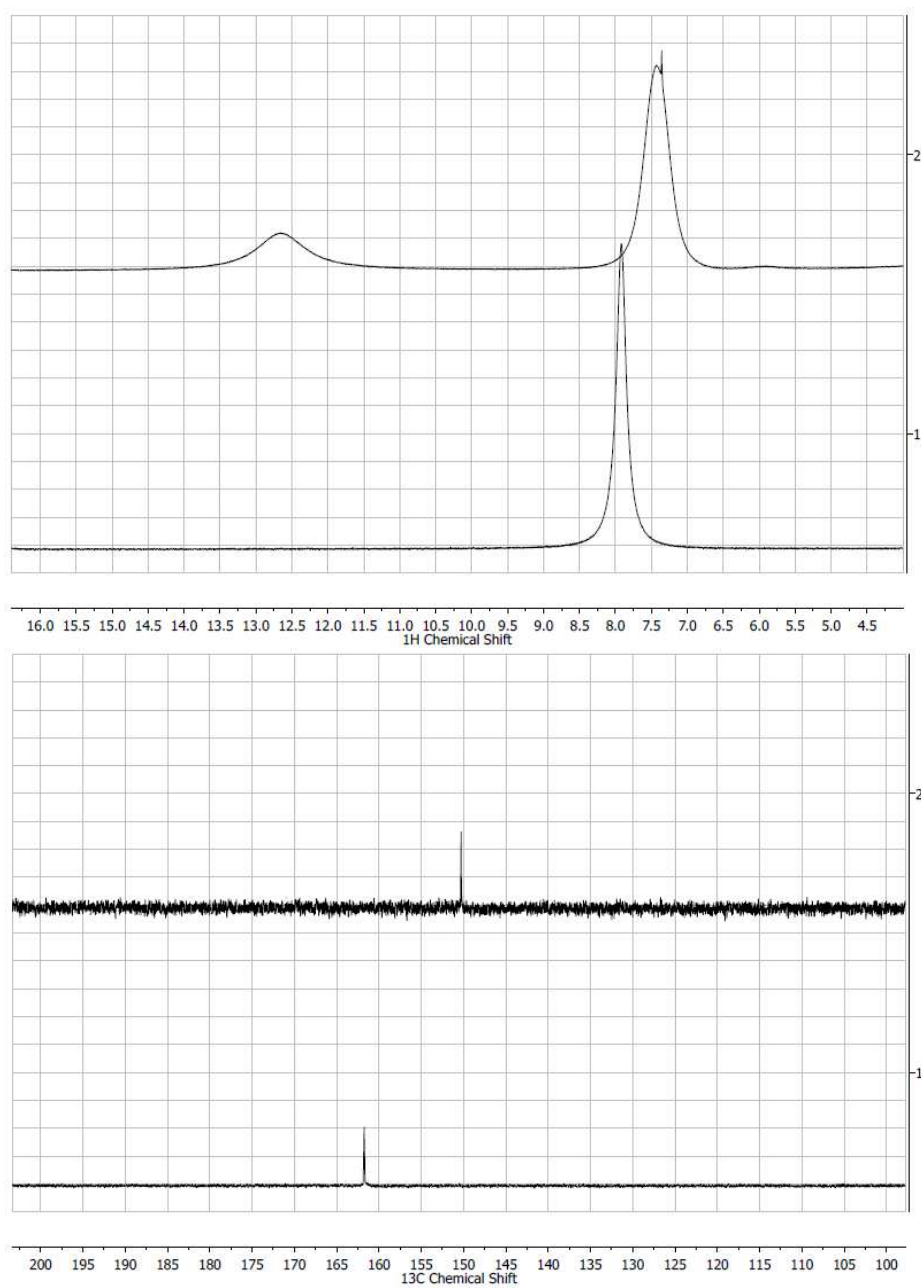
**Figure 6.** ^1H -NMR (top) and ^{13}C -NMR (bottom) of Nitrourea(2) and Urea Nitrate(1)

FIGURE 7

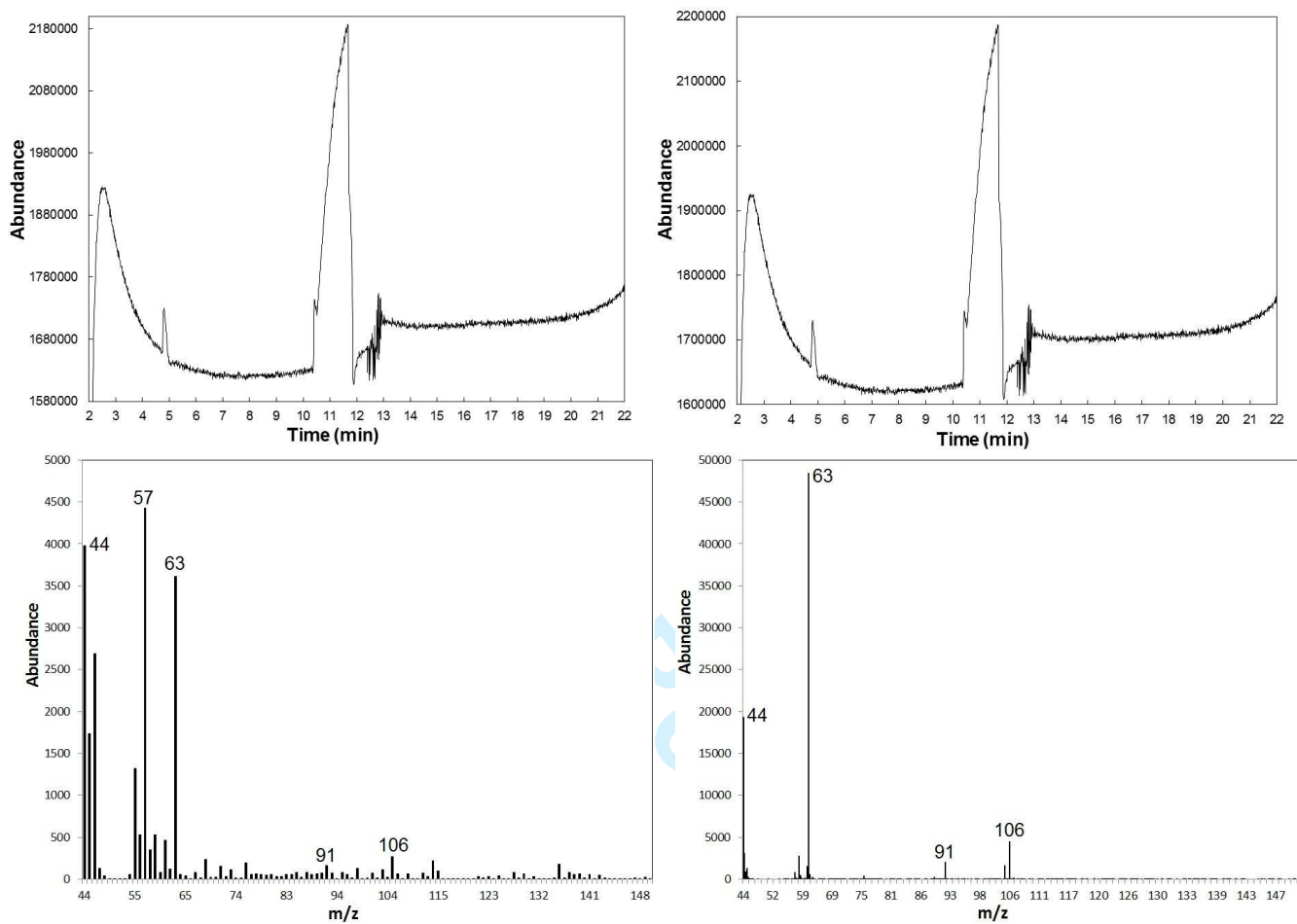


Figure 7. GC/MS chromatograms and spectra with chemical ionization using methane as reagent gas for recrystallized nitrourea synthesized by method 1 (left) and method 2 (right).

FIGURE 8

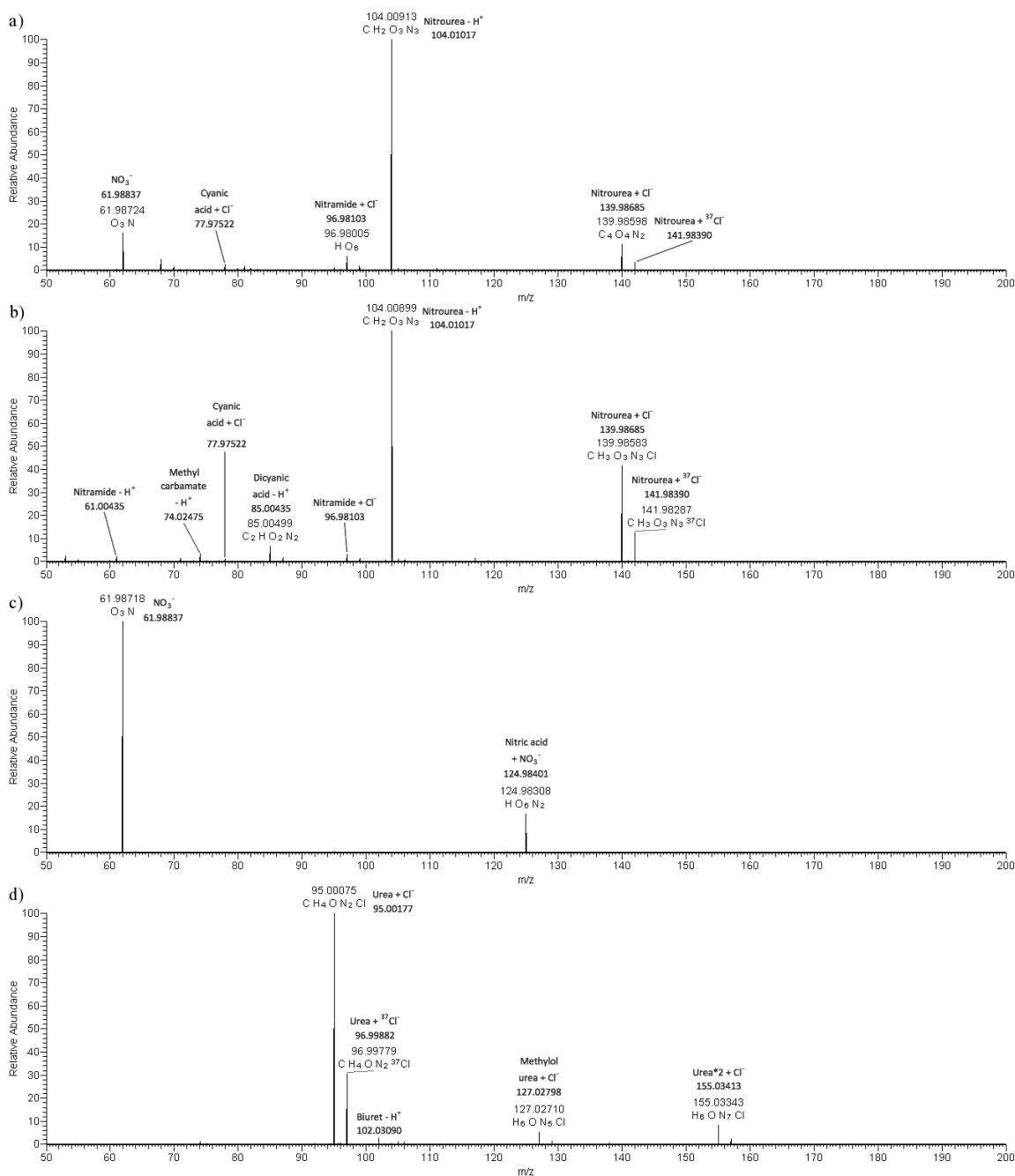


Figure 8. Negative mode mass spectra of NU and UN in 50-50 MeOH-H₂O with CCl₄. a) direct inject NU, b) LC NU, c) direct inject UN, d) LC UN.

FIGURE 9

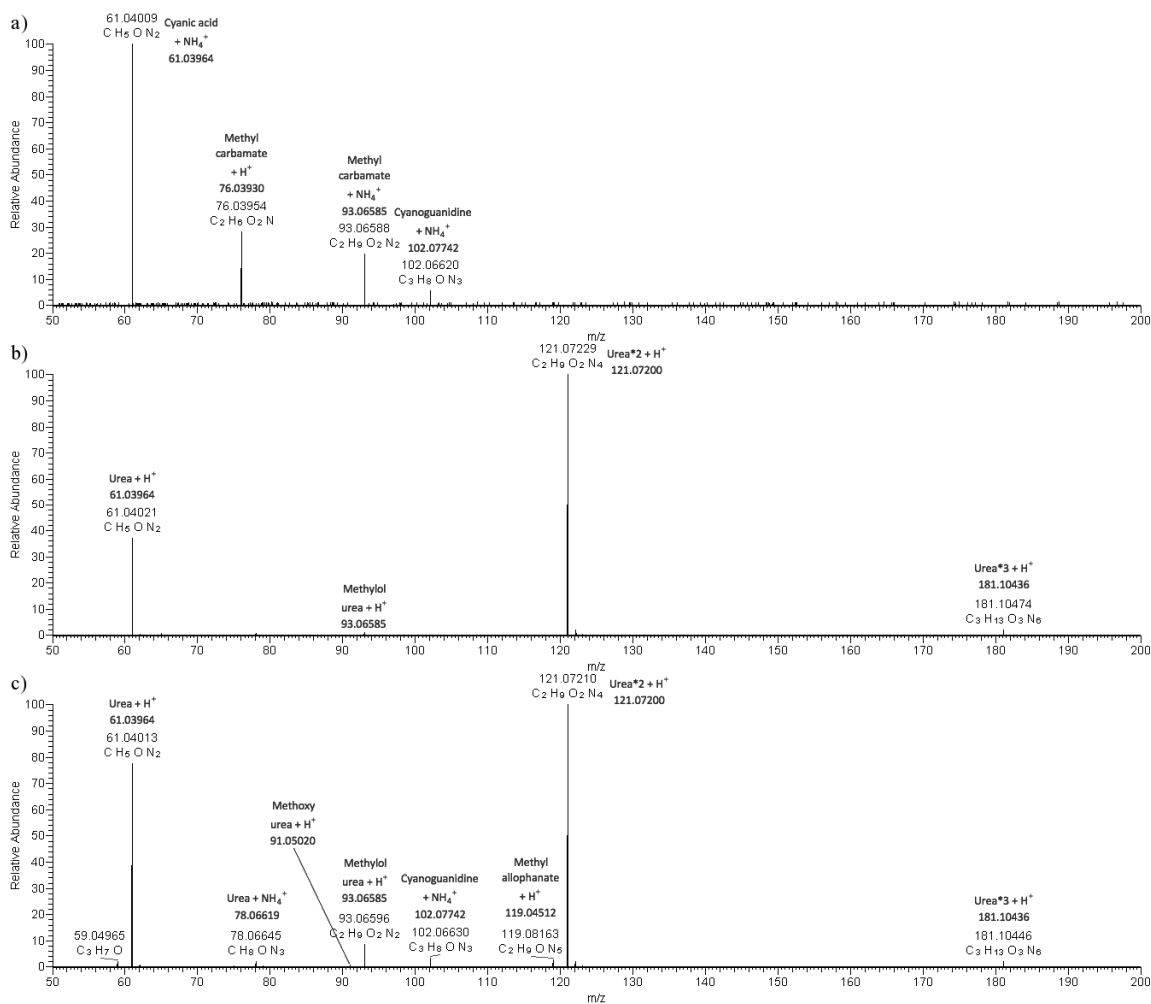


Figure 9. Positive mode mass spectra of NU and UN in 50-50 MeOH-H₂O with CCl₄. a) LC NU, b) direct inject UN, c) LC UN.

FIGURE 10

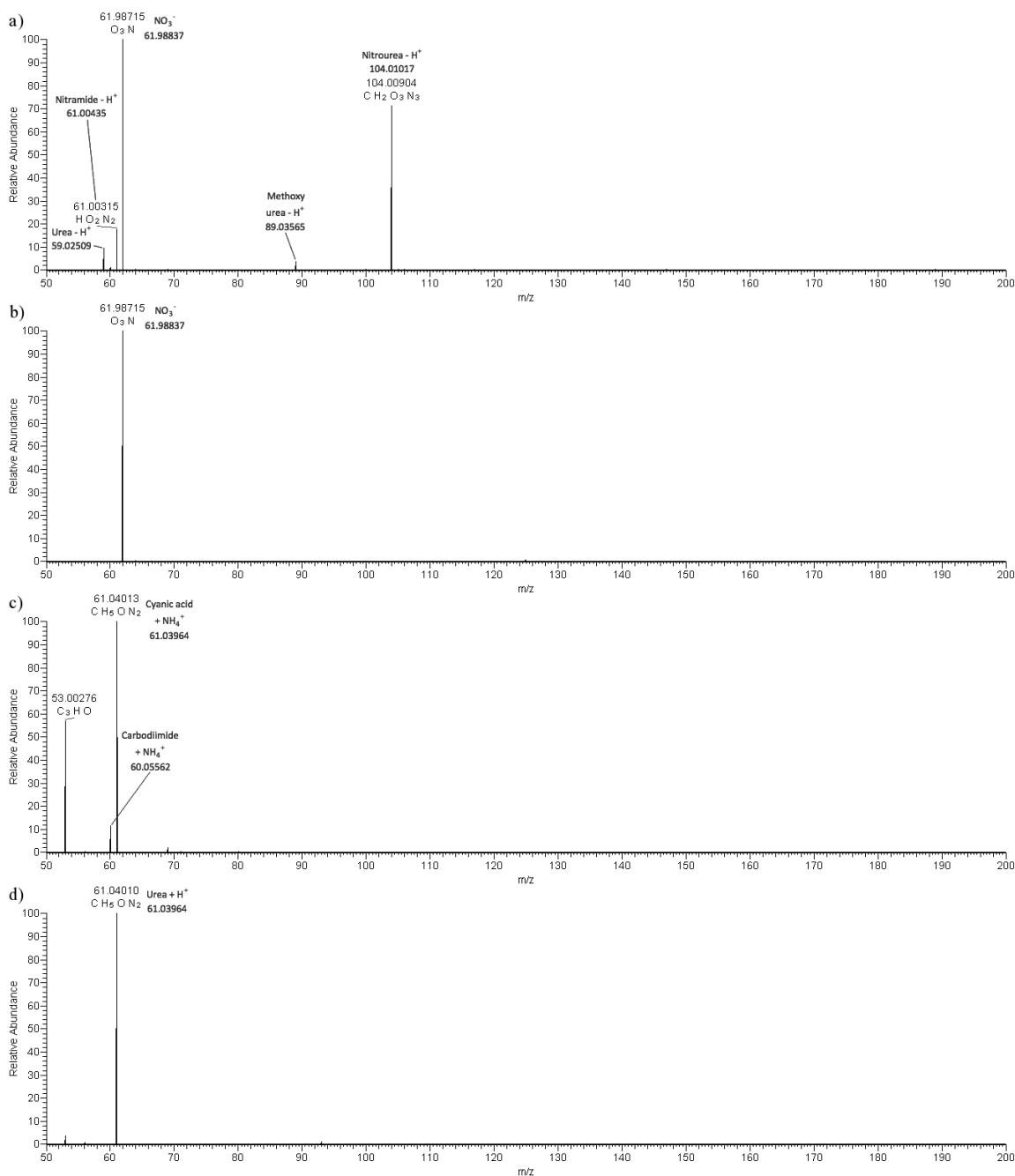


Figure 10. Direct inject mass spectra of NU and UN in 50-50 MeOH-H₂O with ammonium acetate. a) negative mode NU, b) negative mode UN, c) positive mode NU, d) positive mode UN.

FIGURE 11

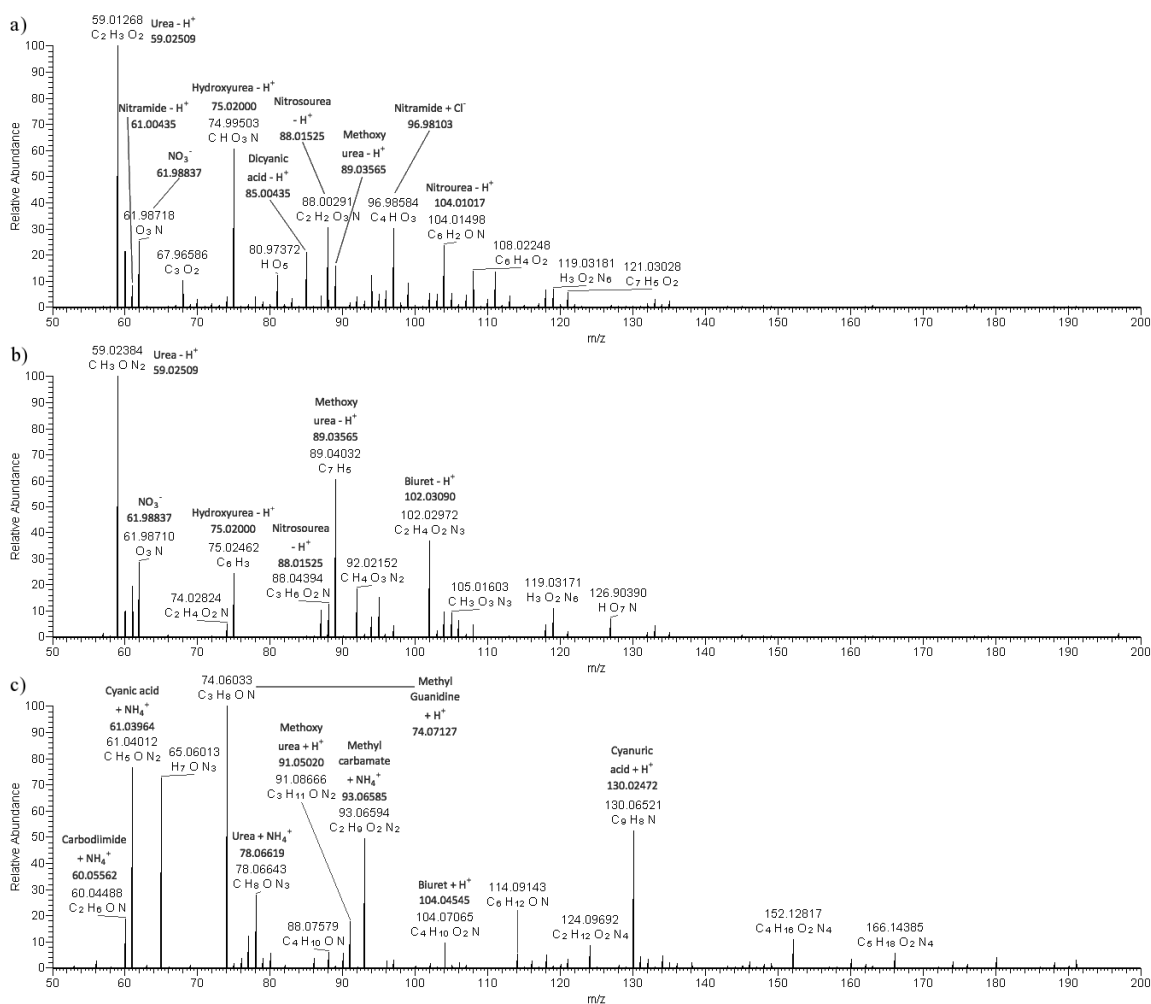


Figure 11. Direct inject mass spectra of NU and UN in 50-50 MeOH-H₂O with no additive. a) negative mode NU, b) negative mode UN, c) positive mode NU.

FIGURE 12

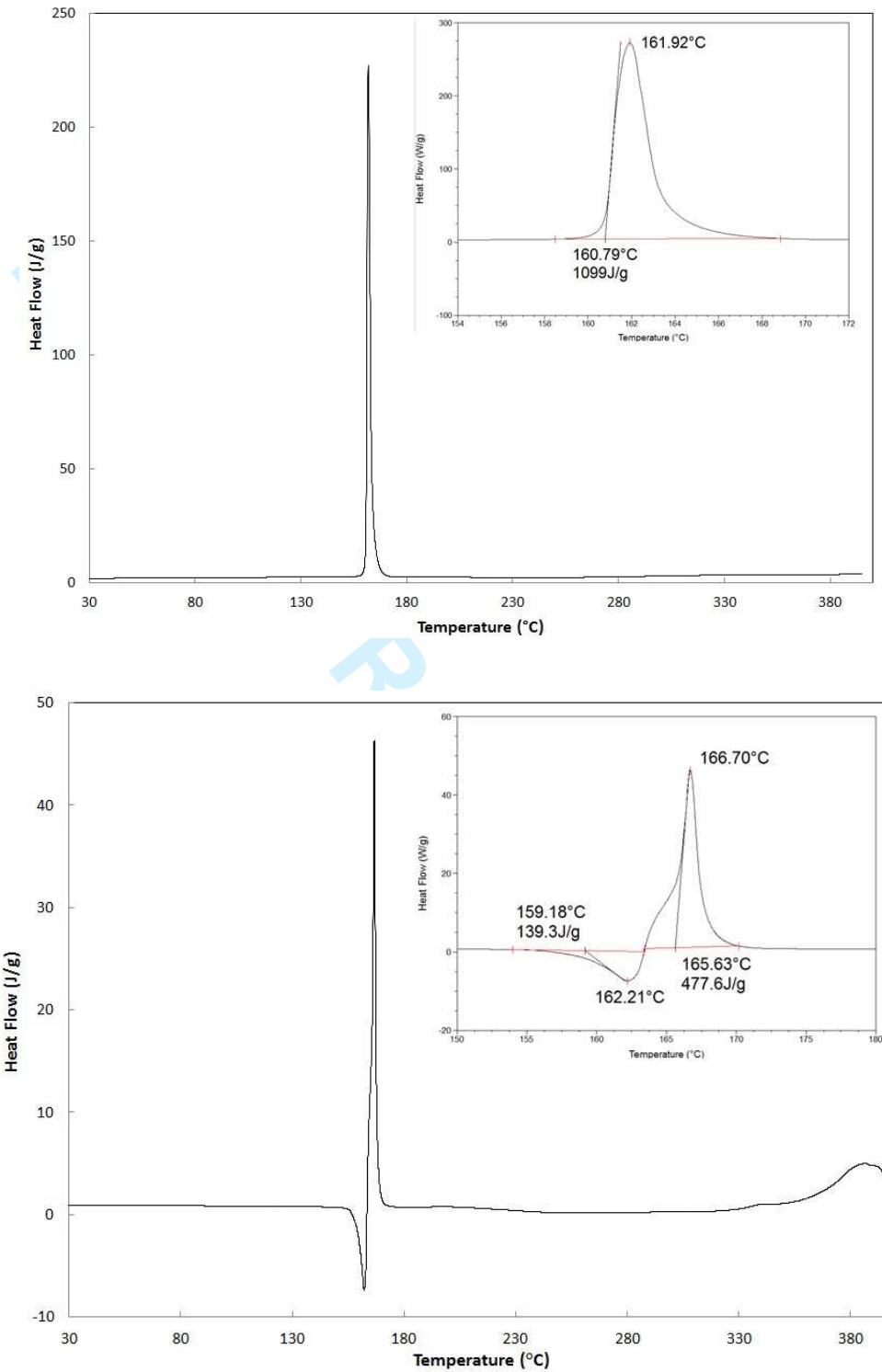


Figure 12. DSC thermograms of nitrourea (top) & urea nitrate (bottom) scanned at 10 °C/minute

FIGURE 13

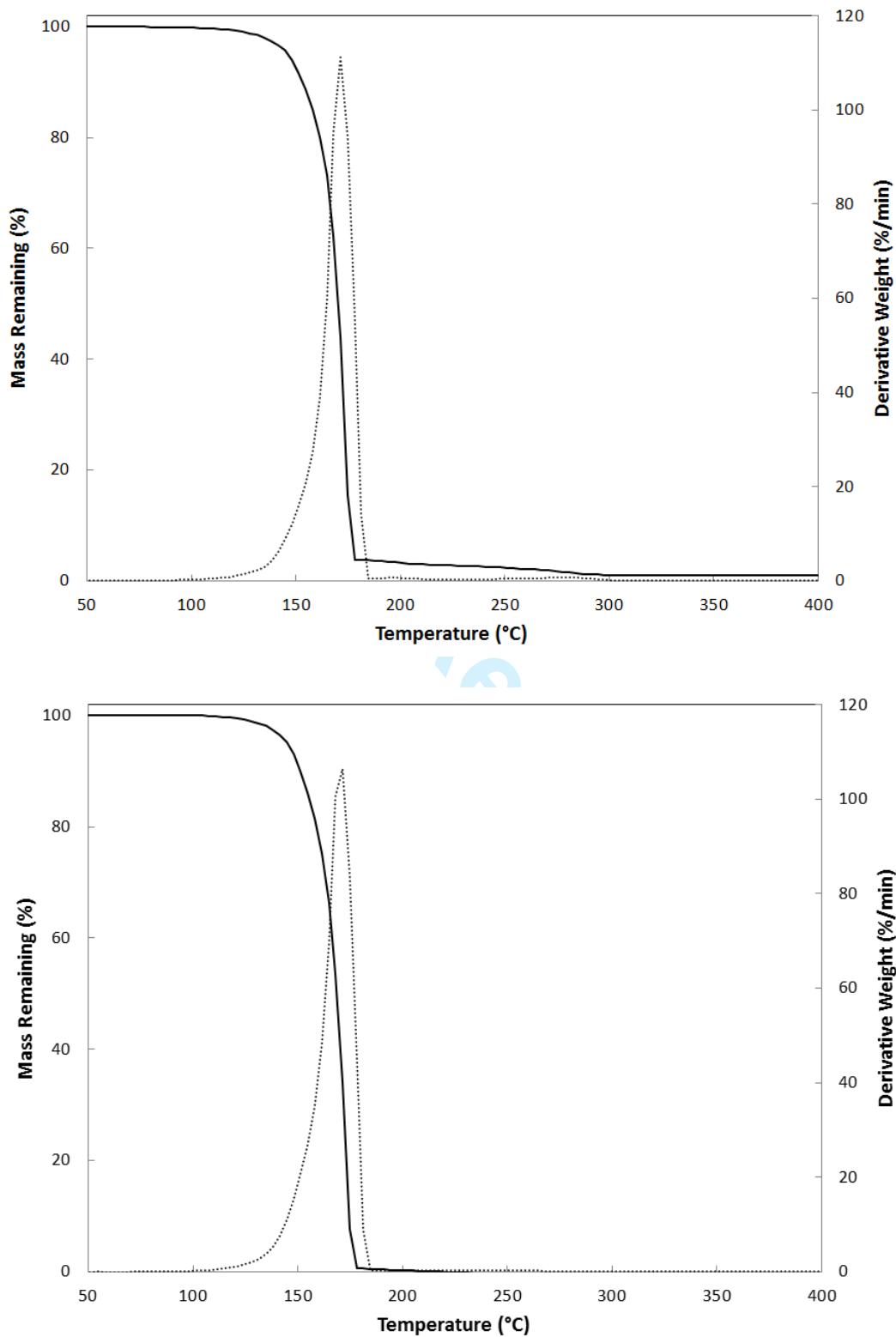
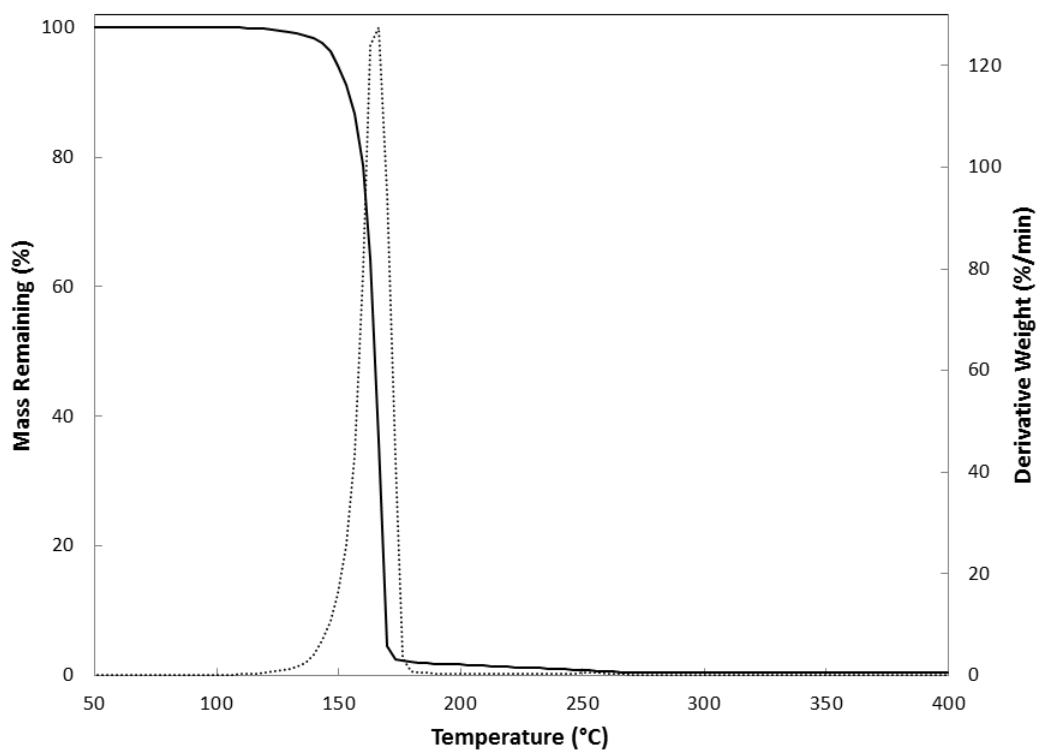
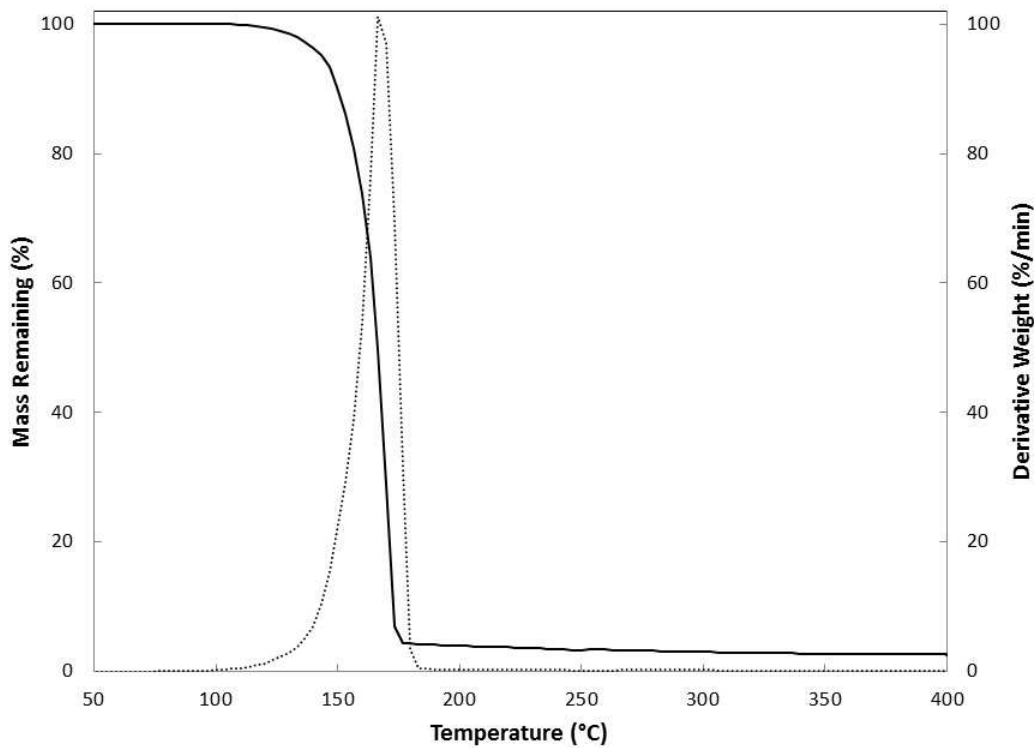


Figure 13. TGA trace crude (top) and re-crystallized (bottom) nitrourea



55
56
57
58
59
60

Figure 14. TGA Trace Recrystallized Nitrourea synthesized using method 1 (top) & method 2 (bottom). Scan rate 20 °C/min.

FIGURE 15

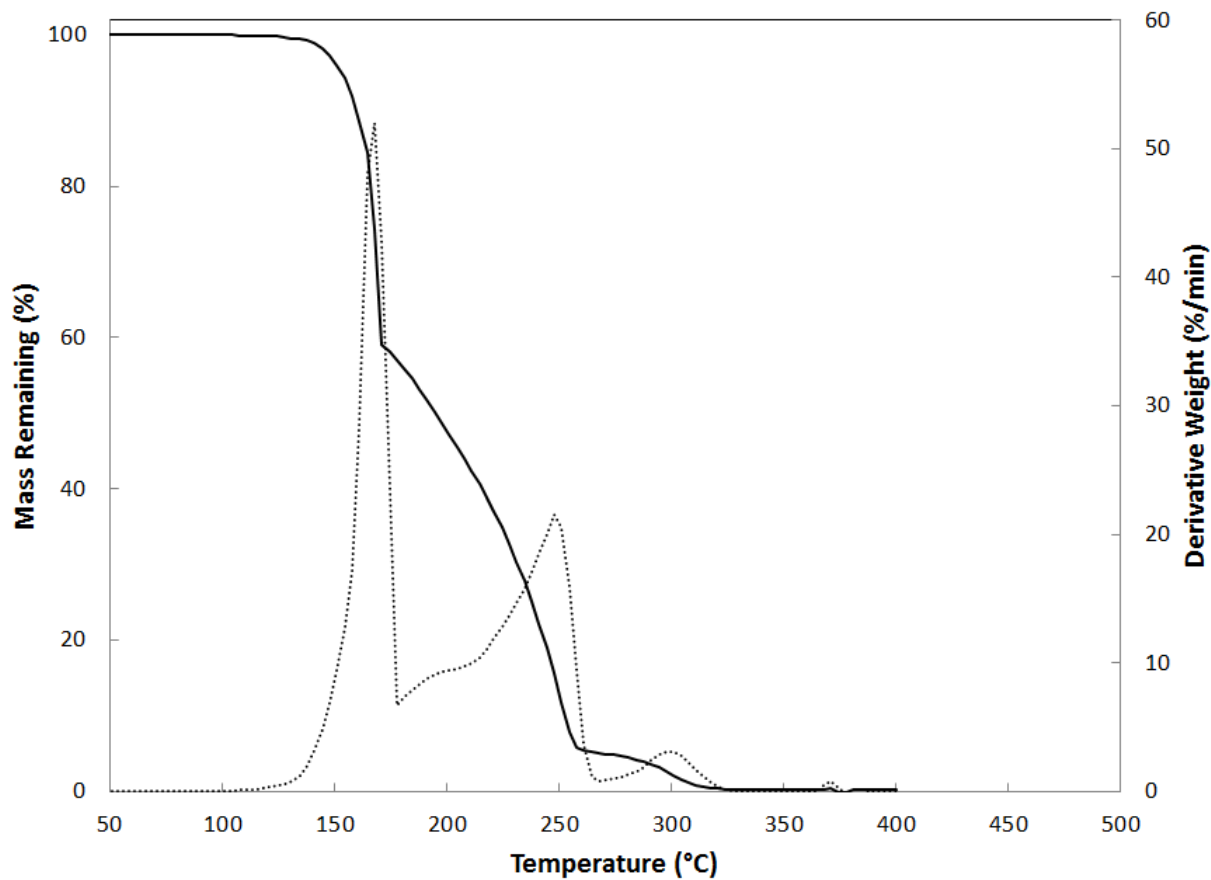


Figure 15. TGA Trace of Recrystallized Urea Nitrate.

FIGURE 16

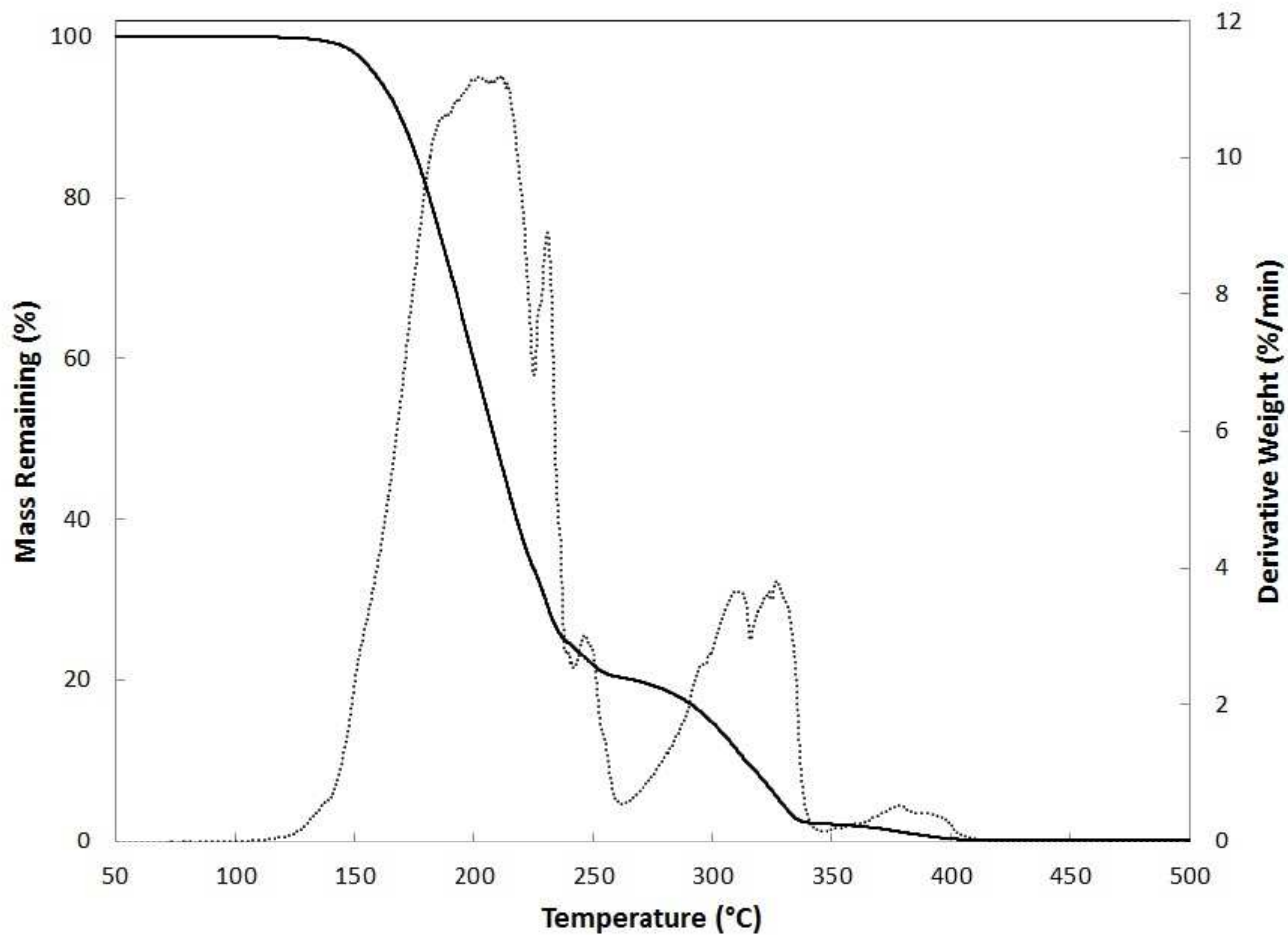


Figure 16. TGA thermogram of urea.

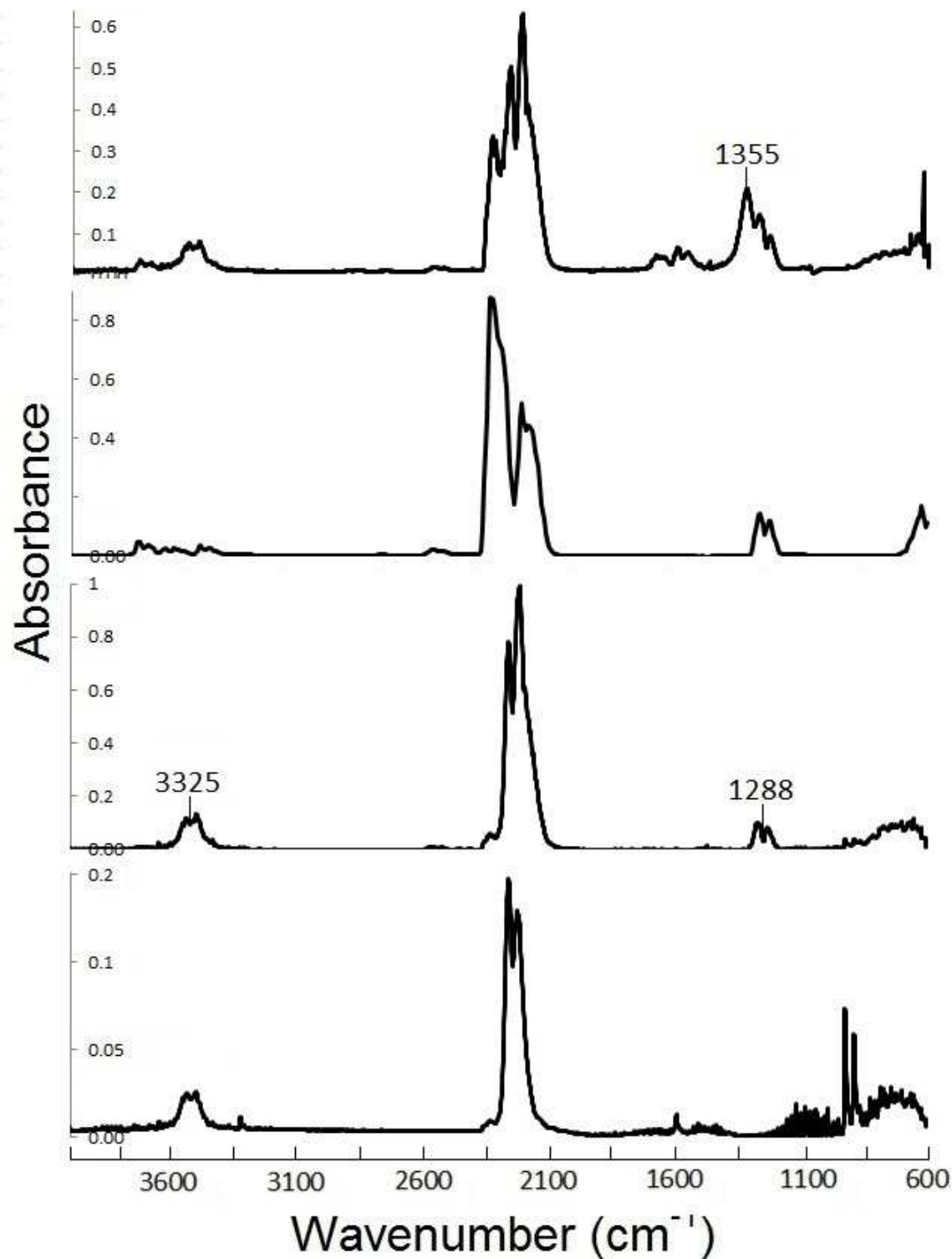


Figure 17. Stacked IR spectra of urea nitrate, CO₂ and N₂O mixture, nitrourea, and urea from top to bottom, respectively. Selected wavenumbers are shown.

FIGURE 18

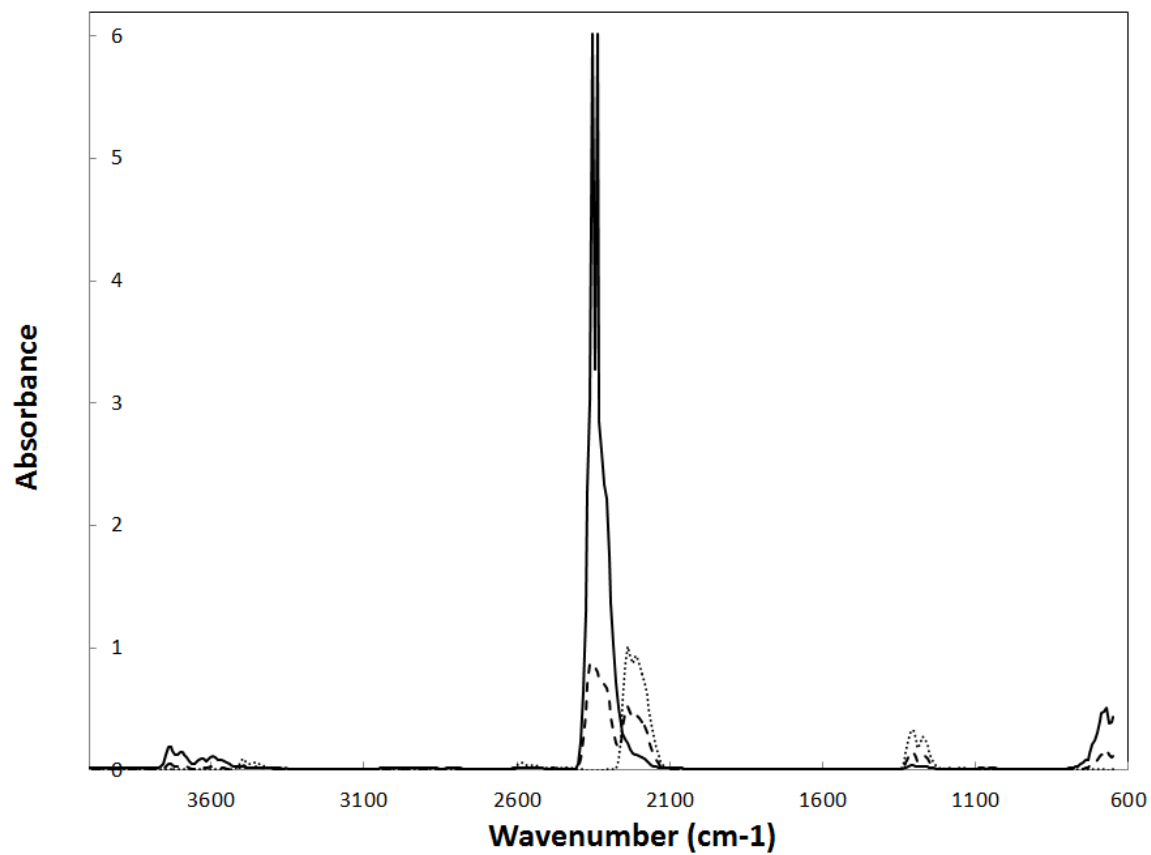


Figure 18. Overlap spectra of CO₂ (—), N₂O (···), and a mixture of both (---).

FIGURE 19

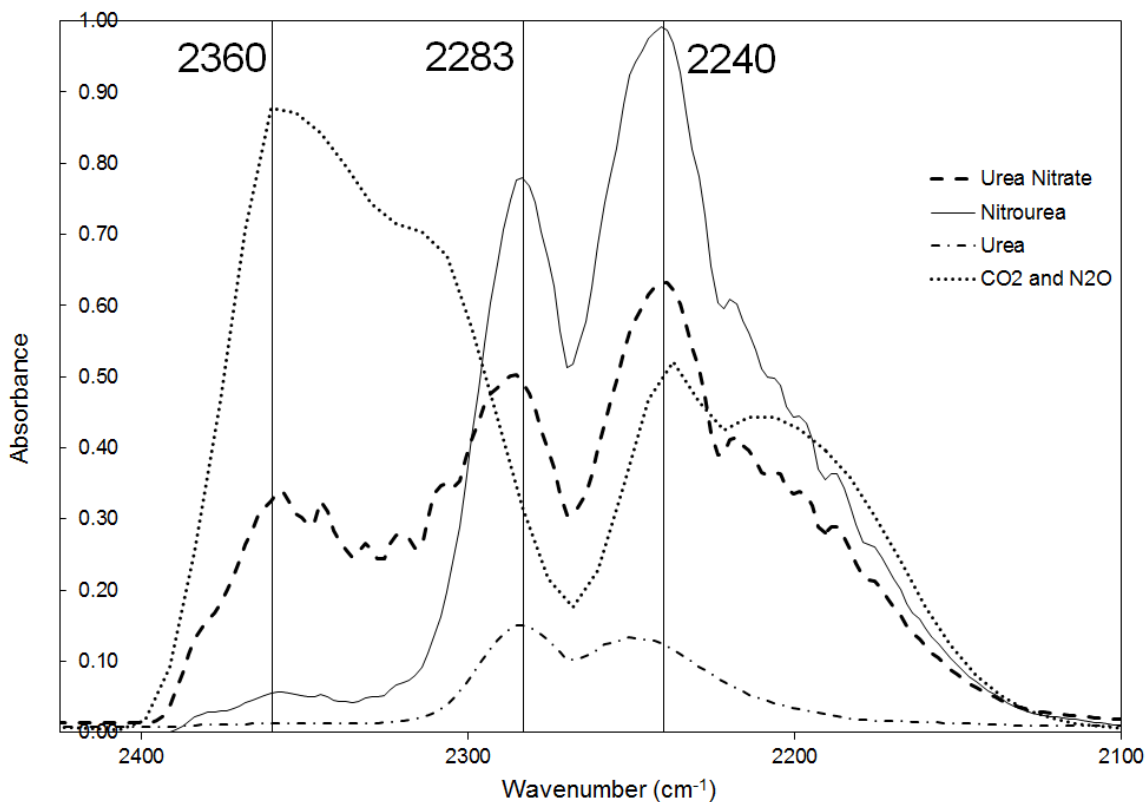


Figure 19. Overlap magnified IR spectra of urea nitrate, nitrourea, urea, and a mixture of CO₂ and N₂O.

Full Paper

Characterization and Analysis of Tetranitrate Esters

Jimmie C. Oxley, James L. Smith,* Joseph E. Brady IV, Austin C. Brown

University of Rhode Island, Chemistry Dept; Kingston, RI 02881, USA
e-mail: jsmith@chm.uri.edu

Received: May 19, 2011

DOI: 10.1002/prop.201100059

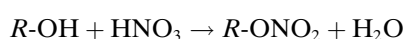
Abstract

Thermal behaviors, vapor pressures, densities, and drop weight impact results, as well as analytical protocols, are reported for three tetranitrate esters: erythritol tetranitrate (ETN), 1,4-dinitrato-2,3-dinitro-2,3bis(nitratomethylene) butane (DNTN), and pentaerythritol tetranitrate (PETN). ETN and DNTN both melt below 100 °C and have ambient vapor pressures comparable to TNT. While LC/MS was shown to be a viable technique for analysis of all three tetranitrate esters, only ETN was successfully analyzed by GC/MS. Performance of these nitrate esters as evaluated in lab using the small-scale explosivity device (SSED) suggested $RDX \gg DNTN > PETN > ETN$. Detonation velocities were calculated using Cheetah 6.0. Since the starting material is now widely available, it is likely that law enforcement will find ETN in future improvised explosive devices. This paper with its analytical schemes should prove useful in identification of this home-made explosive.

Keywords: Erythritol tetranitrate, 1,4-Dinitrato-2,3-dinitro-2,3bis(nitratomethylene) butane, Pentaerythritol tetranitrate, Vapor pressure, Densities, Drop weight impact, Thermal behavior, HPLC-HRMS

1 Introduction

In recent years there has been growth in use of so-called “homemade” explosives (HME). Preparation of HME can require little synthetic expertise. It can be as simple as mixing oxidizers and fuels as opposed to the preparation and isolation of discrete compounds. When specific characteristics are required terrorists do engage in more complex synthetic procedures. Common approaches include preparations of peroxide based explosives or the nitration of alcohols to form nitrate esters:



Formation of the nitrate ester favors use of either sulfuric acid with concentrated nitric acid (68%) or fuming

nitric acid (>86%). Competing with nitration is the oxidation of the alcohol. For example, in the presence of 55% nitric acid diethylene glycol may be oxidized to diglycolic acid or cleaved at the ether and oxidized to oxalic acid [1]; with $\leq 95\%$ nitric acid or a combination of nitric and sulfuric acids, the di-nitrate ester, di-ethylene glycol dinitrate (DEGDN) can be formed [2]. Typically, terrorists and criminals choose to nitrate methanol, ethylene glycol, glycerin, or pentaerythritol. The nitration of erythritol to erythritol tetranitrate (ETN) has been known longer (1849) than that of ethylene glycol (1870) or pentaerythritol (1894) [3]. The nitrate ester ETN had been largely ignored because the erythritol precursor was not readily available. While previously extracted from seaweed [4], algae, and lichen [5], erythritol is now produced on an industrial scale using microbial techniques [6]. With the advent of low-carbohydrate diets, erythritol has become available in bulk to the general public [7].

Recent reports suggest that with availability of erythritol, synthesis of ETN is being targeted by juveniles, criminals and terrorists [8]. The chemical structure of ETN is similar to the military explosive, PETN. The military and law enforcement require physical properties and other characteristics of ETN as they compare to PETN in order to assess the potential risks associated with its availability. We report the properties and analysis characteristics of ETN herein and compare them to PETN and the recently reported dinitro-tetranitrate ester, (DNTN) [9]. Because of DNTN's low melting point and predicted explosive performance, it is an attractive material for use as a military or commercial explosive. Included is an assessment of ETN's sensitivity to initiation and performance as compared to DNTN and PETN, which has been associated with several terrorist plots, e.g. the Shoe Bomber (2001), Christmas Day Bomb Plot (2009), and Cargo Plane Bomb Plot (2010) [10].

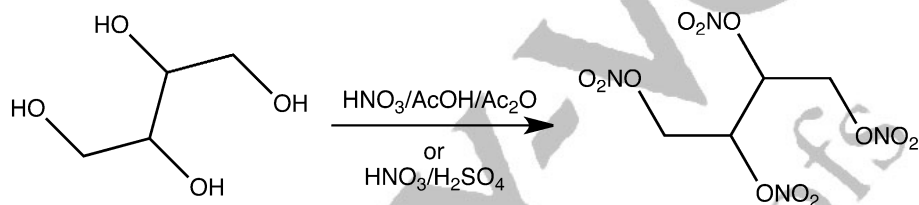
2 Experimental Section

2.1 Preparation of ETN

Erythritol tetranitrate (ETN) was prepared by mixed acid nitration [11] Erythritol (2.0 g, 0.016 mol) was dissolved in concentrated sulfuric acid (96 %, 14.0 g, 0.143 mol) in a 25 mL round bottomed flask at room temperature with stirring. Concentrated sulfuric acid (96 %, 1.4 g, 0.014 mol) was added to the fuming nitric acid (98 %, 14.0 g, 0.222 mol) in a 50 mL round bottomed flask and chilled to 0 °C with stirring. The erythritol/sulfuric acid mixture was added to the nitric/sulfuric acid mixture over 30 minutes while maintaining the temperature below 10 °C. After addition was complete, the mixture was warmed to 35 °C and stirred for 1 hour, initially becoming cloudy and nearly opaque after about 15 minutes. The reaction mixture was poured over shaved ice (400 mL), filtered, rinsed with copious amounts of distilled water and dried for 1 hour over a vacuum aspirator to yield 3.60 g

(0.012 mol, 75 %) of ETN, m.p. 58–59 °C. The product was dissolved in hot methanol. Afterwards, ammonium carbonate was added to neutralize any remaining acid and hot filtered. The recrystallized product had a melting point of 60–61 °C.

Alternatively, ETN may be prepared by nitration with acetyl nitrate. Glacial acetic acid (25 mL) and acetic anhydride (25 mL) were added to a 250 mL round-bottomed flask. The flask was placed in an ice/water bath and cooled to 0 °C. Fuming nitric acid (19 g, 98 %) was added drop wise, maintaining the temperature below 10 °C. The reaction mixture was allowed to stir for 1 hour and erythritol (3.02 g, 0.0247 mol) was added in small portions. The mixture was stirred for 2 hours at 0 °C, the flask was removed from the ice water bath and stirred for an additional 2 hours. The reaction mixture poured over ice (200 mL), the product was filtered, rinsed with copious amounts of water, and allowed to air dry. The resulting crude product (7.25 g, m.p. 59.6–61.0) was recrystallized from 2-propanol (6.34 g, 85 % yield, m.p. 60.5–



Raman Spectrum of ETN

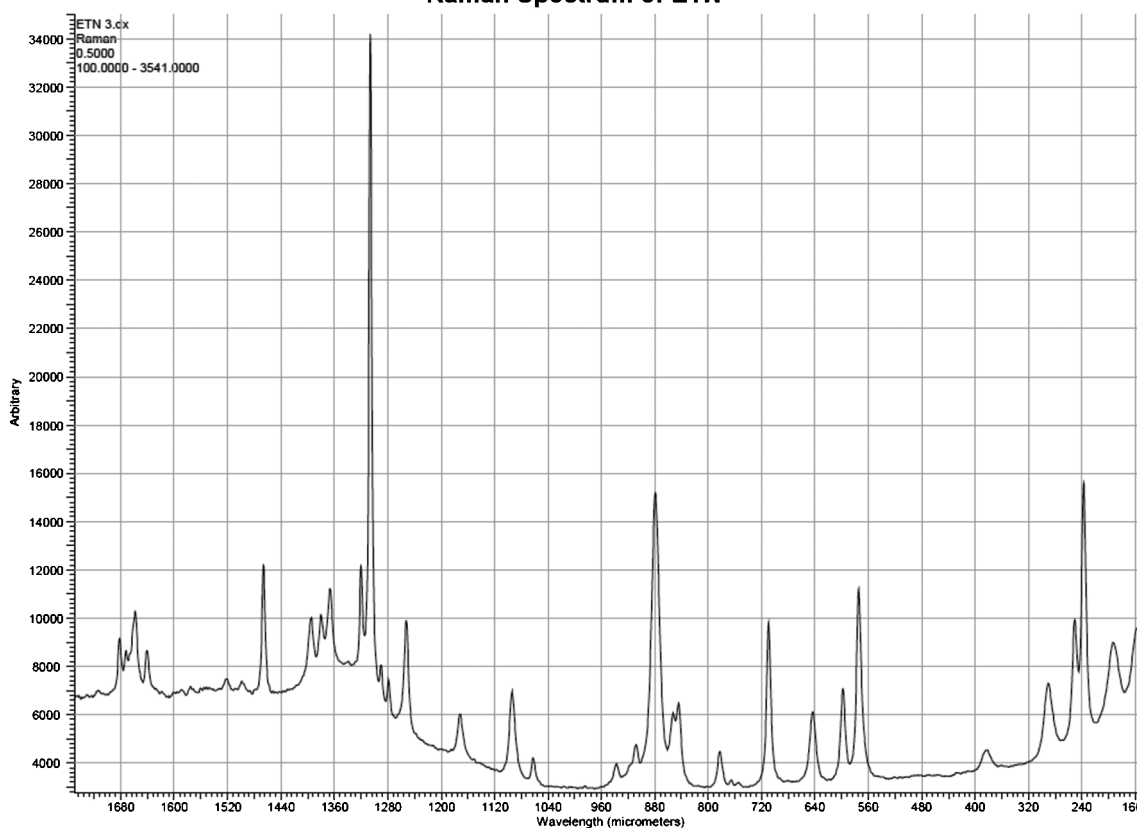


Figure 1. Raman Spectrum of (ETN).

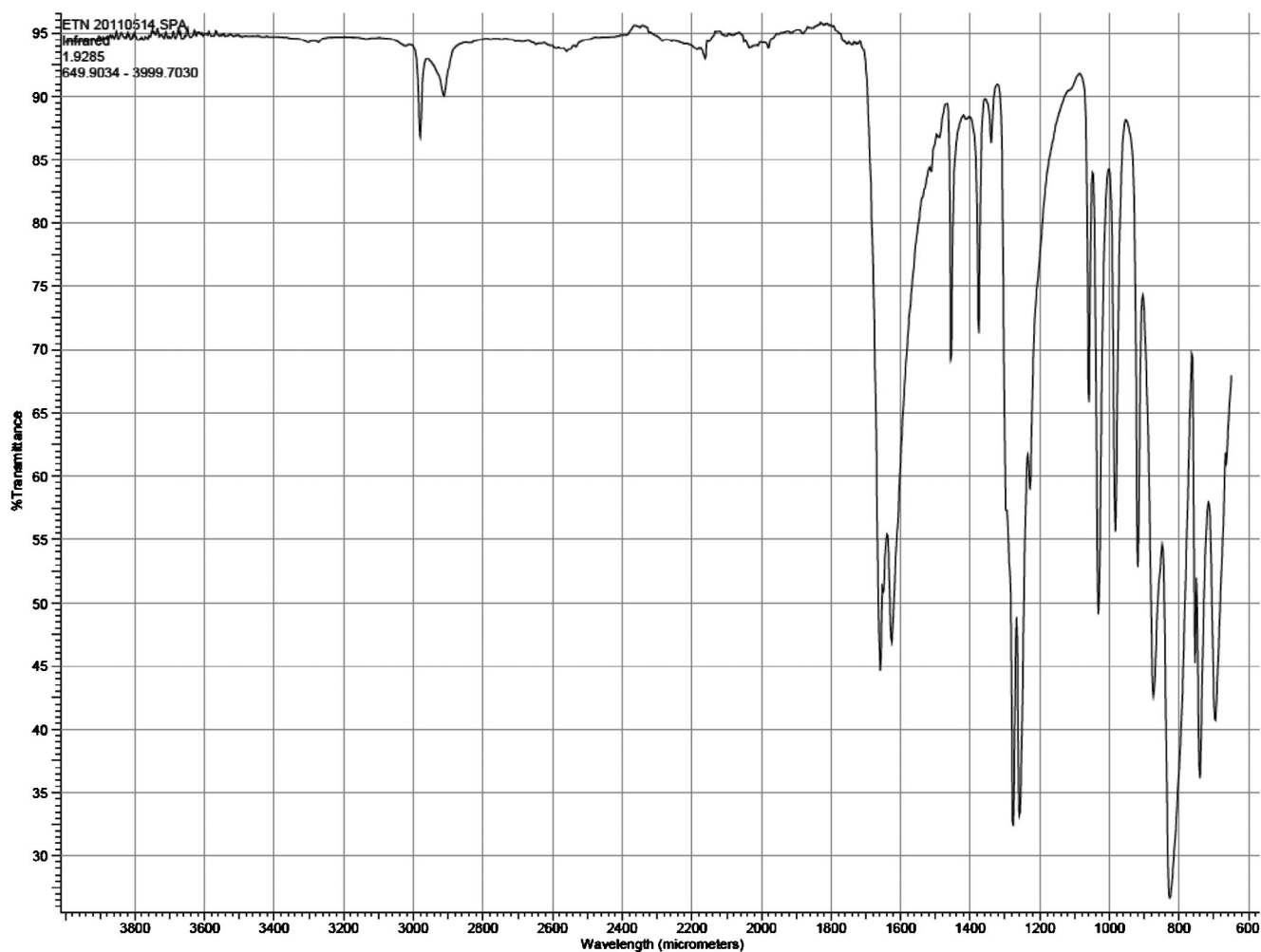
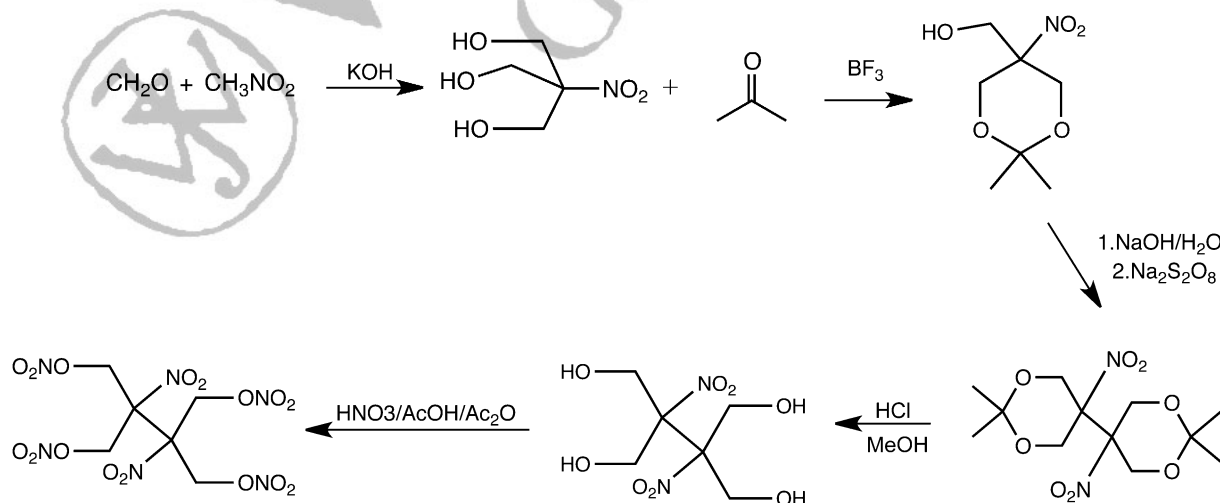


Figure 2. Infrared spectrum of ETN.

61.5°C). ETN is soluble in methanol, ethanol, 2-propanol, acetone and acetonitrile. Infrared and Raman spectra are shown in Figure 1 and Figure 2.

2.2 Preparation of DNTN (1,4-Dinitrato-2,3-dinitro-2,3bis(nitratomethylene) Butane)

Trismethoxy nitromethane (TMNM) was prepared by combining nitromethane (17.9 g, 0.293 mol) and potassi-



Raman Spectrum of DNTN

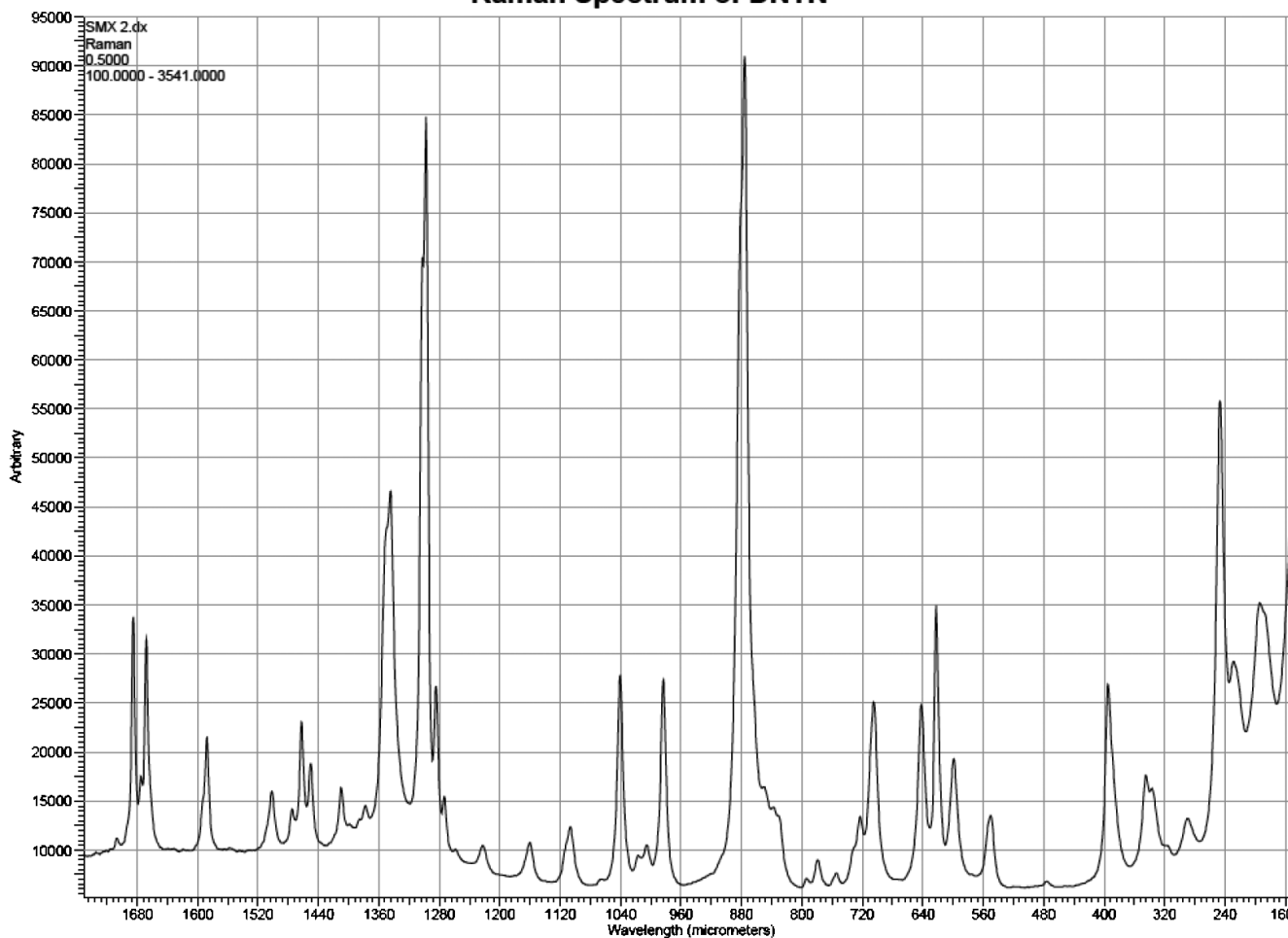


Figure 3. Raman Spectrum of DNTN.

um hydroxide (0.49 g, 8.7 mmol) in methanol (45 mL) and dichloromethane (2 mL) with stirring in a 200 mL round bottomed flask [12]. The flask was cooled in a water bath to 5 °C and the paraformaldehyde (28 g, 0.933 mol) was added gradually over the course of thirty minutes. A condenser was attached to the flask and the mixture was heated to 40 °C and allowed to react for 2 hours. The mixture was cooled to room temperature and placed in a –10 °C freezer for three hours. The precipitate was collected by vacuum filtration and dried overnight in a 50 °C oven to yield a white solid, 21.45 g, 48%, m.p. 150–154 °C. The TMNM was used without further purification.

The ketal was prepared by the acid catalyzed condensation of TMNM with acetone. [13]. The TMNM (30.21 g, 0.2 mol) and acetone (36.31 g, 0.620 mol) were combined and gently heated until the TMNM dissolved. The mixture was cooled to 20 °C and the BF₃ (48% in ether, 34.38 g, 0.243 mol) was added to the mixture in one dose. A condenser was attached and the temperature of the mixture quickly rose to 58 °C. The mixture was stirred for six minutes and poured into a saturated NaHCO₃ (500 mL) solution with shaved ice (100 mL). The cream

colored precipitate (27.49 g, 72%) was collected by vacuum filtration, rinsed with copious amounts of water, and had a melting point of 130–132 °C. Recrystallization from ethyl acetate or methanol yields a lighter colored product, m.p. 133–134 °C.

The dimerized ketal was prepared by combining water (740 g), sodium hydroxide solution (50%, 49.12 g, 0.614 mol) and the ketal (57.08 g, 0.299 mol) in a 2 L round bottomed flask. The mixture was heated to 50 °C and maintained between 50 and 60 °C for 2.5 hours before cooling to 20 °C. The sodium persulfate (146.30 g, 0.615 mol) was added and the mixture was stirred at room temperature for 24 hours. Sodium hydroxide solution was used to raise the pH 11–12 and the precipitate was filtered and washed with cold water. The product (28.09 g, 58%), was a light tan solid, m.p. 129–130 °C.

The dinitro-tetra-ol was prepared by dissolving the coupled ketal (17.45 g, 0.054 mol) in methanol (175 mL) and gently bubbling HCl gas into the solution at room temperature with stirring until the mixture dissolved, approximately 2 minutes. Within five minutes of the addition of the HCl, the mixture became a very dark brown but was still translucent. The reaction vessel was sealed and al-

lowed to react at room temperature for 45 hours. The methanol was removed by rotary evaporation, the mixture was triturated with n-pentane and the solid was filtered to yield 8.27 g (64%) of solid cream-colored material, m.p. 100–101 °C.

In a 250 mL round-bottomed flask, glacial acetic acid (25 mL) and acetic anhydride (25 mL) were combined. This mixture was cooled to 0 °C with stirring and fuming nitric acid (98%, 19 g, 0.299 mol) was added while maintaining the temperature between 0–10 °C. After addition of the nitric acid was complete, the mixture was allowed to react with stirring while maintaining the temperature at approximately 0 °C. The tetra-ol was (5.98 g, 0.025 mol) added to the mixture over the course of 30 minutes and the mixture was stirred for an additional 2.5 hours at 0 °C. The mixture was poured over a mixture of ice/water (200 mL), the solid was filtered, and washed with a 1% Na₂CO₃ solution (200 mL), followed by cold water. After air-drying overnight, the crude material, 7.86 g (75% yield), m.p. 81–84 °C, was recrystallized from reagent alcohol to yield a white solid, m.p. 84–85 °C. DNTN was found to be soluble in methanol, ethanol, 2-propanol,

acetone and acetonitrile. Infrared and Raman spectra are shown in Figure 3 and Figure 4.

The PETN used in this study was obtained from obtained from commercial sources.

3 Analyses

3.1 HPLC/HRMS

Both the crude (mixed acid preparation) and recrystallized ETN were analyzed using high performance liquid chromatography (HPLC) with atmospheric pressure ionization and high-resolution mass spectrometry (HRMS). The strongly electron-withdrawing nature of the nitro and nitrate ester moieties makes these molecules vulnerable to adduct formation with the mobile phase and/or impurities in the mobile phase or elsewhere in the system, further complicating analysis. However, this feature may be exploited by introducing an additive into the system that generates nucleophilic ions [14]. The introduction of chlorinated compounds (CH₂Cl₂, CHCl₃, CCl₄, NH₄Cl) into the mobile phase is known to cause the preferential formation of chlorinated adducts with nitrate esters [R-O-

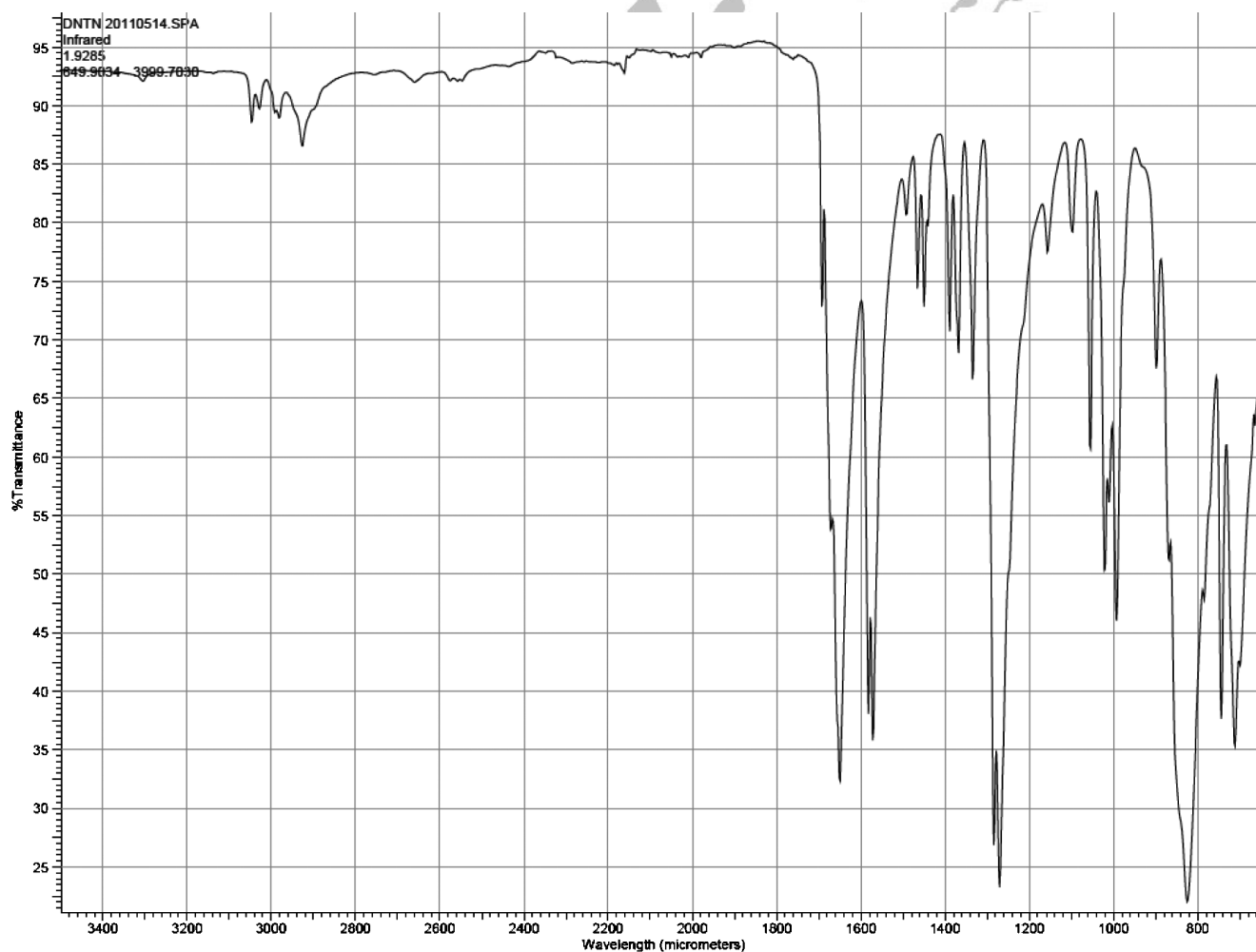


Figure 4. Infrared Spectrum of DNTN.

Table 1. Relative MS abundances of adducts formed during the direct injection of ETN (based on the average of at least three runs).

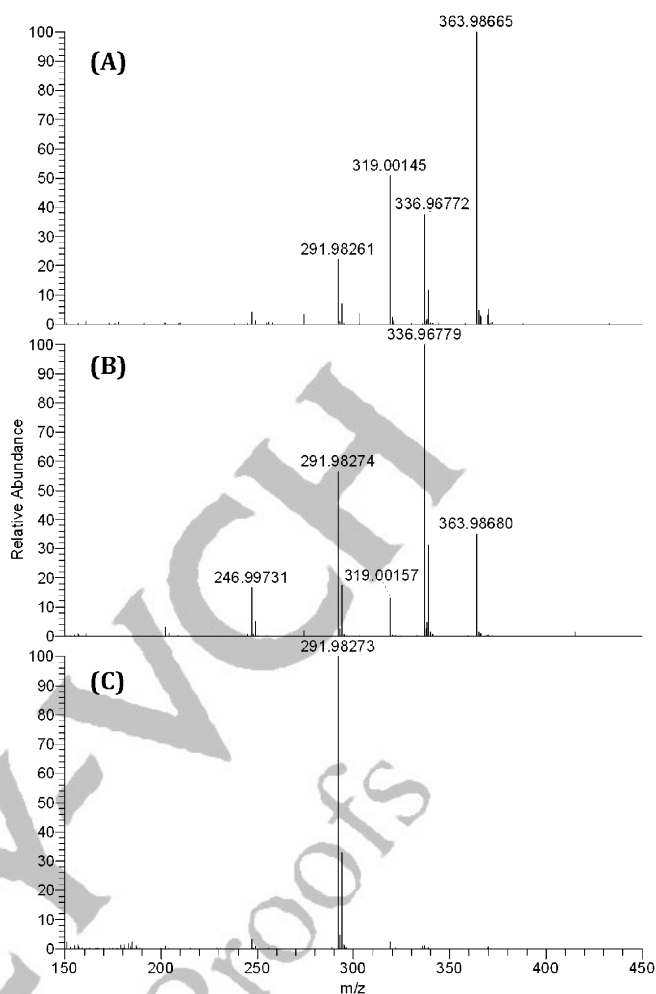
Mass (<i>m/z</i>)	relative abundance/%	Ion	Formula
363.98665	100	[ETN+NO ₃] ⁻	C ₄ H ₆ O ₁₅ N ₅
319.00145	50.9	[ETN-NO ₂ +HNO ₃] ⁻	C ₄ H ₇ O ₁₃ N ₄
336.96772	37.9	[ETN+ ³⁵ Cl] ⁻	C ₄ H ₆ O ₁₂ N ₄ Cl
291.98261	22.4	[EtriN+ ³⁵ Cl] ⁻	C ₄ H ₇ O ₁₀ N ₃ Cl
246.99722	4.2	[EdiN+ ³⁵ Cl] ⁻	C ₄ H ₈ O ₈ N ₂ Cl

NO₂+Cl]⁻, nitramines [R-N-NO₂+Cl]⁻, and to de-protonate nitro-aromatics [Ar-NO₂-H]⁻ [15]. Carbon tetrachloride was added to the mobile phase in this study to generate chloride adducts.

The mass spectrometer was a Thermo Scientific Exactive operated in the negative ion mode using APCI. To minimize decomposition during analysis, the vaporizer was set at 200 °C and capillary was set to 125 °C. The discharge current was 80 μA, and the sheath gas and auxiliary gas were operated at 35 and 10 arbitrary units, respectively. When directly injected into the ionization source via syringe pump, the flow rate was 15 μL min⁻¹, and the material was dissolved in a 50:50 methanol-water solution with 0.25% carbon tetrachloride. The resolution was set to high (50,000 at 2 Hz), and the maximum injection time was 250 ms. Separation by HPLC was performed by gradient elution. The solvents were water (A) and methanol w/ 0.25% CCl₄, v/v, (B). The flow rate was held constant at 300 μL min⁻¹. The mobile phase was changed from 90% A, 10% B to 10% A, 90% B over 7.5 minutes, followed by 90% A, 10% B for 2.5 minutes. Samples (10 μL) of the crude and recrystallized product were analyzed at the 1 mg mL⁻¹ level using a Hypersil GOLD Phenyl column from Thermo Scientific (dimensions 50 mm × 2.1 mm with particle size of 3 μm).

A portion of twice recrystallized ETN was dissolved in 50/50 methanol/water to prepare a 1 mg mL⁻¹ solution. When this solution was directly infused into the source for one minute, there were five prominent signals (Table 1, Figure 5A). While the expected [ETN+³⁵Cl]⁻ was found, signals corresponding to erythritol dinitrate (EdiN) and erythritol trinitrate (EtriN), each with one ³⁵Cl⁻, were also observed. In addition, a nitrate adduct [ETN+NO₃]⁻ and an adduct with a mass corresponding to [ETN+OH]⁻ were detected. More likely than the formation of an [ETN+OH]⁻ adduct is the loss of one NO₂ followed by the addition of HNO₃, [ETN-NO₂+HNO₃]⁻. The formation of nitric acid adducts during negative mode LC/MS-APCI has been reported elsewhere [16].

After finding what appeared to be the di- and tri-nitrat-ed products during direct infusion experiments, the twice-recrystallized ETN sample and a crude sample, both at a concentration of 1 mg mL⁻¹, were separated using HPLC and analyzed by HRMS. The twice-recrystallized sample

**Figure 5.** Mass spectra of ETN by direct injection (A), separated by HPLC (B) and EtriN (C).

was run in triplicate and showed only one chromatographic peak, eluting at 6.74 minutes (Figure 6, Figure 5B). While the ions found in the mass spectrum for this peak were identical to those found during direct infusion, the relative abundance of each mass was significantly different (Table 1, Table 2). The concentration of the sample also affected the distribution of adducts. When the concentration of ETN was reduced from 1 to 0.01 mg mL⁻¹, the [ETN+NO₃]⁻ signal was greatly reduced and the [ETN-NO₂+HNO₃]⁻ was not found. When the concentration of ETN was reduced to 0.001 mg mL⁻¹, [ETN+NO₃]⁻ was not found (Table 3). Since the decomposition of ETN is the most likely source of the nitrate ion, as the concentration of ETN decreased, the amount of nitrate also decreased as did the amount of [ETN+NO₃]⁻ formed.

When the crude ETN (m.p. 58–59 °C), was separated by HPLC, two chromatographic peaks were observed. Examination of the first peak (5.37 min, Figure 6) revealed only two signals of interest. The most prominent signal in the mass spectrum was found to have a mass corresponding to [EtriN+³⁵Cl]⁻ (*m/z* approx. 292, Fig-

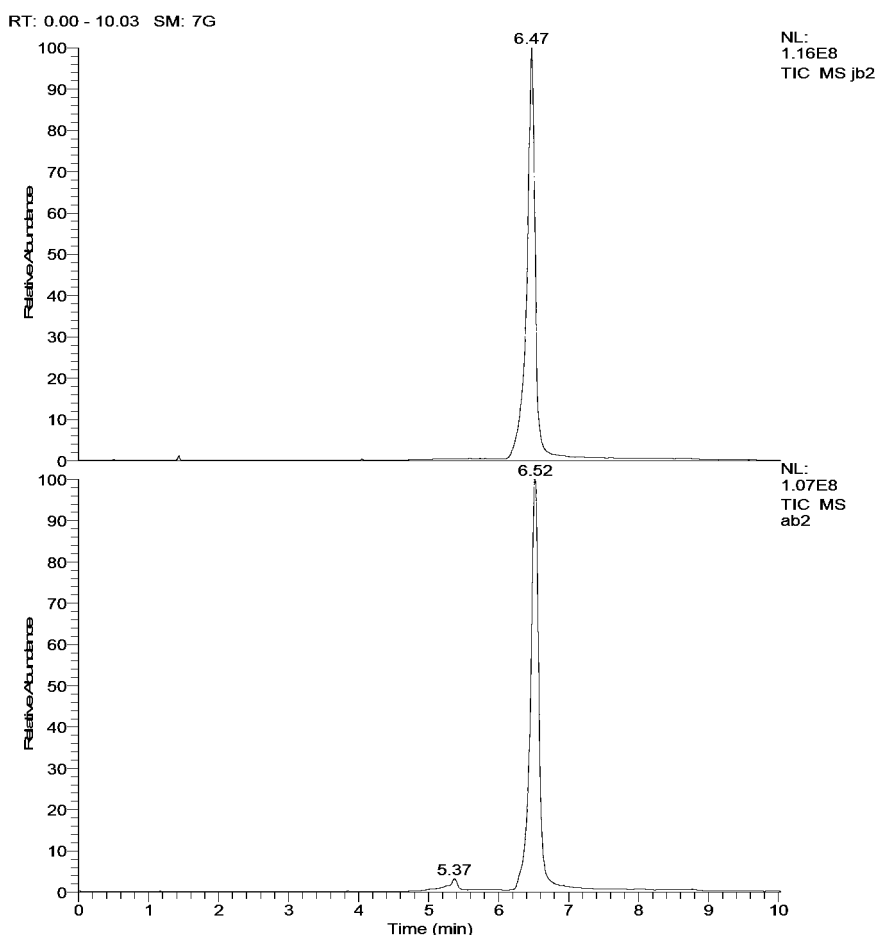


Figure 6. Chromatograms of recrystallized ETN (top) and crude ETN (bottom).

Table 2. Relative MS Abundance of adducts observed by HPLC-HRMS.

Mass (m/z)	relative abundance/%	Ion	Formula
336.96779	100	$[\text{ETN} + ^{35}\text{Cl}]^-$	$\text{C}_4\text{H}_6\text{O}_{12}\text{N}_4\text{Cl}$
291.98274	56	$[\text{ETriN} + ^{35}\text{Cl}]^-$	$\text{C}_4\text{H}_7\text{O}_{10}\text{N}_3\text{Cl}$
363.98680	35	$[\text{ETN} + \text{NO}_3]^-$	$\text{C}_4\text{H}_6\text{O}_{15}\text{N}_5$
246.99731	16	$[\text{EdiN} + ^{35}\text{Cl}]^-$	$\text{C}_4\text{H}_8\text{O}_8\text{N}_2\text{Cl}$
319.00157	13	$[\text{ETN} - \text{NO}_2 + \text{HNO}_3]^-$	$\text{C}_4\text{H}_7\text{O}_{13}\text{N}_4$

ure 5C), while the much smaller signal corresponded to $[\text{EdiN} + ^{35}\text{Cl}]^-$. The second chromatographic peak (approx. 6.5 min, Figure 6) had the same retention time and fragmentation pattern as the twice-recrystallized ETN. The integrated signal of first peak, tentatively assigned as the trinitrated product, was about 3% of the total area of that of ETN.

When PETN was subject to mass spectrometry under the same conditions used for ETN, four major signals corresponding to $[\text{PETN} + \text{NO}_3]^-$, $[\text{PETN} + \text{Cl}]^-$, $[\text{PETriN} + \text{Cl}]^-$, and $[\text{PEDiN} + \text{Cl}]^-$ were observed. Like ETN, the relative abundance of these ions was shown to be concen-

Table 3. Relative abundance of adducts formed during HPLC-HRMS analysis as a function of ETN, DNTN, or PETN concentration (average of 3 runs per concentrations).

Species	Concentration/ mg L^{-1}		
	1000	10	1
$[\text{ETN} + \text{Cl}]^-$	100	100	100
$[\text{ETriN} + \text{Cl}]^-$	56	17	18
$[\text{ETN} + \text{NO}_3]^-$	35	2	0
$[\text{ETN} - \text{NO}_2 + \text{HNO}_3]^-$	13	0	0
$[\text{EdiN} + \text{Cl}]^-$	16	5	7
$[\text{DNTN} + \text{Cl}]^-$	19	100	100
$[\text{DNTN} + \text{NO}_3]^-$	100	56	1
$[\text{PETN} + \text{Cl}]^-$	100	100	100
$[\text{PETN} + \text{NO}_3]^-$	32	1	1
$[\text{PETriN} + \text{Cl}]^-$	22	15	16
$[\text{PEDiN} + \text{Cl}]^-$	6	4	6

tration dependent (Table 3). Interestingly, DNTN did not exhibit fragmentation analogous to ETN or PETN. Aside from the anticipated $[\text{DNTN} + \text{Cl}]^-$, only $[\text{DNTN} + \text{NO}_3]^-$ was found and the relative amount of amount of each adduct was also found to be concentration dependent (Table 3).

3.2 GC/MS

The analysis of explosives, particularly nitrate esters, by gas chromatography is known to be problematic [17]. Therefore, optimization of the conditions for analysis of ETN by gas chromatography-electron impact mass spectrometry (GC-MS) was necessary. An Agilent 6890 gas chromatograph with an Agilent 5973i mass selective detector was used. The column was a DB5-MS, with a nominal diameter of 250 μm and a film thickness of 0.250 μm , cut to 10 m. The column was cut to 10 m after numerous unsuccessful attempts to analyze the material with a 30 m column. Presumably, a shorter column improved sensitivity by reducing the amount of time the analyte spent in the column, simultaneously reducing the thermal decomposition of the analyte. The inlet was a split/splitless inlet from Agilent Technologies operated in either the split (5:1) or splitless mode; the inlet temperature was varied from 100 to 250 °C. The carrier gas was ultra-high purity helium, and the flow rate was either 1.5 or 2.0 mL min⁻¹. Initial temperature of the oven was either 50 or 100 °C, and ramp rates of 10 and 20 K min⁻¹ were used. The temperature of the transfer line was varied between 100 and 300 °C. The conditions were varied iteratively, and thirty-one separate sets of conditions were screened. The mass spectrometer was operated with a solvent delay of 1 min and was tuned daily using Agilent's "STUNE·U" program.

The optimized conditions were a 5:1 split at 100 °C at the inlet, 1.5 mL min⁻¹ flow rate and transfer line temperature of 200 °C. The oven was held at 50 °C for 2 minutes before ramping to 300 °C at a rate of 20 K min⁻¹. The ETN eluted as a single peak at approx. 7.3 minutes. Varying the oven ramp rate, initial oven temperature or carrier gas flow rate varied the retention time with no signifi-

Table 4. Prominent ETN fragments by GC/MS and their assignments.

<i>m/z</i>	Fragment
30	NO, CH ₂ O
46	NO ₂
60	CH ₂ NO ₂
76	CH ₂ NO ₃
89	C ₂ H ₃ NO ₃
118	C ₂ H ₂ N ₂ O ₄
151	C ₂ H ₂ N ₂ O ₆

cant effect on the signal. The mass spectrum of ETN revealed considerable thermal decomposition, and the parent peak was not observed in any of the trials. The three most prominent peaks in the mass spectrum were 30, 46, and 76 *m/z*, most likely corresponding to NO, NO₂ and CH₂NO₃. Other peaks and their tentative assignments are given in Table 4. When holding all other conditions constant, it was observed that as the temperature of the transfer line increased, the relative abundance of NO

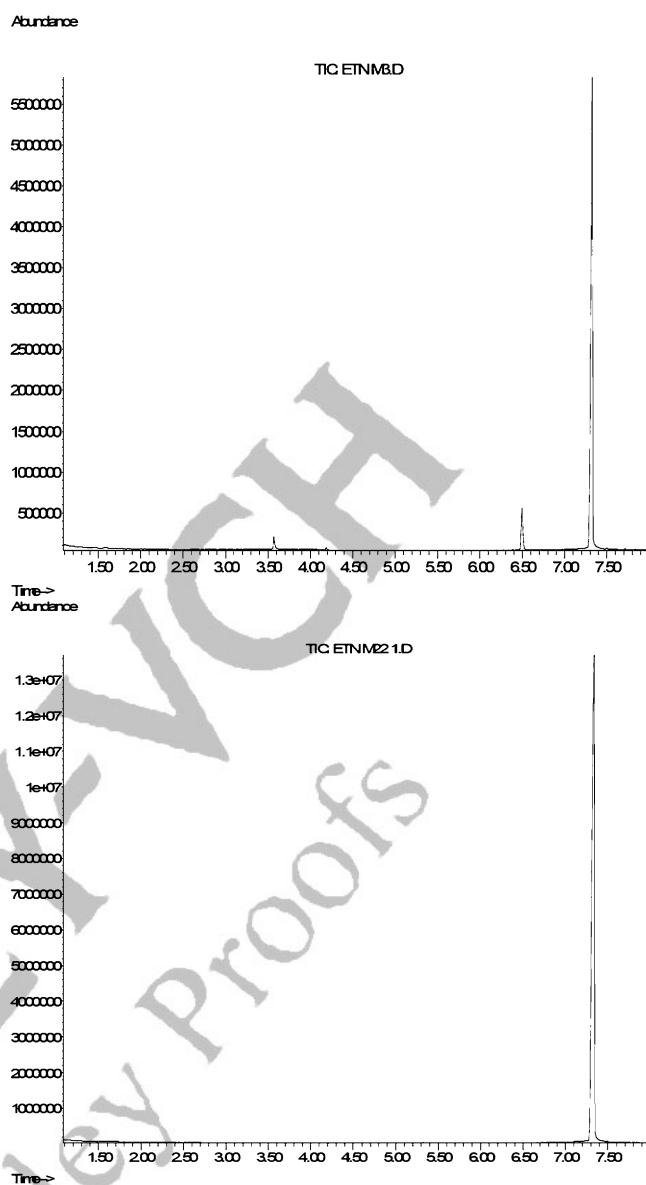


Figure 7. Comparison of gas chromatograms at inlet temperatures of 200 °C (top) and 100 °C (bottom).

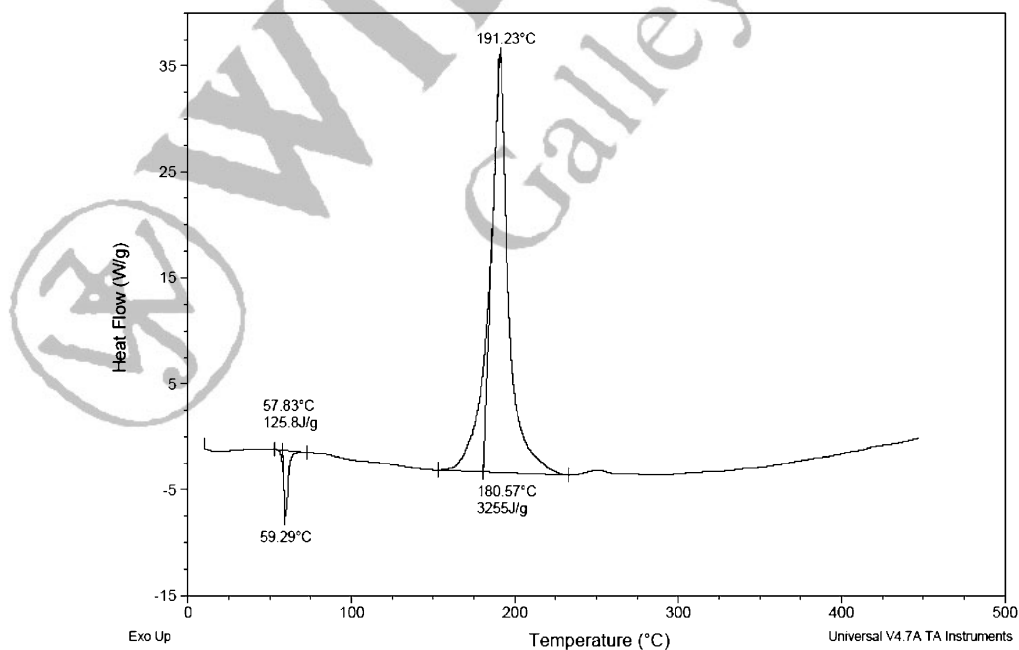
with respect to NO₂ increased, most likely the result of the thermal decomposition of NO₂ to NO. If the temperature of the inlet was 150 °C or above, ETN partially decomposed at the inlet elevating the baseline, reducing the size of the main chromatographic peak and causing the appearance of multiple peaks in the chromatogram (Figure 7). As the inlet temperature was increased, the decomposition peaks increased in size with respect to the ETN peak. When the inlet temperature was 250 °C or higher, the ETN decomposed completely. The chromatogram was identical to an injection of neat methanol, presumably because the decomposition products were molecules small enough to elute before the solvent delay. Seven different concentrations of ETN between 0.0001 and 1000 mg L⁻¹ were prepared and analyzed by GC/MS to evaluate the sensitivity of the technique. The signal for ETN was plainly apparent without magnification or back-

Table 5. DSC Results for ETN, PETN, DNTN at various scan rates.

	$\beta/\text{K min}^{-1}$	n =	mass/mg	Endotherm $T_{\text{min}}/^\circ\text{C}$	$\Delta H_{\text{fus}}/\text{J g}^{-1}$	Exotherm onset/ $^\circ\text{C}$	Exotherm $T_{\text{max}}/^\circ\text{C}$	$\Delta H/\text{J g}^{-1}$
PETN	20	4	0.125	144	109	198	212	1971
	10	4	0.297	143	148	193	202	3874
	9	3	0.280	143	128	192	201	3358
	8	4	0.298	142	147	191	199	4032
	7	3	0.330	142	145	188	196	3634
	6	3	0.326	142	117	189	195	4060
	5	3	0.284	143	110	186	194	3734
	4	3	0.289	142	117	183	192	2985
	3	3	0.282	141	102	181	189	2919
	2	3	0.301	140	120	178	183	3553
ETN	20	4	0.203	60	113	184	199	2233
	10	5	0.200	62	107	182	193	2795
	9	6	0.288	63	105	183	192	2592
	8	5	0.244	63	102	182	191	2437
	7	4	0.255	61	117	182	186	3181
	6	1	0.232	63	102	181	185	2418
	5	2	0.226	59	116	176	180	3253
	4	2	0.219	62	104	176	180	2948
	3	3	0.255	60	114	171	173	2957
	2	2	0.281	61	99	168	169	2551
DNTN	20	4	0.311	88	135	179	185	3185
	10	3	0.279	87	71	170	175	3121
	9	2	0.381	87	99	167	171	3756
	8	3	0.338	86	70	165	169	3116
	7	2	0.354	85	50	166	169	2730
	6	1	0.313	85	80	163	167	3855
	5	3	0.223	84	70	159	163	2809
	4	3	0.433	85	80	155	158	3934
	3	2	0.400	86	89	150	154	3342
	2	3	0.311	86	87	151	149	3257
1	3	0.250	84	81	141	142	3342	

ground subtraction at the 0.005 mg L^{-1} level but did not appear to be present at the 0.001 mg L^{-1} level. A plot of the ions 30, 46, 60 and 76 at the 0.001 mg L^{-1} level yielded

overlapping signals with the correct retention time and with $S/N \geq 3$. These ions show promise as candidates for


Figure 8. Thermogram of ETN at 10 K min^{-1} .

the low-level detection of ETN by GC/MS using selective ion monitoring or tandem mass spectrometry.

Using identical conditions to those successfully used to examine ETN, multiple attempts were made to analyze DNTN and PETN by GC/MS. DNTN eluted as a broad hump, while PETN eluted as a well-defined peak, with a height and area disproportionately small to the amount of PETN in the solution. The major fragments found for DNTN using the method described for ETN are, in order

of intensity, m/z 30, 46, and 114 while the major fragments for PETN are 46, 30, and 76.

3.3 Differential Scanning Calorimetry

Samples (0.190–0.490 mg) were flame sealed in glass micro-ampoules (9.5 mm × 1.0 mm) and examined using a TA Instruments Q100 DSC. The cell resistance, cell capacitance, and cell constant were obtained by calibrating

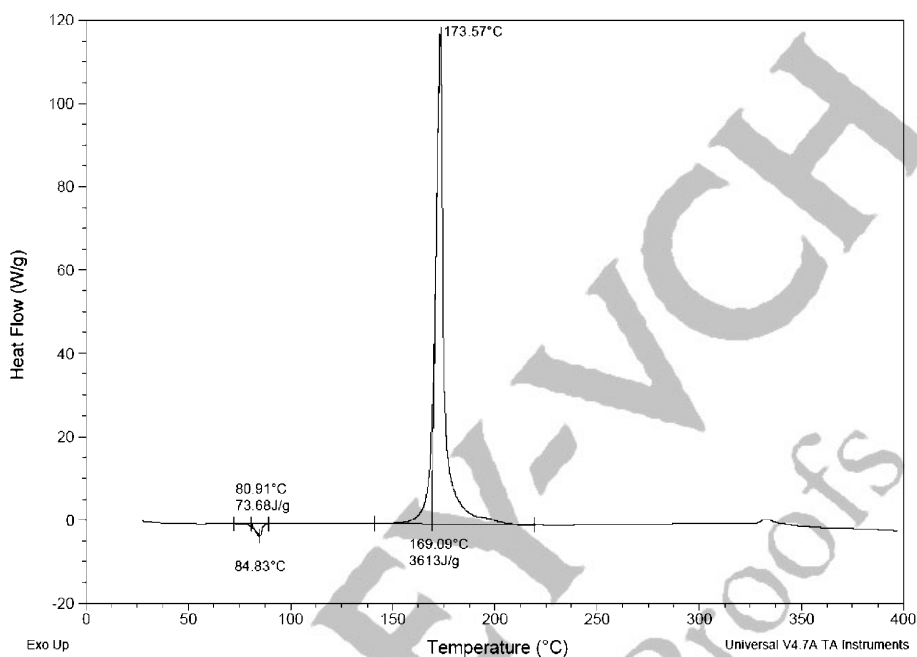


Figure 9. Thermogram of DNTN at 10 K min⁻¹.

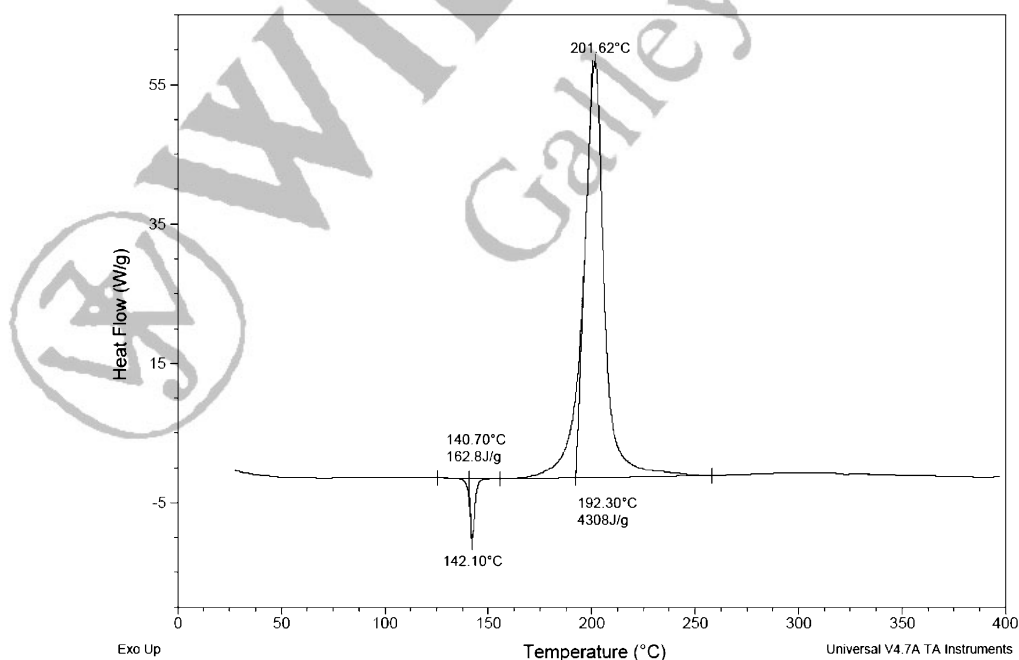


Figure 10. Thermogram of PETN at 10 K min⁻¹.

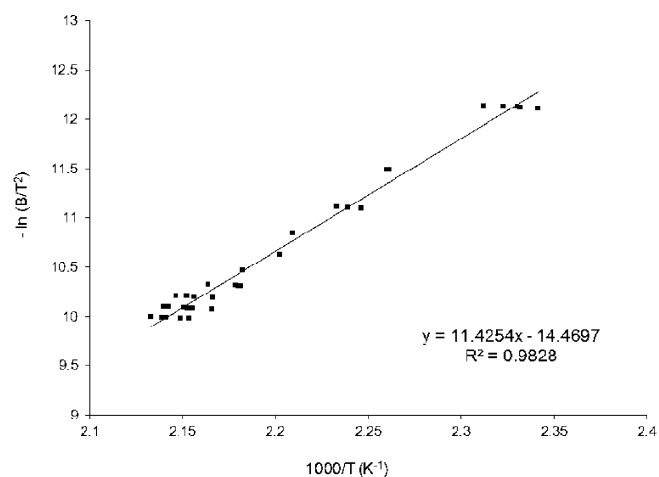


Figure 11. Plot for the determination of activation of ETN energy by DSC.

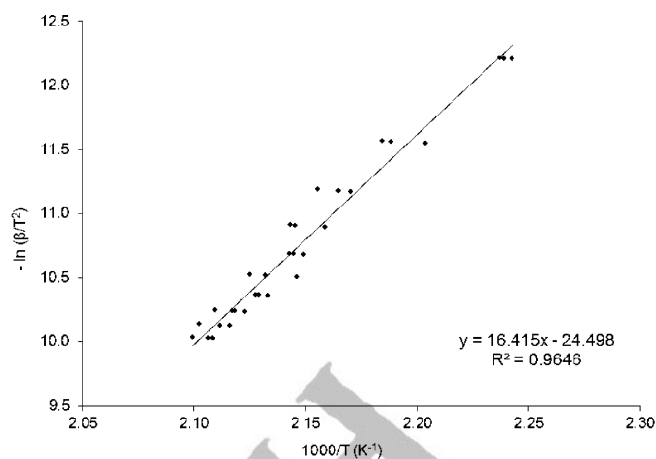


Figure 13. Plot for the determination of activation energy of PETN by DSC.

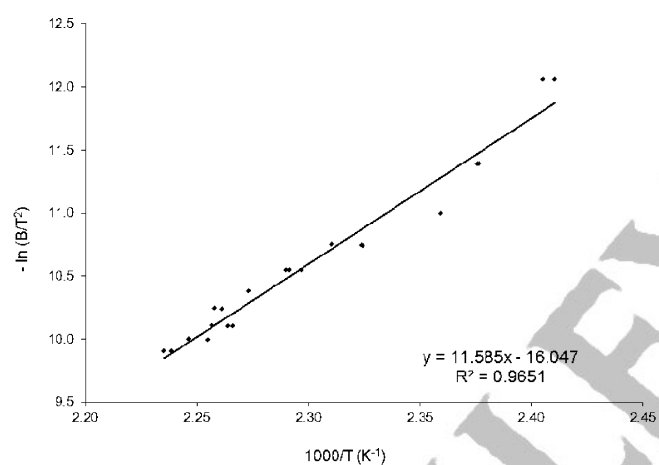


Figure 12. Plot for the determination of activation energy of DNTN by DSC.

against sapphire, and the temperature was calibrated using indium. All experiments were performed under a stream of ultra-high purity nitrogen at 50 mL min^{-1} . The

values shown in Table 5 indicate that a single endothermic melt and exothermic decomposition were observed for ETN, PETN, and DNTN. Figure 8, Figure 9, and Figure 10 show typical DSC traces at 10 K min^{-1} . However, in a few sample of ETN a small exothermic deviation from baseline was observed immediately after the first exotherm (Figure 8). Since the DSC tube was sealed, all the decomposition products were retained in the glass capillary tube, and the second exotherm must be the result of a secondary oxidation involving them.

The activation energies of thermal decomposition and the Arrhenius pre-exponential factors of ETN, DNTN, and PETN were tabulated by employing the methods outlined in ASTM E 698–05 using Equation (1) and (2) and using the individual data which is shown in average in Table 5.

$$E_a = R(d[-\ln(\beta/T^2)]/d[1/T]) \quad (1)$$

$$Z = \beta E e^{E/RT} / RT^2 \quad (2)$$

where R is the gas constant, β is the heating rate in K, T is the maximum temperature for the exothermic decom-

Table 6. Summary of experimentally measured physical properties: DSC & activation energies, vapor pressure, sublimation enthalpies, densities, drop weight impact.

	DNTN	ETN	PETN
	$\text{C}_6\text{H}_8\text{N}_6\text{O}_{16}$	$\text{C}_4\text{H}_6\text{N}_4\text{O}_{12}$	$\text{C}_5\text{H}_8\text{N}_4\text{O}_{12}$
melting points/ $^\circ\text{C}$	85–86	60–61	143
Heat release obs by DSC/ J g^{-1}	3200	2800	3900
DSC Exo T_{max} at 20 K min^{-1}	$184 \text{ }^\circ\text{C}$	$200 \text{ }^\circ\text{C}$	$212 \text{ }^\circ\text{C}$
DSC Exo T_{max} at 10 K min^{-1}	$174 \text{ }^\circ\text{C}$	$193 \text{ }^\circ\text{C}$	$202 \text{ }^\circ\text{C}$
DTA (max. mass loss 10 K min^{-1})	$180 \text{ }^\circ\text{C}$	$200 \text{ }^\circ\text{C}$	$200 \text{ }^\circ\text{C}$
E_a (kJ mol^{-1})	96.3	95.0	136.5
A/s^{-1}	1.03×10^{11}	2.35×10^{10}	7.47×10^{14}
Vapor Pressure/Pa, $25 \text{ }^\circ\text{C}$	4.10×10^{-3}	3.19×10^{-3}	5.21×10^{-6}
$\Delta H_{\text{sub}}/\text{kJ mol}^{-1}$	105.3	117.7	146.6
Pycnometer Density/ g cm^{-3}	1.8238	1.7219	1.7599
Literature X-ray density/ g cm^{-3}	1.917^9	1.55^3	1.778^{28}
Drop Wt (4 Kg) Impact Dh_{50}/cm	27.7	24.0	25.2

position in Kelvin and Z is the Arrhenius pre-exponential factor. Experiments were carried out at $\beta=1-10 \text{ K min}^{-1}$. Figure 11, Figure 12, and Figure 13 show the plots yielding activation energies for ETN, DNTN, and PETN, respectively. The activation energies and Arrhenius pre-exponential factors, calculated using $\beta=5 \text{ K min}^{-1}$, thus determined are shown in Table 6.

3.4 Thermogravimetric Analysis and Vapor Pressure Determinations

Thermogravimetric analysis (TGA) was used to examine the thermal decomposition of ETN, PETN, and DNTN on a Thermal Analysis Q5000. The samples (8 to 10 mg) were loaded into 100 μL open platinum pans. The analytical run consisted of an initial, isothermal hold at ambient operating temperature, 35 to 40 $^{\circ}\text{C}$, for five minutes with a flow to the balance of 20 mL min^{-1} and 50 mL min^{-1} to the furnace of ultra high purity nitrogen. The flows to the balance and furnace were then reduced to 10 and 25 mL min^{-1} , respectively, and the furnace was ramped at a rate of 10 K min^{-1} to 300 $^{\circ}\text{C}$. The experiment was repeated in quadruplicate and representative thermograms are shown in Figure 14.

The thermogram showed a very gradual mass loss for ETN between 40 and 145 $^{\circ}\text{C}$, losing 1% of the total mass. Above 145 $^{\circ}\text{C}$, the mass loss was more rapid but still steady; no ETN remained at 205 $^{\circ}\text{C}$. The rate of mass loss for PETN was also steady but more rapid than that of ETN. Between 165 $^{\circ}\text{C}$ and 199 $^{\circ}\text{C}$, 95% of the PETN was lost, with complete decomposition by 300 $^{\circ}\text{C}$. The majority of DNTN mass loss occurred between 146 $^{\circ}\text{C}$ and 191 $^{\circ}\text{C}$, dropping from 99% to 18%. At 300 $^{\circ}\text{C}$, 8% of the original mass of DNTN remained.

An isothermal gravimetric technique has been reported as a method for measuring of enthalpy of sublimation

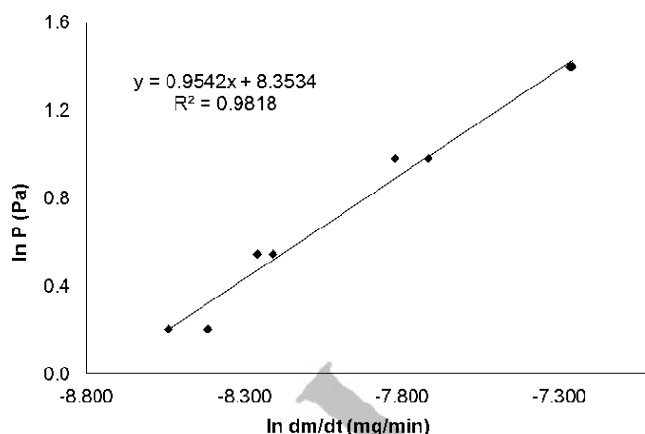


Figure 15. Plot of natural logarithm of the vapor pressure vs. the natural logarithm of the sublimation rate for benzoic acid.

and vapor pressure [18,19]. A material of known vapor pressure, e.g. benzoic acid, is held at constant temperature and the mass loss is measured per unit time. The experiment is repeated at multiple temperatures in order to calibrate the TGA for the purposes of determining the Antoine coefficients of an unknown material. Benzoic acid, 9–11 mg, was loaded into a 110 μL open platinum pan; the furnace was closed and held at fixed temperatures for 250 minutes. The flow to the furnace was 80 mL min^{-1} , the flow to the balance was 20 mL min^{-1} , and the purge gas was ultra high purity nitrogen.

The vapor pressure of benzoic acid at various temperatures is available (<http://webbook.nist.gov>). The natural logarithm of its vapor pressure was plotted vs. the natural logarithm of the sublimation rate (Figure 15). The equation of the line in this plot takes the form

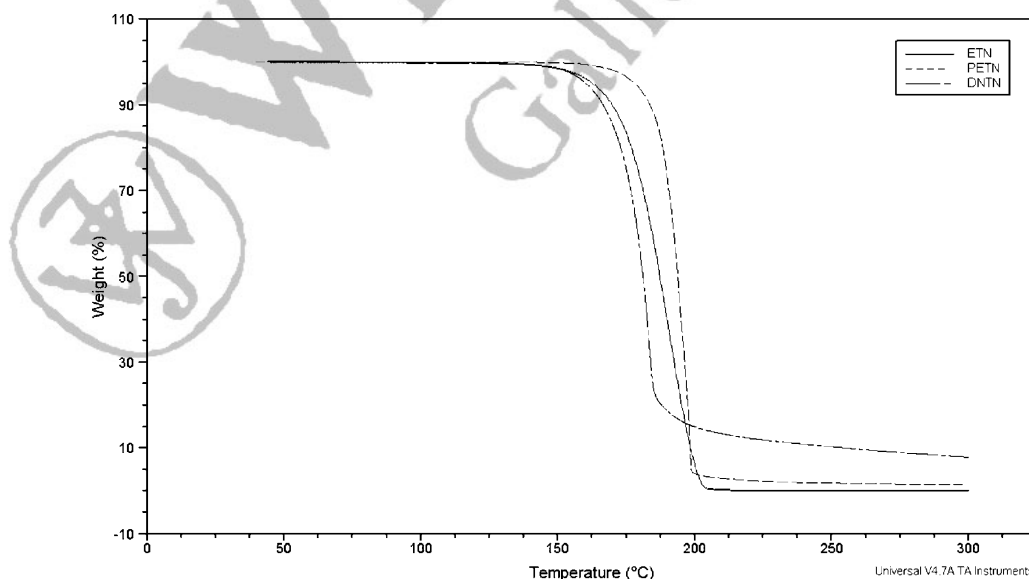


Figure 14. Thermogravimetric plots of ETN, PETN and DNTN.

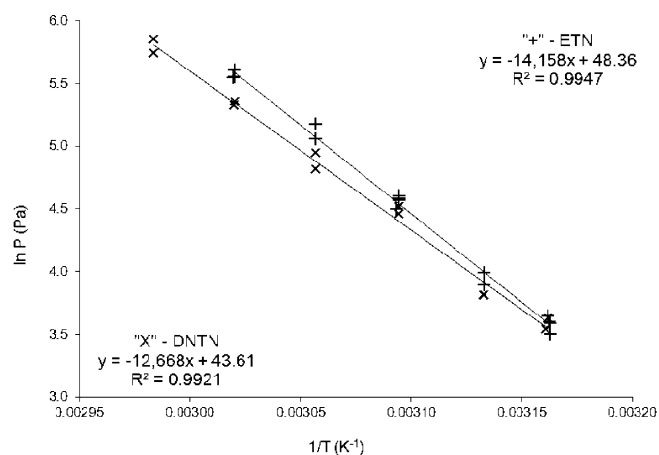


Figure 16. Claperyon plots for ETN and DNTN.

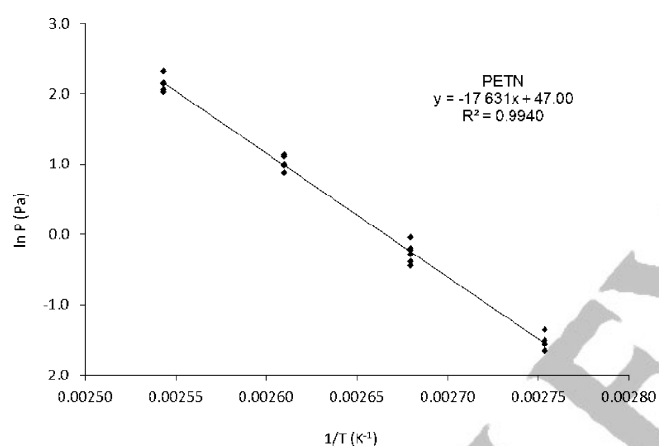


Figure 17. Claperyon plot for PETN.

$$\ln P = A \ln (dm/dt) + B$$

where dm/dt is the sublimation rate in mg min^{-1} , P is the vapor pressure in Pa, and A , the slope, and B , the intercept, are the pseudo-Antoine coefficients. For benzoic acid and the experimental conditions used in this study, the coefficients are $A=0.9542$ and $B=8.3534$. The sublimation rates at specific temperatures of PETN, ETN, and DNTN were determined experimentally and used with the pseudo-Antoine equation above to extrapolate the vapor pressures. The vapor pressures at these temperatures were used to construct Clapeyron plots (Figure 16, Figure 17). Extrapolating to 25°C , the vapor pressures for the three nitrate esters were determined along with their enthalpy of sublimation. The slope of the line in a Clapeyron plot is the enthalpy of sublimation (ΔH_{sub}) divided by the gas constant. This is the first report of vapor pressures for ETN and DNTN. Vapor pressure and sublimation enthalpy of PETN have previously been reported as 1.78×10^{-5} Pa [20], and $150.4 \text{ kJ}\cdot\text{mol}^{-1}$ [21], respectively; these values compare well with those found herein (Table 6).

3.5 Density

The density of mono-molecular explosives is known to have a strong effect on the performance of energetic materials. The densities of ETN, PETN and DNTN were measured using a Micromeritics AccuPyc II helium gas pycnometer. The instrument was calibrated according to the manufacturer's instructions using a steel sphere of known mass and volume. Samples were prepared by filling the provided crucibles to 50–75% of capacity with the material and recording the mass of sample. The cell was purged with helium ten times and ten volume measurements were made. The calibration was verified using $\text{BaCl}_2\cdot 2\text{H}_2\text{O}$ and the value, $3.1048 (\pm 0.0019) \text{ g cm}^{-3}$, found to be close to literature value, 3.097 g cm^{-3} . The densities of the materials discussed in this study were measured. ETN was found to have density $1.7219 (\pm 0.0025) \text{ g cm}^{-3}$; DNTN density $1.8238 (\pm 0.0016) \text{ g cm}^{-3}$; and PETN density $1.7599 (\pm 0.0006) \text{ g cm}^{-3}$ (Table 6).

3.6 Impact Sensitivity

An in-house drop-weight impact sensitivity apparatus and the Bruceton Method were used to compare the sensitivities of ETN, PETN and DNTN to initiation from impact. The apparatus was modeled after the "LLNL Small-Scale Drop-Hammer Impact Sensitivity Test" [22]. The test material ($35 \pm 1 \text{ mg}$) was loaded onto a 1 inch square piece of 120-grit sandpaper and the sample was placed under a cylindrical, steel striker. A steel weight (4 kg) attached to a fixed, vertical rail was raised to a known height and released. The height of the hammer was varied in 1 cm increments until at least 20 measurements could be collected at 6 consecutive heights. A "go" was characterized by a loud report and significant damage to the sandpaper, whereas after a "no-go", the sandpaper was intact and the material remained. By applying the Bruceton Method, the height at which the probability of explosion is 0.5, or " Dh_{50} ", may be determined. These experiments showed that ETN (24.0 cm) is more sensitive to impact than PETN (25.2 cm) while DNTN (27.7 cm) is less sensitive than both (Table 6).

3.7 Small-Scale Explosivity Testing

The performance of ETN was compared to PETN, RDX and DNTN using a small-scale explosivity device (SSED) [23–27]. This technique has been used to compare explosive performance of laboratory-scale quantities of materials using the metric of the weight of intact cartridge remaining. The cartridge employed was a British.303 rifle cartridge, and the fragment to be weighed was the base and all metal remaining attached to it. The explosive (2 g) was loaded into the brass cartridge, and the depth measured in order to calculate the volume and tap density. An RP-3 (29 mg of PETN) exploding bridge wire (EBW) detonator was placed so that the bottom of the detonator was just below the surface (2–4 mm) of the ma-

Table 7. Summary of small-scale explosivity device results.

Sample	Charge depth/mm	Tap Density/g mL ⁻¹	Mass Cartridge/g	Mass Remaining/g	fraction remaining/% (SD)
ETN 1	18	0.71	11.027	3.0412	27.6
ETN 2	25	0.91	10.9242	3.0325	27.8
ETN 3	9	0.58	11.1935	3.1628	28.3
ETN 4	14	0.64	11.2962	2.994	26.5
ETN 5	29	1.07	10.987	3.3665	30.6
ETN 6	30	1.07	11.2383	3.1386	27.9
Average					28.1 (1.4)
PETN 1	17	0.69	11.0747	2.8792	26
PETN 2	14	0.64	11.183	2.9109	26
PETN 3	18	0.71	11.3524	3.0374	26.8
Average					26.3 (0.4)
DNTN 1	21	0.77	11.1826	2.7519	24.6
DNTN 2	17	0.69	11.1314	2.9157	26.2
DNTN 3	20	0.77	11.4555	2.9974	26.2
DNTN 4	26	0.91	11.3384	2.7119	23.9
Average					25.2 (1.1)
RDX 1	30	1.07	11.3428	1.4285	12.6
RDX 2	30	1.07	11.208	1.3939	12.4
RDX 3	30	1.07	11.1956	1.1714	10.5
Average					11.8 (1.2)

Table 8. Summary of physical properties and performance.

	EGDN	DNTN	ETN	PETN	RDX
chemical formula	C ₂ H ₄ N ₂ O ₆	C ₆ H ₈ N ₆ O ₁₆	C ₄ H ₆ N ₄ O ₁₂	C ₅ H ₈ N ₄ O ₁₂	C ₃ H ₆ N ₆ O ₆
molecular weight/g mol ⁻¹	152	420	302	316	222
oxygen balance (% to CO ₂)	0	0	5.3	-10.1	-21.6
melting point/°C	-22	85–86	61	143	204
heat of formation/kJ mol ⁻¹	-243.01	-371.00	-474.80	-538.48	-70.00
Small Scale Explosivity/% remaining		25.1	28.1	26.3	11.8
Stand. Dev.		1.1	1.4	0.4	1.2
pycnometer density/g cm ⁻³	1.492 [27]	1.8238	1.7219	1.7599	1.767 [28]
detonation velocity*/kms ⁻¹	7.517	8.895	8.206	8.481	8.65
CJ pressure*/GPa	20.37	34.97	26.77	30.44	31.56
SSED density/g cm ⁻³	0.69	0.69	0.69	0.69	0.69
detonation velocity*/kms ⁻¹	4.198	4.187	3.998	4.293	4.738
CJ pressure*/GPa	3.594	3.597	3.274	3.717	4.443

* Determined with Cheetah 6.0 [28].

terial. The loaded cartridge was secured in a 5.1 cm thick 1 L steel bolted closure vessel and electronically initiated from a remote location. After detonation, the base of the cartridge, the largest and the only readily identifiable portion remaining, was recovered and sonicated in water (15 min) followed by an acetone rinse (15 min), dried in a 125 °C oven, and weighed to determine the fraction remaining. As seen in Table 7, the relative explosive power of the materials was found to be RDX ≫ DNTN > PETN > ETN.

Cheetah 6.0 [28] was used to predict the detonation velocities of the materials using literature values for the heats of formation [3,9] and calculating at two different densities. For the tetranitrate esters density as measured by pycnometry and reported above were used. For RDX and EGDN literature values were input [28,29] To make calculations more comparable to SSED, the nominal tap density of 0.69 g cm⁻³ was also used to calculate detonation velocities. Results of this latter calculation again indicate RDX performs much better than the nitrate esters.

A summary of the physical properties and performance is given in Table 8.

4 Conclusion

The physical properties and analyses of three tetranitrate esters have been measured and compared. ETN and DNTN both melt below 100 °C, and unlike PETN, they are stable above their melting points (60 and 85 °C, respectively). As the low melting point suggests, they have significant vapor pressures at ambient conditions. In fact, their 25 °C vapor pressures (ETN, 3.19 × 10⁻³; DNTN, 4.10 × 10⁻³ Pa) as measured by isothermal TGA, are slightly higher than those reported for TNT (.0004 to 0.0007 Pa at 25 °C, Table 2 [30]). While LC/MS was shown to be a viable technique for analysis of all three tetranitrate esters, only ETN was successfully analyzed by GC/MS. Initial DSC kinetics suggested the thermal stability of ETN and DNTN is poorer than PETN, but the mol-

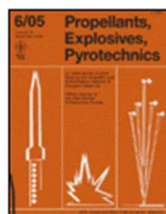
ecules exhibit a more favorable oxygen balance than PETN. Performance of these nitrate esters was tested in the lab using the small-scale explosivity device (SSED) [23–27] and comparing the fraction of the holder remaining to that left by RDX. By that test the most powerful explosive was RDX: RDX \gg DNTN $>$ PETN $>$ ETN. Performance was also judged by calculating detonation velocities using the densities measured in this study. Here the denser DNTN performed better than the other three explosives. Detonation velocities calculated for all four explosives and ethylene glycol dinitrate (EGDN) at the density used in the SSED (approx. 0.69 g cm^{-3}) yielded velocities ranging from 4.7 km s^{-1} to 4.0 km s^{-1} :

RDX \gg PETN $>$ EGDN \approx DNTN $>$ ETN.

Interestingly, DNTN and EGDN have identical oxygen balances and almost identical detonation velocities when calculated at same density.

References

- [1] C. Y. Shen, D. A. Ruest, Production of Diglycolic Acid by Nitric Acid Oxidation of Diethylene Glycol, *Ind. Eng. Chem. Process Des. Dev.* **1980**, *19*, 401–404.
- [2] T. Urbański, *Chemistry and Technology of Explosives*, Pergamon Press, Oxford, **1965**.
- [3] B. T. Fedoroff, O. E. Sheffield, *Encyclopedia of Explosives and Related Items*, Vol. 5. E124–125; Picatinny Arsenal, Dover, NJ, **1972**.
- [4] J. P. Agrawal, R. Hodgson, *Organic Chemistry of Explosives*, John Wiley & Sons Ltd., West Sussex, England **2007**, p. 89.
- [5] T. L. Davis, *Chemistry of Powder and Explosives*, Angriff Press, Hollywood, CA, **1943**, p. 235.
- [6] Lin et al., *Erythritol-Producing Moniliella Strains*, U.S. Patent 6916639, Food Industry Research and Development Institute, Taiwan, **2005**.
- [7] <http://www.amazon.com/Now-Foods-Erythritol-1-lbs/dp/B000Z978SS>; assessed Feb. **2011**.
- [8] a) <http://www.thevillagenews.com/story/52538/>; b) www.gazettenet.com/2009/05/23/trial-opens-amherst-teen-explosives-case_SESSf5277b9c6cedda122d4f2e4a4a4df338=gnews.
- [9] D. E. Chavez, M. A. Hiskey, D. L. Naud, D. Parrish, Synthesis of an Energetic Nitrate Ester, *Angew. Chem.* **2008**, *120*, 8431; *Angew. Chem. Int. Ed.* **2008**, *47*, 8307–8309.
- [10] a) <http://www.time.com/time/world/article/0,8599,203478-4,00.html>; b) <http://articles.cnn.com/2009-12-29/justice/airline.terror.attempt.petrn.1.umar-farouk-abdulmutallab-petrn-explosive>; c) www.guardian.co.uk/world/2010/nov/01/petrn-explosive-airport-cargo-scanners.
- [11] F. H. Bergeim, *Production of Erythritol Tetranitrate*, U.S. Patent 1691954, E. I. Du Pont De Nemours & Company, USA, **1928**.
- [12] Bourguignon et al., *Preparation of Tris(hydroxymethyl)aminomethane*, U.S. Patent 4233245, Societe Chimique de La Grande Paroisse, Azote et Produits Chimiques, Paris, FR, **1980**.
- [13] G. B. Linden, M. H. Gold, Preparation of 2- and 5-Substituted-1,3-Dioxanes, *J. Org. Chem.* **1956**, *21*, 1175.
- [14] R. F. Reich, R. A. Yost, Trace Detection and Quantitation of Explosives Using LC/APCI-MS *49th ASMS Conference on Mass Spectrometry and Allied Topics*, Chicago, Illinois, USA, 27–31 May **2001**.
- [15] X. Zhao, J. Yinon, Identification of Nitrate Ester Explosives by Liquid Chromatography–Electrospray Ionization and Atmospheric Pressure Chemical Ionization Mass Spectrometry, *J. Chromatogr. A* **2002**, *977*, 59–68.
- [16] J. Almog, G. Burda, Y. Shloosh, S. Abramovich-Bar, E. Wolf, T. Tamiri, Recovery and Detection of Urea Nitrate in Traces, *J. Forensic Sci.* **2007**, *52*, 1284–1290.
- [17] J. Yinon, S. Zitrin, *Modern Methods and Applications in Analysis of Explosives*, John Wiley & Sons Ltd, England, **1996**, p. 123.
- [18] J. C. Oxley, J. L. Smith, J. Brady, S. Naik, Determination of Urea Nitrate and Guanidine Nitrate Vapor Pressures by Isothermal Thermogravimetry, *Propellants Explos. Pyrotech.* **2010**, *35*, 278–283.
- [19] M. Xie, T. Ziemba, M. Maurin, Sublimation Characterization and Vapor Pressure Estimation of an HIV Nonnucleoside Reverse Transcriptase Inhibitor using Thermogravimetric Analysis, *AAPS PharmSciTech* **2003**, *4*, 23.
- [20] F. T. Crimmins, The Vapor Pressure of Pentaerythritoltetranitrate (PETN) in the Temperature Range of 50 to 98 Degrees Centigrade, *Lawrence Radiation Laboratory*, UCRL-50704, Jul, **1969**.
- [21] R. C. Cundall, Vapour Pressure Measurements on Some Organic High Explosives, *J. Chem. Soc. Faraday Trans. 1* **1978**, *74*, 1339–1345.
- [22] R. L. Simpson, M. F. Foltz, *LLNL Small-Scale Drop-Hammer Impact Sensitivity Test*, Lawrence Livermore National Laboratory, Livermore, CA, **1995**.
- [23] J. C. Oxley, J. L. Smith, E. Resende, Determining Explosivity Part II: Comparison of Small-Scale Cartridge Tests to Actual Pipe Bombs, *J. Forensic Sci.* **2001**, *46*, 1070–1075.
- [24] J. Oxley, J. Smith, E. Rogers, E. Resende, A. Mostafa, Small-Scale Explosivity Testing, *J. Energ. Mater.* **1999**, *17*, 331–343.
- [25] D. P. Lidstone, *The Assessment of Explosive Performance by Means of a Cartridge Case Deformation Test*, RARDE Memorandum 15/1969.
- [26] A. M. Lowe, *Cartridge Case Test Validation*, DRA Report, November **1995**.
- [27] A. M. Lowe, R. Hilley, Cartridge Case Deformation Test, *J. Energ. Mater.* **1998**, *16*, 289–307.
- [28] S. Bastea, Fried L. E., K. R. Glaesemann, W. M. Howard, I-F. W. Kuo, P. C. Souers, P. A. Vitello, *Cheetah 6.0*, User's Manual, Lawrence Livermore National Laboratory, Livermore, CA, **2010**.
- [29] T. R. Gibbs, A. Popolato, *LASL Explosive Property Data*, UC Press, Berkeley, CA, **1980**, p. 133.
- [30] J. C. Oxley, J. L. Smith, J. Moran, K. Shinde, Determination of the Vapor Density of Triacetone Triperoxide (TATP) Using a Gas Chromatography Headspace Technique, *Propellants Explos. Pyrotech.* **2005**, *30*, 127–130.



Factors Influencing Triacetone Triperoxide (TATP) and Diacetone Diperoxide (DADP) Formation: Part I

Journal:	<i>Propellants, Explosives, Pyrotechnics</i>
Manuscript ID:	Draft
Wiley - Manuscript type:	Full Paper
Keywords:	Denature, Triacetone Triperoxide (TATP), Diacetone Diperoxide (DADP), Small-Scale Explosivity Device (SSED), Drop-weight Impact Sensitivity

SCHOLARONE™
Manuscripts

Factors Influencing Triacetone Triperoxide (TATP) and Diacetone Diperoxide (DADP) Formation: Part I

Jimmie C. Oxley^{*a}; James L. Smith^a; Patrick R. Bowden^b; Ryan C. Rettinger^a

^a*University of Rhode Island,
Chemistry Department
51 Lower College Road
Kingston, RI 02881
joxley@chm.uri.edu

^b*Los Alamos National Laboratory, MS P952,
Los Alamos, NM, 87544*

Abstract

Conditions which result in the formation of triacetone triperoxide (TATP) or diacetone diperoxide (DADP) from acetone and hydrogen peroxide (HP) have been studied for the purposes of inhibiting the reaction. Reaction of HP with acetone precipitates either DADP or TATP, but the overall yield and amount of each was found to depend on (1) reaction temperature; (2) the molar ratio of acid to HP/acetone; (3) initial concentrations of reactants, and (4) length of reaction. Controlling molar ratios and concentrations of starting materials was complicated because both sulfuric acid and hydrogen peroxide were aqueous solutions. Temperature exercised great control over the reaction outcome. Because there is much speculation of the relative stability, sensitivity and performance of DADP and TATP, standard tests (i.e. DSC, drop weight impact, and SSED) were performed.

Keywords: Denature, Triacetone Triperoxide (TATP), Diacetone Diperoxide (DADP), Small-Scale Explosivity Device (SSED), Drop-weight Impact Sensitivity

1 Introduction

Triacetone triperoxide (3,3,6,6,9,9-hexamethyl-1,2,4,5,7,8-hexoxonane, TATP, CAS #17088-37-8), is a sensitive, moderately powerful energetic material first reported in 1895 [1]. The one-pot synthesis from readily available precursors can, if certain precautions are met, produce TATP in high yield. TATP, being highly volatile (odor similar to pepper), does not lend itself to military or commercial applications; however, it has been used successfully by foreign and domestic terrorists. Properties of the pure material are reported in Table 1 along with standard military explosives for comparison. Literature procedures abound for TATP synthesis, from peer-reviewed journals and the internet, but all are similar [1, 4-6, 9-22]. Furthermore, an internet search provides a plethora of videos and forums of individuals who candidly show and speak about making TATP. Beginning in Israel in the 1980's, terrorist attacks have used TATP, either as the main or initiating charge [23]. Some of those incidents are shown in Table 2. Recent papers have investigated TATP synthesis, including unintended synthesis when acetone and hydrogen peroxide are used in cleaning procedures [30]. The focus of this study was to observe how varying reaction conditions affected yield of the reaction products TATP and diacetone diperoxide (DADP) and the extent to which the reaction is reversible or preventable (Scheme 1).

<tabr1>

<tabr2>

<schr1>

2 Experimental Section

2.1 Reagents and Chemicals

Acetone (HPLC-grade) and concentrated sulfuric acid (Certified ACS Plus) were obtained from Fisher Scientific. Hydrogen peroxide was obtained from Univar at 50% w/w in

1
2
3 water and was diluted to 30% and 9wt% using distilled water. Higher concentrations of
4
5 hydrogen peroxide were obtained by removal of water at elevated temperature. All
6
7 concentrations of hydrogen peroxide were verified by refractometry to within +/- 1wt% [31].
8
9
10 Adulterants (102 compounds) were obtained from Fisher Scientific and Sigma-Aldrich with
11
12 varying degrees of purity.
13
14

15 16 **2.2 Preparation of Triacetone Triperoxide (TATP) with and without adulterants**

17
18 Into a glass test tube (16mm x 150mm) containing a small stir bar, 1.53g +/- 0.01g (13.5
19
20 millimols, mmols) of 30wt% hydrogen peroxide was weighed. The test tube was capped with
21
22 Parafilm and placed in a temperature-controlled water bath. Acetone, 0.78g +/- 0.01g
23
24 (13.5mmols), neat or adulterated, was added to the hydrogen peroxide, and they were allowed to
25
26 mix for a minimum of 15 minutes before sulfuric acid (40-96wt%, generally, 1.35 to 0.135
27
28 mmols) was added. If higher concentration of HP were used, i.e. $\geq 50\text{wt}\%$, optimum results
29
30 (~100% yield) was achieved using a 1:1:1 mole ratio of sulfuric acid (65wt%): HP (50wt%) :
31
32 acetone and holding the mixture at 5°C for 24 hours.
33
34
35
36

37
38 The majority of the experiments were performed using a molar ratio of 0.01:1 or 0.10:1
39
40 of 46-50wt% sulfuric acid to hydrogen peroxide. The 1 mol% loading was achieved by using 1
41
42 drop, via pipet, of 40-50wt% sulfuric acid. The 10 mol % loading was achieved by using 0.276g
43
44 of 48wt% sulfuric acid, delivered by pipette. The sulfuric acid concentration was verified by
45
46 density. Acid addition was monitored for several reactions to determine temperature spike; a
47
48 maximum of 8°C rise was seen in samples that were run at 25°C. In one series of experiments,
49
50 90wt% sulfuric acid was added, drop wise, in varying amounts to make step-wise increases in
51
52 catalyst loading.
53
54
55
56
57
58
59
60

The solution was allowed to stir, behind a blast shield, for a minimum of 24 hours before filtration. The theoretical yield was 1.00 gram (4.5mmols) TATP; at this scale, multiple batches were run simultaneously. Following reactions for the specified lengths of time, test tubes were removed and filtered under water aspiration using 4.25cm diameter Fisher P4 (4-8 μ m particle retention) filter paper. Each reaction was washed with 75 to 150mL distilled water at ambient temperature. Due to the high vapor pressure of TATP, the product was only allowed to dry only 15 minutes. If standing beads of water were removed by blotting, this length of time was sufficient to remove water without significant loss of TATP. Once mass of the solid product was obtained, each sample was placed into a glass vial with a plastic push-cap and placed into a -15 $^{\circ}$ C freezer until analyses were performed. When analytically pure samples were required, the re-crystallization protocol cited below (Section 2.5) was employed. Melting point 94-96 $^{\circ}$ C; 1 H NMR 1.46 ppm and 13 C NMR 21 and 107 ppm (CDCl_3); MS fragmentation pattern: $m/z = 222$ (Parent, very small), 117 $[(\text{CH}_3)_2\text{CO}_2\text{CCH}_3\text{O}]^+$ (medium), 101 $[(\text{CH}_3)_2\text{CO}_2\text{CH}_3]^+$ (medium), 91 $[(\text{CH}_3)(\text{CH}_2)\text{C}(\text{OH})(\text{OOH})]^+$ (very small), 89 $[\text{C}_3\text{H}_5\text{O}_3]^+$ (very small), 75 $[\text{C}_3\text{H}_7\text{O}_3]^+$ (large), 73 $[\text{C}_2\text{H}_5\text{O}_2]^+$ (small), 59 $[(\text{CH}_3)_2\text{COH}]^+$ (large), 58 $[(\text{CH}_3)_2\text{CO}]^+$ (large), 43 $[\text{CH}_3\text{CO}]^+$ (dominant), 29 $[\text{CH}_3\text{CH}_2]^+$ (medium), 15 $[\text{CH}_3]^+$ (medium).

2.3 Sample Preparation of Diacetone Diperoxide (DADP)

Similar to the TATP synthesis reactions, 13.5mmols of hydrogen peroxide was combined with 13.5mmols of acetone in a test tube in a temperature controlled bath. The hydrogen peroxide concentration varied from 30wt% to 65wt%; two concentrations of sulfuric acid, 55wt% and 63wt%, were used. The molar ratio of sulfuric acid to hydrogen peroxide was varied from 0.3:1 to 1.5:1 for 65wt% HP; 0.55:1 to 1.8:1 for 50% wt HP; and 1:1 to 2.5:1 for 30wt% HP. Reactions were run at 25 $^{\circ}$ C and 5 $^{\circ}$ C for 24 hours. Reactions were cooled in an ice bath

1
2
3 while acid was added before being transferred to the 25°C bath; reactions at 5°C were not cooled
4
5 further prior to acid addition. Filtration procedures were similar to that for TATP syntheses
6
7 (Section 2.2), but more water (>200mL) was used to rinse precipitate since more acid was used
8
9 in DADP preparation. When high sample purity was required, the re-crystallization protocol
10
11 cited below (Section 2.5) was employed. Melting point 131-133°C; ¹H NMR 1.35 and 1.80 ppm
12
13 and ¹³C NMR 20, 22 and 108 ppm (CDCl₃); MS fragmentation pattern: m/z = 133
14
15 [(CH₃)₂OCO₂C(CH₃)O]⁺ (small), 117 [(CH₃)₂CO₂CCH₃O]⁺ (small), 101 [(CH₃)₂CO₂CH₃]⁺
16
17 (large), 89 [C₃H₅O₃]⁺ (very small), 75 [C₃H₇O₃]⁺ (small), 73 [C₂H₅O₂]⁺ (small), 59
18
19 [(CH₃)₂COH]⁺ (large), 58 [(CH₃)₂CO]⁺ (large), 43 [CH₃CO]⁺ (dominant), 29 [CH₃CH₂]⁺
20
21 (medium), 15 [CH₃]⁺ (medium).
22
23
24
25
26
27

28 **2.4 Preparation of TATP/DADP Mixtures**

29
30 Mixtures of TATP and DADP were prepared by dissolving proportional masses of each
31
32 into 25g acetone, e.g. 75/25, 50/50 and 25/75, with a total mass between 1.50-2.00 g. The
33
34 acetone solution was poured onto 100g of distilled water with vigorous stirring. After 10-15
35
36 minutes of stirring, the mixture was filtered and washed with room temperature distilled water;
37
38 organic solvents were not used as a wash due to differing solubilities of DADP and TATP. The
39
40 solid was allowed to dry for 30 minutes before being weighed and placed into a glass vial with
41
42 plastic push-cap.
43
44
45
46
47

48 **2.5 Recycling of Samples**

49
50 Samples of TATP and DADP no longer needed were recrystallized. Double
51
52 recrystallization was used to prepare TATP for standards. The first recrystallization was from
53
54 methanol, and the solution was allowed to cool slowly to room temperature before being placed
55
56
57
58
59
60

1
2
3 into a freezer. After filtering and washing with cold (-15°C) methanol, the TATP was re-
4
5 dissolved in pentane. The pentane solution was cooled rapidly in an ice water and salt bath with
6
7 continued stirring. In this manner, a smaller particle size was obtained. Recrystallization of
8
9 DADP was performed in methanol or ethyl acetate.
10
11

12 13 14 **2.6 Adulterated TATP**

15
16 Adulterated solutions of acetone were prepared by adding acetone to the desired mass of
17
18 adulterant in a 15mL vial with a total mass of 10g. Over 100 adulterants were tested in a range
19
20 of concentrations from 1wt% to 50wt%. Sparingly soluble adulterants were used as saturated
21
22 solutions; for these adulterants, saturation was below 10wt%. In these cases, rather than
23
24 determine solubility and adjust the mass of acetone solution to maintain a ratio of 1:1 between
25
26 hydrogen peroxide and acetone, the standard mass of acetone, 0.78g, was used. For these
27
28 solutions, the actual mass ratio of hydrogen peroxide to acetone fell between 1:1 and 1.12:1.
29
30 Reactions using adulterated acetone were run in duplicate per concentration and specific reaction
31
32 conditions; few were run only once. Reaction times were measured from the time of addition of
33
34 acid to filtration of the solid precipitate.
35
36
37
38
39

40 41 **2.7 Analytical Methods**

42
43 Melting points were obtained on a Mel-Temp model 1001, without temperature
44
45 corrections; samples containing DADP required sealing both ends of the capillary tubes to
46
47 prevent sublimation. For multiple samples produced under the same conditions, the melting
48
49 point range reported is an average of the onset of melting and completion of melting (i.e. low end
50
51 of the range and the high end of the range) observed for all the samples.
52
53
54
55
56
57
58
59
60

1
2
3 Gas chromatograph (Agilent 6890) coupled to either a mass selective detector (Agilent
4 5793) (GC/MS) or a micro-electron capture detector (GC/ μ ECD) was used to quantify TATP
5 and DADP against pure samples in acetonitrile solutions. Most impurities present in samples
6 could not be positively identified by GC/MS, nor were laborious attempts made to do so.
7
8 Samples for GC analysis were prepared by weighing 9-11mg of sample into a 10mL volumetric
9 flask and filling to mark with acetonitrile; for GC/ μ ECD analysis, a further 1:10 dilution was
10 performed.
11
12
13
14
15
16
17
18

19
20 The GC/MS inlet temperature was 150°C and a flow of 11.6mL/min (helium carrier gas).
21 The inlet was operated in split mode, with a ratio of 5:1 and a split flow of 7.5mL/min. A 10m
22 DB5-MS column (J&W) with a 0.25mm inner diameter and a 0.25 μ m film thickness was
23 operated under a constant flow condition of 1.5mL/min. The oven program had an initial
24 temperature of 50°C with a 4min hold followed by a 10°C/min ramp to 200°C and a post-run at
25 310°C for 1min. The transfer line temperature was 250°C and the mass selective detector source
26 and quadrupole temperatures were 230°C and 150°C, respectively, and electron-impact
27 ionization was used.
28
29
30
31
32
33
34
35
36
37
38

39 The GC/ μ ECD inlet temperature was 170°C, a pressure of 2.36psi (helium carrier gas)
40 and operated in splitless mode. The 6m RTX-TNT2 column (Restek, 0.53mm inner diameter,
41 1.5 μ m film thickness) was held to constant pressure. The oven program had an initial
42 temperature of 40°C and a 2min hold followed by a 20°C/min ramp to 150°C, a 1min hold and a
43 post-run at 250°C for 2mins. The detector was set to 280°C with 30mL/min nitrogen makeup
44 gas flow.
45
46
47
48
49
50
51
52

53 Physical attributes, including density, impact sensitivity, explosivity, and thermal
54 stability, were characterized for pure TATP and DADP and mixtures of TATP/DADP, following
55
56
57
58
59
60

1
2
3 determination of approximate ratios of TATP to DADP using GC/ μ ECD. Crystal densities were
4 obtained on a Micromeritics Helium Pycnometer with barium chloride calibration. A single
5 sample was analyzed ten times by the instrument and a density given with a standard deviation.
6
7 Due to the high vapor pressure of DADP, an accurate density was not obtained for mixtures of
8 TATP and DADP or neat DADP. Impact sensitivity, i.e. drop-weight impact, was performed
9
10 using an apparatus modeled after Lawrence Livermore National Laboratories drop weight impact
11 machine; the weight used was 1.91kg [32]. A small-scale explosivity device (SSED) was used,
12 wherein a mass of material is placed inside a British 0.303 rifle cartridge (primer removed) and
13 detonated with a Teledyne RISI RP-3 (29mg PETN) detonator. Typically the mass of material
14 used was 2.0000g, unfortunately, due to the low tap density and inability to pack TATP or
15 DADP into the cartridge, the mass was significantly less. Relative power output is correlated by
16 finding the percentage of the base remaining versus the initial mass of the cartridge [33, 34].
17
18
19
20
21
22
23
24
25
26
27
28
29
30
31

32 A TA Instruments Q100 differential scanning calorimeter (DSC) was used to determine
33 onset temperature of decomposition, heat release and exothermic maximum temperature.
34 Calibration of the DSC consisted of sapphire disc T_{zero} calibration followed by 4 metal standards
35 for heat release and temperature calibration: indium, tin, lead and zinc. Samples were sealed in
36 glass capillary tubes using 0.1-0.2mg of material. Standard run conditions were: Equilibrate at -
37 10°C, ramp 20°C/min to 30°C, turn data storage on, ramp 20°C/min to 400°C. For mixtures of
38 TATP and DADP, the DSC was used for observing eutectic and non-eutectic melting.
39
40
41
42
43
44
45
46
47

48 In adulteration experiments, percent yield of white precipitate formed was the main
49 metric for determining if adulterants affected the reaction between hydrogen peroxide and
50 acetone. Neat reactions were run using similar reaction times, temperature and catalyst loading
51 for comparison. Percent yields were calculated based on either hydrogen peroxide or acetone,
52
53
54
55
56
57
58
59
60

1
2
3 whichever was the limiting reagent; the ratio between hydrogen peroxide and acetone was 1:1 for
4
5 the majority of the reactions. Purity/identity of the white precipitate was judged primarily by
6
7 melting point, but in some cases GC/MS or GC/ μ ECD analysis was performed. While GC/MS
8
9 could not reveal inorganic salts or solvents which might decrease melting point, it would reveal
10
11 organic impurities. Use of TATP calibration standards allowed determination of whether the
12
13 solid was primarily TATP or whether a large percentage of its mass was some material invisible
14
15 to the GC detector. Hence, in several cases we report a decrease in melting point but a high level
16
17 of purity indicated by GC/MS or GC/ μ ECD analysis.
18
19
20
21
22

23 **3 Results and Discussion**

24 **3.1 Factors Affecting TATP Yield**

25 *3.1.1 Hydrogen Peroxide to Acetone Ratio*

26
27
28 An optimum molar ratio of hydrogen peroxide (HP) to acetone was investigated using
29
30 two different means of varying the ratio: the amount of HP was held constant at 13.5mmols and
31
32 the amount of acetone was varied, or the amount of acetone was held constant at 13.5mmols and
33
34 the amount of HP was varied. The HP-to-acetone molar ratio was varied between 0.25:1 to 4:1
35
36 with two different sulfuric acid (48wt%) amounts, 0.14mmols (1mol%) or 1.35mmols (10mol%)
37
38 (Figure 1). Regardless of which reagent was held constant, a molar ratio between 0.5:1 and 2:1
39
40 resulted in good yield of TATP; outside this range, the yield decreased.
41
42
43
44
45
46

47 <fig1>

48 49 50 *3.1.2 Concentration of HP and Reaction Length*

51
52 Yield of TATP increased with increasing concentration of HP even though the molar
53
54 ratios of HP to acetone of 1:1 and sulfuric acid (48wt%) to HP of 0.01:1 were held constant
55
56
57
58
59
60

(Figure 2). In a 48 hour reaction, 84wt% HP yielded 84% TATP, while 30wt% HP yielded 30% TATP. At low amounts of acid (1mol%), an increase in reaction length increased yield; with 30wt% HP, the yield more than doubled between 24 hours (16%) and 72 hours (35%) (Figure 2).

<figr2>

<figr3>

3.1.3 Reaction Temperature

The temperature of the reaction was varied from 5°C to 40°C. While concentrations of sulfuric acid (48wt%) and HP (30wt%) were not varied, their molar ratio was (Figure 3). At temperatures less than 25°C, molar ratios of acid to HP higher than 0.1:1 increased yield; above 25°C, increasing the molar ratio of acid to HP above 0.1:1 resulted in decreased yield of solid peroxide. With 0.1:1 acid to HP molar ratio, a maximum yield was obtained at 25°C. By GC/μECD analysis, the reactions ran at 40°C with a molar ratio of acid to HP of 0.2:1 yielded 1-3wt% DADP; all other reactions yielded TATP only.

3.1.4 Acid to HP/Acetone Ratio

Two reaction temperatures, 5°C and 25°C, were used to observe product distribution over a wide range of concentrations and amounts of sulfuric acid (48wt%-96wt%) and HP (30wt% - 84wt%); molar ratios ranged from 0.002:1 to 2.5:1 (Figure 4). HP to acetone molar ratio was set as 1:1 and was not varied. At 5°C, an increase in yield was observed with increased acid amount, reaching nearly 100% at an acid to HP molar ratio of 0.8:1, before declining. At 25°C, overall yield reached a maximum at an acid to HP molar ratio of 0.4:1 before declining. Above a molar ratio of acid to HP of 0.5:1, reactions ran at 5°C had greater overall yields than identical reactions ran at 25°C. Presumably, at higher temperatures, the use of larger amounts of acid

1
2
3 resulted in decomposition of the peroxides. Figure 4 is expressed as total yield because analysis
4 was of total precipitate formed, both TATP and DADP.
5
6

7
8 <figr4>
9

10 11 **3.2 Conditions Affecting DADP Formation** 12

13
14 In order to assign percentages of TATP and DADP of the overall mixtures (shown in
15 Figure 4), GC/ μ ECD analysis was performed against standards. Figures 5 and 6 illustrate that
16 high temperature (25°C vs. 5°C) and high acid content favored DADP formation. Temperature
17 affected overall yield (Figure 4) and product distribution; for example, under the same
18 conditions, 1:1 molar ratio of sulfuric acid (63wt%) to HP (65wt%), samples ran at 5°C yielded
19 over 80% TATP, while samples ran at 25°C were almost 100% DADP.
20
21
22
23
24
25
26
27

28
29 <figr5>

30 <figr6>
31
32

33 Both Hernandez and Matyas discussed some aspects of the TATP/DADP conversion.
34 Hernandez reported that the reaction of acetone and hydrogen peroxide at temperatures below
35 0°C gave exclusively TATP, but at 20°C a mixture of TATP and DADP was obtained (amount
36 of acid was not reported) [17]. Matyas noted a dependence on acid concentration. He found that
37 when an acetone and hydrogen peroxide (30wt%) mixture was treated with 1 molar equivalent of
38 96wt% sulfuric acid, DADP formed; when 65wt% sulfuric acid was used, 2.5 molar equivalents
39 of acid were necessary to form DADP [15].
40
41
42
43
44
45
46
47
48

49 In the present experiments, the concentration of hydrogen peroxide was found to dictate
50 the amount of acid necessary to convert TATP to DADP. As the initial concentration of HP was
51 increased (concentration of sulfuric acid held constant), the amount of acid necessary for
52 complete conversion of TATP to DADP decreased. For example, with 30wt% HP and 63wt%
53
54
55
56
57
58
59
60

1
2
3 sulfuric acid, a 1.5:1 acid to HP mol ratio yielded only DADP; when the initial concentration of
4
5 HP was increased to 65wt%, a smaller molar ratio, 0.8:1, induced complete conversion to DADP
6
7 (Figure 7). Raw data collected at 5°C and 25°C is provided in supplemental data.
8
9

10
11 <figr7>
12

13
14 While the importance of acidity on the HP/acetone reaction has long been acknowledged,
15
16 it appears the volume of water in reaction mixture plays an important role. Since both HP and
17
18 acid were aqueous, the relative ratios of reactants were complex. Figure 8 illustrate that water-
19
20 to-sulfuric acid molar ratio alone is insufficient to determine the resultant product mix. As the
21
22 total volume of the reaction mixture decreased with increasing HP concentration, the volume
23
24 occupied by the precipitated solid peroxide remained nearly constant. The result was that less
25
26 TATP transformed into DADP at conditions where similar water-to-sulfuric-acid molar ratios
27
28 achieved by high acid concentration and low HP concentration yielded strictly DADP. Figure 9
29
30 plots the reaction products at 25°C as a function of HP moles per kg of water and sulfuric acid
31
32 moles per kg of water, where water comes into the reaction with both the HP and the acid. This
33
34 allows select synthesis of TATP or DADP. If the desired product is TATP then high
35
36 concentration of HP and low acid must be used (black diamonds, Figure 9); for high yield of
37
38 DADP, lower concentration of HP and higher concentration acid are required (black circles,
39
40
41
42
43
44
45 Figure 9).

46
47 <figr8>
48

49
50 <figr9>
51

52 **3.3 Physical Properties**

53 *3.3.1 TATP/DADP Mixture*

54
55
56
57
58
59
60

1
2
3
4
5
6
7
8
9
10
11
12
13
14
15
16
17
18
19
20
21
22
23
24
25
26
27
28
29
30
31
32
33
34
35
36
37
38
39
40
41
42
43
44
45
46
47
48
49
50
51
52
53
54
55
56
57
58
59
60

On do-it-yourself synthesis web sites there is often speculation on the effect of forming DADP rather than TATP in improvised syntheses. The concern is which peroxide is more sensitive or unstable. The fact that TATP exhibits a lower DSC exotherm (239°C) than DADP (251°C) indicates it is somewhat less thermally stable (Table 3). The DSC thermograms indicated that a low melting eutectic was formed when a small amount of DADP contaminated TATP. Analysis of crude samples showed significant destabilization if quantities of acid exceeded 10mol% or impurities were present caused from adulteration of the acetone with 20wt% 2-butanone or 2-pentanone (Table 3). Mixtures of TATP and DADP were found to be more impact sensitive than either pure chemical. Impact sensitivity was only slightly decreased for crude samples (Table 4). Also in Table 4 are the results of the SSED test. Both TATP and DADP perform poorer than TNT, leaving 42% of the cartridge case attached to the base, but this result was achieved with considerably less TATP (~0.8g) than DADP (~1.3g).

<tabr3>

<tabr4>

3.3.2 *Wetted TATP*

While do-it-yourself “chemists” speculate on the effect of DADP contamination of their TATP, explosive disposal personnel speculate on methods to “desensitize” TATP sufficiently so that it can be safely moved from a domestic location. To illustrate the potential associated hazards, a 4.3kg weight was used in the impact device against 20mg TATP. Pure TATP produced a “go” response at a drop height of 5cm. Wetting it with ethanol (EtOH), a 50/50 mixture of ethanol/water or diesel resulted in a mixture that usually did not “go” even when the weight was raised to 100 cm (Table 5). A popular remedy, WD-40, did not show reproducible desensitization, and water, alone, showed none. We attribute the “desensitizing” effect of certain

1
2
3 liquids and the failure of others to their relative tendency to dissolve TATP. Even though the
4 amount of ethanol was too little to dissolve the TATP and the material did not appear to be
5 dissolving, we believe the outer coating was sufficiently softened to reduce sensitivity to impact.
6
7
8
9
10 Water, in which TATP has little solubility, did not reduce its sensitivity to impact.

11
12
13 <tabr5>

14
15 The entire test series was repeated with a different batch of TATP; less favorable results
16 were obtained (Table 5). Mixtures which showed reduced sensitivity, e.g. EOH/water, now
17 produced a “go”. We believe this is due to the increased particle size observed with this batch of
18 TATP. This observation shows the dangers in judging sensitivity based on one batch as batch to
19 batch particle size and, of course, purity have dramatic effects. Furthermore, if the a batch of
20 TATP desensitized with alcohol were allowed to stand long enough so that the alcohol
21 evaporated from the mixture, TATP clumping could become worse making the final material
22 more sensitive than the first.
23
24
25
26
27
28
29
30
31
32
33
34

35 **3.4 Adulterated Reactions**

36
37 To inhibit the reaction between acetone and hydrogen peroxide we sought chemicals to
38 adulterate the precursors without interfering with their desired usage. The ideal adulterant would
39 be kept at a few percent loading, be relatively non-toxic and completely inhibit formation of
40 TATP under most conditions. Our approach was to seek out additives that destroyed hydrogen
41 peroxide, diverted hydrogen peroxide (by reacting with it), quenched the acid catalyst, or made
42 isolation of TATP cumbersome. Over one hundred adulterants, chosen from eight classes of
43 reagents were tested: (1) antioxidants; (2) radical initiators; (3) metal salts; (4) molecules
44 containing reactive bonds; (5) ketones other than acetone; (6) organic solvents to prevent TATP
45 precipitation; (7) amines and inorganic bases; (8) halides and halogenated organics. Reactions
46
47
48
49
50
51
52
53
54
55
56
57
58
59
60

1
2
3 involving adulterated solutions of acetone used a molar ratio of 1:1 hydrogen peroxide (30wt%)
4 to acetone and either 1) 25°C with 1 mol% sulfuric acid for 48 hours or 2) 5°C with 10 mol%
5 sulfuric acid for 24 hours. DADP was not observed by GC/MS or GC/ μ ECD for any of these
6 reactions. Most of the adulterants failed to retard TATP formation. Adulterants and rationale for
7 choosing them is as follows:
8

9
10 (1) Antioxidants were added in an attempt to quench hydroxyl and hydroperoxy radicals
11 should they be formed during synthesis of TATP. However, butylated hydroxytoluene, vanillic
12 acid, butylated hydroxyanisole, diethyl phthalate, benzoquinone, tannic acid, pyrogallol, 4-
13 hydroxyphenylacetic acid, resorcinol, p-hydroxyphenylacetic acid, gallic acid, butylated
14 hydroxytoluene, vitamin E, dioctyl phthalate, and pyrogallol failed to reduce TATP production
15 even when they were present in up to 30wt% concentration.
16
17

18
19 (2) Radical initiators (t-butyl peroxide, benzoyl peroxide, sodium persulfate, sodium bisulfite,
20 ammonium bisulfite, glycol sulfite, acetone sodium bisulfate) were added in an attempt to
21 destroy hydrogen peroxide before it reacted with acetone. None were successful.
22
23

24
25 (3) Catalytic decomposition of hydrogen peroxide and TATP can be achieved by some metal
26 salts; however, copper salts of nitrate, sulfate, acetate, and iodide; iron salts of acetylacetonate,
27 phosphate, chloride, phthalocyanine, and ferrocene; tin chloride; and zinc sulfate and chloride
28 did not reduce TATP formation, while copper chloride and bromide did.
29
30

31
32 (4) Molecules containing reactive bonds were added to offer hydrogen peroxide an alternative
33 site for reaction. Terephthalaldehyde, benzaldehyde, furfural, formaldehyde, ethyl propiolate, 2-
34 pentyn-1-ol, propargyl alcohol, methyl methacrylate, styrene, 5-vinyl-2-norbornene methacrylic
35 acid, isoprene, t, t-1,4-diphenyl-1,3-butadiene, isobutylene, 7,7,8,8-tetracyanoquinodimethane
36
37
38
39
40
41
42
43
44
45
46
47
48
49
50
51
52
53
54
55
56
57
58
59
60

1
2
3 failed to effectively compete with acetone when added at the 20wt% level. Only at 40wt% to
4
5 50wt% did these adulterants become effective.
6
7

8 (5) To compete with acetone for oxidation formamide, cyclohexanone, cyclopentanone, 2- and
9
10 3-pentanone, 2-butanone, 2,3- and 2,4-butanedione, benzil, 1,4-cyclohexanedione, and 2-
11
12 nonanone were added. At 20wt% they were slightly effective; to eliminate TATP formation they
13
14 needed to be present at 50wt%.
15
16

17 (6) Organic solvents (methanol, carbitol, ethylene glycol, diethyl ether, ethyl acetate, toluene,
18
19 and t-butanol) added to acetone at up to 50wt% did not prevent precipitation of TATP from
20
21 solution.
22
23

24 (7) Amines and other bases ammonium or potassium hydroxide, trimethyl- or triethyl-amine,
25
26 aniline, diaminopropane, diethylamine, diethylene triamine, ethylenediamine, hydrazine
27
28 monohydrate, phenyl hydrazine, diethyl- or diisopropyl-amine, piperidine, or pyridine
29
30 neutralized the acid catalyst [35]. They were effective at the 1wt% level in preventing TATP
31
32 formation. However, their effect was readily overcome by the addition of excess acid.
33
34 Furthermore, many amines are toxic and on a time-scale of months, react with acetone, even
35
36 when kept cold (-15°C).
37
38
39

40
41 Two type of adulterants were effective at reducing TATP formation—bases and iodide
42
43 species. Iodide is known to decompose hydrogen peroxide (Eq. 1) with iodide consumed at a
44
45 molar ratio of 3:1 (I^- : HP); bromide was known to react similarly [36,37]. Therefore, halide
46
47 salts [ammonium iodide (NH_4I), tetrabutylammonium iodide (TBAI),
48
49 methyltriphenylphosphonium iodide (MTPPI), potassium iodide (KI) and tetrabutylphosphonium
50
51 bromide (TBPBr)] and organic halides [diatrizoic acid ($C_{11}H_9N_2O_4I_3$), and N-bromosuccinimide
52
53 (NBS)] were used. Due to the high formula weight of iodine compounds, the molar ratio was
54
55
56
57
58
59
60

1
2
3 low. For example, with a 10wt% NH_4I solution, the molar ratio of I^- : HP was 1:29; however,
4 this was sufficient to disrupt the formation of TATP. Similar to amine adulterants, use of
5 increased acid catalyst could overcome the inhibitory effect of iodide on TATP production.
6 Furthermore, acetone solutions containing iodide salts, especially NH_4I , darken after a few
7 months storage, but the inhibiting effect of iodide was not diminished.
8
9
10
11
12
13

14 15 16 **4 Conclusion**

17
18 The reaction between hydrogen peroxide and acetone was investigated to identify
19 conditions that affect yield and purity of TATP and/or DADP. The molar ratio of HP to acetone
20 was able to be varied between 0.5:1 and 2:1 without yield being drastically affected. Reaction
21 temperature, reactant ratios to each other, and initial reactant concentrations affected overall
22 yield as well as the ratio of TATP to DADP produced. Analysis of reaction conditions was
23 complicated by the fact that both HP and sulfuric acid were aqueous. Some volume of solution
24 was required for TATP conversion to DADP. Figure 9 outlines reaction conditions to be selected
25 toward the desired product. Adulterating acetone to inhibit TATP formation was difficult to
26 achieve at low levels of adulterant. Some materials - amines, iodide salts, ketones, and metal
27 salts - showed promise, but either their toxicity or their adverse effect on solution stability would
28 be hindrances to their use, e.g. amines, iodide and metal salts. Low molecular weight ketones,
29 i.e. methyl ethyl ketone and 2-pentanone at relatively high adulterant concentration ($\geq 20\text{wt}\%$)
30 proved most effective, with no loss in stability and minimal increase in toxicity.
31
32
33
34
35
36
37
38
39
40
41
42
43
44
45
46
47
48
49
50
51
52
53
54
55
56
57
58
59
60

5 References

- [1] R. Wolffenstein, Action of Hydrogen Peroxide on Acetone and Mesityl Oxide, *Ber. Deut. Chem. Ges.*, **1895**, 28, 2265-9.
- [2] V. Egorshv, V. Sinditskii, S. Smirnov, E. Glinkovsky and V. Kuzmin, A Comparative Study on Cyclic Acetone Peroxides, *Proceedings of the 12th Seminar on New Trends in Research on Energetic Materials*, **2009**, 115-125, Pardubice, Czech Republic.
- [3] R. Meyer, J. Kohler and A. Homburg, *Explosives, Sixth, Completely Revised Edition*, Wiley-VCH Verlag GmbH, Weinheim, **2007**, p. 251 & 343.
- [4] R. Matyas, Influence of Oil on Sensitivity and Thermal Stability of Triacetone Triperoxide and Hexamethylenetriperoxide diamine, *Proc. of the 8th Seminar on New Trends in Research on Energetic Materials*, **2005**, 687-692, Pardubice, Czech Republic.
- [5] R. Matyas, J. Selesovsky, Power of TATP Based Explosives, *J. Haz. Mat.*, **2009**, 165, 95-99.
- [6] J. C. Oxley, J. L. Smith, K. Shinde, J. Moran, Determination of the Vapor Density of Triacetone Triperoxide (TATP) Using a Gas Chromatography Headspace Technique, *Propellants, Explos., Pyrotech.*, **2005**, 30, 127-130.
- [7] J. C. Oxley, J. L. Smith, W. Luo, J. Brady, Determining the Vapor Pressures of Diacetone Diperoxide (DADP), and Hexamethylene Triperoxide Diamine (HMTD), *Propellants, Explos., Pyrotech.*, **2009**, 34, 539-543.
- [8] R. B. Cundall, T. F. Palmer, C. E. C. Wood, Vapour Pressure Measurements on Some Organic High Explosives, *J. Chem. Soc. Faraday Trans.*, **1978**, 74(6), 1339-1345.
- [9] M. Costantini, *Destruction of Acetone Peroxides*, US Patent 5003109 **1991**, Rhone-Poulenc Chimie, Courbevoie, France.
- [10] F. Dubnikova, R. Kosloff, J. Almog, Y. Zeiri, R. Boese, H Itzhaky, A. Alt, E. Keinan, Decomposition of Triacetone Triperoxide is an Entropic Explosion, *J. Am. Chem. Soc.* **2005**, 127, 1146-1159.
- [11] L. Jensen, P.M. Mortensen, R. Trane, P. Harris, R. W. Berg, Reaction Kinetics of Acetone Peroxide Formation and Structure Investigations Using Raman Spectroscopy and X-Ray Diffraction, *Appl. Spectrosc.*, **2009**, 63(1), 92-97.
- [12] H. Jiang, G. Chu, H. Gong, Q. D. Qiao, Tin Chloride Catalyzed Oxidation of Acetone with Hydrogen Peroxide to Tetrameric Acetone Peroxide, *J. Chem. Res.*, **1999**, 4, 288-289.
- [13] C. M. Mateo, G. N. Eyler, E. E. Alvarez, A. I. Canizo, New Method for the Synthesis of Cyclic Acetone Triperoxide, *Informacion Tecnologica*, **1998**, 9(2), 19-22.

- 1
2
3 [14] R. Matyas, J. Pachman, Thermal Stability of Triacetone Triperoxide, *Sci. Technol. Ener. Mat.*, **2007**, 68, 111-116.
4
5
6
7 [15] R. Matyas, J. Pachman, Study of TATP: Influence of Reaction Conditions on Product
8 Composition, *Propellants, Explos., Pyrotech.*, **2010**, 35, 31-37.
9
10 [16] N. A. Milas, A. Golubovic, Studies in Organic Peroxides. XXVI. Organic Peroxides
11 derived from Acetone and Hydrogen Peroxide, *J. Am. Chem. Soc.* **1959**, 81, 6461-6462.
12
13 [17] L. C. Pacheco-Londono, A.J. Pena, O.M. Primera-Pedrozo, S.P. Hernandez-Rivera, N.
14 Mina, R. Garcia, R.T. Chamberlain, R.T. Lareau, An Experimental and Theoretical Study
15 of the Synthesis and Vibrational Spectroscopy of Triacetone Triperoxide (TATP),
16 *Proceedings of SPIE-The Int'l. Soc. Optical Engineering*, 403 (Pt. 1: Sensors and
17 Command, Control, Communications, and Intelligence (C31) Technologies for Homeland
18 Security and Homeland Defense III), **2004**, 279-287, Orlando, FL, USA.
19
20
21 [18] O. Reany, M. Kapon, M. Botoshansky, E. Keinan, Rich Polymorphism in Triacetone-
22 Triperoxide, *Cryst. Growth Des.*, **2009**, 9, 3661-3670.
23
24 [19] S. Zeman, W. A. Trzcinski, R. Matyas, Some Properties of Explosive Mixtures Containing
25 Peroxides Part I: Relative Performance and Detonation of Mixtures with Triacetone
26 Triperoxide, *J. Haz. Mat.*, **2008**, 154, 192-198.
27
28 [20] <http://www.totse.info/en/> - accessed June 20, 2011
29
30 [21] <http://www.shadowrx.com/forums/showthread.php?t=931> - accessed June 20, 2011
31
32 [22] http://www.roguesci.org/chemlab/energetics/acetone_peroxide.html-accessed June 20, 2011
33
34 [23] H. Schubert, A. Kuznetsov, *Detection of liquid explosives and flammable agents in*
35 *connection with terrorism*, Springer, The Netherlands, **2008**, p. 36.
36
37 [24] [http://articles.cnn.com/2002-01-07/us/reid.timeline_1_flight-crew-american-airlines-flight-](http://articles.cnn.com/2002-01-07/us/reid.timeline_1_flight-crew-american-airlines-flight-brixton-mosque?_s=PM:US)
38 [brixton-mosque?_s=PM:US](http://articles.cnn.com/2002-01-07/us/reid.timeline_1_flight-crew-american-airlines-flight-brixton-mosque?_s=PM:US), accessed June 20, 2011.
39
40 [25] www.justice.gov/opa/documents/zazi-detention-memo.pdf, accessed June 20, 2011
41
42 [26] [http://p10.hostingprod.com/@spyblog.org.uk/blog/2007/01/16/july-21st-2005-london-](http://p10.hostingprod.com/@spyblog.org.uk/blog/2007/01/16/july-21st-2005-london-bomb-attack-trial-hydrogen-peroxide-chapati-flour-tatp-det.html)
43 [bomb-attack-trial-hydrogen-peroxide-chapati-flour-tatp-det.html](http://p10.hostingprod.com/@spyblog.org.uk/blog/2007/01/16/july-21st-2005-london-bomb-attack-trial-hydrogen-peroxide-chapati-flour-tatp-det.html), accessed June 20, 2011
44
45 [27] <http://www.bbc.co.uk/news/world-europe-11345887>, accessed June 20, 2011
46
47 [28] http://www.masslive.com/localbuzz/index.ssf/2009/06/actionreaction_how_one_teens_c.html,
48 [accessed June 20, 2011](http://www.masslive.com/localbuzz/index.ssf/2009/06/actionreaction_how_one_teens_c.html)
49
50 [29] <http://homelandsecurityus.com/archives/1386>, accessed June 20, 2011.
51
52
53
54
55
56
57
58
59
60

- 1
2
3
4
5 [30] J. C. Oxley, J. Brady, S. A. Wilson, J. L. Smith, The Risk of Mixing Dilute Hydrogen
6 Peroxide and Acetone Solutions, *J. Chem. Health Safety*, **2011**, in press.
7
8 [31] W. C. Schumb, C. N. Satterfield, R. L. Wentworth, *Hydrogen Peroxide*, Reinhold
9 Publishing Corp, New York, **1955**, p. 269-270, 337-338, 467-500.
10
11 [32] L. R. Simpson, M. F. Foltz, *LLNL Small-Scale Drop-Hammer Impact Sensitivity Test*,
12 Report UCRL-ID-119665, **1995**, Lawrence Livermore National Lab, Livermore, CA.
13 [33] J.C. Oxley, J.L. Smith, E. Rogers, M.A. Hamad, E. Resende, Small Scale Explosivity
14 Testing, *J. Ener. Mat.*, **1999**, 17(4), 331-343.
15
16 [34] J.C. Oxley, J.L. Smith, E. Resende, Determining Explosivity Part II: Comparison of Smal-
17 Scale Cartridge Test to Actual Pipe Bombs, *J. For. Sci.*, **2001**, 46(5), 1070-1075.
18
19 [35] E.G.E. Hawkins, Reactions of Organic Peroxides. Part XII. Amino-peroxides from Acyclic
20 Carbonyl Compounds, *J. Chem. Soc (C)*, **1969**, 19, 2678-81.
21
22 [36] H. A. Liebafsky, A. Mohammed, The Kinetics of the Reduction, in Acid Solution, of
23 Hydrogen Peroxide by Iodide Ion, *J. Am. Chem. Soc.*, **1933**, 55 (10), 3977-3986.
24
25 [37] W. C. Bray, R. S. Livingston, The Catalytic Decomposition of Hydrogen Peroxide in the
26 Bromine-Bromide Solution, and a Study of the Steady State, *J. Am. Chem. Soc.*, **1923**, 45
27 (5), 1251-1271.
28
29
30
31
32
33

34 *Acknowledgements*

35 The authors wish to thank the Department of Homeland Security for funding via
36 Cooperative agreement # 2008-ST-061-ED000 through the University Programs Center of
37 Excellence as well as through the Science & Technology Division.
38
39
40
41
42
43
44
45
46
47
48
49
50
51
52
53
54
55
56
57
58
59
60

Table Captions

Table 1. TATP Characteristics

Table 2. Terrorist Use of Peroxide Explosives

Table 3. DSC Data; Ramp Rate: 20°C/min, 30-400°C

Table 4. Drop-Weight Impact (1.91kg weight used) and SSED Data

Table 5. Impact (4.3 kg) Sensitivity of Wetted TATP

Table 1. TATP Characteristics

	Sensitivity		Power		Vap. Pr. at 25°C (torr)
	Impact (J)	Friction (N)	Trauzl	Ballistic Mortar	
TATP	0.2 [2], 0.3 [3], 0.8 [4], 1.0 ^a	0.1 [3], 0.015 [4]	80% [3]	62% [5]	5×10^{-2} [6]
DADP	0.4 [2], 2.3 ^a	--	--	--	1.3×10^{-1} [7]
PETN	3 [3], 6 ^a	60 [3]	--	--	--
TNT	--	--	100%	100%	5.8×10^{-6} [8]

^a This Work

Table 2. Terrorist Use of Peroxide Explosives

Where:	Who:	What:	When:	Ref:
Flight to US	Reid	TATP initiator in "Shoe Bomb"	12/01	[24]
NY/Denver	Zazi	Collected HP as a precursor	~9/09	[25]
London	Group of 6	Subway attempt, TATP & HP/Fuel	7/05	[26]
Denmark	Dukayev	Attempted letter bomb, TATP	9/10	[27]
MA	Robison Jr.	Amateur Chemist, home-made TATP + Other Explosives seized	'07-'08	[28]
TX	Rugo	Killed while grinding TATP + metals	7/06	[29]

Table 3. DSC Data (ramp rate 20deg/min from 50 to 400°C)

Sample	% wt TATP	% wt DADP	# of Runs	DSC Events								
				TATP Melt			DADP Melt			Exotherm		
				Onset (°C)	Heat Absorbed (J/g)	Max Endo (°C)	Onset (°C)	Heat Absorbed (J/g)	Max Endo (°C)	Onset (°C)	Heat Released (J/g)	Max Exo (°C)
TATP	100	0	7	95	85	97	--	--	--	202	2511	239
75/25 TATP/DADP	82-86	14-18	2	77	93	81	--	--	--	207	2775	240
50/50 TATP/DADP	53-61	39-47	2	78	55	81	96	49	105	207	2809	242
25/75 TATP/DADP	37-59	41-63	3	82	98	85	--	62	112	197	3128	243
DADP	0	100	4	--	--	--	130	200	132	219	3253	251
0.1 : 1 (30wt%), 5°C	100	0	2	93	63	98	--	--	--	184	2904	228
0.1 : 1 (30wt%), 5°C	91	0	3	--	37	94	--	--	--	175	2669	235
0.4 : 1 (65wt%), 25°C	98	3	2	88	48	90	--	--	--	96	2822	108
0.8 : 1 (50wt%), 25°C	50	47	3	75	68	80	--	--	--	93	2594	133
0.8 : 1 (50wt%), 25°C	44	47	3	78	28	81	104	61	114	128	2905	147
1.0 : 1 (65wt%), 25°C	0.6	94	2	--	--	--	125	72	128	133	2564	142
1.2 : 1 (50wt%), 25°C	0.5	96	3	--	--	--	124	99	128	149	2844	154
1.8 : 1 (50wt%), 25°C	0.1	91	2	--	--	--	125	90	127	137	2947	141
20wt% 2-Pentanone	84	--	2	88	28	94	--	--	--	139	1220	153
20wt% 2-Butanone	68	--	3	76	42	83	--	--	--	123	1698	143
10wt% Formamide	97	--	2	87	61	98	--	--	--	209	1952	242

Table 4. Drop Weight Impact (1.91 kg) & SSED Data

Sample:	% TATP / % DADP by GC/ μ ECD	Melting Point $^{\circ}$ C	Impact h_{50} (cm)	SSED Data	
				Charge Wt (g)	% Base Rem.
Recrystallized TATP	98 / 0	95-96	5.3	0.7580	42%
75/25 TATP/DADP	86 / 18	74-87	6.0	--	--
50/50 TATP/DADP	53 / 39	77-106	3.4	--	--
25/75 TATP/DADP	37 / 41	83-122	7.6	--	--
Recrystallized DADP	0 / 84	131-133	12.5	1.2989	42%
TNT	--	--	--	2.0000	37%
PETN	--	--	33.7	2.0000	26%
HMTD	--	--	4.7	--	--
0.6:1 (65wt%), 5 $^{\circ}$ C	94 / 0.3	79-82	4.6	--	--
0.8:1 (50wt%), 5 $^{\circ}$ C	85 / 0.4	88-89	4.0	--	--
1.8:1 (50wt%), 25 $^{\circ}$ C	0.1 / 85	108-111	7.3	--	--

Table 5. Impact (4.3 kg) Sensitivity of Wetted TATP

Drop Weight (cm)	5	100	100	100	100	100	100
Additive	None	EtOH	EtOH/H ₂ O		Diesel	WD-40	Water
Additive (μL)	--	200	200	100	200	200	200
	FINE PARTICLES						
Trial							
1	G/NG	G/NG	NG	NG	NG	G?	G
2	G	NG	NG	NG	NG	NG	G
3	G	NG	NG	NG	NG	G?	G
4	NG	NG					
5	G	NG					
6	G	NG					
	COARSE PARTICLES						
Conditions	(a)	(a)	(c)	(b)	(c)	(c)	
(a) - wetted	G	G		G	G	G	
(b) - soaked 12h & wet		NG?	G		G	G	
(c) - soaked 12h & dry		G	G		G	G	

Figure Captions

Figure 1. % Yield vs. molar ratio of hydrogen peroxide to acetone

Figure 2. [HP] and Reaction Length Dependence of TATP Yield at 25°C

Figure 3. Temperature Dependence of TATP Yield

Figure 4. Effect of molar ratio of sulfuric acid to HP/acetone on overall yield of peroxide

Figure 5. Effect of Acid on TATP Formation

Figure 6. Effect of Acid on DADP Formation

Figure 7. % DADP and % Total Yield vs. molar ratio of sulfuric acid to HP (wt% HP indicated)

Figure 8. % Overall Yield & % DADP vs. water to sulfuric acid molar ratio for varying [HP]

Figure 9. Sulfuric Acid moles per kg water vs. HP moles per kg water – regions of DADP vs. TATP formation at 25°C

Scheme 1. Triacetone Triperoxide (TATP) and Diacetone Diperoxide (DADP)

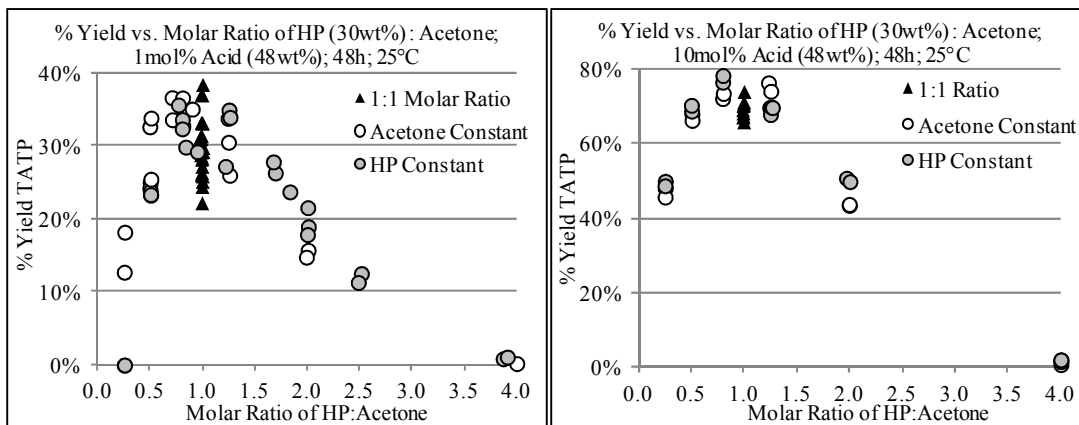
Figure 1. % Yield vs. molar ratio of hydrogen peroxide to acetone

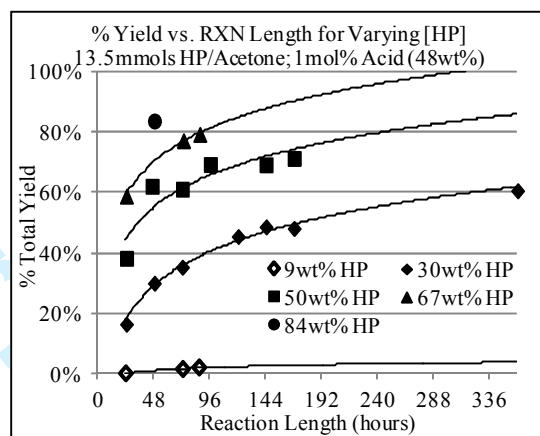
Figure 2. [HP] and Reaction Length Dependence of TATP Yield at 25°C

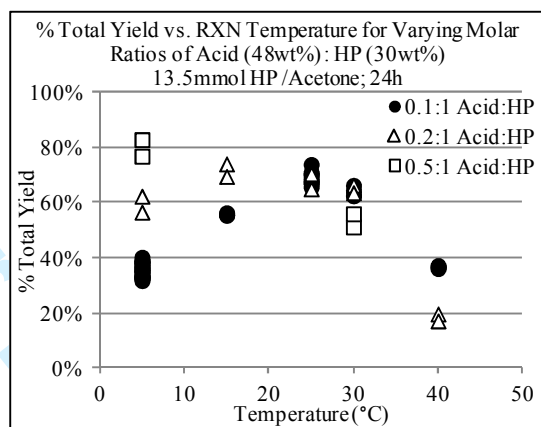
Figure 3. Temperature Dependence of TATP Yield

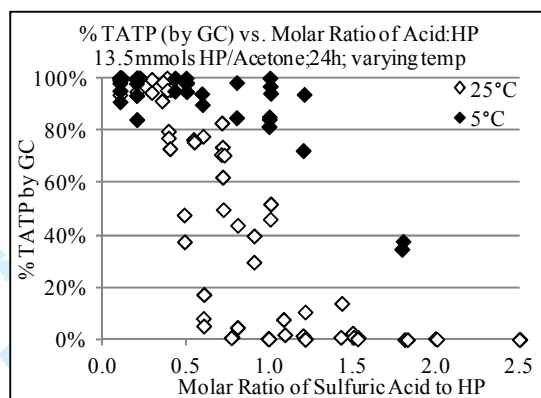
Figure 5. Effect of Acid on TATP Formation

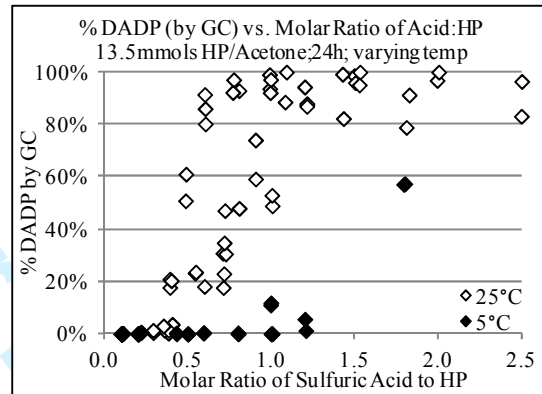
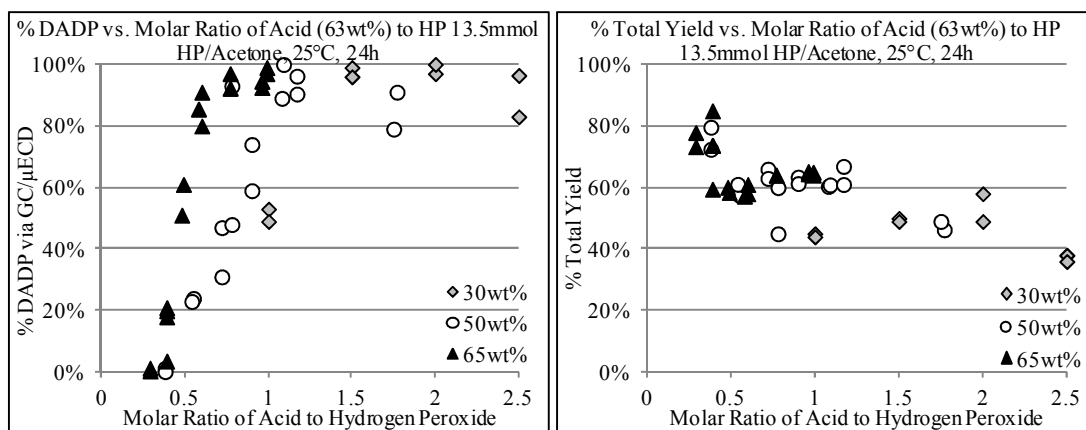
Figure 6. Effect of Acid on DADP Formation

Figure 7. % DADP and % Total Yield vs. molar ratio of sulfuric acid to HP (wt% HP indicated)

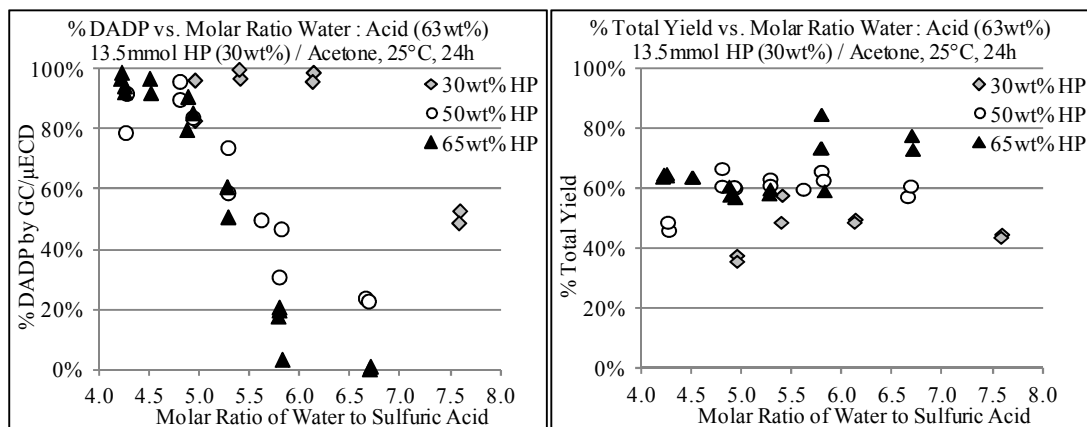


Figure 8. % Overall Yield & % DADP vs. water to sulfuric acid molar ratio for varying [HP]

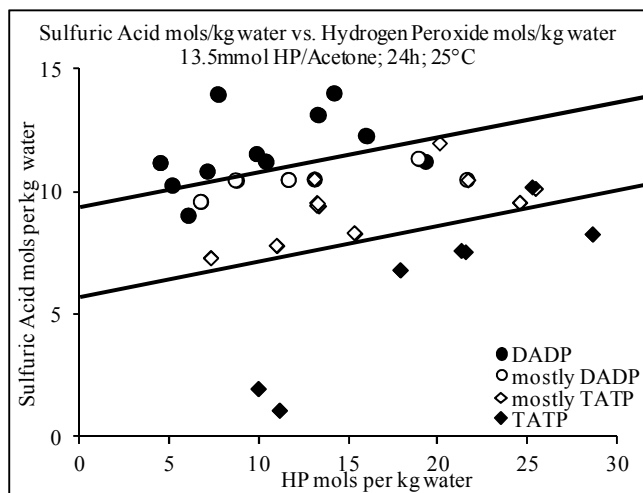
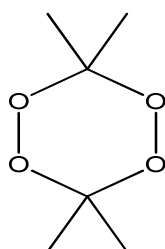
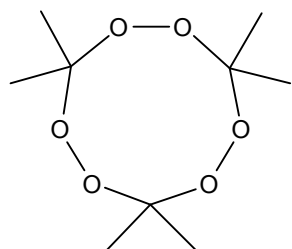


Figure 9. Sulfuric Acid moles per kg water vs. HP moles per kg water – regions of DADP vs. TATP formation at 25°C



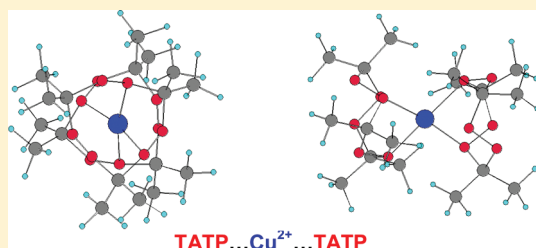
Scheme 1. Triacetone Triperoxide (TATP) and Diacetone Diperoxide (DADP)

For Peer Review Only

Role of Metal Ions in the Destruction of TATP: Theoretical Considerations

Faina Dubnikova,[†] Ronnie Kosloff,[†] Jimmie C. Oxley,[‡] James L. Smith,[‡] and Yehuda Zeiri^{*,§,||}[†]Institute of Chemistry, Hebrew University, Jerusalem, Israel[‡]Chemistry Department, University of Rhode Island, Kingston, Rhode Island 02881, United States[§]Chemistry Division, Nuclear Research Center—Negev, P.O. Box 9001 Beer-Sheva, 84190 Israel^{||}Biomedical Engineering, Ben-Gurion University, Beer-Sheva, 84105 Israel

ABSTRACT: The safe decomposition of solid TATP (triacetone triperoxide) explosive is examined theoretically. The route to destruction starts with formation of metal complexes between a metal ion and the TATP molecule. The second step is decomposition of the molecules into stable final products. We examined the structure and stability of both metal ion (including Na⁺, Cu⁺, Cu²⁺, Co²⁺, and Zn²⁺) and proton complexes with TATP using quantum chemical calculations at the DFT-PBE0 level of theory. In addition, for each ion complex, we determined the initial steps in the pathway to decomposition together with the associated transition states. We find that the products of decomposition, in particular, acetone, are also stabilized by ion metal complexes. In agreement with experiment, we find the best candidates for metal ion induced decomposition are Cu²⁺ and Zn²⁺.



I. INTRODUCTION

The chemistry of organic peroxides, which entails the synthesis, characterization, and transformation of derivatives of hydrogen peroxide, has a long history and strong tradition.^{1,2} The unusual reactivity of peroxides is generally attributed to weakness of the O–O bond; hence, this is the location where it is homolytically cleaved. Cyclic di- and triperoxides derived from aliphatic ketones are objects of numerous studies related to their application as initiators for the polymerization of vinyl monomers. Unfortunately, in high concentrations, the same materials have explosive properties.³

The structures, theoretical details, and properties of TATP and hexamethylene triperoxide diamine (HMTD) have been reported^{4–9} as have forensic issues, such as the analysis, detection, stability, and lab-scale destruction.^{10–18} Decomposition studies, both experimental and theoretical,^{10–18} have been performed at low heating rates (up to 20 K/min) and at isothermal conditions.^{19–23} Based on GC/MS results the dominant decomposition product of TATP is acetone, one of the starting materials of TATP synthesis,²⁰ and calculations by Dubnikova et al.²¹ and van Duin et al.²² confirm this product in the initial reaction pathway.

Terrorist use of peroxide-based explosives such as triacetone triperoxide (TATP) and hexamethylene triperoxide diamine (HMTD; Figure 1), either primaries or the main charge in improvised explosive devices (IED), continues to be of great concern.

For law enforcement agencies, the problems are detection and destruction. These problems are made acute by their extreme sensitivity. Currently, the safest way to dispose illegal explosives is to detonate them on the spot. This procedure safeguards the

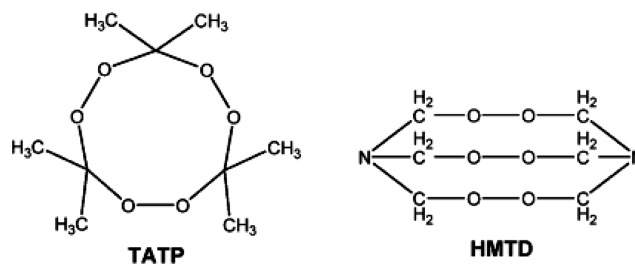


Figure 1. Molecular structures of TATP and HMTD.

law enforcement from handling and transporting these highly sensitive materials. However, in some instances, relatively large quantities (i.e., one kilogram or more) of peroxide explosives are discovered, located in apartments and other high-population density areas. Blow-in-place protocols are impractical in such situations. Hence, there is an urgent need for suitable protocols that will safely destroy large quantities of peroxide-based explosives.

Early work on TATP destruction¹⁶ demonstrated the decomposition of small amounts of TATP using SnCl₂ solutions in water together with organic solvents in an acidic environment. These procedures allowed destruction of TATP in the range of a few grams. In a recent study, the destruction of both TATP and HMTD were examined utilizing various metal ions in acidic water–organic solvent solutions as destroying agents.²⁴ It has

Received: March 7, 2011

Revised: August 11, 2011

been shown that both Zn^{2+} and Cu^{2+} ions in tetrahydrofuran (THF) under acidic conditions could lead to complete destruction of TATP and HMTD, but a large excess of ions was required for efficient destruction. Furthermore, destruction of a gram of TATP using concentrated sulfuric acid resulted in an explosion.

To support the experimental efforts to find a mode for gentle destruction of peroxide explosives on the hundreds of gram scale, we initiated a theoretical analysis of the interaction of various metallic ions with TATP. First, we calculated and reported the binding of various metal ions to TATP.²⁵ These quantum chemical calculations demonstrated that some metal ions bind to the TATP molecules to form complexes in which the TATP structure is not altered. However, a few ions bind to the TATP molecule and lead to destruction of the molecular ring. Other studies demonstrating the importance of the ion–TATP bond include those examining enhanced detection: the Na^+ –TATP interaction for electrospray ionization²⁶ and the use of Zn^{2+} -doped Titania nanocrystals.²⁷ The goal of the present work was to unravel detailed chemical decomposition pathways of TATP induced by different ions. It is based on accurate quantum chemical calculations. The calculations incorporate, in an approximate manner, the effect of solvent as well as acid. We believe that this study will provide a rational design of a more efficient and safe destruction method of TATP.

II. METHOD OF CALCULATIONS

The calculations were carried out using the density functional theory (DFT)-based method, as implemented in the Gaussian 03 package²⁸ with an appropriate basis set. The PBE1PBE hybrid density functional (also known as PBE0)^{29,30} was used in conjunction with the Dunning correlation consistent polarized valence double ξ (cc-pVDZ) basis set³¹ for C, O, H, and Na atoms. Because the bivalent ions (Cu^{2+} , Co^{2+} , Zn^{2+}) have large electron deficiencies we used effective core potential (ECP) in the Christiansen et al. large orbital basis, small core potential (CRENBL ECP).^{32–34} The same CRENBL ECP was used in the calculations related to the Cu^+ –TATP complex. The M06 hybrid functional of Truhlar and Zhao,³⁵ which is known as an appropriate functional for thermochemical, kinetics, and noncovalent interactions was also employed to carry out the calculations for some of the complexes examined. Comparison between the results obtained by the PBE1PBE and M06 functionals show that the differences in relative energies and in free energies are less than 1.5 kcal/mol. Because the use of the M06 functional is in many cases associated with significant convergence difficulties and a much larger computation time, we used PBE1PBE method in all the calculations reported below. The PBE1PBE functional yield reliable results and is quite economic in the computational time requirements for rather large molecular systems as those discussed below. The structures that had biradical character were located using the unrestricted uPBE1PBE wave function with the destructive α – β and spatial symmetry.

The vibrational analysis of the structures was performed at the same level of theory in order to characterize reliably the optimized structures either as local minima or transition states. All the calculated frequencies, the zero point energies, and the thermal energies correspond to harmonic approximation. The calculations of intrinsic reaction coordinates (IRC) using internal coordinates were performed in order to examine whether the transition states under consideration connect the expected reactants and products. These calculations were performed for all the

transition states at the PBE1PBE level of theory. The basis set used was the same as that used for the stationary point optimizations.

Adducts, consisting of two or more nearly separated species, along the decomposition pathways were identified and localized as local minima on the potential energy surface. The energy associated with these complexes did not include basis set superposition error (BSSE) correction. The value of this correction does not exceed 1 kcal/mol, so for our purpose, it does not have a significant importance.

Implicit solvent effect of the experimental THF (tetrahydrofuran) media has been taken into account via the self-consistent reaction field (SCRF) method using C-PCM polarizable conductor calculation model.^{36,37} Gas-phase-like optimized geometries (i.e., molecule without solvent effects) have been used in the single point calculations. In some cases, the full optimization procedure was performed in the solvent and the results compared with those obtained in the solvent-free molecular optimization. In most cases, optimized geometries and energies in the gas-phase-like system and in solvent were in excellent agreement. However, in the case of Cu^{2+} optimization in the solvent resulted in a complex where the TATP ring remains closed and has a slightly higher energy than obtained for gas phase optimization.

III. RESULTS

The first step in the destruction of any solid explosives is its transformation to a molecular form, namely, its dissolution. In the case of TATP, an organic solvent has to be used because the dissolution of TATP in water is very limited. Once the solid is dissolved, the explosive molecules are separated from one another and a chain reaction is much less likely to occur. Moreover, TATP solution is less hazardous to handle because individual molecules are widely separated and evolved heat can be absorbed. The calculations reported below are aimed at the understanding of this second step when metal ions are used to stabilize or transform the TATP molecules to nondetonable species. In a previous study it was shown that metal ions can either form a strongly bound ion–TATP complex or bind to segments of the TATP molecule after the ring shape is destroyed.²⁵ It is clear that the destruction of TATP and any other peroxide based explosive is associated with major alteration of the molecular structure to form decomposition products that are inert. Hence, a natural pathway to examine is the use of metallic ions that cause destruction of the ring structure upon binding to the TATP molecule.

We carried out a series of thorough quantum chemical calculations aimed at the understanding of the details of the ion–TATP complex formation and decomposition. In general, all the ions considered form stable complexes with TATP. Moreover, these ions tend to reduce the energy barrier required to initiate the decomposition of the complex. In this study we considered the following metallic ions: Cr^{3+} , Fe^{3+} , Cu^+ , Cu^{2+} , Zn^{2+} , Co^{2+} , and Na^+ . According to the calculations the first two ions when interacting with TATP open the molecular ring to form spontaneously very stable complexes of the ion bound to three acetone peroxides. We are interested in ions that remain as free ions after the destruction process is over; Cr^{3+} and Fe^{2+} were not considered farther. All the experimental TATP destruction studies^{16,24} were carried out in acidic environments; hence, the complex formed with H_3O^+ was also examined. Below we shall describe the interaction of each ion with a TATP molecule and point out the decomposition pathway of the complex. The calculations

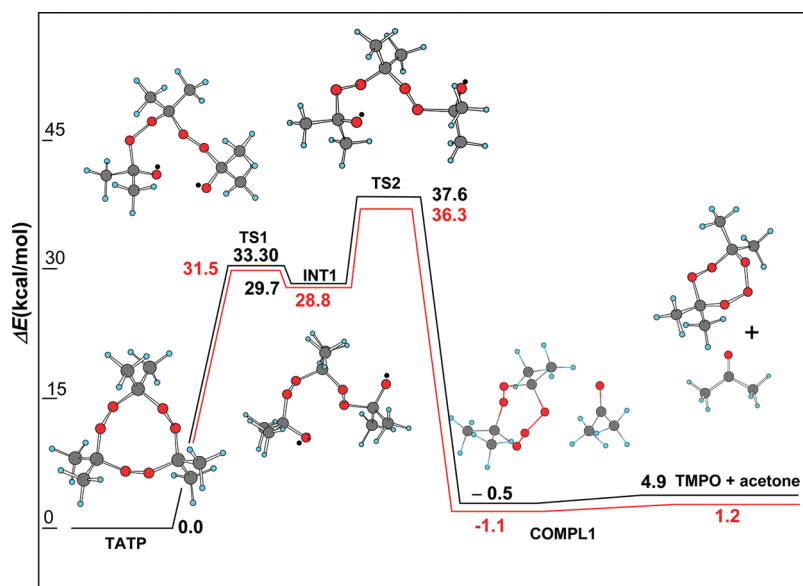


Figure 2. TATP decomposition pathway, black line represents an isolated molecule, while red line corresponds to a molecule dissolved in THF. TMPO means 4,4,7,7-tetramethyl-1,2,3,5,6-pentoxepane.

were carried out both for “gas phase” species as well as for solvated systems (see detailed description in the previous section).

1. TATP. We start with a short description of the decomposition pathway of a single TATP molecule. The initial stages of the decomposition are shown in Figure 2. The black lines show the decomposition of a single isolated TATP molecule while the red line represents the same process when the TATP is dissolved in tetrahydrofuran (THF).

Inspection of these results shows that the initial step in isolated TATP decomposition requires overcoming an energy barrier of 37.6 kcal/mol. This transition state (TS1) is associated with the opening of a peroxide bond. Once the system passed TS2 the molecule decomposes into an acetone molecule and the remaining fragment forms a seven member ring. The existence of a solvent does not change these steps substantially. The magnitude of TS1 and TS2 is slightly reduced but the structures and decomposition products remain the same. The results shown in Figure 2 agree well with those published in the past²¹ with small changes in the numerical values of TS1 and TS2 that are due to the use of a different functional in the present study.

2. Cu⁺–TATP Complex. The interaction between a Cu⁺ ion and a TATP molecule leads to the formation of a stable complex. The decomposition pathway is shown in Figures 3 (initial decomposition stages) and 4 (late decomposition stages).

Inspection of these results shows that formation of the ion–molecule complex lead to a marked reduction in the magnitude of the energy barrier associated with the first step in the decomposition process as compared to the free TATP molecule. The inclusion of solvent leads to a small additional reduction in the barrier size of about 10%. The initial decomposition step is still associated with rupture of a peroxide bond followed by a rearrangement of the molecular structure to form intermediate (INT1). It should be noted that the energy scale is related to the energy of Cu⁺–TATP complex whose energy is 66 kcal/mol below that of Cu⁺ + TATP. Thus, the binding energy of the copper ion to the TATP molecule is 66.2 kcal/mol in the gas phase and reduces to 36.2 kcal/mol for the dissolved complex in THF. The large influence of the THF solvent on the ion–molecule

binding is mainly due to the stabilization of the ion by the solvent molecules defined by eq 1

$$\Delta E_{\text{complex(gasphase-solvated)}} = 6.6(\Delta E_{\text{of TATP}}) + 65.0(\Delta E_{\text{of Cu}^+}) - 41.7(\Delta E_{\text{of TATP-Cu}^+ \text{ complex}}) \quad (1)$$

where $\Delta E_{\text{complex(gas phase-solvated)}} = 29.9$ [kcal/mol].

The intermediate undergoes further rearrangements that are related to two relatively low energy barriers (TS2 and TS3) followed by a large energy release when the Cu⁺ is bound to an eight-member ring on one side and to an acetone molecule in the other side (INT2). The C–O bond opening via TS3 results in some Cu peroxide–three-member ring (Cu–O–O) in INT3 and –O–(CH₃)₂C–O–O–C(CH₃)₂ fragment formation. The next O–O bond rupture leads to the elimination of an acetone molecule (TS4), together with the insertion of a methyl group into the neighboring O–O bond. Thus, instead of the –Cu–O–(CH₃)₂C–O–O–C(CH₃)₂ fragment seen in INT3, we observe the fragment –Cu–O–(CH₃)C–O–CH₃ and acetone molecule in COMPL1–Cu⁺. Endothermic behavior of the COMPL1–Cu⁺ complex to acetone ejection is much lower in the solvent than that in gas phase (i.e., 10.5 compared to 20.5 kcal/mol).

3. Na⁺–TATP Complex. The interaction between a Na⁺ ion and a TATP molecule leads to the formation of a stable complex whose decomposition route is shown in Figure 5. Inspection of these results shows that formation of the ion–molecule complex leads to a reduction in the magnitude of the energy barrier associated with the first step in the decomposition process of a TATP molecule. The reduction in the barrier height is similar to that obtained in the case of Cu⁺. The inclusion of solvent leads in this case to a small increase in the barrier size of TS1 and to a much larger increase for TS2 of about 30%. This different behavior of Na⁺ as compared to Cu⁺ is solvent-dependent. The initial decomposition step, TS1, is still associated with rupture of a peroxide bond followed by a rearrangement of the molecular structure to form INT1 followed by TS2. Note that in THF the stability of INT1 is much lower than that in the gas phase. It should be noted

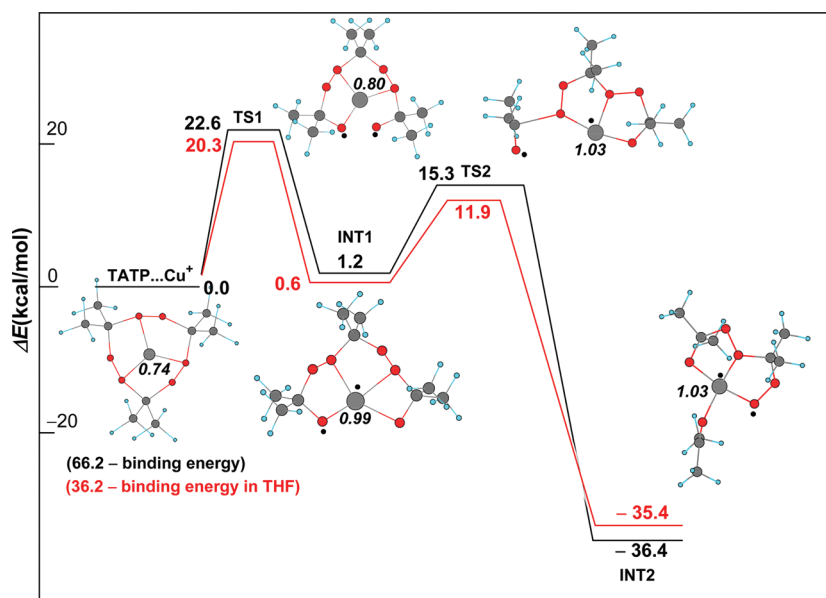


Figure 3. Initial stages of Cu^+ –TATP complex destruction pathway. The symbol \bullet represents the point of maximum spin density. The charge value (Mulliken) on Cu is presented by bold italic font. Black line shows the decomposition of a gas phase complex, while the red line shows the complex in THF.

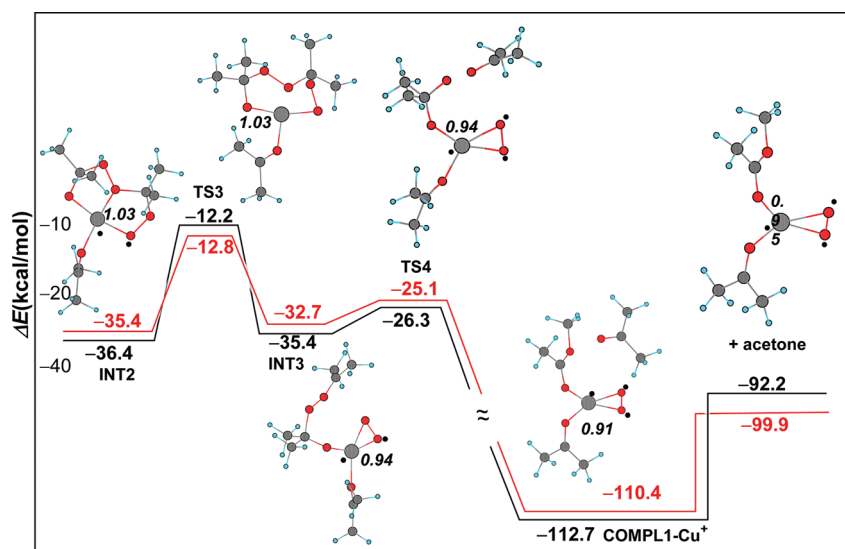


Figure 4. Late stages of Cu^+ –TATP complex destruction until the first acetone molecule is formed. The symbol \bullet represents the point of maximum spin density. The charge value (Mulliken) on Cu is presented by bold italic font. Black line shows the decomposition of a gas phase complex, while the red line shows a complex in THF.

that the energy scale is related to the energy of Na^+ –TATP complex whose energy is 45.2 kcal/mol below that of gas phase Na^+ + TATP and 9.1 kcal/mol below that of the solvated complex. Following TS2 there is further rearrangement to the second intermediate (INT2) in which the Na ion is part of a guarded eight-member ring on one side and bound to an acetone molecule in the other side. The deviation from the Cu^+ pathway is related to the fact that Na^+ has no possibility of forming multiple bonds with oxygen as transition metals can. The intermediate INT2 in Na^+ pathway is much less stable than INT2 in the case of Cu^+ . The formation of a free acetone molecule and an eighth member ring radical requires investment of less energy than in the case of Cu^+ (approximately 11 compared to 21 kcal/mol in

gas phase complexes and about 4 and 10 kcal/mol, respectively, in THF). The formation of a free acetone molecule and an eight-member ring radical is the end of the first stage of the complex decomposition.

4. Cu^{2+} –TATP Complex. The interaction between a Cu^{2+} ion and a TATP molecule leads to the formation of a stable complex whose decomposition pathway is shown in Figure 6. Inspection of these results shows that formation of the ion–molecule complex leads to a large reduction in the magnitude of the energy barrier associated with the first step in the decomposition process of the complex. The reduction in the barrier height in this case is larger than that observed for the singly charged ions described above. The inclusion of solvent leads here to an increase in the barrier

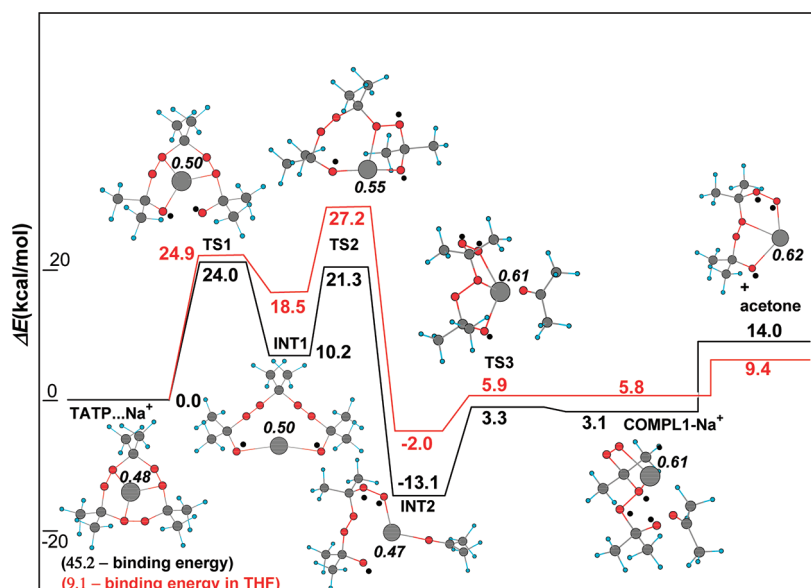


Figure 5. Initial stages of Na^+ –TATP complex destruction pathway. The symbol • represents the point of maximum spin density. The charge value (Mulliken) on Na is presented by bold italic font. Black line shows the decomposition of a gas phase complex, while the red line shows a complex in THF.

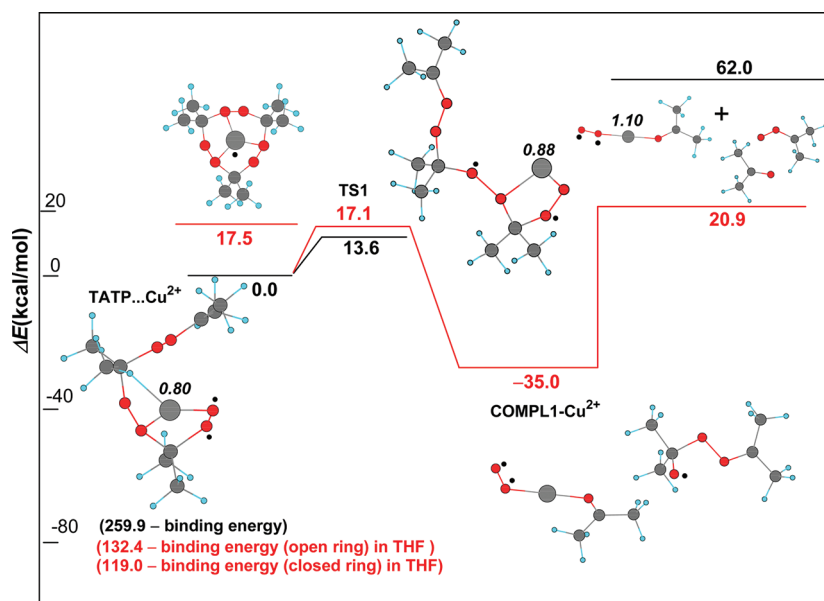


Figure 6. Stages in Cu^{2+} –TATP complex destruction. The symbol • represents the point of maximum spin density. The charge value (Mulliken) on Cu is presented by bold italic font. Black line shows the decomposition of a gas phase complex, while the red line shows a complex in THF. For the gas phase complex, no stable intermediate species could be identified between TS1 and the decomposition products, hence, such a state is missing in the figure.

magnitude of TS1 of about 25%. Another difference is that two stable species are formed upon binding of Cu^{2+} to TATP, a configuration where the metal ion is bonded to the whole molecule above the center of the TATP ring and the other that corresponds to binding of the ion to the TATP after one of the C–O bonds was ruptured. These two forms correspond to slightly different bond strengths (see Figure 6). Comparison between the ion–TATP binding in the gas phase and in the dissolved phase shows that existence of the THF solvent leads to a marked reduction in the binding energy, mainly due to the

stabilization of the ion by the solvent. This difference is calculated using eq 2

$$\Delta E_{(\text{gas phase-THF})} = 6.6(\Delta E_{\text{in TATP}}) + 258.6(\Delta E_{\text{in Cu}^{2+}}) - 143(\Delta E_{\text{in TATP-Cu}^{2+} \text{ complex}}) \quad (2)$$

thus, $\Delta E_{(\text{gas phase-THF})} = 122.3 \text{ kcal/mol}$.

The initial decomposition step, via TS1, is followed in this case by a large energy release, while COMPL1-Cu^{2+} is formed. The separation of the decomposition products is an endothermic

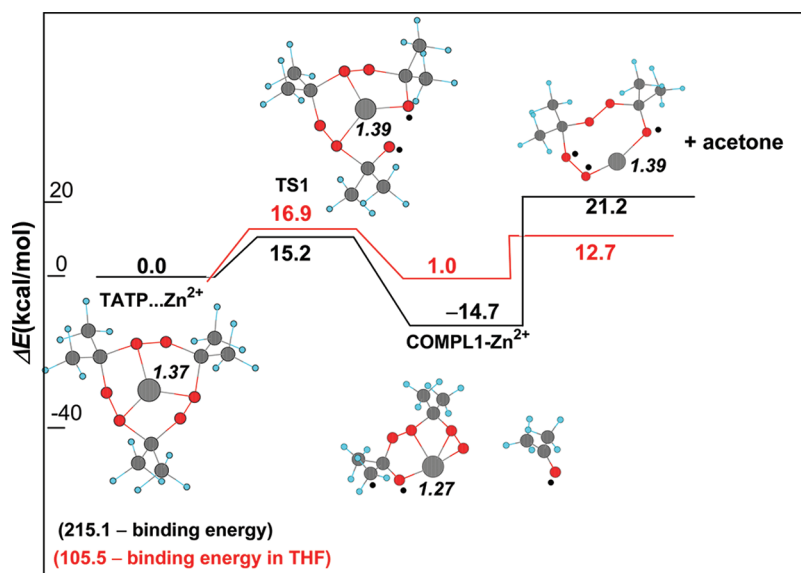


Figure 7. Stages in Zn^{2+} –TATP complex destruction. The symbol • represents the point of maximum spin density. The charge value (Mulliken) on Zn is presented by bold italic font. Black line shows the decomposition of a gas phase complex, while the red line shows that of a complex in THF.

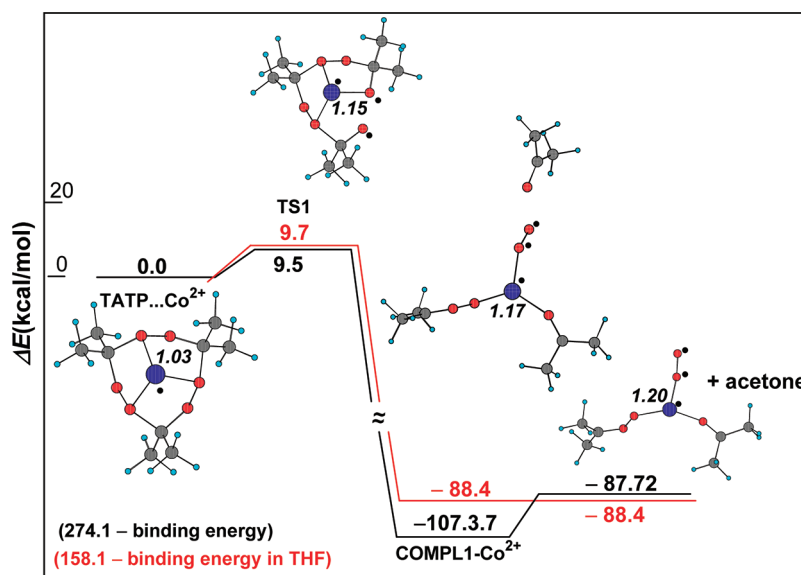


Figure 8. Stages in Co^{2+} –TATP complex destruction. The symbol • represents the point of maximum spin density. The charge value (Mulliken) on Co is presented by bold italic font. Black line shows the decomposition of a gas phase complex, while the red line shows that of a complex in THF.

process. The final products obtained in this part of the decomposition route are an acetone molecule, an acetone peroxide, and an acetone bonded to the metal ion on one side with a peroxide on the other side of the ion. It should be noted that there is a very large difference in the endothermicity of this last stage when comparing gas phase and solvated systems. The decomposition in THF corresponds to a much lower endothermicity value (see Figure 6).

5. Zn^{2+} –TATP Complex. The interaction between a Zn^{2+} ion and a TATP molecule leads to formation of a stable complex; its decomposition pathway is shown in Figure 7 below. The formation of the ion–molecule complex leads to a large reduction in the magnitude of the energy barrier associated with the first step in the decomposition process of the complex. The reduction in the barrier height is larger than that observed for the singly

charged ions and similar to that observed for Cu^{2+} . The inclusion of solvent leads, to a small increase of the energy barrier corresponding to TS1. Comparison between the ion–TATP binding in the gas phase and in the dissolved phase shows that existence of the THF solvent leads to a marked reduction in the binding energy, mainly due to the stabilization of the ion by the solvent. This is similar to the stabilization of Cu^{2+} . This difference is clearly seen in Figure 7.

The initial decomposition step, via TS1, is followed by a much smaller energy release while in COMPL1-Zn^{2+} . Here too the separation of the decomposition products is endothermic. The final products obtained in this part of the decomposition pathway are an acetone molecule and an eight-member ring species that contains the metal ion. It should be noted that the difference in

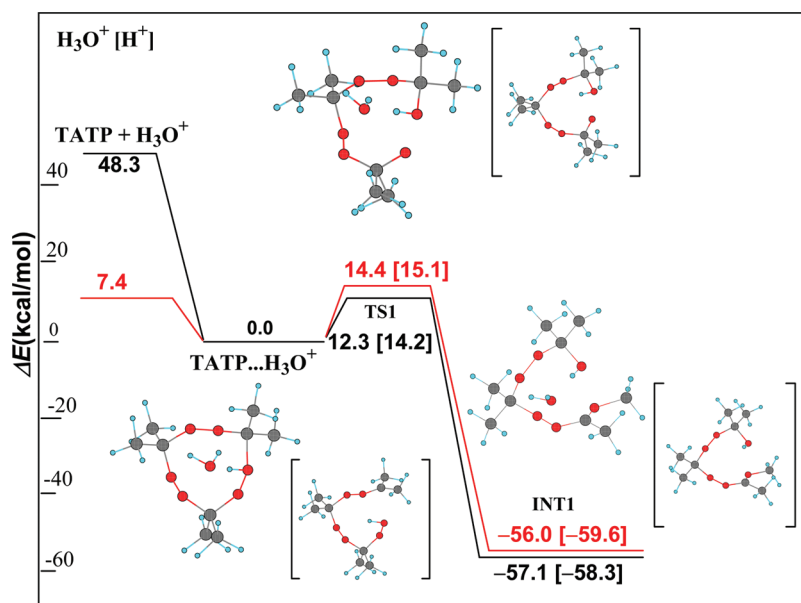


Figure 9. Stages in $\text{H}_3\text{O}^+ - \text{TATP}$ and $\text{H}^+ - \text{TATP}$ complexes destruction. The symbol \bullet represents the point of maximum spin density. Black line shows the decomposition of a gas phase complex, while the red line shows that of a complex in THF. Values in brackets represent the $\text{H}^+ - \text{TATP}$ decomposition pathway.

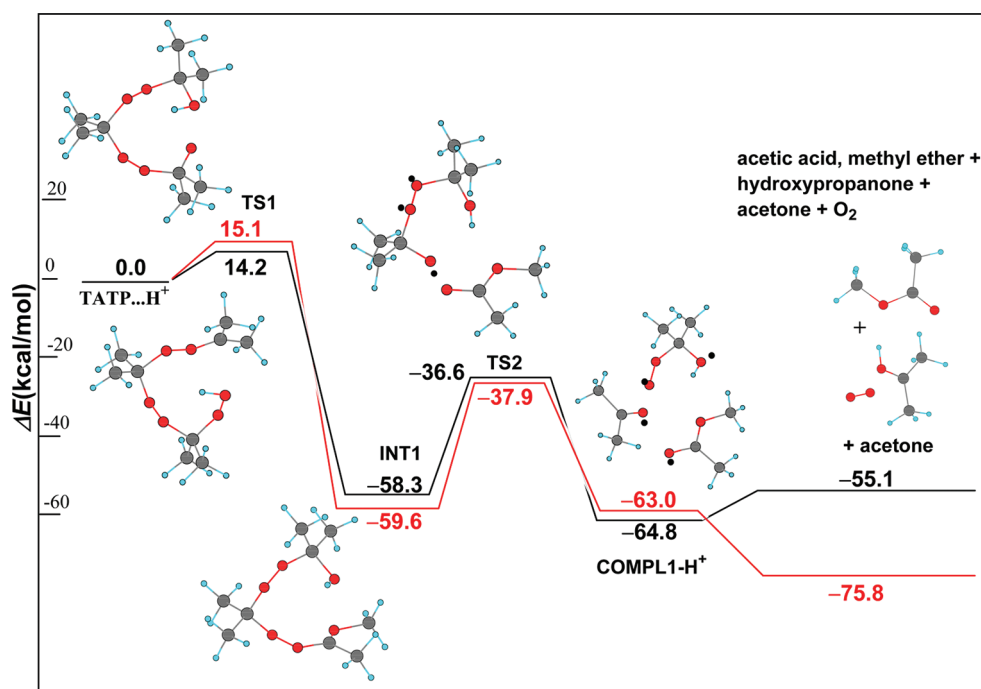


Figure 10. Stages in $\text{H}^+ - \text{TATP}$ complex destruction. The symbol \bullet represents the point of maximum spin density. Black line shows the decomposition of a gas phase complex, while the red line shows that of a complex in THF.

the endothermicity of this last stage when comparing gas phase and solvated systems is reduced for Zn^{2+} as compared to Cu^{2+} . The decomposition in THF corresponds to a lower endothermicity value, see Figure 7.

6. $\text{Co}^{2+} - \text{TATP}$ Complex. The interaction between a Co^{2+} ion and a TATP molecule leads to the formation of a stable complex whose decomposition pathway is shown in Figure 8 below. The formation of the ion–molecule complex leads to a marked reduction in the magnitude of the energy barrier associated with

the first step in the decomposition process of the complex. The reduction in the barrier height is larger than that observed for the ions discussed above. The inclusion of solvent, in this case, does not alter the magnitude of the energy barrier associated with TS1. Following TS1, one of the O–O bonds opens and an acetone molecule starts to separate from the rest of the complex. This step is associated with a large energy release on the order of 100 kcal/mol. The exothermicity of the first stage in the decomposition process, once the acetone separates from the metal

containing the intermediate biradical, is about 90 kcal/mol. This value seems to be independent of the existence of the THF solvent.

7. H_3O^+ –TATP Complex. Because the experimental studies were performed in highly acidic environments,^{16,24} we examined the complexes formed between TATP and a proton. The complex formed between H^+ and a TATP molecule is compared to that formed with H_3O^+ and TATP in Figures 9 and 10. As demonstrated in Figure 9, the H_3O^+ binds to the molecule above the center of the TATP ring by a strong bond in the gas phase that is reduced by a factor of approximately 7 in the solvent. In contrast, inspection of Figure 10 shows that the proton binds to the TATP molecule at one of the oxygen atoms of a peroxide bond following a rupture of a C–O bond. Hence, the H^+ –TATP complex has a structure in which the molecular ring opens. The structure obtained in this case is basically identical to the TS1 in the case of the H_3O^+ –TATP complex, Figure 9. The additional steps to complete the decomposition process for both ions are to a good approximation identical. The magnitude of the energy barrier leading to TS1 (see Figure 9) is very small and it increases by about 15% when a solvated complex is considered. Similar to the case of Cu^{2+} , following TS1 there is a large energy release during relaxation of the structure in the intermediate INT1. The

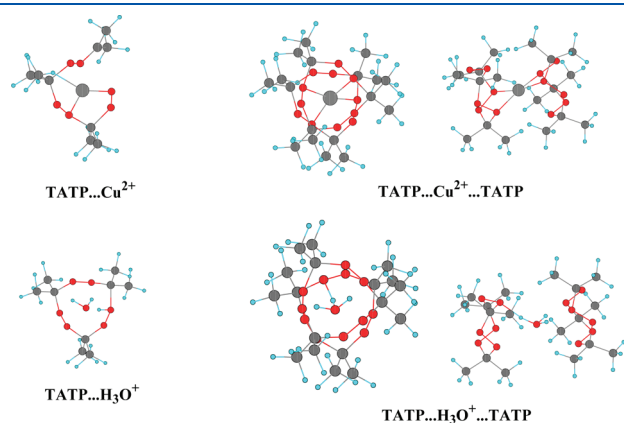


Figure 11. Optimized structures of ion–TATP (left column) and TATP–ion–TATP (right set of four pictures) complexes for Cu^{2+} and H_3O^+ . In the case of sandwich-type complexes, the right column corresponds to the side view, while the left column corresponds to the top view.

amount of energy release is clearly seen in Figures 9 and 10. The steps in the decomposition process following this relaxation step are shown in Figure 10.

Rupture of a peroxide bond proceeds in a second transition state structure (TS2) that is a precursor to further decomposition into a complex that is constituted from an acetone molecule and two smaller radicals. The separation of the decomposition products constitutes an endothermic process. The final products obtained at the end of this part of the decomposition path are an acetone molecule, an oxygen molecule, a hydroxypropanone and acetic acid methyl ester. The separation of these decomposition products is slightly endothermic in the gas phase but it becomes exothermic when system is solvated (Figure 10).

The stability of the ion–TATP complex is enhanced markedly if the cation is sandwiched between two TATP molecules. Such optimized complexes are shown in Figure 11 for Cu^{2+} and H_3O^+ . The sandwich type complexes turn out to be much more stable than the ion–TATP complexes. In the case of Cu^{2+} , the ion leads to opening of the TATP ring when a single molecule participates in the complex, while in the TATP–ion–TATP case, both molecules in the complex have closed rings. It is also easy to see that, in the case of the hydronium ion, the nature of bonding is quite different between single and two TATP complexes. A more detailed comparison between a single and two TATP complexes with the different ions is shown in Table 1. The data clearly shows that formation of a sandwiched ion by two TATP molecules is much more stable than a complex with a single TATP. The increase in stability varies from one ion to another, but in most cases, we find a 30% increase or more. This pattern is true for both gas phase and solvated (i.e., THF) complexes. The only system for which a decreased stability is obtained is for the sandwich complex of Cu^{2+} in THF that is less stable than the Cu^{2+} –TATP complex. Inspection of Table 1 shows that, in all cases, the O–O and C–O distances in the sandwiched ions is shorter than that in the ion–single TATP complexes. Hence, the related bond energies in the sandwiched ions are larger and the corresponding transition state energies are expected to increase compared to the single TATP complexes. The higher stability of the sandwiched complexes together with the larger barriers for decomposition makes these species less favorable to be good initial candidates for TATP destruction. Consequently, the decomposition pathways of the sandwiched ions were not considered.

Table 1. Comparison of Geometries and Energetics of Single and Double TATP Complexes

	number of TATP molecules	binding energy		TS1		$R_{\max}(\text{O}-\text{O})$	$R_{\max}(\text{C}-\text{O})$	$R_{\min}(\text{Cat}-\text{O})$
		gas phase	THF	gas phase	THF			
no ion				33.3	31.5	1.433	1.412	2.338
Na^+	1-TATP	43.8	9.1	24.0	24.9	1.440	1.434	2.338
	2-TATP	73.6	17.9			1.439	1.429	2.457
Cu^+	1-TATP	66.2	36.2	22.6	20.3	1.442	1.445	2.156
	2-TATP	96.6	54.3			1.440	1.433	2.332
Cu^{2+}	1-TATP	264.5	136.1	13.6	17.1	1.448	1.560	1.984
	2-TATP	310.4	81.4			1.450	1.506	2.016
Zn^{2+}	1-TATP	218.2	105.5	15.2	16.9	1.453	1.497	1.987
	2-TATP	292.3	181.2			1.448	1.459	2.188
Co^{2+}	1-TATP	274.1	158.1	9.7	9.5	1.461	1.556	1.862
	2-TATP	351.1	200.3			1.456	1.514	1.972
H_3O^+	1-TATP	48.4	7.4	12.3	14.4	1.441	1.544	$\text{O}_{\text{TATP}}-\text{H}$ 1.001 and $\text{O}_{\text{H}_3\text{O}}-\text{H}$ 1.366
	2-TATP	68.9	17.1			1.440	1.456	$\text{O}_{\text{TATP}}-\text{H}$ 1.624 and $\text{O}_{\text{H}_3\text{O}}-\text{H}$ 1.023

Table 2. Main Energetic Features of the Decomposition of Ion–TATP Complexes (Solvated)^a

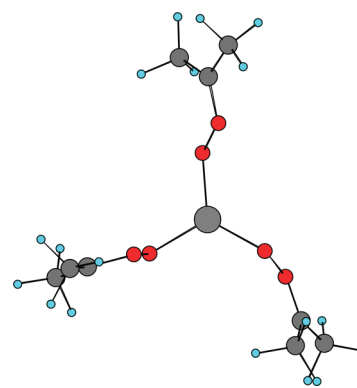
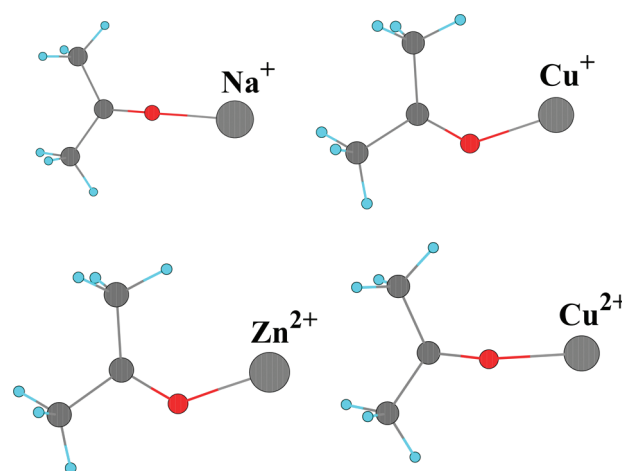
ion	complex stability	barrier height	energy release	energy release to separated products
no ion	0.0	36.3	−1.1	1.2
Cu ¹⁺	36.2	20.3	−35.4	−99.9
Na ¹⁺	9.1	27.2	−2.0	9.4
Cu ²⁺	119.0 (132.4 ^b)	17.1	−35.0	20.9
Zn ²⁺	105.5	16.9	1.0	12.7
Co ²⁺	158.1	9.7	−88.4	−88.4
H ₃ O ¹⁺ (H ¹⁺)	7.4	14.4 (15.1)	−56.0 (−59.6)	−75.8

^aThe second column describes ion–TATP binding energy; third column, the main energy barrier for decomposition; fourth column, the energy release following TS structure relaxation; fifth column, the net energy release following decomposition products separation. All values correspond to solution in THF. Energy values in columns 3–5 are relative to the energy of ion–TATP in THF. Energy units are kcal/mol. ^bStabilization energy for ion–TATP complex in which molecular ring is open.

IV. DISCUSSION AND CONCLUSIONS

If an explosive is diluted with a nonexplosive, its power is depleted. The exact amount of diluents required depends on the particular explosive/diluent considered. For example, commercial nitroglycerin is shipped 50% in acetone. TATP is a hydrophobic molecule, hence, its molecular crystal is poorly soluble in water. TATP destruction methods, published to date, involved the dissolution of TATP. The assumption was that the reaction is less violent with dilute TATP as discussed above. Ref 24 demonstrated effective TATP destruction in THF and ethanol acidic solutions of various metal ions. The enthalpy of TATP sublimation is 17.34 kcal/mol.³⁸ Moreover, electronic structure calculations suggest that the dissolution energy of TATP molecules in THF is practically zero. Because TATP dissolves well in THF, the entropy term has to be the driving force of the dissolution process. The magnitude of the sublimation entropy can be estimated from the pre-exponential term in the Arrhenius curve for TATP in ref 38 to be 62.4 cal mol^{−1} K^{−1}. Hence, at room temperature, the free energy of sublimation is approximately −2.0 kcal/mol and it increases for elevated temperatures. According to the results presented in Table 2, the formation of stable ion–TATP complexes reduces markedly the dissolution enthalpy. Hence, assuming only a small change in the entropy term, one expects that ion–TATP complex formation will increase the stability of the solution. The experiments suggest that a high ratio of ions to TATP molecules is required. This can be rationalized by moving the equilibrium to the solution of TATP complexed ions. A second possibility for the role of the ions is the weakening of the van der Waals forces by the strong salt effect. Furthermore, as will be discussed below, ion complexes may have an important role in the stabilization of TATP decomposition products.

Once the molecular crystal has dissolved, the second step is the decomposition of the ion–molecule complex in solution. Because the production of TATP is catalyzed by acids, a strongly acidic environment has been suggested and employed.²⁴ Metal ions are also known to catalyze the destruction.^{24,25} The detailed mechanism of the ion–TATP decomposition process was the main interest in the present study. As already reported pre-

**Figure 12.** Minimum energy structure of the complex between Cr³⁺ and the three acetone peroxides formed by TATP ring-opening.**Figure 13.** Structure of the complexes formed between acetone and the different ions.**Table 3. Binding Energies and Relative Stabilities of Various Ion–Acetone Complexes^a**

	H ₃ O ⁺	Na ⁺	Cu ⁺	Cu ²⁺	Zn ²⁺	Co ²⁺
R(O–ion) (Å)		2.123	1.881	1.909	1.873	1.834
ΔE ^b (gas phase)	26.9	36.1	54.5	188.4	149.9	212.4
ΔE ^b (THF)	5.8	12.1	34.6	109.4	86.2	137.7

^aEnergy units are kcal/mol. ^bΔE = (E_{acetone} + E_{cation}) – E_{acetone·cation}.

viously,²⁵ some ions form a complex with TATP without altering drastically the molecular structure, while other ions bind to TATP to form charged complexes while rupturing one or more molecular bonds during the complex formation. For the destruction of large TATP quantities, one would like to use the metal ions as catalysts in the destruction process. Otherwise, if the metal ions bond irreversibly to the TATP, vary large quantities of metal ion solutions will be required in the destruction process. Hence, metal ions that lead to the destruction of the TATP ring structure while forming highly stable complexes were not considered here. For this reason, we did not include in the present investigation ions such as Fe³⁺ and Cr³⁺ that spontaneously form highly stable charged complexes of the metal bound to three acetone peroxides, as shown in Figure 12 for Cr³⁺.

The initial steps of the complex decomposition process have common stages for all ions considered here. The first step in the process is to overcome an energy barrier associated with the rupture of a peroxide bond or a C–O bond. The magnitude of this energy barrier dictates the rate of the decomposition initiation. Once the system overcame this energy barrier, the rearrangement of the transition state geometry leads to an energy release. This energy release can lead to an efficient and rapid decomposition process. The next step along the decomposition path is the rupture of one or more additional bonds in the complex and its separation into decomposition products. The energy release and the separation into decomposition products stages may be separated by one or more transition states and intermediates that vary from one ion to another. A summary of the different energy values associated with the various decomposition steps studied here are presented in Table 2.

Inspection of the data in Table 2 shows that the stability of the TATP complex with singly charged ions is smaller by a factor of 3–12 than that of doubly charged ions. This significant stabilization energy of the Cu^{2+} –, Co^{2+} –, and Zn^{2+} –TATP complexes suggest that these ions may have an important role in the dissolution process of the TATP crystals. All ions examined in this study reduce markedly the magnitude of the main energy barrier that controls the initial decomposition step. It is clear that the three doubly charged ions and the hydronium ion lead to energy barriers that are less than half of that in the bare molecule. The decreased energy barriers are expected to result in a very large increase in the rate of the decomposition process.

However, an increased decomposition rate may lead to a violent autocatalytic reaction if it is highly exothermic. The fourth column in Table 2 shows that the hydronium ion as well as Cu^+ , Cu^{2+} , and Co^{2+} complexes with TATP lead to marked energy release, while initial steps along the decomposition path of Zn^{2+} are basically thermoneutral. Once final separated decomposition products are reached Zn^{2+} –TATP is also mildly exothermic. The large energy release together with relatively small energy barrier for decomposition in the case of Co^{2+} , Cu^+ , and H_3O^+ can lead to detonation of the explosive when the destruction of large quantities are required. Experimental evidence related to TATP destruction with pure acids shows samples of gram size detonate, see discussion above. The relatively large energy barrier for initial decomposition in the case of Na^+ is probably the reason why this ion did not show good decomposition ability in the experiments. To summarize, the analysis of the results obtained in the present study suggest that Cu^{2+} and Zn^{2+} are the two best candidates to be used in safe TATP destruction. This finding is in good agreement with the experimental data.

The requirement for high ion concentration in the solution (both metal ions as well as H^+) may be related to an additional aspect, the stabilization of decomposition intermediates. In all decomposition routes discussed in this work, the first stable product formed is acetone. However, in most cases, additional nonstable intermediates are also obtained. Some of these intermediates are charged, due to the incorporation of the metal ion, but some are nonionic radicals. It is possible that existence of ions in the solution may stabilize these intermediates. For example, ions can form stable complexes through bonding to the oxygen end of the acetone molecule, hence, forming a stable ion–acetone complex. The structure of such complexes is shown in Figure 13. The ion–O distances together with the binding energies and relative stabilities of the various ion–acetone complexes are summarized in Table 3.

ACKNOWLEDGMENT

Work supported by The Center of Excellence for Explosives Detection, Mitigation, and Response, Department of Homeland Security.

REFERENCES

- (1) See for example: (a) McCullough, K. J.; Morgan, A. R.; Nonhebel, D. C.; Pauson, P. L.; White, G. J. *J. Chem. Res. Synop.* **1980**, 34–34. (b) McCullough, K. J.; Morgan, A. R.; Nonhebel, D. C.; Pauson, P. L. *Ibid.* **1980**, 36–37.
- (2) Adam, W.; Hadjiarapoglou, L. P.; Curci, R.; Mello, R. In *Organic Peroxides*; Ando, W., Ed.; John Wiley and Sons: Chichester, England, 1992; Chapt. 4.
- (3) Eyler, G. N.; Mateo, C. M.; Alvarez, E. E.; Canizo, A. I. *J. Org. Chem.* **2000**, *65*, 2319–2321.
- (4) Yavari, I.; Hosseini-Tabatabaei, M. R.; Nasiri, F. *J. Mol. Struct.* **2001**, *538*, 239–244.
- (5) Jubert, A. H.; Pis Diez, R.; Castro, E. A.; Canizo, A. I.; Cafferata, L. F. R. *J. Raman Spectrosc.* **1999**, *30*, 45–51.
- (6) Schaefer, W. P.; Fourkas, J. T.; Tiemann, B. G. *J. Am. Chem. Soc.* **1985**, *107*, 2461–2463.
- (7) Edward, J. T.; Chubb, F. L.; Gilson, D. F. R.; Hynes, R. C.; Sauriol, F.; Wiesenthal, A. *Can. J. Chem.* **1999**, *77*, 1057–1065.
- (8) Wierzbicki, A.; Cioffi, E. *J. Phys. Chem. A* **1999**, *103*, 8890–8894.
- (9) Wierzbicki, A.; Salter, E. A.; Cioffi, E.; Stevens, E. D. *J. Phys. Chem. A* **2001**, *105*, 8763–8768.
- (10) Schulte-Ladbeck, R.; Karst, U. *Anal. Chim. Acta* **2003**, *482*, 183–188.
- (11) Fialkov, A. B.; Gordin, A.; Amirav, A. *J. Chromatogr., A* **2003**, *991*, 217–240.
- (12) Schulte-Ladbeck, R.; Kolla, P.; Karst, U. *Anal. Chem.* **2003**, *75*, 731–735.
- (13) Oxley, J.; Zhang, J.; Smith, J. *Propellants, Explos., Pyrotech.* **2000**, *25*, 284–287.
- (14) Schulte-Ladbeck, R.; Kolla, P.; Karst, U. *Analyst* **2002**, *127*, 1152–1154.
- (15) Buttigieg, G. A.; Knight, A. K.; Denson, S.; Pommier, C.; Denton, M. B. *Forensic Sci. Int.* **2003**, *135*, 53–59.
- (16) Bellamy, A. J. *J. Forensic Sci.* **1999**, *44*, 603–608.
- (17) Hiyoshi, R. I.; Nakamura, J.; Brill, T. B. *Propellants, Explos., Pyrotech.* **2007**, *32*, 127–134.
- (18) Pachman, J.; Matyas, R. *Forensic Sci. Int.* **2010**, doi: 10.1016/j.forsciint.2010.10.010.
- (19) Eyler, G. N. *J. Phys. Org. Chem.* **2006**, *19*, 776–779.
- (20) Oxley, J. C.; Smith, J. L.; Chen, H. *Propellants, Explos., Pyrotech.* **2002**, *27*, 209–216.
- (21) Dubnikova, F.; Kosloff, R.; Almog, J.; Zeiri, Y.; Boese, R.; Itzhaky, H.; Alt, A.; Keinan, E. *J. Am. Chem. Soc.* **2005**, *127*, 1146–1159.
- (22) van Duin, A. C. T.; Zeiri, Y.; Dubnikova, F.; Kosloff, R.; Goddard, W. A. *J. Am. Chem. Soc.* **2005**, *127*, 11053–11062.
- (23) Oxley, J. C.; Smith, J. L.; Chen, H.; Cioffi, E. *Thermochim. Acta* **2002**, *388*, 215–225.
- (24) Oxley, J. C.; Smith, J. L.; Huang, J. R.; Luo, W. *J. Forensic Sci.* **2009**, *54*, 1029–1033.
- (25) Dubnikova, F.; Kosloff, R.; Zeiri, Y.; Karpas, Z. *J. Phys. Chem. A* **2002**, *106*, 4951–4956.
- (26) Cotte-Rodriguez, I.; Hernandez-Soto, H.; Chen, H.; Cooks, R. G. *Anal. Chem.* **2008**, *80*, 1512–1519.
- (27) Banerjee, S.; Mohapatra, S. K.; Misra, M.; Mishra, I. B. *Nanotechnology* **2009**, *20*, 1–6.
- (28) Frisch, M. J.; Trucks, G. W.; Schlegel, H. B.; Scuseria, G. E.; Robb, M. A.; Cheeseman, J. R.; Montgomery, J. A., Jr.; Vreven, T.; Kudin, K. N.; Burant, J. C.; Millam, J. M.; Iyengar, S. S.; Tomasi, J.; Barone, V.; Mennucci, B.; Cossi, M.; Scalmani, G.; Rega, N.; Petersson, G. A.; Nakatsuji, H.; Hada, M.; Ehara, M.; Toyota, K.; Fukuda, R.; Hasegawa, J.; Ishida, M.; Nakajima, T.; Honda, Y.; Kitao, O.; Nakai, H.

Klene, M.; Li, X.; Knox, J. E.; Hratchian, H. P.; Cross, J. B.; Bakken, V.; Adamo, C.; Jaramillo, J.; Gomperts, R.; Stratmann, R. E.; Yazyev, O.; Austin, A. J.; Cammi, R.; Pomelli, C.; Ochterski, J. W.; Ayala, P. Y.; Morokuma, K.; Voth, G. A.; Salvador, P.; Dannenberg, J. J.; Zakrzewski, V. G.; Dapprich, S.; Daniels, A. D.; Strain, M. C.; Farkas, O.; Malick, D. K.; Rabuck, A. D.; Raghavachari, K.; Foresman, J. B.; Ortiz, J. V.; Cui, Q.; Baboul, A. G.; Clifford, S.; Cioslowski, J.; Stefanov, B. B.; Liu, G.; Liashenko, A.; Piskorz, P.; Komaromi, I.; Martin, R. L.; Fox, D. J.; Keith, T.; Al-Laham, M. A.; Peng, C. Y.; Nanayakkara, A.; Challacombe, M.; Gill, P. M. W.; Johnson, B.; Chen, W.; Wong, M. W.; Gonzalez, C.; and Pople, J. A. *Gaussian 03*; Gaussian, Inc.: Wallingford, CT, 2004.

(29) Perdew, J. P.; Burke, K.; Ernzerhof, M. *Phys. Rev. Lett.* **1997**, *78*, 1396–1396.

(30) Adamo, C.; Barone, V. *J. Chem. Phys.* **1999**, *110*, 6158–6169.

(31) Dunning, T. H., Jr. *J. Chem. Phys.* **1989**, *90*, 1007–1009.

(32) Hurley, M. M.; Christiansen, P. A.; Ross, R. B.; Ermler, W. C. *J. Chem. Phys.* **1986**, *84*, 6158–6169.

(33) LaJohn, L. A.; Christiansen, P. A.; Ross, R. B.; Atashroo, T.; Ermler, W. C. *J. Chem. Phys.* **1987**, *87*, 2812–2824.

(34) Pacios, L. F.; Christiansen, P. A. *J. Chem. Phys.* **1985**, *82*, 2664–2671.

(35) Zhao, Y.; Truhlar, D. G. *Theor. Chem. Acc.* **2008**, *120*, 215–241.

(36) Barone, V.; Cossi, M. *J. Phys. Chem. A* **1998**, *102*, 1995–2001.

(37) Cossi, M.; Rega, N.; Scalmani, G.; Barone, V. *J. Comput. Chem.* **2003**, *24*, 669–681.

(38) Oxley, J. C.; Smith, J. L.; Luo, W.; Brady, J. *Propellants, Explos., Pyrotech* **2009**, *34*, 539–543.

Density-Dependent Liquid Nitromethane Decomposition: Molecular Dynamics Simulations Based on ReaxFF

Naomi Rom,^{*,†} Sergey V. Zybin,[‡] Adri C. T. van Duin,[§] William A. Goddard, III,[‡] Yehuda Zeiri,^{||,⊥} Gil Katz,[†] and Ronnie Kosloff[†]

[†]Fritz Haber Research Center for Molecular Dynamics, Hebrew University, Jerusalem 91904, Israel

[‡]Materials and Process Simulation Center, 139-74, California Institute of Technology, Pasadena, California 91125, United States

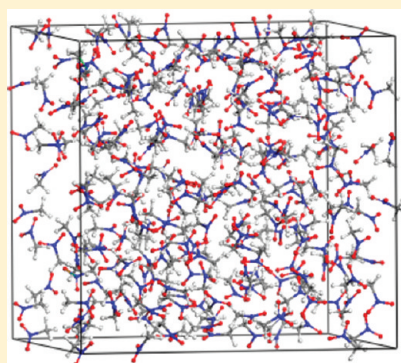
[§]Department of Mechanical and Nuclear Engineering, Pennsylvania State University, University Park, Pennsylvania 16802, United States

^{||}Bio-medical Engineering, Ben Gurion University, Beer-Sheva 84105, Israel

[⊥]Division of Chemistry, NRCN, P.O. Box 9001, Beer-Sheva 84190, Israel

 Supporting Information

ABSTRACT: The decomposition mechanism of hot liquid nitromethane at various compressions was studied using reactive force field (ReaxFF) molecular dynamics simulations. A competition between two different initial thermal decomposition schemes is observed, depending on compression. At low densities, unimolecular C–N bond cleavage is the dominant route, producing CH₃ and NO₂ fragments. As density and pressure rise approaching the Chapman–Jouget detonation conditions (~30% compression, >2500 K) the dominant mechanism switches to the formation of the CH₃NO fragment via H-transfer and/or N–O bond rupture. The change in the decomposition mechanism of hot liquid NM leads to a different kinetic and energetic behavior, as well as products distribution. The calculated density dependence of the enthalpy change correlates with the change in initial decomposition reaction mechanism. It can be used as a convenient and useful global parameter for the detection of reaction dynamics. Atomic averaged local diffusion coefficients are shown to be sensitive to the reactions dynamics, and can be used to distinguish between time periods where chemical reactions occur and diffusion-dominated, nonreactive time periods.



1. INTRODUCTION

Nitromethane (CH₃NO₂, NM), a high explosive (HE), has been studied intensively both experimentally^{1–5} and theoretically.^{3,6–10} Either a liquid phase or a crystal phase was employed as the initial state. The present study focuses on reactive molecular dynamics (MD) simulations of NM in the hot and dense liquid phase. The main goal of this study is to identify and quantify the detailed chemical reactions that occur during detonation. These reactions begin with the first molecular decomposition steps followed by the formation of final products. The calculations were performed under various temperature and compression conditions. These conditions simulate rapid laser heating experiments in diamond anvil cells, where the sample volume is held constant. The purpose of the present study is to obtain insight on the reaction mechanisms governing the initiation and detonation processes. The temperatures and compressions range examined include the typical conditions at the detonation wavefront.

A sample of the possible NM unimolecular decomposition pathways suggested¹¹ are

- CH₃NO₂ → CH₃ + NO₂
- CH₃NO₂ → CH₃ONO → CH₂O + HNO
- CH₃NO₂ → CH₃NO + O

- CH₃NO₂ → CH₃O + NO
- CH₃NO ↔ CH₂NOH
- CH₃NO₂ → CH₂NOOH

In a previous study,⁸ the decomposition of solid NM was calculated using MD simulations with on-the-fly calculations of molecular forces with density functional theory. In these simulations, dense solid NM (1.97 g/cm³ and 2.2 g/cm³) was rapidly heated to 3000 K and 4000 K. The first step revealed in the thermal decomposition was *intermolecular* proton transfer forming [H₃CNO₂H]⁺ and aci ion [H₂CNO₂][−]. The second step observed was *intramolecular* proton transfer forming aci acid [H₂CNO₂H]. Then, additional fragments were formed, such as CH₂NO⁺, OH[−], and H₂O. These reaction products were related to condensed phase reactions, whereas the C–N bond break, being the weakest in the molecule (*D*₀ = 60.1 kcal/mol in the gas phase²³), prevails in gas phase or dilute fluid decomposition.

The hypothesis that hydrogen abduction is the rate-determining step at a pressure of 10 kbar and at a temperature of 273 °C, is

Received: March 3, 2011

Revised: July 20, 2011

Published: August 03, 2011

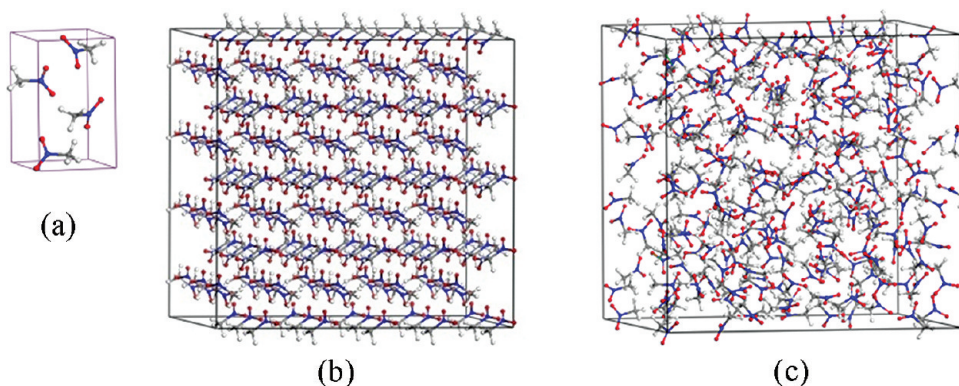


Figure 1. NM Crystal. (a) unitcell (b) $5 \times 4 \times 3$ energy minimized supercell, and (c) liquid NM supercell at ambient conditions.

supported by the measured time to detonation with deuterated NM, which was found to be 10 times longer than with protonated NM.¹ However, interpolation to higher temperatures suggests that above 330 °C the time to denotation of NM is longer than that of deuterated NM. Thus, possibly H-transfer is more important at similar compressions and lower temperatures (<330 °C).

In ref 5, the effect of pressure (<7 GPa) on the thermal decomposition of NM was studied in diamond anvil cell experiments where the samples were heated up to 450 K. It was found that both pressure and temperature accelerate the rate of thermal decomposition, supporting a bimolecular decomposition mechanism. The suggested rate-controlling leading reaction, supported by QM calculation, is



with calculated activation energy of 32.5 kcal/mol.

In the present work, we apply a MD approach based on the reactive force field ReaxFF to study the decomposition of liquid NM at a wide range of compression values ($0.56 \leq V/V_0 \leq 1$, where V is the volume after compression and V_0 is the calculated ambient conditions volume) and temperatures (2500–4500 K). Three regimes of the reaction are identified and analyzed independently: initiation step, intermediate reactions, and stable products creation. We found that the mechanism of the initial rate-determining step in NM decomposition depends strongly on its density (ρ): At ambient density and below 30% compression, C–N bond cleavage is the first event, as in the gas phase. At higher densities, in the vicinity of the Chapman–Jouget (CJ) state (stationary detonation, fully reacted HE, products in chemical equilibrium), CH_3NO is the dominant initial decomposition product. The former process is unimolecular whereas the latter fragment is formed by various mechanisms.

Thermal rate constants were evaluated for the initial endothermic decomposition stage for different initial densities. After some delay (temperature and pressure dependent), various intermediate reactions commence, including autocatalytic ones where NM reacts with its fragments. These reactions are presented in detail in section 3.4. The evolution of final products (H_2O , CO_2 , N_2 , H_2 , CO , NH_3 , and OH) begins in the intermediate stage and terminates when they reach stable amounts, as shown in section 3.5.

The paper is organized as follows: In section 2 the computational approach is described both for the simulations and kinetic analysis. Simulation results and analysis (fragments, rate constants, exothermicity, enthalpy) are presented in section 3, and conclusions are summarized in section 4. Supplementary data (potential parameters and bond order cut off values) are given in the Supporting Information.

2. COMPUTATIONAL APPROACH

The parallel version of the ReaxFF-MD code,^{12,13} GRASP (General Reactive Atomistic Simulation Package) was employed to study the behavior of liquid NM under various conditions. ReaxFF-MD was used in various applications, such as surface catalysis¹⁴ and combustion chemistry.¹⁵ In addition, it was used to study the initial chemical reactions that occur during thermal or shock-induced decomposition of HE materials (e.g., NM,⁹ cyclotrimethylenetrinitramine (RDX),^{16,17} and triacetone triperoxide (TATP)¹⁸), and recently in the calculation of directional anisotropy in pentaerythritoltetranitrate (PETN) single crystals resulting from combined shear and compressive loading.¹⁹ Note that ReaxFF potentials were trained for ground-state processes only, thus fragments obtained in these simulations are radicals or stable molecules (not ionic species). ReaxFF parameters were fitted to results of multiple ab initio quantum mechanical (QM) calculations. ReaxFF-MD simulations were shown to reproduce the QM results with high accuracy. Some examples²⁰ are bonds dissociation (gas phase reactions path), compression curves, geometry distortions (angles and torsion), charges, IR-spectra, condensed phase structures, and equations of state of molecules and crystals with H, C, N and O atoms.

Below we describe the procedure employed to prepare the liquid samples at various compressions followed by the conditions used in the heat-up simulations.

2.1. Sample Preparation. Preparation of liquid NM starts with a solid slab in which the NM molecules are arranged according to their crystal structure. The molecular slab (supercell) is obtained by multiplying solid NM unit cell (orthorhombic cell, Figure 1a, with $a, b, c = 5.228, 6.293, 8.664$ Å, respectively) by an integer along the different directions. Here, $5 \times 4 \times 3$ expansion along $x, y,$ and z directions was employed. Hence, the total number of molecules in the simulation was 240 (1680 atoms). Energy minimization is carried out to obtain optimized equilibrium geometry of the expanded crystal (Figure 1b).

2.1.1. Liquid Creation (Ambient Conditions). In order to obtain a liquid structure at ambient conditions, the following procedure was applied to the relaxed crystal supercell:

- The cell volume was increased by 50%, then its energy was minimized resulting in an optimized geometry (simulation length – 0.25 ps).
- The obtained supercell was heated to 400 K (10 ps), well above the NM melting point (244 K).
- The hot cell was heavily compressed (NPT simulation at 1 GPa and 400 K, 30 ps).

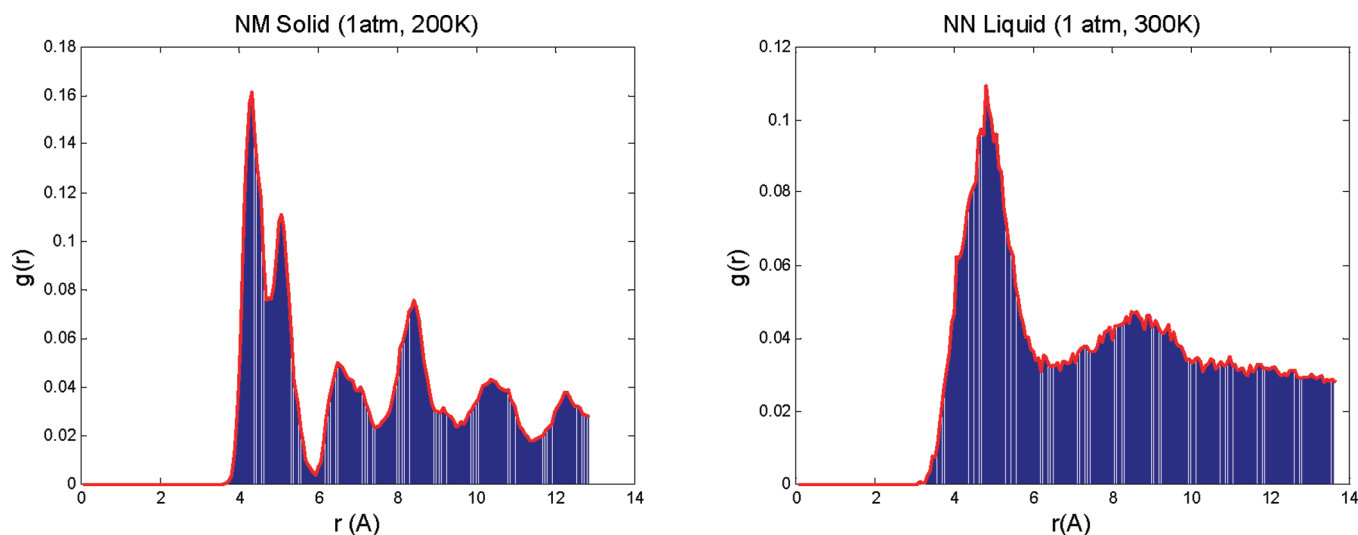


Figure 2. Radial distribution function for NM molecules in the solid (left) and liquid (right) phases. Distance units are Å.

- Cooling and decompression was applied (NPT at 1 atm and 300K, 30 ps). Calculated mass density of the liquefied sample at the end of the simulation was 1.111 gr/cm^3 ($a, b, c = 28.327, 27.386, 28.222 \text{ Å}$, respectively). It differs only by $\sim 2\%$ from the measured density 1.137 gr/cm^3 .
- The liquid cell was thermalized (NVT, $T = 300\text{K}$, 2 ps), and pressure oscillations reduced to $\pm 0.5 \text{ GPa}$.
- Finally the system state was relaxed (NVE simulation, 1 ps). A typical liquid supercell is shown in Figure 1c.

The time step in all the calculations described above was 0.25 fs. In the simulations, a simple rescaling thermostat was used, with temperature correction proportional to half the difference between the target and current temperature.

Radial distribution functions for the solid and liquid simulation cells are presented in Figure 2. Here, r is the distance between two NM molecules. As expected, typical structured behavior and smooth modulations are obtained for the solid and liquid cells, respectively. Results are shown for $r \leq d/2$, where d is the smallest cell vector.

2.2. Liquid Compression ($T = 300 \text{ K}$, $P = 1 \text{ atm}$). In order to obtain liquid in various compressions, we began with the liquid sample prepared by the process described above and volumetrically compressed it by the desired amount. Then, it was energy-minimized for 0.5–1 ps, depending on the magnitude of the compression, until equilibrium atomic positions were obtained. Finally, each sample was thermalized using NVT simulation at 300 K (2 ps), using a velocity rescaling thermostat. It is important to note that none of the NM molecules decomposed during these stages.

2.3. Heat-Up Simulations. Heat-up simulations of liquid NM were made in two stages: Initially, the sample at a fixed density was heated rapidly (within 100 fs, using time step 0.25 fs) from room temperature to the desired final temperature (T_f). Then, NVT simulations were carried out at T_f until the final products approached constant amounts. The rapid heating is carried out on a time scale similar to that of a detonation wave passing through the simulation cell ($\sim 500 \text{ fs}$). The time step used in NVT simulations was 0.1 fs, and the simulations progressed for 60–80 ps.

Thermal rate constants were calculated at three regimes within the simulations:

- Initial decomposition reaction/s (endothermic).

- Intermediate reactions and products.
- Stable products formation with the main products: H_2O , CO_2 , N_2 , H_2 , CO , NH_3 and OH .

The following section describes the methods employed for the chemical kinetics analysis.

2.3.1. Chemical Reactions and Fragments Analysis. Fragments analysis was done with “BondFrag”, a code developed in Goddard’s group at Caltech. For each pair of atoms in the simulation cell, a “bond order” is calculated. Then, according to cutoff values predefined for each pair (given in the Supporting Information), the code determines whether a chemical bond exists or not, thus fragments or molecules are being formed.

According to the reaction regimes mentioned above, fragments were examined in three stages: Creation of primary fragments, representing a reaction bottleneck at the very beginning of liquid NM decomposition; intermediate fragments formation, where many reactions occur simultaneously leading to multiple fragments (unstable and stable); and final products stabilization when thermodynamic equilibrium is reached. The main chemical reactions occurring in the initial stages of NM decomposition are listed below.

2.3.2. Rate Constants Analysis. Thermal rate constants were calculated as a function of density and temperature in the three different reaction stages. The average potential energy (PE) of the system was monitored during the simulation. It was found that PE exhibits a maximum close to the initial stages of the simulation. Fragments analysis (see section 3.4) reveals the nature of the peak: It roughly separates between the initial, endothermic decomposition of NM and the intermediate, multiple reactions stage. The time when the PE reaches a maximum, t_{max} , was determined for each simulation. This was accomplished by fitting a smooth function (sum of decreasing and increasing exponential functions) to the evolution of PE during the simulation and finding its maximum. In cases where the PE maximum was too close to the simulation initiation (namely, at high temperatures), a local polynomial fit was applied in the vicinity of the PE maximum to get t_{max} which was then used to distinguish between NM initial decomposition and the intermediate reactions stage.

For each simulation, rate constants in the three stages are deduced as follows:

- *Initial decomposition stage rate constant, $k_1[\rho, T]$* : The hot liquid NM molecules decay was fitted with a first order decay expression, $N(t)$, from the beginning of the decomposition, at t_0 , until t_{\max} :

$$N(t) = N_0 \cdot \exp[-k_1(t - t_0)] \quad (1)$$

Note that in previous works^{7,16} this fit was made along the full NM decay, including the zone where intermediate reactions take place and hence influence the rate constant, introducing inaccuracy into the single exponential function fit.

- *Intermediate decomposition stage, $k_2[\rho, T]$* : Bypassing the complexity of chemical reactions at this stage, an effective first order rate constant is obtained by fitting a decaying exponential function to the decaying part of PE curve, $U(t)$, starting from t_{\max} :

$$U(t) = U_{\infty} + \Delta U_{\text{exo}} \cdot \exp[-k_2(t - t_{\max})] \quad (2)$$

U_{∞} is the asymptotic value of PE (products) and $\Delta U_{\text{exo}} = U(t_{\max}) - U_{\infty}$. The latter is the exothermicity, or the heat release, in the NM decomposition reaction. This type of fitting was also used in the thermal decomposition study of RDX,¹⁶ triaminotrinitrobenzene (TATB), and octahydro-1,3,5,7-tetranitro-1,3,5,7-tetrazocine (HMX).²⁰ NM decomposition enthalpy change, ΔH , can be estimated from

$$\Delta H = -\Delta U_{\text{exo}} + V(P_{\infty} - P(t_{\max})) \quad (3)$$

As will be seen in section 3.6, ΔH seems to be correlated with the initial decomposition mechanism of NM (which is pressure dependent). If so, it can serve as a simple yet sensitive tool in identifying mechanism changes under various conditions.

- *Final products evolution stage, k_3* : Effective rate constants (due to the variety of reactions leading to their formation) for final products creation can be calculated by fitting the following function to each product's time evolution, $C(t)$:

$$C(t) = C_{\infty} \cdot (1 - \exp[-k_3(t - t_i)]) \quad (4)$$

t_i is the product's time of formation. Note that this fitting needs to be made until each product reaches a stable amount, otherwise the fitted parameters will depend on the simulation length. C_{∞} is the estimated asymptotic amount of the products, and can be compared to measurements²² and results of thermochemical computations²² (see section 3.5).

Following the evaluation of the temperature- and density-dependent rate constants in the initial and intermediate decomposition stages of liquid NM, a fit to the Arrhenius equation is made to obtain activation energies and pre-exponential factors as a function of density for these stages. Kinetic analysis results are presented in the following section.

2.3.3. Diffusion Coefficient and Mean Square Displacement (MSD) of the Atoms. The mobility of atoms during the simulation is influenced by the pressure and temperature, as well as by their participation in chemical reactions. Diffusion

Table 1. Densities, Simulation Cell Volumes and Compressions Used in Heat-Up Simulations

mass density [gr/cm ³]	cell volume, V [cm ³]	Compression, V/V_0
1.111	21894	1
1.234	19704	0.9
1.389	17515	0.8
1.587	15325	0.7
1.852	13136	0.6
1.984	12260	0.56

coefficient, D , can be estimated using Einstein's expression:

$$D = \lim_{t \rightarrow \infty} \frac{1}{6N_m t} \left\langle \sum_{j=1}^{N_m} [r_j(t) - r_j(0)]^2 \right\rangle \quad (5)$$

$r_j(t)$ is the coordinate of atom j at time t . N_m is the number of atoms. In the case of chemically reactive simulations, the diffusion coefficient is not expected to be constant, but rather related to the reactions' evolution. In section 3.6, MSDs are calculated separately for each NM atom (C, H, N, O).

3. RESULTS

Heat-up simulations were carried out at a constant density. The desired temperature was attained by performing rapid heating for 100 fs, followed by a constant, final temperature simulation. Densities used are the calculated ambient mass density (1.111 gr/cm³) and a series of volumetric compressions (10, 20, 30, 40 and 44%; see Table 1). The temperatures vary in the range between 2500 K and 4500 K. The simulation with highest density at ~ 3000 K is close to the CJ state of solid NM, which was studied in detail.^{8,9} Note that in the latter studies 32 NM molecules were included in the simulations, whereas 240 molecules are used here. CJ pressure and particle velocity measured for liquid NM²¹ (initial density 1.14 gr/cm³) are 13.0 ± 0.4 GPa and 1.8 ± 0.05 km/s, respectively, and the CJ detonation velocity is 6.3 km/s. Accordingly, the CJ density is 1.596 ± 0.02 gr/cm³. In ref 25, the measured CJ pressure and detonation velocity are 12.71 GPa and 6.311 km/s, thus CJ density is 1.5805 gr/cm³. Note that the CJ density of liquid NM is at a density of approximately 30% compression (see Table 1).

3.1. Liquid NM Initial Decay. The time evolution of NM (normalized by the initial amount of 240 molecules) is presented in Figure 3, for the different temperature values. Each plot shows results for a different initial density. As expected, the decomposition rate increases with temperature increase.

The initial, rapid heating stage is not shown in these plots. In some cases, one or two NM molecules (<1%) decomposed via a C–N bond break. In the simulation with 20% compression at 4500 K five NM molecules reacted (2%) in this stage: Two molecules formed a van der Waals dimer, and two C–N bonds and one C–H bonds were fractured. In these cases, the initial reactions were sensitive to the time step used. However, in order to be consistent with the other simulations, we proceeded to the NVT simulation with the same time step as in the other cases (0.25 fs).

NM is an insensitive HE. Our simulations show that a relatively high temperature (~ 2500 K) is required for the decomposition process to commence at a pronounced rate. This

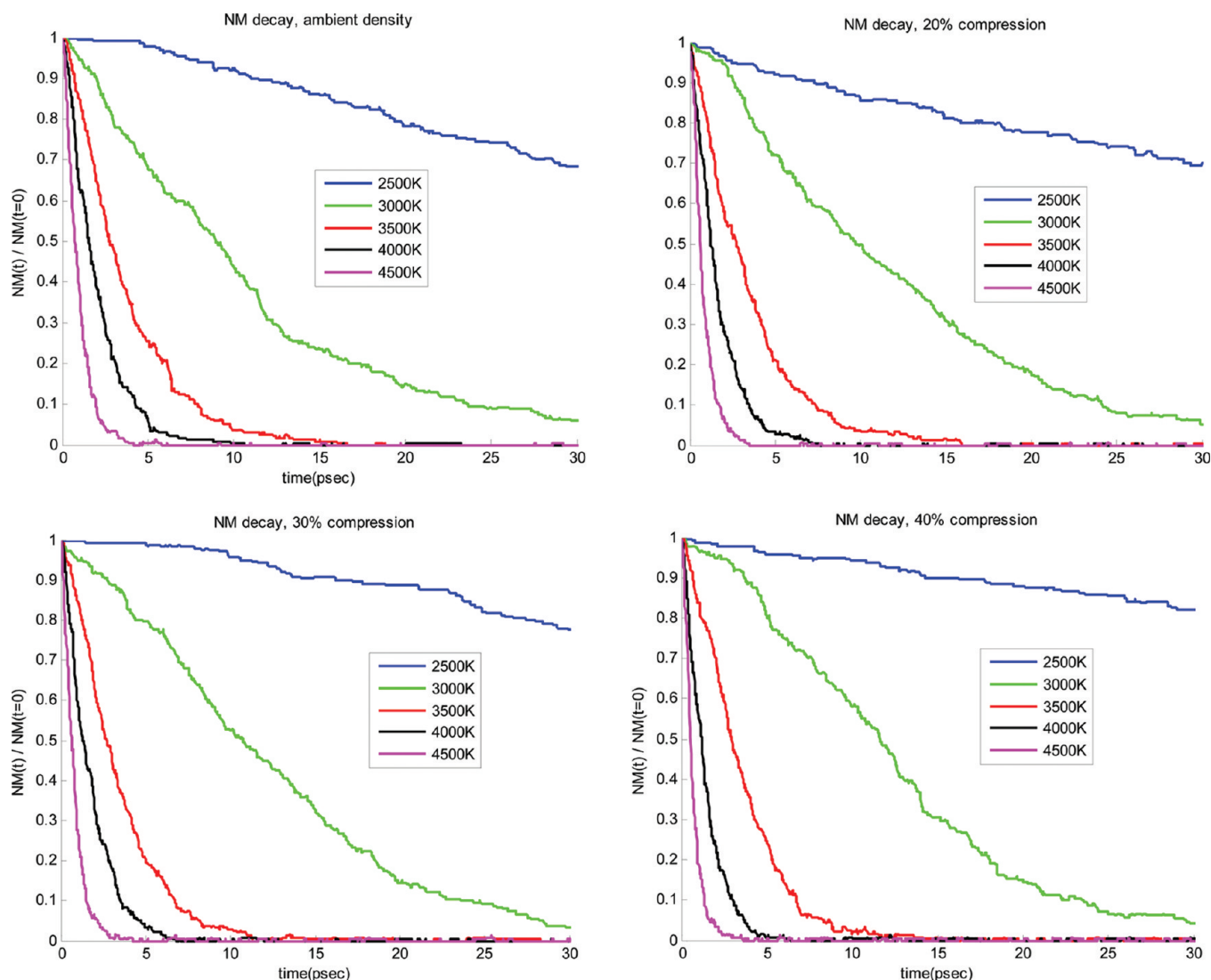


Figure 3. NM decay versus simulation time for various temperatures, plotted separately per density (ambient density, 20, 30, and 40% compressions).

suggests a correlation between the initial temperature in which HE starts to decompose and its sensitivity.

The density-dependent decomposition of NM is shown in Figure 4 for various temperatures. Above 2500 K, in most cases NM decomposition starts as soon as the NVT simulation begins. Two tendencies are seen in the initial decomposition stage of NM, depending on the temperature regime:

- At temperatures ≤ 3500 K, the decay rate of NM slows down as density is increased from ambient density to 40% compression. Further increase of density speeds up NM decay (see Figure 4).
- At temperatures ≥ 4000 K, the decay rate of NM generally increases with density/pressure increase.

These tendencies determine the characteristics of the initial decomposition stage rate constant, k_1 , depending on pressure and temperature, as shown in section 3.3. In Figure 5, a comparison between the density-dependent decay rates at 2500 and 3500 K are presented by shifting the curves such that they coincide at a common decomposition value (3%). The tendency mentioned above for lower temperatures is seen.

Note that in the intermediate reactions regime ($t > t_{\max}$), as decomposition progresses at lower temperatures (≤ 3500 K), the NM decay slopes with 40% and 44% compressions get steeper and bypass lower compression ones (see marks on Figure 4). This increase in NM decay is correlated with the larger PE decay rates obtained at higher compressions (see Figure 6 and section 3.2).

We will further examine the nontrivial dependence of NM decay on pressure and temperature by analyzing the fragments production and chemical reactions (see section 3.4). At this point we note that in the bulk phase at lower temperatures, surrounding molecules act as a “thermal bath” that absorbs energy from excited molecules and cools them down. In the case of unimolecular decomposition, increasing the density strengthens the coupling of the excited vibrational mode to the bath, and the molecule’s decomposition rate is reduced. On the other hand, with bimolecular reactions, increasing the density reduces intermolecular spacing and increases the reaction rate. Hence, increasing the density has a reversed effect on the different types of reaction mechanisms at lower temperatures (≤ 3500 K here). As will be seen below, the reversed tendency of the initial NM decay

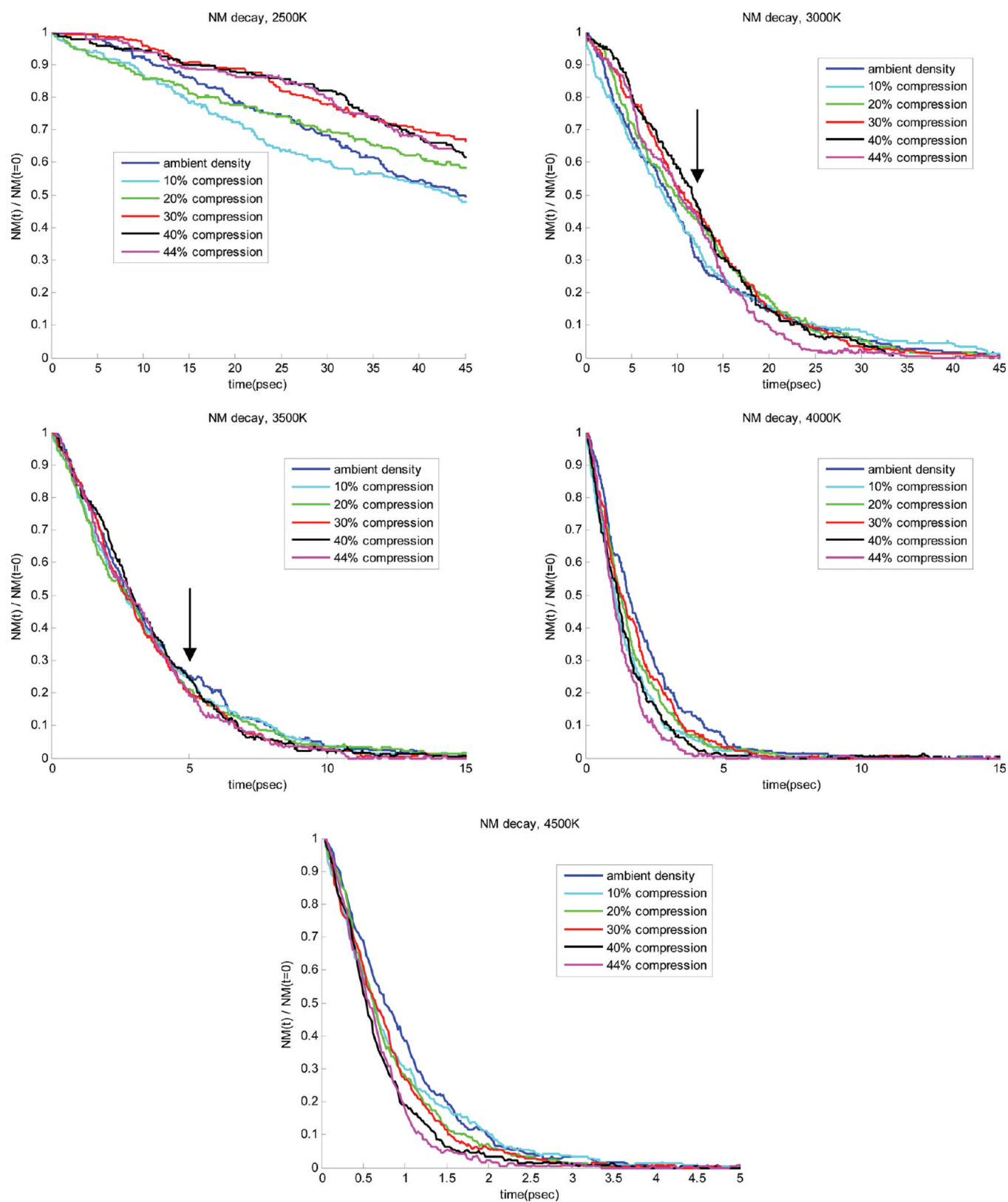


Figure 4. NM decay versus simulation time for various densities, plotted separately per temperature (between 2500 and 4500 K). Note different scales per plot. The arrows mark the time where NM decomposition speeds up for 40% and 44% compressions at 3000 K.

rate as a function of density is related to a transition from a dominant unimolecular decomposition reaction at lower

densities, to a bimolecular path that becomes preferable, in comparison to the unimolecular one, at very high compressions.

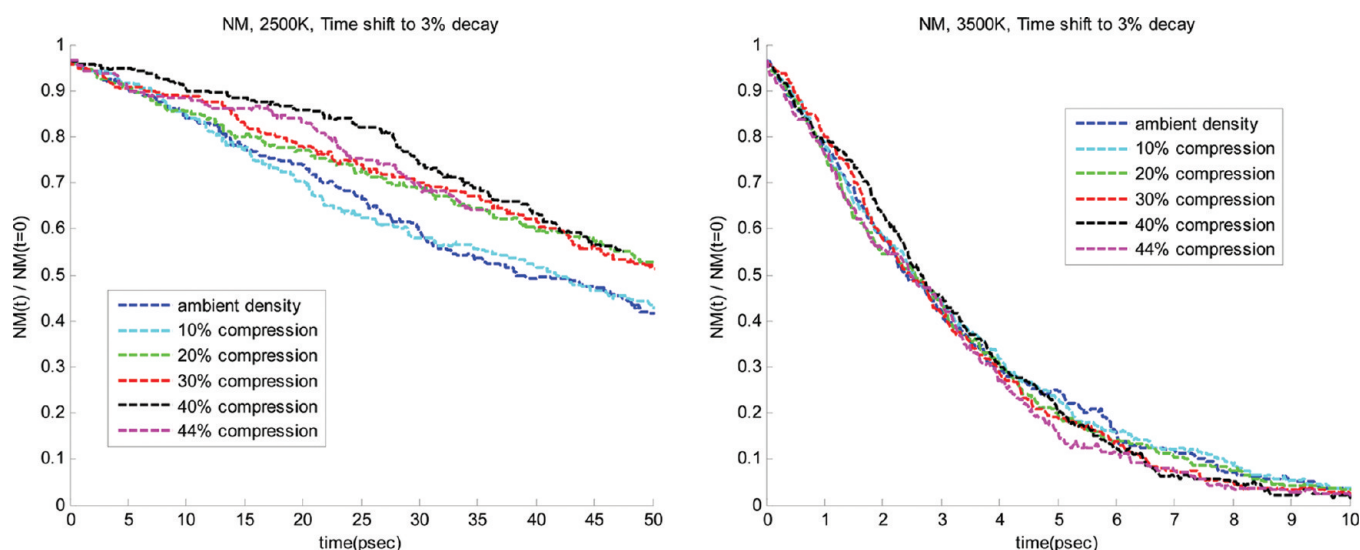


Figure 5. NM decay at 2500 and 3500 K for various densities, plotted versus shifted simulation time such that decomposition at all densities coincides at 3%.

However, at temperatures ≥ 4000 K, increasing the density enhances the decomposition rate monotonically. The NM molecules are highly excited, decomposition reactions occur very fast, and cooling by thermal bath is ineffective.

3.2. Pressure and PE Evolution. The time evolution of the total pressure and PE as a function of density (see Table 1) is presented in Figure 6. Results for each constant temperature are shown separately. Note that the rapid heating stage is not presented. Moving average was applied to the pressure presented in the plots to reduce numeric noise.

Generally, the pressure initially decreases, then in the vicinity of the time where PE is maximal (t_{\max}) it starts to increase gradually toward an asymptotic value, which marks chemical equilibrium. As expected, the pressure rises with density and temperature.

Under all conditions studied, first the PE increases then it exponentially decreases until some asymptotic value is reached. The initial behavior is related to the existence of endothermic reactions in the beginning of NM decomposition (or detonation) process. It is followed by a second stage, where various intermediate reactions take place, some of which involve NM molecules, while in others NM decomposition products participate. The third and last stage marks the termination of chemical reactions with the formation of thermodynamically stable final products that reach a saturation value. Chemical rate constants can be calculated for each of these three regions, as discussed below. The NM decomposition exothermicity (i.e., the heat released in the reactions) is calculated from the difference between the PE maximum and its asymptotic value as well as the pressure change (see section 3.6).

The PE variation with time for temperatures ≥ 3000 K can be divided into two types, depending on the density: In the PE exponential decay region, samples with compression below 30% have slower decay rates, while those with higher compressions decay at a similar, faster rate (see Figure 6 and extended time PE behavior for 3000 K in Figure 7). As mentioned in the previous section, the PE decay rate is related to the NM decay rate at $t > t_{\max}$. Note that the PE decay rate analysis in section 3.3 shows the general attitude of decay rate increase with compression (and temperature).

Finally, the asymptotic value of PE increases with density and temperature.

3.3. Decomposition Reactions Rate Constants: k_1 and k_2 . Rate constants for the initial and intermediate decomposition stages were calculated with the fitting procedure used in ref 1 (also partly in ref 16) and briefly described above (see section 2.3.2). The analysis starts in finding the time where PE reaches its maximal value, t_{\max} . These times are shown in Table 2 for the various densities and temperatures studied, and are plotted in Figure 8. An example of the fitting used for t_{\max} evaluation and PE decay rate (k_2) is shown for 3500 K at ambient density and 30% compression in Figure 9.

Two general observations can be made on the character of secondary reactions initiation (t_{\max}):

- The higher the temperature, the smaller is t_{\max} (secondary reactions start sooner, the barrier is overcome more easily).
- As pressure/density increases, t_{\max} decreases.

The latter can be understood when the reactions involved have more than one reactant. As mentioned above, such reactions are facilitated by pressure and density increase, due to the reduction in intermolecular spacing. This is characteristic of reactions at a time beyond t_{\max} and also for initial decomposition reactions of NM at 30% compression and higher. Both cases will be discussed further in the fragments analysis section 3.4. There are some exceptions to the mentioned density-dependent tendency of t_{\max} due to inaccuracy in its determination when PE curves have a “flat top”, as is the case for $T \leq 3000$ K for all densities, and for 3500 K for densities $\geq 30\%$ compression (see Figure 6). Longer simulations (hundreds of picoseconds) are required to better characterize the evolution of intermediate reactions and products at these conditions.

For the PE fit (k_2), we used temperatures ≥ 3500 K only, since as mentioned, the reaction progress at lower temperatures is relatively slow, and the decay cannot be fitted by a single exponential function (at least within the time regime used in the present simulations).

NM decay rates, $k_1[\rho, T]$, were obtained using eq 1 in the time range $[t_0, t_{\max}]$. Examples of NM decay curve fitting are given in Figure 10 for ambient density and 30% compression at 3000 and

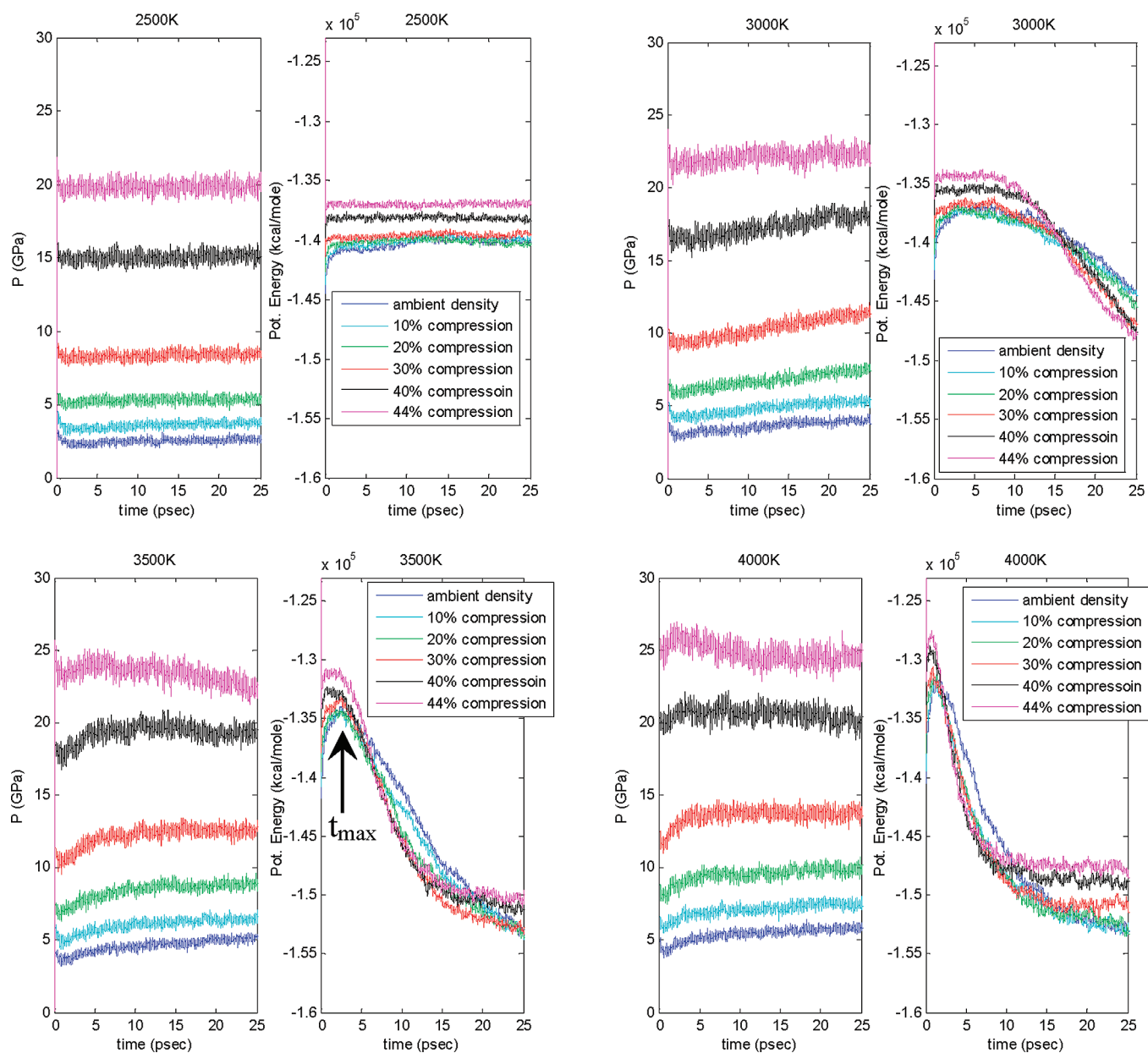


Figure 6. Pressure (left) and PE (right) versus simulation time for various densities, plotted separately per constant temperature simulation (2500–4000 K). Energy units are kcal/mole, where “mole” here refers to a mole of simulation cells. In order to change energy units to kcal/mole of NM molecules, the values in the plots should be divided by 240 (number of molecules/cell).

4000 K. Also shown is a single exponential function fit throughout the whole simulation period, as used, for instance, in ref 7. As can be seen, at the lower temperature and density, as well as in the high temperature and both densities, a single exponential function fit throughout the simulation is fairly good. However, for higher density at 3000 K a single exponent does not fit the NM decay curve well, with a large deviation in the initial reactions region. As will be seen in the next section, at high compressions bimolecular (or higher) mechanisms compete with the initial unimolecular decomposition, causing the large deviation from an overall single exponential function behavior.

Arrhenius plots of the rate constants for the initial and secondary decomposition stages of NM are shown in Figure 11. The behavior of k_2 is monotonic, density (pressure) and

temperature wise, whereas the decay rate of the initial stage, k_1 , shows a more complex behavior with constant-density lines crossing each other above 3500 K. Moreover, their pressure variation is opposite at temperatures ≤ 3500 K and below 44% compression: k_2 increases when pressure increases, whereas k_1 decreases. Conversely, at these temperatures, raising the density from 40% compression to 44% increases the decay rate k_1 . The monotonic behavior of k_2 is understood as it is an averaged energy release rate representing a complex sequence of chemical reactions whose yield improves with pressure increase. On the other hand, as will be seen in the fragments analysis section, the initial decomposition reaction that influences k_1 is pressure dependent, where a transition occurs between a lower pressure mechanism, C–N bond break, to a higher pressure

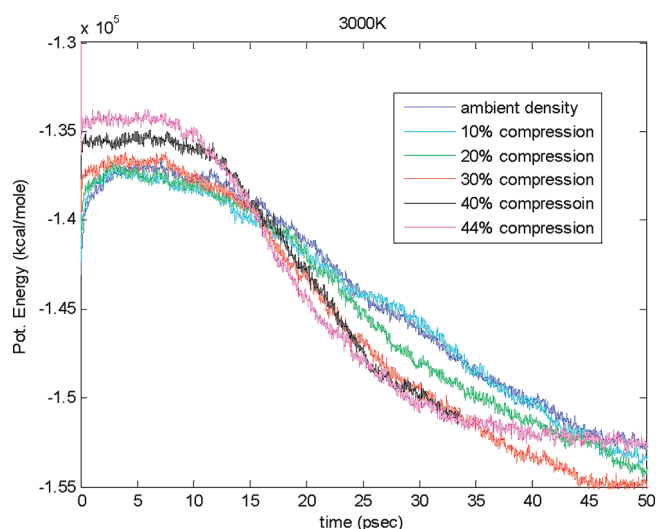


Figure 7. PE versus simulation time for various densities, demonstrating similar decay rates for compressions above 30%. Energy units are kcal/mol of simulation cells.

Table 2. Time of PE Maximum (t_{\max} [ps]) as a Function of Mass Density and Temperature

mass density [gr/cm ³]	2500 [K]	3000 [K]	3500 [K]	4000 [K]	4500 [K]
1.111	21.3	6.9	2.6	1.7	1.0
1.234	16.8	5.0	2.1	1.2	0.9
1.389	14.3	3.4	1.9	1.1	0.8
1.587	20.1	4.2	2.1	1.0	0.6
1.852	11.8	4.5	1.4	0.7	0.5
1.984	15.3	6.2	1.8	0.7	0.5

(near and above CJ pressure) route, CH_3NO production. The former is a unimolecular process, whose rate is suppressed by pressure due to collisions, and the latter fragment is formed mainly by bimolecular (or higher) reactions that speed up with pressure increase. Some of these reactions are listed in the next section.

Arrhenius parameters obtained from the exponential functions fits to NM initial decay (k_1) and PE decay (k_2) are listed in Tables 3 and 4 for the various densities. The Arrhenius fit for k_1 was made with temperatures in the range 2500–4500 K, and in the PE fit (k_2) temperatures ≥ 3500 K were used. Generally, activation energies in the initial reactions stage (E_{a1}) are higher than those in the intermediate stage (E_{a2}). The mean and standard deviation for E_{a2} is $E_{a2} = 37.5 \pm 3.6$ kcal/mol. E_{a1} is almost constant for densities below 30% compression (49.4 ± 1.3 kcal/mol), and it rises with density until 44% compression where it is reduced. On the basis of the fragments analysis in the next section, $E_{a1} = 49.4 \pm 1.3$ kcal/mol is the activation energy of C–N bond cleavage in hot liquid NM below 30% compression. This value is lower than the C–N bond dissociation energy measured in the gas phase, $D_0 = 60.1$ kcal/mol. The difference (reduction in the activation energy by ~ 10 kcal/mol) can be explained by many factors. With NM compression $>30\%$, the initial decomposition of NM is more complex and includes several competing reactions. These reactions are influenced by pressure change, and the activation energy reflects their mutual

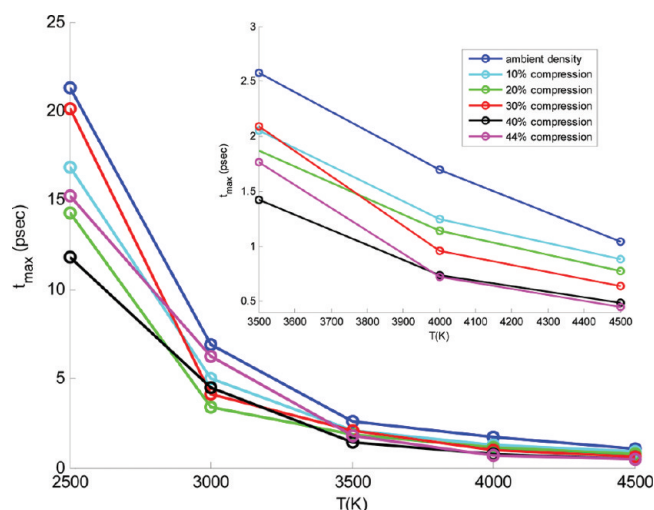


Figure 8. PE maximum time versus temperature for various densities. Also shown is an enlarged region between 3500 and 4500 K. At lower temperatures, PE has a flat top, and the accuracy of t_{\max} is reduced.

contribution to the initial decomposition of NM at higher densities/pressures.

In previous studies,⁷ ReaxFF simulations of liquid NM (ambient density) in the temperature range 2200–3000 K were carried out. Effective activation energy for NM decomposition was obtained by assuming overall first-order reaction during the whole simulation period (until $\sim 95\%$ decomposition of NM). The value of the activation energy obtained was ~ 33 kcal/mol, significantly lower than ~ 50 kcal/mol obtained here. In order to evaluate the difference between the two fitting approaches for E_a extraction in current simulations, a single exponential function was fitted to NM decay until the end of the simulations. The results are shown in Table 5. Comparing to Table 3 it is seen that at compressions below 30% there is a small deviation ($<3\%$) between values obtained with the fitting method suggested here (time between $[t_0, t_{\max}]$) and those obtained with fitting the entire simulation period. At larger compressions, the mismatch is higher (5–12%), as seen also in Figure 10. In any case, these values do not compensate for the large difference between E_a obtained here and in ref 7. These might be related to the large deviations between the fitted curves and the simulation results in ref 7, the different temperature interval, and possibly the difference in potentials used in both studies. Interestingly, E_{a2} at ambient density is 32.8 kcal/mol (see Table 4), resembling the value obtained in ref 7. It can be generally stated that when intermediate reactions evolution dominates and dictates the decay of NM molecules, the effective overall activation energy is lower.

Arrhenius parameters calibrated for liquid NM decomposition in shock initiation experiments⁴ are $A_0 = 2.6e9 \text{ s}^{-1}$ and $E_a = 23$ kcal/mol. These values are lower than those obtained here (and in ref 7) for constant temperature and volume simulations.

3.4. Fragments Analysis: Initial and Intermediate Reactions. Fragments created in the early stages of NM decomposition are analyzed for different initial densities and temperatures using BondFrag code. Stable products, obtained at later stages of the simulation, are analyzed separately (see section 3.5). Fragments that reach over 3% of the initial amount of NM molecules

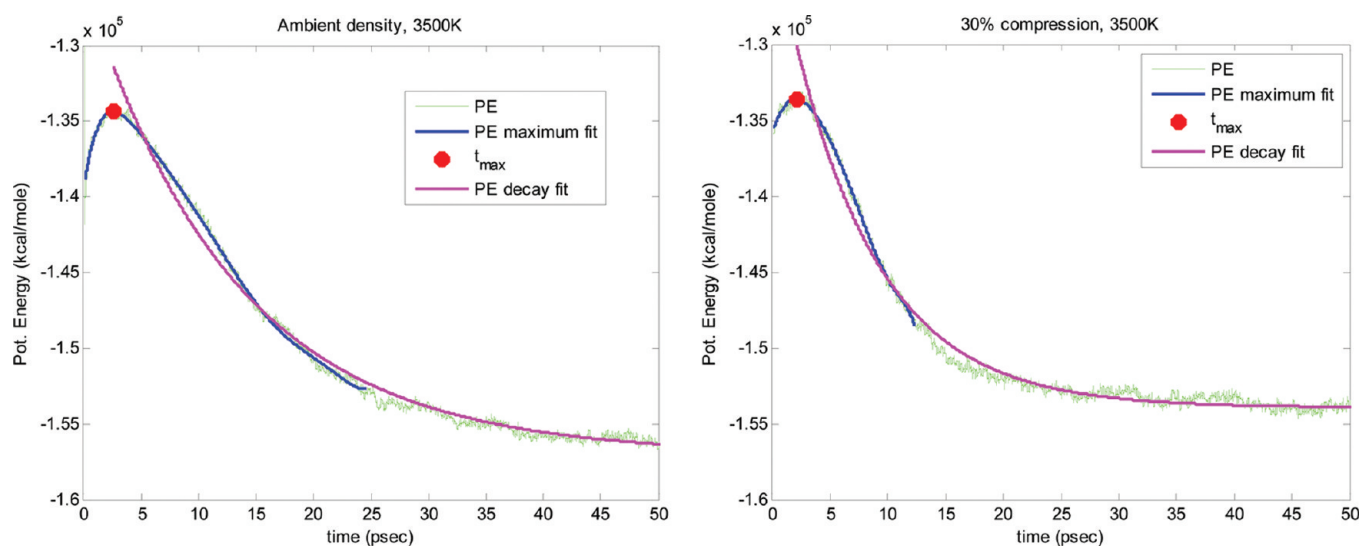


Figure 9. PE fitting for ambient density (left) and 30% compression (right) at 3500 K. Fittings for evaluation of (a) PE maximum time, t_{\max} (red point), and (b) decay rate, k_2 , are shown in blue and pink, respectively.

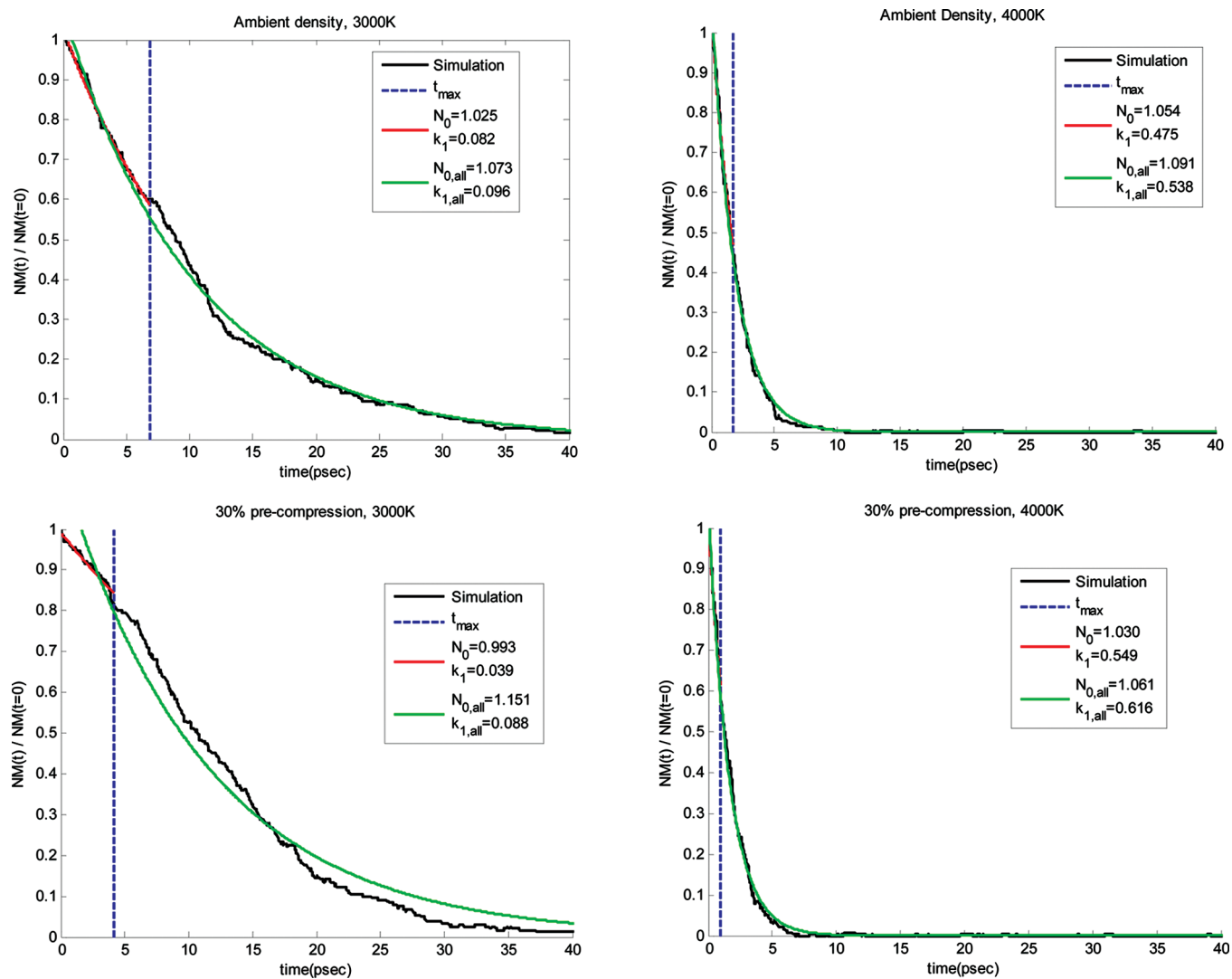


Figure 10. NM decay curve (black), for ambient density and 30% compression, in 3000 K (left) and 4000 K (right) simulations. Single exponential functions (eq 1) were fitted to each curve until t_{\max} (red) and throughout simulation length (green, denoted “all”).

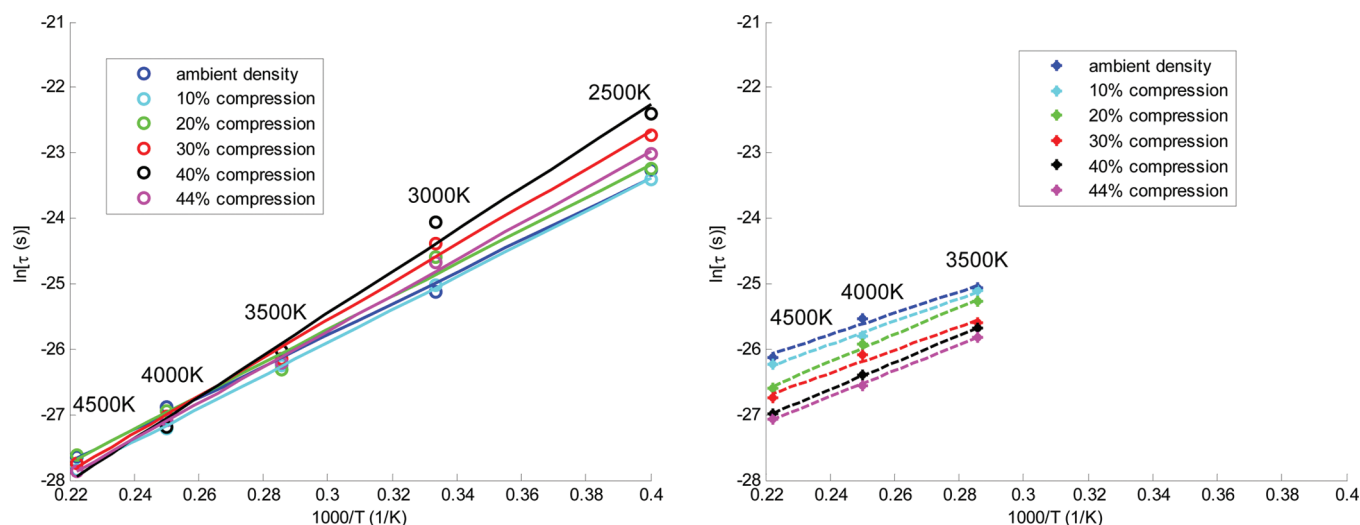


Figure 11. Arrhenius plots (shown is reaction time, $\tau = 1/k$) for NM initial decomposition (left - k_1 , solid lines) and PE decay (right - k_2 , dashed lines), for various densities.

Table 3. Arrhenius Parameters Fitted to NM Exponential Decay Rates, $k_1[\rho, T]$, over a $[t_0, t_{\max}]$ Time Interval for Various Initial Densities^a

mass density [gr/cm ³]	$\ln(A_0[\text{s}^{-1}])$	Ea [kcal/mol]
1.111	33.0	47.9
1.234	33.5	49.9
1.389	33.3	50.3
1.587	34.2	57.4
1.852	35.0	63.4
1.984	34.0	54.6

^a Temperature range used: 2500–4500 K.

Table 4. Arrhenius Parameters Fitted to PE Exponential Decay Rate, $k_2[\rho, T]$, for various initial densities^a

mass density [gr/cm ³]	$\ln(A_0[\text{s}^{-1}])$	Ea [kcal/mol]
1.111	29.8	32.8
1.234	30.2	35.2
1.389	31.2	41.6
1.587	30.6	35.0
1.852	31.6	40.9
1.984	31.5	39.2

^a Temperature range used: 3500–4500 K.

(240) during simulation period are presented for ambient density and various compressions (20%, 30%, 40% and 44%) at 3000 K and 4000 K in Figure 12, and at 2500 K in Figure 13.

Figure 12A (ambient density, 3000 K) shows that CH₃ (red line) and NO₂ (green line) are created rapidly at the beginning of the simulation. Around 5 ps, the rapid rise stops, and a plateau followed by decrease is seen. On the other hand, the CH₃NO fragment (blue dashed line) is not created initially; only after ~2 ps does its amount rise at a relatively slow rate.

Figure 12B (20% compression, 3000 K) again shows a rapid growth of CH₃ and NO₂ fragments as simulation begins. After ~3 ps, the CH₃NO amount starts to increase at a high rate (relative to the growth in Figure 12A), while CH₃ and NO₂ production stops. At ~5 ps, the concentration of CH₃NO surpasses that of CH₃. On the basis of this behavior, it is concluded that CH₃ and CH₃NO are produced by competitive reactions, and the creation of one inhibits the formation of the other.

Figure 12C (30% compression, 3000 K) shows that already at the beginning of the simulation both NO₂ and CH₃NO are produced at the same rate. CH₃NO becomes the most abundant fragment within the simulation time shown. Note that CH₃ concentration is very low (<3%) compared to its maximal amount with 20% compression (~8%) and at ambient density (~15%). This is due to its quick consumption by other reactions at high densities (e.g., with NM molecule or H atom).

Table 5. Arrhenius Parameters Fitted to NM Exponential Decay Rates, $k_1[\rho, T]$, over the Entire Simulation Period for Various Initial Densities^a

Mass density [gr/cm ³]	$\ln(A_0[\text{sec}^{-1}])$	Ea [kcal/mol]
1.111	33.0	46.8
1.234	33.3	48.4
1.389	33.8	51.8
1.587	33.9	52.3
1.852	34.5	56.2
1.984	34.7	57.4

^a Temperature range: 2500–4500 K.

In Figure 12D,E (40% and 44% compression, 3000 K) CH₃NO is by far the dominant fragment in the initial and intermediate stages of NM decomposition.

A more detailed investigation of the difference in the *initial* decomposition mechanism of liquid NM as a function of density is demonstrated in Figure 14. Here, the number of broken C–N bonds as a function of time is calculated at 3000 K for all densities studied (left). It is clearly seen that C–N bond scission is inhibited by the density increase. Initially ($t < 1$ ps), at all densities, there is some amount of C–N bonds breaking. However, below 30% compression, the quantity of broken

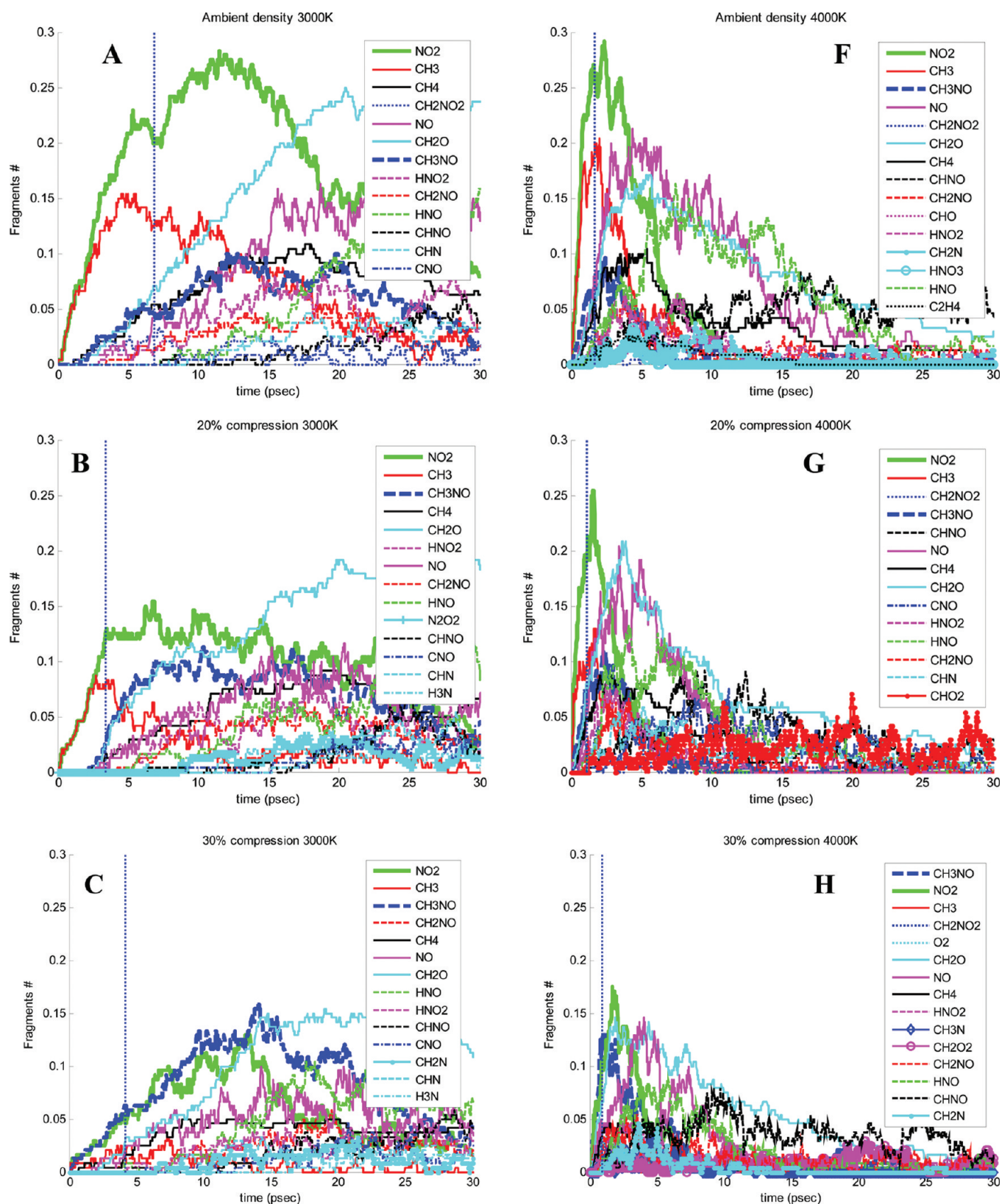


Figure 12. Continued

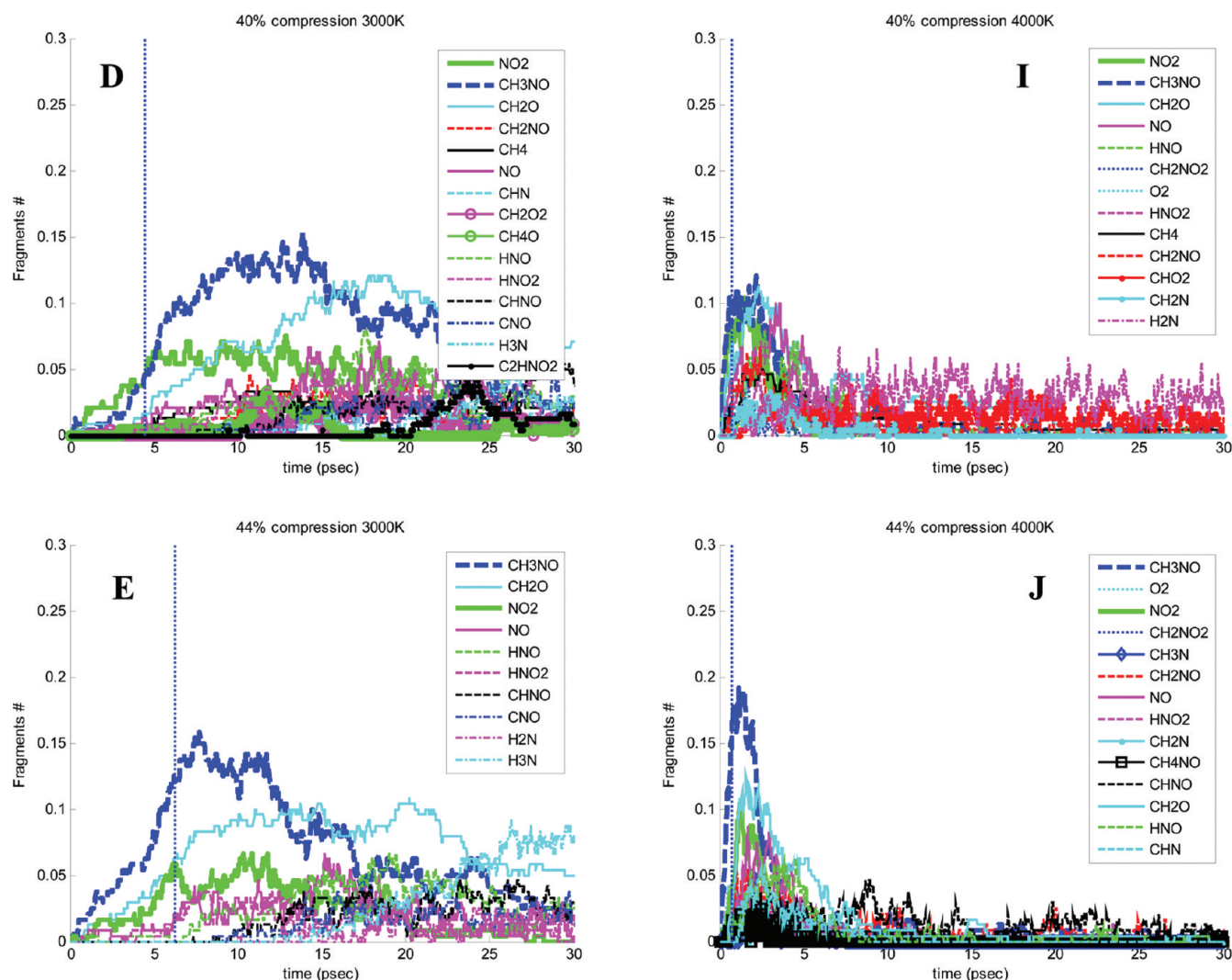


Figure 12. Initial and intermediate fragments obtained in 3000 K and 4000 K simulations at various densities. Dashed vertical lines are t_{\max} (PE maximum). Shown are fragments reaching >3% of initial NM molecules, normalized relative to 240 initial NM molecules.

C–N bonds keeps increasing at a pronounced faster rate compared to the growth of broken C–N bonds at higher densities. On the right-hand side of Figure 14, the total number of broken C–N bonds per density is shown at 7 psec. There is a sharp transition from the high amount of total broken C–N bonds at lower densities (>35%) to the smaller amount at compressions above 30% (<25%).

In summary, the analysis of the initial decomposition reactions and fragments of hot liquid NM shows that they are density dependent:

1. Below 30% compression, the first reaction is a unimolecular C–N bond break forming CH_3 and NO_2 . Then, after some time delay ($\sim t_{\max}$), a variety of intermediate reactions occur producing mostly CH_3NO , CH_2O , CH_4 , NO , and HNO_2 .
2. At 30% compression, the amount of the two competing initial fragments, NO_2 and CH_3NO , is about equal. After some delay, the third abundant fragment, CH_2O , is created together with others. At yet higher compressions, the dominant initial fragment becomes CH_3NO , and C–N

bond breaking is inhibited. Additional fragments formed at smaller amounts in the intermediate decomposition stage at high compressions are CH_2O , NO_2 , NO , CH_4 , and HNO_2 .

The density of NM at 30% compression, $1.587\text{gr}/\text{cm}^3$, is close to CJ density, $1.596 \pm 0.02\text{ gr}/\text{cm}^3$, and the temperatures employed in the simulations are in the vicinity of CJ temperature ($\sim 3000\text{ K}$). It is interesting to compare the initial pressure obtained in the NVT simulations studied, where decomposition of NM begins, with CJ pressure. In Table 6, approximate values of the initial pressures are given for various NVT simulations. As can be seen, only above 30% compression the pressure is higher than CJ pressure, $13 \pm 0.4\text{ GPa}$. Under these conditions the initial fragment formed is CH_3NO . Hence, it can be concluded that above 30% compression the leading fragment formed in the initial step of liquid NM detonation is CH_3NO .

The general density-dependent trend described above is not temperature dependent (see 4000 K and 2500 K results in Figure 12F–J and Figure 13A–E, respectively). The main effect of temperature is speeding up the reactions.

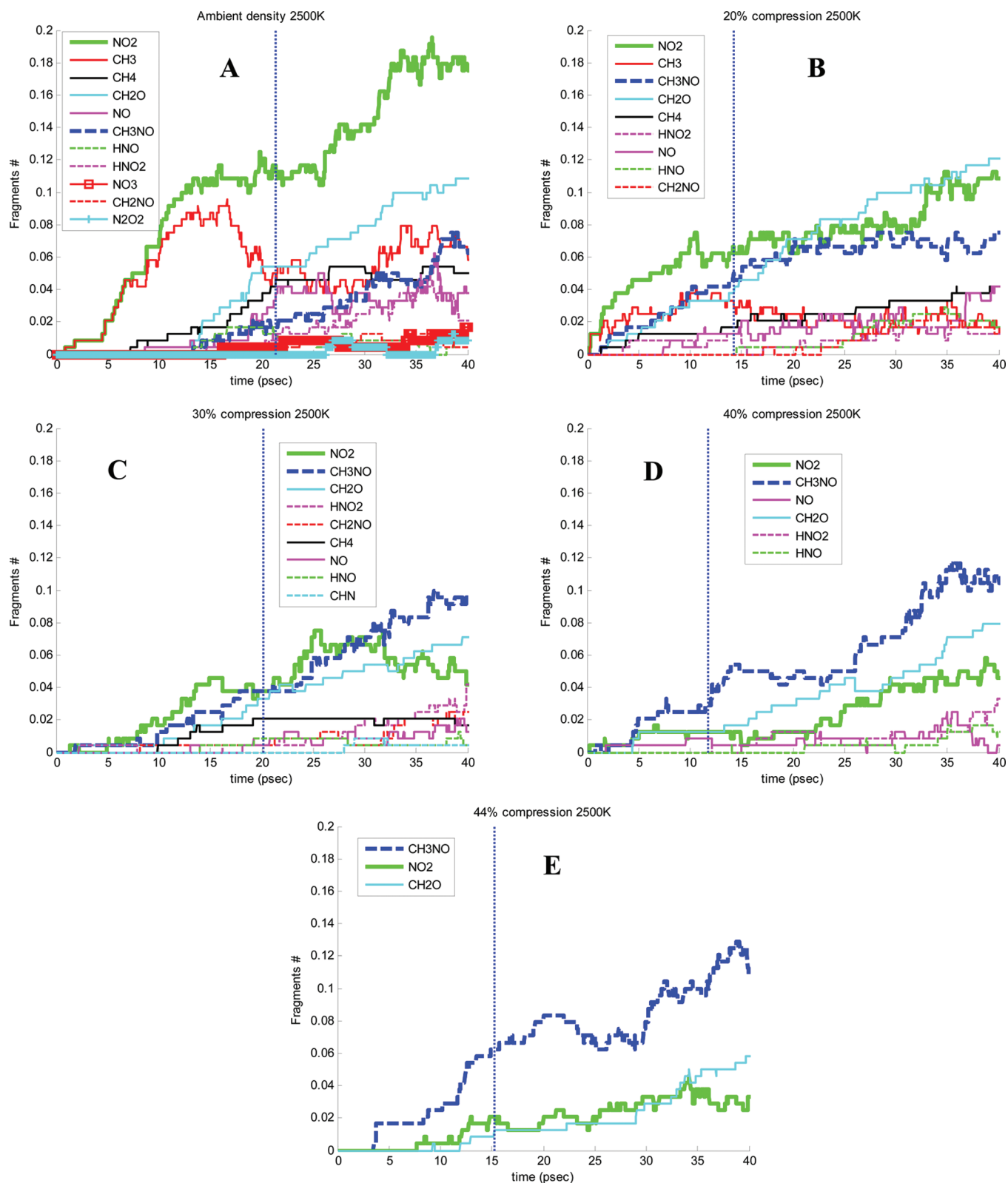


Figure 13. Initial and intermediate fragments in 2500 K simulations at various densities. See caption in Figure 12.

In Figures 12 and 13, the time where PE reaches its maximal value, t_{max} is marked (vertical blue dashed line). As can be seen, it is closely related to the onset of secondary reactions where a variety of exothermic reactions occur.

In Figure 15, the time evolution of NO₂ (left) and CH₃NO (right) fragments is shown as a function of initial density at 3000 K and 4000 K. As can be seen, NO₂ fragment amount and production rate monotonically decrease as

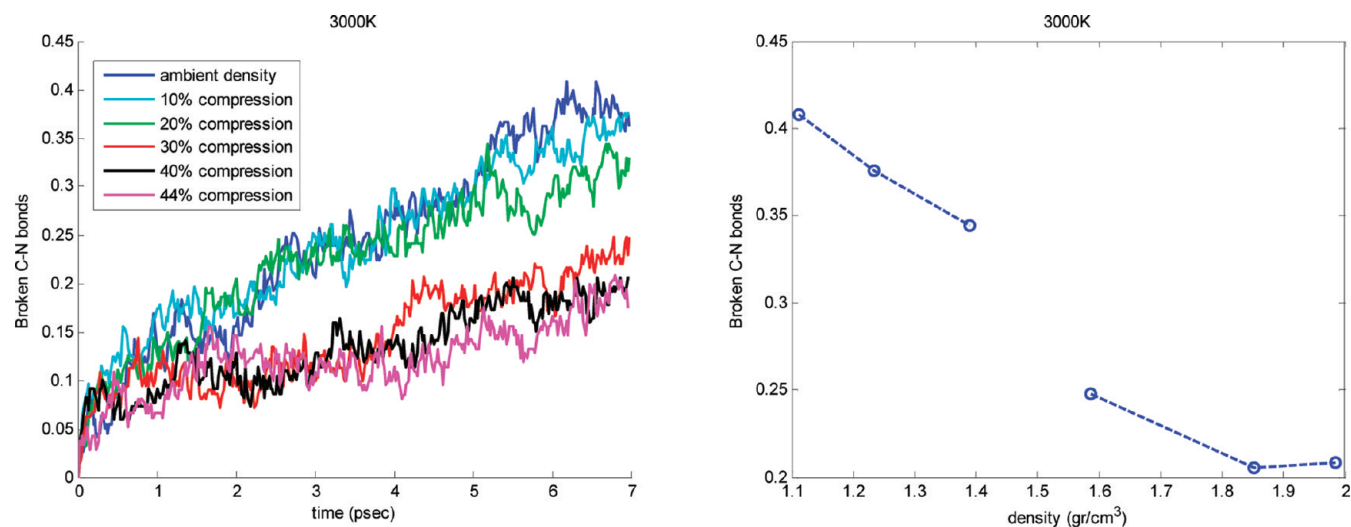


Figure 14. Left: Time dependence of broken C–N bonds as a function of density. Right: Total number of broken C–N bonds at 7 ps, as a function of density. The broken bonds number is normalized by the initial NM molecules (240).

density/pressure increases. On the other hand, CH_3NO overall amount increases with density. As seen above, at lower densities there is almost no production of CH_3NO at the beginning of NM decomposition, whereas at higher densities ($\geq 30\%$ compression) it is created as soon as the decomposition begins.

Figure 15 demonstrates the correlation between the competing reactions governing the initial production of these fragments: At low densities C–N unimolecular bond break is energetically favorable (lower activation barrier, ~ 50 kcal/mol; see Table 3). At higher densities, the unimolecular reaction is suppressed, via collisions with surrounding molecules that absorb energy from the excited molecule. At the same time, with these higher densities, bimolecular reactions that produce CH_3NO become dominant due to more frequent and effective collisions, whereas they are inferior energetically at lower compressions (e.g., N–O bond scission in the gas phase of NM is highly endothermic,²⁴ $D_0 = 94.7$ kcal/mol).

Here also, increasing the temperature accelerates the reactions but does not quantitatively modify the density tendency described above.

Under the high densities and temperatures studied here, the assignment of atoms to molecules is not unique. However, on average, the trends of fragments creation are trustworthy. Some of the leading reactions in the initial and intermediate decomposition stages of NM obtained from BondFrag analysis are (main fragments are bold-faced):

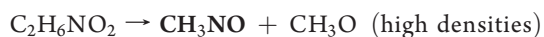
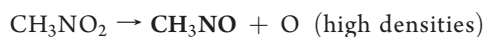
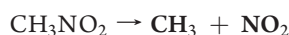
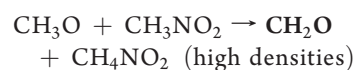
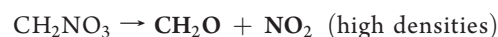
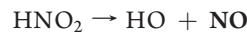
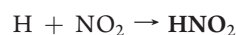


Table 6. Approximate Minimal Pressures (GPa) Reached in the Initial Stage of NM Decomposition with Various Densities and Temperatures^a

density [gr/cm ³]	2500 K	3000 K	4000 K
1.111	<3	3.2	4.5
1.389	5.3	6	8.5
1.587	8.4	10	12
1.852	15	16.5	20
1.984	20	21.5	25

^a Values were taken from Figure 6.



Unless specified, the above reactions occur at all compressions. Excluding the first reaction, the fragments react among themselves or decompose to smaller species.

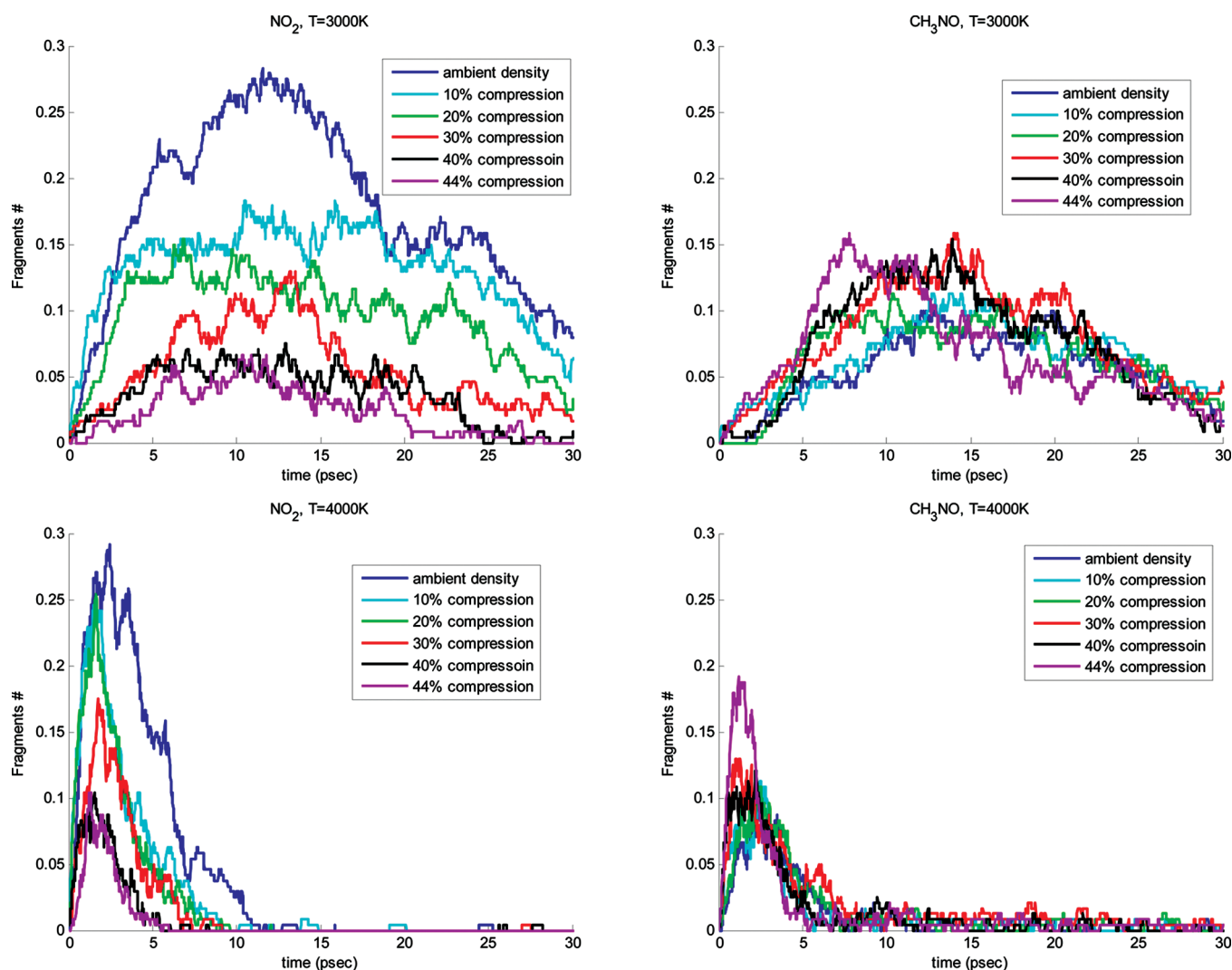


Figure 15. NO_2 (left) and CH_3NO (right) fragments time evolution as a function of density at 3000 K and 4000 K.

Some additional reactions that produce fragments participating in these reactions are



As can be seen, some of the above are autocatalytic reactions, involving parent NM molecules.

3.5. Final Products Analysis: Formation and Asymptotic Amounts. The main products obtained in the thermal decomposition of NM are N_2 , H_2 , H_2O , CO_2 , CO , NH_3 , and OH . Note that no significant amount of stable, carbon-rich clusters was observed among the fragments produced in the present simulations. This implies that NM detonation is not expected to

produce carbon soot or carbon clusters, unlike TATB²⁰ or trinitrotoluene (TNT).²⁶

An increasing exponential function (see eq 4) was fitted to the time evolution curves of these products in simulations where the final products approached saturation values. In Figure 16, simulation results and fitted curves are presented for various densities at 4000 K, and asymptotic amounts extracted per product are listed in Table 7. The latter are plotted in Figure 17 as well as measured liquid NM detonation products.²² Both in measurement and calculations, the most abundant product is H_2O . As seen, excluding NH_3 , OH and H_2O , the amount of all calculated fragments is reduced when pressure increases. There is a very good agreement between the experimental and calculated amounts of all measured products, excluding CO . It should be noted that the experimental values were measured after expansion and cooling down of the gaseous products, whereas the calculated products are at the same density and temperature as the original liquid NM. The OH fragment is unstable at ambient conditions, but is obtained in our simulations. Assuming OH combines with $1/2 \text{H}_2$ molecule to produce H_2O during cooling and decompression, the amount of H_2O expected to be obtained when ambient conditions are reached is also plotted in Figure 17

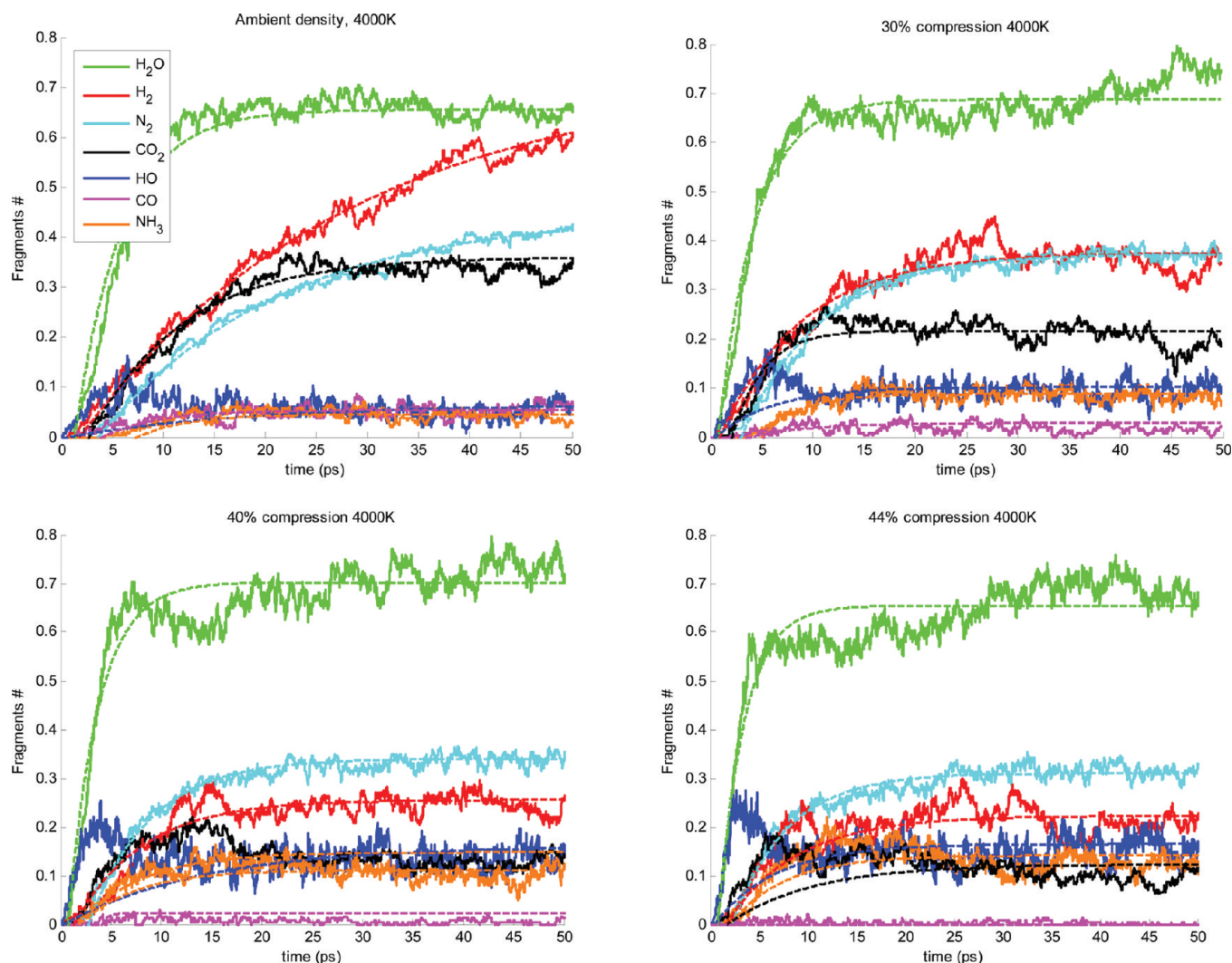


Figure 16. Products creation (solid lines) and increasing exponential functions fits (dashed lines, see eq 4) at 4000 K and various compressions.

Table 7. Final Products Asymptotic Amounts at 4000 K and Various Densities^a (d_0 represents the Calculated Density at Ambient Conditions)

fragment	d_0	$1.1d_0$	$1.2d_0$	$1.3d_0$	$1.4d_0$	$1.44d_0$
OH	0.066	0.080	0.088	0.102	0.161	0.165
H ₂	0.730	0.572	0.542	0.375	0.255	0.223
H ₂ O	0.655	0.663	0.654	0.687	0.703	0.654
CO	0.054	0.047	0.035	0.029	0.022	<0.02
N ₂	0.447	0.406	0.412	0.374	0.340	0.311
CO ₂	0.360	0.314	0.288	0.217	0.148	0.123
NH ₃	0.046	0.052	0.075	0.088	0.111	0.141

^aValues are normalized with respect to the initial amount of NM molecules.

(dotted green line). The agreement between the calculated H₂O amount at CJ density and the measured value improves, and the deviation between the measured and calculated amounts of H₂ decreases (not shown).

Finally, in Figure 18, gaseous product isotherms are plotted at various temperatures. Note that the product composition varies with

temperature and density. The isotherms were produced from *final* total pressure values per simulation (Figure 6). At 3000 K, the product formation may possibly not be fully completed within the simulation time, thus the accuracy of this products isotherm is slightly lower.

3.6. Decomposition Reactions Exothermicity and Change of Enthalpy. Two additional parameters that can be obtained from the MD simulations are decomposition exothermicity, ΔU_{exo} (eq 2), and enthalpy change (eq 3). These quantities are a measure of the exothermic part in the NM decomposition process. In Figure 19, ΔH is plotted as a function of density for the temperatures 3500, 4000, and 4500 K. As seen, the exothermicity temperature dependence is relatively weak (<10%). However, a pronounced modification in ΔH occurs when density varies, as can be seen in Figure 19: As density increases, ΔH increases (less exothermic), until ~30% compression where the slope is reversed and ΔH decreases with density (more exothermic). This change might be related to the transition from initial decomposition of NM by the C–N bond break (low densities) to initial CH₃NO fragment formation (higher compressions). Apparently, in the low compression range (<30%), as C–N bond cleavage is reduced with density rise, the decomposition process is less exothermic, while in the higher compression

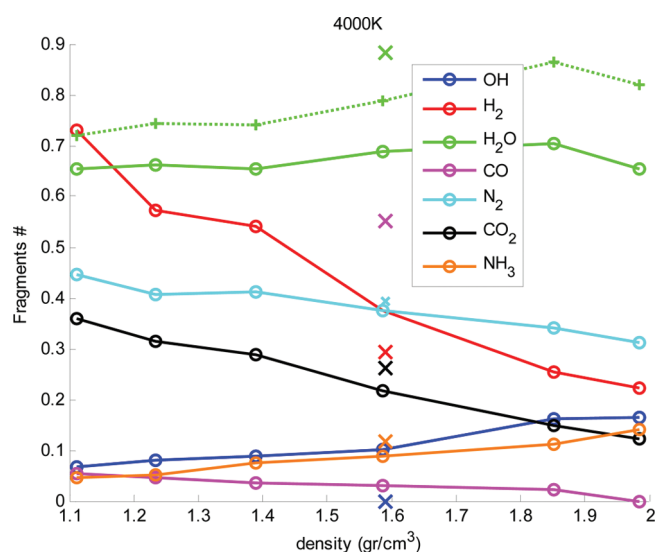


Figure 17. Calculated stable fragments fraction as a function of NM density at 4000 K (○, solid lines). Crosses represent measured detonation products²² (plotted at CJ density). Also shown is the sum of H₂O and OH fragments (+, dotted line).

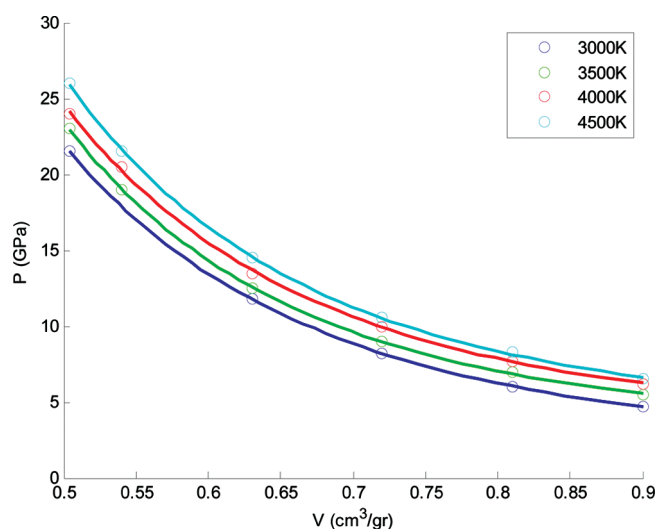


Figure 18. Liquid NM final product isotherms. The circles are calculation results, and the lines are second-order polynomial fits to them.

regime, the NM decomposition becomes more exothermic, in accordance with CH₃NO fragment enhanced production.

In Figure 20, the contributions to enthalpy change are presented (ΔU_{exo} and $V\Delta P$). As seen, the density variation of ΔU_{exo} is slow and monotonic, but $V\Delta P$ shows a more pronounced change.

The measured heat of reaction for liquid NM detonation in calorimetric bomb experiments²² is 1227 ± 7 cal/g, which is in very good agreement with the ΔH calculated at ambient density (see Figure 19): <3% deviation, depending on temperature. Note that Tarver uses 1060 cal/g as the NM heat of reaction for his detonation model.²⁵

3.7. Diffusion Coefficients Analysis. MSDs for the four atomic constituents of NM (C, H, N, O) were calculated for ambient and 30% compression at 3000 K and 4000 K, as presented in Figures 21

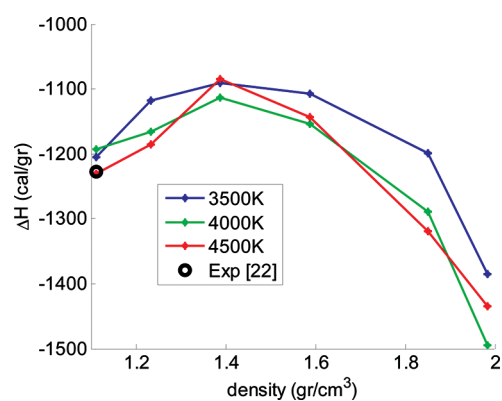


Figure 19. NM decomposition enthalpy change versus density for various temperatures. Also marked is the measured heat release in NM detonation²² (plotted at ambient density).

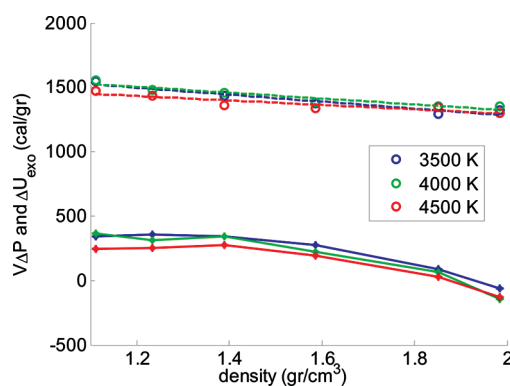


Figure 20. The density dependence of the energy contributions to enthalpy change: PE change (dashed lines) and $V\Delta P$ (solid lines) for various temperatures.

and 22. The atomic coordinates used in the calculation were corrected to remove periodic boundary conditions. As expected, the atoms mobility increases with temperature and decreases when pressure (density) rises. The density dependence of the calculated MSD for hydrogen and carbon atoms is presented in Figure 23 at 3000 K.

The diffusion coefficient can be determined using eq 5 as the slope of MSD time variation. As can be seen in Figure 21 and Figure 22, in the beginning of NM decomposition (initial and intermediate reactions stages) the mobility of all atoms is similar, whereas after a time interval, t_b , the slopes break and the atomic MSD lines split ($t_b \sim 15$ ps and ~ 5 ps at 3000 and 4000 K, respectively). The slope increase for hydrogen atoms is most pronounced, whereas for carbon atoms the diffusion coefficient remains almost constant throughout the simulation. The behavior of nitrogen and oxygen atoms resembles that of hydrogen, but with smaller slope differences. The slope change time is longer than t_{max} and seems to be related to decomposition reaction stage where final products approach saturation values.

In Tables 8 and 9, diffusion coefficients obtained by fitting the MSD curve in two time regions, $[t_0 t_b]$ (D_1) and $[t_b t_{\text{end}}]$ (D_2 , where t_{end} is the simulation length) are summarized for 3000 and 4000 K, respectively, at various densities.

Finally, comparison between D_1 and D_2 values as a function of density is plotted in Figure 24 for 3000 and 4000 K and all atoms. Generally, diffusion coefficients in the later stage of decomposition

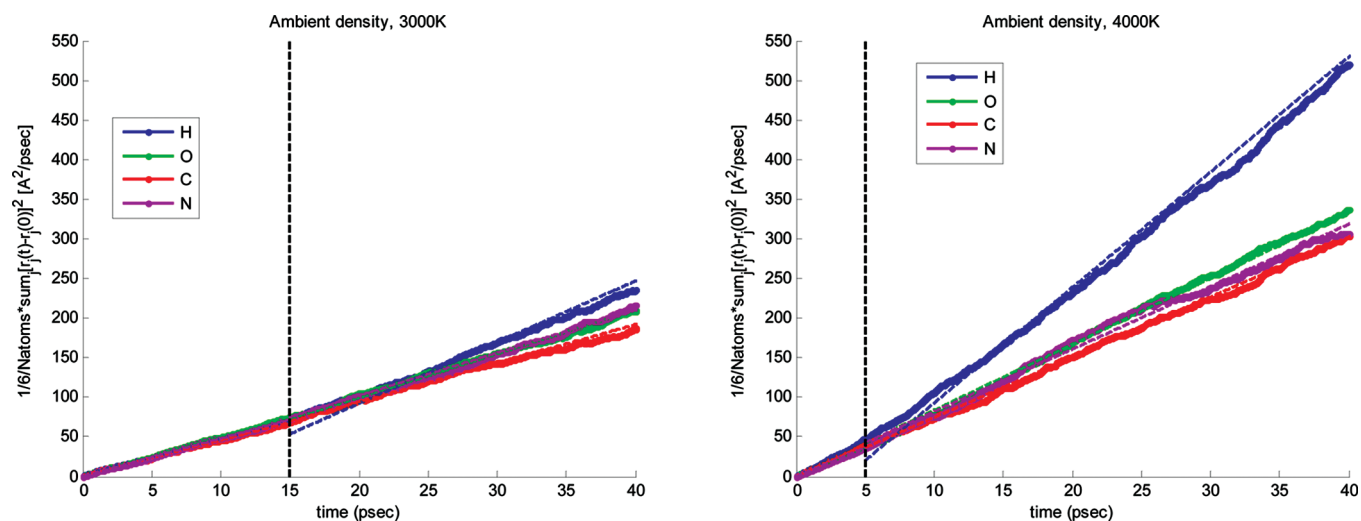


Figure 21. MSD of NM atoms during simulations at ambient density at $T = 3000$ K and 4000 K. Vertical line marks t_b . Linear fits to the time intervals $[0, t_b]$ and $[t_b, t_{\text{end}}]$ are also shown as thin dashed lines.

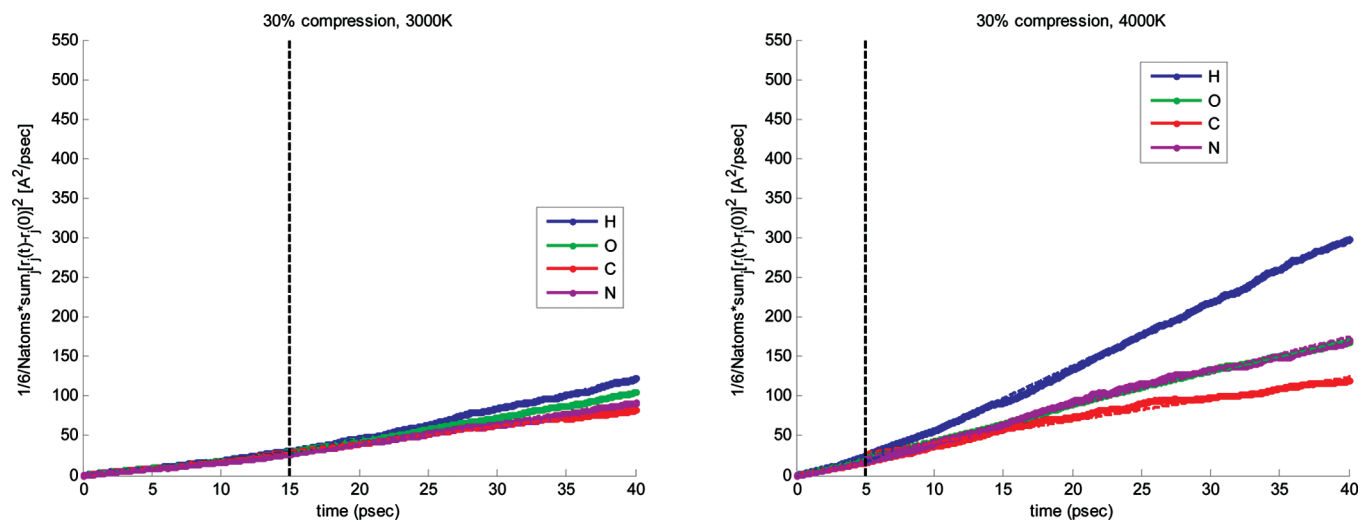


Figure 22. Same as Figure 21, for 30% compression.

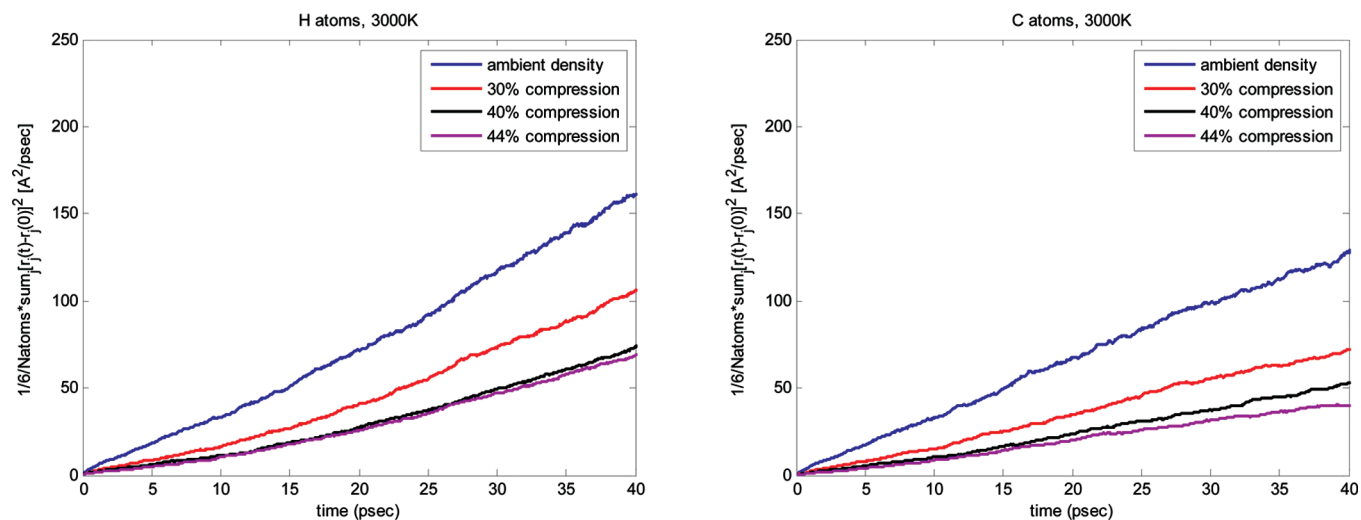


Figure 23. MSD for H (left), and C (right) atoms at various densities and $T = 3000$ K.

reactions (D_2) are larger than those in the initial stage (D_1). This is due to the progress of exothermic reactions, transferring PE to kinetic energy of the formed fragments. The difference between D_1

Table 8. Atomic Diffusion Coefficients in the Time Region $[t_0, t_b]$ of NM Decomposition (D_1) ($T = 3000/4000$ K)

density [g/cm ³]	D_H [Å ² /ps]	D_O [Å ² /ps]	D_C [Å ² /ps]	D_N [Å ² /ps]
1.111	4.6/9.2	4.9/7.0	4.4/7.8	4.8/7.2
1.587	2.0/4.7	1.9/3.9	1.9/3.2	1.7/3.5
1.852	1.1/3.5	1.1/2.7	1.0/2.1	1.0/2.3
1.984	1.1/3.4	1.0/2.5	0.9/1.9	1.0/1.9

Table 9. Atomic Diffusion Coefficients in the Time Region $[t_b, t_{end}]$ of NM Decomposition (D_2) ($T = 3000/4000$ K)

density [g/cm ³]	D_H [Å ² /ps]	D_O [Å ² /ps]	D_C [Å ² /ps]	D_N [Å ² /ps]
1.111	7.7/14.6	5.5/8.3	4.9/7.6	5.4/7.9
1.587	3.7/8.1	3.0/4.2	2.1/2.7	2.7/4.4
1.852	2.5/5.2	1.8/2.9	1.4/1.8	1.9/3.3
1.984	2.2/4.9	1.6/2.6	1.1/1.5	1.4/2.8

and D_2 is maximal for hydrogen atoms and minimal for carbon atoms. In addition, as mentioned above, both diffusion coefficients decrease when pressure increases.

In Figure 25 the averaged time derivative of the atomic MSD, denoted hereafter as averaged local diffusion coefficient (ALDC), is shown for all atoms in 3000 K heat-up simulations with ambient density and 44% compression. [A filter is used to smooth out short-term fluctuations and highlight longer-term trends of the time derivative of the atomic MSD. A forward and reversed direction equal weight filter was applied, with 300 points (6 ps) window in each direction.] The ALDC curves are more sensitive to the reaction dynamics than the monotonous MSD curves, and can be used to differentiate between time periods where chemical reactions occur and diffusion-dominated non-reactive ones. In nonreactive time periods, the ALDC curve is expected to be constant. The atomic ALDC includes contributions from all relevant fragments at a given time.

Figure 26 illustrates the correlation between the hydrogen atoms ALDC curves and the time evolution of fragments that include hydrogen atoms. When such fragments are created at a high rate, the calculated hydrogen ALDC increases, and when the fragment creation rate slows down, the ALDC curve slope

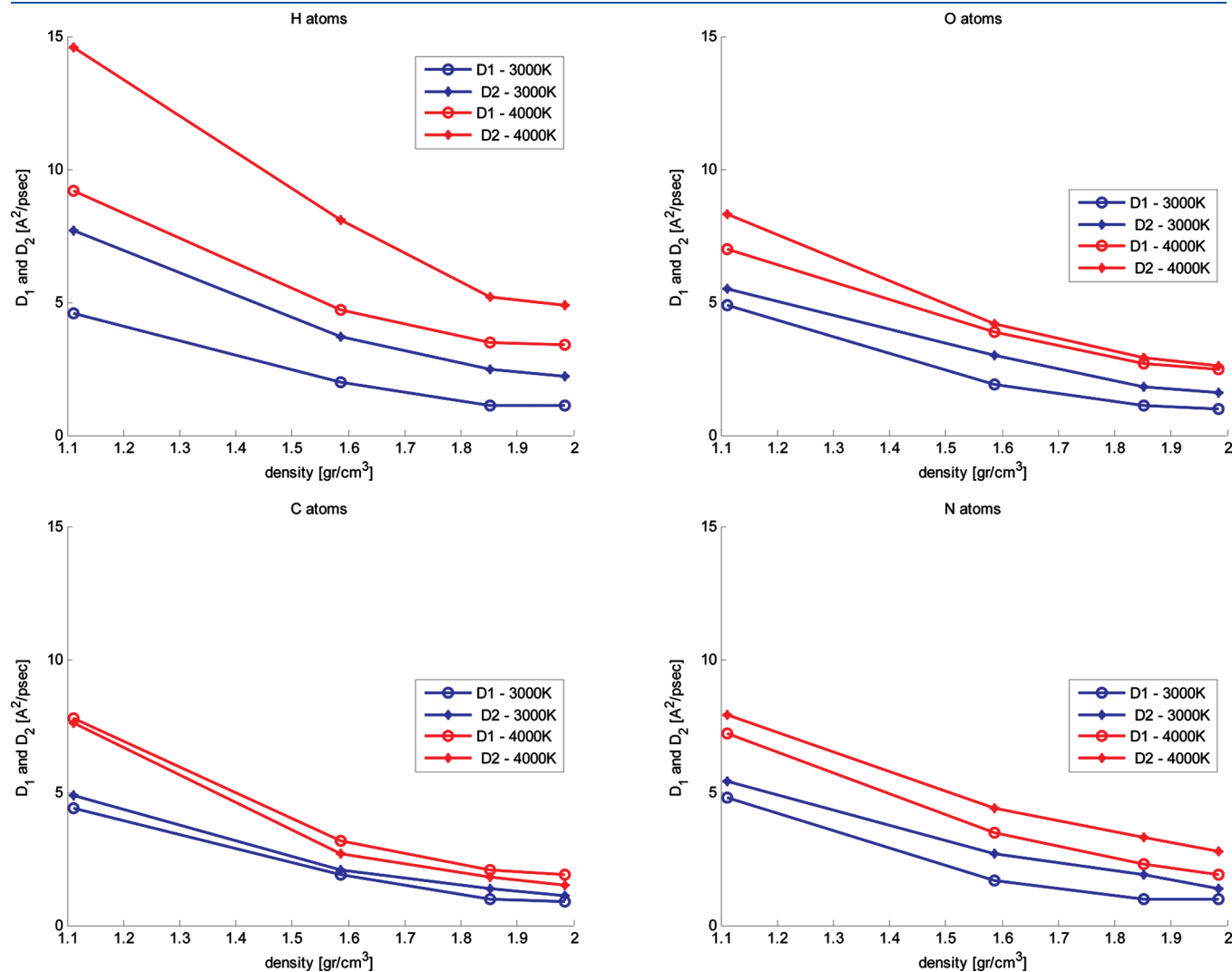


Figure 24. Diffusion coefficients in the time region $[t_0, t_b]$ (D_1) and $[t_b, t_{end}]$ (D_2), as a function of density, for hydrogen, oxygen, carbon, and nitrogen atoms.

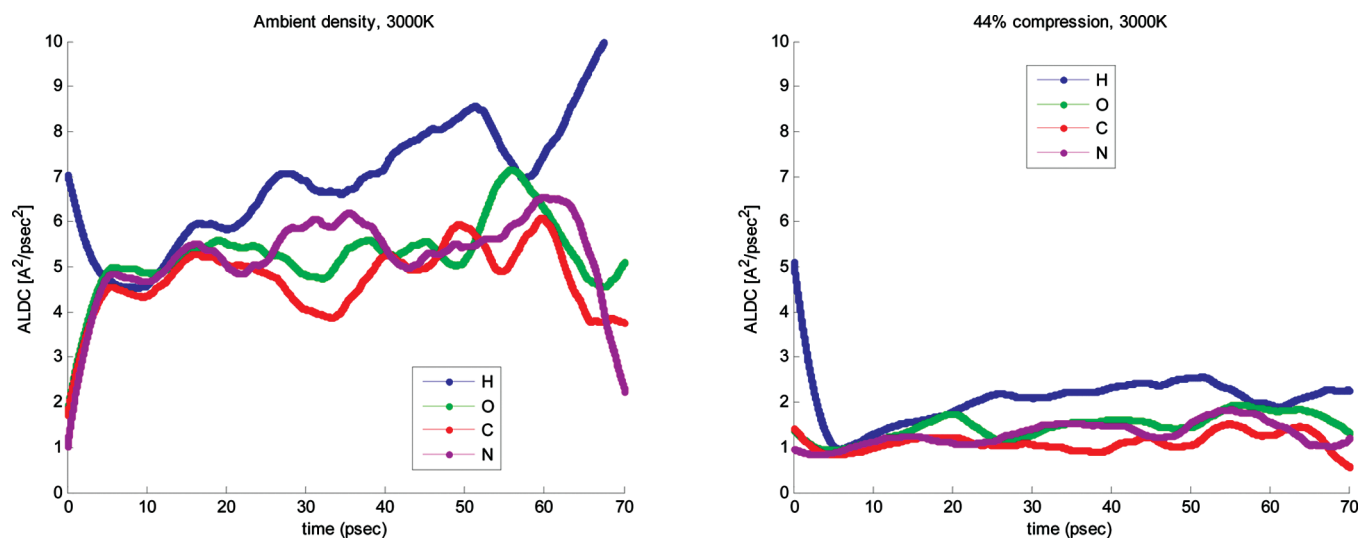


Figure 25. Atomic ALDC curves for ambient density (left) and 44% compression (right) simulations at 3000 K (note that the initial values of the curves have no physical significance at times shorter than the filter time-window, 6 ps).

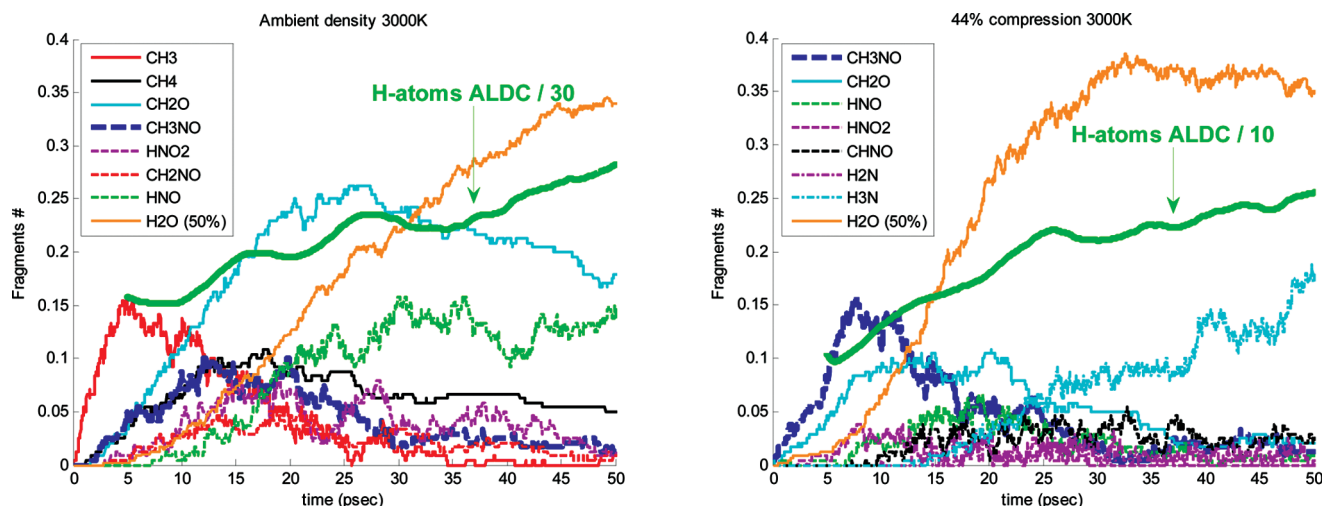


Figure 26. Evolution of the primary hydrogen containing fragments formed in 3000 K simulations at ambient density (left) and 44% compression (right), versus hydrogen ALDC (thick green line). For clarity, ALDC is divided by 30 (10) for the ambient density (44% compression) simulation, and the amount of H₂O molecules is halved.

becomes more moderate and can become negative. This dynamic correlation is more pronounced for hydrogen atoms and is weaker for heavier atoms.

CONCLUSIONS

The decomposition kinetics of hot liquid NM was studied at densities varying from ambient density to 44% compression, and at temperatures in the range 2500–4500 K using ReaxFF MD simulations. A change of mechanism was observed in the initial stage of NM decomposition as a function of density:

- At lower densities, the unimolecular C–N bond cleavage is the dominant reaction, producing CH₃ and NO₂ fragments.
- As density and pressure rise approaching CJ detonation conditions (~30% compression, ~3000 K) the dominant mechanism switches to the formation of the CH₃NO fragment via H-transfer and/or N–O bond rupture.

This behavior leads to a different kinetic and energetic behavior, as well as products distribution, depending on the density.

Thermal rate constants were calculated for the initial (k_1) and intermediate (k_2) decomposition stages of NM. Their density dependence is opposite at temperatures ≤ 3500 K and below 44% compression: k_2 increases when density increases, whereas k_1 decreases. At these temperatures, however, k_1 increases when the compression increases from 40% to 44%. k_2 is an averaged energy release rate, representing multiple chemical reactions whose yield improves with pressure increase. The nonmonotonic behavior of k_1 when density is varied can be understood based on the transition between the lower pressure initial decomposition mechanism, unimolecular C–N bond break, and the higher pressure initial route (around CJ state), CH₃NO production. The rate of the former unimolecular reaction is suppressed by pressure rise due to

collisions, whereas the rate of the bimolecular (or higher) reactions forming CH_3NO increases with pressure.

The activation energies extracted in the initial and intermediate stages of NM decomposition are $E_{a1} = 49.4 \pm 1.3$ kcal/mol (C–N bond break energy, for compression <30%) and $E_{a2} = 37.5 \pm 3.6$ kcal/mol (an effective value for multiple reactions). The activation energy E_{a1} for compression $\geq 30\%$ increases with density due to competing reactions involving CH_3NO production.

The calculated enthalpy change for hot NM decomposition at ambient liquid density is in a very good agreement (<3% deviation) with the measured value.²² Starting from ambient density, ΔH increases until it reaches a peak between 20 and 30% compression; thereafter it begins to decrease when compression increases. This variation of ΔH with density might be related to the initial decomposition path of NM: C–N bond break at low densities versus CH_3NO fragment formation at higher compressions. The observed correlation between ΔH and initial reaction needs to be further explored for other materials. If this is shown to be a general behavior, the high sensitivity of ΔH to the decomposition mechanism, together with its straightforward extraction from simulations, makes it a convenient and useful global parameter for detecting reaction dynamics under various conditions.

Final gaseous fragments asymptotic amounts were calculated. A very good agreement between the measured and calculated amounts was obtained. Both in measurement and simulation, H_2O was found to be the most abundant molecule.

It was shown that atomic ALDCs are more sensitive to the reactions dynamics than the monotonous MSD curves, and can be used to distinguish between time periods where chemical reactions occur and time periods that are diffusion-dominated and nonreactive. The hydrogen average local diffusion coefficient is more sensitive to reaction dynamics than heavier atoms.

Simulations of the various chemical paths in HE decomposition as a function of density and temperature provide detailed insight and understanding that may enable controlling initiation and propagation of detonation waves in HE materials.

■ ASSOCIATED CONTENT

Supporting Information. Cut off parameters in fragments analysis using “BondFrag” code and potential parameters used in ReaxFF. This material is available free of charge via the Internet at <http://pubs.acs.org>.

■ ACKNOWLEDGMENT

S.V.Z. and W.A.G. were supported by ARO (MURI-W911NF-05-1-0345) and ONR (N00014-05-1-0778, N00014-09-1-0634). Simulations were performed at DOD Major Shared Resource Centers under a DoD/HPCMP Challenge award (ARON27203C3K). R.K. and Y.Z. acknowledge support of The Center of Excellence for Explosives Detection, Mitigation and Response, Department of Homeland Security.

■ REFERENCES

- (1) Shaw, R.; Decarli, P. S.; Ross, D. S.; Lee, E. L.; Stromberg, H. D. *Combust. Flame* **1979**, *35*, 237.
- (2) Rice, S. F.; Foltz, M. F. *Combust. Flame* **1991**, *87*, 109.
- (3) Citroni, M.; Bini, R.; Pagliai, M.; Cardini, G.; Schettino, V. *J. Phys. Chem. B* **2010**, *114*, 9420.

- (4) Hardesty, D. R. *Combust. Flame* **1976**, *27*, 229.
- (5) Piermarini, G. J.; Block, S.; Miller, P. J. *J. Phys. Chem.* **1989**, *93*, 462.
- (6) Bourasseau, E.; Dubois, V.; Desbiens, N.; Maillet, J. B. *J. Chem. Phys.* **2007**, *127*, 084513.
- (7) Hervouet, A.; Desbiens, N.; Bourasseau, E.; Maillet, J. B. *J. Phys. Chem. B* **2008**, *112*, 5070.
- (8) Manaa, M. R.; Reed, E. J.; Fried, L. E.; Galli, G.; Gygi, F. *J. Chem. Phys.* **2004**, *120*, 10146.
- (9) Han, S. P.; Strachan, A.; van Duin, A. C. T.; Goddard, W. A. *J. Phys. Chem. A* **2011** in press.
- (10) Melius, C. F. *J. Phys. IV* **1995**, C4–535.
- (11) For example, Asatryan, R.; Bozzelli, J. W.; Simmie, J. M. *J. Phys. Chem. A* **2008**, *112*, 3172.
- (12) van Duin, A. C. T.; Dasgupta, S.; Lorant, F.; Goddard, W. A. *J. Phys. Chem. A* **2001**, *105*, 9396.
- (13) van Duin, A. C. T.; Strachan, A.; Stewman, S.; Zhang, Q. S.; Xu, X.; Goddard, W. A. *J. Phys. Chem. A* **2003**, *107*, 3803.
- (14) Mueller, J. E.; van Duin, A. C. T.; Goddard, W. A. *J. Phys. Chem. C* **2010**, *114*, 4939.
- (15) Chenoweth, K.; van Duin, A. C. T.; Dasgupta, S.; Goddard, W. A. *J. Phys. Chem. A* **2009**, *113*, 1740.
- (16) Strachan, A.; Kober, E. M.; van Duin, A. C. T.; Oxgaard, J.; Goddard, W. A. *J. Chem. Phys.* **2005**, *122*, 054502.
- (17) Nomura, K.; Kalia, R. K.; Nakano, A.; Vashishta, P.; van Duin, A. C. T.; Goddard, W. A. *Phys. Rev. Lett.* **2007**, *99*, 148303.
- (18) van Duin, A. C. T.; Zeiri, Y.; Dubnikova, Y. F.; Kosloff, R.; Goddard, W. A. *J. Am. Chem. Soc.* **2005**, *127*, 11053.
- (19) Zybin, S. V.; Goddard, W. A.; Xu, P.; van Duin, A. C. T.; Thompson, A. P. *Appl. Phys. Lett.* **2010**, *96*, 081918.
- (20) Zhang, L.; Zybin, S. V.; van Duin, A. C. T.; Dasgupta, S.; Goddard, W. A.; Kober, E. M. *J. Phys. Chem. A* **2009**, *113*, 10619.
- (21) Mochalova, V. M.; Torunov, S. I.; Utkin, A. V.; Garanin, V. A. 14th International Detonation Symposium, Idaho, April 11–16, 2010.
- (22) Ornellas, D. L. *J. Phys. Chem.* **1968**, *72*, 2390.
- (23) Benson, S. W. *Thermochemical Kinetics*, 2nd ed.; John Wiley: New York, 1976.
- (24) Hu, W. F.; He, T. J.; Chen, D. M.; Liu, F. C. *J. Phys. Chem. A* **2002**, *106*, 7294.
- (25) Tarver, C. M. *Combust. Flame* **1982**, *46*, 157.
- (26) Hobbs, M. L.; Kaneshige, M. J.; Gilbert, D. W.; Marley, S. K.; Todd, S. N. *J. Phys. Chem. A* **2009**, *113*, 10474.

■ NOTE ADDED AFTER ASAP PUBLICATION

This article posted ASAP on August 24, 2011. The 8th equation beneath Table 6 on page 10195 has been revised. The correct version posted on September 8, 2011.

Molecular dynamics simulations of weak detonationsMorag Am-Shallem,¹ Yehuda Zeiri,^{2,3} Sergey V. Zybin,⁴ and Ronnie Kosloff¹¹*Fritz Haber Research Center, Hebrew University, Jerusalem 91904, Israel*²*Department of Biomedical Engineering, Ben-Gurion University, Beer-Sheva 84105, Israel*³*Chemistry Department, NRCN, P.O. Box 9001, Beer-Sheva 84190, Israel*⁴*Materials and Process Simulation Center, California Institute of Technology, Pasadena, California 91125, USA*

(Received 13 June 2011; revised manuscript received 31 October 2011; published 12 December 2011)

Detonation of a three-dimensional reactive nonisotropic molecular crystal is modeled using molecular dynamics simulations. The detonation process is initiated by an impulse, followed by the creation of a stable fast reactive shock wave. The terminal shock velocity is independent of the initiation conditions. Further analysis shows supersonic propagation decoupled from the dynamics of the decomposed material left behind the shock front. The dependence of the shock velocity on crystal nonlinear compressibility resembles solitary behavior. These properties categorize the phenomena as a weak detonation. The dependence of the detonation wave on microscopic potential parameters was investigated. An increase in detonation velocity with the reaction exothermicity reaching a saturation value is observed. In all other respects the model crystal exhibits typical properties of a molecular crystal.

DOI: [10.1103/PhysRevE.84.061122](https://doi.org/10.1103/PhysRevE.84.061122)

PACS number(s): 47.40.Rs, 62.50.Ef, 82.40.Fp

I. INTRODUCTION

Explosives are characterized by a detonation wave which propagates through the material. After initiation, the velocity of the detonation front reaches a steady state that exceeds the speed of sound in the material. The present paper is devoted to the analysis of a model solid explosive with the purpose of correlating the microscopic structure and interatomic forces to the bulk detonation properties. The investigation is based on a classical molecular dynamics simulation with a simple force field. The initial goal was to construct a first-principle model that is able to qualitatively reproduce a stable detonation wave. The microscopic parameters considered are the crystal structure, the intermolecular forces that stabilize this structure, and the intramolecular potentials that yield the driving chemical reaction. The present investigation unravelled a new type of a solitary-like detonation wave that is directly driven by the one-step exothermic chemical decomposition. From a hydrodynamical perspective it can be classified as a weak detonation.

A common theoretical framework for simulating detonations relies on a continuum picture of the material properties using a hydrodynamic description and is based on the conservation of mass, momentum, and energy [1–4].

In the Chapman-Jouguet (CJ) model, the detonation wave is considered as a discontinuity between “unburnt” and “burnt” material, assuming that the transition from one state to another does occur instantaneously. It assumes an infinite reaction rate and requires only the knowledge of the thermodynamic equilibrium state of the burnt material to satisfy the conservation relations on the Hugoniot curve of compressed detonation products. The resulting detonation wave has zero-width reaction zone and should satisfy the minimum entropy solution of the Rankine-Hugoniot equations, which corresponds to *sonic condition* for downstream flow (downstream velocity with respect to the front, which equals the isentropic sound speed in reacted material). Freely propagating one-dimensional (1D) detonation wave without the piston (*unsupported detonation*) attains the steady-state velocity satisfying the sonic condition.

The CJ model is used extensively as an engineering tool enabling quick calculation of the detonation velocity and pressure in the design of explosive devices.

An extension of the CJ model was proposed by Zel’dovich, von Neumann, and Döring [5–7] (ZND) that incorporates finite-rate reaction kinetics resulting in a chemical reaction zone of finite length. It assumes that the unreacted explosive material behind the front is initially compressed to a high pressure resulting in a so-called von Neumann pressure spike. Then the chemical reactions are initiated behind the spike, leading to the exothermic energy release, temperature increase, and expansion of the reaction products to the lower pressure. The structure and length of the reaction zone is determined by the equation of state of intermediate products. After completion of the reactions, the products reach the final equilibrium state, at the end of the reaction zone. The final state determines the detonation velocity and depends only on the equation of state of the reaction products. For an unsupported detonation wave, this state satisfies the sonic condition as in the CJ model and is called the CJ state.

In the ZND model, besides the minimum-entropy (or, correspondingly, minimum-velocity) solution to the conservation equations, there are two other possible detonation propagation regimes. In a case of piston-supported detonation, the downstream flow can be subsonic in respect to the front and is called *strong or overdriven detonation*. Another type of possible hydrodynamical solutions is termed weak detonation. It is characterized by a downstream flow behind the detonation front that is supersonic in respect to the burnt material and effectively *decouples* from it (i.e., no disturbances from the burnt material can overtake the front). In addition, the weak detonation wave is characterized by only a moderate increase in density and pressure, which is smaller than the CJ pressure on the detonation products Hugoniot.

Zel’dovich [8] stresses that the weak detonation solution satisfies the boundary conditions of shock propagation and therefore is an admissible hydrodynamical solution. He argues that the reason that the weak detonation phenomenon has

not been observed experimentally is the unattainability of the steady-state conditions of this solution. In particular, a typical ZND route from the unreacted shock-compressed state to the burnt material gets trapped in the stable CJ point of minimum entropy production. Von Neumann, however, has shown that if the Hugoniot curves of partially reacted products intersect, then the weak detonation solution is possible [6]. For example, explosives that have very rapid initial exothermic decomposition followed by a slower endothermic reaction may exhibit such behavior, sometimes called *pathological detonation*. It has been also speculated by Tarver, based on a hydrodynamical equations, that in porous materials weak detonation could be stable [9]. Though standard ZND model assumes that chemical reactions are triggered by the high temperature due to the initial shock compression, it is also possible to consider an alternate ignition mechanism without preliminary shock heating at the von Neumann spike. Zel'dovich [10] discussed possible initiation of weak detonation by triggering chemical reactions with a sequence of sparks artificially fired along a tube.

Can a first-principle molecular dynamics (MD) simulation converge to the hydrodynamical detonation model?

There has been a continuous effort to develop MD simulation methods of explosives [11,12]. An interaction potential, known as the Reactive Empirical Bond Order potential (REBO), was introduced in Ref. [13]. This potential has a complex functional form and several parameters. Molecular dynamics simulations of detonation through a model two-dimensional (2D) crystal using this potential showed agreement with the predictions of the CJ model [14].

A significant step was the development of a reactive force field that accounts for breaking and forming chemical bonds during the passage of the shock wave through the solid [15]. Simulations of actual explosives, such as RDX, PETN, and TATP, have been attempted [16–23]. The main goal is to compare the simulation output to known experimental characteristics of the system, such as detonation velocity and final reaction products distributions. These studies were devoted to establish a realistic simulation scheme that converges to the framework of the hydrodynamic models. It was found that the goal of reaching steady-state detonation conditions requires a major computational effort. The phenomenon stabilizes only in a mesoscopic scale (micrometers), which requires very large-scale calculations including many millions of atoms. To establish such a method as a predictive tool, many such simulations should be performed and compared with experiment. A second round of improvements should then be applied to the force field. At present, this task is still in its infancy.

Schemes to bridge the gap between the hydrodynamical description of detonation and the MD approach have been explored. The idea is to replace a group of molecules by a single mesoparticle with an internal thermodynamic degree of freedom [24,25] or to describe a hydrodynamical cell by fictitious particles [26]. In both these schemes individual molecular properties are overlooked.

In the present study a different MD approach was utilized. We limited the objective to establish a relationship between the forces governing the dynamics in the microscopic system and the macroscopic phenomena. The simple molecular force

field employed is constructed to have only a small number of adjustable parameters. In a three-dimensional (3D) model, we observed stable detonation waves, their characteristics being independent of the initial conditions. It required a more thorough investigation to identify that these detonation waves are of a different character from those in the standard ZND model.

A first indication of a new phenomenon can be inferred from the 1D model of Peyrard *et al.* [27], constructed from a chain of unstable diatomic molecules. The dissociation reaction generated an accelerating detonation wave. In order to obtain a stable detonation wave artificial dissipation channels were added. Our analysis of their model revealed that a detonation wave in the 1D chain resembles a solitary wave. Further understanding requires a full 3D crystal model that should supply a natural dissipative mechanism.

The initiation of detonation wave in solids is closely related to the propagation of a shock wave through a crystal lattice. Both waves are quasi-1D. Early MD simulations of a planar shock wave in a perfect fcc crystal [28,29] revealed the formation of a solitary-like train at the shock front over a wide range of shock velocities. It has oscillatory structure and exhibits significant deviation from the thermal equilibrium inside the train. In addition, the MD simulations of shocks in a perfect bcc crystal have shown [30] that an isolated solitary wave can be emitted from the shock front and run ahead it at significantly faster speed than the shock front velocity. This links the present study to the subject of solitary waves propagation in a discrete lattice. Solitons are characterized by a group velocity that is proportional to the amplitude of the wave. For a 1D lattice we refer to the work of Toda, who established a relationship between the microscopic parameter of the repulsive part of the potential and the group velocity [31,32]. Holian has performed MD simulations of shock waves in the 1D Toda lattice to study the dependence of solitary train structure at the shock front on the interaction potential parameters [33].

Can the energy release reaction occur directly at the shock front as in the CJ model? The prerequisite is a metastable molecule whose one-step exothermic decomposition is triggered by the shock front, and its energy is immediately fed back into the detonation wave. By definition, shock wave propagation is faster than any linear elastic wave in the same material. As a result it will always confront *fresh* unperturbed molecules. For these molecules to contribute to the detonation event, their initial decomposition time scale should be similar or faster than the time scale determined by the front propagation velocity. Slower processes can take place behind the shock front. These processes may include thermal equilibration and heat dissipation as well as slower chemical reactions that lead to the final product distribution. If the slower reactions are endothermic, the weak detonation wave can be initiated.

In the present study we identified a diatomic molecule where the exothermic decomposition is sufficiently fast and can proceed directly at the detonation front. We observed a propagation of fast supersonic reactive wave initiated by the impulse impact in a 3D perfect molecular crystal. We analyze the dependence of the detonation wave parameters on the interaction potential and the molecule decomposition

kinetics. We find that the downstream flow is supersonic, and the density increase behind the front is very small, which is typical for a weak detonation. We also observe the decoupling of supersonic front propagation from the dissipative dynamics of the decomposed material left behind the front. Our analysis suggests that the weak detonation wave in the simulated crystal resembles behavior of a solitary wave propagating at the supersonic speed through the lattice. The molecule decomposition is triggered at the detonation front where a significant thermal nonequilibrium exists. The released energy is directly channelled into acceleration of the atoms from the dissociated molecules pushing solitary detonation front forward. Remarkably, the front propagation dynamics significantly depends on the relative orientation of the light and heavy atoms in the molecule with respect to the shock direction.

The simulation results show a possibility of fast initiation of the molecule decomposition reactions at the supersonic solitary wave front in contrast to the standard ZND model where the reactions take place behind the shock front, initiated by the shock compression. Summarizing, the solitary front ignition can provide a mechanism for a direct transition to the weak detonation regime from the initial uncompressed state without going first to the high-pressure state by the shock compression.

II. THE COMPUTATIONAL MODEL

An explosive is defined as a molecular crystal that can decompose to smaller particles, generating a stable detonation wave. The front of the detonation wave moves faster than the speed of the linear compression wave in the molecular crystal. MD simulation of detonations requires a scheme of molecular forces, initial geometry, boundary conditions, and atomic masses. The model should be able to sustain a stable crystal structure. Simulation of the system is based on the solution of the classical equations of motion with sufficient accuracy, using a modified version of the MD code MOLDY, which is described in Appendix A.

A. The reactive molecule model

The model crystal is represented by a slab of diatomic molecules arranged in a crystal structure. Each of the atoms can represent also a group of atoms. The two effective particles will be marked as N and C, and the masses are 47 amu for N and 15 for C. These notations and masses originated from nitromethane: the N corresponds to the NO₂ group, and the C to the CH₃ group. The difference between the masses is essential in such reactive molecular model [27]. However, no other similarity to nitromethane exists in our model. The chemical bond between N and C is designed to be metastable. When energized it can dissociate exothermally. The shape of the potential energy curve as a function of the N-C distance is shown in Fig. 1. When the distance N-C is smaller than the barrier position the molecule is bound. However, when this distance is increased beyond this position the molecule disintegrates. In an energetic perspective, the molecule absorbs sufficient energy such that its internal energy is higher than the energy barrier. Separation of the N-C atoms results in

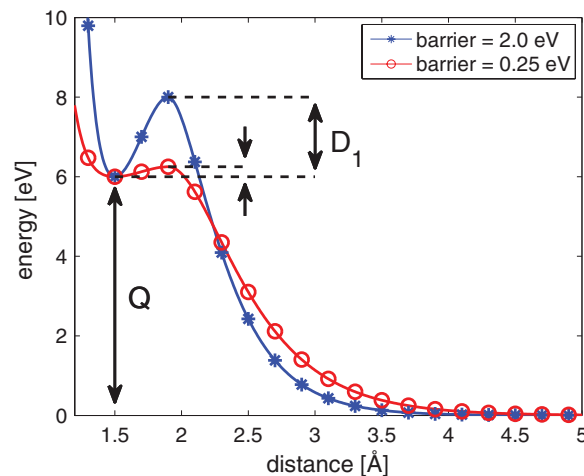


FIG. 1. (Color online) The reactive internal potential as a function of the N-C distance for two different ratios between the barrier height and the exothermicity. When the distance N-C is smaller than the barrier position (here at 1.9 Å, the local maximum) the molecule is bound. When the distance is increased beyond this position the molecule dissociates. Initially the N-C distance is at the equilibrium distance (here at 1.5 Å, the local minimum). Q represents the exothermicity, and D_1 the barrier height for the N-C dissociation.

decomposition of the molecule to its constituents accompanied by energy release. The evaluation of the potential and force during the trajectory calculations was carried out by generating and storing a table of the potential and force values at different N-C distances, according to the potential shown in Fig. 1, or similar potentials. A cubic spline interpolation was used to extract the values. There are functional forms that can be used to generate such an exothermic reactive potential; some of them are described in Ref. [11]. We used a piecewise defined function to generate the potential; its functional forms are described in Appendix B.

B. The molecular crystal

The molecular crystal was constructed by a lattice of N-C molecules with a bonding interaction between similar groups in neighboring molecules. The N entity interacts with other N and C interacts with other C entities. A Morse potential was chosen to describe these interactions:

$$V(r) = D(e^{-2\beta(r-r_0)} - 2e^{-\beta(r-r_0)}). \quad (1)$$

The parameters used are shown in Table I. The initial distances between nearest neighbor molecules was chosen as $r_0 = 7.5 \text{ \AA}$. A long and narrow slab of this molecular crystal was assembled with FCC symmetry. Other structures studied, the BCC and simple cubic crystals, were found to be unstable with this type of pair potentials. This finding is consistent with analysis of stability of Lennard-Jones crystals [34].

C. Boundary conditions and initial conditions

We expect the detonation wave to be quasi-1D. Hence, the reactive crystal slab used is chosen to be long and narrow. The direction of the propagation axis was chosen as Z, and it coincides with the [111] crystallographic axis. The molecular

TABLE I. Potential parameters used for the intermolecular interaction. The third line shows the parameters of the inner part of the intramolecular reactive bonding potential (see Appendix B). The same potentials were used for N-C atoms of different molecules.

Interaction	D (eV)	β (\AA^{-1})	r_0 (\AA)
N-N	0.08	1.0	7.5
C-C	0.016	1.0	7.5
N-C (inner part):			
Barrier of 0.25 eV	0.25	4.33	1.5
Barrier of 2.0 eV	2.0	4.33	1.5

axes were also oriented along the Z direction. Thus, the crystal is very nonisotropic. The length of the periodic unit in the $[111]$ direction of an FCC crystal is $\sqrt{6}$ times r_0 . In our case $r_0 = 7.5\text{\AA}$, so the length of the periodic unit is $\approx 18.37\text{\AA}$. This distance will be referred to in the following as the unit cell length. The length of the crystal was 295 unit cells along the Z direction, and, in some cases, a crystal with a length of 587 unit cells was used. Periodic boundary conditions were imposed along the perpendicular directions X and Y . To check that the size of the cross section is sufficient we ran simulations of crystals with various cross sections. It was found that detonation properties are converged in the larger cross sections. The converged cross section that was eventually used consists of 48 molecules in the XY plane.

The shock wave was initiated by a small crystal pellet, assigned with an initial high velocity in the Z direction. The pellet collided with one of the small faces (XY plane) of the slab. The velocity of the pellet was not kept constant: The MD simulations were of NVE type, and the positions and velocities of the pellet's particles were calculated with no distinction. The pellet was composed of three crystal layers along the Z direction and had 48 N-C molecules in each layer. The collision of this pellet was sufficient to initiate a sustainable shock in the primary crystal.

Most of the simulations were carried with initial temperature of 0°K . A few simulations were carried with higher initial temperatures.

III. WEAK DETONATION WAVES IN THE CRYSTAL

The analysis of weak detonation wave starts from the static properties of the reactive crystal. The second step describes the initiation process, showing that a stationary detonation wave is formed, independent of initiation process. The classification as a weak detonation relies on thermodynamics analysis of the phenomena.

The equilibrium properties of the crystal model were characterized. The details are summarized in Appendix C. A linear relation was found between the velocity of the elastic p -wave and the stiffness of the potential [the β parameter in Eq. (1)].

A. Initiation of stable detonation waves

We ran NVE simulations of shock waves in the model reactive crystal, initiated by the small pellet described above. After initiating a shock wave, a transient emerges, eventually

stabilizing into a stable shock front. Such simulations were run with different crystal parameters and different initial velocities of the pellet. The propagating shock wave initiated a decomposition reaction in crystals composed of reactive molecules. When the decomposition reaction kept pace with the shock front, the shock wave transformed into a detonation wave. The simulations were carried with initial temperature of 0°K . A few simulations were carried with higher initial temperatures, in order to verify that the phenomenon is not restricted to 0°K .

A stable detonation wave is independent of initial conditions. This was verified by using different initial pellet velocities leading to shock waves that are independent of these initial velocities. The details can be found in Appendix D, and in Fig. 17.

A snapshot of the detonation process is shown in Fig. 2. A distinction between the unperturbed crystal and the burnt material is clearly seen. An enlarged section of the reaction zone is shown on the bottom.

Similar simulations, with an endothermic intramolecular Morse potential, yielded decaying shock waves, with propagation velocity that depends on the initial pellet velocity.

B. Classification of the detonation waves as weak detonations

After the short transient the shock wave stabilized into a stable weak detonation wave. The shock front propagated in a very high Mach number, practically decoupled from other processes in the crystal. The number of molecules that were decomposed by this shock front changed from one simulation to another, depending on internal potential parameters such as the exothermicity and the barrier height for C-N dissociation. Only a small compression was associated with this front. Other properties, such as the mass velocity (see Sec. III C 2) and the kinetic energy (see Sec. III C 3), also exhibit an increase in magnitude. This shock wave will be referred to as the reaction wave in the following.

The reaction wave travels through an unperturbed crystal, and therefore its velocity is determined by the crystal properties (see Sec. IV). The reaction wave propagation velocity, as well as its amplitude, are independent of the initial impact (see Appendix D). The velocity does depend on the exothermicity of the reaction, which is an intrinsic property of the material. The dependence of the detonation velocity on the reaction exothermicity will be discussed later (see Sec. IV A).

After the reaction wave, another shock front appeared, characterized by a large increase of both the mass velocity and the kinetic energy. In the second shock front most of the remaining molecules dissociated, leading to a decomposition yield of above 85%. This second shock wave will be referred to as the compression wave in the following. In contrast to the reaction wave, the amplitude of the compression wave decays during its propagation. The compression wave velocity depends on the impact strength but not on the exothermicity.

The reaction wave is faster than the compression wave: $u_{\text{reaction}} > u_{\text{compression}}$ (see Figs. 3 and 4). *This fact categorizes the reaction wave as a weak detonation:* The compression wave is a typical shock wave. It moves faster than sound waves in the reacted material; therefore it sets an upper limit for the sound wave velocity: $u_{\text{compression}} > u_{\text{sound}}$. Thus,

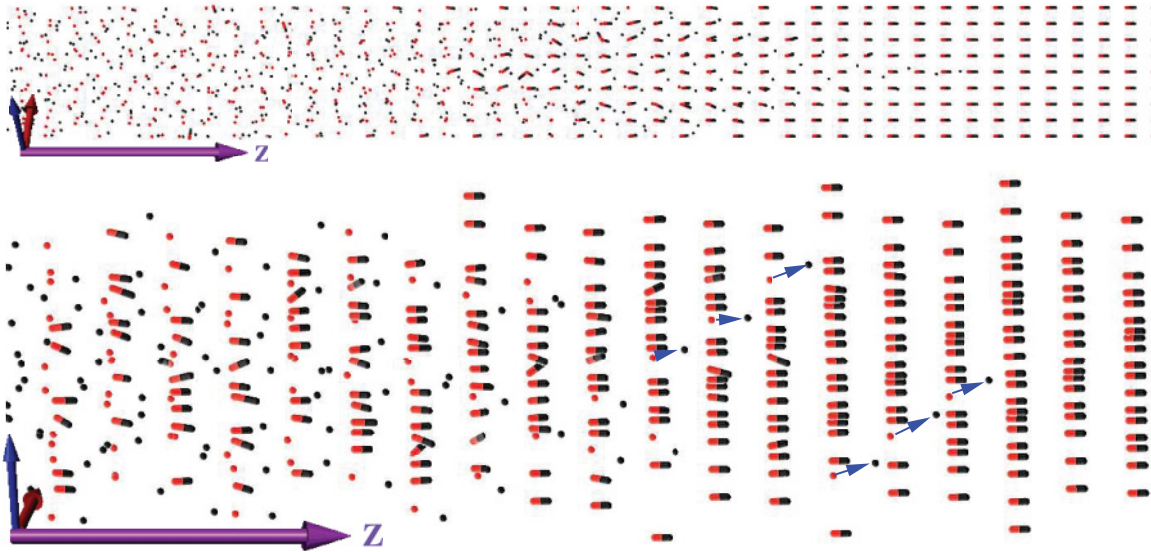


FIG. 2. (Color online) A snapshot of the detonation wave. The propagation axis is the Z direction. Periodic boundary conditions are used in the X, Y directions. The right-hand side shows the unperturbed crystal structure. The red (gray) objects represent the heavy particles (N). The black objects represent the light particles (C). On the left-hand side of the image one can observe the burnt material after the passage of the shock wave. The shock front is characterized by pilot cascades of light particles that are emitted from the decomposed molecules and initiate the next layer in a domino-like effect. The lower panel is an enlarged viewpoint of the detonation front. The arrows indicate decomposed N-C pairs, corresponding to the pilot cascade. This simulation was carried out with exothermicity of 6 eV and a barrier of 0.25 eV. Eventually, in this simulation, in approximately 20 layers, most of the material is decomposed.

$u_{\text{reaction}} > u_{\text{sound}}$. We see that the reaction wave is supersonic with respect to the matter behind it. This is the hydrodynamical definition of weak detonation [4 p. 280].

C. Thermodynamics profiles of the weak detonation waves

The profiles of weak detonations differ from those of normal detonations: In weak detonations there is no compression of the material before the reaction. After the reaction front, there is only a small change in the density, pressure, and velocity of the particles.

1. Different dissociation barrier height

Figure 3 compares the decomposition fraction of two simulations as a function of time and position. The first corresponds to molecules that have an N-C dissociation barrier of 2 eV (left plot). The second corresponds to molecules with a dissociation barrier height of 0.25 eV. The reaction exothermicity in both simulations is 6 eV. For a dissociation barrier of 2 eV, $\sim 35\%$ of the molecules are decomposed by the reaction wave. When the compression wave passes through the partially “burnt” material, most of the remaining molecules decompose (small fluctuations around 90%). For a smaller dissociation barrier, 0.25 eV, more than 85% of the molecules are decomposed simultaneously with the *reaction* shock front.

The reaction wave velocities are almost independent of the dissociation barrier height, as can be seen in Fig. 3. The barrier does influence the mass velocity and the decomposition fraction. The decoupling of the reaction wave from the compression wave and from the dissociation process results from the fact that this is the fastest wave in the material,

leaving behind the slower processes. This phenomenon is another signature of a weak detonation wave.

2. Mass velocity profile

The mass velocity characterizes the mass current and is defined as $\langle v \rangle = \frac{\sum_i m_i v_i}{\sum_i m_i}$. Figure 4 shows a contour plot of the Z component of the mass velocity during the simulation. The mass velocity plot shown can be compared to the decomposition percentage during the same simulation (right-hand side of Fig. 3): The decomposition front and the discontinuity of the mass velocity coincide, and define the reaction wave. The compression wave is observed on the mass velocity plot, but is absent from decomposition plot since the majority of the molecules have already decomposed.

Figure 5 shows profiles of mass velocity at different snapshots during the simulation. The values were averaged over bins with a constant number of particles, 96, in each bin. The top plot shows the Z component of the mass velocity along the solid for three time values. The largest amplitude (the left peak for each time) is associated with the compression wave. At later times the peak mass velocity decays due to dissipation. The first shock front (the right sudden change in velocity for each time) is associated with the reaction wave. The insert shows a zoom-in on the reaction fronts. The average mass velocity after the reaction front, ~ 0.3 km/s, is much smaller than the reaction front velocity, ~ 65 km/s. This is consistent with a small increase of density after the reaction front (see Fig. 8). It is clear that the reaction wave amplitude does not decay. When comparing simulations with different parameters, we find that the reaction wave amplitude depends on the reaction exothermicity and is independent of the impact strength. As

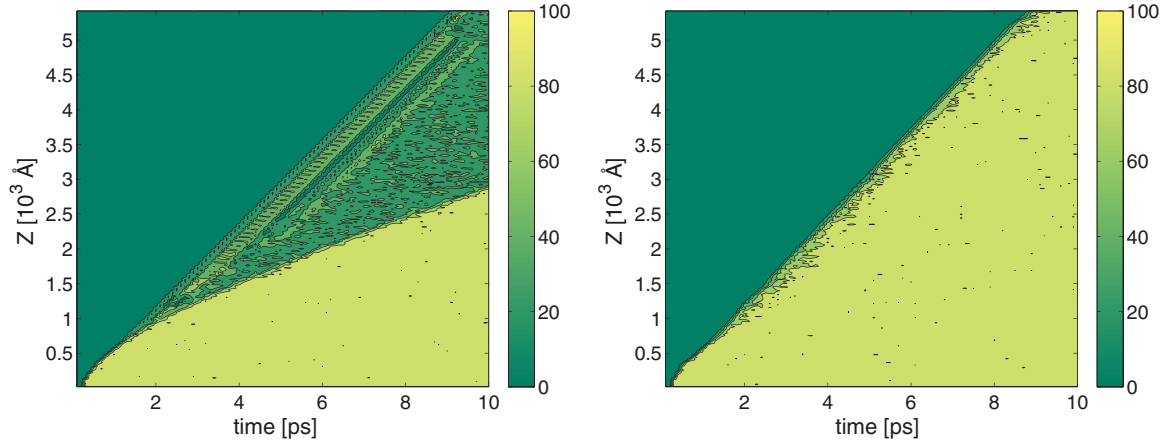


FIG. 3. (Color online) Contour plots of decomposition percentage during two different simulations. The left plot is obtained in a simulation with a dissociation barrier of 2 eV. Some of the molecules are decomposed by the reaction wave. Most of the other molecules (around 90%) are decomposed by the compression wave. The right plot is obtained in a simulation with a decreased dissociation barrier of 0.25 eV. More than 85% of the molecules are decomposed by the reaction wave. In both cases the exothermicity is 6 eV, and the initiating pellet velocity is ~ 90 km/s. The reaction front velocity in the case of the higher barrier, ~ 60 km/s, is very similar to the case of the smaller one, ~ 62.5 km/s.

discussed above, in the Introduction and in Appendix D, this is a characteristic of a detonation wave. The compression wave behaves differently: It has a decaying amplitude that does not depend on the exothermicity but does depend on the impact strength. The compression wave is a regular

compression shock wave. It travels through an unstructured matter composed of reaction decomposition products.

The X component of the mass velocity is shown in the bottom plot for a single snapshot. The shock front is characterized with a abrupt onset of fluctuations. There is a minor change after the first shock front.

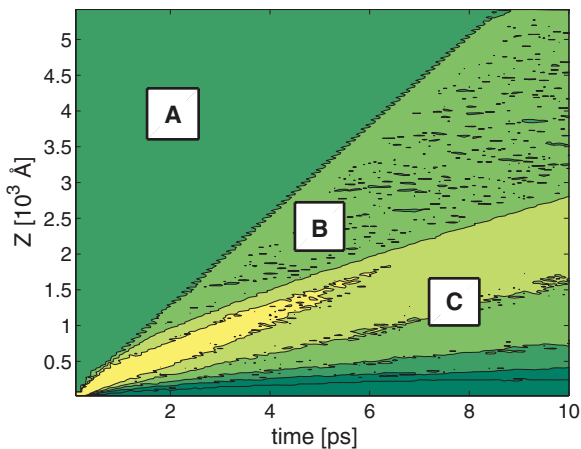


FIG. 4. (Color online) Contour plot of mass velocity along the Z direction. The dissociation barrier height in this simulation was 0.25 eV, and the reaction exothermicity was 6 eV. The initiating pellet velocity was ~ 90 km/s. Three regions are marked in the plot: Region A is the preshocked material. The mass velocity here is 0. Region B is the material after the reaction wave. The mass velocity here fluctuates around an average value of 0.3 km/s (see Fig. 5 for more detailed profiles). The mass velocity plot shown here can be compared to the decomposition percentage during the same simulation, which is shown on the right plot of Fig. 3: The decomposition front and the discontinuity of the mass velocity coincide, characterizing the reaction wave. Region C is the material after the compression wave. The mass velocity on the peak of the compression wave decays from around 20 km/s at 1 ps to 8.5 km/s at 10 ps. The compression wave is visible on the mass velocity plot but is almost absent on the decomposition plot: For this barrier height, most of the molecules have already decomposed before the compression wave reached them.

3. Energies and temperature

Further insight on the detonation process can be obtained by inspection of the kinetic energy and the local temperature profiles, shown in Figs. 6 and 7, respectively. The profiles correspond to an intermediate time of 10 ps. The local temperature is defined as $T_l = \frac{1}{Nk_B} \sum_i^N m_i (v_i - \langle v \rangle)^2$, where $\langle v \rangle$ is the mass velocity defined above. The values were determined by averaging over bins with a constant (96) number of particles. The reaction wave front can clearly be seen as a sharp change in kinetic energy and temperature. The insert in the local temperature figure shows a small region after the first shock front, which is not thermalized. The increase of the Z component of the local temperature precedes the corresponding increase of the X component.

Figure 8 shows the potential energy and the density profiles at the same time step. On the right, a small increase of the potential energy is observed, followed by a large decrease. The small increase is caused by a minor compression before the dissociation starts, as seen in the density profile. The large decrease that follows is caused by the energy release of the exothermic decomposition process. The average density after the reaction front is only slightly larger than the density before this front. This is consistent with the small increase in the mass velocity (see Fig. 5). This phenomenon characterizes weak detonations.

IV. SATURATION OF THE WEAK DETONATION VELOCITY

The detonation wave can be characterized by a stable detonation velocity independent of initiation parameters, as

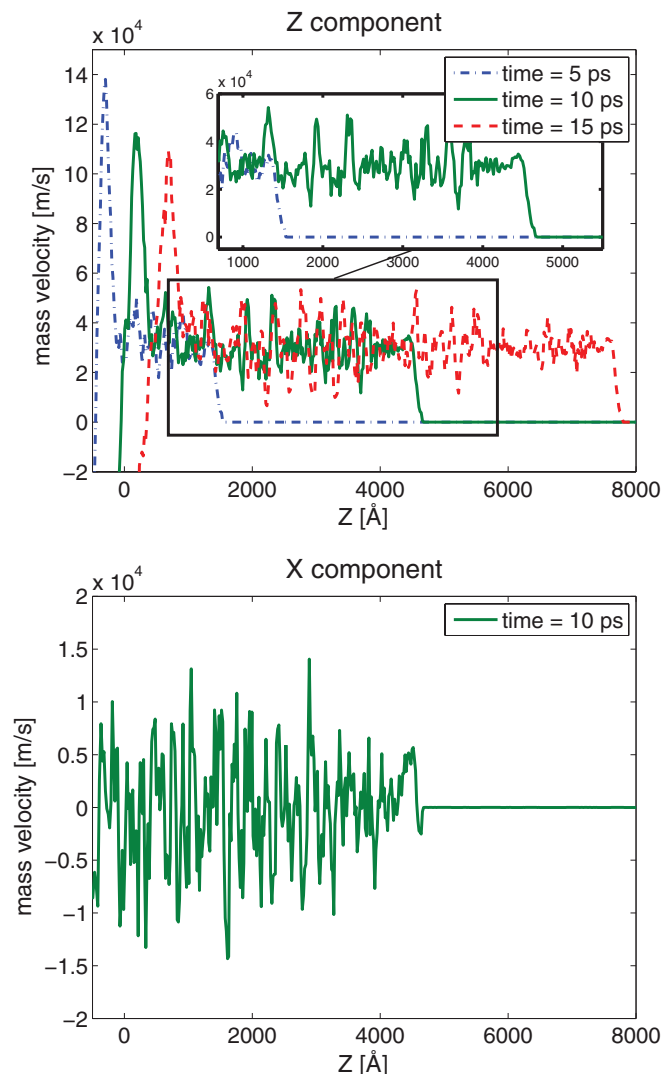


FIG. 5. (Color online) Mass velocity profiles along Z and X directions. The exothermicity of the reaction in this simulation was 6 eV, and the barrier was 0.25 eV. The values were determined by averaging over bins with constant 96 particles in each bin. The left edge of the crystal is placed at -500\AA . The top plot shows the profile of the mass velocity in the Z direction, at three time values. The bottom plot presents the mass velocity along the X direction at a single time value. Along the Z direction (top figure), the largest amplitude (the left peak on each time step) is associated with the secondary compression wave. At later times the peak mass velocity decays due to dissipation. The first shock front (the right peak on each time step) is associated with the reaction wave. The reaction wave amplitude does not decay. The insert shows a zoom of the first shock fronts for the two shorter times. The average mass velocity after the reaction front, ~ 0.3 km/s, is much smaller than the reaction front velocity, ~ 65 km/s.

discussed in Appendix D. The terminal velocity of the wave is a function of the microscopic parameters used in the model. Insight aimed at deciphering the phenomena is obtained by a systematic study of the variation of the detonation velocity as a function of the parameters of interest.

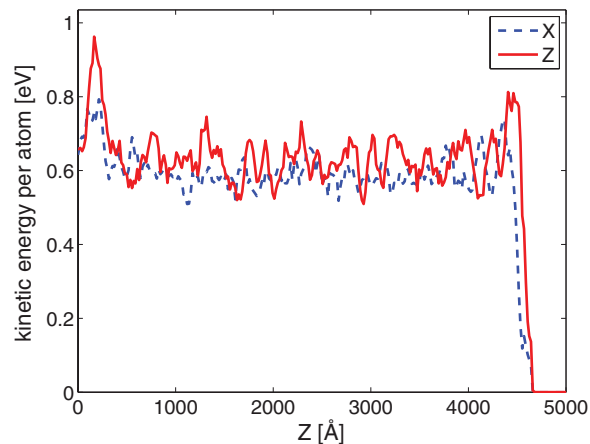


FIG. 6. (Color online) Normalized kinetic energy profile at time = 10 ps. The exothermicity of the reaction in this simulation was 6 eV, and the dissociation barrier was 0.25 eV. The values were averaged over bins with constant number of particles, 96, in each bin. The blue dashed line corresponds to kinetic energy along the X direction, and the red solid line to kinetic energy along the Z direction. The large peak on the right corresponds to the reaction wave front.

A. Intramolecular potential parameters: Exothermicity of the reaction

Simulations of detonation using reactive slabs were carried out with different values of the exothermicity. All other parameters, such as crystal structure, impact magnitude, intermolecular potential, particles masses, initial conditions, were kept constant. Figure 9 displays the reaction propagation, which is determined by the dissociation front, in crystals with different exothermicity values. In the exothermicity range displayed in

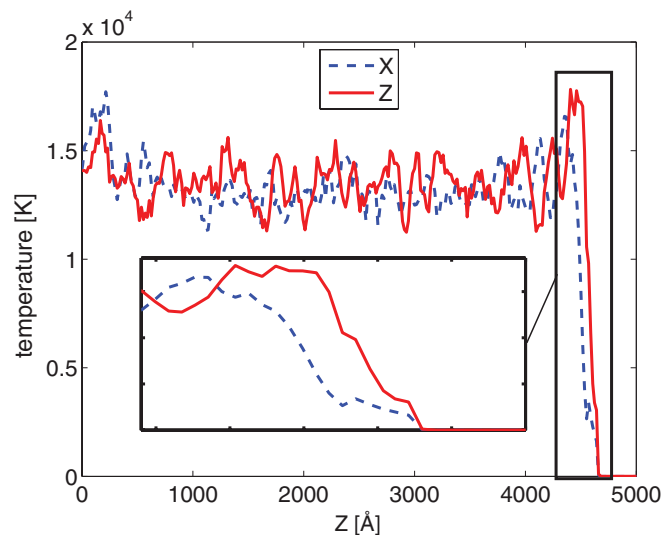


FIG. 7. (Color online) Local temperature profile at time = 10 ps. The parameters are the same as in Fig. 6. The blue dashed line represents temperature along the X direction, and the red solid line along the Z direction. The insert shows an unthermalized region: The large peak on the right is the reaction wave front. The increase of the Z component of the local temperature precedes the increase of the X direction.

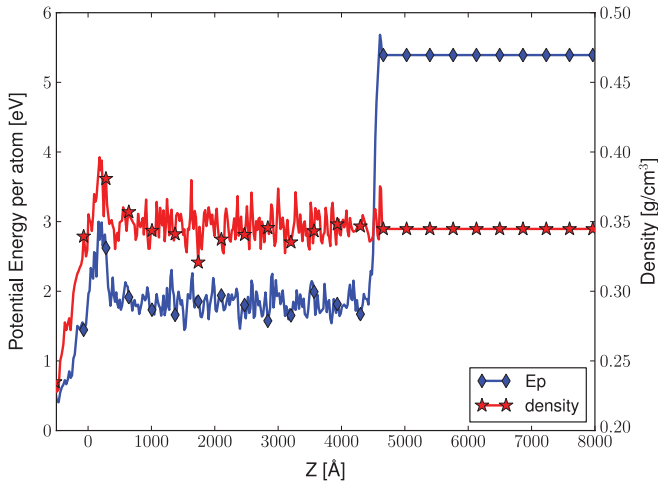


FIG. 8. (Color online) Potential energy (E_p) and density profiles at $t = 10$ ps. The parameters are the same as in Fig. 6. The first shock front displays a small increase of the potential energy, due to a small compression before the dissociation. This small increase is followed by a large decrease of the potential energy, due to the energy release of the exothermic decomposition. The average density after the reaction front is not significant higher than the density before this front. The peak on the left is associated with the compression wave.

the figure (1.0–3.5 eV), the detonation velocity increases as a function of exothermicity. At larger exothermicity values, the detonation velocity reaches saturation: Simulations with exothermicity values above 3.0 eV show only a minor increase in the detonation velocity. Figure 10 displays the variation in detonation velocity as a function of reaction exothermicity. The kinetic energy of the particles behind the reaction wave was found to depend linearly on the exothermicity of the reaction. Thus it is responsible for the energy balance. Nevertheless, in weak detonations this additional kinetic energy is decoupled from the reaction shock front.

The saturation effect is an interplay between three factors: the crystal rigidity, responsible for the nonlinear wave propagation, shear effects, responsible for energy dissipation at the reactive shock front, and kinematic effects, which determine

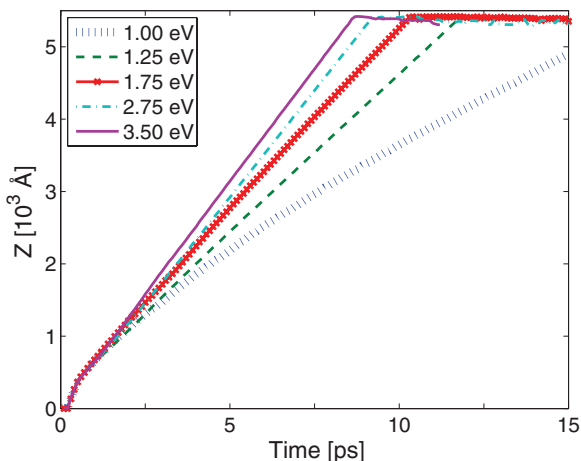


FIG. 9. (Color online) Reaction front propagation in crystals with different exothermicity values. All other parameters are identical.

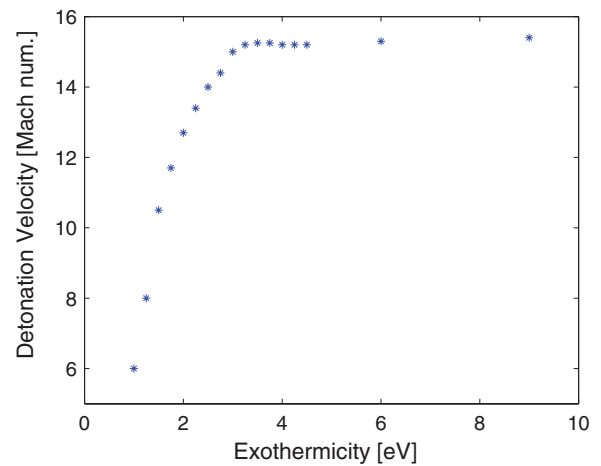


FIG. 10. (Color online) Detonation velocity in the crystal as a function of reaction exothermicity. The detonation velocity is measured in reduced units, normalized to the p -wave velocity, which is 4.6 km/s. We can see the increase of detonation velocity as a function of exothermicity at low exothermicity values, until approximately 3 eV. The saturation of the detonation velocity at high exothermicity values can also be seen. The saturation was verified by simulations with very high exothermicity values: There is a very small increase of the detonation velocity in crystals with higher exothermicity values (12, 15, 18, and even 27 eV; these results are not shown here).

the partitioning of the energy release during the decomposition of a single molecule.

Some insight regarding kinematic effects and the crystal rigidity is discussed in the following; see Secs. IV B and IV C. The nonlinear effect of shear was not explored systematically in this study. The convergence of the calculations was checked to an increase in the XY cross section (see Sec. II C). While checking convergence, we found that increasing the cross section decreases the detonation velocity. This is an indirect indication that the detonation velocity is sensitive to shear.

B. Kinematic effects

In weak detonations the decomposition mechanism of the reactive molecules has to be linked to the characteristics of the detonation wave. A propagation by a domino-like effect, as seen in Fig. 2, requires the decomposition to be asymmetric with respect to the Z direction. Insight is obtained by examining a simplified 1D model of decomposition of a single diatomic molecule. Initially the molecule is at rest. A light particle emerges from the decomposition of the neighboring molecule and hits the molecule from the heavier side (Fig. 11, top). The collision initiates the decomposition process. At the end of the decomposition, the light particle of this molecule is emitted toward the next molecule (Fig. 11, bottom). The mass of the light particle is denoted by m , and the mass of the heavier particle is αm ($\alpha > 1$). After the initiation collision, the molecule decomposes, and the heat of the reaction, E , releases as kinetic energy. The velocity of the colliding particle is denoted by v_1 . After the decomposition, the velocities are denoted by u_1, u_2, u_3 , for the colliding particle, the heavy particle, and the light particle, respectively.

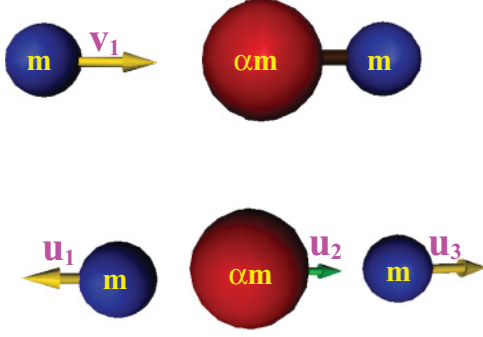


FIG. 11. (Color online) A molecule is hit by a light particle, emitted from neighboring decomposition (top diagram). After the collision, the molecule decomposes (bottom diagram).

Under these conditions the equations for momentum and energy conservation become

$$\begin{aligned} mv_1 &= mu_1 + \alpha mu_2 + mu_3, \\ \frac{1}{2}mv_1^2 + E &= \frac{1}{2}mv_1^2 + \frac{1}{2}\alpha mu_2^2 + \frac{1}{2}mu_3^2, \end{aligned} \quad (2)$$

where we assume that the collision is complete, meaning that all potential energy has been consumed. In steady-state detonation, the initial velocity of the colliding particle should be equal to the velocity of the emitted light particle:

$$v_1 = u_3, \quad (3)$$

and this should also become the group detonation velocity.

Two mechanisms come to mind: a direct and a delayed decomposition. In the direct decomposition mechanism, Eqs. (2) and (3) give the complete kinematic picture. Substituting Eq. (3) into Eq. (2) cancels out the terms v_1 and u_3 . Therefore, the detonation velocity is undetermined without further assumptions. In order to determine the wave propagation velocity, more details on the dissipation mechanism, the crystal structure and the nonlinear properties are needed.

Next, we analyze the delayed decomposition mechanism. This mechanism has two steps: First, the colliding particle has an elastic encounter with the molecule. The molecule after the collision will acquire a velocity of u_{23} and mass of $(\alpha + 1)m$. In the second step, the molecule will dissociate into its components. The equations for momentum and energy conservation of the first step are

$$\begin{aligned} mv_1 &= mu_1 + (\alpha + 1)mu_{23}, \\ \frac{1}{2}mv_1^2 &= \frac{1}{2}mu_1^2 + \frac{1}{2}(\alpha + 1)mu_{23}^2 \end{aligned} \quad (4)$$

And the equations for momentum and energy conservation of the second step are

$$\begin{aligned} (\alpha + 1)mu_{23} &= \alpha mu_2 + mu_3, \\ \frac{1}{2}(\alpha + 1)mu_{23}^2 + E &= \frac{1}{2}\alpha mu_2^2 + \frac{1}{2}mu_3^2. \end{aligned} \quad (5)$$

Again, we require the steady-state condition, Eq. (3). Solving these equations shows that the velocities $v_1 = u_3$, which are equal to the detonation velocity, are proportional to $\sqrt{E/m}$.

A strong detonation process is adequately described by a delayed mechanism, since there is a delay between the compression (which leads to collisions) and the decomposition. The $\sqrt{E/m}$ dependence of the strong detonation velocity

is in accordance with the hydrodynamical theory. This \sqrt{E} dependence was obtained in Ref. [35] in MD simulations of detonations in the REBO model and in Ref. [36] in another crystal model. A different result was obtained in an earlier study [37], in which a linear dependence of the detonation velocity on the energy released is reported.

A weak detonation process is adequately described by the direct mechanism since the reaction coincides with the shock front. In weak detonations, we find the detonation velocity to saturate, becoming independent of the energy release. This means that in our 1D model, only the results of a direct decomposition mechanism can fit this phenomenon. The relation of direct reaction mechanism to weak detonations was shown also in hydrodynamic analysis of the ignition stage [38].

The mechanism discussed above suggests a difference between the two possible reaction wave propagation directions: Different behavior is expected if the reaction wave emits the heavier particle of the molecule, which in turn collides with the lighter particle of the neighboring molecule. This anisotropic behavior of the reaction wave was examined by initiating the shock wave in the opposite edge, impacting from the lighter side of the molecules. Under these conditions, no stable constant velocity reaction waves were formed.

The dependence of the detonation wave velocity on the mass of the emitted particle was also examined. We performed simulations of detonations where the mass of the lighter particle was varied while maintaining the same structure and force field. In order to keep the total mass unchanged, the mass of the heavier particle was also changed. The masses used were 22, 10, and 5 amu for the C particle (and 40, 52, and 57 amu for N , respectively). Several simulations were performed, with different exothermicity values. We expect that decreasing the mass of the C lighter particle will result in a higher velocity, hence faster detonation. This has been already suggested by Peyrard *et al.* [27] in a 1D model. The magnitude of exothermicity at which the detonation velocity saturated was found in all cases to be close to 3 eV. However, the saturation velocity depended on the mass of the emitted C particle. Lower mass of this particle led to an increased detonation velocity. These results are presented in Fig. 12, in log-log scale. A linear fit to the velocity logarithm as a function of the mass logarithm was calculated and is displayed in the graph. The resulting slope is close to 0.5 (0.49), which reveals a $1/\sqrt{m}$ dependence of the detonation velocity on the mass of the emitted group. This dependence is identical to the dependence of the shock velocity of solitons in a Toda lattice.

C. Crystal rigidity: Intermolecular potential parameters

Simulations of the propagation of small amplitude displacements in the crystal showed that the elastic p -wave velocity depends linearly on the β parameter of the intermolecular Morse potential Eq. (1), i.e., the stiffness. This is in agreement with the propagation of elastic waves in a 1D crystal model. See Appendix C2b and Fig. 16 for details.

The shock wave velocity is crucially dependent on the rigidity of the crystal, which is determined by β . To explore this dependence we carried out simulations of detonations in

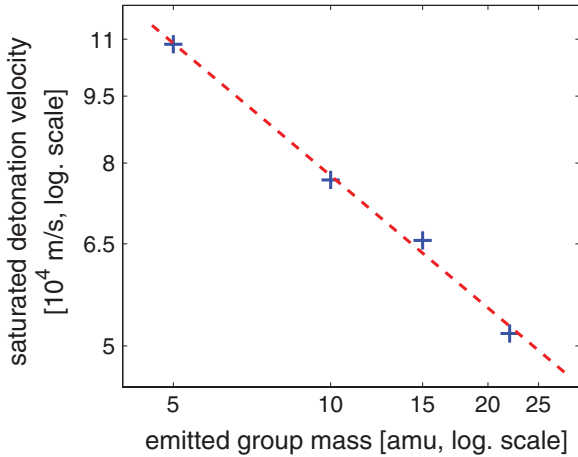


FIG. 12. (Color online) Saturation values of detonation velocities, marked with asterisks, as a function of the mass of the emitted C group. The graph is plotted in logarithmic scale on both axis. In all cases this saturation value is obtained when the exothermicity is close to 3 eV. A linear fit of the data in the log-log scale is also plotted. The slope of the linear fit is close to -0.5 (-0.49), indicating that the detonation velocity is proportional to $1/\sqrt{m}$.

crystals with different β values. The first effect observed is that an increase in β leads to an increase in magnitude of the exothermicity for which the saturated reaction wave velocity is observed. The second effect found is that the saturation reaction wave velocity increased exponentially as a function of β . Figure 13 shows the logarithm of the saturated reaction wave velocity as a function of β . The exponential dependence can be clearly seen. The exponential dependence suggests that the saturation of the reaction wave velocity depends on the repulsive part of the intermolecular potential. This is different from the elastic p -wave velocity, which is governed by the

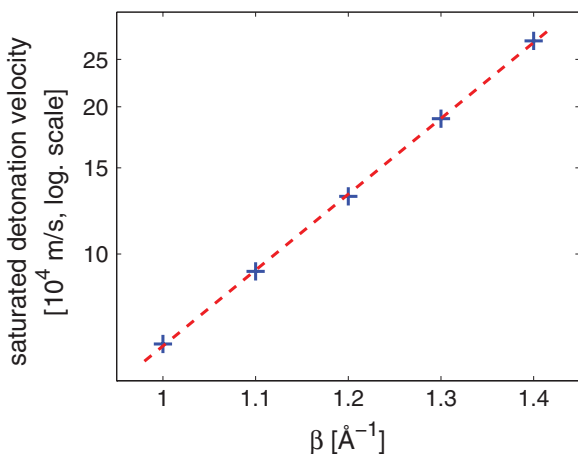


FIG. 13. (Color online) Comparison of reaction propagation velocities (scaled logarithmically) in five different crystals, β ranges from 1 to 1.4 \AA^{-1} (when β is the coefficient inside the Morse potential's exponent). The exponential dependence suggests that the saturation of the detonation velocity is caused by the repulsive part of the intermolecular potential. This is different from the elastic p -wave velocity dependence, which is governed by the behavior of the potential near the equilibrium point (see Appendix C2b and Fig. 16).

shape of the potential near equilibrium and varies linearly as a function of β .

To verify that the saturation of the reaction wave velocity is governed by the repulsive part of the intermolecular potential, we ran additional simulations. In these simulations we varied the stiffness of the inner part of the repulsive potential without altering other parameters of the crystal: The potential was combined from a repulsive part of Morse potential with $\beta = 1.2 \text{ \AA}^{-1}$ and an attractive part of Morse potential with $\beta = 1.0 \text{ \AA}^{-1}$. The reaction shock wave velocities in these crystals were compared to the previous simulations. We found that the reaction waves velocities were almost identical to those with $\beta = 1.2 \text{ \AA}^{-1}$. To conclude the reactive shock-wave velocity is governed by the repulsive part, and independent of the soft long range part of the potential. This phenomenon characterizes solitary waves, as has been suggested by Toda [31,32] and by Rolfe *et al.* [39].

V. DISCUSSION

The purpose of this study was to bridge the gap between a first-principle microscopic model of detonation and bulk hydrodynamical theories. The first task was to obtain a stable detonation wave independent of initial conditions. For this task we constructed a reactive molecular crystal model characterized by pair potentials. The equilibrium properties of the crystal are typical. It is stable at low temperatures and melts at temperatures that scale with the binding energy. The model crystal also possesses linear elastic waves. The detonation potential was added by making the molecule metastable to dissociation releasing a significant amount of energy. The model fulfilled the expectations and a stable detonation wave was identified.

Further analysis, which compared the results obtained in the simulations to hydrodynamical theory, revealed a puzzling picture. The detonation wave did not have the characteristics of the common solutions of the ZND model. Some of the differences are the following:

- (1) The compression at the shock front was minor.
- (2) The chemical reaction coincided with the shock front.
- (3) The shock velocity was supersonic with respect to the burnt material left behind.

Searching for a meeting point with hydrodynamical theory, we conclude that the phenomenon we observed in the MD simulation is a *weak detonation*. Weak detonation is a possible hydrodynamical solution in which the shock wave is supersonic with respect to the material left behind. The characteristics of weak detonations are different from normal detonations: The weak detonation velocity is higher, and the pressure after completion of the reaction is smaller than in the normal detonation case. Also, in weak detonations there is no compression of the material before the reaction. Zel'dovich argues that such solutions are usually unattainable for substances that are initially inert [8]. However, he points out that weak detonations might occur if the chemical reaction would start in the initial state without preliminary heating of the substance by the shock wave [40]. Dremin states that if self-ignition occurs at a pressure lower than the CJ pressure, a weak detonation wave is observed [41].

Why are weak detonations attainable and stable in our case? The answer is in the kinematic behavior of the crystal. The shock propagates with characteristic of a nonlinear solitary wave. The propagation velocity is determined by the repulsive part of the interatomic potential which is similar to solitons on a Toda lattice. The other kinematic property is the mass of the group that emitted from the dissociating molecule. When the shock front comes from the heavy side, the light particle is breaking out with the majority of the kinetic energy, initiating the reaction on the next crystal plane. This can be imagined as a shock propagation by the domino effect which never looks back. The ideal domino effect has no change in the density after the front. This is accompanied by a negligible increase in the mass velocity. The melting of the crystal and the equilibration of the burnt material lag behind the shock front and are decoupled from it due to the supersonic velocity. Remarkably, when the molecule orientation is the opposite (heavy particle is placed ahead of the light one in the shock direction), then the detonation does not reach a steady state. It explains the details of the solitary wave ignition mechanism. If the light particle is pushed forward at the high (supersonic) velocity after the decomposition, it quickly hits another molecule in the next crystal plane, allowing the reaction to propagate at supersonic speed due to the domino effect. On the contrary, if the heavy particle is placed ahead, it breaks out at much slower velocity, delaying the propagation of the decomposition reaction.

These observations pose additional questions:

- (1) What are the conditions that are necessary to observe weak detonation in experiments?
- (2) What are the conditions that an MD simulation will reconstruct the standard solutions of the ZND model?

It seems that a prerequisite for a stable weak detonation is a stiff molecular crystal that supports fast propagation of nonlinear shock waves. In addition, the crystal should be very nonisotropic. The molecules are oriented with the light particle pointing toward the propagation direction. We have carried out preliminary simulations with triatomic molecules with similar effects. Anisotropic shock initiation sensitivity has been observed in detonation of explosives composed of single molecular crystals [42]. Recent calculations reveal this anisotropic sensitivity [43,44]. Weak detonations were shown to occur in the shock initiation process in the case of inhomogeneous explosives or inhomogeneous initial conditions [45–47]. Weak detonations in mixtures which have nonmonotonic energy release were shown experimentally [48]. It has been demonstrated that a quasisteady form of weak detonation plays an integral role in describing shock-induced transition to detonation in an explosive material [49]. The transition to normal detonation was shown to occur effectively at the point where the weak detonation slows to the CJ velocity. In cases of very porous materials it can happen that the decomposition wave will remain faster than the compression wave, stabilizing the weak detonation solution [9]. Finally, a weak detonation requires a decomposition reaction which can follow pace with the shock front even at relatively low temperatures. This dictates a time scale of a few tens of femtoseconds.

The prerequisite for the MD simulation to generate the standard results of the Chapman-Jouguet or the more elaborate ZND model is a more complex and slower chemical reaction

which can justify the quasi-equilibrium assumption. This influence of the speed and complexity of the reaction can be seen even in 1D models: Elert *et al.* [50] used three-body interaction potentials in a 1D model and got a stable detonation without introducing artificial frictional forces. The studies in Ref. [23] using realistic force fields aim at this direction. Nevertheless, the quasi-equilibrium assumption has been criticized [21]. In the present study we find that most regions of the detonating crystal are well described by quasi-equilibrium assumptions, except the vicinity of the shock front.

ACKNOWLEDGMENTS

We would like to thank Matania Ben-Artzi for insightful and fruitful discussions. We also want to thank Naomi Rom and Ido Schaefer for helpful discussions. The study was partially supported by the Center of Excellence for Explosives Detection, Mitigation and Response, DHS.

APPENDIX A: MOLLY: THE MOLECULAR DYNAMICS PROGRAM

The basic simulation program used to integrate the molecular dynamics equations was MOLLY [51]. MOLLY is suitable for the present purpose due to two primary reasons:

(1) The equations of motion are integrated in MOLLY using a modified version of the Beeman algorithm [51,52]. During detonation simulations there is rapid energy exchange between potential and kinetic energy. Simulations carried out with the Verlet algorithm failed to conserve energy properly. The Beeman algorithm, with higher accuracy in velocities, was found to be adequate.

(2) The neighbor list in MOLLY is built using the linked cell method (see, for example, Ref. [53]). In shock wave simulations the system is not homogeneous: Near the shock front there is a domain with high density, and the common neighbor list algorithm is not efficient for such a situation [11].

Two modifications of the MOLLY code were introduced to fit the requirements of detonation simulations:

(1) MOLLY is constructed to calculate potential energy and forces from a wide set of common analytic potentials. We added an option to calculate the potentials and forces from a pre-prepared stored table, using cubic spline interpolation.

(2) The initial velocities in MOLLY's simulations are sampled from the Maxwell Boltzmann (MB) distribution. The pellet initial velocity were modified so that they could be preassigned, while the velocities of the slab atoms are sampled from the MB distribution.

APPENDIX B: THE FUNCTIONAL FORM OF THE EXOTHERMIC POTENTIAL

The interatomic potential described in Fig. 1 can be constructed by a piecewise defined function, which is composed from three segments, each having a different functional form:

$$V(r) = \begin{cases} D_1(e^{-\beta_1(r-r_{\min})} - 1)^2 + Q & 0 < r < r_{\min} \\ c_3r^3 + c_2r^2 + c_1r + c_0 & r_{\min} < r < r_{\text{bar}} \\ D_2[1 - (e^{-\beta_2(r-r_{\text{bar}})} - 1)^2] & r_{\text{bar}} < r < r_{\text{cut}} \end{cases} \quad (\text{B1})$$

With $r_{\min} = 1.5 \text{ \AA}$, $r_{\text{bar}} = 1.9 \text{ \AA}$, and $r_{\text{cut}} = 7 \text{ \AA}$ refer to the positions of the local minimum, the barrier, and the cutoff, respectively. $D_1 = 0.25 \text{ eV}$ is the energy barrier height, Q is the energy release during decomposition of the molecule (the exothermicity of the reaction), and D_2 should satisfy the requirement $D_2 = D_1 + Q$, so the function will be continuous. On the first segment there is a shifted Morse potential, so under small displacements, the molecule's behavior is similar to the behavior under standard Morse potential. The third segment is an inverted Morse potential, and it serves as the repulsive potential at the decomposed state. The role of the polynomial in the intermediate segment is to link between the two edge segments. Therefore, the coefficients c_0 , c_1 , c_2 , and c_3 , are chosen to make the function and its first derivative continuous.

We determined the polynomial coefficients by the requirements for continuity of the potential and its first derivative at the points r_{\min} and r_{bar} (the derivative vanishes at these points). There are four requirements, so the coefficients are determined uniquely. Using $Q = 1.5 \text{ eV}$ and $D_1 = 0.25 \text{ eV}$ (and, consequently, $D_2 = 1.75 \text{ eV}$), and using \AA as the length unit, we got $c_3 = -7.8125$, $c_2 = 39.8437$, $c_1 = -66.7969$, and $c_0 = 38.4141$, with the appropriate units. One can see that we can obtain continuity of the second derivative as well, by choosing $\beta_1 = \sqrt{3}/(r_{\text{bar}} - r_{\min}) = 4.3301 \text{ \AA}^{-1}$ and $\beta_2 = \beta_1 \sqrt{D_1/D_2} = 1.6366 \text{ \AA}^{-1}$. However, this is not essential, since the actual calculations during the simulations were done using cubic spline interpolation. This interpolation guarantees continuity of the second derivative.

For other exothermicity values (i.e., different Q), we used the same functional form on the first and second segments, with the same parameters' values, except Q and c_0 , which determine the exothermicity. On the third segment, we determined the potential values in a way that made only little gap of the function at r_{cut} . We also constructed potentials with different values for the barrier energy, using the same method.

APPENDIX C: CRYSTAL CHARACTERIZATION

Before shock propagations are examined the equilibrium structure and characteristics has to be determined. This was

carried out by evaluating the position correlation function at different temperatures. In addition, the acoustical sound velocity was calculated.

1. Stability and phase transition temperature

Equilibrium *NPT* molecular dynamics simulations were performed under constant pressure of 1 bar, and at different temperatures. Under these conditions the stability of the N-C molecules as well as the stability of the crystal and its melting point were evaluated.

We found that the molecules are stable in the temperature range between $0 \text{ }^\circ\text{K}$ and $250 \text{ }^\circ\text{K}$. When the temperature was raised beyond $250 \text{ }^\circ\text{K}$, some of the N-C bonds started to dissociate. This is consistent with the low dissociation barrier of the molecule under examination, which is 0.25 eV .

The radial distribution functions (RDFs) of the N-N pairs were calculated. The results of the calculations for $50 \text{ }^\circ\text{K}$ and $250 \text{ }^\circ\text{K}$ are shown in Fig. 14. The observed peaks are in positions reflecting the FCC lattice. The RDFs verify that the crystal is solid up to $250 \text{ }^\circ\text{K}$. As the temperature is raised from $50 \text{ }^\circ\text{K}$ to $250 \text{ }^\circ\text{K}$, The peaks of the RDFs get broadened, and at $250 \text{ }^\circ\text{K}$ the RDF does not vanish after the third peak, as a result of large fluctuations.

On higher temperature, at $500 \text{ }^\circ\text{K}$, some of the molecules decompose and the slab melts. The RDF of the system at this temperature shows liquid behavior. In Fig. 15 there is a plot of the RDF of N-N pairs on $500 \text{ }^\circ\text{K}$. There are no sharp peaks at distances greater than the distance of the first nearest-neighbors peak. This character of the RDF is typical for the liquid phase.

2. Elastic sound velocity

a. The elastic sound velocity of our crystal

The MD simulation was used to determine velocity of the pressure *p*-wave in the crystal. A small longitudinal displacement of few crystal layers along the $[111]$ direction was used to induce these waves. The perturbation propagation velocities was then determined. In order to ensure that the

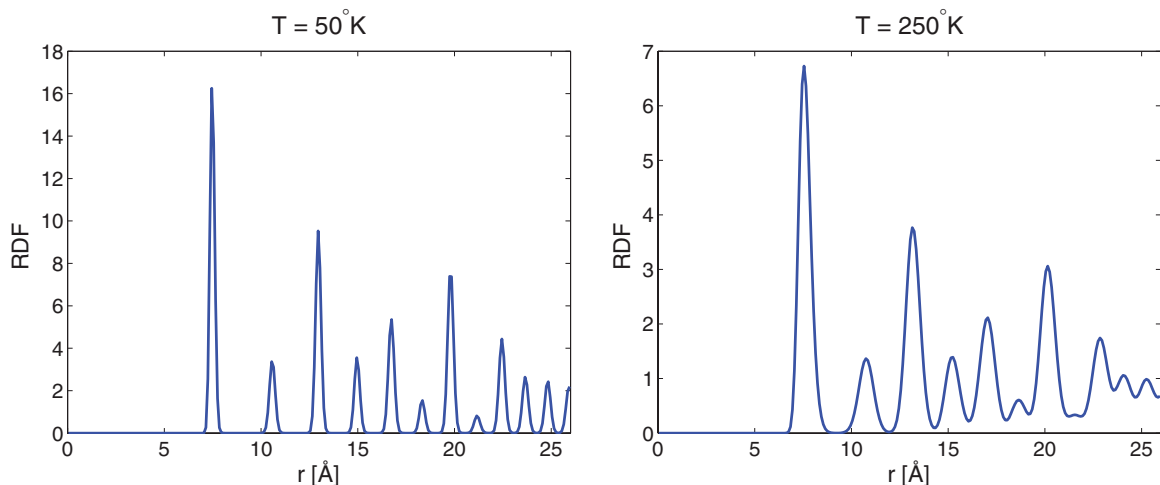


FIG. 14. (Color online) Radial distribution function of the crystal. Results are of a *NPT* simulations with 504 molecules at pressure of 1 bar. The left plot corresponds to $50 \text{ }^\circ\text{K}$, and the right plot corresponds to $250 \text{ }^\circ\text{K}$.

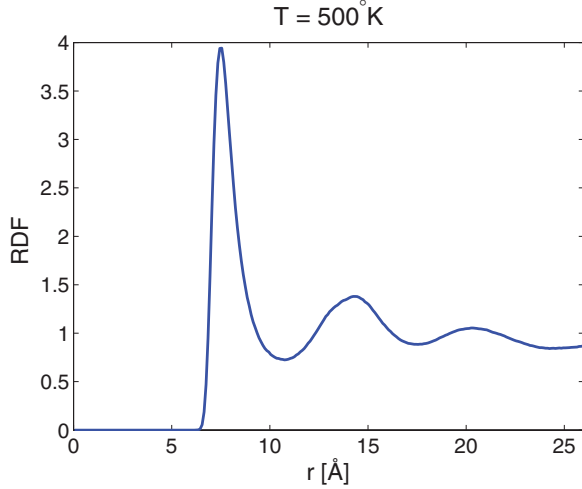


FIG. 15. (Color online) Radial distribution function of a NPT simulations with 504 molecules at pressure of 1 bar and temperature of 500 °K.

displacements are small enough, the simulations were repeated with various displacement amplitudes. It was then verified that the propagation velocity is independent of the displacement amplitude. We found that the p -wave velocity is approximately 2.6 unit cells per picosecond ($\approx 4.6 \times 10^3$ m/s).

b. P-waves velocity on Morse crystals: A discussion

A simple 1D model may give an insight regarding the p -wave velocity in crystals for which the pair interaction is described by the Morse function. In this model there is an infinitely long chain of masses. Let us consider first an infinite harmonic chain. In this case the interaction between neighboring masses is harmonic, with a spring constant α . We

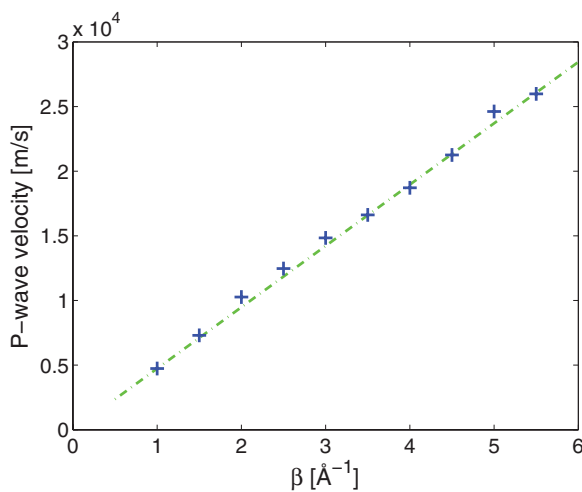


FIG. 16. (Color online) p -wave velocity in the crystal as a function of the β parameter in the intermolecular Morse potential. Each velocity was calculated by simulating propagation of small displacements in a crystal, with the relevant β parameter, and marked in the figure by a cross. The dashed line is an extrapolation to small β values assuming linear scaling.

denote the distance between two neighboring masses l . The equation of motion for the n th mass is

$$m\ddot{x}_n = \alpha(x_{n+1} - 2x_n + x_{n-1}). \quad (C1)$$

If we assume that the time-dependent position is given by

$$x_n(t) = (A_+ e^{+iknl} + A_- e^{-iknl}) \cos(\omega t + \phi), \quad (C2)$$

we get the dispersion relation:

$$\omega(k) = 2\omega_0 \sin\left(\frac{kl}{2}\right), \quad (C3)$$

where we defined $\omega_0 = \sqrt{\alpha/m}$. The p -wave velocity for this case is

$$v_s = \left. \frac{d\omega}{dk} \right|_{k=0} = \omega_0 l \cos\left(\frac{kl}{2}\right) \Big|_{k=0} = \omega_0 l = \sqrt{\frac{\alpha}{m}} l. \quad (C4)$$

This model can be used to describe the harmonic approximation of small vibrations around the equilibrium distance

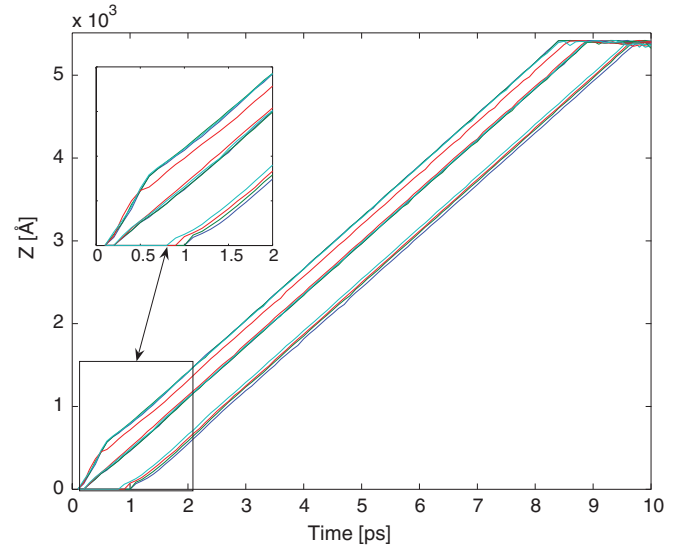


FIG. 17. (Color online) Reaction front location versus time in simulations with three different initial velocities of the pellet. The location was determined by a significant dissociation ratio. The results are grouped in three categories: The rightmost bundle represents five different simulations with the lowest pellet velocity used (≈ 10 km/s). The central bundle corresponds to simulations (five runs) with medium pellet velocity (≈ 50 km/s), while the leftmost bundle corresponds to simulations with the largest pellet velocity (≈ 120 km/s). (These high values of initial velocities are used for demonstration: pellet velocities of 10, 50, and 120 km/s give rise to initial transient shock waves that are, respectively, slower, similar, and higher than the developing stable detonation wave, which is approximately 65 km/s. Smaller values of pellet velocities were used throughout most of this paper.) The different simulations in each one of the three groups correspond to different initial conditions used (slightly different initial pellet-crystal distance). A short time after the pellet collision with the slab, different shock wave velocities develop in each simulation. The differences between the trajectories at short times are shown in the insert of the figure. A stable, steady-state, velocity is reached after an additional propagation period. The shock velocity depends only on crystal parameters, which are identical in all simulations.

in the Morse potential (and other potentials). If the vibration amplitude is small enough for the harmonic approximation to hold, the propagation velocity of small perturbations should be independent of the perturbation amplitude. In such cases, we substitute $\alpha = 2\beta^2 D$, the second derivative near the minimum of the potential. Now the p -wave velocity is

$$v_s = \sqrt{\frac{\alpha}{m}} l = \sqrt{\frac{2D}{m}} \beta l. \quad (\text{C5})$$

This result suggests that the p -wave velocity scales linearly with β .

The p -wave velocity in this simple 1D model is not directly comparable to the p -wave velocity in the 3D fcc slab, since the elastic waves on anisotropic crystal is determined by the elastic tensor σ , which has several parameters [54]. However, some insights can be gained: The MD simulation was employed to evaluate the p -wave velocity along the [111] direction of our slab. The assumption of the velocity's linear scaling as a function of β is tested by simulating propagation of small displacements in different crystals, while changing β . The results are shown in Fig. 16, marked by crosses. The dashed line in this figure is an extrapolation of the $\beta = 1$ case, assuming

linear scaling. We can see that our assumption is valid in a wide range of the β values.

APPENDIX D: THE TRANSITION TO STATIONARY DETONATION WAVES

A stable detonation wave is independent of initial conditions. To check this hypothesis different initial pellet velocities were tested. The location of the reaction front was defined as the first point where molecular decomposition is identified. Figure 17 shows the location of the reaction front as a function of time in simulations with three different initial pellet velocities. Inspection of these results shows that a short time after the pellet collision with the slab, different shock wave velocities develop in each simulation. This is a transient: A stable, steady-state, velocity is reached after a short additional propagation period. The steady-state shock velocity depends only on crystal parameters. Therefore, it is clear that the pressure wave induced by the pellet in this model crystal develops into a constant velocity detonation wave. A similar transition from initiation dependent velocity to a steady-state velocity that depends only on crystal parameters was previously reported [55].

-
- [1] W. Fickett and W. C. Davis, *Detonation: Theory and Experiment* (Dover Publication, Mineola, NY, 2000).
- [2] J. A. Zukas and W. P. Walters, *Explosive Effects and Applications* (Springer-Verlag, New York, 2002).
- [3] A. N. Dremin, *Toward Detonation Theory* (Springer-Verlag, New York, 1999).
- [4] M. Ben-Artzi and J. Falcovitz, *Generalized Riemann Problems in Computational Fluid Dynamics* (Cambridge University Press, Cambridge, 2003).
- [5] Ya. B. Zel'dovich, *Zh. Eksp. Teor. Fiz.* **10**, 542 (1940).
- [6] J. Von Neumann, in *John von Neumann, Collected Works*, edited by A. J. Taub, Vol. 6 (Permagon Press, New York, 1963), pp. 178–202.
- [7] W. Döring, *Ann. Phys.* **435**, 421 (1943).
- [8] Ya. B. Zel'dovich, *J. Exp. Theor. Phys.* **12**, 389 (1942).
- [9] C. M. Tarver, *Combust. Flame* **46**, 157 (1982).
- [10] J. P. Chesick, *J. Chem. Ed.* **38**, 330 (1961).
- [11] B. M. Rice, in *Modern Methods for Multidimensional Dynamics Computations in Chemistry*, edited by D. L. Thompson (World Scientific Publishing, New York, 1998), pp. 472–528.
- [12] D. C. Sorescu, B. M. Rice, and D. L. Thompson, in *Energetic Materials, Part I. Decomposition, Crystal and Molecular Properties*, edited by Peter Politzer and Jane S. Murray, *Theoretical and Computational Chemistry 12* (Elsevier B.V., Amsterdam, 2003), pp. 125–184.
- [13] D. W. Brenner, D. H. Robertson, M. L. Elert, and C. T. White, *Phys. Rev. Lett.* **70**, 2174 (1993).
- [14] B. M. Rice, W. Mattson, J. Grosh, and S. F. Trevino, *Phys. Rev. E* **53**, 611 (1996).
- [15] A. C. T. Van Duin, S. Dasgupta, F. Lorant, and W. A. Goddard III, *J. Phys. Chem. A* **105**, 9396 (2001).
- [16] A. Strachan, A. C. T. van Duin, D. Chakraborty, S. Dasgupta, and W. A. Goddard, *Phys. Rev. Lett.* **91**, 098301 (2003).
- [17] A. Strachan, E. M. Kober, A. C. T. van Duin, J. Oxgaard, and W. A. Goddard, *J. Chem. Phys.* **122**, 054502 (2005).
- [18] F. Dubnikova, R. Kosloff, J. Almog, Y. Zeiri, R. Boese, H. Itzhaky, A. Alt, and E. Keinan, *J. Am. Chem. Soc.* **127**, 1146 (2005).
- [19] A. C. T. van Duin, Y. Zeiri, F. Dubnikova, R. Kosloff, and W. A. Goddard, *J. Am. Chem. Soc.* **127**, 11053 (2005).
- [20] W.-G. Liu, S. V. Zybin, S. Dasgupta, T. M. Klappoetke, and W. A. Goddard III, *J. Am. Chem. Soc.* **131**, 22 (2009).
- [21] A. C. Landerville, I. I. Oleynik, and C. T. White, *J. Phys. Chem. A* **113**, 12094 (2009).
- [22] J. Budzien, A. P. Thompson, and S. V. Zybin, *J. Phys. Chem. B* **113**, 13142 (2009).
- [23] S. V. Zybin, W. A. Goddard III, P. Xu, A. C. T. van Duin, and A. P. Thompson, *Phys. Lett. A* **96**, 081918 (2010).
- [24] G. Stoltz, *Europhys. Lett.* **76**, 849 (2006).
- [25] J. B. Maillet, L. Soulard, and G. Stoltz, *Europhys. Lett.* **78**, 68001 (2007).
- [26] E. J. Reed, L. E. Fried, W. D. Henshaw, and C. M. Tarver, *Phys. Rev. E* **74**, 056706 (2006).
- [27] M. Peyrard, S. Odier, E. Lavenir, and J. Schnur, *J. App. Phys.* **57**, 2626 (1985).
- [28] V. V. Zhakhovskii, S. V. Zybin, K. Nishihara, and S. I. Anisimov, *Phys. Rev. Lett.* **83**, 1175 (1999).
- [29] S. V. Zybin, V. V. Zhakhovskii, M. L. Elert, and C. T. White, *AIP Conf. Proc.* **706**, 310 (2004).
- [30] J. Roth, *Phys. Rev. B* **72**, 014126 (2005).
- [31] M. Toda, *Suppl. Prog. Theor. Phys.* **59**, 1 (1976).
- [32] M. Toda, *IEEE Trans. Circuits Syst.* **30**, 542 (1983).

- [33] B. L. Holian, H. Flaschka, and D. W. McLaughlin, *Phys. Rev. A* **24**, 2595 (1981).
- [34] E. R. Dobbs and G. O. Jones, *Rep. Prog. Phys.* **20**, 516 (1957).
- [35] A. J. Heim, N. Grnbech-Jensen, T. C. Germann, B. L. Holian, E. M. Kober, and P. S. Lomdahl, *Phys. Rev. E* **76**, 026318 (2007).
- [36] V. Fomin, I. Golovnev, and A. Utkin, *Shock Waves* **15**, 325 (2006).
- [37] M. L. Elert, J. J. C. Barrett, D. H. Robertson, and C. T. White, *AIP Conf. Proc.* **429**, 293 (1998).
- [38] J. W. Dold and A. K. Kapila, *Combust. Flame* **85**, 185 (1991).
- [39] T. J. Rolfe, S. A. Rice, and J. Dancz, *J. Chem. Phys.* **70**, 26 (1979).
- [40] Ya. B. Zel'dovich, *Theory of Combustion and Detonation of Gases* (Akademiia Nauk SSSR, Moscow, 1944).
- [41] A. N. Dremin, *Combust. Explos. Shock Waves* **36**, 704 (2000).
- [42] C. S. Yoo, N. C. Holmes, P. C. Souers, C. J. Wu, F. H. Ree, and J. J. Dick, *J. App. Phys.* **88**, 70 (2000).
- [43] M. W. Conroy, I. I. Oleynik, S. V. Zybin, and C. T. White, *Phys. Rev. B* **77**, 094107 (2008).
- [44] M. W. Conroy, I. I. Oleynik, S. V. Zybin, and C. T. White, *J. Phys Chem. A* **113**, 3610 (2009).
- [45] Ya. B. Zel'dovich, *Combust. Flame* **39**, 211 (1980).
- [46] J. B. Bdzil and A. K. Kapila, *Phys. Fluids A* **4**, 409 (1992).
- [47] A. K. Kapila, D. W. Schwendeman, J. J. Quirk, and T. Hawa, *Combust. Theor. Model.* **6**, 553 (2002).
- [48] V. Balalaev, G. Dronin, and I. Veremeev Russian, *J. Phys. Chem. B* **2**, 172 (2008).
- [49] M. Short and J. W. Dold, *Combust. Theor. Model.* **6**, 279 (2002).
- [50] M. L. Elert, D. M. Deaven, D. W. Brenner, and C. T. White, *Phys. Rev. B* **39**, 1453 (1989).
- [51] K. Refson, *Comp. Phys. Comm.* **126**, 310 (2000).
- [52] D. Beeman, *J. Comp. Phys.* **20**, 130 (1976).
- [53] M. P. Allen and D. J. Tildesley, *Computer Simulation of Liquids* (Oxford University Press, New York, 1989).
- [54] J. M. Carcione, D. Kosloff, and R. Kosloff, *Q. J. Mech. Appl. Math.* **41**, 319 (1988).
- [55] M. Peyrard, S. Odier, E. Oran, J. Boris, and J. Schnur, *Phys. Rev. B* **33**, 2350 (1986).

DETONATION FAILURE CHARACTERIZATION OF NON-IDEAL EXPLOSIVES

Authors:

Robert S. Janesheski

rjanesh@gmail.com

Lori J. Groven

lgroven@purdue.edu

Steven F. Son

sson@purdue.edu

*500 N. Allison Rd., West Lafayette IN 47907
School of Mechanical Engineering, Purdue University,*

Abstract. A small scale experiment has been developed to characterize non-ideal explosives such as ammonium nitrate-fuel oil mixtures. A microwave interferometer is applied to small scale confined transient experiments, yielding time resolved characterization of a failing detonation that is initiated with an ideal booster charge. Experiments were performed with ammonium nitrate and two fuel compositions (diesel fuel and mineral oil). It was observed that the failure dynamics were influenced by factors such as the chemical composition, confiner thickness, and applied shock wave strength. Thin steel walled confiners with 0.71 mm wall thickness experienced detonation failure and decoupling of the shock wave from the reaction zone. Confiners with a wall thickness of 34.9 mm only showed a decrease in detonation velocity and a steady detonation was achieved. Varying the applied shock strength by using an attenuator showed corresponding changes in the initial overdriven detonation velocity in the non-ideal explosives. The distance to detonation failure was also shown to depend on the attenuator length when thin wall confinement was used. This experimental method is shown to be repeatable and can be performed with little required material (about 2 grams). The data obtained could be useful to model development and validation.

Keywords: Non-ideal explosives, ammonium nitrate, microwave interferometry, detonation, shockwave.

1. INTRODUCTION

The characterization and understanding of the detonation phenomenon associated with non-ideal explosives has been given great attention in the past 10 years [1-5]. There is a strong interest in characterizing, modeling, and understanding non-ideal explosives as their availability and low cost make them terrorist accessible. In order to more adequately mitigate and respond to these threats, characterization coupled with modeling of non-ideal explosives has become of the utmost importance. Presently, the lack of experimental data and characterization has limited the development of detonation models for non-ideal explosives. This is especially challenging because of the wide variety of mixtures that can be used.

Explosives are typically labeled as non-ideal when they exhibit a large reaction zone length, previously defined as 1 mm in scale [1]. A large critical diameter is a characteristic associated with non-ideal explosives also due to this thick reaction zone. Ammonium nitrate (AN), a typical non-ideal explosive component, has yielded a critical diameter of 100 mm when confined in a steel tube that is loosely packed [6]. When neat AN is pressed within a 36.5 mm diameter steel confiner with an 11 mm wall thickness to a packing density of 1.61 g/cm³, no detonation occurs [6]. When fuel is added to AN, it has been shown that the critical diameter can vary from 10 mm with fine AN particles to 50 mm with course AN particles [7]. It is evident that many parameters such as AN particle size, confiner diameter, packing, and confiner thickness have an effect on the detonation properties of non-ideal explosives. This fact makes large scale characterization of every composition that is available to terrorists prohibitive.

A steady detonation experiment is typical for the measurement of detonation properties such as velocity, reaction zone length, and detonation front curvature [5]. Producing a steady detonation with a non-ideal explosive requires a large amount of material, on the order of hundreds of grams, in order to satisfy the critical diameter constraint. Previous work performed to characterize non-ideal explosives during a steady detonation (all requiring amounts on the scale of hundreds of grams [2-4]) has included the study of the effects of confiner diameter on the detonation velocity [2], the effect of the confiner wall thickness on the steady detonation velocity [3], and the effect of particle diameter and pore volume on the steady detonation velocity [4]. Rate stick and front curvature measurements have also been performed for non-ideal explosives, requiring approximately 125 kg of non-ideal explosive [5]. It is evident that small scale experiments are desirable.

The large scale required to sustain a detonation in non-ideal explosives has also made it a challenge to perform transient measurements, such as deflagration to detonation transition (DDT) [8] or shock initiation [9]. Conventionally, to study initiation, the experimental setup needs to be sized to allow for steady detonation to be reached. Shock initiation measurements have been used for the calibration of parameters for reaction models [9], such as Forest-Fire [10] and ignition and growth [11], for ideal explosives. Transient data provides rich data sets for model validation.

The data available involving transient measurement during a detonation transition for non-ideal explosives is very limited. Some work has been performed to fit equation of state (EOS) parameters for non-ideal explosives using high pressure x-ray diffraction and gas gun-driven plate impact experiments [12]. Reaction and growth modeling parameters have also been measured with non-ideal explosives by using a hybrid Hopkinson bar experiment (modified plate impact experiment) [13]. While these methods are successful in measuring ignition and growth parameters, they do not allow for the entire detonation process from the beginning to end of detonation to be calibrated to the same degree that a transition experiment allows. Transient experiments of detonation failure in non-ideal explosives have not received much attention. The need for an experimental technique to study the transient dynamics during detonation of a non-ideal explosive is evident, especially if the experiment spans a wide parameter space. A small scale transient experiment may be especially useful to modelers and could provide valuable insight as well.

In the past, microwave interferometry has been used as a non-intrusive measurement for burning rates for propellants [14] and for the study of the detonation of ideal explosives including tetryl [15], TNT, Pentolite, Amatol, and Tritonal [16]. Low power microwaves are used to develop interference signals produced from microwave reflection off of the detonation front. The position and velocity of the detonation front can be calculated non-intrusively with the interference signal. The spatial and temporal resolution of the microwave interferometry technique is dependent on the frequency and wavelength of the microwave system. Over the years, the technique has been refined and wavelengths have decreased from 3 cm [16] to 2 mm [17]. It has been shown that a single experiment can measure the regression rate of propellants as a function of pressure [18] due to the ability to make continuous phase angle measurements that include transient effects. The technique has also been previously used to characterize ideal explosives in deflagration-to-detonation transition (DDT) experiments [8]. Therefore, this diagnostic tool could be applied to detonation failure in non-ideal explosives.

The objective of this work is to develop a small scale experiment to characterize non-ideal explosives in such a detonation failure experiment. Transient effects are measured while using a microwave interferometer to obtain position-velocity data during propagation of an unsteady, weakening detonation through a non-ideal explosive. The non-ideal explosives exhibit an initial overdriven detonation that can eventually fail. This provides broad parameter space for model validation or calibration. Material composition, various confinement properties, and leading shock strength is also investigated to quantify the effects on the failing detonation through non-ideal explosives.

2. EXPERIMENTAL PROCEDURE

2.1 Materials and Equipment

The non-ideal explosives used in this work consisted of ammonium nitrate (AN) mixed with various fuels. Kinepak™ ammonium nitrate produced by SEC, Orica Manufacturing Company, was used. Sizing of the AN was conducted with a Malvern Mastersizer with hexane as the dispersing medium. The material is trimodal with a mean volume diameter of ~200 μm and d(50) of ~175 μm. Various weight percentages of diesel and mineral oil were mixed with AN as the fuels of interest. In these experiments, 1.9 g of ideal explosive and 2 to 2.5 g of non-ideal explosive were required. The non-ideal explosive mixtures characterized in this work include AN with 2, 5 and 10 wt.% diesel fuel as well as AN with 2 and 15 wt.% mineral oil. The explosives were pressed within the confiner in increments to allow for uniform density throughout the length of the sample. Samples ranged from 60% TMD for compositions with 2 wt.% fuel up to 70% TMD for compositions with 15 wt.% fuel. Primasheet 1000, an ideal explosive, was used to develop a steady leading overdriven detonation into the non-ideal explosive. A Teledyne Risi, Inc. RP-502 detonator was used to initiate the detonation.

Three confinement conditions were used that included very weak confinement (polypropylene tube with a wall thickness of 0.2 mm and I.D. of 6.95 mm), thin-wall confinement (304 stainless steel tube with 0.71 mm wall thickness and I.D. of 6.53 mm) and thick-wall confinement (1018 steel tube with a wall thickness of 34.9 mm and I.D. of 6.35 mm). To study the effect of applied shock strength leading into the non-ideal explosives, poly(methyl methacrylate) (PMMA) attenuators with thicknesses ranging from 1 to 8 mm were used.

A custom built microwave interferometer was used to produce position measurements of the detonation front. The microwave system produced microwaves with a frequency of 35 GHz and a free space vacuum wavelength of 8.6 mm. The output signal from the microwave interferometer was recorded with a 500 MHz sampling rate using a Tektronix DPO4034 Digital Phosphor Oscilloscope. Microwave transmission to the sample was made possible by an expendable 6.35 mm O.D. cylindrical Teflon™ waveguide. Fiber optics with Thorlabs, Inc. M34L02 patch cables having a 600 μm core diameter were used to transmit light to Thorlabs, Inc. DET10A photo-detectors with a 1 ns rise time.

2.2 Experimental Configuration

The experimental configuration within the confiner is shown in Fig. 1. Detonation begins with the detonator initiating a steady detonation through the ideal explosive. When present, a PMMA attenuator transmits a shock wave to the non-ideal explosive. The PMMA attenuator was only used when different shock strengths leading to the non-ideal explosive were investigated. When the attenuator was omitted, the ideal and non-ideal explosives were placed together to allow for the steady detonation developed by the ideal explosive to transition to the non-ideal explosive. Due to the inner diameter of the confiner being below the critical diameter, the overdriven detonation weakens and decelerates in velocity during propagation through the non-ideal explosive.

The waveguide was placed on the opposite end of the detonator in the confiner tube. The microwave interferometer produces microwaves that are transmitted by the waveguide to the explosives within the confiner. The experimental setup showing the connection of the waveguide to the microwave interferometer is shown in Fig. 2. The explosives and PMMA attenuator are dielectric mediums, allowing for transmission of the microwave signal from the waveguide. Reflection of the microwave signal occurs with the presence of a dielectric discontinuity that can either be caused by an ionizing reaction zone or a shock wave [19, 20]. The reflected signal returns through the unreacted dielectric mediums and waveguide to the interferometer for output of the data.

A fiber optic was located at the interface of the detonator/ideal explosive to trigger the oscilloscope. A second fiber optic was placed at the ideal/non-ideal explosive interface to determine the time the detonation front transitions from the ideal to non-ideal explosive. A third location was either at 1.5 cm away from the ideal/non-ideal interface into the non-ideal explosive for position calibration or at the end of the confiner to verify that a detonation was sustained through the entire length of the non-ideal explosive.

2.3 Microwave Interferometry Technique

As previously mentioned microwaves are partially reflected off of the detonation front, a shock wave, or other dielectric discontinuity and returned back through the waveguide to the interferometer. The reflected signal is mixed with the reference signal to develop an interference signal.

The frequency of the interference signal is proportional to the velocity. Using this relation, the position can be determined using the zero-axis crossing method with

$$x(t) = \frac{\lambda_I N(t)}{2}, \quad (1)$$

where x is the position, λ_I is the wavelength of the interference signal through the medium, and N is the number of wavelengths present at a specified time [modified from ref. 19]. The spatial resolution is limited to half the wavelength of the interference signal. Each instance the interference signal crosses the zero-axis indicates that advancement in phase by π has occurred. The interference signal advancing in phase by 2π indicates that the detonation front has advanced in position a distance equivalent to the wavelength of the interference signal.

Higher spatial resolution (sub-wavelength) can be obtained between each zero-axis crossing using the quadrature method [21]. The microwave interferometer can be designed to output a second signal shifted 90 degrees from the interference signal by use of a quadrature mixer. The two output signals are then combined to calculate the position using a discontinuous arctangent function,

$$x(t) = \frac{\lambda_I}{4\pi} \tan^{-1} \frac{V_2(t)}{V_1(t)}, \quad (2)$$

where V_1 is the interference signal and V_2 is the 90 degree shifted interference signal. The arctangent function is pieced together to yield a continuous position. This gives resolution below the wavelength of the interference signal.

The raw data from each experiment was also filtered and normalized before position analysis was performed. Again, the input for position measurement is phase angle (arctangent function) produced by reflection of microwaves off of the detonation front, etc. Implemented using MATLAB®, low-pass filters were used to ensure high frequency noise would not be interpreted as advancement of the detonation front's position. High-pass filters were used to remove the DC shift by reducing the low frequency oscillations that were produced by the large voltage discharge that occurred during initiation of the EBW detonator or other noise sources. Normalization of the signal from -1 to 1 V allows for an improved visual representation of the frequency (detonation front velocity) as a function of time.

Each method requires knowledge of the interference wavelength of the interference signal for the material being measured. This was calibrated dynamically using fiber optic probes at two known locations of the medium. The wavelength is found using

$$\lambda_I = \frac{L}{N} = \frac{2x}{N}, \quad (3)$$

where L is the total distance the microwave travels from one fiber optic to the next, N is the number of wavelengths that are present in the interference signal between the time the fiber optics were triggered, and x is the length between the fiber optics. The number of wavelengths present can be found by producing a Lissajous curve with both interference signals between the time intervals indicated by the fiber optics. Since both signals are in quadrature, one full revolution of the data in the Lissajous curve represents advancement in phase by one

wavelength. Fractions of a wavelength are then calculated by calculating the phase angle of an incomplete revolution for more accuracy.

A numerical differentiation method by Fast Fourier Transform (FFT) [22] was used to calculate the velocity of the detonation front with position measurements. This method was chosen to reduce the error produced during numerical differentiation associated with experimental data.

2.4 Numerical Predictions

The Chapman-Jouguet (C-J) pressures were predicted for a range of compositions using CHEETAH 6.0 with the standard equation of state product library [23]. Compositions for investigation were chosen based on the predicted C-J pressure; assuming that the failure dynamics of these non-ideal explosives correlate to the predicted C-J pressures and detonation energy.

3. RESULTS AND DISCUSSION

The results from a typical test will be shown first and the analysis steps will be illustrated. Figure 3 shows raw data (top) and the filtered/normalized data of the interference signal (bottom) for an experiment with AN/10 wt.% diesel fuel. The signal prior to $t=0$ is measurement of the detonation front as it is propagating through the ideal explosive. It is seen in the normalized data (bottom of Fig. 3) that a constant frequency is present during this time, representing a constant velocity of the detonation through the ideal explosive. At $t=0$, the shock reaches the non-ideal explosive and overdrives it. The frequency of the interference signal decreases as a function of time, representing the detonation front slowing as it fails.

Using an algorithm to implement the quadrature method, the normalized voltage signals are used to calculate the position and velocity of the detonation front. Using the interference signal shown in Fig. 3 and the 90 degrees off phase interference signal (not shown), the position and velocity of the detonation front is calculated and shown in Fig. 4 with the position (top) and the velocity (bottom). A constant slope of the position (top of Fig. 4) as well as a constant detonation velocity (bottom of Fig. 4) is shown through the ideal detonation prior to $t=0$. At $t=0$, the measured position no longer has a constant slope as a function of time. A concave-down curve is shown representing a decelerating detonation front as a function of time. A decelerating detonation is also evident in the bottom plot of Fig. 4 (velocity) as the detonation slows as it advances through the non-ideal explosive as a function of time. This trend shows the non-ideal detonation weakening during propagation through the sample. The plots in Fig. 4 show the ability of the microwave interferometry technique to measure the entire dynamic process that occurs during the failure of an overdriven detonation through a non-ideal explosive.

3.1 Verification

It is important to verify that measurements made using the microwave interferometer with non-ideal explosives were indeed of a detonation front and not of a shock wave or compaction of the material. To distinguish between a signal produced by reflection off of a shock wave and a detonation, experiments with an inert material and a non-ideal explosive were considered.

Data was collected using a thick-walled confiner with compositions consisting of non-iodized table salt/2 wt.% mineral oil (inert) and AN/2 wt.% mineral oil (non-ideal explosive). The interference signal produced from the salt/2 wt.% mineral oil is shown in the top of Fig. 5. The amplitude of the interference signal stays approximately constant for the duration of the measurement. The interference signal produced when AN/2 wt.% mineral oil was used is shown in the bottom of Fig. 5. The amplitude increases generally as a function of time. There is a clear difference between the signal recorded from the salt/2 wt.% mineral oil and AN/2 wt.% mineral oil. It was previously noted that the amplitude of the interference signal has no effect on the measurement of position. However, the amplitude can provide information on whether a shock wave or reaction zone is causing the reflection of the microwave signal as there is a clear difference in the interference signal between an inert material and non-ideal explosive. Previous work has shown that microwave reflections within an inert material due to a shock wave produce constant amplitudes and are caused by dielectric discontinuities from compaction (density changes) [19]. It

has also been shown that during a reaction, the amplitude of the reflected signal will steadily increase with the presence of ionization zones [20]. The increasing amplitude indicates that a reaction is occurring within the non-ideal explosive.

The higher frequency signal of the non-ideal explosive in Fig. 5 also indicates that the wave causing the reflection of the microwaves is traveling at a faster rate compared to the shock wave within the inert material. The amplitude of the interference signal cuts off much sooner in time for the signal with the non-ideal explosive when compared to the inert material. This signifies that the point of reflection reached the end of the confiner much sooner. Fiber optic probes placed near the end of the confiner when AN/2 wt.% mineral oil were used also shows evidence that a reaction zone was present as emitted light was measured. As anticipated, no emission of light was recorded with the inert material shown in the top of Fig. 5. A few oscillations of the interference signal are seen after the fiber optic triggers for AN/2 wt.% mineral oil, which occurred due to the waveguide being forced out of the confiner as the detonation reached the end of the non-ideal explosive. However, beyond the end of the tube the data is not relevant.

3.2 Experimental Accuracy

All subsequent results reported are measurements exclusively of the non-ideal explosive as the steady detonation leading to the attenuator or non-ideal explosive interface for each experiment was held constant. Four experiments were performed using thin wall confiners with each composition of 2 and 10 wt.% diesel fuel to determine the accuracy of the microwave interferometry method during detonation failure. The mean position along with the standard deviation of AN/2 wt.% diesel fuel is shown in Fig. 6. Maximum standard deviations calculated were +/- 1.1 mm for AN/2 wt.% diesel fuel and +/- 2.5 mm for AN/10 wt.% diesel fuel. It is noted that the standard deviation was observed to be the largest near the end of the non-ideal explosive's position. The increased standard deviation can be explained by the method used to calculate the position from the interference signal. The advancement in position of the detonation front calculated for each time step is added to the previously calculated position. Any error produced during each step will then accumulate leading to maximum deviation occurring near the end of the measurement.

3.3 Thin-walled Confinement with AN/Diesel Compositions

A typical position vs. velocity result with AN/2 wt.% diesel fuel may be seen in Fig. 7. Position and velocity temporal profiles were combined to produce results that allow for the speed of the detonation front to be followed as it propagates through the non-ideal explosive within the confiner. A position of zero indicates the leading edge of the non-ideal explosive. Two distinct slopes are observed. The initial slope is the weakening of the overdriven detonation as it travels through the AN/2 wt.% diesel fuel composition. The second velocity slope is less steep. The location of the two slopes intercepting is defined to be the location that detonation fails and measurement of a decoupled shock wave begins. The location is shown in Fig. 7. This is analogous to analysis of shock initiation to determine run-to-detonation. The velocity oscillation may correspond to a pulsating, failing detonation.

The stoichiometric mixture of AN/diesel fuel was calculated to consist of 5.56 wt.% diesel fuel. Predictions using CHEETAH, shown in Fig. 8, indicate that the C-J energy is largest at the stoichiometric composition (near 5 wt.% diesel fuel). A higher C-J energy correlates to larger detonation energy available to support the detonation. The extra energy released by the stoichiometric mixture should allow for the detonation front to be sustained further through the non-ideal explosive.

Measurements of the location within the non-ideal explosive where detonation fails and decoupling of the shock wave occurs are shown for compositions of AN with 2, 5, and 10 wt.% diesel fuel in Table 1 for thin wall confiners. It is shown in Table 1 that the mixture consisting of AN/5 wt.% diesel sustained the detonation the furthest into the non-ideal explosive. It is shown that the fuel lean (2 wt.% diesel) and fuel rich (10 wt.% diesel) were not able to sustain the detonation as far. Consequently, we see that they run-to-failure. Measurements agree that higher calculated C-J pressures (or energy) lead to a longer run to failure.

Unreacted non-ideal explosive was recovered from the thin confiner and observed to be compacted due to a shock wave. The recovered samples after the experiments verified that the detonation failed in the non-ideal explosive. All thin wall confinement experiments exhibited complete failure with recovered non-ideal explosive. When the detonation fails the shock wave will decouple and the shock wave strength would decrease without the additional energy from the reaction zone, eventually leading to no deformation of the thin-wall confiner. An example of a recovered thin walled steel confiner is shown in Fig. 9. This shows that the shock wave does weaken and a portion of the confiner is recovered without evidence of deformation. The remaining lengths of the recovered confiners were measured. The lengths for the confiners recovered were approximately 3.9, 4.0, and 4.4 cm long for AN with 2, 5, and 10 wt.% diesel fuel respectively. The recovered confiners show that deformation occurred further through the confiners for mixtures closest to stoichiometric. It is noted that these measurements are approximate due to the poorly defined edges produced by the detonation as shown in Fig. 9, and further illustrates why a dynamic measurement technique is valuable.

3.4 Thin-walled Confinement with AN/Mineral Oil Compositions

A similar relationship was seen when diesel fuel was replaced with mineral oil (MO). Velocity slope intercepts were used to determine the location of detonation failure in the same way previously shown for AN/diesel fuel. Figure 10 shows that increasing the fuel percentage will decrease how far the failing detonation can sustain itself through the non-ideal explosive (or run-to-failure). The AN/2 wt.% MO composition sustained the detonation front through 3.9 cm of non-ideal explosive while the AN/15 wt.% composition only sustained the detonation for 2.5 cm, as shown in Table 2. Assuming that mineral oil is similar in composition to diesel fuel, it was shown that a mixture closer to the stoichiometric composition (2 wt.% MO) sustained the detonation further through the non-ideal explosive, much like what was previously observed for diesel fuel.

3.5 Various Confinement Conditions with AN/2 wt.% Mineral Oil

Different behaviors in the failure dynamics are observed when the material composition is held constant and the confinement conditions are changed. Figure 11 shows the detonation front velocity as it travels through AN/2 wt.% mineral oil for various confinement conditions. The condition emulating no confinement (plastic tube) showed deceleration of the overdriven detonation much more rapidly when compared to the other confinement conditions. The radial loss of energy is greatest with conditions of little confinement and the failing detonation does not continue beyond 2 cm of the non-ideal explosive.

The difference in the failure dynamics shown between the different confinements is due to the mechanisms that lead to energy loss behind the reaction zone. Within the thin wall confiners, there are lateral losses due to plastic deformation and expansion. With sizing of the non-ideal explosive below the critical diameter, the loss in energy due to plastic deformation of the confiner can surpass the amount of energy supplied to the leading shock by the reaction zone. The detonation weakens until the reaction zone can no longer be sustained and the shock wave decouples from the detonation front.

Unlike with thin wall confinement, the velocity of the thick wall confiner never drops below 1000 m/s. The transition zone for a decoupled shock wave seen with the thin wall confiners was not evident with the thick wall confiners. This indicates that although the detonation is weakening, with a decreasing detonation velocity, complete failure never occurs for thick walled confiners.

The amount of deformation that occurs within the thick wall confiner should depend on the amount of energy lost from the reaction zone. Energy is required to result in the expansion of the inner diameter of the confiner. Measuring the amount of deformation that occurred after detonation of the non-ideal explosive would verify whether or not detonation occurred through the entire length of the confiner. The thick-wall confiners were cut in half to produce one side that would allow for the measurement of the inner diameter, as seen in the bottom of Fig. 12, to determine if expansion of the original diameter of 6.35 mm occurred. Inner diameter measurements (top of Fig. 12) showed that a detonation occurred through the entire length of AN/2 wt.% mineral oil, as the measured I.D. never dropped below 6.46 mm. The fiber optic placed at the end of the non-ideal explosive in the thick wall confiner was also triggered indicating that a luminous reaction occurred through the entirety of the sample.

Previous work has shown that energy lost due to expansion of the confiner can be distributed in front of the detonation by pressure waves when the sound speed of the confiner is larger than the velocity of the explosive [24]. The speed of sound for steel is 5790 m/s [25]. The detonation front velocities measured in this work decelerated to values below the sound speed of the steel confiners, allowing for the detonation energy lost due to deformation of the confiners to be distributed in front of the detonation front. The distributed energy could have an effect on the detonation velocity. It was also shown by Jackson et al. [24] that when energy transport within the confiner occurs, increasing the confiner thickness would increase the detonation velocity of ammonium nitrate-fuel oil. In this work, increasing confinement thickness showed a similar trend as the sustainment of the detonation was shown to increase. Consequently, simulations of these data should certainly account for confiner wall thickness.

3.6 Effect of Attenuator Thickness with AN/2 wt. % Diesel Fuel

Experiments were performed using PMMA attenuators in thin and thick wall confiners with various attenuator thicknesses. These experiments allow for examination of the transient dynamics due to shock strength. The strength of the shock wave transmitted to the non-ideal explosive (AN/2 wt.% diesel fuel) is dependent on the thickness of the attenuator. Thicker attenuators result in weaker applied shock waves. The weaker shock waves should lower initial detonation velocities in the non-ideal explosives. Also, the distance to failure can be obtained as a function of attenuation when thin wall confiners are used, similar to "Pop-plots" for shock initiation.

3.6.1 Thick wall Confinement

Using thick wall confinement with AN/2 wt.% diesel fuel, attenuators 2, 4, and 8 mm thick were used along with a base case without attenuation. As shown in Fig. 13, the detonation velocity without an attenuator produced an initial detonation velocity at higher speeds. Using the 2 mm thick attenuator reduced the initial detonation velocity, but the deceleration is seen to be similar to the deceleration of the detonation without an attenuator. Increasing the attenuator thickness to 4 mm showed very little difference compared to the 2 mm case. It would be expected that a lower initiating detonation velocity would be observed with a slightly thicker attenuator. The additional 2 mm thickness of the attenuator may not have as large of an effect on the leading shock strength compared to just the effect of having the presence of the attenuator as previously shown. However, when doubling the attenuator thickness to 8 mm, the largest decrease in initiating detonation velocity is seen. The deceleration of the detonation in all three cases has a common slope indicating that the dynamics occurring (losses in energy to deformation of the confiner walls) are similar. The key difference is that the initial detonation velocity is dependent on the incoming shock wave strength (attenuator thickness), which was expected.

Results for all cases in Fig. 13 show a steady detonation velocity near 2000 m/s. The C.J. particle velocity was calculated using CHEETAH to be 1865 m/s for AN/2 wt.% diesel. With the thick wall confinement, a steady wave may be reached to sustain the detonation of the non-ideal explosive with low detonation speeds. The fiber optics placed at the end of the confiners indicates that complete detonation occurs through the entire non-ideal explosive sample, further supporting that decoupling of the shock wave is not occurring at this speed in a similar way to what was observed in the thin wall confiners. There was no recovery of non-ideal explosive for any of the thick wall confinement experiments.

3.6.2 Thin wall Confinement

Experiments were also conducted in thin wall confiners. Attenuators of different thicknesses (0, 1, 4, and 8 mm) were used with a non-ideal explosive composition of AN/2 wt.% diesel fuel. Decreased leading detonation velocities were observed with larger attenuator lengths similar to the thick wall confinement examples. The deceleration of the detonation front was similar between each case, with the difference in leading velocity proportional to the transmitted shock strength. As observed in previous results with thin wall confinement, complete failure of the detonation occurred along with the decoupling of a shock wave. A run to failure (RTF) distance is shown to depend on the attenuator thickness (leading shock strength), as shown in Fig. 14. The case without an attenuator was able to sustain the detonation the furthest through the non-ideal explosive, while the cases with attenuation showed a linear relationship between the RTF distance and the attenuator thickness. The RTF plot will be beneficial for calibrating a model of AN/2 wt.% diesel fuel in a thin wall confiner.

4. CONCLUSIONS

A unique method has been developed to characterize the failure dynamics of non-ideal explosives at small scales. The experimental work presented could be used for calibration of models using hydrocodes such as Sandia's CTH [26] or other shock physics code. The calibrated models could then be compared to large scale data for validation. If successful, it will show that this small scale experimental technique can be used for the characterization of non-ideal explosives and still be valid for large scale configurations. Regardless, this experiment is useful for improving the understanding of detonation failure in non-ideal explosives.

Experiments have been performed using AN with diesel fuel and mineral oil. High resolution spatial measurements of the position and velocity were attained indicating factors such as chemical composition, confiner thickness, and initiating shock wave strength all affect the detonation failure dynamics. Thin wall experiments showed that stoichiometric compositions sustained a detonation further through the non-ideal explosives. Various confinement conditions used with AN/2 wt.% mineral oil showed how the confinement had an effect on sustaining a detonation through a non-ideal explosive. Complete failure of the detonation was accompanied by a decoupling shock wave with thin wall confinement. It was shown that the thick wall confiner sustained the detonation through the entire length of non-ideal explosive by limiting the lateral loss of detonation energy compared to the thin wall confiners and likely propagating energy ahead of the shock wave.

The strength of the shock wave transmitted to the non-ideal explosive corresponded to the resulting initial detonation speed. In thin wall confinement, it was shown that the run to detonation failure increased as the attenuator length decreased. Higher initiating shock strengths yielded additional energy for sustaining the detonation further into the non-ideal explosive. This experimental technique shows potential to reduce the time and cost required to dynamically characterize non-ideal explosives and rapidly characterize a variety of materials and confinement conditions.

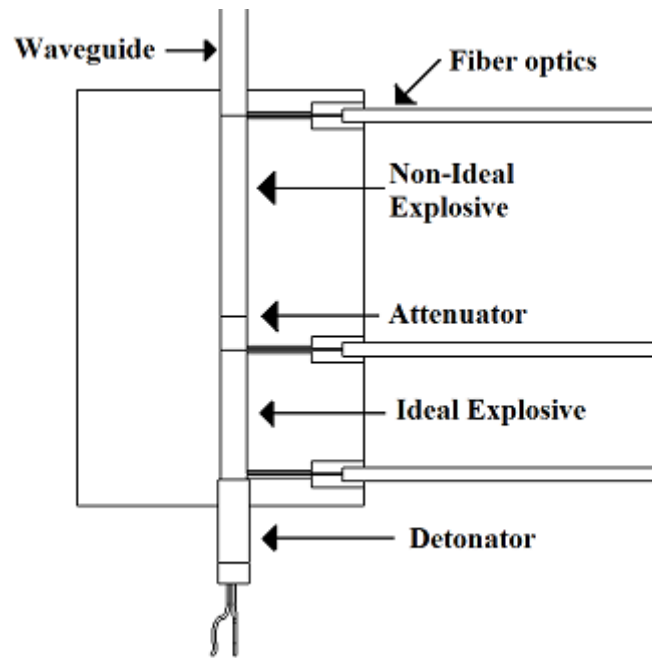
5. ACKNOWLEDGEMENTS

This project was funded by the Department of Homeland Security through the Center of Excellence for Explosive Detection, Mitigation, and Response under award number 080409/0002251. Discussions with Dr. Blaine Asay were also very useful.

6. REFERENCES

- [1] W. M. Howard, L. E. Fried, P. C. Souers, Modeling of Non-Ideal Aluminized Explosives, AIP Conference Proceedings 505.1 (2000) 389.
- [2] A. Miyake, H. Echigoya, H. Kobayashi, T. Ogawa, K. Katoh, S. Kubota, Y. Wada, Non-Ideal Detonation Properties of Ammonium Nitrate and Activated Carbon Mixtures, Int. J. Mod. Phys. b 22.9-11 (2008) 1319-1324.
- [3] S. I. Jackson, C. B. Kiyanda, M. Short, Experimental Observations of Detonation in Ammonium-nitrate-fuel-oil (ANFO) Surrounded by a High-sound-speed, Shockless, Aluminum Confiner, Proceedings of the Combustion Institute. 33.2 (2011) 2219-2226.
- [4] A. Miyake, K. Takahara, T. Ogawa, Y. Ogata, Y. Wada, H. Arai, Influence of Physical Properties of Ammonium Nitrate on the Detonation Behavior of ANFO, Journal of Loss Prevention in the Process Industries 14.6 (2001) 533-538.
- [5] F. W. Sandstrom, R. L. Abernathy, M. G. Leone, M. L. Banks, Diameter Effect and Detonation Front Curvature of Ideal and Non-ideal Explosives, AIP Conference Proceedings 505 (2000) 825-828.
- [6] B. M. Dobratz, LLNL handbook of explosives, UCRL-52997, Lawrence Livermore National Laboratory, March 1981 (updated Jan. 1985).
- [7] C. H. Johansson, P. A. Persson, Detonics of High Explosives, Academic Press, London, 1970.
- [8] N. J. Burnside, S. F. Son, B. W. Asay, P. M. Dickson, Deflagration to Detonation Experiments in Granular HMX, Conference: 1997 Joint Army, Navy, NASA, Air Force (JANNAF) CS/propulsion systems hazards subcommittee meeting, West Palm Beach, FL (United States), 27-31 Oct 1997.
- [9] E. L. Lee, C. M. Tarver, Phenomenological Model of Shock Initiation in Heterogeneous Explosives, Phys. Fluids. 23 (1980) 2362-272.
- [10] R. Menikoff, M. S. Shaw, Review of the Forest fire Model for High Explosives, Combustion Theory and Modeling 12.3 (2008) 569-604.
- [11] R. Menikoff, M. S. Shaw, Reactive Burn Models and Ignition & Growth Concept, EPJ Web of Conferences 10 (2010) 00003.
- [12] D. L. Robbins, S. A. Sheffield, D. M. Dattelbaum, N. Velisavljevic, D. B. Stahl, Equation of State of Ammonium Nitrate, AIP Conference Proceedings 1195 (2009) 552-555.
- [13] E. J. Cart, R. H. Granholm, V. S. Joshi, H. W. Sandusky, R. J. Lee, Measurement of Ignition and Reaction Parameters in Non-Ideal Energetic Materials, AIP Conference Proceedings 845 (2006) 1045-1048.
- [14] V. S. Bozic, D. D. Blagojevic, B. A. Anicin, Measurement System for Determining Solid Rocket Propellant Burning Rate using Reflection Microwave Interferometry, J. Propulsion and Power 13.4 (1997) 457-462.
- [15] G. F. Cawsey, J. L. Farrands, S. Thomas, Observations of Detonation in Solid Explosives by Microwave Interferometry, Proceedings - Royal Society. Mathematical, Physical and Engineering Sciences 248.1255 (1958) 499-521.
- [16] M. A. Cook, R. L. Doran, G. J. Morris, Measurement of Detonation Velocity by Doppler Effect at 3-centimeter Wavelength, J. Appl. Phys. 26.4 (1955) 426-428.
- [17] V. E. Zarko, D. V. Vdovin, V. V. Perov, Methodical Problems of Solid-Propellant Burning-rate Measurements Using Microwaves, Comb. Explosion, and Shock Waves 36.1 (2000) 62-71.
- [18] B. A. Anicin, B. Jojic, D. Blagojevic, M. Adzic, V. Milosavljevic, Flame Plasma and the Microwave Determination of Solid-Propellant Regression Rates, Combust. Flame 64.3 (1986) 309-319.
- [19] A. D. Krall, B. C. Glancy, H. W. Sandusky, Microwave Interferometry of Shock Waves .1. Unreacting Porous-media, J. Appl. Phys. 74.10 (1993) 6322-6327.
- [20] B. C. Glancy, A. D. Krall and H. W. Sandusky, Microwave Interferometry of Shock Waves .2. Reacting Porous-media, J. Appl. Phys. 74.10 (1993) 6328-6334.
- [21] N. Burnside, Deflagration to Detonation Transition in Granular HMX, MS thesis Brigham Young University, 1999.
- [22] R. D. Levie, S. Sarangapani, P. Czekaj, Numerical Differentiation by Fourier Transformation as Applied to Electrochemical Interfacial Tension Data, Anal. Chem. 50 (1978) 110-115.
- [23] L. E. Fried, W. M. Howard, P. C. Souers, Cheetah 6.0 User's Manual, USA: Lawrence Livermore National Laboratory (2010).
- [24] S. I. Jackson, C. B. Kiyanda, M. Short, Precursor Detonation Wave Development in ANFO Due to Aluminum Confinement, 14th International Detonation Symposium, Coeur d'Alene, Idaho, 11-16 Apr. 2009.
- [25] CRC Handbook of Chemistry and Physics, 90th ed., CRC Press, Boca Raton, FL., 2009.
- [26] D. A. Crawford, A. L. Brundage, E. N. Harstad, E. S. Hertel, Jr., R. G. Schmitt, S. C. Schumacher, J. S. Simmons, CTH User's Manual and Input Instruction, USA: Sandia National Laboratories (2011).

Figures:



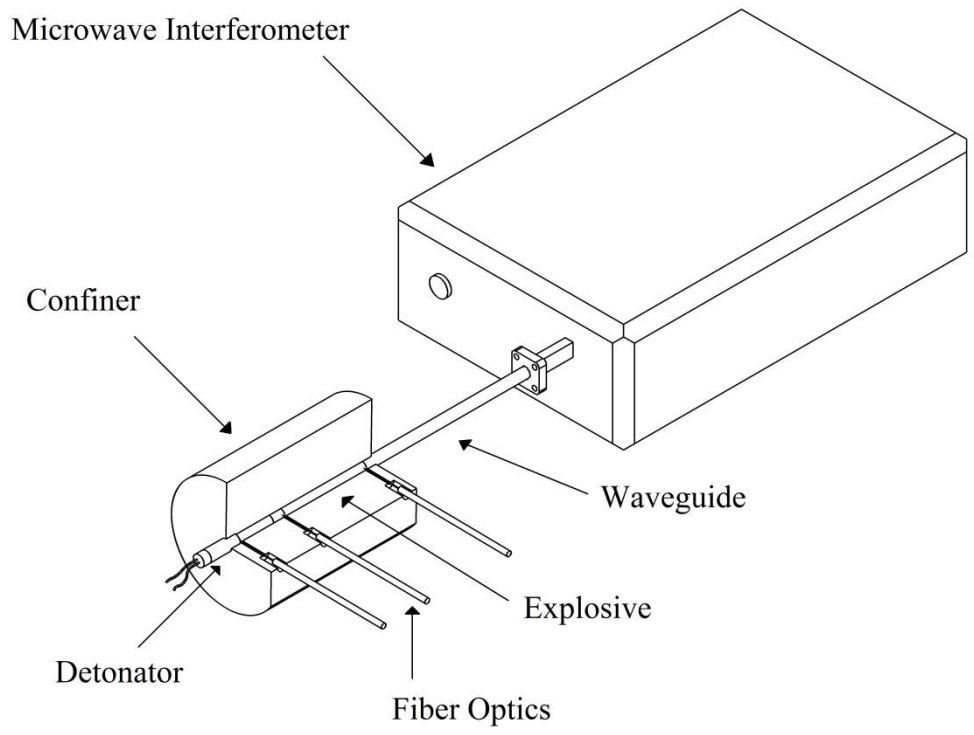


FIG. 2. Schematic of the experimental configuration.

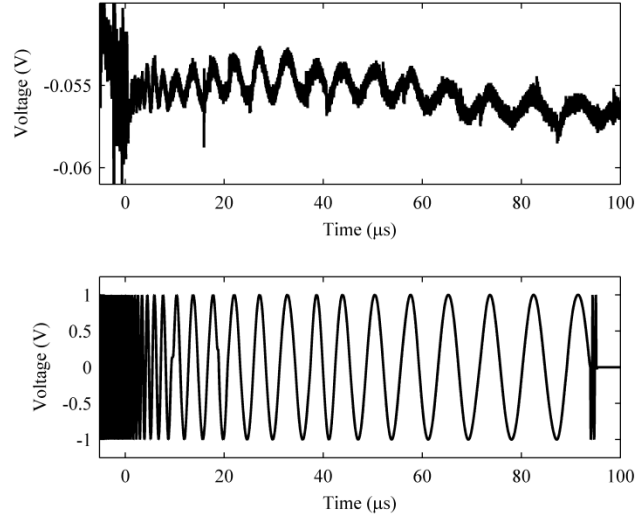


FIG. 3. Raw interference signal (top) and normalized signal (bottom) of detonation through ideal explosive transitioning to AN/10 wt.% diesel ($t = 0$).

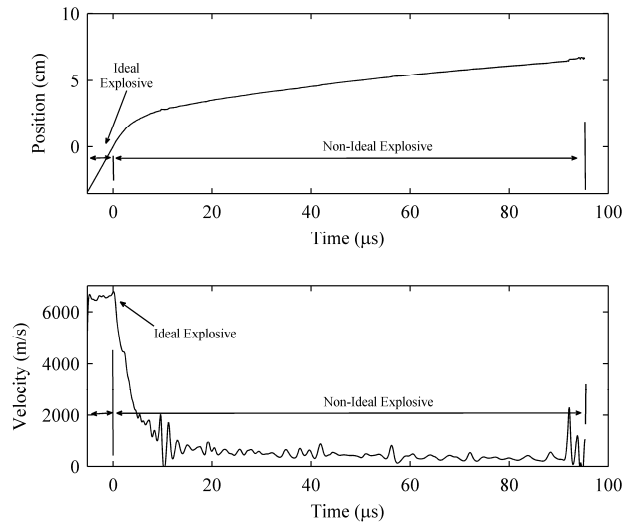


FIG. 4. Position (top) and velocity (bottom) of detonation through ideal explosive transitioning to AN/10 wt.% diesel ($t = 0$). FIG. 1. Cross-section of confiner showing location of the detonator, ideal explosive, non-ideal explosive, PMMA attenuator, waveguide, and fiber optics.

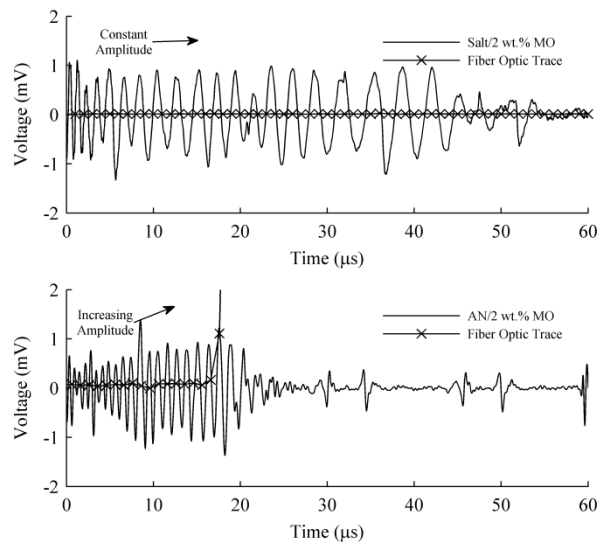


FIG. 5. Interference signal produced due to reflection through salt/2 wt.% mineral oil (bottom) and AN/2 wt.% mineral oil (top).

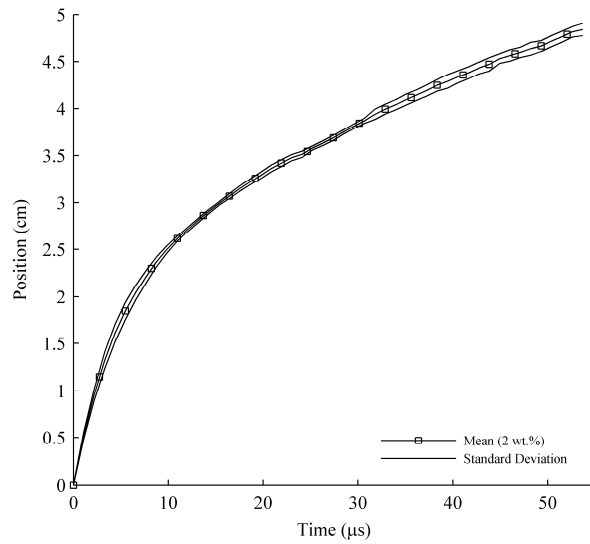


FIG. 6. Result showing the detonation velocity of the detonation front through AN/2 wt.% diesel fuel in thin-wall confiners.

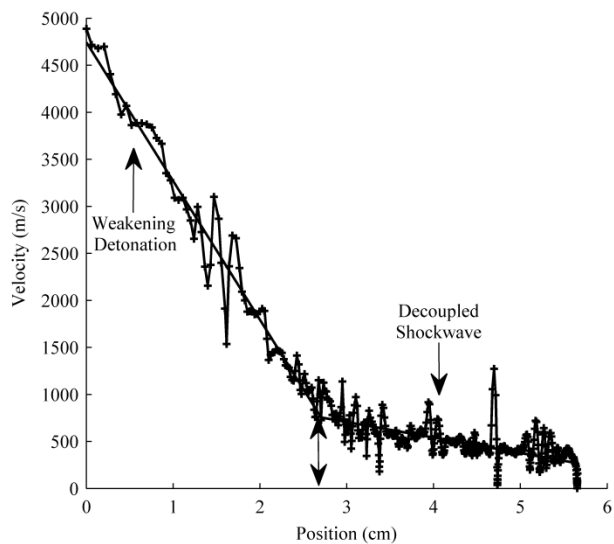


FIG. 7. Wave velocity as a function of position through AN/2 wt.% diesel fuel.

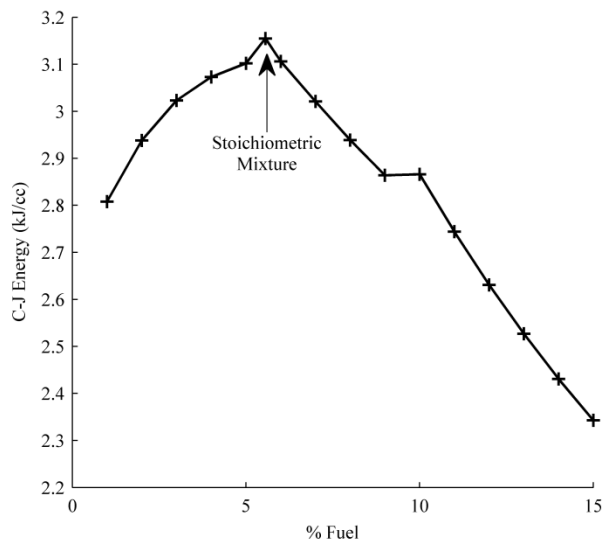


FIG. 8. C-J energy predictions for AN/diesel mixtures at various compositions using CHEETAH 6.0.



FIG. 9. Recovered thin-walled confiner after detonation of a non-ideal explosive fails.

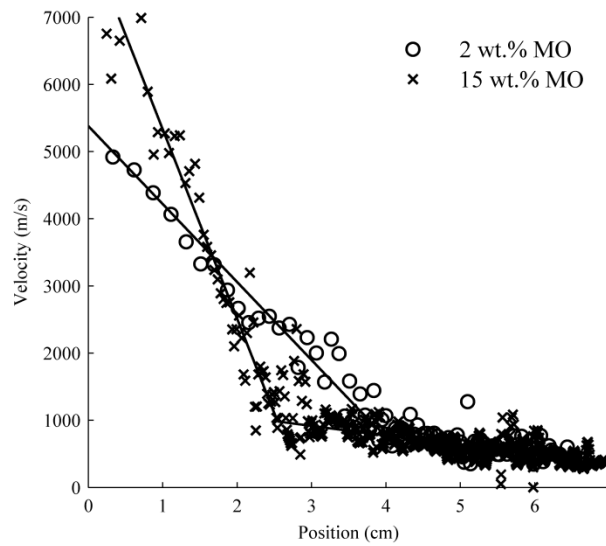


FIG. 10. – Results showing the velocity of the detonation front through non-ideal explosives with various mineral oil compositions in thin-wall confiners.

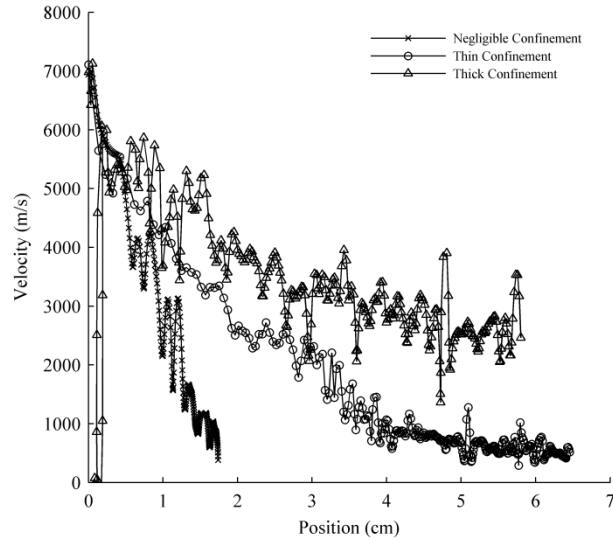


FIG. 11. Results between no confinement, thick confinement, and thin wall confiner using AN/2 wt.% mineral oil showing the velocity as a function of position through the non-ideal explosive.

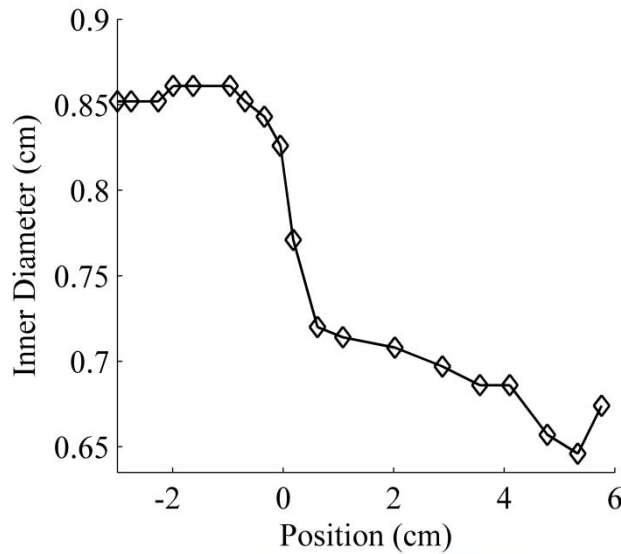


FIG. 12. Measurement of the I.D. of the recovered thick wall confiner (top) where $x=0$ is the location that the detonation transfers to the non-ideal explosive along with the cross-section of the thick-wall confiner cut in half used to measure the inner diameter I.D. (bottom).

TABLE 1. Failure position and velocity measured at the location of the velocity slope intercepts for various AN/diesel fuel compositions.

Diesel Fuel (wt.%)	Position (cm)	Velocity (m/s)
2	2.7	760
5	3.2	850
10	2.9	640

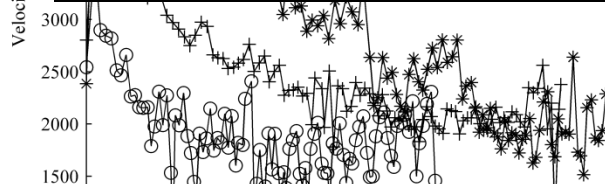


TABLE 2. Failure position and velocity measured at the location of the velocity slope intercepts for various AN/mineral oil compositions.

Mineral Oil (wt.%)	Position (cm)	Velocity (m/s)
2	3.9	910
15	2.5	980

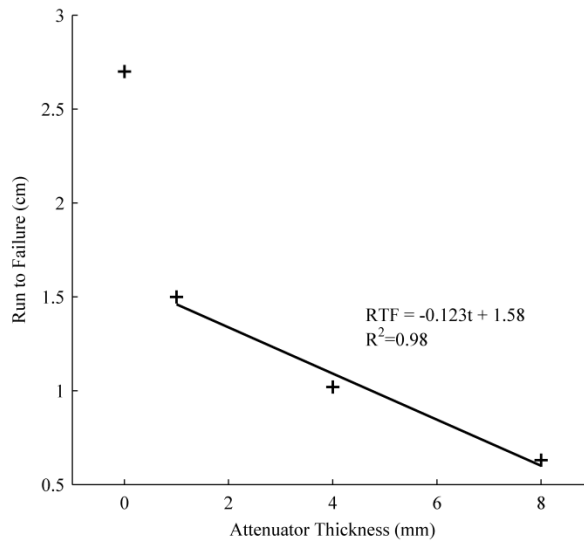


FIG. 14. Run to failure as a function of attenuator thickness in a thin steel wall confiner for AN/2 wt.% diesel fuel.

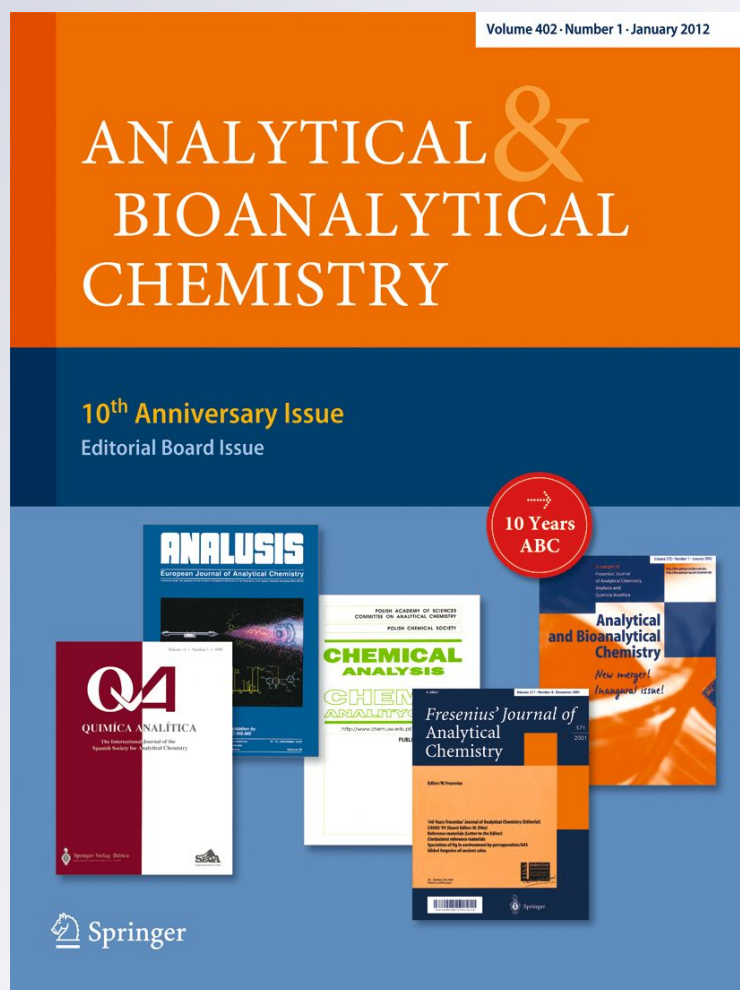
Fast detection of triacetone triperoxide (TATP) from headspace using planar solid-phase microextraction (PSPME) coupled to an IMS detector

Wen Fan, Mimy Young, Jon Canino, James Smith, Jimmie Oxley & Jose R. Almirall

Analytical and Bioanalytical Chemistry

ISSN 1618-2642
Volume 403
Number 2

Anal Bioanal Chem (2012) 403:401–408
DOI 10.1007/s00216-012-5878-x



Your article is protected by copyright and all rights are held exclusively by Springer-Verlag. This e-offprint is for personal use only and shall not be self-archived in electronic repositories. If you wish to self-archive your work, please use the accepted author's version for posting to your own website or your institution's repository. You may further deposit the accepted author's version on a funder's repository at a funder's request, provided it is not made publicly available until 12 months after publication.

Fast detection of triacetone triperoxide (TATP) from headspace using planar solid-phase microextraction (PSPME) coupled to an IMS detector

Wen Fan · Mimy Young · Jon Canino · James Smith · Jimmie Oxley · Jose R. Almirall

Received: 6 December 2011 / Revised: 10 February 2012 / Accepted: 14 February 2012 / Published online: 2 March 2012
© Springer-Verlag 2012

Abstract Triacetone triperoxide (TATP) is a high explosive synthesized from easily available reactants making it accessible for illicit uses. In this study, fast detection of TATP is achieved using a novel planar solid-phase microextraction (PSPME) as a preconcentration and sampling device for headspace analysis offering improved sensitivity and reduced sampling time over the conventional fiber-based solid-phase microextraction (SPME) when followed by ion mobility spectrometer (IMS) detection. Quantitation and comparison of the retention capabilities of PSPME as compared to the commercially available SPME were determined using TATP standards and analyzed using gas chromatography–mass spectrometry for SPME analysis and a commercial IMS with no instrumental modification for PSPME. Static and dynamic headspace extractions were used and compared for PSPME extractions, in which low milligram quantities of TATP were detected within 30 s of static mode sampling and less than 5 s in the dynamic mode sampling for PSPME–IMS.

Keywords Ion mobility spectrometer (IMS) · Planar solid-phase microextraction (PSPME) · Solid-phase microextraction (SPME) · Triacetone triperoxide (TATP)

Introduction

Triacetone triperoxide (TATP) was first discovered and prepared in 1895 by Wolffenstein [1]. Its extreme sensitivity to friction, shock, and impact makes it unfavorable for many commercial or military uses [1]; however, the ease of synthesis from readily available chemicals, the simple requirements of preparation, and the detonation effect attract much interest in criminal and terrorist activities [2, 3]. Thus, development of a fast, on-site, contact-free, and reliable method for the detection of TATP has received increasing attention within the last decade [4, 5].

Since TATP lacks a nitro group and aromatic functionalities, well-established detection methods for the nitro-containing explosives such as 2,4,6-trinitrotoluene, nitroglycerin, and 1,3,4-trinitro-1,3,5-triazacyclohexane are not suitable for this peroxide-based compound [6, 7]. Various analytical methods have been developed for the separation and detection of TATP for different purposes. Liquid chromatography [8] and gas chromatography (GC) [9] are used for the separation of TATP, and infrared [6] and Raman spectroscopy [6, 10] techniques have been used to detect TATP in the laboratory. In addition, TATP can also be detected by either mass spectrometry which includes desorption electrospray ionization [11] and selected ion flow tube [12] or sensor-based techniques such as luminescence [13, 14], electrochemical [15–17], and biological [18] sensors. However, very few of these techniques can fully accomplish two important detection requirements: fast on-site analysis with unambiguous identification and low limits of detection from post-explosion debris with high selectivity. Ion mobility spectrometry (IMS) is another robust tool for the detection of TATP [6, 19–22] and has been used by law enforcement and homeland security in airports, government buildings, and at border crossings to detect explosives for

W. Fan · M. Young · J. R. Almirall (✉)
Department of Chemistry and Biochemistry and International
Forensic Research Institute, Florida International University,
11200 SW 8th St. OE 116A,
Miami, FL 33199, USA
e-mail: almirall@fiu.edu

J. Canino · J. Smith · J. Oxley
Department of Chemistry and DHS Center of Excellence on
Explosives Detection, Mitigation and Response,
University of Rhode Island,
Kingston, RI 02881, USA

several decades due to the characteristics of fast detection, high sensitivity, ease of use, and on-site analysis, making this detection system attractive over other techniques [23]. However, IMS has not been widely exploited for the detection of TATP, and limited research has been published due to the lack of efficient sampling methods that can be coupled to this instrument.

In 2010, a novel preconcentration and sampling technique, planar solid-phase microextraction (PSPME) [24], was reported for rapid air sampling in the field. The PSPME devices can be easily and inexpensively made in the laboratory and have similar chemical characteristics as the solid-phase microextraction (SPME) fiber [24]. The increased surface area of PSPME significantly shortens the extraction time and increases the extraction recovery over the fiber SPME, and analytes extracted onto the PSPME device can be thermally desorbed into a commercial IMS instrument without modification of the IMS inlet. PSPME extractions can be accomplished in two different modes: static sampling and dynamic sampling. Static sampling is similar to the SPME equilibrium extraction from a confined headspace. Dynamic sampling is assisted with a continuous pumped flow of air through the PSPME device and has been shown to shorten sampling time [24] and improve the detection over fiber SPME. Additionally, PSPME does not suffer from potential damage for SPME fiber and limited adsorption/absorption capacity [25, 26].

In this study, we describe a fast method of sampling TATP from headspace followed by detection of IMS within seconds. In addition, a comparative study between SPME and PSPME was conducted to determine the increased retention capability and faster sampling time as a result of increased surface area and phase volume. Additionally, the PSPME device can be coupled to a portable IMS instrument to allow for on-site analysis with high sensitivity and selectivity. Furthermore, this contact-free air sampling approach reduces the potential for clutter and background commonly found in real-world contact sampling scenarios.

Experimental section

Instrumentation

Headspace sampling of solid TATP was carried using previously described SPME [27] and PSPME [24] devices and coupled to a commercial GE Ion Track (Wilmington, MA) ITEMIZER 2 IMS instrument containing a radioactive ^{63}Ni source (10.0 mCi). GE N-mode (positive mode) calibration traps containing cocaine were used to calibrate the instrument. Further TATP detection experiments were performed using the Smiths Detection IONSCAN[®]-LS (Smiths

Detection, Warren, NJ) IMS. For Smiths Detection IMS, two different dopants were used, nicotinamide (original dopant in the positive mode) and isobutyramide purchased from Smiths Detection [28]. The IMS operating conditions for both IMS instruments are shown in Table 1.

Absolute mass quantitation with SPME was analyzed using a Varian (Palo Alto, CA) CP 3800 gas chromatograph coupled to a Saturn 2000 ion trap mass spectrometer and equipped with a CP 8400 autosampler (Varian Inc., Walnut Creek, CA). The GC-MS conditions are listed in Table 2. The MS was operated in electron ionization mode (-70 eV) with a scan range of 40–450 m/z and a delay of 3.5 min.

Chemicals and methods

TATP explosives were synthesized and prepared in the University of Rhode Island laboratory [29]. Cocaine standards were purchased from Cerilliant (Round Rock, TX) for the positive mode IMS calibration. PSPME sampling devices were prepared by spin coating a sol-gel polydimethylsiloxane (PDMS) solution on an activated glass fiber filter as previously described [24] and used for both static and dynamic extractions. Approximately 10 mg of solid TATP explosive was placed in a half-gallon glass jar and was allowed to equilibrate for 30 min. For static extractions, the PSPME devices were suspended over the solid TATP sample at the opening of the jar. Various sampling times (10 s, 30 s, 1 min, 2 min, 5 min) and temperatures (20, 25, and 40 °C) were tested in triplicates to determine the minimum amount of time required for the detection of TATP using the PSPME devices. For dynamic extractions, the PSPME device was inserted into a nozzle of a handheld vacuum sampler (Barringer) in order to allow the air sample to flow through the PSPME device at a rate of 0.17 L s⁻¹. All static extractions were equilibrated at different temperatures; however, all dynamic sampling was performed at room temperature (20 °C).

Further headspace static extraction studies were conducted using certified TATP standards of 0.1 mg mL⁻¹

Table 1 Conditions for the IMS instruments used as detectors for both SPME and PSPME sampling/preconcentration

IMS operating conditions	GE ion track ITEMIZER	Smiths detection IONSCAN [®] -LS
Polarity	Positive (+)	Positive (+)
Desorber temperature (°C)	175	250
Drift tube temperature (°C)	195	235
Sample flow (mL min ⁻¹)	500	200
Drift flow (mL min ⁻¹)	350	351
Reagent gas	Ammonia	Nicotinamide/ isobutyramide

Table 2 GC–MS conditions for SPME headspace mass quantitation

Column type	Restek 15 m×0.25 mm ID×0.25 μm Rxt-5 fused silica
Carrier gas	Helium at a flow rate of 1.0 mL min ⁻¹
Split ratio	5:1
Injector temperature	180 °C
Column oven parameters	40 °C, hold for 1 min 100 °C at 5 °C min ⁻¹ , hold for 6 min 250 °C at 10 °C min ⁻¹ , hold for 5 min
MS transfer line temperature	280 °C
MS ion trap temperature	180 °C

(AccuStandard, New Haven, CT) in acetonitrile. The TATP stock solution was diluted to concentrations 5, 10, 15, 20, 25, and 30 ng μL⁻¹ using methanol or acetonitrile of optima grade (Fisher Scientific, Fair Lawn, NJ) for absolute mass quantitation in the SPME–GC–MS and PSPME–IMS sampling/detector configurations. Static extractions were performed in a similar manner in which a quart can was spiked with 10 μL of varying concentrations of TATP solutions (5–40 ng μL⁻¹), and the PSPME device was suspended over the TATP sample for different extraction times (0.5 to 10 min). Calibration of the IMS instrument was conducted by directly spiking 2 μL of standard TATP solutions of varying concentration. Calibration and confirmation of TATP in the GC–MS was performed by spiking 1-μL TATP solutions in the instrument with the CP 8400 autosampler.

The optimum equilibrium time was obtained by conducting the static extractions at different times in triplicate. Once the optimized equilibrium time was achieved, 10-μL standard solutions of known concentration ranging from 5 to 30 ng μL⁻¹ were spiked into a quart-sized can containing a suspended PSPME filter and sealed

immediately for 5-min static extractions. The signals were recorded and plotted to give a quantitative mass calibration of TATP in the PSPME devices.

Surface area analysis of the PSPME was performed in the Pacific Northwest National Laboratory (Richland, WA) using a Quantachrome FloVac Degasser (Boynton Beach, FL) for degassing the sample and a Quantachrome Autosorb iQ₂ for nitrogen Brunauer–Emmett–Teller (BET). First, a PSPME filter and an uncoated glass filter were cut into ~6×9-mm strips and were placed into two large bulb 9-mm BET tubes separately. The Quantachrome FloVac Degasser was used for degassing the samples for 3 h at 150 °C. After degassing, nitrogen BET was performed on the samples using the Quantachrome Autosorb iQ₂ by taking 40 adsorption and 40 desorption points. Surface area calculations were then performed using a 5-point multipoint BET isotherm. Pore sizes and distributions were calculated using Barrett–Joyner–Halenda adsorption isotherm.

Evaluation of the extraction recovery of SPME and PSPME was achieved by spiking the desired amount of TATP on a quart can and extracting immediately without

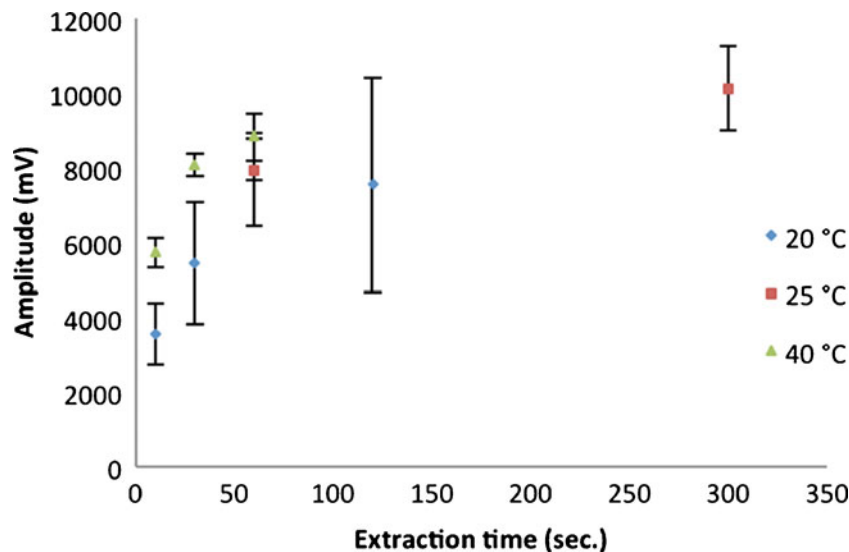
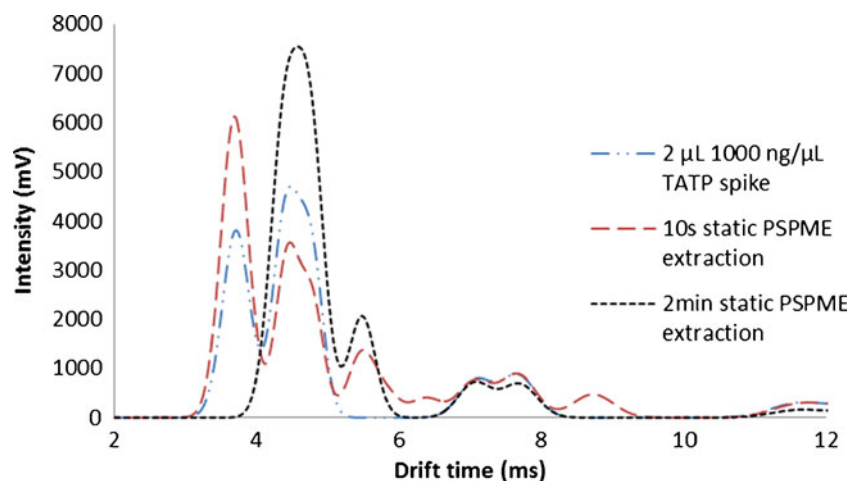
Fig. 1 Signal observed at 4.3 ms at different static extraction times of TATP at different temperature profiles

Fig. 2 IMS plasmagram of static PSPME TATP extractions performed at 20 °C with varying extraction times (10 s–2 min.). Confirmation of TATP was performed by manually spiking 1,000 ng μL^{-1} onto the PSPME device followed by detection via IMS



headspace equilibrium development. Detection of TATP extracted by SPME was performed using the Varian GC–MS, using the conditions described in Table 2. Detection of TATP extracted by PSPME was analyzed with Smiths Detection IONSCAN®-LS IMS without further modification.

Results and discussion

Detection of TATP

Various static extraction times were used at room temperature (20 °C), 25 and 40 °C to determine the shortest extraction times for the detection of a 10-mg TATP sample. Detection of TATP was achieved within a 1-min extraction of the headspace of a half-gallon glass container at room temperature (Fig. 1). In fact, after a 1-min static extraction, the pool of protonated clusters associated as the reactant ion peak (RIP) in the IMS

was completely depleted by the TATP on the PSPME device, giving two strong signals at 4.3 and 4.7 ms separately corresponding to reduced mobilities (K_0) of 2.13 and 1.95 $\text{cm}^2 \text{V}^{-1} \text{s}^{-1}$ in GE-IMS. The identity of the peak was confirmed by directly spiking 2 μL of 1,000 ng μL^{-1} TATP in dichloromethane onto a PSPME device forming two peaks with the same drift time as shown in Fig. 2, and the drift time agrees with a previous publication under the same conditions [19]. Similar results were obtained at elevated temperatures with even shorter extraction times and greater signals. Detection for TATP was achieved within 10 s of static extractions at 40 °C.

Dynamic extractions using the PSPME devices produced greater IMS signals with shorter extraction times. A 5-s extraction at room temperature (20 °C) produced a strong signal of TATP (4.3- and 4.7-ms peaks in the plasmagram), completely depleting the RIP (3.7 ms) by the saturated amount of TATP present in the PSPME device, after sampling a total volume of 0.85 L.

Fig. 3 TATP calibration by spiking 2 μL TATP of the following concentrations: 0.5, 1.0, 1.5, 2.0, 2.5, 3.0, 5.0 ng μL^{-1} onto a PSPME device

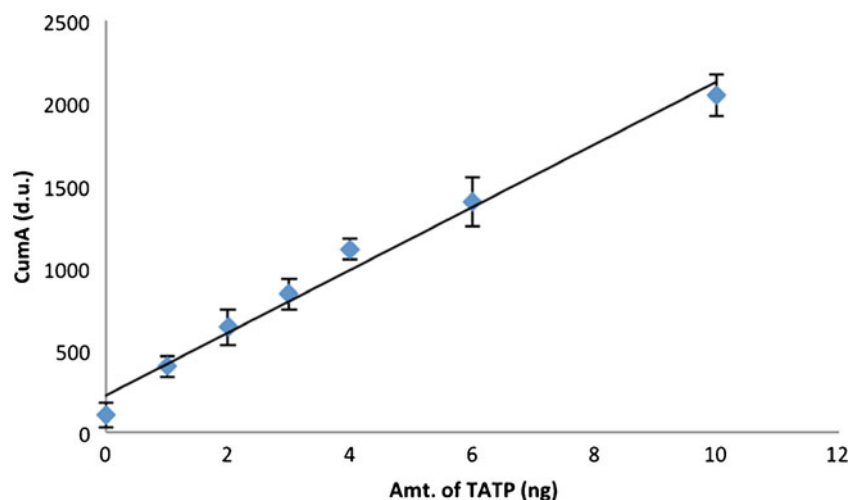
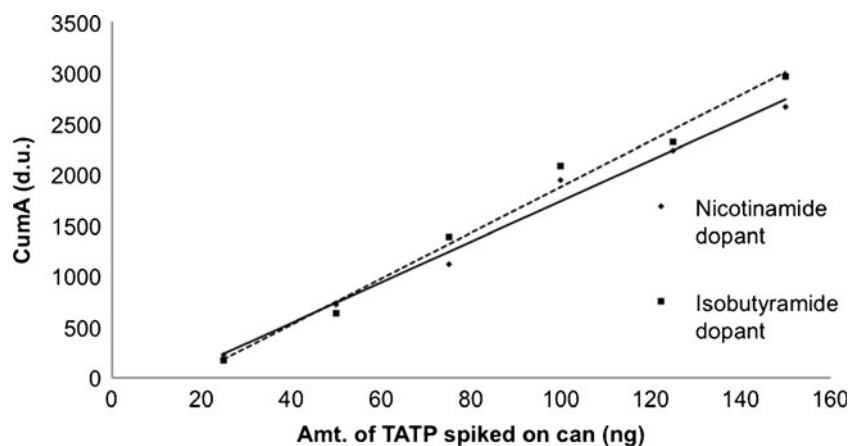


Fig. 4 TATP headspace calibration obtained from 5 min static PSPME headspace extraction of TATP (spiking 5 μL of solutions of the following concentrations: 5, 10, 15, 20, 25, 30 $\text{ng } \mu\text{L}^{-1}$)



Detection of TATP in the Smiths IMS was observed within 1 min of static extraction with 0.5- μg spike of a TATP standard in the quart container, generating a peak with a drift time of 6.7 ms and a reduced mobility (K_0) of $2.57 \text{ cm}^2 \text{ V}^{-1} \text{ s}^{-1}$ in close agreement with previously stated reduced mobility of TATP [6]. This reduced mobility is different from other reported values [30, 31] and could be caused by decomposition of TATP at an increased temperature and/or formation of different adducts with different dopants applied. Additional identification and quantitation of the TATP were conducted by directly spiking 2 μL of certified standard solutions diluted to concentrations ranging from 0.5 to 5.0 $\text{ng } \mu\text{L}^{-1}$ (Fig. 3).

Absolute mass calibration of TATP in PSPME filters

A response curve was generated using the observed maximum amplitude (d.u.) from the Smiths IONSCAN resulting in the following linear regression line Eq. 1:

$$(y) = 190.05(x) - 229.72, r^2 = 0.984 \quad (1)$$

From this method, the minimum detectable amount of TATP was determined to be 1.4 ng.

Since a PSPME extraction is an equilibrium technique similar to SPME, this technique can be used for quantitative analysis. Headspace calibration was achieved by spiking a

Fig. 5 Microscope image of the surface and cross section of the uncoated glass filter, **a** and **c**, respectively, and image of the surface and cross section of the coated PSPME devices, **b** and **d**, respectively

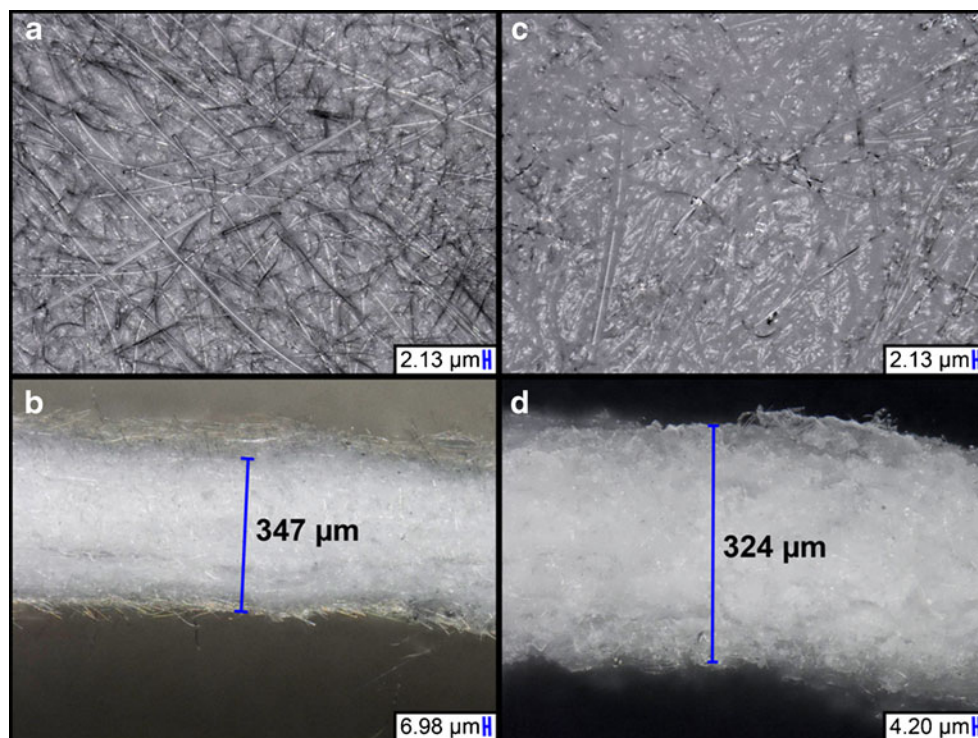
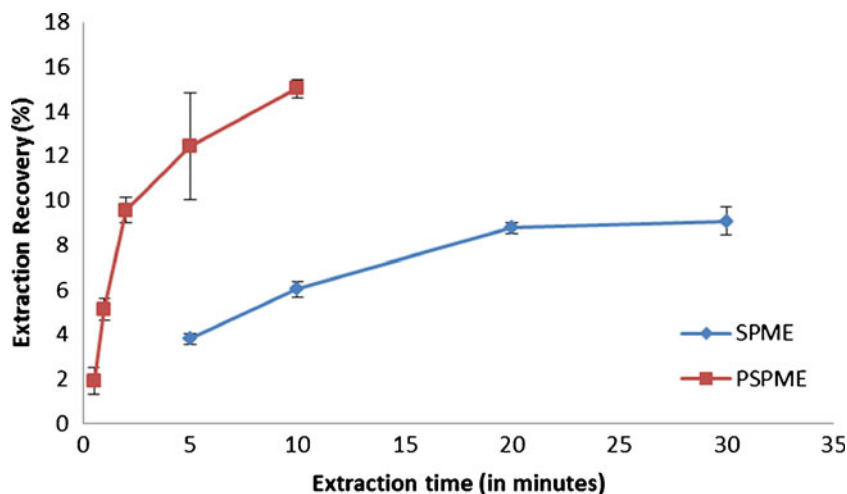


Fig. 6 Percent recovery comparison of PSPME and SPME by different static extraction time (0.5–30 min) of 100 ng TATP



known amount of TATP into a closed system and headspace sampling using PSPME at the equilibrium time of 5 min (Fig. 4). Dopant selection is essential for optimal instrument performance in order to form stable and identifiable analyte ions and suppressing ionization of unwanted analytes. Isobutyramide was used for calibration of TATP due to its reported more accurate detection on peroxide-based explosives [28]. Response curves from the Smiths IONSCAN using the nicotinamide and isobutyramide are given in Eqs. 2 and 3, respectively:

$$(y) = 20.04(x) - 272.3, r^2 = 0.986 \tag{2}$$

$$(y) = 22.58(x) - 384.5, r^2 = 0.986 \tag{3}$$

The response signals observed in the IMS were similar using either the nicotinamide or the isobutyramide dopant; thus, majority of the experiments were performed using the initially installed nicotinamide dopant. After 5 min of static PSPME extractions, the minimum amount of detectable TATP when spiked in the can using both dopants was determined to be approximately 19 ng, as shown in Fig. 4.

Headspace extraction recovery comparison of PSPME and SPME

In comparison to SPME fiber, PSPME has a $\sim 2 \times 10^4$ -fold increase ($\sim 0.15 \text{ m}^2$) in surface area than SPME fiber ($\sim 9.5 \times 10^{-6} \text{ m}^2$), and the extraction phase volume of a planar SPME disk is calculated to be approximately 300 mm^3 , compared to the commercial fiber SPME with a maximum phase volume of 0.6 mm^3 [27], offering greater than 500 times more volume capacity. Digital microscope imaging (Keyence) was performed to characterize the surface of the PSPME in comparison to the uncoated glass filter (Fig. 5). The cross-section thickness of a PSPME device was determined to be $\sim 324 \mu\text{m}$ (Fig. 5d) while an uncoated glass filters had a cross-section thickness of $\sim 347 \mu\text{m}$ (Fig. 5b). No increase in cross-sectional thickness indicates the sol-gel-based PDMS is well incorporated into the glass filter surface. Furthermore, surface images (Fig. 5a and c) show increased thickness of the glass fibers by $\sim 2 \mu\text{m}$ in PSPME, thus enhancing the capacity and phase volume. Further surface analysis studies show a decrease in glass filter surface area after coating, declining from 5.244 m^2 /

Table 3 Percent recovery comparison of PSPME and SPME by 5-min static extraction of different amounts of TATP

Amt. spiked in can (ng)	PSPME		SPME	
	Amt. of TATP recovered (ng)	Recovery %	Amt. of TATP recovered (ng)	Recovery %
50.0	2.58	5.2	2.63	5.3
75.0	4.63	6.2	4.26	5.7
100	9.00	9.0	3.45	3.5
150	21.0	14.0	7.03	4.7
200	35.1	18.0	9.35	4.7
300	61.8	21.0	13.2	4.4
400	79.2	20.0	16.9	4.3

g (uncoated glass filter) to 2.196 m²/g (coated glass filter), in agreement with the thickness measurements of the PSPME in Keyence digital microscope (Fig. 5).

Minimum amount of extraction time for detection of 100 ng of TATP for PSPME was observed to be 0.5 min compared to 5 min using SPME (Fig. 6). Comparison of the extraction recovery by varying the concentration of TATP was performed by spiking different nanogram levels of TATP standard and extracting for 5 min. The minimum amount of TATP required to be spiked into the cans in order to detect TATP was 100 ng. The amount of TATP recovered using PSPME was calculated by using an external calibration curve with the regression line in Eq. 1. For SPME analysis on the GC–MS, the following linear regression curve Eq. 4 was used:

$$(y) = 2,539(x) - 3,592, r^2 = 0.988 \quad (4)$$

Recovery of TATP on PSPME and SPME was determined to be approximately 15 and 5%, respectively, as shown in Table 3. Thus, the increased surface area and phase volume of PSPME offers much greater recovery rate and faster detection in comparison to the commercially available fiber-based SPME.

Conclusions

As a result of the increased surface area and phase volume in PSPME, TATP was sampled and preconcentrated on a PSPME device in less than 30 s by both static and dynamic extractions followed by detection using a commercial off-the-shelf IMS that does not require any modification to the sample inlet of the instrument. When using IMS as the detection method, the sampling and detection time of TATP was very short, highlighting the potential use of this method in field analysis with both high selectivity and high sensitivity detection. The total sampling and analyzing time of TATP was significantly simplified and shortened (~35 s), in comparison with fiber-based SPME sampling and analysis in GC–MS (~22 min). Compared with fiber-based SPME, the recovery of TATP is increased from approximately 5% to almost 20% when using PSPME. Sufficient recovery approximating 5% was possible with only a 1-min extraction using PSMPE. For the example of a 100-ng spike of total analyte available, this translates to the accumulation of 5 ng of TATP on the PSPME device, which is more than sufficient to produce a signal in the IMS detector. These results suggest that PSPME devices can be coupled with various commercial IMS systems to provide a high-throughput,

sensitive detection of different explosives in the field. Future work will include developing receiver operator characteristic curves to evaluate the utility of PSPME–IMS in real-world environments.

Acknowledgments The development of PSPME was supported by Award No. 2006-DN-BX-K027 from the National Institute of Justice, Office of Justice Programs, U.S. Department of Justice. The opinions, findings, and conclusions or recommendations expressed in this publication are those of the author(s) and do not necessarily reflect those of the Department of Justice. The authors would also like to acknowledge the University of Rhode Island DHS CoE for financial support for this project, and Dr. Jeannette Perr and Dr. Patricia Diaz for helpful discussions. In addition, the authors would also like to acknowledge Dr. Raymond S. Addleman from the Pacific Northwest National Laboratory for the determination of the PSPME surface area.

References

- Beveridge A (1998) Forensic investigation of explosions. Taylor & Francis, New York
- Naughton P (2005) TATP is suicide bombers' weapon of choice. Times Online
- Townsend M (2006) The real story of 7/7. The Observer
- Schulte-Ladbeck R, Vogel M, Karst U (2006) Recent methods for the determination of peroxide-based explosives. Anal Bioanal Chem 386(3):559–565. doi:10.1007/s00216-006-0579-y
- Burks RM, Hage DS (2009) Current trends in the detection of peroxide-based explosives. Anal Bioanal Chem 395(2):301–313. doi:10.1007/s00216-009-2968-5
- Buttigieg GA, Knight AK, Denson S, Pommier C, Bonner Denton M (2003) Characterization of the explosive triacetone triperoxide and detection by ion mobility spectrometry. Forensic Sci Int 135 (1):53–59
- Schulte-Ladbeck R, Kolla P, Karst U (2002) A field test for the detection of peroxide-based explosives. Analyst 127(9):1152–1154
- Schulte-Ladbeck R, Edelmann A, Quintas G, Lendl B, Karst U (2006) Determination of peroxide-based explosives using liquid chromatography with on-line infrared detection. Anal Chem 78 (23):8150–8155. doi:10.1021/ac0609834
- Stambouli A, El Bouri A, Bouayoun T, Bellimam MA (2004) Headspace-GC/MS detection of TATP traces in post-explosion debris. Forensic Sci Int 146(Supplement 1):S191–S194
- Wackerbarth H, Salb C, Gundrum L, Niederkruger M, Christou K, Beushausen V, Viol W (2010) Detection of explosives based on surface-enhanced Raman spectroscopy. Appl Opt 49 (23):4362–4366
- Cotte-Rodriguez I, Hernandez-Soto H, Chen H, Cooks RG (2008) In situ trace detection of peroxide explosives by desorption electrospray ionization and desorption atmospheric pressure chemical ionization. Anal Chem 80(5):1512–1519. doi:10.1021/ac7020085
- Sovova K, Dryahina K, Spanel P, Kyncl M, Civiš S (2010) A study of the composition of the products of laser-induced breakdown of hexogen, octogen, pentrite and trinitrotoluene using selected ion flow tube mass spectrometry and UV–vis spectrometry. Analyst 135(5):1106–1114
- Mills A, Grosshans P, Snadden E (2009) Hydrogen peroxide vapour indicator. Sensors Actuators B-Chem 136(2):458–463. doi:10.1016/j.snb.2008.12.032

14. Girotti S, Ferri E, Maiolini E, Bolelli L, D'Elia M, Coppe D, Romolo FS (2011) A quantitative chemiluminescent assay for analysis of peroxide-based explosives. *Anal Bioanal Chem* 400(2):313–320. doi:10.1007/s00216-010-4626-3
15. Lu DL, Cagan A, Munoz RAA, Tangkuaram T, Wang J (2006) Highly sensitive electrochemical detection of trace liquid peroxide explosives at a Prussian-blue 'artificial-peroxidase' modified electrode. *Analyst* 131(12):1279–1281. doi:10.1039/b613092e
16. Lin HW, Suslick KS (2010) A colorimetric sensor array for detection of triacetone triperoxide vapor. *J Am Chem Soc* 132(44):15519–15521. doi:10.1021/ja107419t
17. Xie YQ, Cheng IF (2010) Selective and rapid detection of triacetone triperoxide by double-step chronoamperometry. *Microchem J* 94(2):166–170. doi:10.1016/j.microc.2009.10.016
18. Walter MA, Pfeifer D, Kraus W, Emmerling F, Schneider RJ, Panne U, Weller MG (2010) Triacetone triperoxide (TATP): Hapten design and development of antibodies. *Langmuir* 26(19):15418–15423. doi:10.1021/la1018339
19. Oxley JC, Smith JL, Kirschenbaum LJ, Marimnganti S, Vadlamanati S (2008) Detection of explosives in hair using ion mobility spectrometry. *J Forensic Sci* 53(3):690–693. doi:10.1111/j.1556-4029.2008.00719.x
20. Räsänen R-M, Nousiainen M, Peräkörpi K, Sillanpää M, Polari L, Anttalainen O, Utriainen M (2008) Determination of gas phase triacetone triperoxide with aspiration ion mobility spectrometry and gas chromatography–mass spectrometry. *Anal Chim Acta* 623(1):59–65
21. Hilton CK, Krueger CA, Midey AJ, Osgood M, Wu J, Wu C (2010) Improved analysis of explosives samples with electrospray ionization-high resolution ion mobility spectrometry (ESI-HRIMS). *Int J Mass spectrom* 298(1–3):64–71. doi:10.1016/j.ijms.2010.08.011
22. Cook GW, LaPuma PT, Hook GL, Eckenrode BA (2010) Using gas chromatography with ion mobility spectrometry to resolve explosive compounds in the presence of interferents. *J Forensic Sci* 55(6):1582–1591. doi:10.1111/j.1556-4029.2010.01522.x
23. Eiceman GA, Karpas Z (2005) *Ion mobility spectrometry*, 2nd edn. CRC Press, Boca Raton
24. Guerra-Diaz P, Gura S, Almirall JR (2010) Dynamic planar solid phase microextraction-ion mobility spectrometry for rapid field air sampling and analysis of illicit drugs and explosives. *Anal Chem* 82(7):2826–2835. doi:10.1021/ac902785y
25. Isetun S, Nilsson U (2005) Dynamic field sampling of airborne organophosphate triesters using solid-phase microextraction under equilibrium and non-equilibrium conditions. *Analyst* 130(1):94–98
26. Tollbäck J, Isetun S, Colmsjö A, Nilsson U (2010) Dynamic non-equilibrium SPME combined with GC, PICI, and ion trap MS for determination of organophosphate esters in air. *Anal Bioanal Chem* 396(2):839–844. doi:10.1007/s00216-009-3221-y
27. Pawliszyn J (ed) (1999) *Applications of solid phase microextraction*. Royal Society of Chemistry, Cambridge
28. Stott WR, Nacson S, Eustatiu GI (2006) *Chemical identification of peroxide-based explosives*
29. Oxley JC, Smith JL, Chen H (2002) Decomposition of a multiperoxidic compound: triacetone triperoxide (TATP). *Propellants Explos Pyrotech* 27(4):209–216. doi:10.1002/1521-4087(200209)27:4<209::aid-prep209>3.0.co;2-j
30. Marr AJ, Groves DM (2003) Ion mobility spectrometry of peroxide explosives TATP and HMTD. *Int Ion Mobil Spectrom* 6(2):59–62
31. Ewing RG, Waltman MJ, Atkinson DA (2011) Characterization of triacetone triperoxide by ion mobility spectrometry and mass spectrometry following atmospheric pressure chemical ionization. *Anal Chem*: Null-Null. doi:10.1021/ac200466v

The adhesion of particles of standard explosives to model surfaces

Yevgeny Zakon^{1,2}, N. Gabriel Lemcoff¹, Abraham Marmur³ and Yehuda Zeiri^{2,4}

¹ Department of Chemistry, Ben-Gurion University, Beer-Sheva 84105, Israel

² Division of Chemistry, NRCN, P.O. Box 9001, Beer-Sheva 84190, Israel

³ Department of Chemical Engineering, Technion-Israel Institute of Technology, Haifa 32000, Israel

⁴ Biomedical Engineering, Ben-Gurion University, Beer-Sheva 84105, Israel
(yehuda@bgu.ac.il)

Abstract

Atomic force microscope (AFM) measurements are reported in which the adhesion of explosive particles to substrates with tailored chemical nature were measured. Four different explosives were studied: TNT, RDX, HMX and PETN. Two types of measurements were performed: in the first a self assembled monolayer (SAM) with different end groups was deposited on the tip and used to measure adhesion forces to an explosive particle surface. In the second type of experiments the explosive particle was glued to the cantilever and its adhesion force to SAM covered gold plated glass substrate was measured. All the experiments were performed in both ambient air and under water. These measurements show that -OH and -C₆H₅ end groups of the SAM lead to increased adhesion. In addition, we found that capillary forces have a major contribution to adhesion of explosive particles.

Introduction

Most of the standard solid explosives exhibit very low vapor pressure at room temperature.¹⁻³ One of the highest vapor pressures corresponds to 2,4,6-trinitrotoluene (TNT), whose magnitude is about 10⁻⁶ torr at room temperature.^{4-5,8-9} At the other end of the vapor pressure spectrum one finds pentaerythritol tetranitrate (PETN)⁶⁻⁹ and 1,3,5-trinitroperhydro-1,3,5-triazine (RDX)⁸⁻⁹ with vapor pressures in the range of 10⁻⁹-10⁻¹⁰ torr at room temperature. Thus, trace detection of most explosives is limited to their solid particle form. Consequently, law enforcement authorities need efficient particle sampling procedures to collect trace amounts of explosives required for detection by the analytical systems.¹⁰

Sample collection from passenger belongings and luggage in airports is aimed at the detection of energetic material residues. Trace amounts of material are expected to remain on items belonging to individuals involved in preparation or transportation of explosives. Presently, sampling of trace amounts of explosives is mostly carried out using the swab sample collection. In this procedure, particle collection is based on wiping a swab material over the surface suspected to be contaminated by explosive residues. The particles collected by the swab material are then transferred to a suitable detection system for their chemical analysis (the most widely used detection system is the ion mobility spectrometer (IMS)).¹¹ Different compounds are employed for the fabrication of the swab material. These include glass fiber, Teflon or cotton based cloths that serve as the main matrix. This substrate is usually coated by various polymer layers whose purpose is to increase the efficiency of explosive particle collection by the cloth.

A proper design of the swab material can lead to a marked enhancement in particle sampling efficiency. For this, the affinity of the swab material to the explosive particles must be increased. To engineer such improved material, the nature of the forces acting between the explosive particle and the surface of the swab material must be understood. Therefore, the main objective of the present study is to enhance the understanding of the contribution of forces from diverse origins to the adhesion of explosive particles to substrates with different chemical nature.

The adhesion of particles to solid substrates has been studied for many decades.^{12,13} In general, the contact area upon adhesion depends on the detailed topology of the two surfaces. The estimation, experimentally or theoretically, of the contact area between a particle and a substrate is not trivial and requires development of sophisticated modeling procedures.^{14,15} The main types of interactions that contribute to particle adhesion include: electrostatic (if charges are present), van der Waals (vdW),

chemical bonding and capillary forces. The domain, in which each type of these interactions has significant contribution to adhesion, varies. The shortest range interaction corresponds to chemical binding whose main contribution is in the range of 0.1-0.3 nm. Both vdW and electrostatic interactions extend to much longer particle-substrate distances, up to 50 nm, while capillary forces can extend to the micrometer range.

The present study is concerned with four widely used explosives: pentaerythritol tetranitrate (PETN), 1,3,5-trinitroperhydro-1,3,5-triazine (RDX), cyclotetramethylene-tetranitramine (HMX), and 2,4,6-trinitrotoluene (TNT). Force measurements, using atomic force microscopy (AFM), between the explosive particles and a self-assembled monolayer (SAM) of molecules with different functional end groups were carried out to estimate the magnitude of the attractive interactions. Two experimental arrangements were considered; in the first, the SAM was located on the AFM tip while the explosive particle was glued to a glass substrate; in the second setup, the SAM was formed on a gold plated glass substrate while the explosive particle was glued to the AFM cantilever. The experiments were carried out in ambient air as well as in water. Comparison between the results allows the assessment of the contribution of capillary forces to the adhesion of these particles.

Methods and Materials

All force measurements were carried out using a Veeco system model Dimension 3100 SPM. The cantilevers used for the measurements were Veeco NP-010 with force constants of 0.06 and 0.32 N/m as well as cantilever by Budget Sensors SiNi with Gold/Chromium coating and force constants of 0.06 and 0.27 N/m. We have used 15-30 μm size particles received from Rafael Ltd (P.O. Box 2250, Haifa, 321021 Israel). Particles were glued to the cantilever using a home built apparatus based on micrometer movements of the cantilever in the X-Y-Z directions. The gluing process was carried out under a stereoscopic Nikon microscope (STZ-1000 model). Before each measurement with a new cantilever, the force constant of the cantilever, after the particle was glued to it, was measured by comparison of the deflection to that of a standard cantilever on a standard flat substrate.

The self-assembled monolayer was formed by exposure of a 50 nm deep gold layer to a 1 mM solution in ethanol of thiol molecules. The gold layer was plated on a glass substrate or on the AFM tip (by the manufacturer) depending on the type of measurement to be performed. The gold plated substrate was cleaned with ethanol and then immersed for 20 min into a 1 mM ethanol solution of thiol. Subsequently, the sample was removed from the solution, rinsed with ethanol and dried by exposure to a dry air jet for 10 min. This monolayer preparation was based on published procedures in the literature.¹⁷⁻²¹ Eight different molecules were used to construct the various SAMs. They are listed in Table 1 together with the measured contact angle (no hysteresis measured) and the corresponding value obtained in the literature. All chemicals used in this study were purchased from Sigma-Aldrich, Israel.

Two sets of measurements were performed. In the first, the SAM was deposited on the gold plated AFM tip while the explosive particle examined was glued to a glass microscope plate. In this set of experiments the contact area between the SAM covered tip and the explosive surface is small (few nanometers) but with well defined magnitude. In the second set of experiments the SAM was deposited on a 50 nm thick gold layer plated on the glass substrate and the explosive particle was glued to the cantilever. Since the structure and roughness of the explosive particles are not well defined, the contact area between the particle and the substrate is not known. However, this experimental arrangement is expected to yield more accurate and realistic adhesion force values. In both types of experiment a low force constant cantilever (0.06 N/m) was used. The diameter of the explosive particles used was in the range of 15-25 μm . Both types of experiments were carried out using two different scanning rates and no dependence of the measured adhesion force on the scanning rate was found.

Table 1: List of molecules used to construct the various SAMs used in this study. The contact angle measurements reported below were carried out using the SAM deposited onto the gold plated glass slide.

Contact angle [$^{\circ}$]	Measured contact angle [$^{\circ}$]	Molecule used	End Group
75.9 ¹⁷	75	Au layer	none
26.1 ¹⁷	27	11-mercapto-1-undecanol	-OH
108.9 ¹⁷	102	Octadecane thiol	-CH ₃
34 ¹⁸	38	cysteamine	-NH ₂
150 ¹⁹	150	Perfluorodecanethiol	-CF ₃
40-50 ²⁰	45	3-mercaptopropionic acid	C ₃ -COOH
40-50 ²⁰	52	8-mercaptooctanoic acid	C ₈ -COOH
65 ²¹	65	4-Phenylthiazole-2-thiol	-C ₆ H ₅
	85	2-mercapto-2-thiazoline	C ₃ H ₄ SN

All AFM measurements were repeated at ten randomly chosen sites on the substrate examined. At each site 10-20 force measurements were performed to obtain statistically meaningful adhesion force values. The standard deviations in the measurements at a given site were typically up to 10% of the average force value. This spread is associated mainly with variations in substrate morphology. For each type of explosive the data presented corresponds to two different particles used to carry out the measurements. All measurements were carried out in two environments: the first was air at ambient conditions, temperature of 24±2⁰C and relative humidity of 35-60%; the other was under liquid water.

All electronic structure calculations were carried out using the Gaussian 09 code²² on a PC work station. The calculations were carried out using density functional theory (DFT) employing the

WB97XD functional with the 3-21G basis set. This level of calculations yields accurate thermochemical data for the different explosives examined. For each explosive-end group pair the optimized lowest energy was calculated for 5-10 different initial relative orientations.

Results and Discussion

Adhesion forces of explosive particles using two different arrangements were examined: adhesion of a SAM covered tip to explosive particle surface and the adhesion between a particle glued to the tip and a flat SAM covered gold plated glass substrate. In both types of experiments the goal in using a SAM covered surface was to examine the importance of chemical interactions in the adhesion process. Hence, the end groups of the molecules used to form the SAM were changed to obtain information about the chemical interactions in the system.

In general, the adhesion force, F_{ad} , can be written as a sum of four main components:¹⁶

$$(1) \quad F_{ad} = F_{el} + F_{vdW} + F_{cap} + F_{chem}$$

where F_{el} denotes electrostatic force, F_{vdW} contribution from dispersion forces, F_{cap} stands for capillary forces and F_{chem} for contribution of chemical interactions. Each one of these forces has its range of applicability, the shortest being F_{chem} which is limited to the range of 0.1-0.4 nm, F_{el} and F_{vdW} to the range 0.4-50 nm. F_{cap} starts to contribute when a bridge of water molecules is formed between the two approaching surfaces. Such a bridge of water molecules can be formed starting at a separation of 1 nm extending out to several micrometers depending on the amount of adsorbed water molecules layers on the solid surface. As noted above, we did not find any evidence to contribution of electrostatic forces in the experiments reported here. Also of interest is the simple theoretical observation that the electrostatic force (under water), the capillary force (in air), and the contribution of the chemical interactions can be affected by the chemical nature of the SAM. In general, the SAM is much too thin to affect the vdW forces.

The contribution of capillary forces is expected to be more pronounced when the system under investigation is exposed to increased humidity. The AFM employed in this study did not allow control of humidity, hence, all measurements were carried out also under water where capillary forces are eliminated. However, when the adhesion forces are measured under water additional contributions to F_{ad} might exist.¹⁶ One possibility is the electrostatic double layer force, F_{edl} , associated with the interaction of the double layers at the particle and substrate surfaces. The magnitude and sign of this force depends on ion concentration, surface charges and the distance between the particle and the substrate. Typical magnitude and range of the electrostatic double layer interaction for ionic solids (i.e. metal oxides) at low ion concentrations is 0.2-2.0 kcal/mol in the distance range of 4-70 nm respectively. This force is probably negligible in the present case since triply distilled water with very low ion concentration was used (although dissolved CO_2 may lead to very small concentration of CO_3^{2-} ions) and both particle and substrate are non ionic substances. Another type of force is the one associated with hydration, F_{hyd} .¹⁶ The source of this force is the hydration layers at the particle and substrate surface. F_{hyd} is short range, 0.2-1.5 nm, it decays exponentially and results in repulsion between the particle and the substrate. These interactions for smooth surfaces are very small, and usually do not exceed 0.2 kcal/mol, hence will not be considered here. The last and probably most important contribution to adhesion can be due to Hydrophobic attractive interaction.¹⁶ Hydrophobic surfaces in water attract each other if the contact angle with both surfaces (particle and substrate) is larger than 90° . Typical values of hydrophobic interactions span the range of 2.0-25.0 kcal/mol. Inspection of Table 1 shows that only two SAMs exhibit contact angle larger than 90° , Octadecane thiol and Perfluorodecanethiol while the contact angle for the explosives examined is in the range of $50-70^\circ$.²³⁻²⁴ Thus, for most systems examined here no major contributions of hydrophobic forced to adhesion are expected.

The non-uniform structure of real explosive particles and the morphology of their surfaces were examined by scanning electron microscopy (SEM). The images of typical large particles as those used to glue to the glass substrate are shown at two magnification values in Figs. 1 and 2. In all cases the

images were taken after the particles were covered with a 20 nm deep gold layer. The highly irregular shape with steep surfaces at different orientations is clearly seen in Fig.1 for all four explosives. Inspection of the larger magnification images' Fig. 2, shows that the surface morphology of all four explosives exhibit complex structure with micrometer and smaller scale. Thus, randomly chosen sites on these type of surfaces may correspond to widely different morphologies around the sites. The implications of this high degree of site heterogeneity will be discussed below in more detail.

The presentation and discussion of the experimental results below will be divided into two parts. First we shall describe the outcome in the measurements of the interaction between the SAM-covered tip and the surface of an explosive particle glued to a glass substrate. Next, the outcome of experiments employing an explosive particle glued to the cantilever and a SAM deposited on a thin gold film substrate will be described. In both types of experiments it was not possible to obtain accurate normalized quantification of the measured forces. This limitation is due to the irregular shape and roughness of the explosive particle surface that prevents quantitative determination of the contact area between the two surfaces in contact (i.e. tip-particle or particle-gold film substrate). In both types of measurements the SAM was prepared following the prescriptions found in the literature (except in the case of 2-mercapto-2-thiazolin end group).¹⁷⁻²¹ No efforts were made to reveal the detailed morphology and arrangement of the SAM except contact angle measurements. It is assumed that the SAM arrangements in this study are identical to those reported in the literature.¹⁷⁻²¹ At the end of this section results of electronic structure calculations will be presented to support the experimental findings.

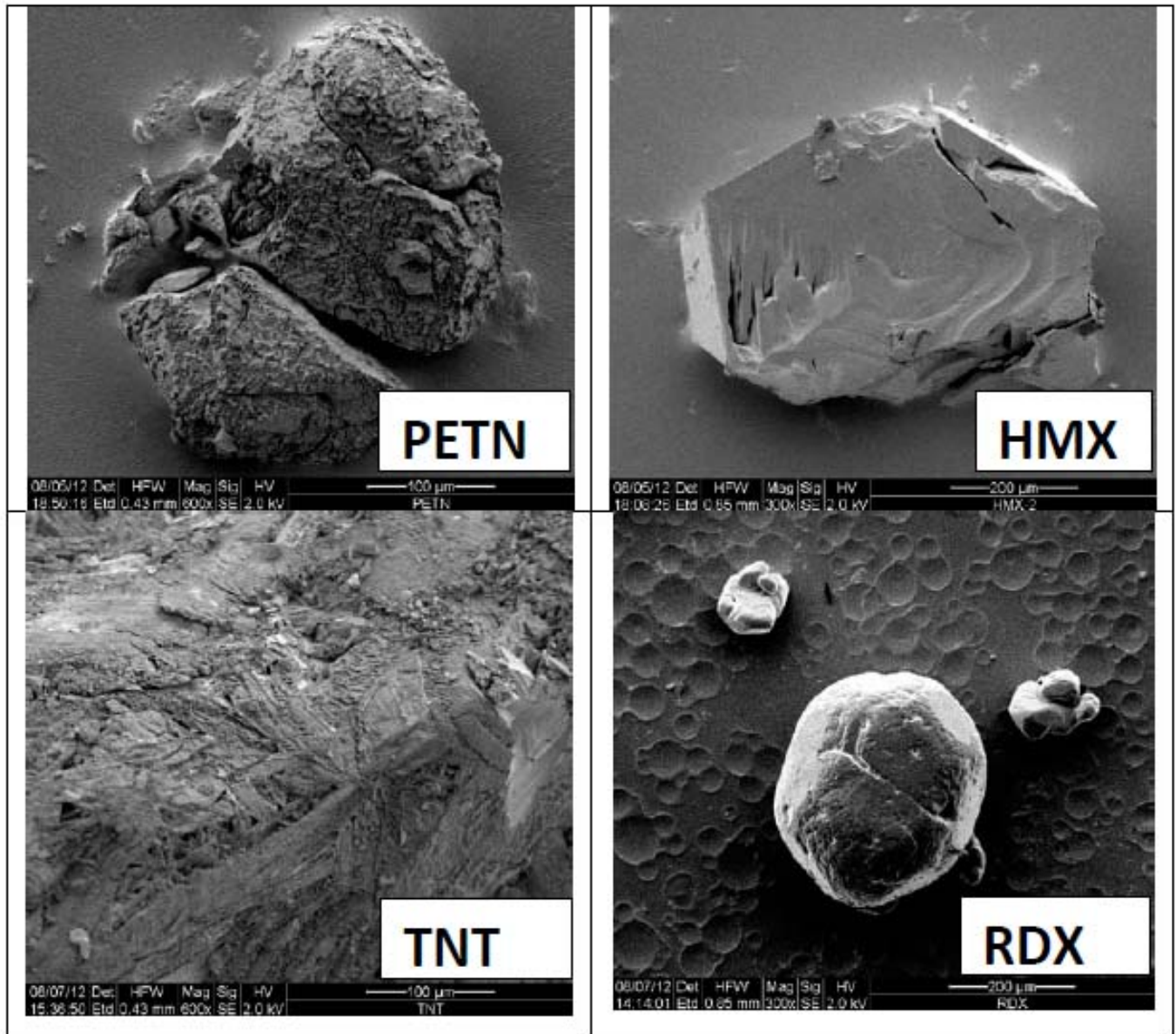


Fig. 1: Low magnification SEM images of the large explosive particles glued to the glass substrate.

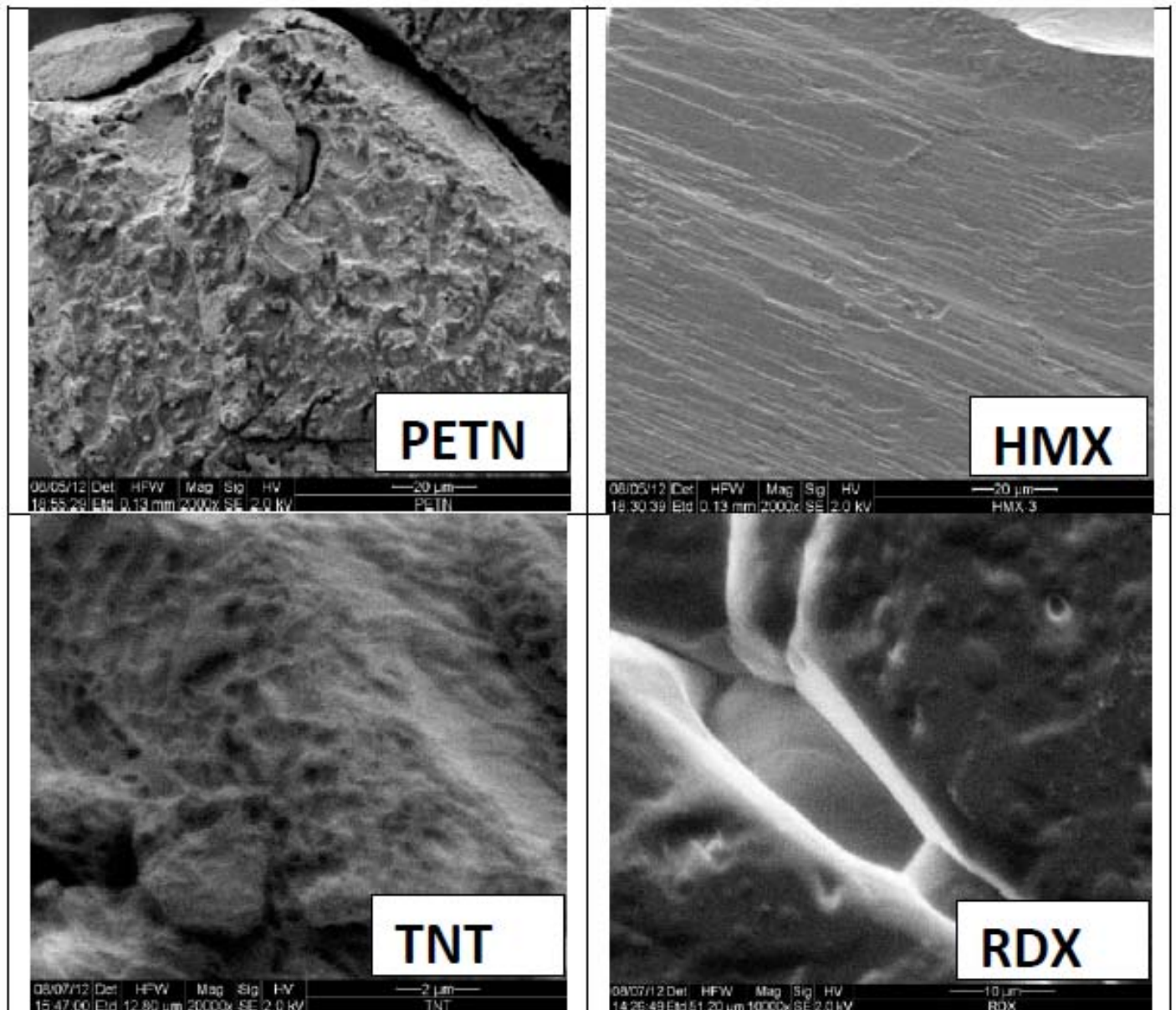


Fig. 2: High magnification (5-10 time larger than in Fig. 1) SEM images of randomly chosen sites on the surface of the large explosive particles glued to the glass substrate.

SAM on tip

The van der Waals interaction between the SAM and the explosive particle surface can be deduced from the magnitude of cantilever bending at the "jump to contact" distance, Z_{jtc} , that occur during the approach of the tip to the substrate. Once this quantity is measured, one can use the force terms derived by Hamaker²⁵ for the interaction between system of different shapes, assuming that vdW forces dominate at this point.¹⁶ In SAM on tip type of measurements one would expect well defined contact area between the tip and the substrate and a well defined curvature at the contact (i.e. the tip curvature). The irregular shape of the particle and its high surface roughness, see Figs. 1 and 2, leads to large variation in Z_{jtc} obtained at different randomly chosen sites on the substrate surface. These limitations do not allow a detailed comparison of the Hamaker constant for the different SAMs examined. However, comparison between the magnitude of Z_{jtc} obtained in the different experiments shows that the Z_{jtc} values obtain in the under water measurements are smaller, typically by a factor of four or more, than those obtained in ambient air measurements. This finding is associated with a large contribution of

capillary forces in the case of the ambient air data. It is well established that a capillary bridge can be formed between the tip and the substrate even at low relative humidities.²⁶⁻²⁸ These studies clearly show that even at low relative humidity values, strong contributions of capillary forces are expected at tip-substrate separations smaller than 10 nm. This phenomenon is more pronounced for rough substrates.²⁸ The fluctuations in the magnitude of Z_{jtc} did not allow any meaningful comparison between values obtained for different SAMs.

Next, the retraction part of the force curves are analyzed to obtain the adhesion forces. The average values of the adhesion forces between the tip and the explosive particles in ambient air and underwater are presented in Figs. 3 and 4 respectively. The values shown are averages of the adhesion forces measured at 10 random sites on the explosive particle surface. It is easy to see that the observed variations in the magnitude of F_{ad} are not too large. Inspection of these results shows that in both environments the magnitude of adhesion forces are similar. The results in ambient air, Fig. 3, suggest that the interaction of the explosive particles with SAMs that have -OH and -Phenyl end groups lead to slightly stronger adhesion forces than those observed for the other end groups. A 2-40 times enhancement in adhesion by these two end groups is observed compared to the other end groups. In ambient air, HMX and PETN exhibit stronger adhesion forces towards most SAMs than those for RDX and TNT. Similar examination of the data obtained underwater, Fig. 4, shows that in this case the -OH end group does not exhibit much stronger binding compared to the other SAMs, however, the -Phenyl end group exhibits increased F_{ad} values.

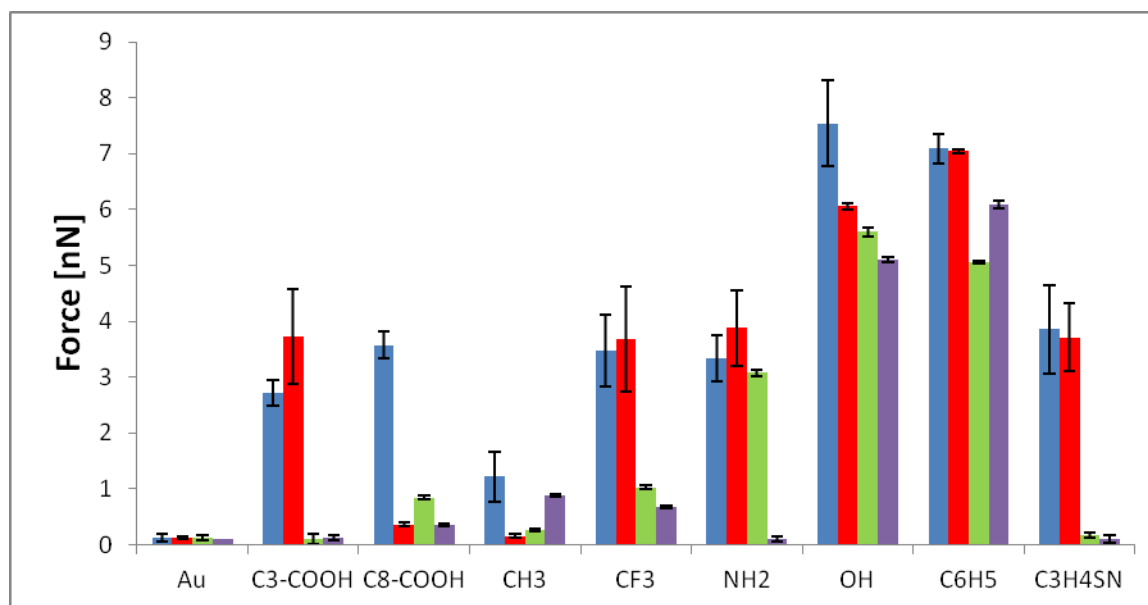


Fig. 3: Adhesion force between different explosive and end groups of the SAM deposited on the tip measured in ambient air. Blue columns correspond to HMX, red columns to PETN, green columns to RDX and purple columns to TNT.

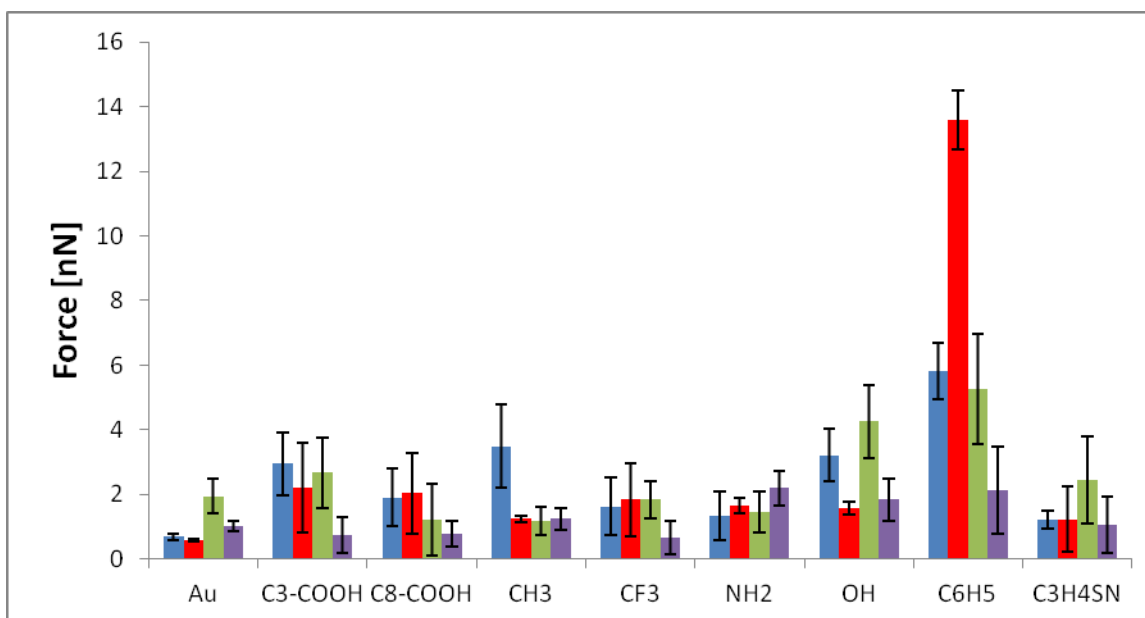


Fig. 4: Adhesion force between different explosive and end groups of the SAM deposited the tip, measured under water. Blue columns correspond to HMX, red columns to PETN, green columns to RDX and purple columns to TNT.

Inspection of the results presented in Figs. 4 and 5 shows some interesting features. The first is that in the case of ambient air measurements the variation between the four explosives is much larger than that in the under water measurements. The adhesion of the SAM covered tip to HMX and PETN surfaces seem to be stronger than to the other two explosives. The second is the similarity in the magnitude of F_{ad} obtained in the two different environments. Some of the adhesion forces obtained in ambient air are larger than the corresponding values obtained under water while some are smaller. The last feature is the variation of F_{ad} as a function of the end group on the SAM. In the ambient air measurements the adhesion forces to -OH and -Phenyl groups is larger than to the other end groups examined. For the under water measurements, the adhesion to -Phenyl is stronger than to the other end groups.

The magnitude of the standard deviations in these measurements (used to define the error bar shown) varies in the range of 5%-30% of the average value. These variations are related to the changes in the tip-substrate contact area at different site. The irregular shapes of the particles together with their roughness can lead to marked changes between tip-substrate contact area at the randomly chosen sites. Although the curvature at the edge of the tip used is rather small (15 nm according to the manufacturer), the height and base sizes of the pyramidal shaped tip are 17 ± 2 and $5 \mu\text{m}$ respectively. Thus, the variations in local morphology at the randomly chosen site can easily be responsible to the error observed. However, the standard deviation values obtained are small enough to eliminate the possibility that they are responsible to some of the features described above.

The larger adhesion forces observed in some of the ambient air measurements are related to contributions of capillary forces to F_{ad} . Once the capillary bridge between the tip and the substrate is formed, the adhesion of the tip to the particle is expected to increase due to the inclusion of F_{cap} .²⁶⁻²⁸ Formation of the capillary bridge depends on the relative humidity and the amount of adsorbed layers of water molecules on the two approaching surface. The amount of adsorbed water on the explosive particle surface can be responsible to the variation in F_{ad} observed in the ambient air data. As described above, the results in Fig. 3 show that the adhesion to HMX and PETN surfaces tend to be stronger than F_{ad} to RDX and TNT surfaces. Since this behavior is not observed in the case of under water

measurements, it is related to contributions of capillary forces to F_{ad} for HMX and PETN. Large variations in contact angle have been measured for different crystal phases of explosives.²⁴⁻²⁵ Moreover, it has been proved that variation of surface roughness scales correspond to different magnitude F_{cap} .²⁹⁻³¹ Thus, the heterogeneity in local surface polarity and variation on roughness suggests that different sites on the explosive particle surface may adsorb largely different amounts of humidity. Consequently, different contributions of capillary forces to F_{ad} are expected.

The results presented in Figs. 3 and 4 clearly suggest that the interaction between -Phenyl end group and all four explosives examined is larger than for the other end groups. The measurements in ambient air show that chemical interactions have marked contributions to F_{ad} also by the -OH end group, this behavior is not exhibited so clearly in the under water data. The adhesion forces corresponding to all the other end groups may have contributions due to chemical interactions but they are less dominant. The relatively strong binding to -OH and -Phenyl groups are also substantiated by model electronic structure calculations (see discussion below). **Particle on tip**

We turn now to force measurements where the explosive particle is glued to the cantilever and the SAM is deposited on a thin gold layer deposited on a glass substrate. In this case, the highly irregular shape and morphology of the glued particle prevents one from any knowledge or possibility to estimate the contact area between the explosive and the substrate. Moreover, unknown structure of the particle-substrate interface does not allow a meaningful definition of the particle curvature, R , at the contact points and the number of such points. Thus, one cannot use the magnitude of cantilever bending at the jump-to-contact point along the approach route of the tip to estimate the magnitude of A_H .

The adhesion forces obtained by analysis of the retraction part in the force curve for the different explosive particles are presented in Figs. 5 and 6 for ambient air and under water measurements, respectively. Comparison between these results and those obtained in the "SAM on tip" measurements, Figs. 3 and 4, shows that for ambient air measurements the adhesion forces now are for all explosives larger by an order of magnitude or more. For under water measurements we obtain F_{ad} values that are comparable with those obtained for "SAM on tip" measurements. The large increase in the adhesion forces observed for ambient air measurements can be associated with the increased contact area between the explosive particle and the SAM covered gold substrate. While in the "SAM on tip" case the contact area is dictated by the size of the tip and the local morphology of the substrate at the measurement site, here it is expected to be much larger due to the high probability for multiple macroscopic size contact regions. Such a multiple contacts are expected due to the irregular shape of the particles and the surface roughness of both bodies in contact, see Figs. 1 and 2. Such an increased multiple contact areas should lead also to increased F_{ad} values for under water measurements in the case of "particle on tip" configuration compared with the "SAM on tip" measurements. Comparison of the results in Figs. 4 and 6 shows that this is clearly not the case. In both arrangements similar adhesion forces are obtained. Another difference observed is an increase in the standard deviations for the "particle on tip" measurements compared to the "SAM on tip" experiments. This difference in standard deviation values is associated with the larger variation of contact area due to surface irregular shape of the particles and the roughness of both particle and substrate morphologies for "particle on tip" case, see Figs. 1 and 2.

The large increase in the adhesion forces for all systems examined in the ambient air measurements are associated with large contributions of capillary forces to F_{ad} . As discussed above, the contribution of capillary forces strongly depends on the relative humidity that in turn determines the amount of adsorbed water molecules on the two surfaces in contact. In addition, capillary force contribution to adhesion will increase linearly as a function of the number of contact points between the two surfaces. The irregular shapes of the explosive particles used, see Fig. 1, and their rough surface morphology, Fig. 2, suggests that a large number of contact points between the particle and the substrate exists at each randomly chosen site. At each contact point one expects contribution of F_{cap} to F_{ad} , hence in such situation capillary forces may become dominant. This behavior rationalizes the observed marked increase in F_{ad} obtained for ambient air measurements compared to under water experiments.

For all four explosives, the variation of adhesion force as a function of the end group on the SAM is irregular with a tendency for increased adhesion forces observed for the-Phenyl end groups as well as

for -OH and -NH₂. These variations in F_{chem} as a function of the different end groups seem to be much smaller than the contributions due to F_{cap} . However, the identity of the end group may have an indirect contribution through its ability to adsorb water molecules. It is expected that for ambient air measurements hydrophilic end groups will increase the amount of adsorbed water molecules on the SAM, hence, lead to an increase in the number of water bridges formed between the two surfaces. Thus, the identity of the end group can influence the contribution of F_{cap} to F_{ad} . The variation of F_{ad} for the different end groups seem to be similar for both ambient air and under water measurements. This suggests that the magnitude of F_{chem} is small compared to that of F_{cap} but its indirect influence described above will scale as a function of contact area and number of contact point. The factor of 2-5 variation in F_{ad} for the various end groups and explosives examined can be used to improve sample collection, see discussion below.

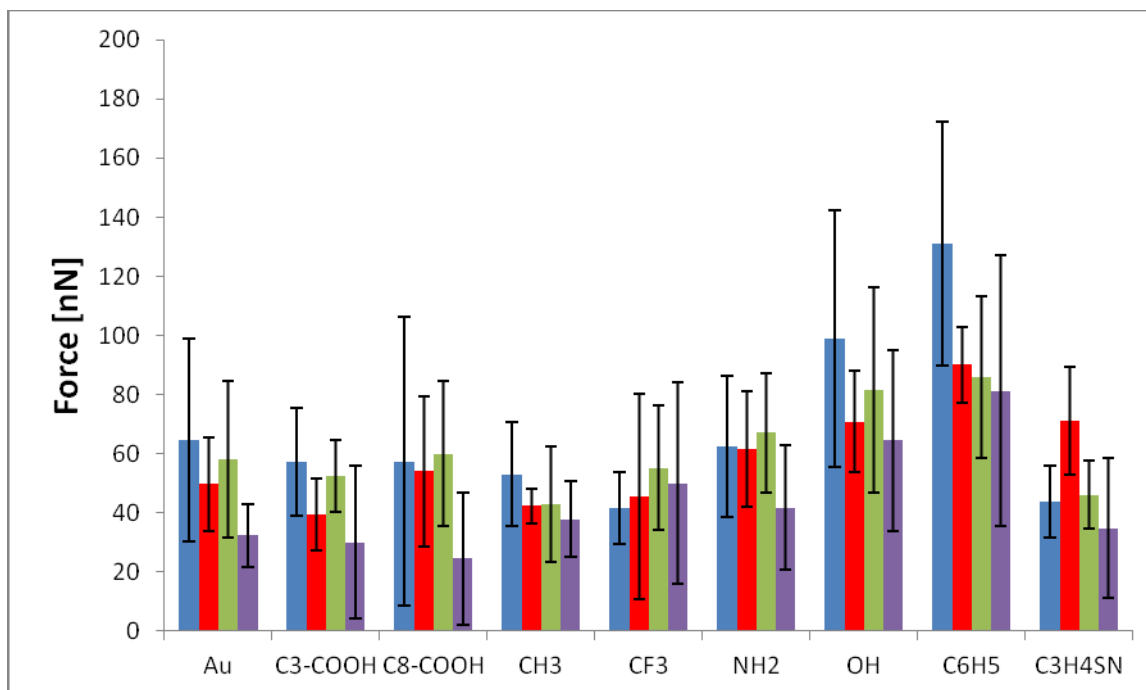


Fig. 5: Adhesion force between different explosive particles and end groups of the SAM deposited on a glass substrate measured in ambient air. Blue columns correspond to HMX, red columns to PETN, green columns to RDX and purple columns to TNT.

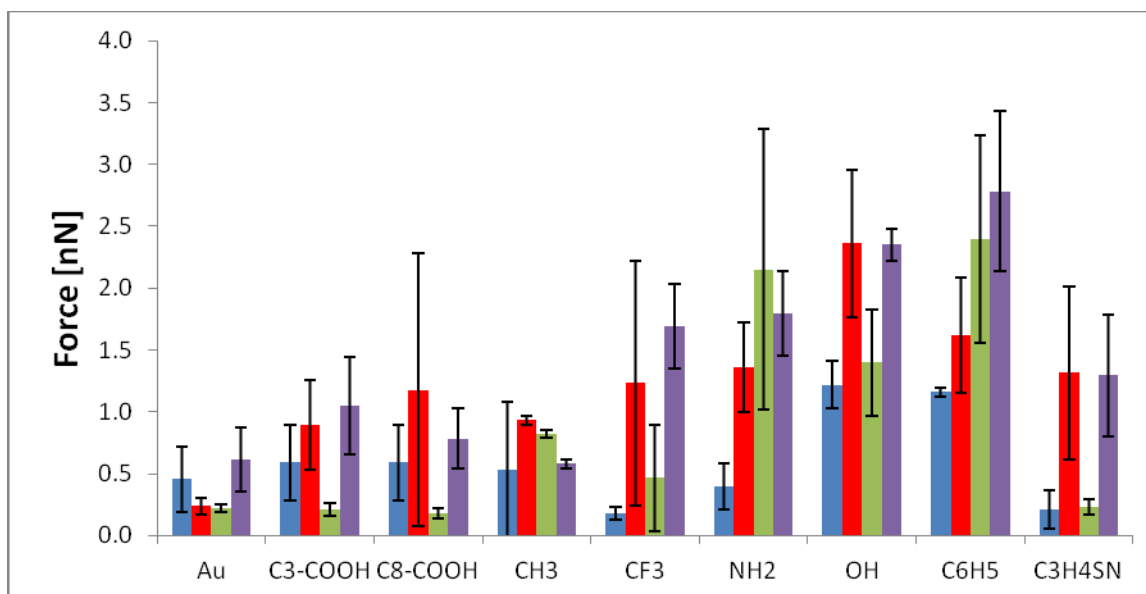


Fig. 6: Adhesion force between different explosive particles and end groups of the SAM deposited on a glass substrate measured under water. Blue columns correspond to HMX, red columns to PETN, green columns to RDX and purple columns to TNT.

DFT calculations

To obtain an estimate of the chemical interactions between different end groups and a simplified model of the explosive particle surface, electronic structure calculations were performed. The simulations considered interaction between a single explosive molecule, PETN or RDX, and a hydrocarbon chain attached to one of the end groups examined. In all cases the hydrocarbon chain contained five carbon atoms. The system was optimized to obtain the lowest energy configuration of the system considered. For each pair of explosive-end group 5-10 different initial configurations, distances and relative orientations, were chosen randomly. In each initial configuration, the end group studied was pointed towards a different region of the explosive molecule. In all cases the hydrocarbon chain was pointing away from the molecule. The average values obtained for the various initial configurations examined are presented in table 3.

Table 3: Optimized lowest average energies of complexes between an explosive molecule and different end groups examined. All energies are in units of kcal/mol.

	PETN (Kcal/mol)	RDX (Kcal/mol)
Pentane	3.32±1.5	4.60±2.6
CH ₃ (CH ₂) ₃ CF ₃	13.85±2.9	10.78±4.5
Pentamine	26.65±1.4	26.35±5.0
Pentanol	27.76±4.7	19.91±2.6
Phenyl-C5*	31.13±1.7	30.60±2.6

* Represents a toluene molecule where the methyl group was replaced by a hydrocarbon chain with five carbon atoms.

The results in Table 3 clearly show that the interaction between both PETN and RDX and methyl (or fluorinated methyl) groups is 2-4 times smaller than that with -OH, -NH₂ and -Phenyl end groups. These results are in good qualitative agreement with the experimental data. The explosive molecules in the experiment are part of small crystals, hence, the interaction of end groups with them depends on the crystal phase and the micro-crystal orientation relative to the SAM. This means that the values in Table 3 can serve only as an upper limit for the end group-explosive interaction strength, and in most cases it is expected to be smaller due to deviations from the optimal relative orientation and distance.

Conclusions

The present study reports results of adhesion force measurements between four different explosives and substrates with different chemical characteristics. Two types of experiments were performed, in the first, "SAM on tip" a self-assembled monolayer was deposited to the AFM tip and then the adhesion force between the tip and the surface of an explosive particle was measured. The second class of experiments, "particle on tip" measured the adhesion between an explosive particle and a gold plated glass substrate on which SAM was deposited. Both types of experiments were carried out in ambient air as well as under water. For all the experiments we used explosive particles collected at explosive manufacturing sites without changing their shapes and roughness. SEM images of the particles used show that they have highly irregular shapes and surface roughness of the order of sub-micrometers or larger. These irregular shapes and rough surfaces are responsible to many of the observed results. For example, we could not determine the Hamaker constant, in both types of experiments performed, since the curvature and contact areas could not be well defined.

The actual adhesion forces were evaluated from the retraction parts of the force curves. In both experimental configurations, "SAM on tip" and "Particle on tip", there is a clear indication to contributions of capillary forces as well as of chemical interactions to the adhesion force. This contribution is manifested by the variations in F_{ad} observed when the end group on the SAM is changed. There is a clear indication that -OH, -Phenyl and probably -NH₂ end groups lead to increased contributions to F_{ad} . For the case of "particle on tip", the increased contact area and number of contact points between the explosive particle and the substrate results in marked contribution of capillary and chemical forces to the adhesion. These findings were qualitatively substantiated by electronic structure calculations.

This study reveals some aspects related to the nature of interactions that have contributions to explosive particles adhesion. It should be emphasized that we used explosive particles collected at explosive manufacturing site without changing particle shape or roughness. The results revile the role of various force types in the determination of the total adhesion force. Moreover, the observed results suggest that sample collection efficiency could be improved by increasing the direct and indirect contributions of F_{chem} to F_{ad} . These can be achieved by fictionalization of the swab material by a high density of -Phenyl, -OH and probably -NH₂ end groups.

Acknowledgments

Yehuda Zeiri acknowledge partial support of The Center of Excellence for Explosives Detection, Mitigation and Response, Department of Homeland Security.

References

1. R.B. Cundall, T.F. Palmer, C.E.C. Wood, "Vapor pressure measurements on some organic high explosives", J. Chem. Soc. Farad. Trans., 1978, 74, 1339-1345.
2. B.C. Dionne, D.P. Rounbehehler, E.K. Achter, J.R. Hobbs, D.H. Fine, "Vapor pressure of explosives", *J. Energ. Mater.*, **1986**, 4, 447-472
3. J. M. Rosen, C. Dickinson, "Vapor pressures and heats of sublimation of some high-melting organic explosives", J. Chem. Eng Data, 1969, **14**, 120-124
4. A.P. Gershanik, Y. Zeiri, "Sublimation Rate of TNT Microcrystals in Air", *J. Phys. Chem. A*, 2010, 114, 12403-12410 (and references therein).
5. G. Edwards, "The vapor pressure of 2,4,6-trinitrotoluene", Trans Faraday Soc., 1950, 46, 423-427
6. A. Burnham, R. Gee, A. Maiti, R. Qiu, P. Rajasekar, B. Weeks, L. Zepeda-Ruiz, *LLNL Technical Report UCRL TR 216963*, 2005. Experimental results on vapor pressure of PETN documented in this work are from R. Behrens, presentation in: "Update on the Analysis of Thermally and Chemically Stabilized PETN Powders," *JOWOG Focused Exchange Meeting*, May **2003**, Sandia National Lab, Albuquerque, NM.
7. F.T. Crimmins, "The vapor pressure of Pentaerythritoltetranitrate (PETN) in the temperature range of 50 to 98 degrees centigrade", Report UCRL- 50704, Lawrence Radiation Lab. Ca, **1969**

8. A. Eiceman, D. Preston, G. Tiano, J. Rodrigues, J.E. Parmeter, "Quantitative calibration of vapor levels of TNT, RDX, and PETN using a diffusion generator with gravimetry and ion mobility spectrometry", *Talanta*, **1997**, 45, 57-74.
9. J. E. Parmeter, G. A. Eiceman, D. A. Preston, G. S. Tiano, "Calibration of an explosives vapor generator based on vapor diffusion from a condensed phase", *Sandia Report SAND-96-2016C, Conf--960767- 2 I*, **1996**, Sandia National Laboratories, Albuquerque, NM
10. Jessica L. Staymates, Jessica Grandner and Greg Gillen, "Fabrication of adhesive coated swabs for improved swipe-based particle collection efficiency", *Anal. Methods*, 2011, **3**, 2056.
11. Scott D. Harvey & Robert G. Ewing and Melanie J. Waltman, "Selective sampling with direct ion mobility spectrometric detection for explosives analysis", *Int. J. Ion Mobil. Spec.* (2009) **12**, 115–121.
12. D. S. Rimai and L. P. DeMejo, "Physical interactions affecting the adhesion of dry particles", *Annu. Rev. Mater. Sci.* **1996**. 26, 21-41.
13. W W Gerberich and M J Cordill, "Physics of adhesion", *Rep. Prog. Phys.* **2006**, 69, 2157–2203.
14. Sean Eichenlaub, Anne Gelb ad Steve Beaudoin, "Roughness models for particle adhesion", *Journal of Colloid and Interface Science* **2004**, 280, 289–298.
15. Ravi P. Jaiswal, Gautam Kumar, Caitlin M. Kilroy, and Stephen P. Beaudoin, "Modeling and Validation of the van derWaals Force During the Adhesion of Nanoscale Objects to Rough Surfaces: A Detailed Description", *Langmuir*, **2009**, 25, 10612-10623.
16. Hans-Juergen Butt, Brunero Cappella and Michael Kappl, "Force measurements with the atomic force microscope: Technique, interpretation and applications", *Surface Science Reports* 2005, 59, 1–152.
17. Hyo-Sok Ahn, Pham Duc Cuong, Sangkwon Park, Yong-Wook Kim and Jong-Choo Lim, "Effect of molecular structure of self-assembled monolayers on their tribological behaviors in nano- and microscales", *Wear*, **2003**, 255, 819-825.
18. Joong Ho Moon, Jin Ho Kim, Ki-jeong Kim, Tai-Hee Kang, Bongsoo Kim, Chan-Ho Kim, Jong Hoon Hahn, and Joon Won Park, "Absolute Surface Density of the Amine Group of the Aminosilylated Thin Layers: Ultraviolet–Visible Spectroscopy, Second Harmonic Generation, and Synchrotron-Radiation Photoelectron Spectroscopy Study", *Langmuir*, **1997**, 13, 4305–4310.
19. Hideo Notsu, Wakana Kubo, Isao Shitanda and Tetsu Tatsuma, "Super-hydrophobic/super-hydrophilic patterning of gold surfaces by photocatalytic lithography", *J. Mater. Chem.*, 2005, **15**, 1523-1527.
20. Inhee Choi, Younghun Kim, Changmook Kim, Jinsoo Kim, Kyunghee Choi and Jongheop Yi, "Site-Defined Micropatterning Using Atomic Force Microscopic Lithography", *Key Engineering Materials* **2005**, Volumes **277-279**, 903-906, 10.4028/www.scientific.net/KEM.277-279.903.
21. O.N. Tretinnikov, "Hydrophilic (Hydrogen-Bonding) Polystyrene Surface by Substrate-Induced Surface Segregation of Benzene Groups", *Langmuir*, 2000, **16**, 2751-2755.
22. Gaussian 09, Revision **A.1**, M. J. Frisch, G. W. Trucks, H. B. Schlegel, G. E. Scuseria, M. A. Robb, J. R. Cheeseman, G. Scalmani, V. Barone, B. Mennucci, G. A. Petersson, H. Nakatsuji, M. Caricato, X. Li, H. P. Hratchian, A. F. Izmaylov, J. Bloino, G. Zheng, J. L. Sonnenberg, M. Hada, M. Ehara, K. Toyota, R. Fukuda, J. Hasegawa, M. Ishida, T. Nakajima, Y. Honda, O. Kitao, H. Nakai, T. Vreven, J. A. Montgomery, Jr., J. E. Peralta, F. Ogliaro, M. Bearpark, J. J. Heyd, E. Brothers, K. N. Kudin, V. N. Staroverov, R. Kobayashi, J. Normand, K. Raghavachari, A. Rendell, J. C. Burant, S. S. Iyengar, J. Tomasi, M. Cossi, N. Rega, J. M. Millam, M. Klene, J. E. Knox, J. B. Cross, V. Bakken, C. Adamo, J. Jaramillo, R. Gomperts, R. E. Stratmann, O. Yazyev, A. J. Austin, R. Cammi, C. Pomelli, J. W. Ochterski, R. L. Martin, K. Morokuma, V. G. Zakrzewski, G. A. Voth, P. Salvador, J. J. Dannenberg, S. Dapprich, A. D. Daniels, Ö. Farkas, J. B. Foresman, J. V. Ortiz, J. Cioslowski, and D. J. Fox, Gaussian, Inc., Wallingford CT, 2009.
23. W. L. Elban "Surface energies of high explosives PETN and RDX from contact angle measurements" *J. Mater. Sci.* **14**, 1008 (1979)
24. L. Yang, "Surface Polarity of β -HMX Crystal and the Related Adhesive Forces with Estane Binder", *Langmuir* 2008, **24**, 13477 13482

25. H.C. Hamaker, "The London – van der Waals attraction between spherical particles", *Physica*, 1937, **4**, 1058.
26. Xu L., Lio A., Hu J., Ogletree D. F. and Salmeron M., "Wetting and Capillary Phenomena of Water on Mica" *J. Phys. Chem. B* 1998, **102**, 540
27. Major R.C., Houston J.E., McGrath M.J., Siepmann J.I. and Zhu X. -Y., "Viscous Water Meniscus under Nanoconfinement" *Phys. Rev. Lett.* 2006, **96**, 177803
28. van Zwol P. J., Palasantzas G. and De Hosson J. Th. M., "Influence of roughness on capillary forces between hydrophilic surfaces" *Phys. Rev. E* 2008, **78**, 031606.
29. Wenzel, R. N., "Resistance of Solid Surfaces to Wetting by Water", *Ind. Eng. Chem.* 1936, **28**, 988–994.
30. Krasowska, M. and Malysa K., "Kinetics of Bubble Collision and Attachment to Hydrophobic Solids: I. Effect of Surface Roughness" *Int. J. Miner. Process.* 2007, **81**, 205–216.
31. P. M. Hansson, A. Swerin, J. Schoelkopf, P. A. C. Gane, and E. Thormann, "Influence of Surface Topography on the Interactions between Nanostructured Hydrophobic Surfaces", *Langmuir*, 2012, **28**, 8026-8034.



Composites of carboxylate-capped TiO₂ nanoparticles and carbon black as chemiresistive vapor sensors

Edgardo García-Berríos^a, Ting Gao^b, Don Walker^a, Bruce S. Brunshwig^c, Nathan S. Lewis^{a,*}

^a Beckman Institute and Kavli Nanoscience Institute, 210 Noyes Laboratory, 127-72 Division of Chemistry and Chemical Engineering, California Institute of Technology, Pasadena, CA 91125, United States

^b Polymer, Ceramics, Technical Services Laboratories, Tyco Electronics Corporation, Technology Group, 306 Constitution Drive, Menlo Park, CA 94025, United States

^c Beckman Institute, California Institute of Technology, Pasadena, CA 91125, United States

ARTICLE INFO

Article history:

Received 11 November 2010

Accepted 6 April 2011

Available online 14 April 2011

Keywords:

Titanium (IV) dioxide nanoparticles

Carbon black composites

Electronic nose

Principal components analysis (PCA)

ABSTRACT

Titanium (IV) dioxide (TiO₂) nanoparticles (NPs) with a 1–5 nm diameter were synthesized by a sol–gel method, functionalized with carboxylate ligands, and combined with carbon black (CB) to produce chemiresistive chemical vapor sensor films. The TiO₂ acted as an inorganic support phase for the swellable, organic capping groups of the NPs, and the CB imparted electrical conductivity to the film. Such sensor composite films exhibited a reproducible, reversible change in relative differential resistance upon exposure to a series of organic test vapors. The response of such chemiresistive composites was comparable to, but generally somewhat smaller than, that of thiol-capped Au NPs. For a given analyte, the resistance response and signal-to-noise ratio of the capped TiO₂-NP/CB composites varied with the identity of the capping ligand. Hence, an array of TiO₂-NP/CB composites, with each film having a compositionally different carboxylate capping ligand, provided good vapor discrimination and quantification when exposed to a series of organic vapors. Principal components analysis of the relative differential resistance response of the sensor array revealed a clear clustering of the response for each analyte tested. This approach expands the options for composite-based chemiresistive vapor sensing, from use of organic monomeric or polymeric sorbent phases, to use of electrically insulating capped inorganic NPs as the nonconductive phase of chemiresistive composite vapor sensors.

© 2011 Elsevier B.V. All rights reserved.

1. Introduction

Chemiresistive vapor sensors arrays have been prepared from composites of monomeric [1,2], or polymeric organic phases [3,4], as well as from metal nanoparticles (NPs) capped with organic ligands [5–10]. Specifically, arrays of metal NPs functionalized with different ligands have attracted significant interest for their ability to detect and discriminate between different analyte vapors [6,11–13]. The ability to synthesize NPs with different functionalities allows the detection of various analytes and produces unique sensor array responses for a large range of different analytes. Pattern recognition algorithms can then be employed to obtain information on the physicochemical properties, and concentration, of the vapor(s) exposed to the sensor array [14–17].

Sensors composed of organothiol-capped Au-NPs are interesting because they have shown high sensitivity towards certain test vapors [5,18], and because such sensors allow for good discrimination between organic vapors [6,11–13]. Given that the Au core

of such capped NPs serves as a supporting and conducting phase for the organic ligands that effect the vapor sorption and resulting swelling of the sensor film, it ought to be possible to replace the Au core by other chemically inert inorganic nanoparticulate phases, such as titanium (IV) dioxide (TiO₂). TiO₂-NPs must however contain an additional component to provide electrical conductivity through the chemiresistive sensor film, such as a percolative network of carbon black (CB) particles.

Capped TiO₂-NPs have been synthesized previously [19], with the surface ligation produced by binding carboxylate groups [20–25] to the oxide/hydroxide functionality on the TiO₂-NPs. A wide variety of carboxylated organic ligands groups are readily prepared, thereby facilitating the straightforward preparation of a diverse array of capped groups for TiO₂-NP, or other inorganic oxides (e.g. ZnO), for use in chemiresistive composite vapor detectors.

In this work, we describe the vapor response of an exemplary set of such functionalized, metal oxide based, NP composites, using capped TiO₂-NPs with CB as the electrically conductive phase of the vapor sensors. TiO₂-NPs with a 1–5 nm size range were synthesized by a sol–gel method, and were capped with seven different carboxylate-functionalized ligands (Table 1). Composites of these

* Corresponding author. Tel.: +1 626 395 6335; fax: +1 626 395 8867.
E-mail address: nslewis@caltech.edu (N.S. Lewis).

Table 1
TiO₂-NP capping ligands and their respective abbreviations.

Carboxylate ligand	Abbreviation
1-Octanoic acid	C8
1-Dodecanoic acid	C12
Tetracosanoic acid	C24
12-Hydroxydodecanoic acid	C12-OH
1-Adamantaneacetic acid	C2(2cC10)
2-Hexyldecanoic acid	C10(C6)
3-Methyl-2-phenylvaleric acid	C5(2Ph)(3C)

insulating, capped inorganic NP phases, with a percolative CB conductive network phase, were prepared and their performance was measured in a representative series of vapor detection, classification, and quantification tasks.

2. Experimental

2.1. Materials

The chemicals 2-propanol (anhydrous, 99.5%), titanium (IV) isopropoxide (99.999%), nitric acid (99.999%), 1-octanoic acid (99.5%), 1-dodecanoic acid (99.5%), tetracosanoic acid (99%), 12-hydroxydodecanoic acid (97%), 1-adamantaneacetic acid (98%), 2-hexyldecanoic acid (96%) and 3-methyl-2-phenylvaleric acid (97%), and the solvents used to generate the test organic vapors (*n*-hexane, *n*-heptane, *n*-octane, iso-octane, cyclohexane, ethanol and ethyl acetate) were obtained from Sigma–Aldrich. All chemicals were used as received. 18 MΩ-cm resistivity deionized water was obtained from a Barnstead Nanopure purification system.

2.2. TiO₂ nanoparticle synthesis and carboxylation

The TiO₂-NPs were prepared by a procedure reported by Khoudiakov et al. [19]. To obtain the TiO₂-NPs, a solution of 0.9 mL of titanium (IV) isopropoxide in 9 mL of anhydrous 2-propanol was added dropwise at a rate of 1 drop min⁻¹ to a vigorously stirred solution that contained 100 mL of H₂O and HNO₃ at a pH of 1.3 under N₂(g). The solution was maintained at 1 °C for 24 h after the addition of the titanium (IV) isopropoxide solution. A slightly cloudy solution was obtained when the desired particle sizes (1–5 nm in diameter) had been produced. The TiO₂-NP solution was then centrifuged with a Sorvall RC-5B (DuPont) refrigerated superspeed centrifuge and was washed by subsequent additions of 2-propanol, ethanol and hexane.

The TiO₂-NPs were then combined with stoichiometric amounts (mol ratio 1:1) of the desired carboxylate capping ligand in acetone. The resulting solutions were sonicated for 24 h. The different carboxylate-capped TiO₂-NPs were then filtered and redispersed in acetone. Thermogravimetric analysis of the particles showed that the amount of ligands present on the TiO₂-NPs comprised 4–7% of the total capped-nanoparticle by mass.

2.3. Characterization by TEM and FTIR

2.3.1. Transmission electron microscopy

Transmission electron microscopy (TEM) was performed using a Philips EM430 (300 KV) with a point-to-point resolution of 2.3 Å. Samples for TEM analysis were prepared by placing a drop of the non-capped TiO₂-NPs suspended and sonicated (1 h) in 2-propanol (0.5 mg mL⁻¹) onto a Cu TEM grid that had been coated with amorphous carbon. TEM images were obtained two days after the NPs had been initially synthesized.

2.3.2. Fourier transform infrared spectroscopy

KBr-pressed pellets were used to characterize the carboxylate-capped TiO₂-NPs by Fourier transform infrared spectroscopy (FTIR).

Spectra were recorded on a Vertex 70 FTIR spectrometer (Bruker Optics Inc., Billerica, MA) that was equipped with a liquid N₂(1)-cooled HgCdTe detector (InfraRed Associates Inc.). The spectral resolution was 4 cm⁻¹ and 64 scans were collected per spectrum. A KBr background spectrum was subtracted from the measured spectrum of the NPs to provide the desired FTIR characterization data.

2.4. Sensor fabrication

The capped NP solutions were in acetone with 50% CB by mass relative to the TiO₂-NPs, followed by sonication for 2 h. These solutions were sprayed on substrates using an airbrush spray. The substrates were 0.5 cm × 2.5 cm glass slides that had a 2 mm gap between the electrical contact regions. The metalized contact regions were formed by evaporation, through a contact mask, of 35 nm of Cr followed by 65 nm of Au.

All chemiresistive sensors were dried under vacuum (~10⁻¹ Torr) for 30 min. The sensor films were then conditioned by exposure to analytes for 24 h to reach a steady baseline resistance, and a reproducible, steady sensor response, prior to the data collection reported herein.

2.5. Sensing measurements

Typically, 4 nominally identical vapor sensors were prepared at a time. The sensors were loaded into a rectangular, 40-slot chamber, with sensor film replicates positioned randomly. No dependence was observed on the performance of a given sensor on the spatial position of the sensors in the array. The 45.5 cm × 3.0 cm × 1.5 cm (*w* × *l* × *d*) chamber was connected by Teflon tubing to the gas delivery system. The internal cross-sectional area of the chamber was 1 cm². The dc resistance of the sensor array was measured with a digital multimeter (Keithley Model 2002) that was connected to a multiplexing unit (Keithley Model 7001). The resistance data were collected every 5–7 s from the array. A computer-controlled (LabVIEW) flow system delivered pulses of analyte vapor at a given fraction of the analyte's vapor pressure. Oil-free air was obtained from the house compressed air source (1.10 ± 0.15 ppt of water vapor) and was controlled with a mass flow controller. The test analytes used were *n*-hexane (Hex), *n*-heptane (Hept), *n*-octane (Oct), iso-octane (*i*Oct), cyclohexane (*c*Hex), ethyl acetate (EtOAc), and ethanol (EtOH). The sensor response as a function of vapor concentration was studied over the concentration range that corresponded to 0.0010 ≤ *P*/*P*⁰ ≤ 0.0500, where *P* and *P*⁰ are the partial pressure and vapor pressure of the analyte at room temperature (22 °C), respectively. Each analyte presentation consisted of 70 s of air, followed by 80 s of analyte vapor, followed by 60 s of air to purge the system. The total flow rate for each analyte presentation was 5 L min⁻¹.

The sensor response was expressed as the maximum relative differential resistance change ($\Delta R_{\max}/R_b$), where *R*_b is the baseline resistance of the sensor in the absence of analyte, and ΔR_{\max} is the average of five maximum resistance data points measured at the end of each analyte exposure response. During the pre-exposure period, a correcting spline was used to fit the baseline drift [5]. The values of $\Delta R_{\max}/R_b$ were calculated by subtracting the values of the spline extrapolated over the time of the exposure from the observed resistance.

2.6. Principal components analysis

Differences in the sensor response data were visualized using principal components analysis (PCA). The normalized $\Delta R_{\max}/R_b$ data were mean-centered, and diagonalization of the covariance matrix of the data set provided a transformed set of dimensions that

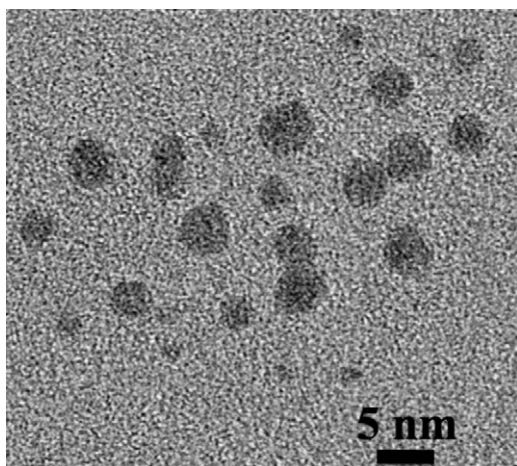


Fig. 1. Transmission electron micrograph of TiO₂-NPs on a Cu grid. The NPs were dispersed in 2-propanol (0.5 mg mL⁻¹).

best described the data in terms of principal components (PCs). The 1st PC captured the largest amount of variance in the data; the 2nd PC captured the second most variance in the data (subject to being orthogonal to the 1st PC), etc. The mean-centered data were then projected onto the first and second PCs, and the data were plotted with respect to these coordinate vectors to observe the natural clustering of the data points. The eigenvalues of the mean-centered covariance matrix provided the relative amounts of variance in each of the corresponding eigenvectors, allowing quantification of the amount of the variance that was captured in the 2-dimensional PC space.

3. Results

3.1. Characterization

3.1.1. Transmission electron microscopy

Fig. 1 shows a TEM micrograph of the TiO₂-NPs, revealing particles having diameters between 1 and 5 nm. A consistent slow addition of the Ti complex was required to produce particles that had such small diameters. Particles with a larger diameter (>10 nm) were obtained if large aggregates formed in the acidic solution after the addition of the metal precursor. Such particles were not used for the fabrication of chemiresistive vapor sensors that were evaluated in this work.

3.1.2. Fourier transform infrared spectroscopy

Fig. 2 shows the FTIR absorption spectra of three different carboxylate-capped TiO₂-NPs. When a carbonyl stretch was observed at ~1710 cm⁻¹, due to the presence of physisorbed carboxylic acid, the capped NPs were re-filtered. The asymmetric and symmetric bound carboxylate group vibrations at ~1530 cm⁻¹ and ~1420 cm⁻¹ respectively, were observed for C12, C12-OH and C5(2Ph)(3C)-capped NPs. The vibration of the C5(2Ph)(3C) ligand overlapped the scissoring frequency of -CH₂- at ~1460 cm⁻¹, and consequently the band was broadened. The observed C=O stretching frequency suggests a bidentate (chelate) structure [26]. The C5(2Ph)(3C) spectrum also displayed an aromatic C=C stretch at ~1600 cm⁻¹.

3.2. Sensor response

Different CB loadings were tested (25, 50, and 75% CB by mass), and composites having 50% CB yielded the highest signal-to-noise ratio (SNR). Fig. 3 shows the response of several sensors upon expo-

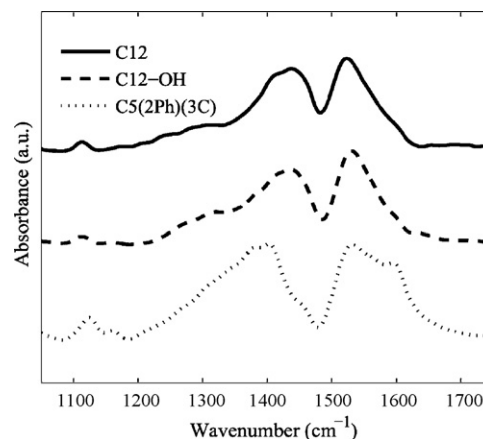


Fig. 2. FTIR spectra of carboxylate-capped TiO₂-NP on a KBr pellet at a resolution of 4 cm⁻¹, with KBr as the background.

sure to Hex and EtOAc at $P/P^0 = 0.0050$. All of the sensors showed rapid, reversible responses to each analyte vapor tested. Fig. 4 displays the average values of $\Delta R_{\max}/R_b$ obtained from 200 exposures to each analyte. The responses of two well studied CB-based polymer composites, poly(ethylene-co-vinyl acetate) (PEVA) and poly(ethylene oxide) (PEO) [27–29], are presented for comparison. Each sensor responded differently to each of the test vapors. For the hydrocarbons, among the TiO₂-NP/CB composites, the highest $\Delta R_{\max}/R_b$ values were obtained for the C5(2Ph)(3C) sensor. For all of the vapors, C24 showed the lowest $\Delta R_{\max}/R_b$ values. For the TiO₂-NP/CB composites, the $\Delta R_{\max}/R_b$ values obtained upon exposure to EtOH were very similar to each other. The reference PEVA/CB sensor produced $\Delta R_{\max}/R_b$ values that were higher than those of

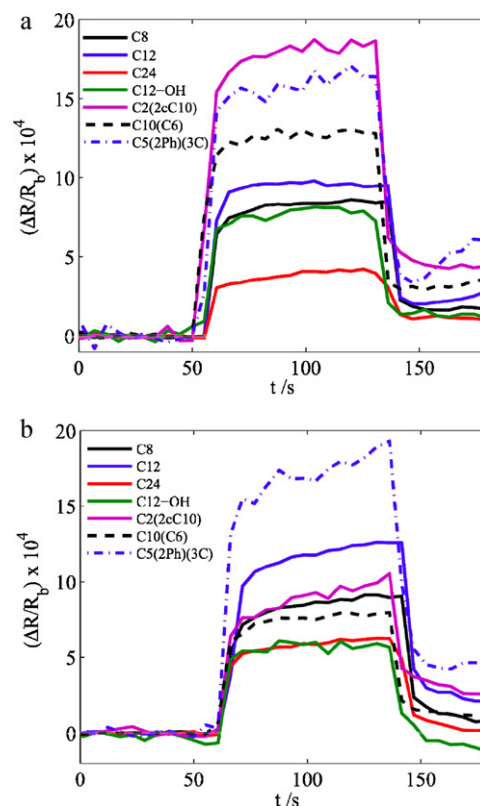


Fig. 3. Relative differential resistance response, $\Delta R/R_b$, for the seven carboxylate-capped TiO₂-NP/CB composites: (a) response to Hex at $P/P^0 = 0.0050$; (b) response to EtOAc at $P/P^0 = 0.0050$.

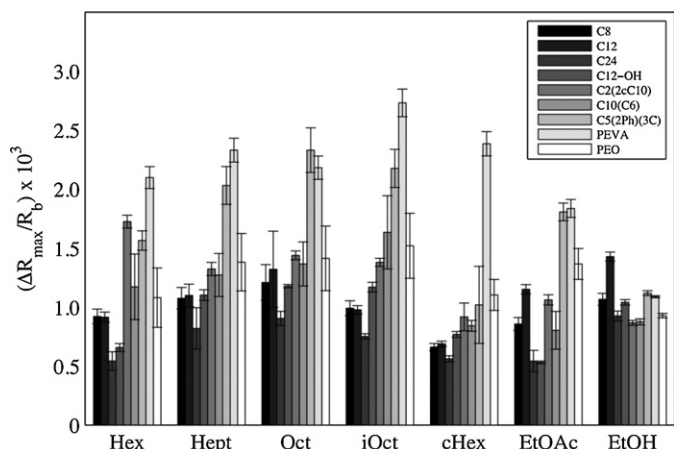


Fig. 4. Maximum relative differential resistance, $\Delta R_{\max}/R_b$, for all carboxylate-capped TiO_2 -NP/CB sensors at $P/P^0 = 0.0050$. The values for PEVA/CB and PEO/CB are presented for comparison.

the TiO_2 -NP/CB sensors, however the $\Delta R_{\max}/R_b$ values obtained from PEO/CB sensors were generally comparable to those obtained from the TiO_2 -NP/CB composites.

Fig. 5 shows the $\Delta R_{\max}/R_b$ response as a function of analyte concentration over the range $0.0010 \leq P/P^0 \leq 0.0500$ for Hex and for EtOH. For Hex, the highest $\Delta R_{\max}/R_b$ values were obtained for the C2(2cC10) sensor, whereas C12-OH produced the lowest $\Delta R_{\max}/R_b$ values. However, the slope for the four sensors displayed was approximately the same, specifically for $0.0100 \leq P/P^0 \leq 0.0500$. For EtOH, C12-OH produced the highest $\Delta R_{\max}/R_b$ values, whereas C12 produced the lowest $\Delta R_{\max}/R_b$ values. The slopes at $0.0010 \leq P/P^0 \leq 0.0500$ were different among the different sensors.

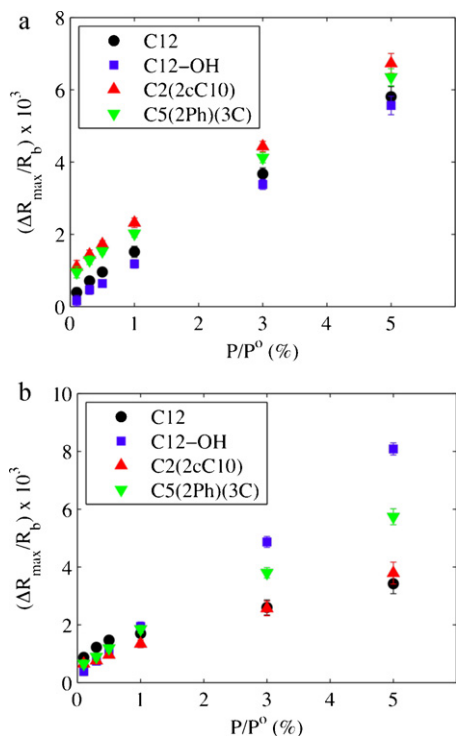


Fig. 5. Maximum relative differential resistance change as a function of P/P^0 ($0.0010 \leq P/P^0 \leq 0.0500$) for four different carboxylate-capped TiO_2 -NP/CB chemiresistors upon exposure to (a) Hex and (b) EtOH.

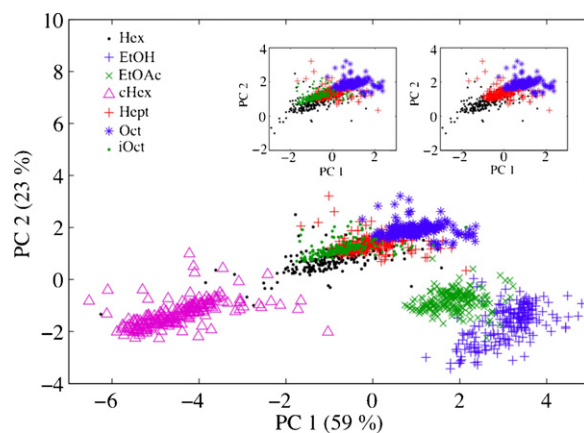


Fig. 6. Principal components analysis projection of the response of an array of the carboxylate-capped TiO_2 -NP/CB chemiresistors upon exposure to seven analytes, each presented to $P/P^0 = 0.0050$. The left figure inset displays the PC projection of Hex, Hept, Oct and *i*Oct, and the right figure inset displays the PC projection of Hex, Hept and Oct (displayed in one inset).

3.3. Principal components analysis

Fig. 6 shows the PCA projection of the 1st and 2nd PCs of the sum-normalized data. The PCA projection showed clear separation between cHex, EtOAc, EtOH and the saturated alkane vapors. The left inset depicts the alkane region of Fig. 6, and displays the overlap of the alkane vapors. The *i*Oct cluster interfered with the other three solvents, and prevented good separation. The right inset of Fig. 6 shows a fairly good separation between the tested analytes Hex, Hept and Oct, after removing the projection of the *i*Oct cluster.

4. Discussion

4.1. Sensor response

The interparticle spacing, and thus the sensitivity, of the sensor films can be controlled at the molecular level using capping ligands with different lengths, structure and functionalities. The magnitude of the $\Delta R_{\max}/R_b$ values for the carboxylate-capped TiO_2 -NP/CB composites was somewhat smaller than the $\Delta R_{\max}/R_b$ values of other chemiresistive CB composite sensors, such as CB composites with insulating polymers [3], monomers [1], or thiol-capped Au-NPs [5]. The small $\Delta R_{\max}/R_b$ magnitude for the capped TiO_2 -NP/CB composites is likely due to the lower surface ligand coverage of the NPs, which resulted in a lower mass of analyte sorbed into the sensing films. Consequently, the SNR values ($\text{SNR} = \Delta R_{\max}/s_{\text{baseline}}$, s_{baseline} is the standard deviation of R_b) obtained were lower than those observed for other chemiresistive sensing materials in response to the same set of test analytes (Table 2) [1,2].

The responses of sensors made using C8 and C12 were also larger, in general, than those of sensors that were made using C24

Table 2

Signal to noise ratios (SNR) of seven carboxylate-capped TiO_2 -NP/CB composites in response to seven analytes over 200 exposures to each analyte delivered in random order at $P/P^0 = 0.0050$.

	Hex	Hept	Oct	<i>i</i> Oct	cHex	EtOAc	EtOH
C8	93	130	190	99	34	230	86
C12	99	150	190	120	25	250	110
C24	65	89	140	48	18	200	76
C12-OH	88	110	130	120	47	120	120
C2(2cC10)	170	200	260	210	89	130	110
C10(C6)	130	200	220	190	66	120	83
C5(2Ph)(3C)	180	250	270	260	47	150	130

ligand caps. The C24 ligand has a low solubility, which prevents vapor analyte molecules from partitioning and thus from separating C24-capped TiO₂-NPs. The hydroxy termination of the C12-OH film produced a higher sensitivity towards EtOH than was observed for the C12, C2(2cC10) and C5(2Ph)(3C) sensors. For $P/P^0 = 0.0050$, the C5(2Ph)(3C)-capped TiO₂-NP composite was the most sensitive material for the all vapors (Fig. 4), and produced the highest SNR values (Table 2).

A percolative network of CB particles had to be incorporated into the sensing films to produce the required dc electrical conduction needed, for a chemiresistive sensor. For carboxylate-capped TiO₂-NP/CB composites, limited information could be obtained on the mechanism of vapor-induced volume change that resulted from each of the film components. Both film components, the TiO₂-NPs and the CB particles, are able to sorb analyte and thus contribute to the overall observed film resistance change. Another limitation is that if TiO₂-NPs are functionalized with a specific chemistry, the effects on vapor sorption of such functionality will be reduced by the presence of CB, because only ~5% by mass of the capped NP film contained the desired functional group.

4.2. Discrimination performance

The PC projections for the first and second PCs (Fig. 6) show that the TiO₂ NP sensor array was clearly able to separate the polar and nonpolar analytes. Both PCs differentiated analytes based on their polarity. Particularly for the alkanes, overlaps between the response clusters for Hex, and Hept and Oct were observed. Furthermore, the *i*Oct cluster slightly overlapped with that of Hex, whereas high overlap was observed between the Hept and *i*Oct clusters. The latter is a consequence of the similar vapor pressures of these two analytes ($P_{\text{Hept}}^0 = 5.1 \times 10^4$ ppm, $P_{\text{iOct}}^0 = 5.6 \times 10^4$ ppm).

5. Conclusions

TiO₂ NPs capped by seven different carboxylate-functionalized ligands having variable chain lengths and polarities were synthesized by a sol-gel method, characterized by TEM and FTIR, and investigated as chemical vapor sensors. The capped NPs were mixed with CB and exposed to seven different analytes of varying polarity. The sensing materials responded uniquely to each analyte and responded in an approximately linear dependence with vapor concentration for Hex and EtOH. The SNR value of each TiO₂ NPs sensor varied with the ligand functionality for every analyte. PCA showed a fair clustering of the analytes tested, with the alkanes being the most difficult analytes to separate.

Acknowledgments

The authors thank Dr. Marc D. Woodka for helpful discussions and data analysis, Heather Agnew for helping with the FTIR analysis, Carol M. Garland for the TEM analysis and Juan S. Ramirez for the centrifugation of the nanoparticles. Edgardo García-Berriós acknowledges the NSF for a graduate fellowship. Ting Gao acknowledges the support from Tyco Electronics. Research was carried out in the Molecular Materials Research Center of the Beckman Institute at Caltech. This work was supported by the NSF, grant CHE-0604894, and by DHS, grant HSARPA 2008-ST-061-ED0002.

References

- [1] T. Gao, M.D. Woodka, B.S. Brunnschwig, N.S. Lewis, Chemiresistors for array-based vapor sensing using composites of carbon black with low volatility organic molecules, *Chem. Mater.* 18 (2006) 5193–5202.
- [2] S. Maldonado, E. García-Berriós, M.D. Woodka, B.S. Brunnschwig, N.S. Lewis, Detection of organic vapors and NH₃(g) using thin-film carbon-black-metallophthalocyanine composite chemiresistors, *Sens. Actuators B* 134 (2008) 521–531.
- [3] E.J. Severin, B.J. Doleman, N.S. Lewis, An investigation of the concentration dependence and response to analyte mixtures of carbon black/insulating organic polymer composite vapor detectors, *Anal. Chem.* 72 (2000) 658–668.
- [4] E.J. Severin, N.S. Lewis, Relationships among resonant frequency changes on a coated quartz crystal microbalance, thickness changes, and resistance responses of polymer-carbon black composite chemiresistors, *Anal. Chem.* 72 (2000) 2008–2015.
- [5] E. García-Berriós, T. Gao, S. Maldonado, M.D. Woodka, M.W. Ellsworth, B.S. Brunnschwig, N.S. Lewis, Response vs. chain length of alkanethiol-capped Au nanoparticle chemiresistive chemical vapor sensors, *J. Phys. Chem. C* 114 (2010) 21914–21920.
- [6] E. García-Berriós, T. Gao, J.C. Theriot, B.S. Brunnschwig, N.S. Lewis, Response and discrimination performance of arrays of organothiol-capped Au nanoparticle chemiresistive chemical vapor sensors, *J. Phys. Chem.* 115 (2011) 6208–6217.
- [7] J.W. Grate, A sorptive behavior of monolayer-protected gold nanoparticle films containing alkanethiols and alkanedithiols, *Anal. Chem.* 75 (2003) 6759–6759.
- [8] J.W. Grate, D.A. Nelson, R. Skaggs, Sorptive behavior of monolayer-protected gold nanoparticle films: implications for chemical vapor sensing, *Anal. Chem.* 75 (2003) 1868–1879.
- [9] H. Wohltjen, A.W. Snow, Colloidal metal-insulator-metal ensemble chemiresistor sensor, *Anal. Chem.* 70 (1998) 2856–2859.
- [10] W.P. Wuelfing, S.J. Green, J.J. Pietron, D.E. Cliffel, R.W. Murray, Electronic conductivity of solid-state, mixed-valent, monolayer-protected Au clusters, *J. Am. Chem. Soc.* 122 (2000) 11465–11472.
- [11] L. Han, X.J. Shi, W. Wu, F.L. Kirk, J. Luo, L.Y. Wang, D. Mott, L. Cousineau, S.I.I. Lim, S. Lu, C.J. Zhong, Nanoparticle-structured sensing array materials and pattern recognition for VOC detection, *Sens. Actuators B* 106 (2005) 431–441.
- [12] L.Y. Wang, N.N. Kariuki, M. Schadt, D. Mott, J. Luo, C.J. Zhong, X.J. Shi, C. Zhang, W.B. Hao, S. Lu, N. Kim, J.Q. Wang, Sensing arrays constructed from nanoparticle thin films and interdigitated microelectrodes, *Sens. Basel* 6 (2006) 667–679.
- [13] L.Y. Wang, X.J. Shi, N.N. Kariuki, M. Schadt, G.R. Wang, Q. Rendeng, J. Choi, J. Luo, S. Lu, C.J. Zhong, Array of molecularly mediated thin film assemblies of nanoparticles: correlation of vapor sensing with interparticle spatial properties, *J. Am. Chem. Soc.* 129 (2007) 2161–2170.
- [14] J.A. Burns, G.M. Whitesides, Feedforward neural networks in chemistry—mathematical systems for classification and pattern-recognition, *Chem. Rev.* 93 (1993) 2583–2601.
- [15] R.O. Duda, P.E. Hart, *Pattern Classification and Scene Analysis*, John Wiley & Sons, New York, 1973.
- [16] P. Geladi, B.R. Kowalski, Partial least-squares regression: a tutorial, *Anal. Chim. Acta* 185 (1986) 1–17.
- [17] B.R. Kowalski, C.F. Bender, K-nearest neighbor classification rule (pattern-recognition) applied to nuclear magnetic-resonance spectral interpretation, *Anal. Chem.* 44 (1972) 1405.
- [18] A.W. Snow, H. Wohltjen, *Materials, Method and Apparatus for Detection and Monitoring of Chemical Species*, MicroSensor Systems Inc., United States, 2001, pp. 1–9.
- [19] M. Khoudiakov, A.R. Parise, B.S. Brunnschwig, Interfacial electron transfer in Fe-II(CN)₆(4-)-sensitized TiO₂ nanoparticles: a study of direct charge injection by electroabsorption spectroscopy, *J. Am. Chem. Soc.* 125 (2003) 4637–4642.
- [20] S.J. Hug, B. Sulzberger, In-situ Fourier-transform infrared spectroscopic evidence for the formation of several different surface complexes of oxalate on TiO₂ in the aqueous-phase, *Langmuir* 10 (1994) 3587–3597.
- [21] K. Kilsa, E.I. Mayo, B.S. Brunnschwig, H.B. Gray, N.S. Lewis, J.R. Winkler, Anchoring group and auxiliary ligand effects on the binding of ruthenium complexes to nanocrystalline TiO₂ photoelectrodes, *J. Phys. Chem. B* 108 (2004) 15640–15651.
- [22] Y.X. Weng, L. Li, Y. Liu, L. Wang, G.Z. Yang, Surface-binding forms of carboxylic groups on nanoparticulate TiO₂ surface studied by the interface-sensitive transient triplet-state molecular probe, *J. Phys. Chem. B* 107 (2003) 4356–4363.
- [23] A.P. Xagas, M.C. Bernard, A. Hugot-Le Goff, N. Spyrellis, Z. Loizos, P. Falaras, Surface modification and photosensitization of TiO₂ nanocrystalline films with ascorbic acid, *J. Photochem. Photobiol. A* 132 (2000) 115–120.
- [24] H.J. Jeon, S.D. Moon, Y.S. Kang, Synthesis of photodegradable TiO₂/stearate complex and characterization of its Langmuir monolayer at the air/water interface, *Colloids Surf. A: Physicochem. Eng. Aspects* 257–58 (2005) 165–169.
- [25] X. Wu, D. Wang, S. Yang, Preparation and characterization of stearate-capped titanium dioxide nanoparticles, *J. Colloid Interf. Sci.* 222 (2000) 37–40.
- [26] K. Nakamoto, *Infrared and Raman Spectra of Inorganic and Coordination Compounds*, 5th ed., John Wiley & Sons, Inc., New York, 1997.
- [27] M.C. Burl, B.C. Sisk, T.P. Vaid, N.S. Lewis, Classification performance of carbon black-polymer composite vapor detector arrays as a function of array size and detector composition, *Sens. Actuators B* 87 (2002) 130–149.
- [28] M.S. Freund, N.S. Lewis, A chemically diverse conducting polymer-based electronic nose, *Proc. Natl. Acad. Sci. U.S.A.* 92 (1995) 2652–2656.

- [29] M.C. Lonergan, E.J. Severin, B.J. Doleman, S.A. Beaber, R.H. Grubbs, N.S. Lewis, Array-based vapor sensing using chemically sensitive, carbon black–polymer resistors, *Chem. Mater.* 8 (1996) 2298–2312.

Biographies

Edgardo Garcia-Berrios received his B.S. in Chemistry from the University of Puerto Rico at Cayey in 2004. He is currently a Ph.D. candidate graduate student in the research group of Prof. Nathan S. Lewis. His research interests are the design and study of novel chemiresistive materials for gas/vapor detection.

Dr. Ting Gao received her B.S. and M.S. in Physics from Nanjing University in 1994 and 1997, respectively, and her Ph.D. in Inorganic Chemistry from the University of California in San Diego in 2002. She is currently a Senior Scientist for Tyco Electronics and her research interests are in the field of applied material science, in particular novel touchscreen technology, and polymeric composites and nanomaterials for chemical and gas sensors.

Dr. Don Walker received his B.S. in Chemistry from the Southern University in 2003 and his Ph.D. from the California Institute of Technology in 2010. He is currently a Member of the Technical Staff at the Aerospace Corporation and his research inter-

ests are in the field of dye-sensitized solar cells for efficient solar-to-electrical energy conversion.

Dr. Bruce S. Brunshwig received his B.A. in Chemistry from the University of Rochester in 1966 and his Ph.D. in Chemistry from Polytechnic University in 1972. He is currently the director of the Molecular Materials Research Center at the California Institute of Technology. His research interests include kinetics and mechanisms of photochemical and thermal reactions involving dissolved transition–metal complexes, experimental studies of charge-transfer reactions both in homogenous solution and on electrode surfaces, development of models for electron-transfer reactions, quantum chemistry calculations of transition–metal complexes, and solar energy conversion.

Prof. Nathan S. Lewis received his B.S. and M.S. in Chemistry from the California Institute of Technology in 1977 and his Ph.D. in Chemistry from the Massachusetts Institute of Technology in 1980. He is currently the George L. Argyros Professor of Chemistry at the California Institute of Technology. His research interests include light-induced electron transfer reactions, both at surfaces and in transition–metal complexes, surface chemistry and photochemistry of semiconductor/liquid interfaces, novel uses of conducting organic polymers and polymer/conductor composites, and development of sensor arrays that use pattern recognition algorithms to identify odorants, mimicking the mammalian olfaction process.

The Kinetics of the Thermal Decomposition of the Chloride Adduct of Ethylene Glycol di-nitrate : An Ion Mobility Spectrometry and *ab initio* Calculation Study

R.M.M.Y. Rajapakse^a, G.A. Eiceman^a and J.A. Stone^b

^a*Department of Chemistry and Biochemistry, New Mexico State University, Las Cruces, NM, 88003, USA*

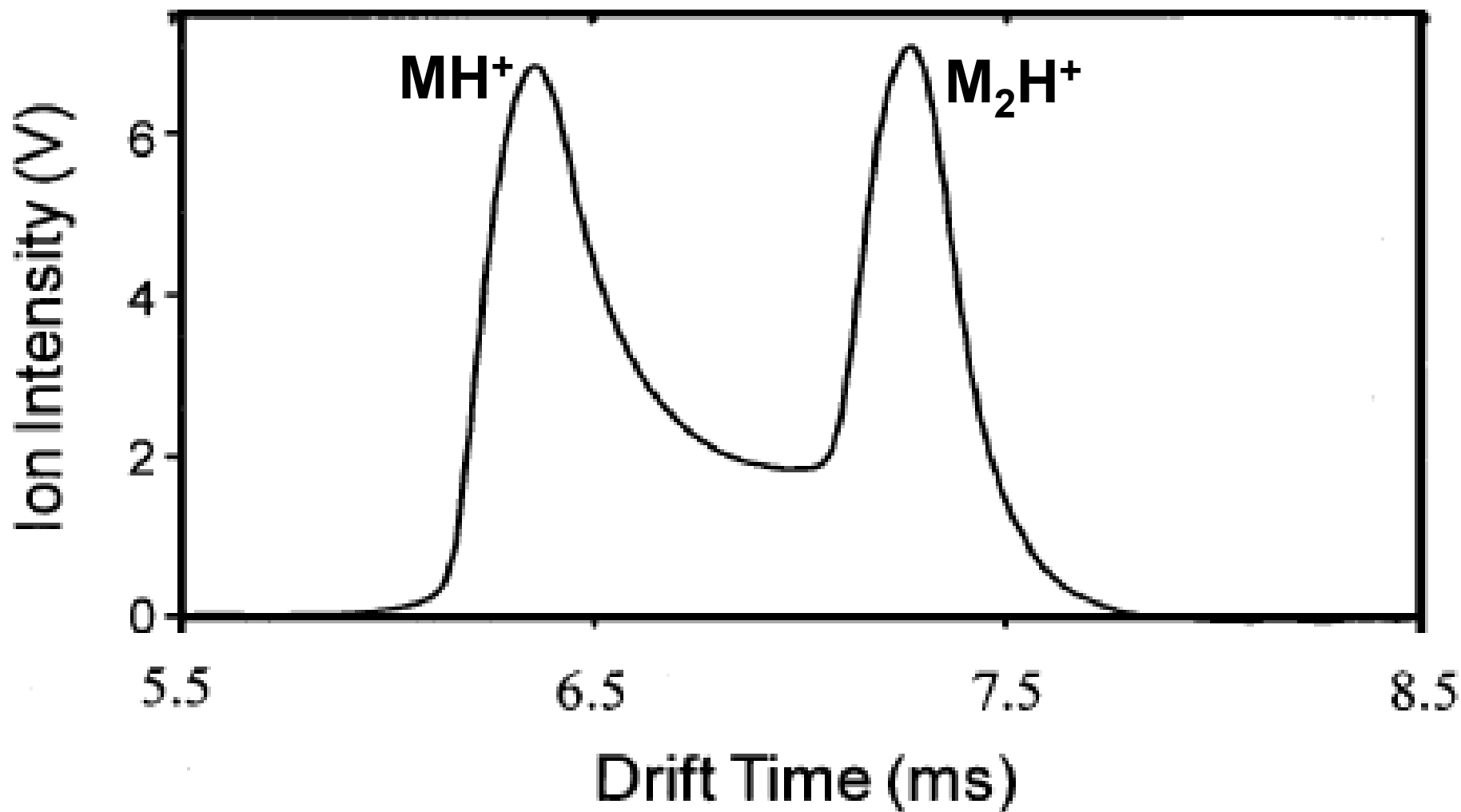
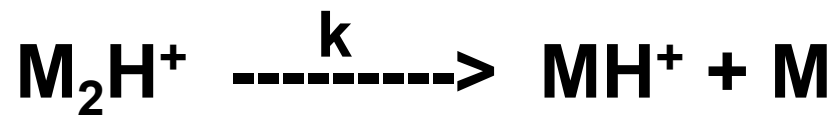
^b*Department of Chemistry, Queen's University, Kingston, Ontario, Canada K7L3N6*



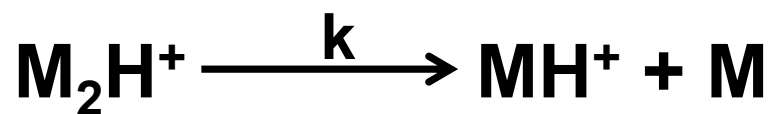
Prior studies of kinetics of ion reactions with mobility-based instruments

- Biondi (1961) *Electron attachment in atmospheric gases*
- Spangler and Collins, (1975) *Reactant ions in negative ion plasma chromatography*
- Grimsrud , et al. (1992) *Displacement reaction of chlorine anion with a series of alkyl bromides,*
- Ewing et al (1996-2000) *Dissociation of Proton bound dimers of DMMP,DMP*
- An, et al, (2006-2010) *Fragmentation and dissociation of acetates and ketones_in IMS and DMS*
- Jazan and Tabrizchi, (2009) *Formation of proton bound dimers of DMMP, DMP, ketone*
- Rajapakse, et al, (2012) *Dissociation of chloride adducted explosives, in preparation*

Prior studies by kinetic IMS from New Mexico State University and Friends



Prior studies by kinetic IMS from New Mexico State University and Friends

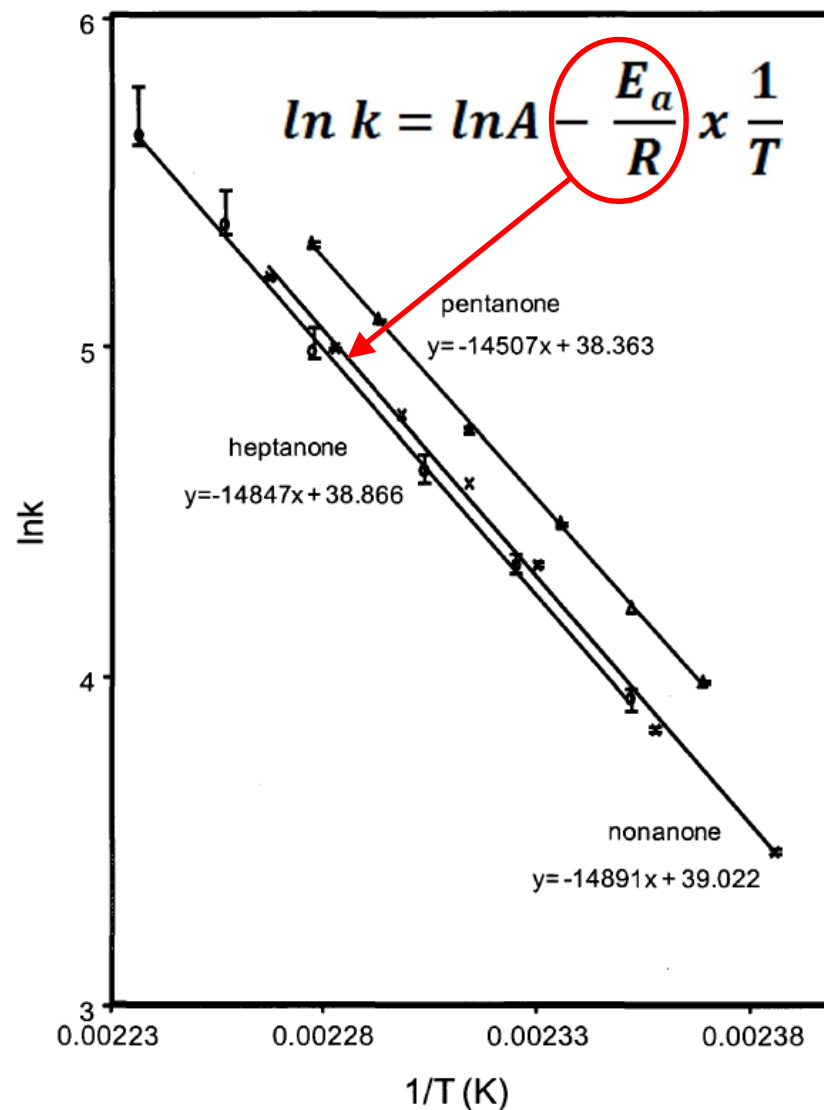


$$-\frac{d[M_2H^+]}{dt} = k [M_2H^+]$$

An et al, Kinetics of decomposition of gas phase ions of esters and ketones in air at ambient pressure using differential mobility spectrometry and ion mobility spectrometry, J. Phys Chem 2012 submitted

Temperature range 146 °C – 174 °C

Activation energies for $E_a = 122$ kJ/mol



Methods to determine gas phase ion kinetics

Comments

High Pressure Mass Spectrometry
(50 to 100 torr)

- a. Value for [Vapor Sample] must be known with a **high degree of precision**
- b. Ions not necessarily thermalized

Differential Mobility Spectrometry

- a. Field heating of ions is interesting but **not fully understood or developed**
- b. Heating is ion mass dependent

Ion Mobility Spectrometry

- a. Ions ***thermalized*** with MB distribution
- b. Direct measure of ion lifetimes

Goals for present research effort

Obtain kinetic rate data for gas phase ions of explosives and other thermochemical values associated with decomposition or dissociation reactions.

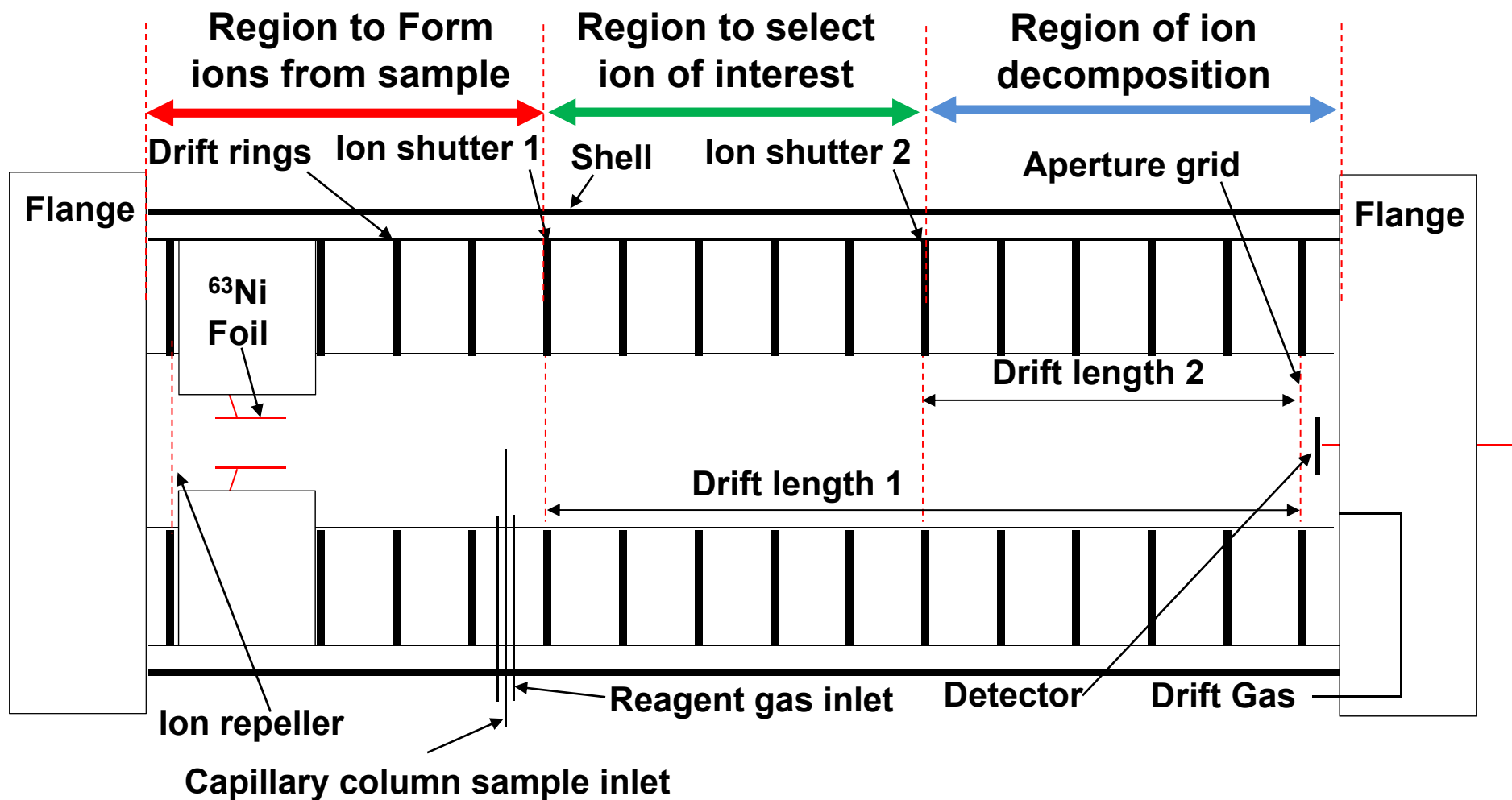
Objectives

- A. Refine instrumentation for a kinetic IMS design with constant temperature throughout the drift tube and with neutral-free gas atmosphere in drift region.....(use gas bath oven and dual shutter design).**
- B. Complete measurements with high confidence in purity of sample vapor without interferences..... pre-fractionate sample by gas chromatography.**

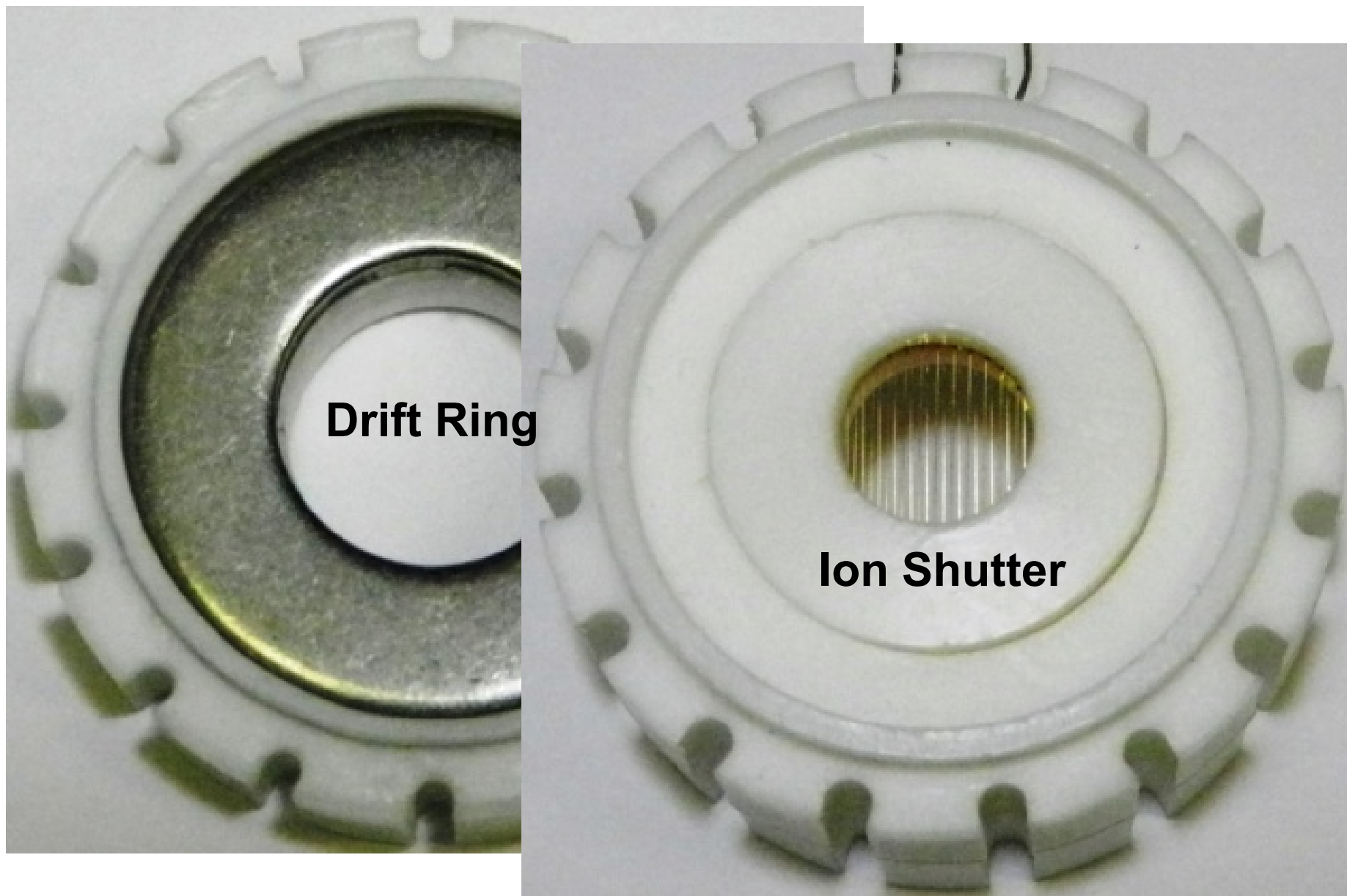
The NMSU Kinetic IMS (2012)



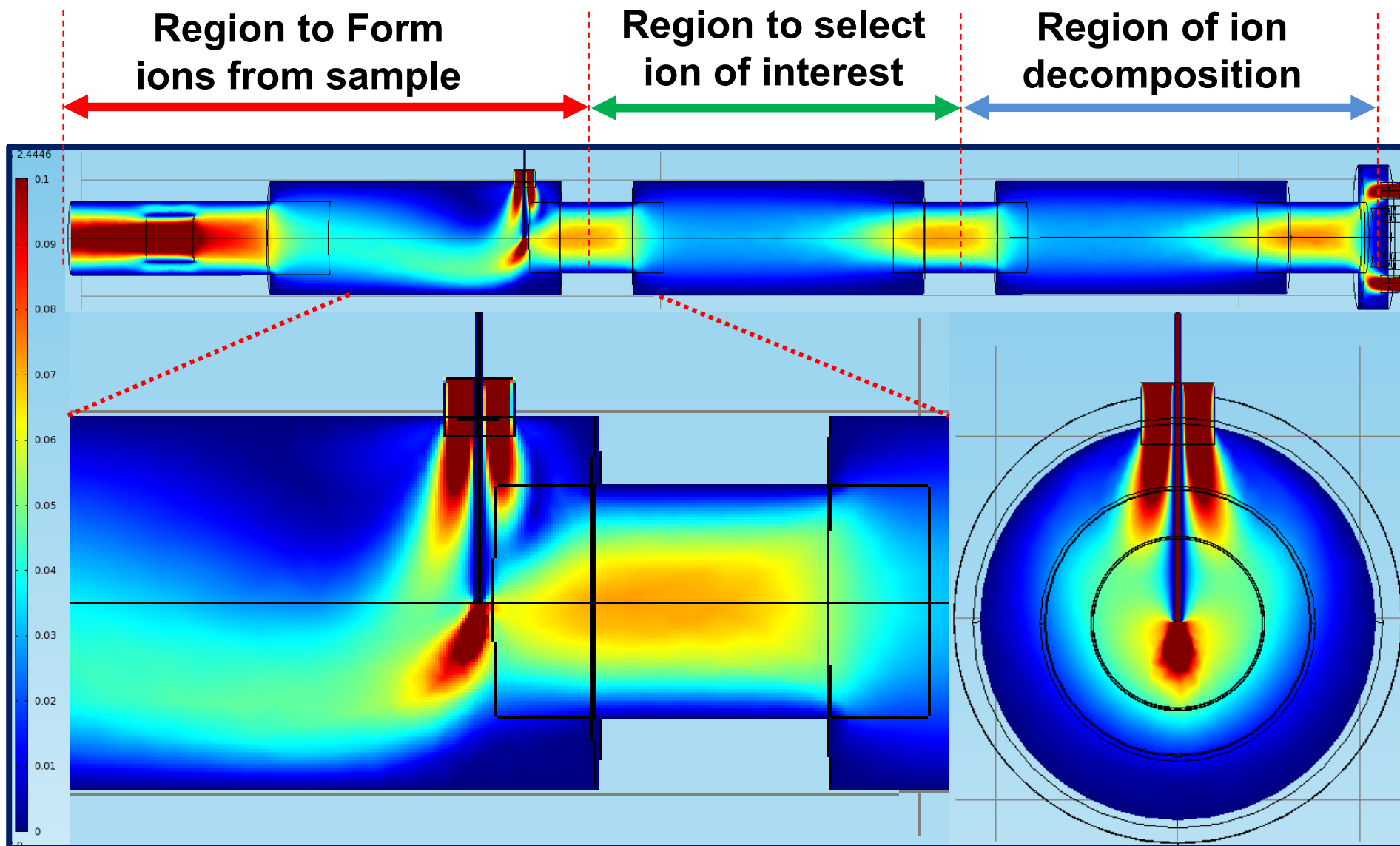
Three regions of the NMSU kinetic ion mobility spectrometer



Conventional ring structures of NMSU used in kinetic IMS drift tube

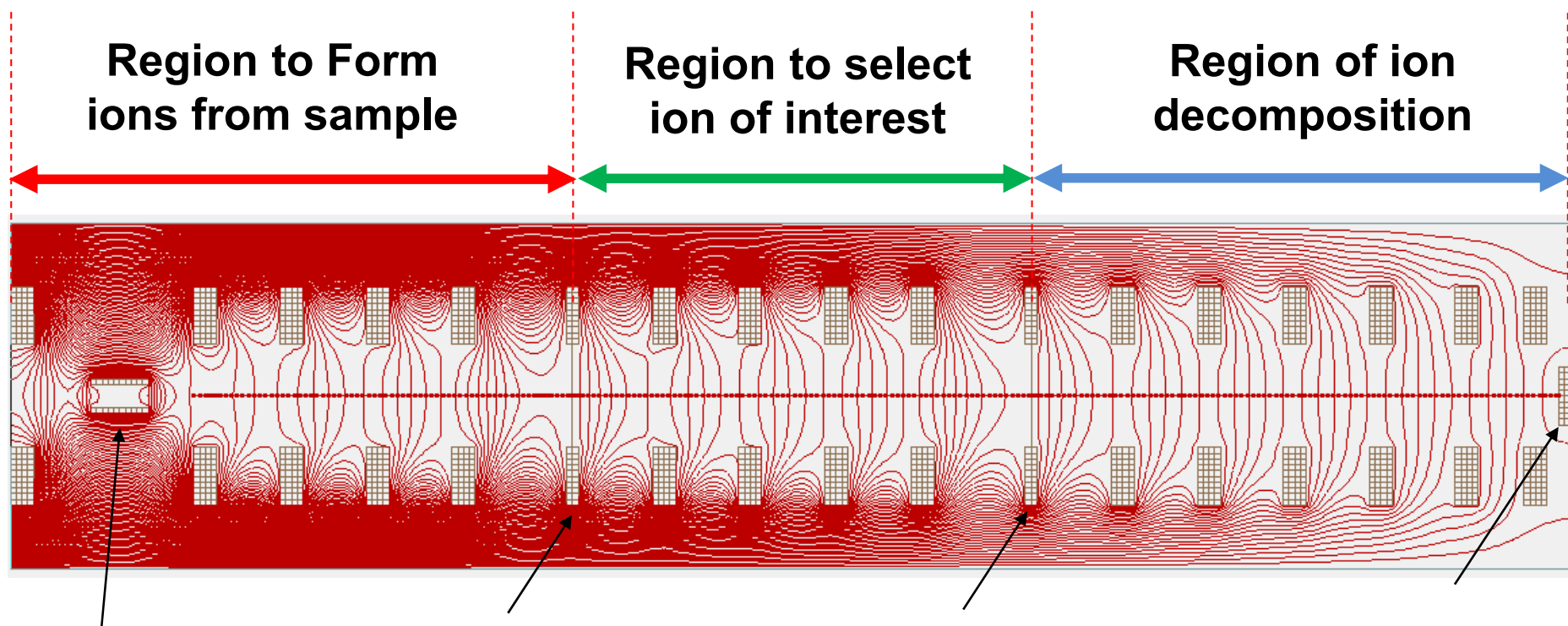


Computer simulation of flows in kinetic IMS drift tube



COMSOL model for the velocity magnitude (m/s) for the gas flows of the dual shutter mobility spectrometer, Drift flow = 280 mL/min , Dopant flow = 100 mL/min , Sample Flow = 6 mL/min

Computer simulations of electric fields in kinetic IMS drift tube

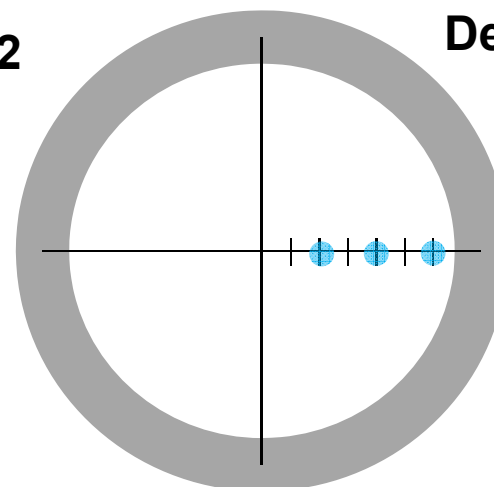


Source

Ion shutter 1

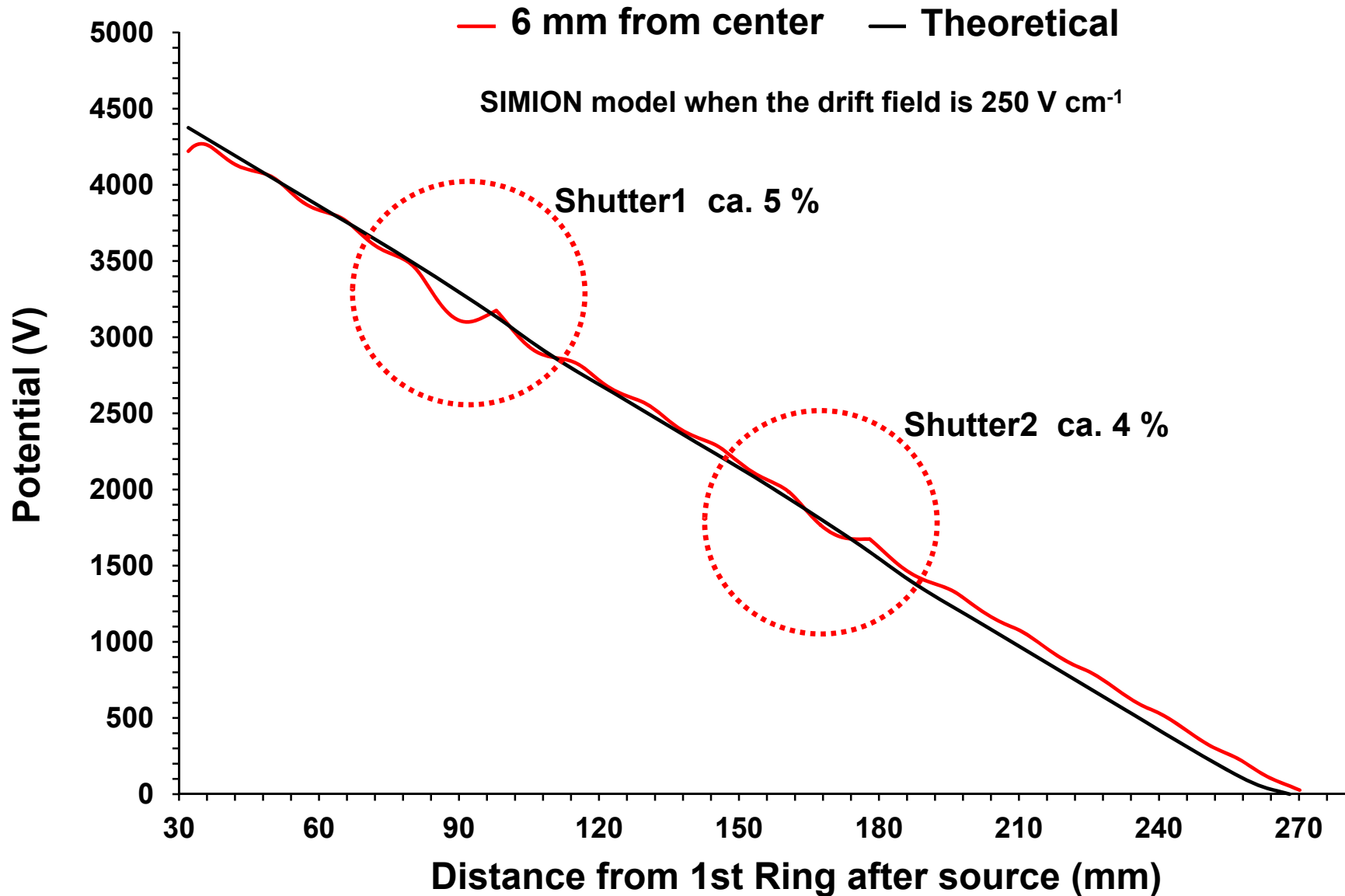
Ion shutter 2

Detector

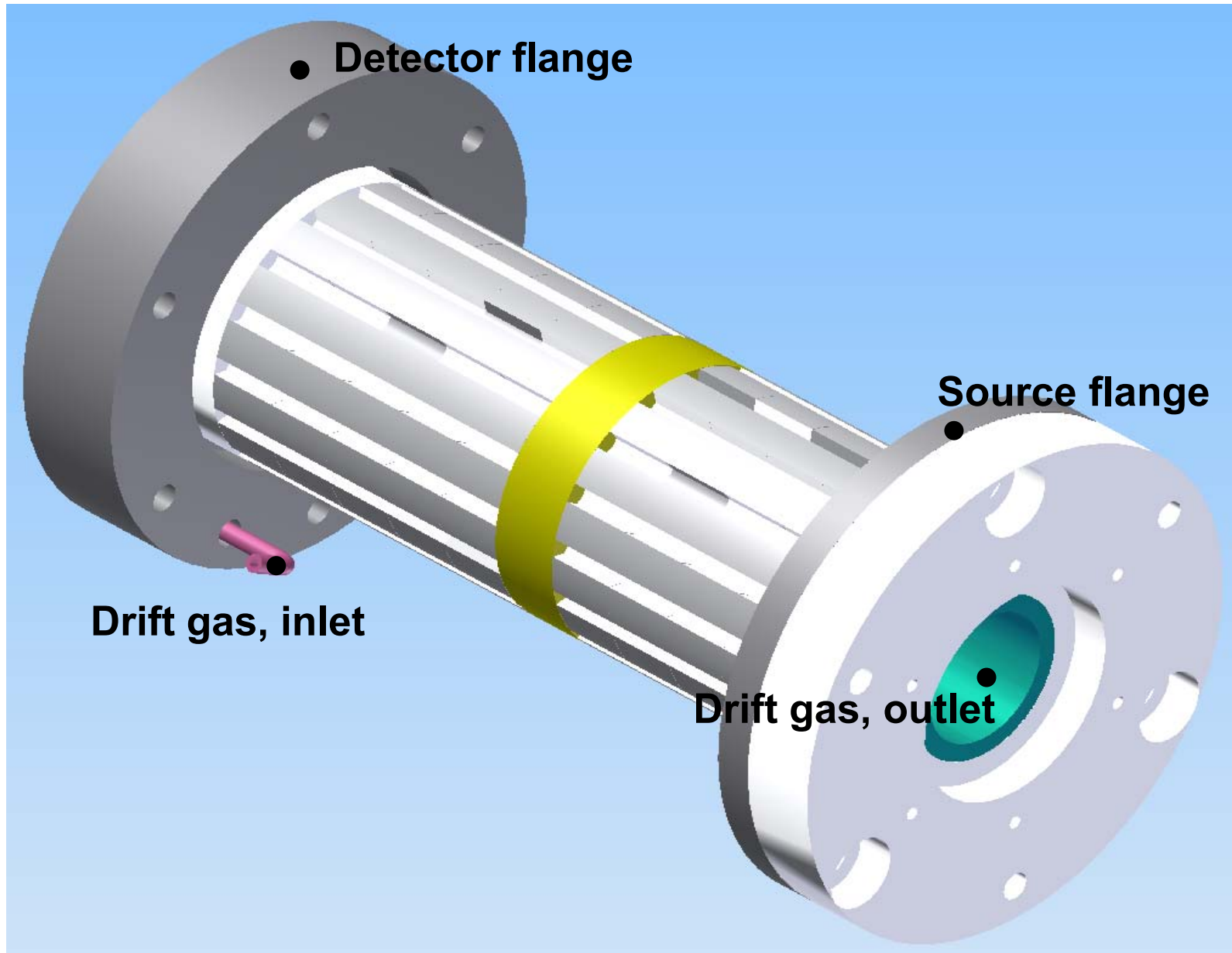


A study of the performance of an ion shutter for drift tubes in atmospheric pressure ion mobility spectrometry: Computer models and experimental findings, F.K. Tadjimukhamedov, J. Puton, J.A. Stone, G.A. Eiceman, Rev. Sci. Instrum. 80, (2009)

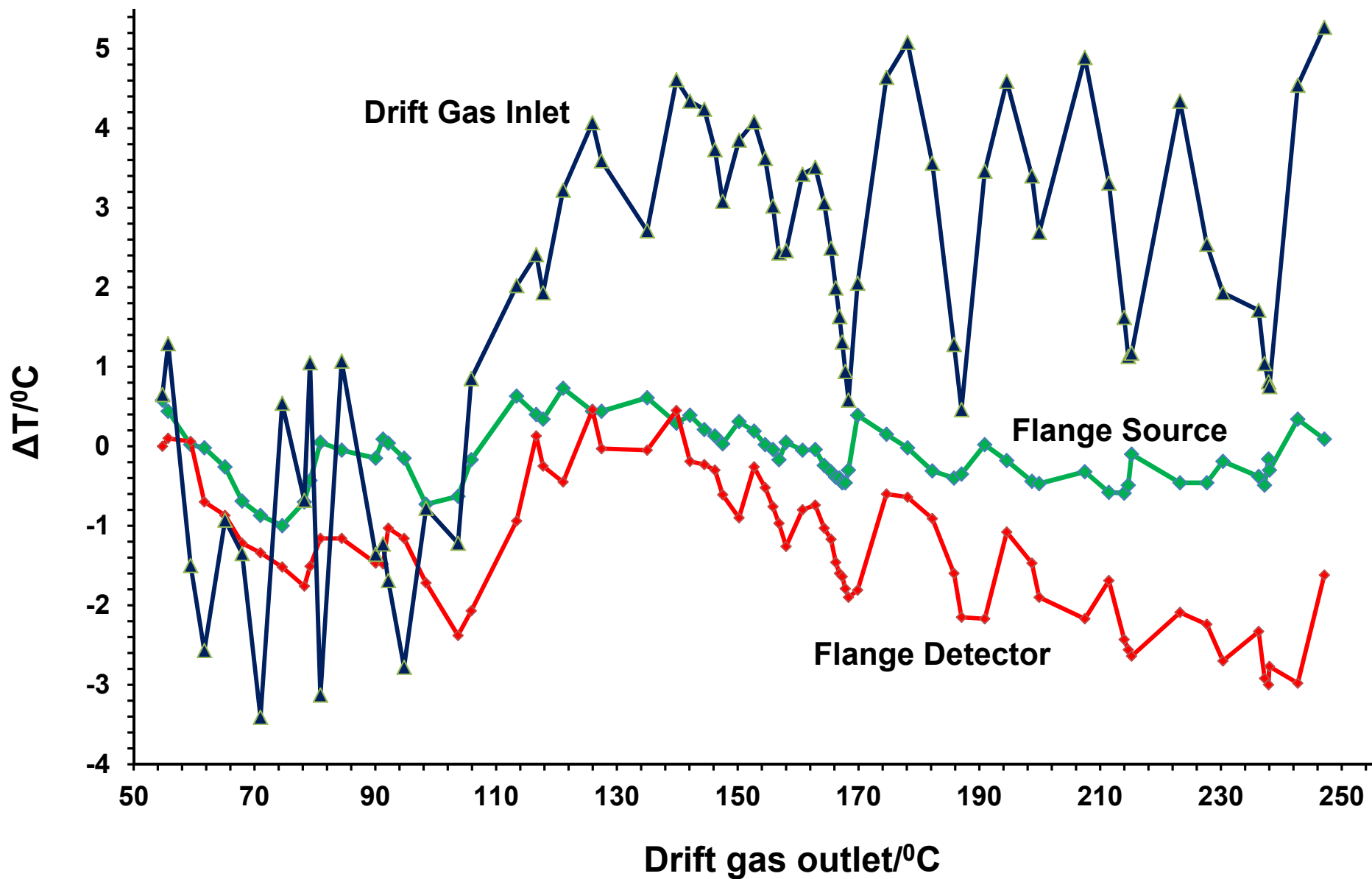
Computer simulations deviations in potentials inside tube: worst condition for deviations at 6 mm from center (near wall)



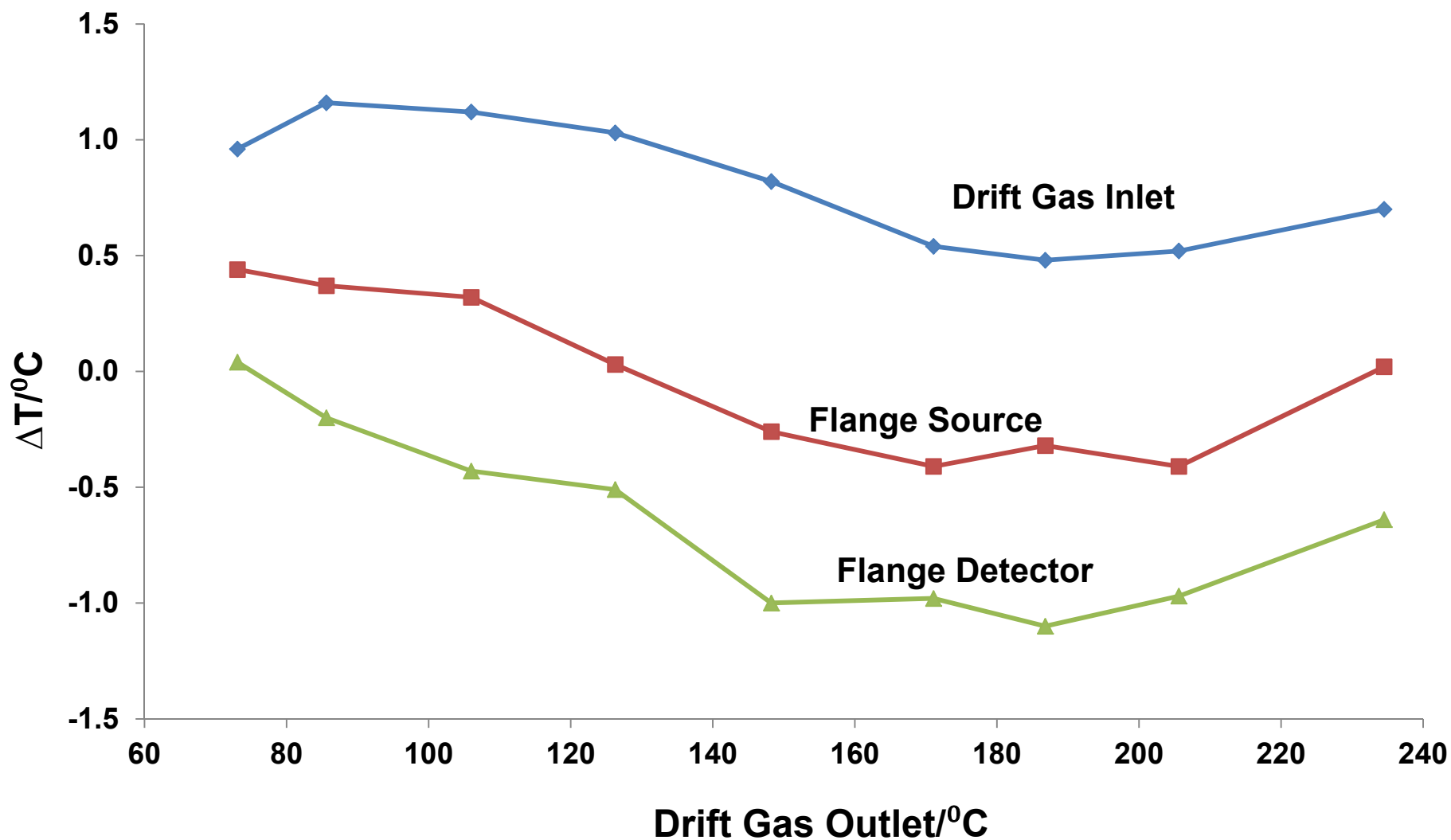
Temperature variations with drift tube: location of thermocouples



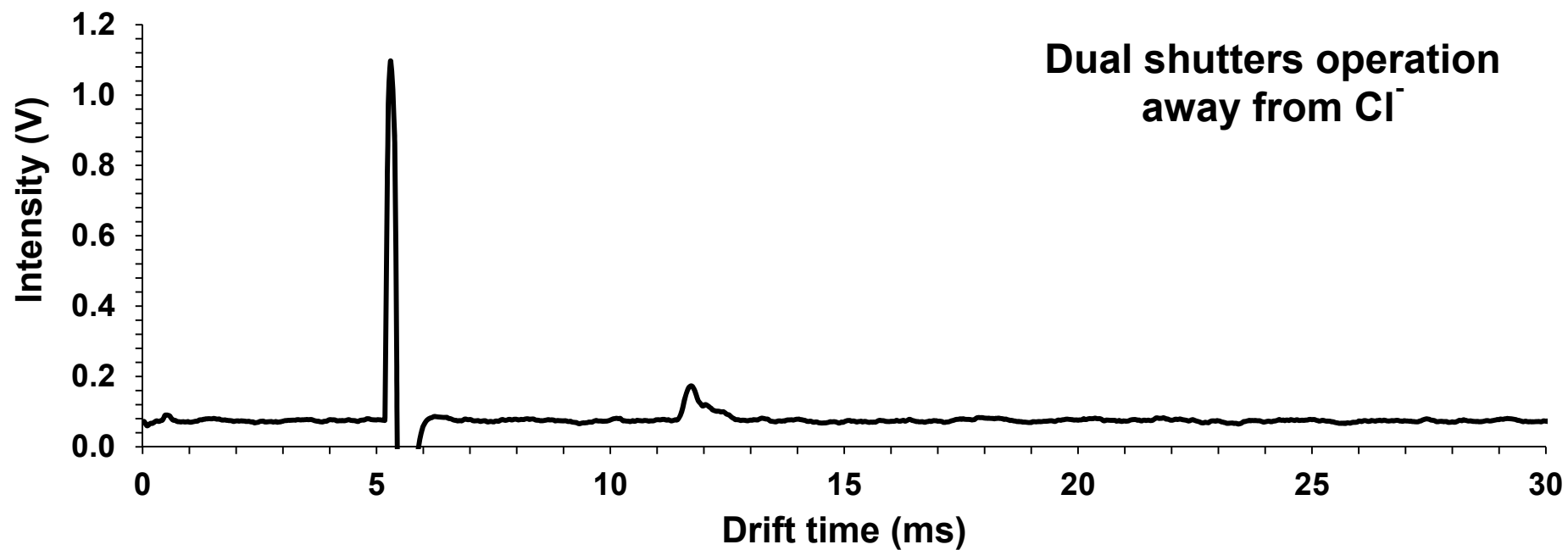
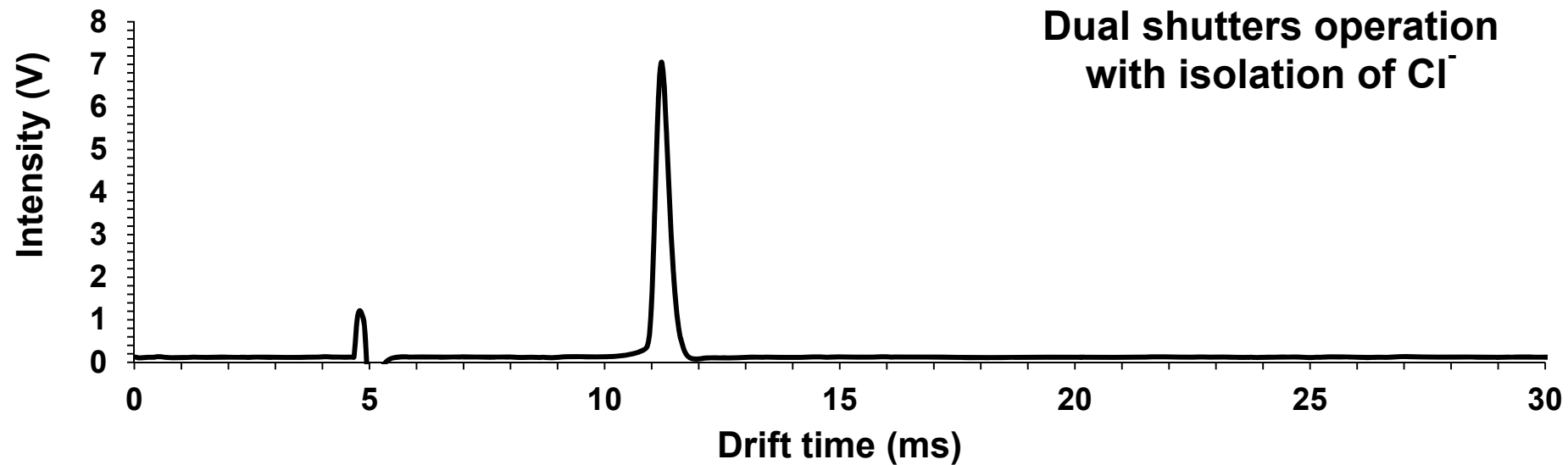
Difference in temperature with only 2 hr intervals against drift gas temperature at outlet



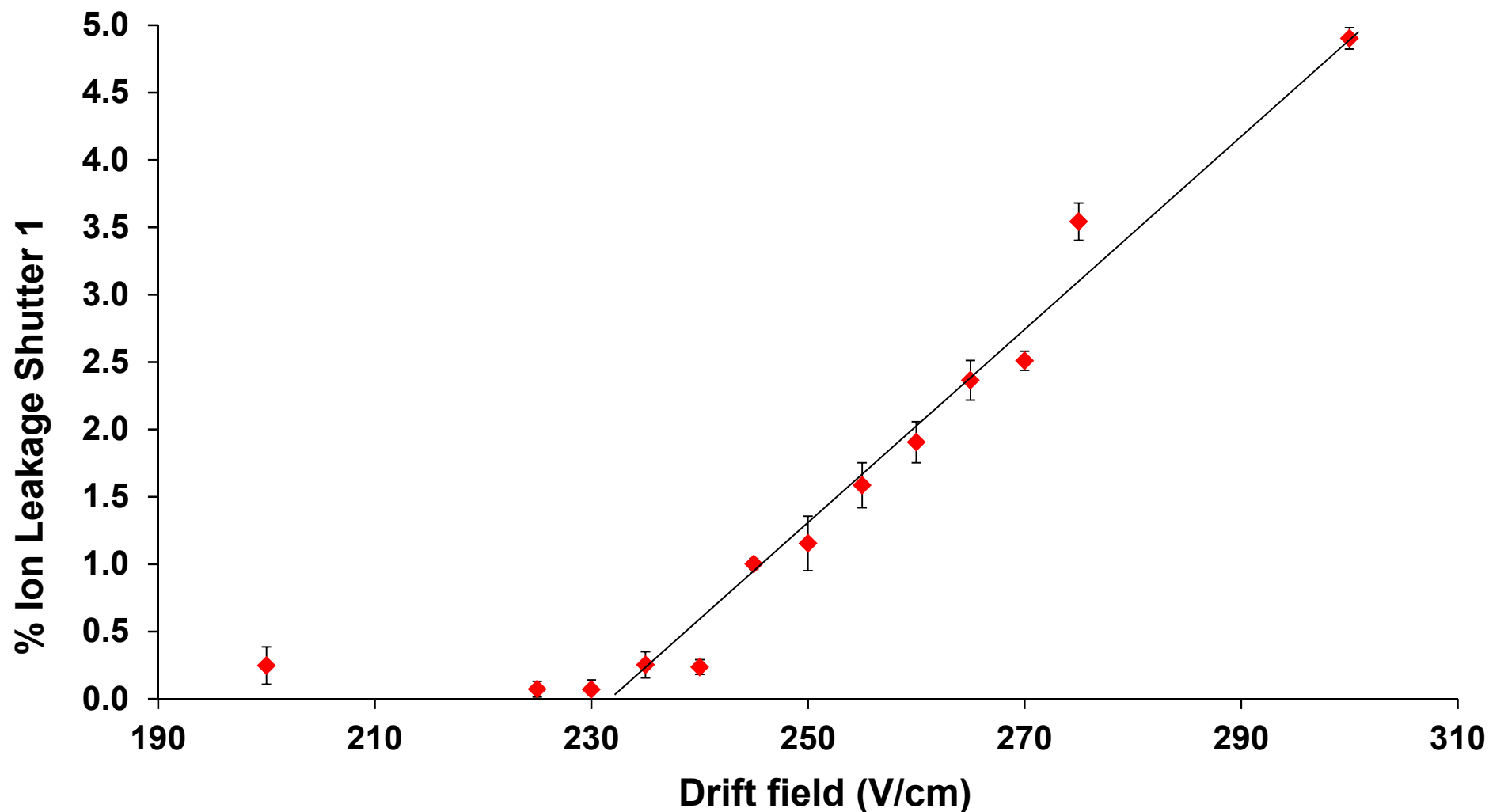
Difference in temperature with only 24 hr intervals against drift gas temperature at outlet



Ion leakage through ion shutter no. 1: as low as 0.1%

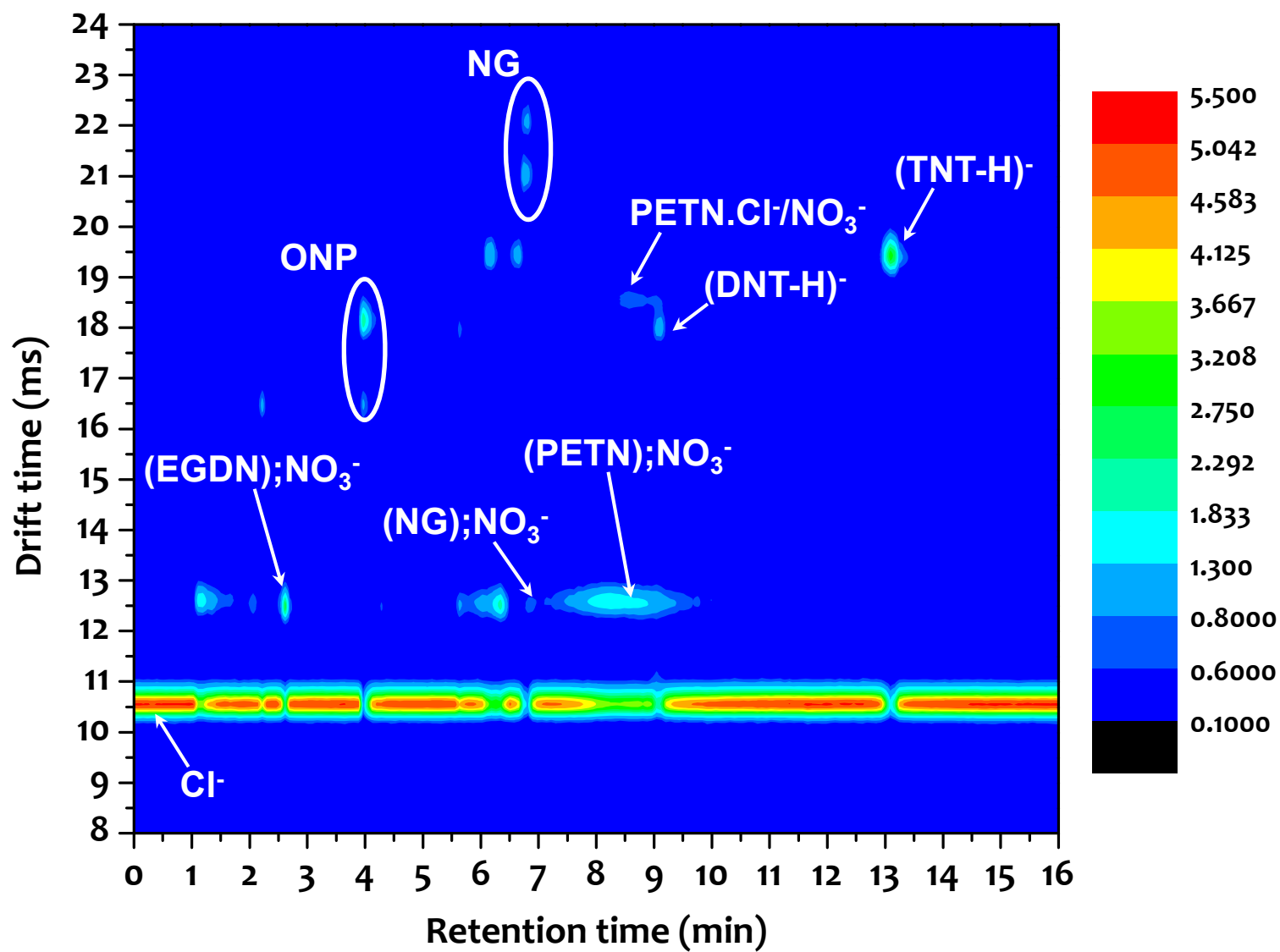


Leakage in Ion shutter no. 1 increases with increased drift field



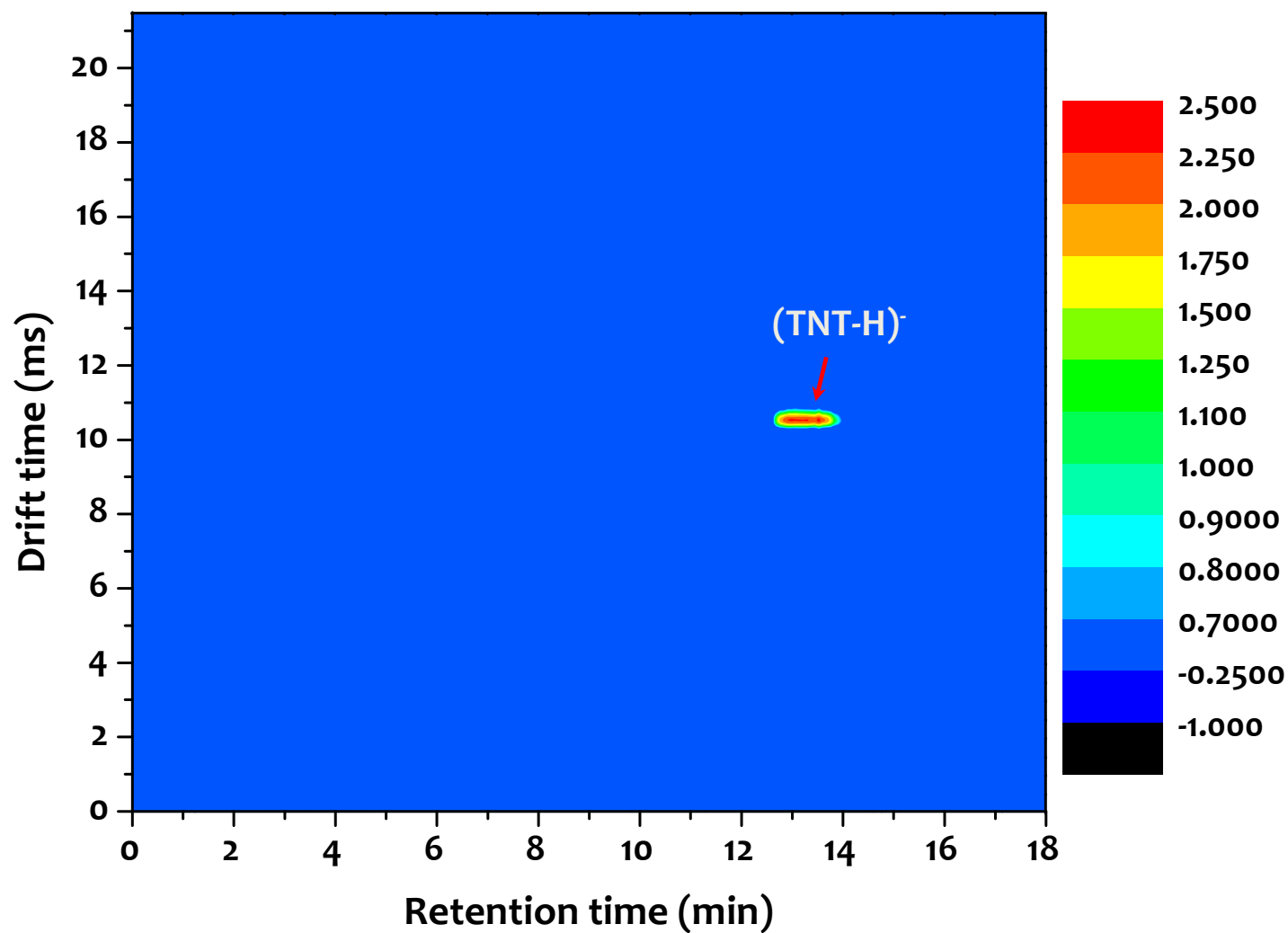
A study of the performance of an ion shutter for drift tubes in atmospheric pressure ion mobility spectrometry: Computer models and experimental findings, F.K. Tadjimukhamedov, J. Puton, J.A. Stone, G.A. Eiceman, Rev. Sci. Instrum. 80, (2009)

GC Pre-fractionation of complex mixture



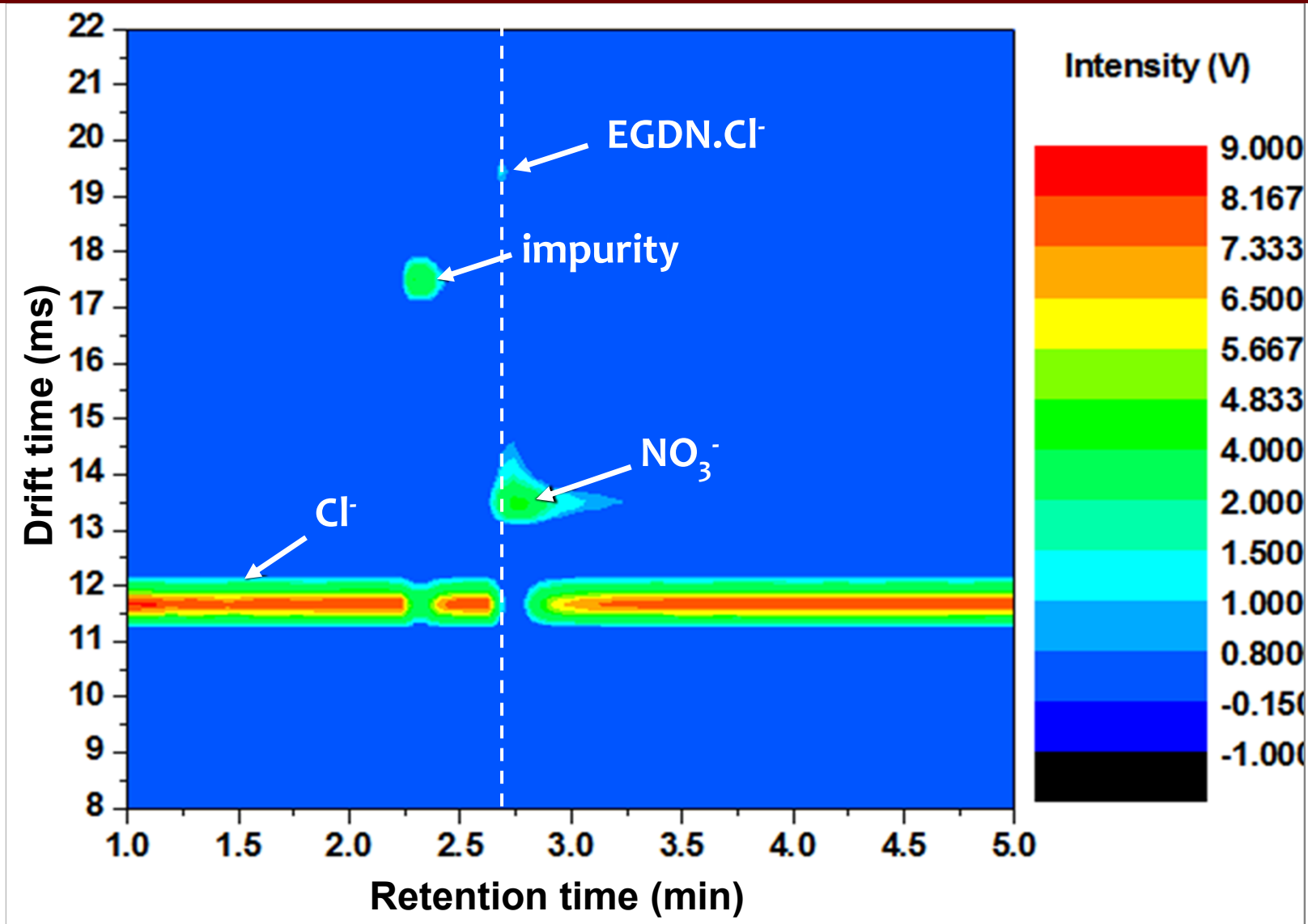
six nitrate explosives at 111 °C and 250 V cm⁻¹

Mobility-based isolation, with dual shutter, of (TNT-H)⁻ from complex mixture with GC pre-fractionation



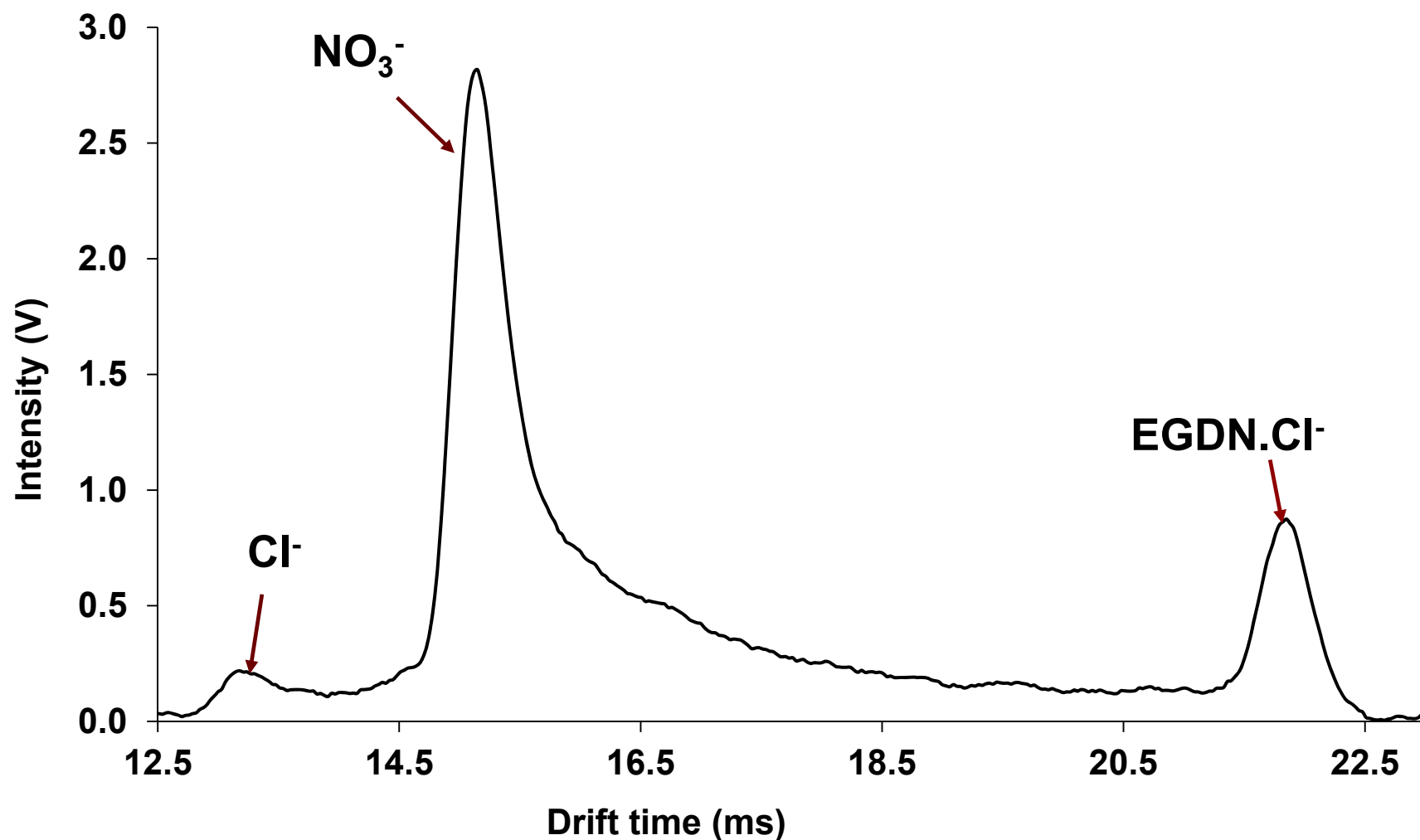
A mixture of six nitrate explosive ions and adducts at 111 °C and 250 V cm⁻¹

First data on decomposition of EDGN Cl⁻ in air at ambient pressure



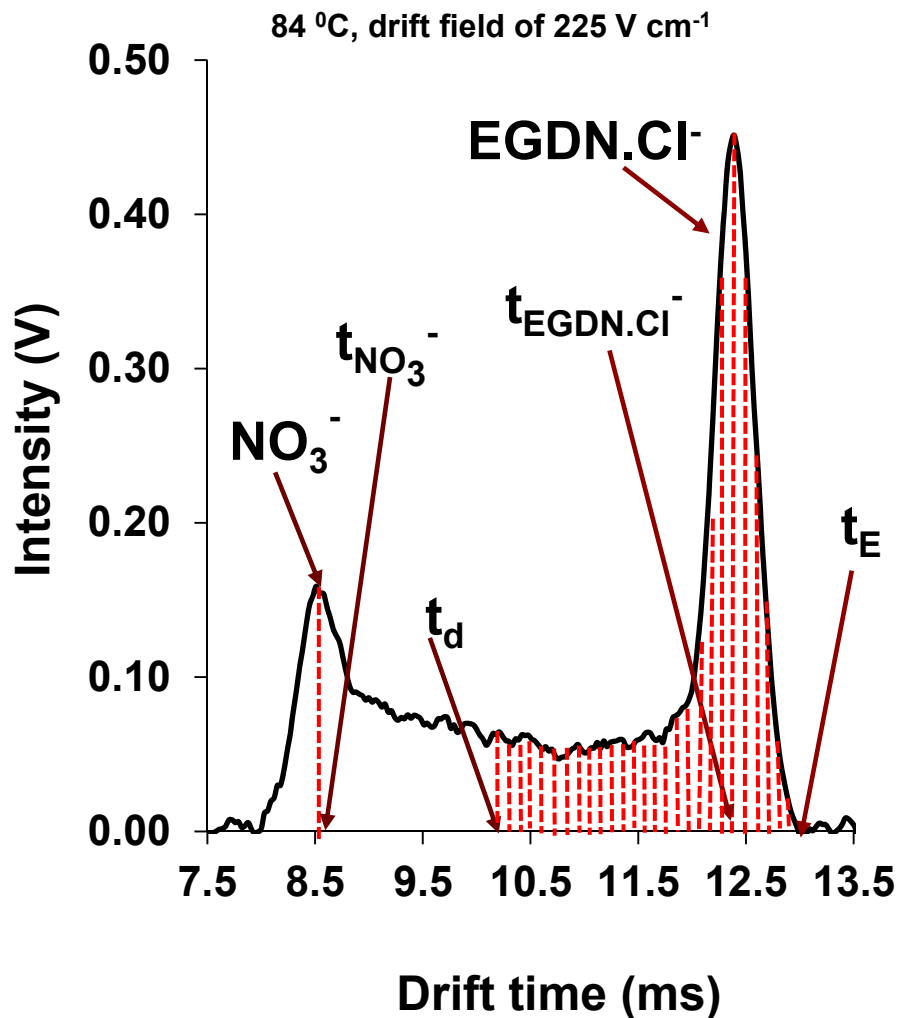
88 °C.....250 V cm⁻¹ion shutter no. 1 only

Decomposition of EGDN Cl⁻ with ion shutter no. 1



Detection of ethylene glycol dinitrate vapors by ion mobility spectrometry using chloride reagent ions, A. H. Lawrence, Pavel Neudorfl, *Anal. Chem.*, 1988, 60 (2), 104–109

Isolation of EGDN.Cl⁻ with dual shutter operation



$$t_x = (t_{EGDN.Cl^-}) \left[\frac{(t_d) - (t_{NO_3^-})}{(t_{EGDN.Cl^-}) - (t_{NO_3^-})} \right]$$

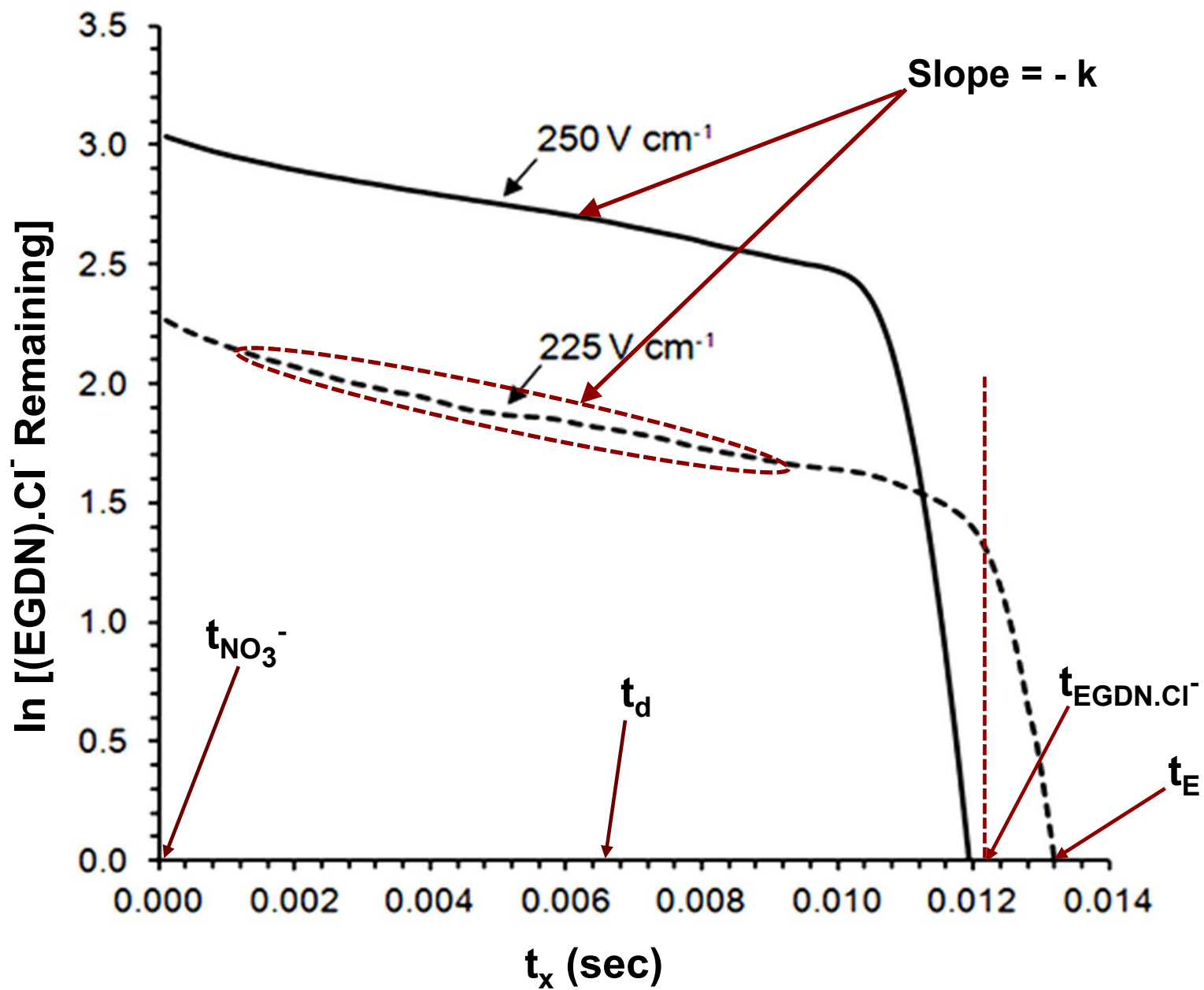
$$t_x = 0 \rightarrow t_{EGDN.Cl^-}$$

$$-\frac{d[EGDN.Cl^-]}{dt} = k[EGDN.Cl^-]$$

$$\ln [EGDN.Cl^- \text{ remaining at } t_x] \text{ vs } (t_x)$$

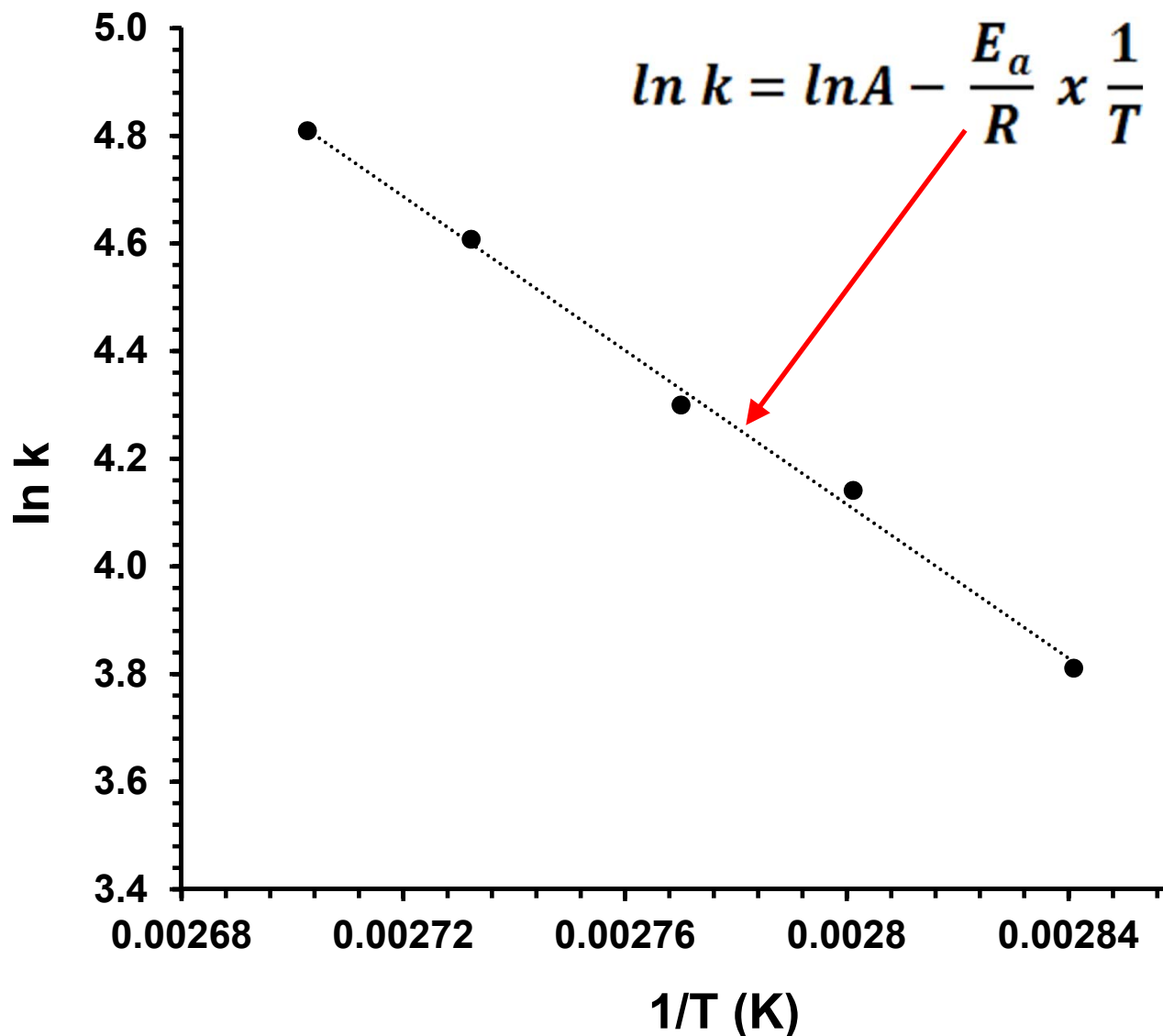
The kinetics of the decompositions of the proton bound dimers of 1,4-dimethylpyridine and dimethyl methylphosphonate from atmospheric pressure ion mobility spectra, R.G. Ewing, G.A. Eiceman, C.S. Harden, J.A. Stone, I.J. Mass Spec, 2006,76-85

Rate plots for EGDN.Cl⁻ decomposition at 84 °C



Arrhenius plot for the decomposition of EGDN-CF

T (°C)	k (s ⁻¹)
79	45.2
84	62.9
88	73.7
93	100.3
97	122.7

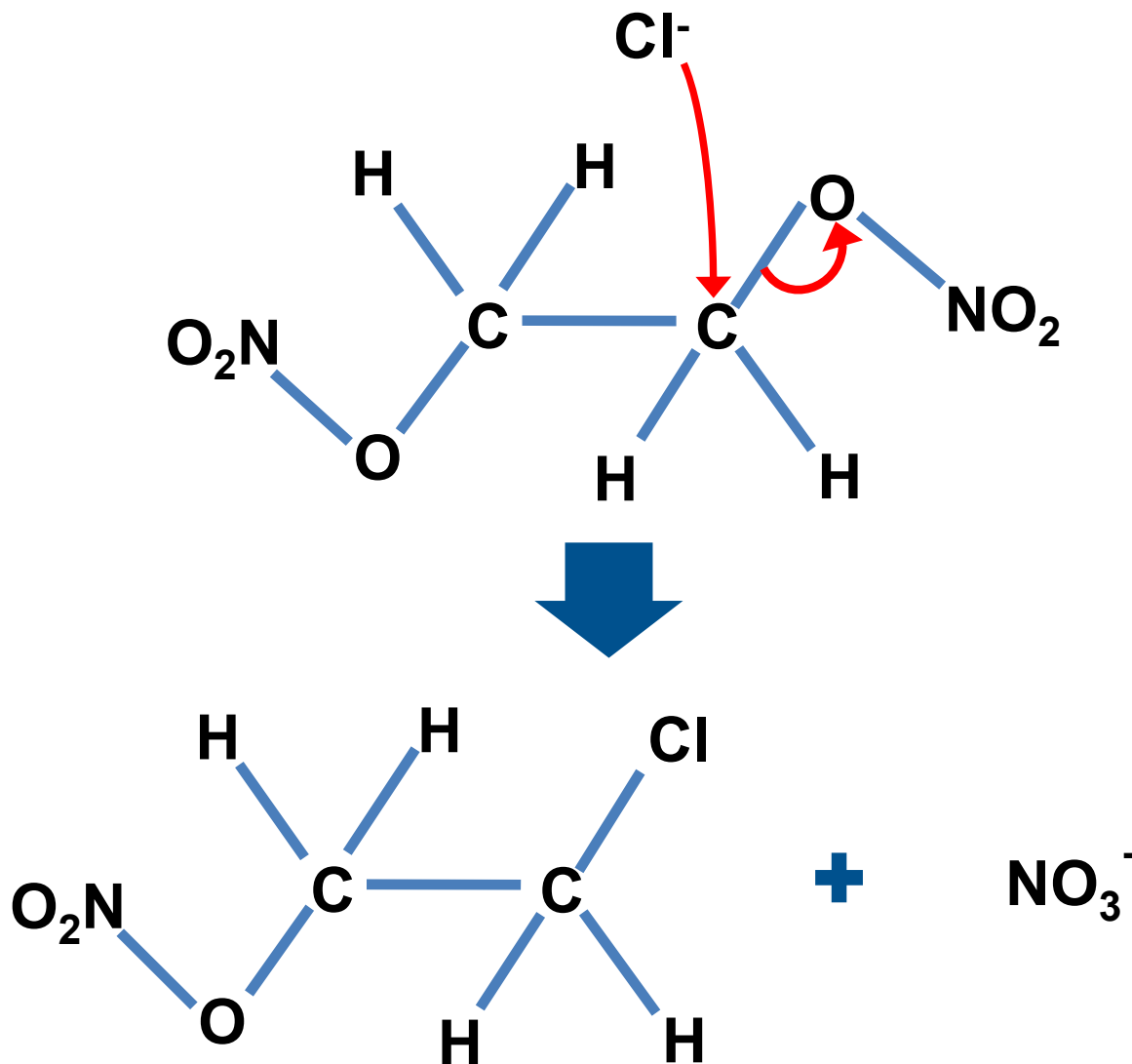


$\Delta H^\circ = E_a + RT$ provides the std Enthalpy change for the reaction

ab initio calculations for reaction paths

Spartan 10

Ground state geometries were optimized using Density Function Theory using B3LYP/6-311 G (D,P) basis set



Comparison experimental and theoretical results



Experimental

$$E_a = 60 \text{ kJ mol}^{-1}$$

$$\Delta H^\circ = E_a + RT \text{ (when } T = 298 \text{ K)}$$

$$\Delta H^\circ = 62 \text{ kJ mol}^{-1}$$

Theoretical

$$\Delta H^\circ = 56 \text{ kJ mol}^{-1} \text{ SPARTAN}$$

$$\Delta H^\circ = 61 \text{ kJ mol}^{-1} \text{ GAUSSIAN}$$

Conclusions

- Kinetic IMS instrument characterized quantitatively for sources of error in temperature, electric field, gas flows, and ion shutter performance.
- Pre-fractionation of sample before drift tube provides demonstrated control over vapor composition and confidence in kinetic rate constants (not due to impurities).
- Dual shutter operation permits isolation of one ion peak only for uncomplicated rate measurements demonstrated with TNT-H⁻ and EDGN.Cl⁻.
- Difference in Experimental versus *ab-initio* calculation for $\Delta H^\circ \sim 1$ kJ/mole, or $\sim 1.5\%$ relative error.

Acknowledgements



THE
UNIVERSITY
of RHODE ISLAND

Center of Excellence for Explosives
Detection, Mitigation and Response

Eiceman Research Group, NMSU

- Dr. Stephen Davilla
- Dr. Ryan Blase, now at Southwest Science Center
- Dr. C-H Yuan
- Marlen Menlyadiev
- Aldo Maldonado

Solution-based direct readout surface enhanced Raman spectroscopic (SERS) detection of ultra-low levels of thiram with dogbone shaped gold nanoparticles

Benjamin Saute and Radha Narayanan*

Received 1st August 2010, Accepted 4th November 2010

DOI: 10.1039/c0an00594k

We report the use of two different sizes of dogbone shaped gold nanoparticles as colloidal substrates for surface enhanced Raman spectroscopy (SERS) based detection of ultra-low levels of thiram, a dithiocarbamate fungicide. We demonstrate the ability to use a solution based, direct readout SERS method as a quantitative tool for the detection of ultra-low levels of thiram. The two different sizes of dogbone shaped gold nanoparticles are synthesized by using the seed-mediated growth method and characterized by using UV-visible spectroscopy and transmission electron microscopy (TEM). The smaller dogbone shaped nanoparticles have an average size of 43 ± 13 nm. The larger dogbone shaped gold nanoparticles have an average size of 65 ± 15 nm. The nanoparticle concentration is 1.25×10^{11} nanoparticles per mL for the smaller dogbone shaped gold nanoparticles and is 1.13×10^{11} nanoparticles per mL for the larger dogbone shaped gold nanoparticles. Different concentrations of thiram are allowed to bind to the two different sizes of dogbone shaped gold nanoparticles and the SERS spectra are obtained. From the calibration curve, the limit of detection for thiram is 43.9 ± 6.2 nM when the smaller dogbone shaped gold nanoparticles are used as colloidal SERS substrates. In the case of the larger dogbone shaped gold nanoparticles, the limit of detection for thiram is 11.8 ± 3.2 nM. The lower limit of detection obtained by using the larger dogbone shaped gold nanoparticles as colloidal substrates is due to the lightning rod effect, higher contributions from the electromagnetic enhancement effect, and larger number of surface sites for thiram to bind.

Introduction

Surface-enhanced Raman scattering (SERS) was discovered in 1977 by Van Duyne¹ and by Creighton.² SERS is a phenomenon in which there are greatly enhanced Raman signals when Raman scattering molecules are placed very near or attached onto metal substrates or metal nanoparticles. While of long standing fundamental importance,^{3–6} its potential as a quantitative analytical tool has only recently begun to take place.^{7–10} Some types of quantitative applications of SERS are biological sensing,^{5,11–23} environmental monitoring,^{16,24} trace analysis,²⁴ and explosive and contaminant detection.^{5,24–26} The ability to use SERS as a quantitative analytical tool reflects advances in the ability to reproducibly synthesize and manipulate the size and shape of gold and silver nanoparticles.

The EPA have set maximum concentration limit (MCL) of <1 ng mL⁻¹ for pollutants present in water. As a result, it is necessary to be able to detect ultra-low levels of pesticides, insecticides, fungicides, and other environmental pollutants. SERS has been used for the detection of different types of environmental pollutants.^{27–30} SERS has also been used for the detection of polychlorinated biphenyls (PCBs).^{27–29} Different types of pesticides^{27–34} have also been detected by using SERS. In addition, SERS has been used for the detection of fungicides.^{35–38} It is worth noting that in many of these studies, SERS is used qualitatively for identification of the different pollutants, PCBs,

pesticides and fungicides as well as structural studies on the binding process. In our paper, we use SERS as a quantitative analytical tool for detecting ultra-low levels of thiram, which is a dithiocarbamate fungicide.

SERS has traditionally been conducted with gold and silver substrates as well as colloidal gold and silver nanoparticles. It has been recently shown that using cubic, block, and dogbone shaped gold nanoparticles result in ~ 100 times higher SERS enhancements of 4-mercaptobenzoic acid compared to spherical gold nanoparticles.³⁹ This SERS enhancement has been attributed to the lightning rod effect in which there is greater amount of localized electromagnetic fields at the corners and edges of the nanoparticles.³⁹

We show that we can use two different sizes of dogbone shaped gold nanoparticles as colloidal SERS substrates for quantitative detection of ultralow levels of thiram, which is a dithiocarbamate fungicide. In this paper we demonstrate the ability to use a solution based, direct readout SERS method as a quantitative tool for the detection of ultra-low levels of thiram. In our method, we use two different sizes of dogbone shaped gold nanoparticles as colloidal SERS substrates for a solution based direct readout SERS based detection of ultra-low levels of thiram. Thiram has a disulfide bond which spontaneously breaks upon exposure to the gold nanoparticles and binds to the nanoparticles through the Au–S bond, which is the gold thiolate bond. It was observed that there is a lower limit of detection when the larger dogbone shaped gold nanoparticles are used as colloidal SERS substrates. Different sources that give rise to higher enhancements will also be discussed in the paper.

Department of Chemistry, University of Rhode Island, 51 Lower College Road, Kingston, RI, 02881, USA. E-mail: rnarayanan@chm.uri.edu; Fax: +1 401-874-5072; Tel: +1 401-874-2298

Experimental

Synthesis of two different sizes of dogbone shaped gold nanoparticles

The smaller dogbone shaped gold nanoparticles were synthesized by a slightly modified seed mediated growth method reported previously.^{40–42} This synthesis consists of two distinct steps: preparation of the nanoparticle seeds and preparation of the nanoparticle growth solution. To prepare the seeds, 250 μL of 0.01 M HAuCl_4 is added to a solution containing 4.75 mL deionized water and 5 mL of 0.2 M CTAB. Next, 600 μL of ice-cold 0.01 M NaBH_4 is added to the solution, acting as a rapid reducing agent. The seed solution is allowed to age for approximately one hour. After the seed is aged, the growth solution is prepared. The growth solution consists of 95 mL of 0.1 M CTAB, 800 μL of 0.01 M AgNO_3 , 5 mL of 0.01 M HAuCl_4 , 550 μL of 0.1 M ascorbic acid, and 120 μL of the previously prepared seed solution. After the growth solution is prepared, the jar is left undisturbed overnight to allow the nucleation and growth process to occur. The resulting nanoparticle solution appears navy blue. In the case of the synthesis of larger dogbone shaped nanoparticles, the same type of seed mediated growth method was used and 0.25 M ascorbic acid is used in the growth solution instead of 0.1 M ascorbic acid.

UV-visible spectroscopic characterization

The two different sizes of dogbone shaped gold nanoparticles were characterized by using UV-visible spectroscopy to determine the surface plasmon band λ_{max} of the nanoparticles. The two different sizes of dogbone shaped nanoparticles were filtered by using a 0.22 micron PVDF syringe filter. Two mL of the dogbone shaped gold nanoparticles were placed into a quartz cuvette and placed in the sample holder of the Agilent 8453 diode array UV-visible spectrophotometer. The smaller dogbone shaped nanoparticles have a surface plasmon band λ_{max} of 671 nm and the larger dogbone shaped nanoparticles have a surface plasmon band λ_{max} of 758 nm.

Transmission electron microscopic characterization

TEM characterization allows for determination of the size and shape distributions of our gold nanoparticles. The different sizes of dogbone shaped gold nanoparticles are filtered in the same way as the UV-vis sample preparation. The nanoparticles are then centrifuged twice at 12 000 rpm for 10 minutes each time. This removes excess CTAB that is present in solution. One drop of the filtered and centrifuged nanoparticles is spotted on the TEM grid.

Size distribution analysis

The UTHSCSA ImageTool for Windows—Version 3 image analysis software was used to determine the size distributions of the two different sizes of dogbone shaped gold nanoparticles. The Distance tool in the Analysis pull-down menu is used to measure the number of pixels in the scale bar of the TEM image. Based on the number of pixels for the fixed size associated with the scale bar and measuring the number of pixels for ~ 200

nanoparticles in several TEM images, the size of the dogbone shaped gold nanoparticles can be calculated by dividing the number of pixels for the nanoparticles by the number of pixels of the scale bar and multiplying by the fixed size associated with the scale bar of the TEM image. We then plotted the histogram of % dogbone shaped gold nanoparticles vs. nanoparticle size and obtained a Gaussian fit to the histogram. From the Gaussian fit, we can determine the average size and standard deviation of the dogbone shaped gold nanoparticles.

Surface enhanced Raman spectroscopy (SERS)

The SERS spectra of thiram were obtained by using a Raman Systems R-3000QE Raman spectrometer. The laser excitation wavelength is 785 nm. One mL of the dogbone shaped gold nanoparticles with thiram bound to it is placed in a cuvette. The cuvette is placed in the self-contained dark chamber. The L cap is used since these are solution samples that are being analyzed. A 30 second integration time is used for acquisition of the SERS spectra. The SERS spectra are acquired in the range from 200 to 1800 cm^{-1} .

Results and discussion

There are a few papers in the literature which report the SERS spectra for thiram and discuss the binding modes to silver colloids and gold films.^{43–45} In addition, there has been a paper in which the authors have made assignments of the SERS bands associated with thiram when it is bound to silver colloids.³⁵ We have developed a solution-based direct readout SERS method for quantitative detection of ultralow levels of thiram, which is a dithiocarbamate fungicide. Two different sizes of dogbone shaped gold nanoparticles have been used as colloidal SERS substrates for the detection of thiram.

Synthesis of the two different sizes of dogbone shaped gold nanoparticles

We have synthesized two different sizes of dogbone shaped gold nanoparticles by using the seed-mediated growth method described previously.^{40–42} Fig. 1 shows a representative TEM image of the smaller dogbone shaped gold nanoparticles as well as the size distribution histogram with the average size of the particles. The size distributions were determined by using the ImageTool software. The smaller dogbone shaped gold nanoparticles have an average size of 43 ± 13 nm. The concentration

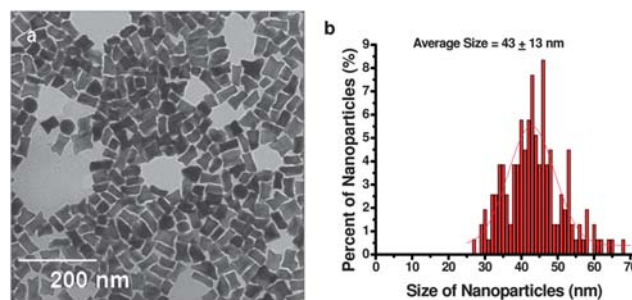


Fig. 1 TEM image of the smaller dogbone shaped gold nanoparticles (a) and size distribution histogram of the nanoparticles (b).

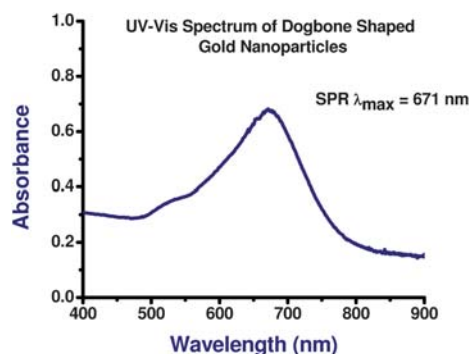


Fig. 2 UV-visible spectrum showing the surface plasmon band λ_{\max} of the smaller dogbone shaped gold nanoparticles.

of the smaller dogbone shaped nanoparticles is calculated to be 1.25×10^{11} nanoparticles per mL. We have also characterized the smaller dogbone shaped gold nanoparticles by using UV-visible spectroscopy to characterize the surface plasmon band λ_{\max} . It can be seen in Fig. 2 that the smaller dogbone shaped gold nanoparticles have a λ_{\max} of 671 nm.

TEM images and size distribution plots were also obtained for the larger dogbone shaped gold nanoparticles. Fig. 3 shows a representative TEM image of the larger dogbone shaped gold nanoparticles as well as the size histogram with the average size of the nanoparticles. The larger dogbone shaped gold nanoparticles have an average size of 65 ± 15 nm. The concentration of the larger dogbone shaped gold nanoparticles is calculated to be 1.13×10^{11} nanoparticles per mL. We have also used UV-visible spectroscopy to obtain the surface plasmon band λ_{\max} . It can be seen in Fig. 4 that the larger dogbone shaped gold nanoparticles have a surface plasmon band λ_{\max} of 758 nm.

The dogbone shaped gold nanoparticles are much more attractive as colloidal SERS substrates compared to the spherical gold nanoparticles since the dogbone shaped gold nanoparticles have surface plasmon bands (671 nm and 758 nm) that are in greater resonance to the laser excitation wavelength. The spherical gold nanoparticles have surface plasmon band in the range between 520 and 560 nm, which are not in good resonance to the laser excitation wavelength. The larger dogbone shaped gold nanoparticles have a surface plasmon band λ_{\max} which is in greater resonance to the laser excitation wavelength than that of the smaller dogbone shaped gold nanoparticles. As a result, we

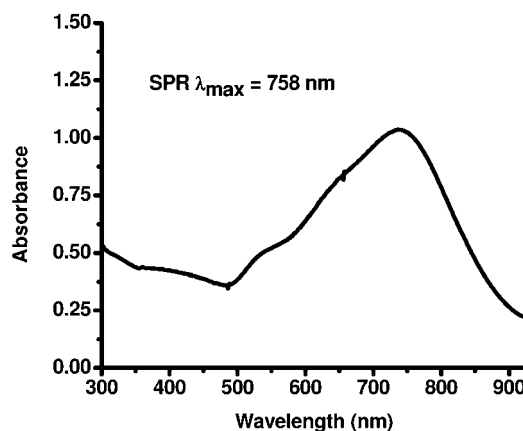


Fig. 4 UV-visible spectrum showing the surface plasmon band λ_{\max} of the larger dogbone shaped gold nanoparticles.

would expect to obtain higher SERS signals using the larger dogbone shaped gold nanoparticles compared to the smaller dogbone shaped gold nanoparticles. This is discussed in more detail later on in the paper.

SERS bands of thiram

There has been a previous study where the SERS spectrum of thiram has been obtained in which the assignments of the different bands has been determined.³⁵ Table 1 shows the SERS peaks that we observe when the thiram is bound to the dogbone

Table 1 Table of the SERS bands associated with thiram^a

SERS band	Assignment ³⁵
339 (vw)	δ (S=CS), δ (CSS)
486 (vw)	δ (CH ₃ NC), ν (C=S)
556 (m)	ν (SS)
755 (vw)	—
928 (m)	ν (CH ₃ N), ν (C=S)
1139 (m)	ρ (CH ₃), ν (CN)
1379 (vs)	δ s(CH ₃), ν (CN)
1444 (m)	δ as(CH ₃)
1508 (m)	ρ (CH ₃), ν (CN)

^a s = strong, w = weak, m = medium, sh = shoulder, v = very, ν = stretching, δ = deformation, ρ = rocking.

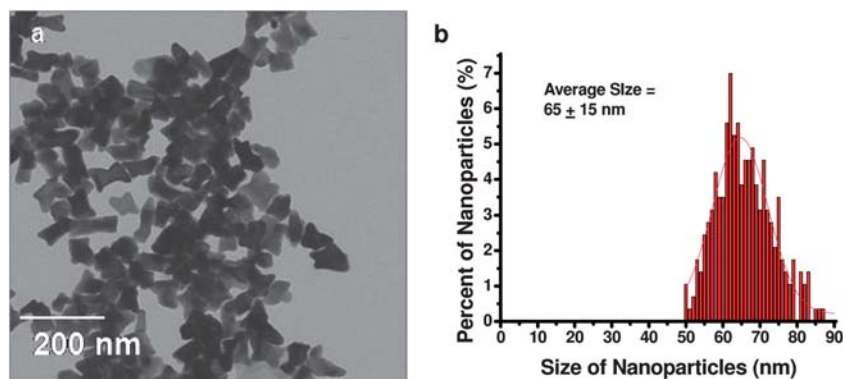


Fig. 3 TEM image of the larger dogbone shaped gold nanoparticles (a) and size distribution histogram of the nanoparticles (b).

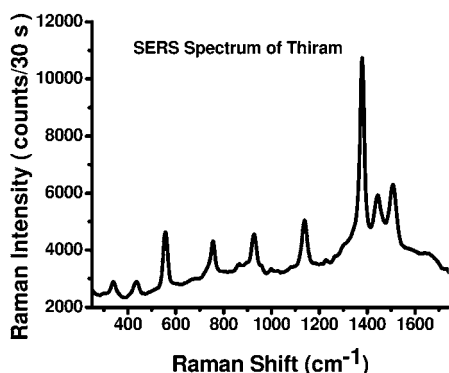


Fig. 5 Example of a SERS spectrum of thiram bound to dogbone shaped gold nanoparticles.

shaped gold nanoparticles and Fig. 5 shows an example of the SERS bands observed when thiram binds to the nanoparticles. There are many peaks in the SERS spectrum of thiram. The strongest peak is at 1379 cm⁻¹ which is the CN stretching mode and symmetric CH₃ deformation mode. Since this is the strongest peak in the SERS spectra, this is the band we use for monitoring the SERS intensity as a function of the thiram concentration. The asymmetric CH₃ deformation mode occurs at 1444 cm⁻¹. The CN stretching mode also occurs at 1508 cm⁻¹ as well as the rocking CH₃ mode. The CN stretching mode and rocking CH₃ mode also occurs at 1139 cm⁻¹. The stretching CH₃N and C=S modes occur at 928 cm⁻¹. The peak at 556 cm⁻¹ is associated with the SS stretching mode. The peak at 486 cm⁻¹ is due to the CH₃NC deformation and C=S stretching modes. The S=CS deformation and the CSS deformation occur at 339 cm⁻¹.

SERS calibration curve

Thiram is a dithiocarbamate fungicide which has a disulfide bond. It is known that there is cleavage of the disulfide bond upon exposure to gold nanoparticles or gold substrates.⁴⁶ When the disulfide bond in thiram breaks, it can bind to the dogbone shaped gold nanoparticles *via* the gold thiolate bond. Different concentrations of thiram are added to the dogbone shaped gold nanoparticles and allowed to bind overnight. The SERS spectra were obtained in triplicate sets for different concentrations of thiram that is covalently bound to the smaller dogbone shaped gold nanoparticles. Fig. 6 shows a representative raw SERS spectra as well as the calibration curve of the SERS intensity as a function of the thiram concentration obtained by using the smaller dogbone shaped gold nanoparticles. The error bars represent the standard deviation of the average Raman intensity (counts per 30 s) obtained with three sets of SERS measurement. It can be seen from the linear fit that the SERS measurements are reproducible. The limit of detection (LOD) is determined by first calculating the minimum distinguishable signal which is the average signal of the blank + 3 times the standard deviation of the blank. The minimum distinguishable signal is then plugged into the best-fit equation of the calibration curve to calculate the limit of detection. The limit of detection obtained for thiram by using the smaller dogbone shaped gold nanoparticles is 43.9 ± 6.2 nM.

Fig. 7 shows a representative set of raw SERS spectra from triplicate sets as well as the calibration curve of the SERS

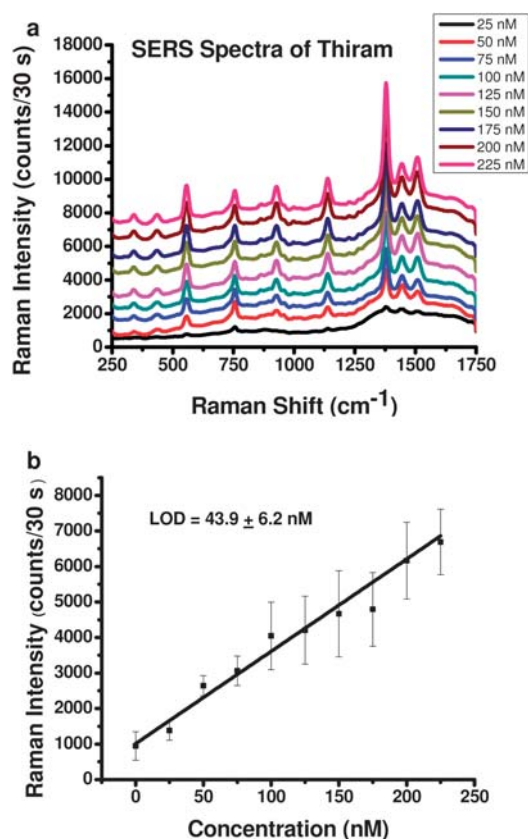


Fig. 6 Raw SERS spectra (a) and SERS calibration curve of SERS intensity with 30 second integration time as a function of the thiram concentration obtained by using the smaller dogbone shaped gold nanoparticles as colloidal SERS substrates (b).

intensity as a function of the thiram concentration obtained by using the larger dogbone shaped gold nanoparticles. The error bars represent the standard deviation of the average Raman intensity (counts per 30 s) obtained with three sets of SERS measurement. It can be seen from the linear fit that the SERS measurements are reproducible. In the case of the larger dogbone shaped Au nanoparticles, the limit of detection is 11.8 ± 3.2 nM. Using the larger dogbone shaped Au nanoparticles as colloidal SERS substrates results in 3.7× lower limit of detection. Several sources that give rise to the higher SERS enhancements are discussed in the next section.

Sources of higher SERS activities

It has been previously shown that cubic, block, and dogbone shaped gold nanoparticles result in ~100× higher SERS enhancements for 4-mercaptobenzoic acid compared to spherical nanoparticles.³⁹ In the case of these nanoparticles, the higher SERS enhancements are attributed to the lightning rod effect. The two types of dogbone shaped gold nanoparticles that we have synthesized have a similar concentration in which the smaller nanoparticles have a concentration of 1.25 × 10¹¹ nanoparticles per mL and the larger dogbone shaped gold nanoparticles have a concentration of 1.13 × 10¹¹ nanoparticles per mL. In the case of our smaller dogbone shaped gold nanoparticles, the source of the SERS enhancement is due to the

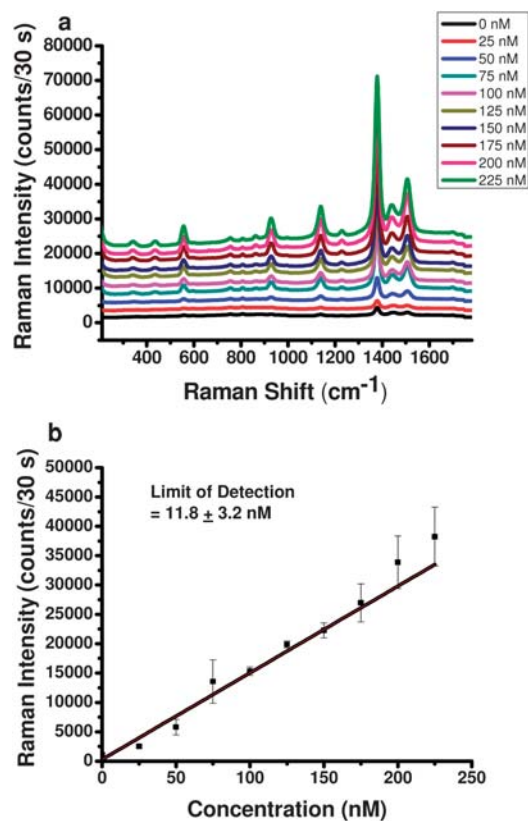


Fig. 7 Raw SERS spectra (a) and SERS calibration curve of SERS intensity with 30 second integration time as a function of the thiram concentration obtained by using the larger dogbone shaped gold nanoparticles as colloidal SERS substrates (b).

lightning rod effect in which there are greater electromagnetic fields at the corners and edges of the nanoparticles. In the case of the larger dogbone shaped gold nanoparticles, in addition to the lightning rod effect, there are much greater contributions from the electromagnetic enhancement effect since the surface plasmon band λ_{max} is 758 nm which is close to the laser excitation wavelength of 785 nm. This gives rise to some of the higher SERS enhancement that is observed. Also, since the surface area of the larger dogbone shaped gold nanoparticles (6276.07 nm²) is larger than the surface area of the smaller dogbone shaped gold nanoparticles (5175.85 nm²) more thiram can bind to the nanoparticle surface resulting in some of the higher enhancements that is observed. Overall, there are higher SERS enhancements and lower limits of detection for thiram observed for the larger dogbone shaped gold nanoparticles. The sources that contribute to the higher SERS enhancements and lower limits of detection observed for the larger dogbone shaped gold nanoparticles are lightning rod effect, surface plasmon band λ_{max} being in much greater resonance to the laser excitation wavelength resulting in greater contributions from the electromagnetic enhancement effect, and more surface sites for thiram to bind to the nanoparticle surface due to a higher surface area.

Conclusions

We have developed a quantitative analytical solution-based direct readout SERS method for detection of thiram which is

a dithiocarbamate fungicide. Two different sizes of dogbone shaped gold nanoparticles are used as colloidal SERS substrates for SERS based detection of thiram. It is observed that using larger dogbone shaped gold nanoparticles results in lower limits of detection compared to using the smaller dogbone shaped gold nanoparticles. The lower limits of detection observed for the larger dogbone shaped gold nanoparticles could be attributed to the lightning rod effect, surface plasmon band λ_{max} being in much greater resonance to the laser excitation wavelength, and more surface sites for thiram to bind. There are higher contributions in the SERS intensities from the electromagnetic enhancement effect.

Acknowledgements

We thank Dr Richard Kingsley at the Electron Microscopy Facility for assistance in acquiring the TEM images. We thank the University of Rhode Island start-up funds, RI-INBRE Pilot Program, as well as the Society for Analytical Chemists of Pittsburgh starter grant for funding of this work.

References

- 1 D. L. Jeanmaire and R. P. VanDuyne, Surface Raman spectroelectrochemistry. Part I. Heterocyclic, aromatic, and aliphatic amines adsorbed on the anodized silver electrode, *J. Electroanal. Chem.*, 1977, **84**, 1.
- 2 M. G. Albrecht and J. A. Creighton, Anomalous intense Raman spectra of pyridine at a silver electrode, *J. Am. Chem. Soc.*, 1977, **99**, 5215.
- 3 M. Moskovits, Surface-enhanced Raman spectroscopy. A brief perspective, *Top. Appl. Phys.*, 2006, **103**, 1.
- 4 J. A. Dieringer, A. D. McFarland, N. C. Shah, D. A. Stuart, A. V. Whitney, C. R. Yonzon, M. A. Young, X. Zhang and R. P. Van Duyne, Surface enhanced Raman spectroscopy: new materials, concepts, characterization tools, and applications, *Faraday Discuss.*, 2006, **132**, 9.
- 5 C. L. Haynes, A. D. McFarland and R. P. VanDuyne, Surface-enhanced Raman spectroscopy, *Anal. Chem.*, 2005, **77**(17), 338A–346A.
- 6 M. Moskovits, Surface-enhanced Raman spectroscopy: a brief retrospective, *J. Raman Spectrosc.*, 2005, **36**(6–7), 485.
- 7 W. E. Smith, K. Faulds and D. Graham, Quantitative surface-enhanced resonance Raman spectroscopy for analysis, *Top. Appl. Phys.*, 2006, **103**, 381.
- 8 C. L. Haynes, C. R. Yonzon, X. Zhang and R. P. VanDuyne, Surface-enhanced Raman sensors: early history and the development of sensors for quantitative biowarefare agent and glucose detection, *J. Raman Spectrosc.*, 2005, **36**(6–7), 471.
- 9 S. C. Pinzaru, I. Pavel, N. Leopold and W. Kiefer, Identification and characterization of pharmaceuticals using Raman and surface-enhanced Raman scattering, *J. Raman Spectrosc.*, 2004, **35**(5), 338.
- 10 T. Vo-Dinh, SERS chemical sensors and biosensors: new tools for environmental and biological analysis, *Sens. Actuators, B*, 1995, **B29**(1–3), 183.
- 11 K. Faulds, W. E. Smith and D. Graham, DNA detection by surface enhanced resonance Raman scattering (SERRS), *Analyst*, 2005, **130**(8), 1125–1131.
- 12 A. E. Grow, L. L. Wood, J. L. Claycomb and P. A. Thompson, New biochip technology for label-free detection of pathogens and their toxins, *J. Microbiol. Methods*, 2003, **53**(2), 221–233.
- 13 K. Kneipp, H. Kneipp, I. Itzkan, R. R. Dasari and M. S. Feld, Surface-enhanced Raman scattering and biophysics, *J. Phys.: Condens. Matter*, 2002, **14**(18), R597–R624.
- 14 A. G. Ryder, Surface enhanced Raman scattering for narcotic detection and applications to chemical biology, *Curr. Opin. Chem. Biol.*, 2005, **9**(5), 489–493.
- 15 Z. Q. Tian, Surface-enhanced Raman spectroscopy: advancements and applications, *J. Raman Spectrosc.*, 2005, **36**(6–7), 466–470.

- 16 T. Vo-Dinh, Surface-enhanced Raman spectroscopy using metallic nanostructures, *TrAC, Trends Anal. Chem.*, 1998, **17**(8–9), 557–582.
- 17 T. Vo-Dinh, D. L. Stokes, in *Surface-Enhanced Raman Scattering (SERS) for Biomedical Diagnostics*, 2003, pp 64/1–64/39.
- 18 T. Vo-Dinh, F. Yan and D. L. Stokes, Plasmonics-based nanostructures for surface-enhanced Raman scattering bioanalysis, *Methods Mol. Biol.*, 2005, **300**, 255–283, Protein Nanotechnology.
- 19 S. Xu, X. Ji, W. Xu, B. Zhao, X. Dou, Y. Bai and Y. Ozaki, Surface-enhanced Raman scattering studies on immunoassay, *J. Biomed. Opt.*, 2005, **10**(3), 031112.
- 20 W. E. Doering, M. E. Piotti, M. J. Natan and R. G. Freeman, *Adv. Mater.*, 2007, **19**(20), 3100.
- 21 R. G. Freeman, W. E. Doering, I. D. Walton, S. G. Penn, G. Davis, F. Wong and M. J. Natan, *Proc. SPIE*, 2005, **5705**, 114.
- 22 S. P. Mulvaney, M. D. Musick, C. D. Keating and M. J. Natan, *Langmuir*, 2003, **19**(11), 4784.
- 23 M. El-Kouedi, C. D. Keating, *Nanobiotechnology*, 2004, p. 429.
- 24 G. A. Baker and D. S. Moore, Progress in plasmonic engineering of surface-enhanced Raman-scattering substrates toward ultra-trace analysis, *Anal. Bioanal. Chem.*, 2005, **382**(8), 1751–1770.
- 25 K. M. Spencer, J. M. Sylvia, P. J. Marren, J. F. Bertone and S. D. Christesen, Surface-enhanced Raman spectroscopy for homeland defense, *Proc. SPIE*, 2004, **5269**, 1–8, Chemical and Biological Point Sensors for Homeland Defense.
- 26 W. E. Smith, P. C. White, C. Rodger and G. Dent, Raman and surface enhanced resonance Raman scattering: applications in forensic science, *Pract. Spectrosc.*, 2001, **28**, 733–748, Handbook of Raman Spectroscopy.
- 27 A. M. Alak and D. Tuan Vo, Surface-enhanced Raman spectrometry of chlorinated pesticides, *Anal. Chim. Acta*, 1988, **206**(1–2), 333–337.
- 28 S. Bonora, M. Di Foggia and M. Iafisco, SERS in the analysis of pesticides (triazinic herbicides), *Chim. Ind.*, 2008, **90**(10), 98–100.
- 29 C. J. Lee, H. J. Kim, M. R. Karim and M. S. Lee, Surface-enhanced Raman spectroscopy of ethephone adsorbed on silver surface, *Bull. Korean Chem. Soc.*, 2006, **27**(4), 545–548.
- 30 D. Lee, S. Lee, G. H. Seong, J. Choo, E. K. Lee, D.-G. Gweon and S. Lee, Quantitative analysis of methyl parathion pesticide in a polydimethylsiloxane microfluidic channel using confocal surface-enhanced Raman spectroscopy, *Appl. Spectrosc.*, 2006, **60**(4), 373–377.
- 31 V. Lee and S. Farquharson, SERS sample vials based on sol-gel process for trace pesticide analysis, *Proc. SPIE*, 2001, **4206**, 140–146, Photonic Detection and Intervention Technologies for Safe Food.
- 32 J. Qiao, G. Zheng and F. Li, Determination of trace pesticide in water by surface enhanced Raman spectroscopy, *Huaxue Tongbao*, 2006, **69**(6), 462–464.
- 33 C. Shende, A. Gift, F. Inscore, P. Maksymiuk and S. Farquharson, Inspection of pesticide residues on food by surface-enhanced raman spectroscopy, *Proc. SPIE*, 2004, **5271**, 28–34, Monitoring Food Safety, Agriculture, and Plant Health.
- 34 C. S. Shende, F. Inscore, A. Gift, P. Maksymiuk and S. Farquharson, Analysis of pesticides on or in fruit by surface-enhanced Raman spectroscopy, *Proc. SPIE*, 2004, **5587**, 170–176, Nondestructive sensing for food Safety, Quality, and Natural Resources.
- 35 J. S. Kang, S. Y. Hwang, C. J. Lee and M. S. Lee, SERS of dithiocarbamate pesticides adsorbed on silver surface; thiram, *Bull. Korean Chem. Soc.*, 2002, **23**(11), 1604–1610.
- 36 M. S. Kim, J. S. Kang, S. B. Park and M. S. Lee, Surface-enhanced Raman spectroscopy of quinomethionate adsorbed on silver colloids, *Bull. Korean Chem. Soc.*, 2003, **24**(5), 633–637.
- 37 S. Sanchez-Cortes, C. Domingo, J. V. Garcia-Ramos and J. A. Aznarez, Surface-enhanced vibrational study (SEIR and SERS) of dithiocarbamate pesticides on gold films, *Langmuir*, 2001, **17**(4), 1157–1162.
- 38 S. Sanchez-Cortes, M. Vasina, O. Francioso and J. V. Garcia-Ramos, Raman and surface-enhanced Raman spectroscopy of dithiocarbamate fungicides, *Vib. Spectrosc.*, 1998, **17**(2), 133–144.
- 39 C. J. Orendorff, A. Gole, T. K. Sau and C. J. Murphy, Surface-enhanced Raman spectroscopy of self-assembled monolayers: sandwich architecture and nanoparticle shape dependence, *Anal. Chem.*, 2005, **77**(10), 3261–3266.
- 40 L. Gou and C. J. Murphy, Fine-tuning the shape of gold nanorods, *Chem. Mater.*, 2005, **17**(14), 3668–3672.
- 41 C. J. Murphy, T. K. Sau, A. M. Gole, C. J. Orendorff, J. Gao, L. Gou, S. E. Hunyadi and T. Li, Anisotropic metal nanoparticles: synthesis, assembly, and optical applications, *J. Phys. Chem. B*, 2005, **109**(29), 13857–13870.
- 42 T. K. Sau and C. J. Murphy, Room temperature, high-yield synthesis of multiple shapes of gold nanoparticles in aqueous solution, *J. Am. Chem. Soc.*, 2004, **126**(28), 8648–8649.
- 43 A. Torreggiani, Z. Jurasekova, M. D’Angelantonio, M. Tamba, J. V. Garcia-Ramos and S. Sanchez-Cortes, Fabrication of Ag nanoparticles by 1-irradiation: application to surface-enhanced Raman spectroscopy of fungicides, *Colloids Surf., A*, 2009, **339**, 60–67.
- 44 S. Sanchez-Cortes, M. Vasina, O. Francioso and J. V. Garcia-Ramos, Raman and surface-enhanced Raman spectroscopy of dithiocarbamate fungicides, *Vib. Spectrosc.*, 1998, **17**, 133–144.
- 45 S. Sanchez-Cortes, C. Domingo, J. V. Garcia-Ramos and J. A. Aznarez, Surface-enhanced vibrational study (SEIR and SERS) of dithiocarbamate pesticides on gold films, *Langmuir*, 2001, **17**, 1157–1162.
- 46 H. A. Biebuyck and G. M. Whitesides, Interchange between monolayers on gold formed from unsymmetrical disulfides and solutions of thiols: evidence for sulfur-sulfur bond cleavage by gold metal, *Langmuir*, 1993, **9**(7), 1766–1770.

Standoff detection via single-beam spectral notch filtered pulses

Adi Natan, Jonathan M. Levitt, Leigh Graham, Ori Katz, and Yaron Silberberg

Citation: *Appl. Phys. Lett.* **100**, 051111 (2012); doi: 10.1063/1.3681365

View online: <http://dx.doi.org/10.1063/1.3681365>

View Table of Contents: <http://apl.aip.org/resource/1/APPLAB/v100/i5>

Published by the [American Institute of Physics](#).

Related Articles

A two-color tunable infrared/vacuum ultraviolet spectrometer for high-resolution spectroscopy of molecules in molecular beams

Rev. Sci. Instrum. **83**, 014102 (2012)

Fast magneto-optical spectrometry by spectrometer

Rev. Sci. Instrum. **83**, 013103 (2012)

High resolution far-infrared Fourier transform spectroscopy of radicals at the AILES beamline of SOLEIL synchrotron facility

Rev. Sci. Instrum. **82**, 113106 (2011)

Tunable excitation source for coherent Raman spectroscopy based on a single fiber laser

Appl. Phys. Lett. **99**, 181112 (2011)

Characterization of near-terahertz complementary metal-oxide semiconductor circuits using a Fourier-transform interferometer

Rev. Sci. Instrum. **82**, 103106 (2011)

Additional information on *Appl. Phys. Lett.*

Journal Homepage: <http://apl.aip.org/>

Journal Information: http://apl.aip.org/about/about_the_journal

Top downloads: http://apl.aip.org/features/most_downloaded

Information for Authors: <http://apl.aip.org/authors>

ADVERTISEMENT



LakeShore Model 8404 developed with **TOYO Corporation**
NEW AC/DC Hall Effect System Measure mobilities down to 0.001 cm²/V s

Standoff detection via single-beam spectral notch filtered pulses

Adi Natan,^{a)} Jonathan M. Levitt, Leigh Graham, Ori Katz, and Yaron Silberberg
Department of Complex Systems, Weizmann Institute of Science, Rehovot 76100, Israel

(Received 22 November 2011; accepted 13 January 2012; published online 3 February 2012)

We demonstrate single-beam coherent anti-Stokes Raman spectroscopy (CARS), for detecting and identifying traces of solids, including minute amounts of explosives, from a standoff distance (>50 m) using intense femtosecond pulses. Until now, single-beam CARS methods relied on pulse-shapers in order to obtain vibrational spectra. Here, we present a simple and easy-to-implement detection scheme, using a commercially available notch filter that does not require the use of a pulse-shaper. © 2012 American Institute of Physics. [doi:10.1063/1.3681365]

Laser based remote detection and identification of hazardous materials, including biological warfare agents and explosives have recently been the focus of intense research efforts.^{1–7} In particular, it has been shown that the vibrational response of molecules provides a unique fingerprint for various molecular species and, hence, vibrational spectra can be used for identification.^{5–11} One such suitable technique for identifying vibrational spectra is coherent anti-Stokes Raman spectroscopy (CARS).¹² In CARS, pump ω_p and Stokes ω_s photons excite a vibrational level ω_{vib} that is subsequently probed with a probe photon ω_{pr} . The vibrational levels are resolved by measuring the scattered anti-Stokes photons located at $\omega_{vib} + \omega_{pr} = \omega_{AS}$, and coherent signal buildup occurs when $k_p - k_s + k_{pr} - k_{AS} = 0$. In conventional CARS, narrowband (ps) pump and probe beams are tuned such that $\omega_p - \omega_s = \omega_{vib}$ where a *single* vibrational level is excited. Multiplex CARS can also be achieved by using spectrally broader (fs) Stokes pulses to excite *multiple* bands of vibrational levels and identify them by measuring the spectrally resolved anti-Stokes photons.

CARS is typically challenging to implement due to the strict spatiotemporal overlap requirement of several beams from several sources.^{11–13} To overcome this issue, single-beam techniques have been developed using shaped, spectrally broad femtosecond pulses to simultaneously provide the necessary pump, Stokes, and probe photons.^{14–17} By employing single-beam techniques, spatiotemporal overlap is inherently achieved; however, the exclusive use of temporally short, femtosecond pulses results in a nonresonant four-wave mixing (FWM) signal that is orders of magnitude greater than the resonant CARS signal.^{15,16} The measured CARS signal is, therefore, the coherent sum of the resonant and nonresonant signals, as shown in Eq. (1).

A variety of CARS schemes have been developed in order to suppress the nonresonant background signal, such as tailoring the temporal width and delay of the probe-pulse,¹⁰ using polarization pulse shaping techniques,^{4,8} and employing coherent control.¹⁴ These schemes exploit different properties of the nonlinear FWM interaction to achieve the goal of background-free measurements. While these methods are effective for applications such as microscopy,^{14,18} they are

not necessarily suitable for long-range standoff probing of scattering samples. Under such conditions, polarization shaping is sensitive to the depolarization caused by the multiple random scattering in the sample. Furthermore, the nonresonant signal can serve to amplify the resonant signal and, thus, suppression can result in a remaining resonant signal that is too weak to be detected.

In this work, we demonstrate single beam standoff detection of traces of solids without using a complex pulse shaping apparatus or nonresonant background suppression. Instead, we use a commercially available notch filter as passive optical element and exploit the nonresonant signal in a homodyne amplification scheme.

For the notch filter, we use a resonant photonic crystal slab (RPCS), which is a waveguide etched with a subwavelength grating that creates a tunable notch feature in the spectrum (Figs. 1(a) and 1(b)). The notch can be adjusted over a wide spectral range by changing its angle with respect to the incident beam.¹⁹ The use of an RPCS as a passive shaping element has been recently demonstrated in single-pulse CARS micro-spectroscopy.²⁰ In this technique, the spectral notch feature serves as a narrow probe that allows for multiplex CARS detection. We exploit the strong nonresonant background and use it as a local oscillator in a homodyne amplification scheme:

$$I(\omega) = |P^{NR}(\omega) + P^R(\omega)|^2 \\ \simeq |P^{NR}(\omega)|^2 + 2|P^R(\omega)||P^{NR}(\omega)|\cos\phi(\omega), \quad (1)$$

where $I(\omega)$ is the measured signal intensity at frequency ω , P^R , and P^{NR} are the resonant and nonresonant signals, respectively, and ϕ is the relative spectral phase between them. Usually, with ultrashort pulses $|P^{NR}(\omega)|^2 \gg |P^R(\omega)|^2$, making the resonant signal challenging to measure.^{10,15,16}

However, the cross term is the product of a strong, smooth, and featureless nonresonant signal, with a weak resonant signal that has a typical spectral phase modulation around a vibrational resonance. The phase modulation is governed by the vibrational resonance lineshape and the phase structure of the RPCS notch resonance.¹⁵ As a result, the resonant feature is amplified by several orders of magnitude, allowing detection of the much weaker coherent Raman signal.

To demonstrate the ability to remotely detected back-scattered CARS signal, we probed samples with 30 fs pulses

^{a)}Author to whom correspondence should be addressed. Electronic mail: natan@stanford.edu.

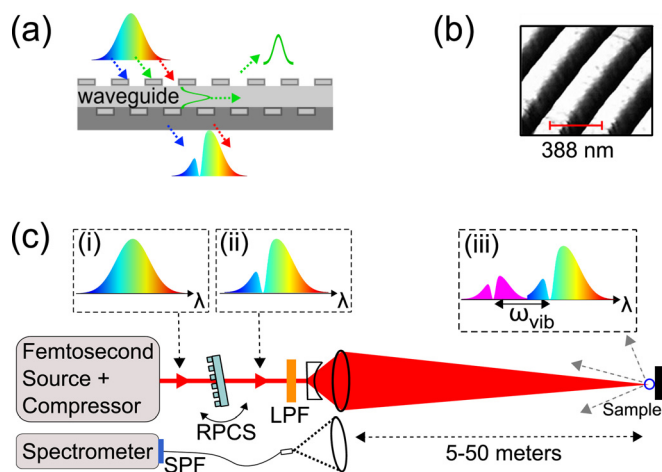


FIG. 1. (Color online) (a) Schematic diagram of the RPCS filter. (b) AFM image of the RPCS surface (from Thayil *et al.*, *Optics Express* **16**(17), 13315 (2008). Copyright © 2008). Reproduced with permission, © 2012 Optical Society of America. (c) The experimental setup. The broadband excitation pulse (i) is shaped with a tunable narrowband spectral notch by the RPCS filter (ii). A long-pass filter (LPF) is then used to attenuate the short-wavelength region. The spectral notch serves as a probe for the CARS process, generating narrow features which are blue-shifted from the probe by the vibrational frequencies (iii). The scattered light is collected, then short-pass filtered (SPF) and coupled to a spectrometer.

(Femtolasers GmbH) that were notch filtered by an RPCS filter. The pulses were then long-pass filtered around the spectral region that overlapped with the CARS signal, and focused on samples at distances of 5–50 m (Fig. 1(c)). The beam diameter on the sample was ≈ 1.5 mm, resulting in peak powers of $\approx 10^{11}$ W/cm². We collected the backscattered CARS signal from various materials using a single 7.5 in. lens imaging configuration. The light was then short-pass filtered and fiber coupled to a spectrometer (Horiba Jobin Ivon, Triax 321). We placed a black absorptive material behind the samples to eliminate the possibility of collecting specular reflections of the much stronger forward CARS signal. This is in contrast to previous studies that placed the sample on a reflective surface,⁸ while assuming the worst-case scenario for real-life situations, where a minute contribution to the signal due to diffusive reflections from the background material will occur. Such contribution can be estimated by $\rho D^2/16r^2$, with background reflectivity ρ , collecting lens diameter D at distance r from the sample, yielding an attenuation of at least 10^{-7} for the setup used. For each acquisition, we obtained two measurements, corresponding to different notch positions, spectrally separated by the notch width (≈ 1 nm). The CARS spectra were obtained with integration times ranging from 1 to 5 s. The typical signal power collected by the spectrometer was ≈ 1 pW. The dispersion induced by the propagation in air was compensated using the internal prism compressor of the laser source.

Typical CARS spectra from complimentary notch locations are shown in Fig. 2. The interference feature due to the resonant contribution at 1051 cm^{-1} is evident in the KNO_3 spectrum. In order to extract the Raman line, we normalized the differential measurement by P^{NR} (Ref. 20)

$$I_{CARS}(\omega) \propto \frac{I_n(\lambda+\Delta\lambda)(\omega)}{P_{n(\lambda+\Delta\lambda)}^{NR}(\omega)} - \frac{I_n(\lambda)(\omega)}{P_{n(\lambda)}^{NR}(\omega)}, \quad (2)$$

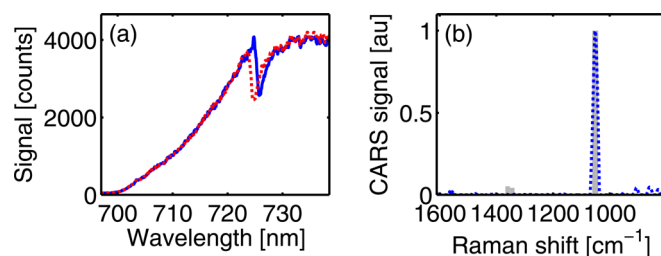


FIG. 2. (Color online) (a) Raw spectra of trace amount (<1 mg) of KNO_3 collected from a distance of 5 m, using two notch positions: 784 nm (dashed line) and 785 nm (solid line) with integration time of 3 s. (b) Taking the normalized difference of the two spectra by the non-resonant spectra (dashed line), the Raman line (solid line) is retrieved.

where $I_n(\lambda)$ is the intensity measured with a notch at wavelength λ , of width $\Delta\lambda$, and P^{NR} is approximated by smoothing $\sqrt{I_n(\lambda)(\omega)}$ using a moving average filter with 1 nm window following a median filter with 3 nm window. We have found that estimating P^{NR} for each notch acquisition helps reduce beam pointing fluctuations effects between the two acquisitions.

Experimentally resolved Raman spectra of traces of solids and explosives particles are presented in Fig. 3. The measured spectra are in a good agreement with the known Raman lines of the probed materials.⁹ In our experiments, the acquisition time was limited by the beam-point stability of the experimental setup. For example, the missing Raman lines in Fig. 3(a) were detectable in shorter distances (not shown); however, the limited beam pointing stability and the available laser bandwidth obscure them at longer distances. Actively stabilizing the beam would reduce signal fluctuations between measurements and allow shorter measurement times. Other alternative shaping techniques could also be used to generate a similar spectral notch-like feature. For example, the use of an interference filter, Fabry-Perot interferometer, or fiber Bragg grating would yield similar results.

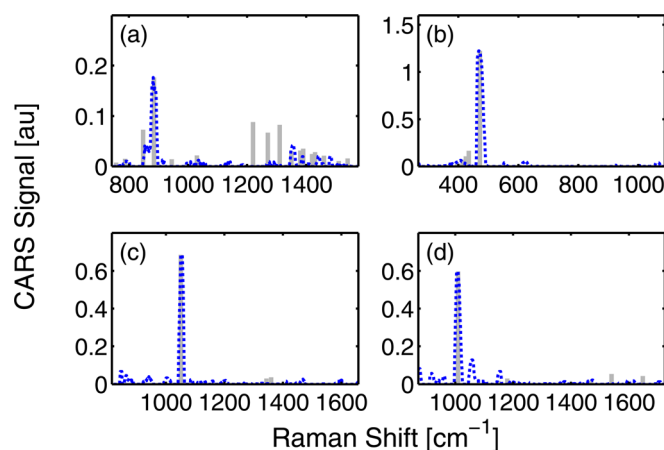


FIG. 3. (Color online) Resolved CARS spectra of several scattering samples (dashed line). (a) Cyclotrimethylene-trinitramine (RDX/T4) <1 mg (b) sulfur powder $<500\ \mu\text{g}$ (c) crystallized potassium nitrate (KNO_3) <1 mg (d) crystallized urea <4 mg. Spectra were obtained at a standoff distances of (a) 24 m and (b-d) 50 m, with integration times of (a) 3 s (b) 5 s (c) 5 s (d) 1 s. The samples have glass like morphology. The Raman lines (solid line) are plotted for reference.

However, these lack the simplicity, compactness, and compatibility with high intensities.

Femtosecond CARS spectroscopy using a spectral notch filter has numerous advantages over other single beam techniques. The RPCS is virtually alignment free and has broad tunability allowing for flexibility in the detection window, while nearly eliminating the inherent losses of grating based pulse shapers. A transmission of almost unity is particularly beneficial as the CARS signals are cubically proportional to the pulse intensity. Moreover, the RPCS can be mounted on a galvanometric mirror to achieve rapid (KHz) modulation rates that are 1.5 orders of magnitude faster than typical liquid crystal spatial light modulators (LC-SLMs) allowing lock-in detection and fast scanning. Additional signal enhancement can be made using multiple notch filters. By spectral positioning of several notches spaced by the vibrational lines of a known substance, the coherent addition of signals from several vibrational levels will generate a feature, which is significantly larger than the linear sum of the individual contributions.²¹

We thank S. Soria for providing the RPCS filter and the AFM image used in this work.¹⁹ We also thank E. Grinvald, G. Elazar, and G. Han for invaluable help. This work was supported in parts by DHS Center of Excellence of Explosives Detection, Mitigation, Response and by NATO Project No. SfP-983789. J.M.L. was supported by the European MC-ITN FASTQUAST.

¹National Research Council, Committee on the Review of Existing and Potential Standoff Explosives Detection Techniques, *Existing and Potential Standoff Explosives Detection Techniques* (National Academies, Washington, DC, 2004).

- ²S. Wallin, A. Pettersson, H. Östmark, and A. Hobro, *Anal. Bioanal. Chem.* **395**, 259 (2009).
- ³P. R. Hemmer, R. B. Milesb, P. Polynkinc, T. Sieberta, A. V. Sokolova, P. Spranglee, and M. O. Scully, *Proc. Natl. Acad. Sci. U.S.A.* **108**, 3130 (2011).
- ⁴M. T. Bremer, P. J. Wrzesinski, N. Butcher, V. V. Lozovoy, and M. Dantus, *Appl. Phys. Lett.* **99**, 101109 (2011).
- ⁵A. Portnov, S. Rosenwaks, and I. Bar, *Appl. Phys. Lett.* **93**, 041115 (2008).
- ⁶J. C. Carter, S. M. Angel, M. Lawrence-Snyder, J. Scaffidi, R. E. Whipple, and J. G. Reynolds, *Appl. Spectrosc.* **59**, 6 (2005).
- ⁷D. Pestov, X. Wang, G. O. Ariunbold, R. K. Murawski, V. A. Sautenkov, A. Dogariu, A. V. Sokolov, and M. O. Scully, *Proc. Natl. Acad. Sci. U.S.A.* **105**, 2 (2008).
- ⁸H. Li, D. A. Harris, B. Xu, P. J. Wrzesinski, V. V. Lozovoy, and M. Dantus, *Opt. Express* **16**, 5499 (2008).
- ⁹O. Katz, A. Natan, Y. Silberberg, and S. Rosenwaks, *Appl. Phys. Lett.* **92**(17), 171116 (2008).
- ¹⁰D. Pestov, R. K. Murawski, G. O. Ariunbold, X. Wang, M. Zhi, A. V. Sokolov, V. A. Sautenkov, Y. V. Rostovtsev, A. Dogariu, Y. Huang *et al.*, *Science* **316**, 265 (2007).
- ¹¹B. Schrader, *Infrared and Raman Spectroscopy* (VCH, Weinheim, 1995).
- ¹²A. Volkmer, *J. Phys. D: Appl. Phys.* **38**, R59 (2005).
- ¹³C. L. Evans and S. X. Xie, *Annu. Rev. Anal. Chem.* **1**(1), 883 (2008).
- ¹⁴N. Dudovich, D. Oron, and Y. Silberberg, *Nature* **418**(6897), 512 (2002).
- ¹⁵D. Oron, N. Dudovich, and Y. Silberberg, *Phys. Rev. Lett.* **89**(27), 273001 (2002).
- ¹⁶S. H. Lim, A. G. Caster, and S. R. Leone, *Opt. Lett.* **32**, 10 (2007).
- ¹⁷C. Müller, B. Tiago, B. von Vacano, and M. Motzkus, *J. Raman Spectrosc.* **40**, 809 (2009).
- ¹⁸X. S. Xie, J. Yu, and W. Y. Yang, *Science* **312**, 228 (2006).
- ¹⁹A. Thayil, A. Muriano, J. P. Salvador, R. Galve, M. P. Marco, D. Zalvidea, P. Loza-Alvarez, T. Katchalski, E. Grinvald, A. A. Friesem *et al.*, *Opt. Express* **16**(17), 13315 (2008).
- ²⁰O. Katz, J. M. Levitt, E. Grinvald, and Y. Silberberg, *Opt. Express* **18**, 22693 (2010).
- ²¹D. Oron, N. Dudovich, and Y. Silberberg, *Phys. Rev. A* **70**, 023415 (2004).

Development of Novel Composite Materials & Structures for Blast Mitigation

Arun Shukla

with Nate Gardner, Erheng Wang, Puneet Kumar, Jefferson Wright
Mechanical Engineering Dept, University of Rhode Island

Details

Task 1: Gas Compressibility during Air-blast (Shock wave) Loading

A new fluid-structure interaction model that considers high gas compressibility has been developed using the Rankine-Hugoniot relations. The impulse conversion between the gas and the structure was utilized to determine the reflected pressure profile from the known incident pressure profile. The physical parameters of the gas such as the shock front velocity, gas density, local sound velocity, and gas particle velocity, as well as the impulse transmitted onto the structure were also evaluated. A series of one-dimensional shock wave loading experiments on free-standing monolithic aluminum plates were conducted using a shock tube apparatus to validate the proposed model. The momentum was evaluated using high-speed digital imagery. The experimental reflected pressure profile, along with the peak reflected pressure, and the momentum transmitted onto the plate were compared to the predicted results. The comparisons show that the gas's compressibility significantly affects the fluid-structure interaction behavior, and the new model can predict more accurate results than the existing models. The effects of factors, such as the areal density of the plate and the peak incident pressure, on momentum transfer are also discussed using the present model. Moreover, the maximum achievable momentum and the fluid-structure interaction time are defined and calculated.

Theoretical Considerations – Fluid-Structure Interaction

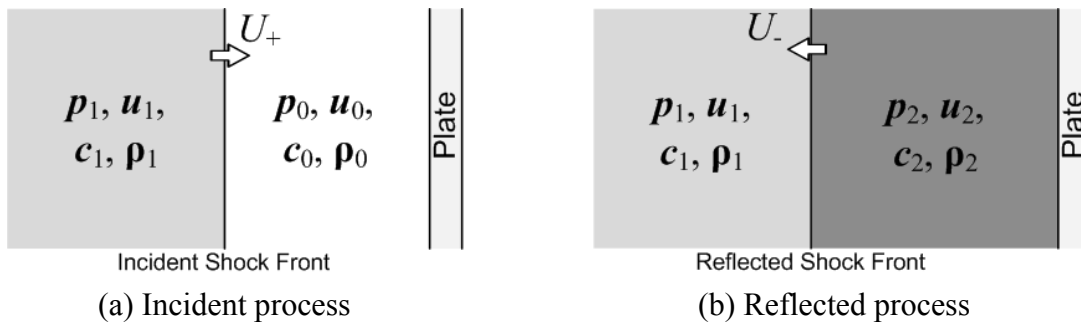


Fig. 4 Sketch of the incident and the reflected shock processes

Consider a planar shock wave impinging normally and uniformly upon an infinite free-standing monolithic plate with an areal density m_s . Fig. 4 shows a typical shock wave loading process. A planar incident shock wave front is traveling from the left side to the right side (incident process, Fig. 4a). The right side of the incident wave front is undisturbed gas, while the left side of incident wave front is the high pressure gas driven by the incident shock wave. After the incident shock wave impinges on a static free-standing flat plate, a reflected planar shock wave is generated and travels from the right side to the left side (reflected process, Fig. 4b). The

left side of the reflected wave front is still the high pressure gas driven by the incident shock wave, while the right side of the reflected wave front is now the gas that is disturbed by the reflected shock wave. Moreover, at this time the plate will move with a velocity that is equal to the particle velocity of the gas behind the reflected shock wave front. U_+ and U_- are the velocities of the incident and the reflected shock wave fronts, respectively. The state of the gas can be defined using the following physical parameters:

- p the pressure
- u the particle velocity
- c the sound velocity
- ρ the density

The subscript 0 on the parameters denotes the initial state of the gas. Subscript 1 represents the state of the gas located behind the incident shock wave front and this is defined as the incident state. Subscript 2 represents the state of the gas located behind the reflected shock wave front and this will be defined as the reflected state.

The incident pressure p_1 behind the incident shock wave front and reflected pressure p_2 behind the reflected shock wave front are all assumed to have exponential decay profiles. This will be shown to be true later from experimental data. They can be expressed as,

$$p_1(t) = p_{1_peak} e^{-\frac{t}{\theta_1}}, \quad 0 \leq t \leq \infty \quad (1a)$$

$$p_2(t) = p_{2_peak} e^{-\frac{t}{\theta_2}}, \quad 0 \leq t \leq \infty \quad (1b)$$

where, p_{1_peak} and p_{2_peak} are the peak pressures for the incident and reflected pressure pulses, respectively. θ_1 and θ_2 are the time constants for the incident and reflected pressure. Furthermore, assume t_{1+} and t_{2+} are the positive time periods for the incident and reflected pressures.

From the shock wave loading processes described in Fig. 4, it can be seen that the plate is subjected to the reflected pressure, p_2 , during the entire reflection process. Therefore, the impulse per unit area transmitted to the specimen, i.e. the final momentum per unit area of the specimen, is,

$$I_{impulse} = \int_0^{t_{2+}} [p_2(t) - p_0] dt \quad (2)$$

Normally, the physical parameters of the undisturbed gas, p_0 , u_0 , c_0 , and ρ_0 are known parameters. The pressure profile p_1 behind the incident shock wave front can be measured. However, other parameters, such as p_2 , u_1 , u_2 , c_1 , c_2 , ρ_1 , ρ_2 , U_+ and U_- are all unknown parameters and are difficult to measure on-site. The absence of these physical parameters makes it difficult to evaluate the loading history of the plate. The following analysis proposes a methodology to calculate all of these unknown parameters based on the one-dimensional gas-dynamic theory.

Comparison of Experimental and Analytical Results – Reflected Pressure Profile

The experimental and analytical results of the peak reflected pressure as a function of the incident pressures are shown in Fig. 5. The peak reflected pressure at time $t = 0$ from Taylor's model is also shown in this figure. It can be seen that the experimental data follows the predicted trend very well. Taylor's model gives much lower prediction results. The model prediction has

also been compared with the experimental data for various other materials tested in our lab and the results are shown in Fig. 6. It is evident that the reflected peak pressure only depends on the incident peak pressure, and the compressibility of the gas highly affects the results.

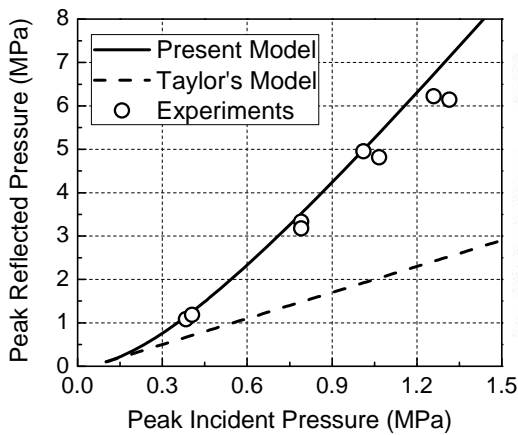


Fig. 5 The relation between peak incident and peak reflected pressures

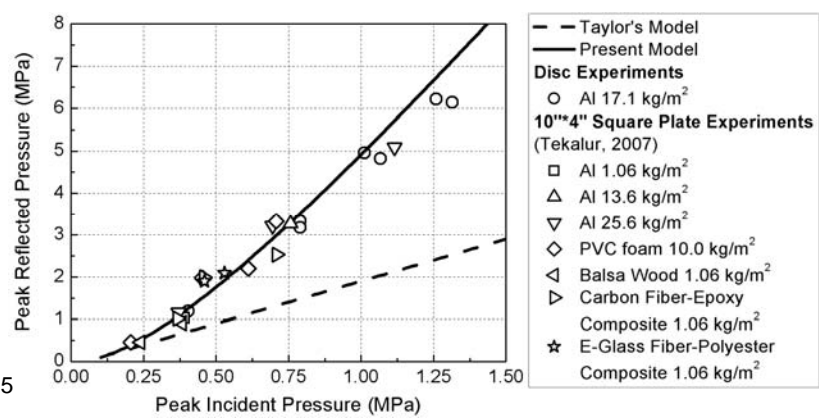


Fig. 6 The relation between peak incident and peak reflected pressures (more experimental results)

Task 2: Blast Response Carbon-fiber Composite Panels

Experimental studies were conducted to understand the effect of plate curvature on the blast response of 32 layered carbon-fiber epoxy panels. A shock tube apparatus was utilized to impart controlled shock loading on carbon-fiber panels having three different radii of curvatures; infinite (panel A), 305 mm (panel B), and 112 mm (panel C). These panels with dimensions of 203 mm x 203 mm x 2 mm were held under clamped boundary conditions during the shock loading. A 3-D Digital Image Correlation (DIC) technique coupled with high-speed photography was used to obtain out-of-plane deflection and velocity, as well as in-plane strain on the back face of the panels. There were two types of dominant failure mechanisms observed in all the three panels: fiber breakage and inter-layer delamination. The fiber breakage initiated from the face exposed to shock loading (front face) and continued to the interior. Delamination occurred on the side of the specimen as well as on the front face. Energy analysis was also performed which showed that panel C had the best energy dissipation property. Macroscopic post-mortem analysis and DIC results showed that panel C can mitigate higher intensity (pressure) shock waves without initiation of catastrophic damage in the panel. Panel B could sustain the least shock wave intensity and exhibited catastrophic failure. Panel A exhibited intermediate blast mitigation capacity.

Material details

Carbon fiber epoxy panels with three different radii of curvature were utilized in the experiments: infinite radius of curvature (Panel A), 304.8 mm radius of curvature (Panel B) and 111.8 mm radius of curvature (Panel C). The specimens are shown in Fig. 7. The specimens were fabricated using ready-to-cure sheets of unidirectional AS4/3501-6 material manufactured by the Hercules Corporation of Magna, Utah. These sheets were manufactured by pulling a row of uniformly spaced fibers through resin bath. The spacing between the fibers determines the ratio

of fiber volume to total volume of the material. After stacking 32 plies of this unidirectional material in the desired orientation, the panels were vacuum bagged and then placed in autoclave for curing. The curved panels were manufactured in the same way as described above with a difference that cylindrically curved pre-forms were used for laminate lay-up and curing.

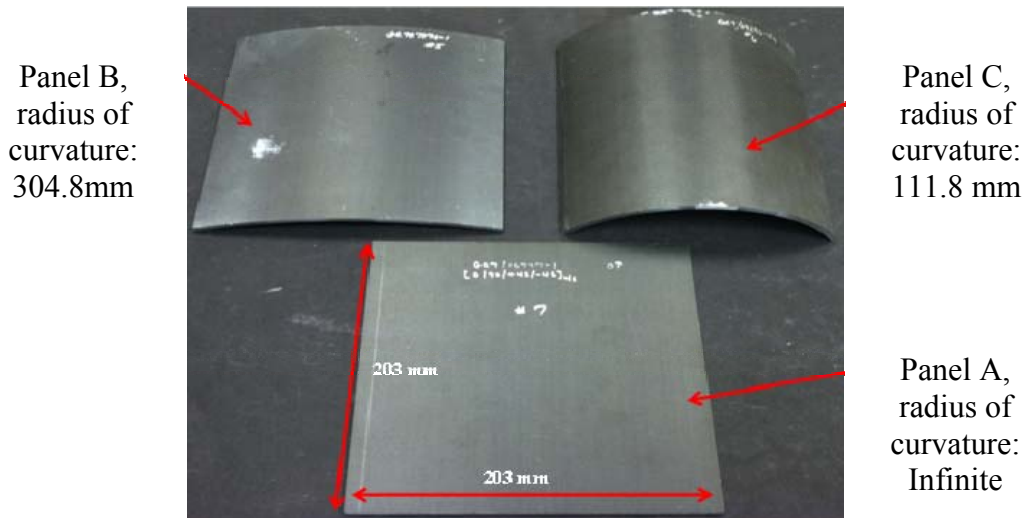


Fig. 7 Specimens and geometries

The orientation of the individual unidirectional plies that comprised the composite laminate was selected to simulate quasi-isotropic properties ($[0/90/+45/-45]_{4s}$). The specimens were 203 mm long x 203 mm wide x 2 mm thick, made out of 32 layers of carbon fibers. For the case of curved panels, the arc length of the curved edges corresponds to the plate length.

Digital Image Correlation (DIC) Analysis

The DIC technique was used to better understand the overall behaviors and deformations of the various specimens (three geometries). The shock tube used in this study provides a uniform pressure pulse over a circular area of 4562 mm^2 (muzzle area). This is verified by the DIC image of the out of plane displacement on flat plate during shock impingement as shown in Fig. 8. The image taken at $50 \mu\text{s}$ shows that the flat panel had a uniform deflection of $3 \text{ mm} \pm 0.2 \text{ mm}$ within a central region of diameter 70 mm. As the muzzle diameter of the shock tube is 76 mm, the uniform deflection contour constitutes about 92% of the total loaded area. This out of plane deflection decays to 0 mm from 3 mm in an area of thickness 3 mm beyond this central region. As the radius of

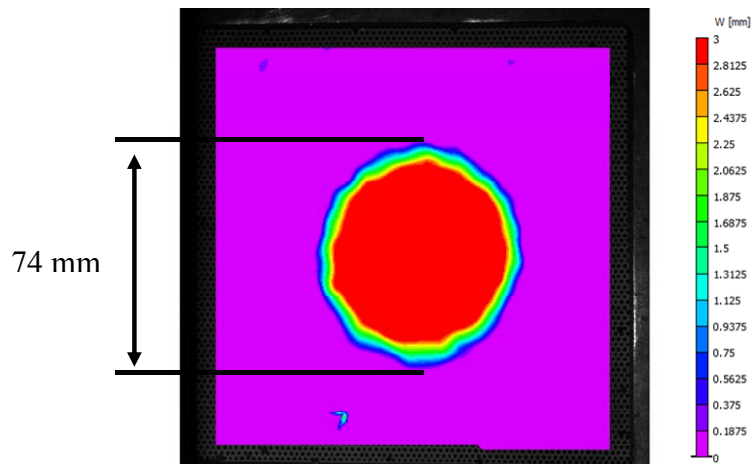


Fig. 8 DIC analysis showing the loading area during shock impingement on a flat panel at $t = 50 \mu\text{s}$.

curvature decreases the circular loading area changes to elliptical loading area (Fig. 9a). As the panels become curved, the shock loading starts acting on the projected area which causes it to change its shape from circular to elliptical.

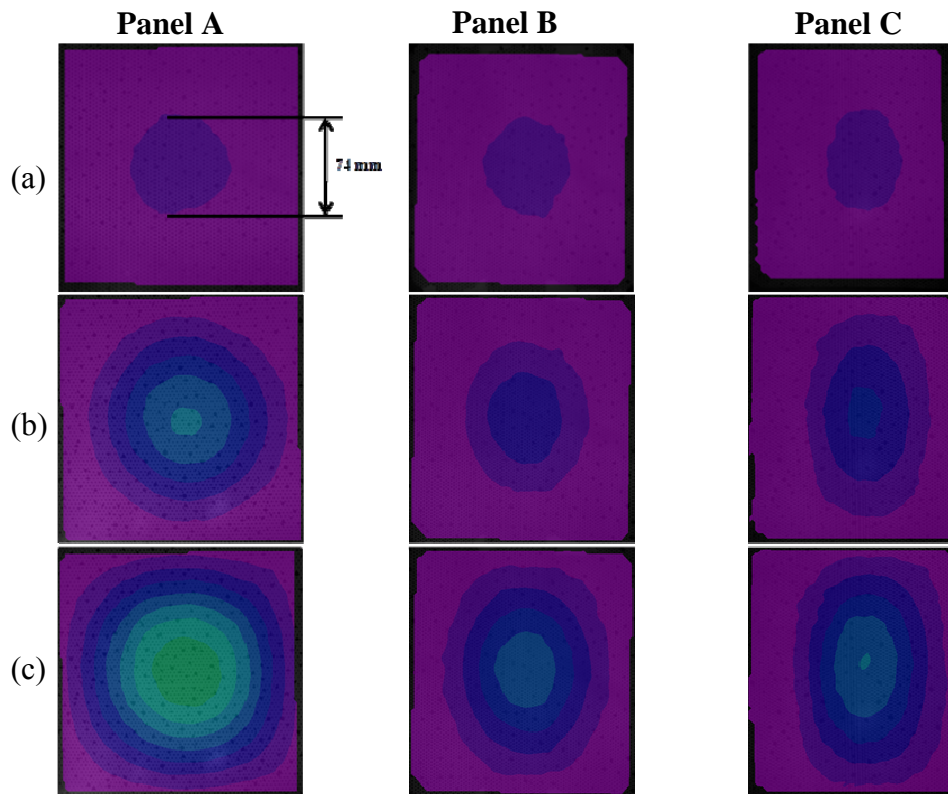


Fig. 9 DIC analysis showing the loading area during shock impingement at (a) $t = 50 \mu\text{s}$, (b) $t = 100 \mu\text{s}$, (c) $t = 150 \mu\text{s}$.

The full-field deflection at $100 \mu\text{s}$, $150 \mu\text{s}$ is shown in Fig. 9b and Fig. 9c respectively. During the early part of shock loading, the out-of-plane deflection contours are not influenced by the boundary conditions. The deflection in panel A starts as a circular region (Fig. 9), which continues till $150 \mu\text{s}$. This is a localized circular deflection contour, which has roughly the same diameter as that of the muzzle (at $t = 50 \mu\text{s}$). At $t = 150 \mu\text{s}$, the boundary conditions start affecting the development of deflection contours in the panel. The stress waves generated in the specimen travel outward and are reflected from the boundary. This reflected stress wave causes the change in the shape of the deflection contours.

The full-field deflection at the failure loading for the panels is shown in Fig. 10. The total deflection in these panels subjected to blast loading comprises of two distinct regions, namely, the indentation region followed by the flexural deflection (Fig. 11). During indentation, localized deflection superposes onto the overall deflection. In case of flexure, the overall deflection starts to overpass the localized deflection. The indentation deflection is localized around the loading area whereas a full field deflection over the area of the specimen being loaded is predominant in flexural mode. Also, the boundary conditions affect the deflection in case of flexural mode. Panels B and C had elliptical deflection contour at $200 \mu\text{s}$ (Fig. 9 & 10). Since both these panels are curved, the shock wave impinges on the projected area and creates localized elliptical

deflection contour (it is more clearly seen in Fig. 9). In panel B, the boundary condition starts affecting the deflection development after 200 μs (Fig. 9 & 10). Thus, the elliptical deflection contour in panel B starts changing to rectangular shape. Also, the deflection mode in panel B changes from indentation to flexural mode at this time. The deflection in panel C continues to develop further with elliptical contour. The deflection is primarily because of indentation and boundary conditions do not affect the deflection contours. As such, it retains its elliptical deflection profile throughout the loading process (Fig. 9 & 10).

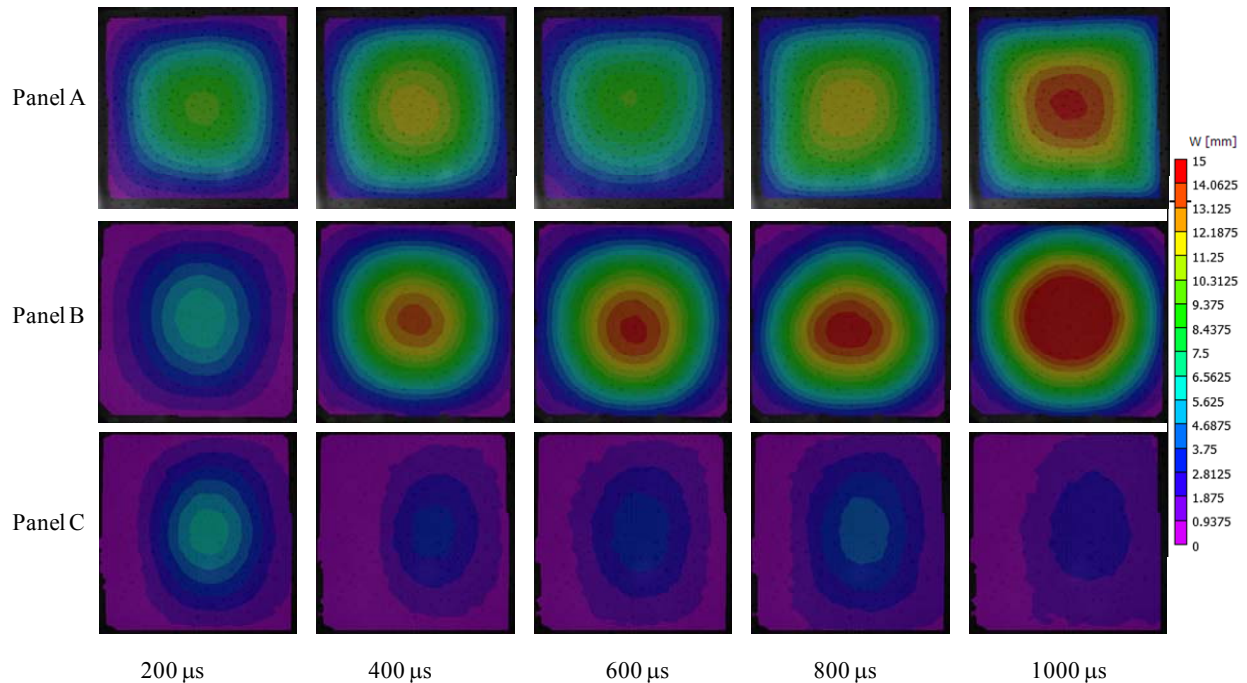


Fig. 10 Full field deformation of panels from 3-D-DIC analysis

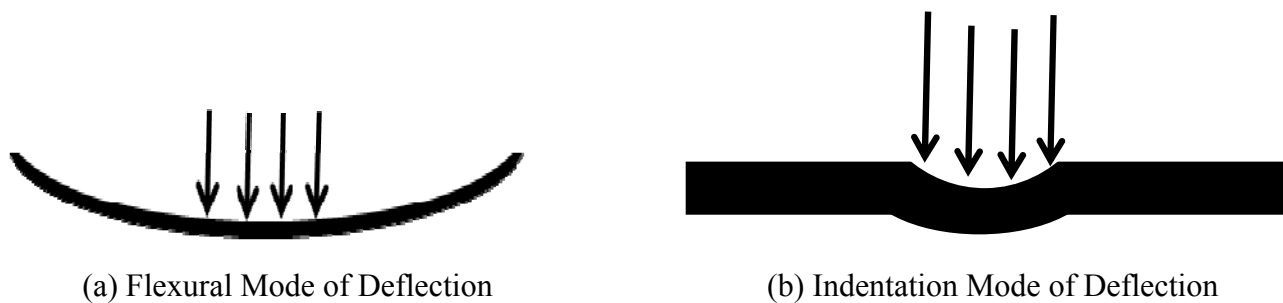


Fig. 11 Modes of deflections for the panels

Macroscopic Post-mortem Analysis

The results of post-mortem evaluation of the shock loaded carbon fiber epoxy panels are shown in Fig. 12. The post-mortem analysis of Panel A (flat panel, infinite radius of curvature) and Panel B (radius of curvature of 304.8 mm), as shown in Fig. 12a and Fig. 12b respectively, reveals heavy inter-laminar delamination and fiber breakage. Unlike Panel A and Panel B, Panel C (Fig. 12c) exhibited no fiber breakage or delamination, even though it was subjected to twice the blast pressure as the other two panels. It did however show some charring on the front face due to the ionization of the impinging gas (occurs at higher levels of loading/pressure)



Panel A



Panel B



Panel C

Fig. 12 Post-mortem evaluation of carbon-fiber epoxy panels

Task 3: Effect of Equivalent Core Layer Thickness vs. Equivalent Core Layer Mass on Blast Response of Sandwich Structures

The dynamic behavior of sandwich composites made of E-glass Vinyl-Ester (EVE) facesheets and Corecell™ A-series foam were studied using a shock tube apparatus. The materials, as well as the core layer arrangements, and overall specimen dimensions were identical, with the only difference appearing in the core layers; one configuration utilized equivalent core layer thickness, while the other configuration utilized equivalent core layer mass. The foam core itself was layered based on monotonically increasing the acoustic wave impedance ($Z = \rho C$, where ρ is the density of the material and C is the one-dimensional wave speed) of the core layers, with the lowest wave impedance facing the shock loading. During the shock tube testing, high-speed photography system coupled with the optical technique of 3-D Digital Image Correlation (DIC) was utilized to capture the real-time deformation process as well as mechanisms of failure. Post-mortem analysis was carried out to evaluate the overall blast performance of these two configurations. The results indicated that with a decrease in areal density of $\sim 1 \text{ kg/m}^2$ (5%) from the sandwich composites with equivalent core layer thickness to the sandwich composites with equivalent core layer mass, an increase in deflection (20%), in-plane strain (8%) and velocity (8%) was observed.

Material details

The facesheet materials that were utilized in this study are E-glass Vinyl-Ester (EVE) composites. The woven roving E-glass fibers of the skin material consisted of 8 layers of plain weave fabric placed in a quasi-isotropic layout $[0/45/90/-45]_s$. The fibers were made of the 0.61 kg/m^2 areal density plain weave. The resin system used was Ashland Derakane Momentum 8084, with the front and back skins (facesheets) consisting of identical layups and materials. The EVE

composite consisted of a 55% / 45% volume fraction of glass (fiber) to resin, as determined using proper ASTM standard D 2584. Fig. 13 shows a schematic of the sandwich composite with skin and core materials.

The core materials used in the present study are Corecell™ A-series styrene acrylonitrile (SAN) foams, which are manufactured by Gurit SP Technologies specifically for marine sandwich composite applications. The two types of Corecell™ A-series foam that were used in present study were A300 and A800. The cell structures for the two foams are similar and the only difference appears in the cell wall thickness and node sizes, which accounts for the different densities of the foams.

The Vacuum Assisted Resin Transfer Molding (VARTM) process was utilized to fabricate the sandwich specimens. During the VARTM process, the sandwich specimens were infused under the same conditions, i.e. temperature, humidity, and vacuum pressure (760 mmHg (1 atm)), with the same volume of resin. The overall dimensions for the samples were approximately 102 mm wide, 254 mm long and 48 mm thick. The foam core itself was approximately 38 mm thick, while the skin thickness was approximately 5 mm.

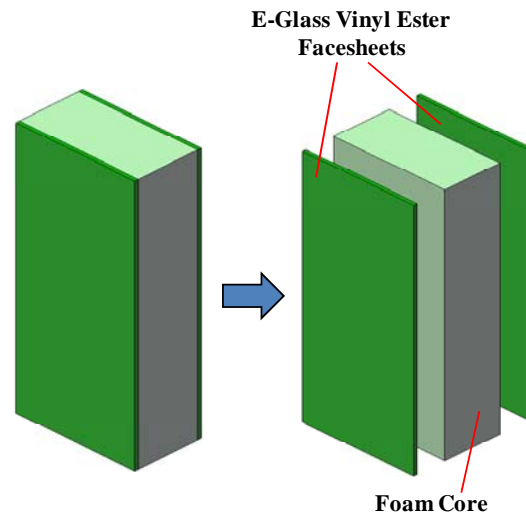


Fig. 13 Schematic of sandwich composite with skin and core

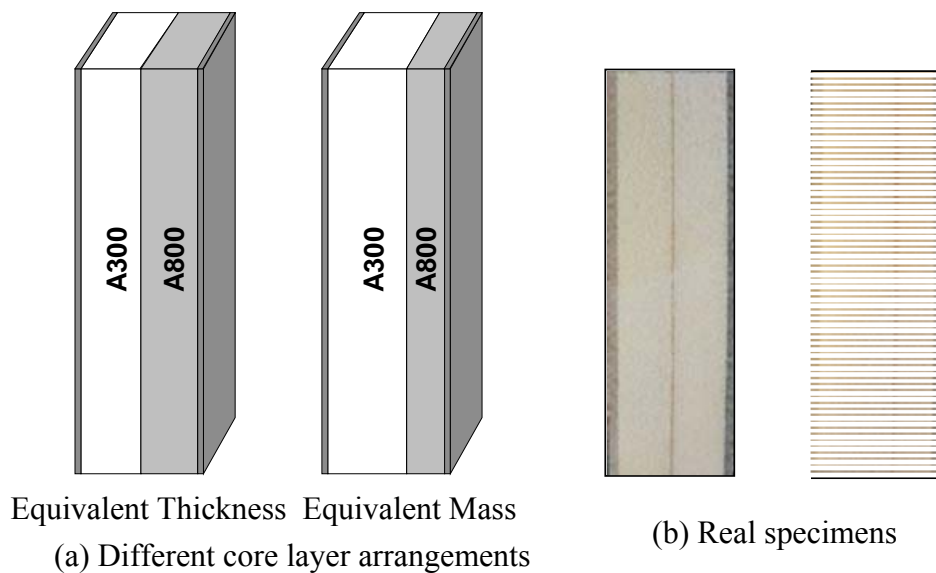


Fig. 14 Specimen design and core configuration

For the sandwich composites utilized in this study, two different core layer arrangements were investigated (as shown in Fig. 14). Both configurations consisted of two core layers of foam, A300 and A800 respectively, and were arranged based on monotonically increasing the acoustic wave impedance (A300/A800). It should be noted that the first core layer of foam,

A300, is the one first exposed to the shock wave loading. For the sandwich composites with equivalent core layer thickness, both foam layers had equivalent layer thickness (19 mm), resulting in an overall areal density of approximately 18.5 kg/m^2 . For the sandwich composites with equivalent core layer mass, the mass of the individual foam layers was equivalent. Due to specific dimensions and material availability from the manufacturer [Gurit SP Technology], the thickness of the A300 and A800 foam were 25.4 mm and 12.7 mm respectively. This resulted in panels with an overall areal density of approximately 17.6 kg/m^2 .

Real – time Deformation and Analysis

The real-time observations of the transient behavior for both sandwich composite panels subjected to shock wave loading are shown in Fig. 15. The shock wave (pressure wave) propagates from the right side of the image to the left side and some detailed deformation mechanisms are pointed out in the figures. It should be noted that the time scheme used to represent the images in each configuration is identical. Therefore, for each of the four configurations investigated, the images are correlated based on the same time per frame. This allows for a better comparison between the different configurations in regards to the failure mechanisms and extent of damage observed.

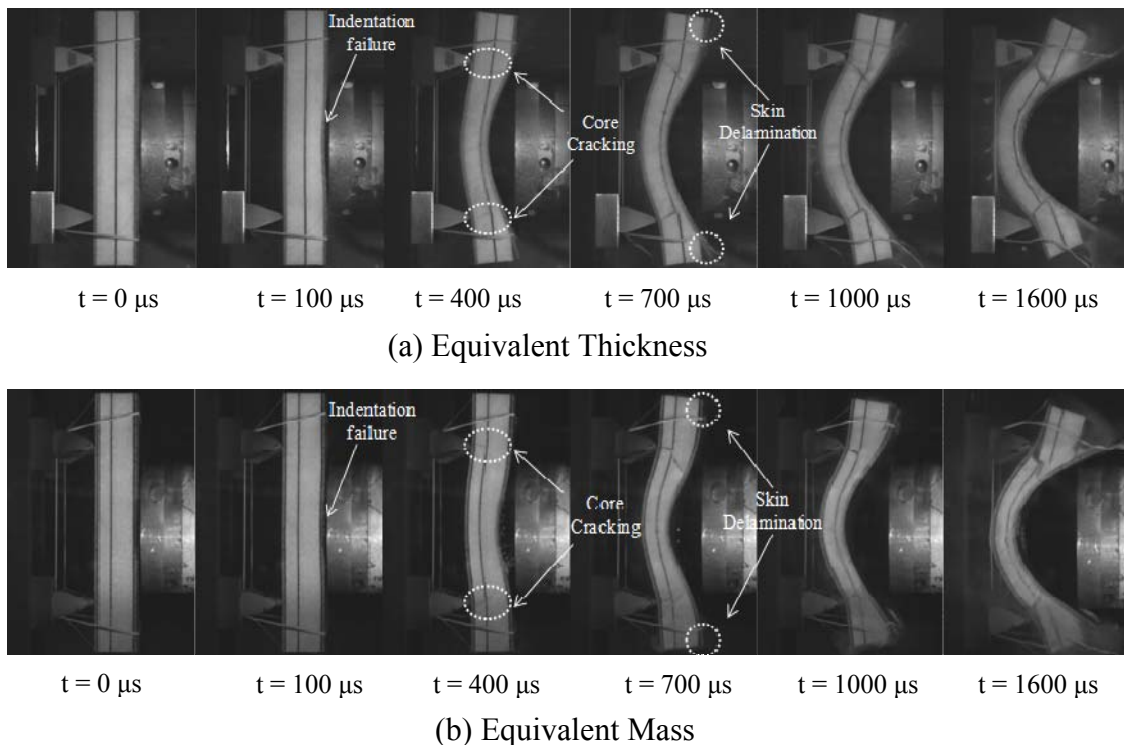


Fig. 15 High-speed images for both core configurations

For the sandwich composites with equivalent core layer thickness, as shown in Fig. 15a, it can be observed that at $t = 100 \mu\text{s}$ indentation failure of the core has initiated. This means that compression has initiated in the first core layer of foam (A300). By $t = 400 \mu\text{s}$, the A300 layer has continued to compress and core cracking has initiated in the A800 layer where the supports are located. By $t = 700 \mu\text{s}$ more core cracking can be observed, as well as skin delamination

between the front skin and the first core layer of foam (located at the top and bottom of the specimen). Also at this time, the core compression in the first layer of foam (A300) has reached a maximum (13 mm), approximately 75% of its original layer thickness (19 mm). After this time, the response of the specimen is global bending and by $t = 1600 \mu\text{s}$, no new failure mechanisms were observed. Also the core cracks have propagated completely through the foam core to the front facesheet, and there is heavy skin delamination between the front facesheet and the first core layer of foam.

For the sandwich composites with equivalent core layer mass, as shown in Fig. 15b, it can be observed that at $t = 100 \mu\text{s}$ indentation failure of the core has initiated. This means that compression has initiated in the first core layer of foam (A300). By $t = 400 \mu\text{s}$, the A300 layer has continued to compress and core cracking has initiated in the A800 layer where the supports are located. By $t = 700 \mu\text{s}$ more core cracking can be observed, as well as skin delamination between the front skin and the first core layer of foam (located at the top and bottom of the specimen). By $t = 1000 \mu\text{s}$, the damage mechanisms have continued to propagate, and the core compression in the first layer of foam (A300) has reached a maximum (19 mm), approximately 75% of its original layer thickness (25.4 mm). After this time, the response of the specimen is global bending and by $t = 1600 \mu\text{s}$, no new failure mechanisms were observed. Also the core cracks have propagated completely through the foam core to the front facesheet, and there is heavy skin delamination between the front facesheet and the first core layer of foam.

It was observed in both configurations, equivalent core layer thickness and equivalent core layer mass, that the deformation mechanisms were identical. Both configurations exhibited a double-winged deformation shape which means both configurations were under shear loading. Indentation failure was followed by core compression of the first layer of foam (A300) and core cracking, and finally skin delamination between the front facesheet and foam core. The extent of the damage mechanisms varies between configurations, but the time at which the damage mechanisms were observed is identical.

Macroscopic Post-mortem Analysis

After the blast loading event occurred, the damage patterns of the sandwich composites with both core layer arrangements were visually examined and recorded using a high resolution digital camera and are shown in Fig.16. Note the locations and damage mechanisms were identical for both configurations; the only difference was in the extent of damage observed. When the sandwich composite with equivalent core layer thickness was subjected to highly-transient loading, as shown in Fig. 16a, the damage was confined to the areas where the supports were located in the shock tube and core cracking is visible in these two areas. The core cracks propagated completely through the foam core. Core delamination is visible between the front facesheet and the foam core. Also, the core cracks lead to back skin delamination, where the core separated from the back facesheet. Some core compression is also visible in the first core layer (A300) of foam.

For the sandwich composite with equivalent core layer mass, the damage patterns after being subjected to the shock loading are shown in Fig. 16b. For this core configuration, the damage was again confined to the areas where the supports were located in the shock tube and

core cracking is evident. The core cracks propagated completely through the foam core. Skin delamination is obvious between the front facesheet and the foam core, as well as back skin delamination between the back facesheet and the foam core. Also, heavy front face fiber delamination and core compression in the first layer of foam (A300) can be observed.

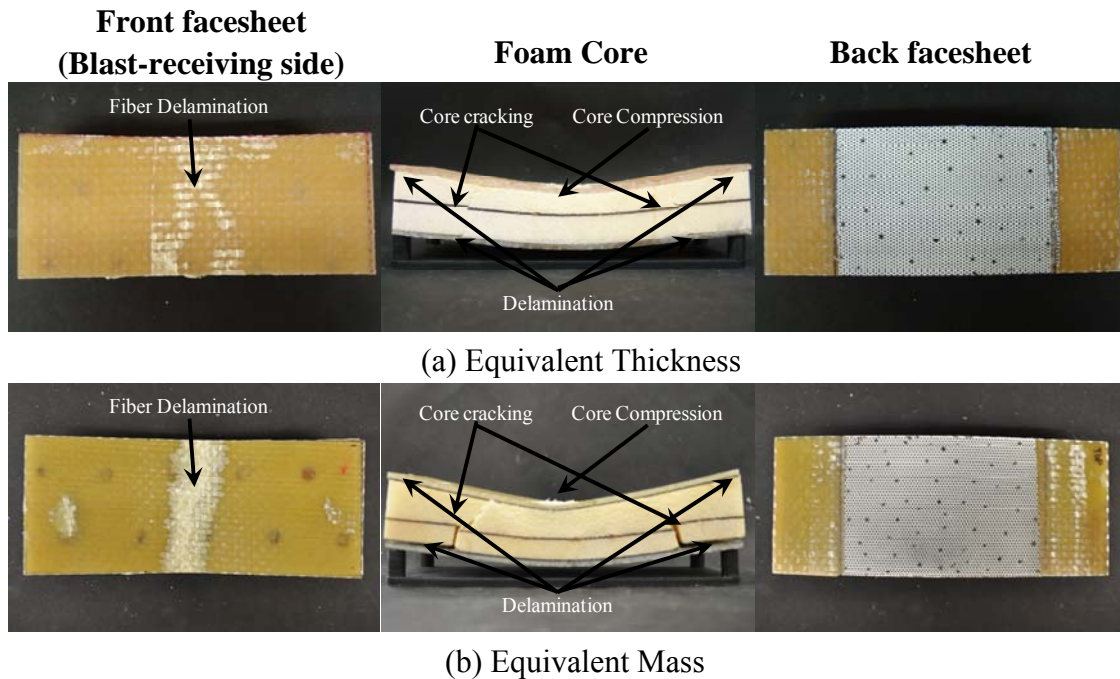


Fig. 16 Visual examination of both configurations after being subjected to high intensity blast load

Task 4: Response of Functionally Graded Sandwich Beams to Blast Loading

The dynamic behavior of sandwich composites made of E-glass Vinyl-Ester (EVE) facesheets and graded Corecell™ A-series foam was studied using a shock tube apparatus. The foam core was monotonically graded based on increasing acoustic wave impedance, with the foam core layer of lowest wave impedance facing the blast. The specimen dimensions were held constant for all core configurations, while the number of core layers varied, resulting in specimens with one layer, two layer, three layer, and four layers of foam core gradation. Prior to shock tube testing, the quasi-static and dynamic constitutive behavior (compressive) of each type of foam was evaluated. During the shock tube testing, high-speed photography coupled with the optical technique of Digital Image Correlation (DIC) was utilized to capture the real-time deformation process as well as mechanisms of failure. Post-mortem analysis was also carried out to evaluate the overall blast performance of these configurations. The results indicated that increasing the number of monotonically graded foam core layers, thus reducing the acoustic wave impedance mismatch between successive layers, helped maintain structural integrity and increased the blast performance of the sandwich composite.

Material details

For the sandwich composites utilized in this study, they were fabricated in an identical manner to those used in Task 3, i.e. the manufacturing conditions (temperature, humidity, amount of resin, etc), materials (E-glass Vinyl-Ester facesheets and styrene acrylonitrile (SAN) foams) and overall specimen dimensions. The core materials used in the present study are Corecell™ A-series styrene acrylonitrile (SAN) foams, which are manufactured by Gurit SP Technologies specifically for marine sandwich composite applications. The four types of Corecell™ A-series foam that were used in present study were A300, A400, A500, and A800. The cell structures for the four foams are similar and the only difference appears in the cell wall thickness and node sizes, which accounts for the different densities of the foams.

For the sandwich composites with a functionally graded/layered core, a series of four different core layer arrangements were studied (as shown in Fig. 17). For the 1 layer gradation, sandwich composites were created using A500 foam alone, and the core layer arrangement was A500/A500 (middle / middle density). For the 2 layer gradation, sandwich composites were fabricated using A300 and A800 foams, and the core layer gradation was A300/A800 (lowest / high density). For the 3 layer gradation, sandwich composites were created using A300, A500 and A800 foams, and the core layer gradation was A300/A500/A800 (lowest / middle / high density). Finally, for the 4 layer gradation, sandwich composites were fabricated using A300, A400, A500, and A800 foams, and the core layer gradation was A300/A400/A500/A800 (lowest / low / middle / high density). With these configurations it should be noted that the first core layer is the one first subjected to the shock wave loading. Actual samples can be seen in Fig.17b.

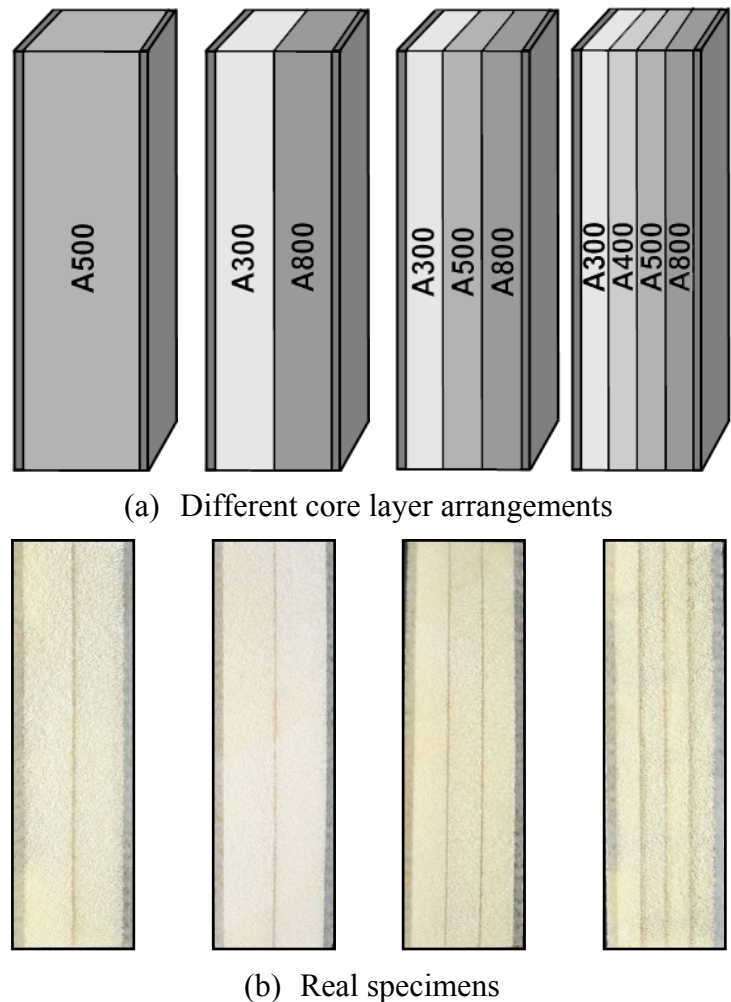
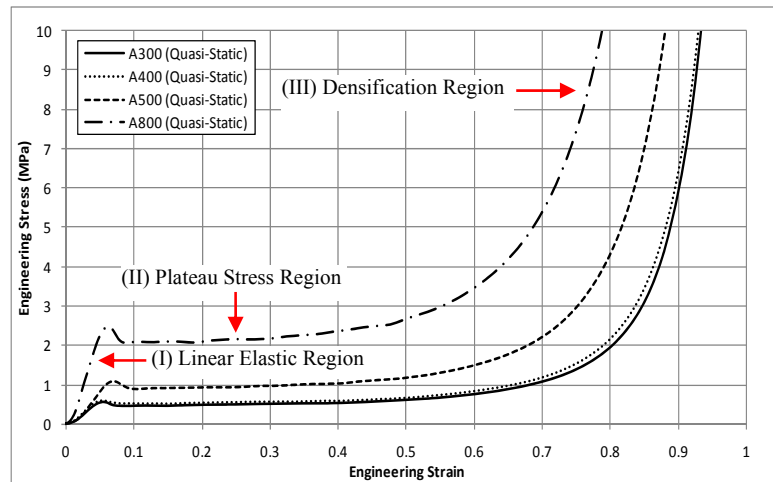


Fig. 17 Specimen configuration and core gradation

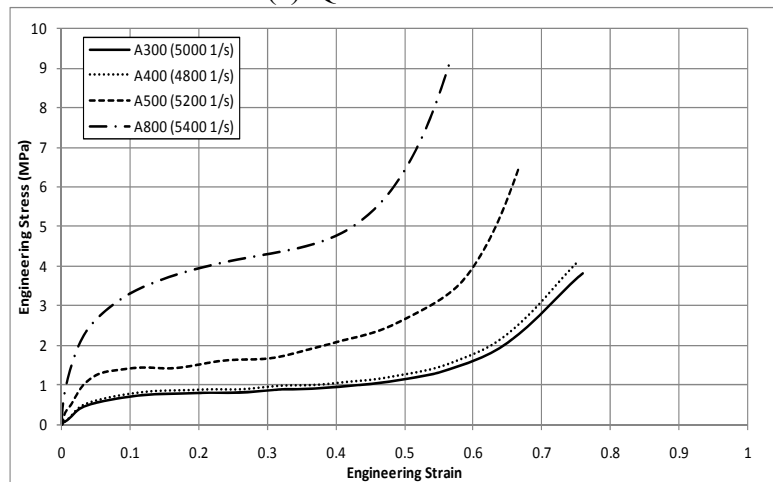
Dynamic Behavior of Core Material

The four types of Corecell™ A-series foams have different quasi-static and dynamic compressive behavior. For the same type of Corecell™ foam, the material shows strain rate dependency from quasi-static to dynamic loading.

Fig.18 shows the quasi-static (Fig. 18a) and high strain rate (Fig. 18b) compressive behavior of the different types of Corecell™ A-series foams. For the quasi-static compressive behavior (Fig. 18a), the stress-strain curves show three deformation regions; (I) the linear elastic region, (II) the plateau stress (plastic yielding) region and (III) the densification region [Gibson and Ashby, 1988]. For high strain rate compressive behavior, the stress-strain curves also show the three deformation regions, even though the densification region is much harder to achieve. Note the plateau stress regions for both instances have a large strain range.



(a) Quasi-Static



(b) Dynamic

Fig. 18 Compressive behavior of different types of Corecell™ A-series foams

As seen in Fig.18, the quasi-static and dynamic stress-strain responses have an obvious trend for the different types of foams. Lower density foam has a lower strength and stiffness, as well as a larger strain range for the plateau stress.

The high strain rate yield stresses and plateau (flow) stresses are much higher than the quasi-static ones for the same type of foams. The dynamic strengths of A500 and A800 foam increase approximately 100% in comparison to their quasi-static strengths, while the dynamic strengths of A300 and A400 foam increase approximately 50% in comparison to their quasi-static strengths. The high yield stresses and long stress plateaus indicate that these foams can withstand higher stresses and absorb larger amounts of energy. Therefore, they show great potential in being used as core materials in sandwich structures subjected to high intensity blast loading.

Macroscopic Post-mortem Analysis

After the blast loading event occurred, the damage patterns of the sandwich composites with four different core layer arrangements were visually examined and recorded using a high resolution digital camera, as shown in Fig. 19. When the sandwich composite with one layer core gradation was subjected to highly-transient loading, as shown in Fig. 19a, the damage was confined to the areas where the supports were located in the shock tube and core cracking is visible in these two areas. The core cracks propagated completely through the foam core. Core delamination is visible between the two core layers of A500 foam. Also one of the core cracks lead to back skin delamination, where the core separated from the back facesheet. Some core compression is also visible in the first core layer of A500 foam.

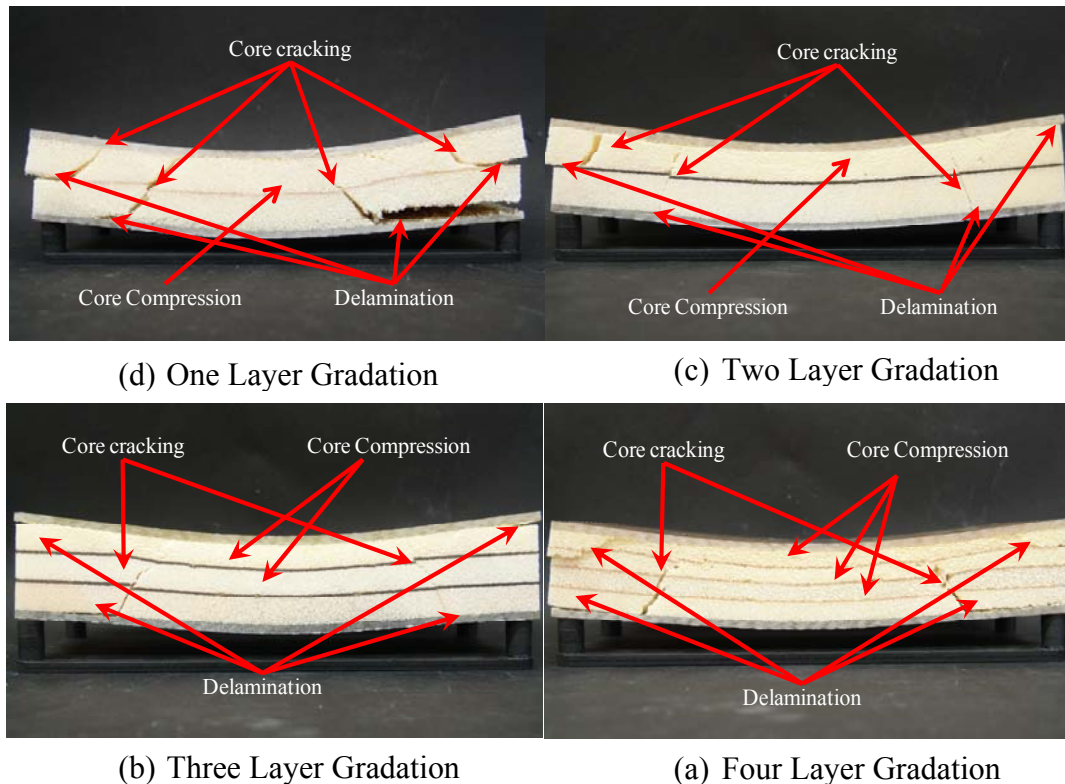


Fig. 19 Visual examination of all core configurations after being subjected to high-intensity blast loading

For the sandwich composite with two layers of core gradation, the damage patterns after being subjected to the shock loading are shown in Fig. 19b. For this core configuration, the damage was again confined to the areas where the supports were located in the shock tube and core cracking is evident. The core cracks propagated completely through the foam core. Skin delamination is obvious between the front facesheet and the foam core, as well as back skin delamination between the back facesheet and the foam core. Core delamination between the first and second core layers of foam, A300 and A800 respectively, is also evident, along with core compression in the first core layer of foam (A300).

Fig. 19c shows the damage patterns of the sandwich composite with three layers of core gradation after the blast loading event occurred. Again, the damage to this core configuration was confined to the areas where the supports were located in the shock tube and core cracking is

visible in these two areas. These core cracks propagated completely through the foam core. Also skin delamination is visible between the front facesheet and the foam core, as well as back skin delamination located between the back facesheet and the foam core. Core compression is also evident in both the first and second core layers of foam, A300 and A500 respectively.

When the sandwich composite with four layers of core gradation was subjected to the shock loading, as shown in Fig. 19d, the damage was again confined to the areas where the supports from the shock tube were located and core cracking is evident in these two areas. Unlike the previous three configurations, the core cracks did not propagate completely through the foam core. Core delamination is obvious between the first and second core layers of foam, A300 and A400, as well as back skin delamination between the back facesheet and the foam core. Core compression is very obvious in this configuration. The first, second and third layers of foam, A300, A400 and A500 respectively, all exhibit various amounts of core compression.

Task 5: Functionally Graded Corrugated Structures for Blast Mitigation (Collaboration with the University of Connecticut)

Blast loading experiments on graded, corrugated steel sandwich panels were conducted using a shock tube apparatus in combination with high-speed digital photography and pressure sensors. Various combinations of multilayer corrugation cores were experimentally evaluated in order to understand the effects of gradation on the shock response of the corrugated panels. The results show that a gradual, linearly graded corrugation, from the thinnest corrugation on the front face to thickest corrugation on the back face, mitigates back face deflection of the panel the most, especially when normalized due to areal density. This arrangement leads to a new sequential collapse mode which helped in mitigating the blast and thus reduces back face deflection.

Material details

Each specimen is composed of two face sheets, a back face and a front face, and different core configurations. The two face plates of each specimen were made from 1018 steel of dimensions 203.2 mm long, 50.8 mm wide, and 3.2 mm thick and weighed approximately 250 g each. The core of the specimens consisted of four layers of differing corrugated thicknesses constructed in seven different configurations (written with the first letter being on the back face and continuing forward): AAAA, BBBB, CCCC, AABC (shown in Fig. 20), ABBC, ABCC, and AACC where A = 0.762 mm thick, B = 0.508 mm thick, and C = 0.254 mm thick each having an average mass of 60 g, 37 g and 18 g, respectively. These corrugated components were made from 1010 steel. As-delivered, sheets were annealed in air at 910 °C and then furnace cooled. Afterwards, the surface oxide layers were removed with wire brushing. The sheets were then compressed in a specifically designed die to induce the corrugated shape. The intrinsic mechanical properties of the individual sheets were identical, but due to the thickness differences their load-bearing property differed. Each panel was constructed via spot welding at each node on both sides of the panel.



Fig. 20 Sinusoidal graded sandwich specimen with white paint - AABC Core

Real – time Deformation and Analysis

The side-view history of the AABC specimen (Fig. 21) shows immediate C level corrugation collapse which begins to extend to the elastic/plastic deformation of the B level after about 400 μ s with local buckling near the welding nodes at the center of the specimen, near the loading area (see Figure 9 for partial deformation history). During these initial 400 μ s an elastic deformation can be observed in all four layers of corrugation. In this specimen minimal plastic deformation is observed in either of the back two A thickness corrugations. No weld breakings are observed until the complete collapse of the top most layer (C) and only sporadic breakings are observed there. The maximum average deflection occurs at 2800 μ s with minimal plastic deformation of the faces observed. A quick coupled face sheet response is observed for this type of specimen.

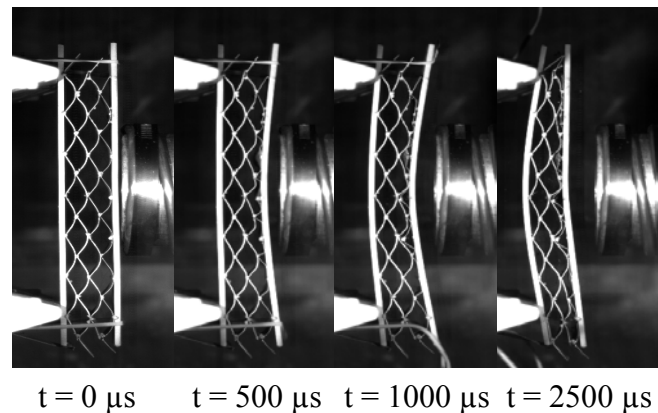


Fig. 21 AABC Side-view history

Macroscopic Post-mortem Analysis

The damage patterns in the graded corrugated sandwich specimens after the shock event occurred were visually examined and recorded using a high resolution digital camera and are shown in Fig. 22.

After experiencing a shock loading the AAAA specimens exhibited slight bending in the front and back face plates with the back face being more prominently bent, 3.0 and 5.3 mm respectively. The overall specimen only compressed 3.5%, the smallest amount of the sandwiches although not the smallest BFD.

The post-mortem BBBB specimens both have an uneven collapse of their layers in which some cells, even within the same layer, were completely collapsed, partially collapsed or entirely un-collapsed. The front and back face deflections for these specimens averaged 8.4 and 5.8 mm respectively with a core compression of 28.9%.

After experiencing a shock loading the CCCC specimens exhibited large bending in the front and back faces plates, an average of 12.8 and 13.3 mm, as well as the complete collapse of all four layers with the accompanying highest percent compression at 62.6%.

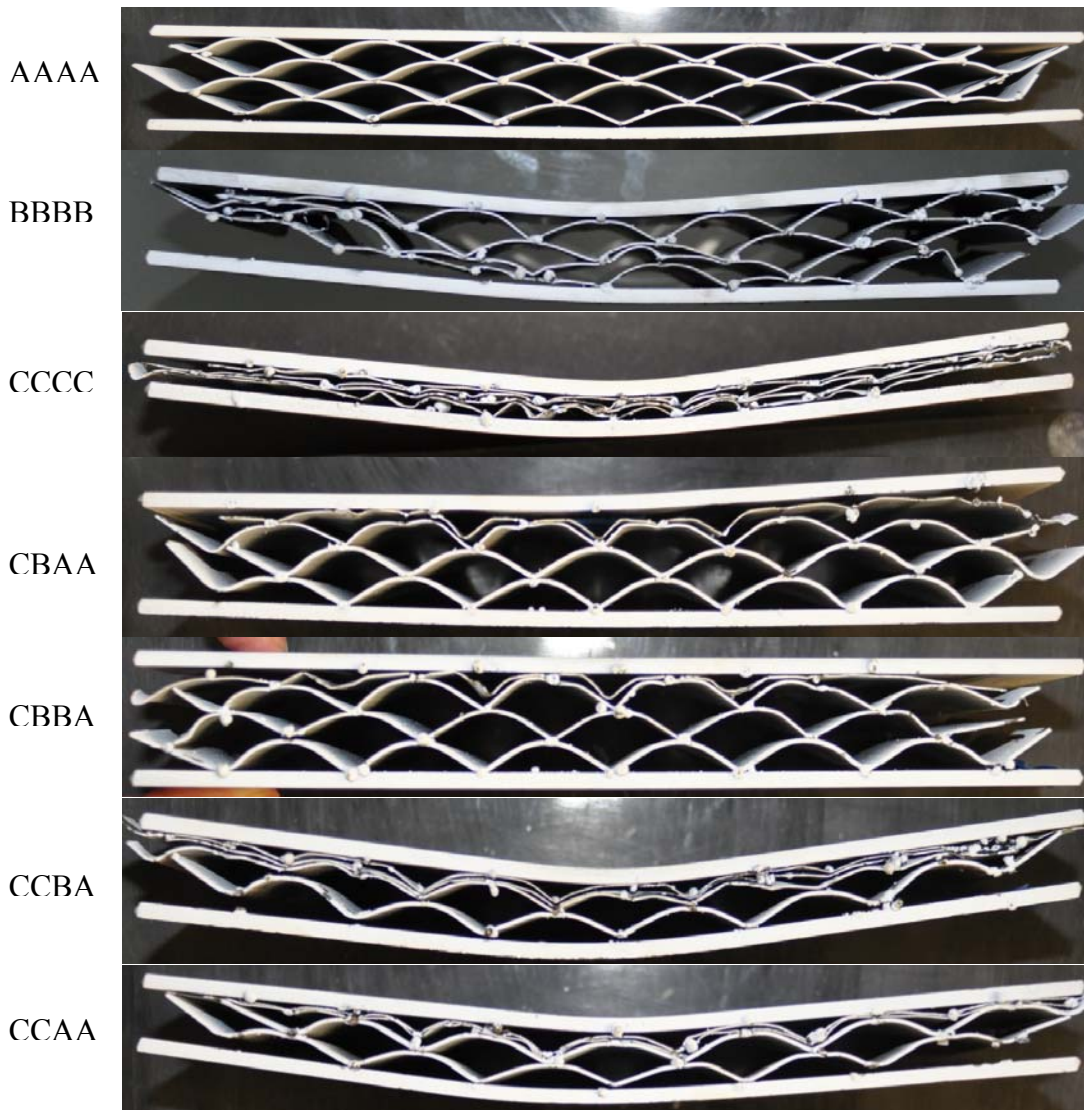


Fig. 22 Post-mortem of specimens

The AABC specimens after being loaded exhibited very slight bending in both the front and back face plates, an average of 4.1 and 2.6 mm, less BFD than AAAA. The most notable damage occurred in the first two layers (C/B) where the front most C layer has entirely collapsed and the B layer has been slightly buckled. This led to a 16.7% compression.

The ABBC specimens have blast damage very similar to that seen in AABC. Its average permanent deflections are also very small: the FFD is 1.0 mm and BFD is 0.1 mm, an almost negligible amount and the smallest permanent deflection of the specimen types. The core, however, has compressed slightly more than the AABC to 19.7% which includes a complete collapse of the front most C layer and buckling in both of the middle B layers.

Post-mortem observations of ABCC indicate a great degree of permanent FFD - 10.5 mm and BFD - 9.3 mm with a highly compressed core - 41.5%. This is due to the complete collapse of the front two C layers and subsequent slapping of the front face plate into the thicker A/B layers as discussed above.

As expected, AACC behaves similarly with high permanent average FFD of 9.3 mm and BFD of 7.6 mm. Its compression is also high at 37.2% almost entirely from the compression of the two front C layers.

Task 6: Collaboration with Industry / Transition to Customer

Novel material systems and sandwich structures, including but not limited to laminated glass panels, corrugated steel armor, and sandwich composites with a functionally graded foam core (Fig. 23) were designed and fabricated to withstand blast loadings and mitigate blast overpressures. Technical collaboration with XO Armor®, Specialty Products Inc., Gurit SP Technology and TPI Composites helped in facilitating sample preparation. This effort also aligns with the mission of DHS to transition technology and allow for a unified effort to protect our homeland.



Fig. 23 Collaborations with Industry

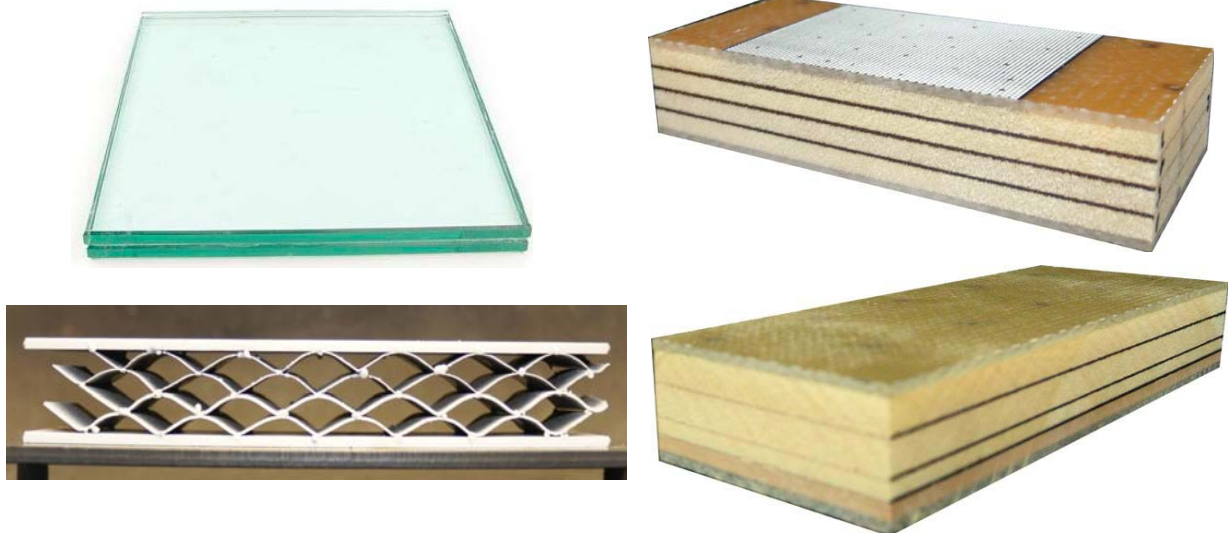


Fig. 24 Novel material systems fabricated with help from Industry

Students Supported

1. Nate Gardner (Ph.D)
2. Puneet Kumar (Ph.D)
3. Dan Gracia (M.S)
4. Jefferson Wright (M.S)
5. Payam Fahr (M.S)
6. Chris Shillings (Undergraduate)



Fig. 25 Students working on shock tube experiments

Journal Publications

1. E. Wang, N Gardner and A. Shukla, "The Blast Resistance of Sandwich Composites with Stepwise Graded Cores", *International Journal of Solid and Structures*, 46, 3492-3502, 2009.
2. E. Wang and A. Shukla, "Analytical and Experimental Evaluation of Energies during Shock Wave Loading", *International Journal of Impact Engineering*, 1188-1196, 2010.
3. M. Jackson, A. Shukla, "Performance of Sandwich Composites Subjected to Sequential Impact and Air Blast Loading", *Composites: Part B*, 42, 155–166, 2011.
4. P. Kumar and A. Shukla, "Dynamic Response of Glass Panels Subjected to Shock Loading", *Journal of Non-Crystalline Solids*, Vol. 357 (24), 3917-3923, 2011.
5. E. Wang, J. Wright and A. Shukla, "Analytical and Experimental Study on the Fluid Structure Interaction During Air Blast Loading", *Journal of Applied Physics*, Vol. 110, 114901-1 – 114901-12, 2011.
6. N. Gardner, E. Wang, P. Kumar and A. Shukla, "Blast Mitigation in a Sandwich Composite Using Graded Core and Polyurea Interlayer", *Experimental Mechanics*, Vol. 52, 119-133, 2012.
7. N. Gardner, E. Wang and A. Shukla, "Performance of Functionally Graded Sandwich Composite Beams under Shock Wave Loading", *Composite Structures*, Vol. 94 (5), 1755–1770, 2012

8. E. Wang and A. Shukla, "Blast Performance of Sandwich Composites with In-Plane Compressive Loading", *Experimental Mechanics*, Vol. 52, 49-58, 2012.
9. P. Kumar, J. LeBlanc, D. Stargel and A. Shukla, "Effect of Plate Curvature on Blast Response of Aluminum Panels", *International Journal of Impact Engineering*, Vol. 46, 74-85, 2012.

Conference Proceedings

1. E. Wang, N. Gardner and A. Shukla, "Experimental Study on the Performance of Sandwich Composites with Stepwise Graded Cores Subjected to a Shock wave Loading", SEM Annual Conference and Exposition on Experimental and Applied Mechanics, Albuquerque, New Mexico, June 1-4, 2009.
2. N. Gardner, "Blast Performance of Sandwich Composites with Discretely Layered Core", SEM Annual Conference and Exposition on Experimental and Applied Mechanics, Albuquerque, New Mexico, June 1-4, 2009.
3. S.A. Tekalur, E. Wang, M. Jackson and A. Shukla, "Failure Behavior and Energy Absorption of Sandwich Composites under Dynamic Loading", SEM Annual Conference and Exposition on Experimental and Applied Mechanics, Albuquerque, New Mexico, June 1-4, 2009.
4. E. Wang and A. Shukla, "Evaluation of Incident, Reflected and Deformation Energies During Blast Experiments", SEM Annual Conference and Exposition on Experimental and Applied Mechanics, Albuquerque, New Mexico, June 1-4, 2009.
5. N. Gardner and A. Shukla, "The Blast Response of Sandwich Composites With a Functionally Graded Core", SEM Annual Conference and Exposition on Experimental and Applied Mechanics, Indianapolis, Indiana, June 7-10, 2010.
6. N. Gardner and A. Shukla, "The Blast Response of Sandwich Composites With a Functionally Graded Core and Polyurea Interlayer", SEM Annual Conference and Exposition on Experimental and Applied Mechanics, Indianapolis, Indiana, June 7-10, 2010.
7. E. Wang and A. Shukla, "The Blast Response of Sandwich Composites with In-Plane Pre-Loading". SEM Annual Conference and Exposition on Experimental and Applied Mechanics, Indianapolis, Indiana, June 7-10, 2010.
8. P. Kumar and A. Shukla, "Blast Loading Response of Glass Panels", SEM Annual Conference and Exposition on Experimental and Applied Mechanics, Indianapolis, Indiana, June 7-10, 2010.
9. E. Wang and A. Shukla, "Core Deformation of Sandwich Composites under Blast Loading", SEM Annual Conference and Exposition on Experimental and Applied Mechanics, Indianapolis, Indiana, June 7-10, 2010.
10. E. Wang and A. Shukla, "Blast Response of Sandwich Composites using Digital Image Correlation Technique", 9th International Conference on Sandwich Structures (ICSS9), Caltech, Pasadena, California, June 14 - 16, 2010.

11. E. Wang and A. Shukla, "Performance of Pre-Stressed Sandwich Composites Subjected to Shock Wave Loading", 14th International Conference on Experimental Mechanics (ICEM 14), Poitiers, FRANCE July 4-9, 2010.
12. N. Gardner and A. Shukla, "The Blast Resistance of Sandwich Composites with a Functionally Graded Core and Polyurea Interlayer", IMPLAST 2010, SEM Fall Conference, Providence, RI, October 12-14, 2010.
13. P. Kumar and A. Shukla, "Dynamic Response of Glass Panels Subjected to Shock Loading", IMPLAST 2010, SEM Fall Conference, Providence, RI, October 12-14, 2010.
14. N. Gardner and A. Shukla, "The Blast Response of Sandwich Composites with Graded Core: Equivalent Core Layer Mass vs. Equivalent Core Layer Thickness", SEM Annual Conference and Exposition on Experimental and Applied Mechanics, Uncasville, Connecticut, June 13 - 16, 2011.
15. P. Kumar and A. Shukla, "Dynamic Response of Shock Loaded Architectural Glass Panels", SEM Annual Conference and Exposition on Experimental and Applied Mechanics, Uncasville, Connecticut, June 13 - 16, 2011.
16. P. Kumar and A. Shukla, "Effect of Curvature on Shock Loading Response of Aluminum Panels", SEM Annual Conference and Exposition on Experimental and Applied Mechanics, Uncasville, Connecticut, June 13 - 16, 2011.
17. P. Kumar and A. Shukla, "Blast Response of Architectural Glass Panels", SEM Annual Conference and Exposition on Experimental and Applied Mechanics, Uncasville, Connecticut, June 13 - 16, 2011.

Boundary Layer Profile Behind Gaseous Detonation as it Affects Reflected Shock Wave Bifurcation

J. Damazo,* J. Odell,† and J. E. Shepherd‡

California Institute of Technology, Pasadena, CA, 91125, USA

The present study explores the flow field created by reflecting detonations using heat transfer and pressure measurements near the location of detonation reflection. Schlieren imaging techniques are used to examine the possibility of shock wave–boundary layer interaction. These measurements are compared to laminar boundary layer theory and a one-dimensional model of detonation reflection. Experiments were carried out in a 7.6 m long detonation tube with a rectangular test section using mixtures of stoichiometric hydrogen–oxygen with argon dilution of 0, 50, 67, and 83% at an initial pressure of 10, 25, and 40 kPa. Optical observations show that minimal interaction of the reflected shock wave results when propagating into the boundary layer created by the incident wave. The heat transfer rate is qualitatively consistent with the time dependent laminar boundary layer predictions, however the magnitude is consistently larger and substantial (factor of three) peak-to-peak fluctuations are observed. The pressure measurements show good agreement between predicted ideal incident and reflected wave speeds. The pressure amplitudes are under-predicted for no argon dilution cases particularly at 40 kPa, but in reasonable agreement for lower pressures and higher dilutions.

Nomenclature

Subscripts

- 1 Initial experimental conditions
- 2 Post-detonation (Chapman–Jouguet) conditions
- 3 Burned equilibrium conditions

Symbols

- η Similarity variable used in the solution to the laminar boundary layer equations
- γ Ratio of specific heats
- ν Kinematic viscosity
- c Fluid sound speed
- c_p Specific heat at constant pressure
- f Non-dimensionalized velocity used in the similarity solution to the laminar boundary layer equations
- h Enthalpy
- k Fluid heat conductivity
- p Pressure
- p_R Pressure at the reflecting end-wall
- q Heat transfer per unit area
- u Fluid velocity
- Re Reynolds number

*PhD Candidate at the Graduate Aerospace Laboratories California Institute of Technology, 1200 E California Blvd, MC 105-50, Pasadena, CA, 91125. AIAA student member.

†Senior Mechanical Engineer at the California Institute of Technology, 1200 E California Blvd, MC 105-50, Pasadena, CA, 91125. AIAA student member.

‡C.L. “Kelly” Johnson Professor of Aeronautics and Professor of Mechanical Engineering at the Graduate Aerospace Laboratories California Institute of Technology, 1200 E California Blvd, MC 105-50, Pasadena, CA, 91125. AIAA senior member.

Re_1	Reynolds number evaluated 1 m behind the detonation
St	Stanton number
T	Temperature
U_I	Measured incident detonation speed
U_{CJ}	Theoretical Chapman–Jouguet detonation speed

I. Introduction

A PARTICULARLY important situation in laboratory testing or accidental explosions is the initiation of a flame followed by deflagration to detonation transition (DDT), resulting in a detonation propagating in a piping system.¹ Gaseous detonations^{2,3} inside piping or vessels create both structural and thermal loads and in extreme cases may lead to plastic deformation or rupture.⁴ When the detonation reaches a closed end, the boundary condition of zero flow velocity leads to the creation of a reflected shock wave that propagates back towards the point of ignition.⁵ The speed and strength of this reflected shock wave changes with time as the shock propagates through the unsteady Taylor–Zel’dovich wave.^{6,7} The reflected shock wave is also complicated by the possibility of interaction with the boundary layer created by the flow induced by the incident gaseous detonation.⁸ Recent work in our laboratory by Karnesky et al.,^{4,8} has suggested that the internal pressure and resulting plastic deformation of thin-walled cylindrical shells due to internal detonation loading is influenced by these viscous effects. There is evidence that the boundary layer created by the fluid motion induced by the detonation interacts with the reflected shock wave created when the detonation normally impinges upon a planar wall. The goal of this paper is to present analytical and experimental findings on the behavior and nature of the boundary layer induced by the detonation and its effects on the reflected shock wave created when a detonation normally impinges upon an end wall.

Reflected shock wave bifurcation occurs when a normally reflected shock wave splits into a lambda shock as shown in Figure 1 due to interaction with the boundary layer created by the incident shock. Previous researchers have extensively examined bifurcation in shock tubes as it pertains to shock tube performance.^{9–12} Mark developed the foundational theory that explains and predicts under what conditions bifurcation will occur.⁹ Mark shows that gases exhibiting a low ratio of specific heats, γ , bifurcate under the widest range of conditions; this suggests that reflected detonations, which have an especially low value for γ , will readily bifurcate and makes bifurcation a likely candidate for explaining the two-dimensional effects observed in our laboratory’s previous work. However, Mark’s analysis assumes the temperature is constant and equal to the initial conditions. This assumption is invalid for the detonation case and is one of the motivations for this study of the boundary layer behind a detonation and interaction with the reflected shock wave.

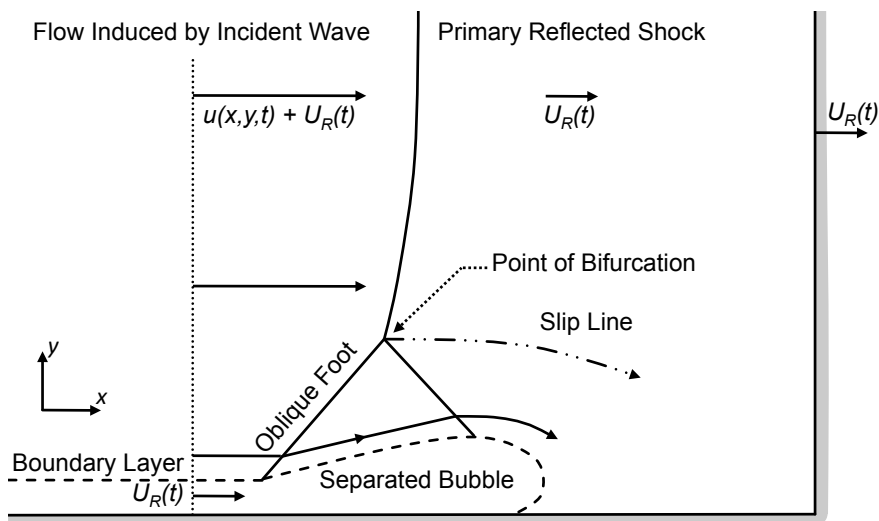


Figure 1. Archetypical reflected shock wave bifurcation sketched in the shock fixed frame.

Numerous researchers have studied boundary layer growth behind shock waves. Mirels^{13,14} developed much of the pioneering work on boundary layer growth behind shock waves. Sturtevant and Okamura¹⁵

solved the boundary layer equation in the shock-fixed frame and explored the effects of shock strength on the boundary layer profile. Liu et al.¹⁶ applied boundary layer analyses to the case of hemi-spherical blast and detonation waves. Here we adapt these models of boundary layer development behind shock waves to the case of boundary layer growth behind detonation. We compare the results to pressure and heat flux measurements recorded during gaseous detonation experiments of stoichiometric hydrogen–oxygen at varying initial pressure and varying argon dilution, conditions which result in varying free-stream conditions as well as detonation cell size. Alongside these measurements we present schlieren photographs of the incident detonation and reflected shock. These pictures reveal novel behavior of the shock wave where it is made up of multiple shock waves. The photographs further reveal the presence of shock wave–boundary layer interaction over a range of argon dilutions.

II. Analytical Formulation

One approach to modeling the detonation reflection process is numerical simulation of reacting viscous compressible flows.^{17–20} Previous studies on reflecting shock waves^{9,21} however, suggest that much may be gained in understanding the shock wave–boundary layer interaction by applying simple models in analyzing the boundary layer growth and propagation of the reflected shock wave. As a first step, we apply previous models for boundary layer growth and detonation reflection to the experimental cases of stoichiometric hydrogen–oxygen detonations with argon dilution. At the present stage, we are still developing an analytical model that includes the strong property variations within the boundary layer and the present experimental results serve to inform our efforts in that direction.

Although gaseous detonations are inherently three-dimensional due to their cellular structure, their mean properties are well approximated by one-dimensional wave propagation theory.²² This results in the detonation exhibiting the behavior sketched in the x – t diagram shown in Figure 2. The detonation propagates

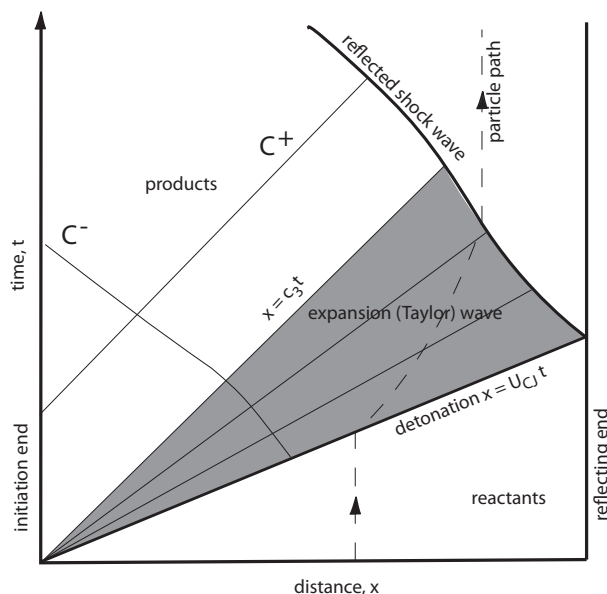


Figure 2. One-dimensional behavior of a detonation in a tube.

away from the point of ignition at the constant theoretical Chapman–Jouguet (CJ) velocity, U_{CJ} , towards the closed end of the tube. The Taylor–Zel’dovich (TZ) expansion wave trails the detonation and gradually brings the fluid to rest. Once the detonation impinges upon the tube’s closed end, a reflected shock wave propagates into the TZ expansion at a non-constant speed. Analysis of the speed and strength of this unsteady reflected wave is discussed in previous work.⁴ To simplify the analytical investigation of reflecting detonation waves, we will consider the less complicated case shown in Figure 3 where the TZ expansion wave is neglected and the properties behind the detonation are the constant CJ values. This assumption becomes

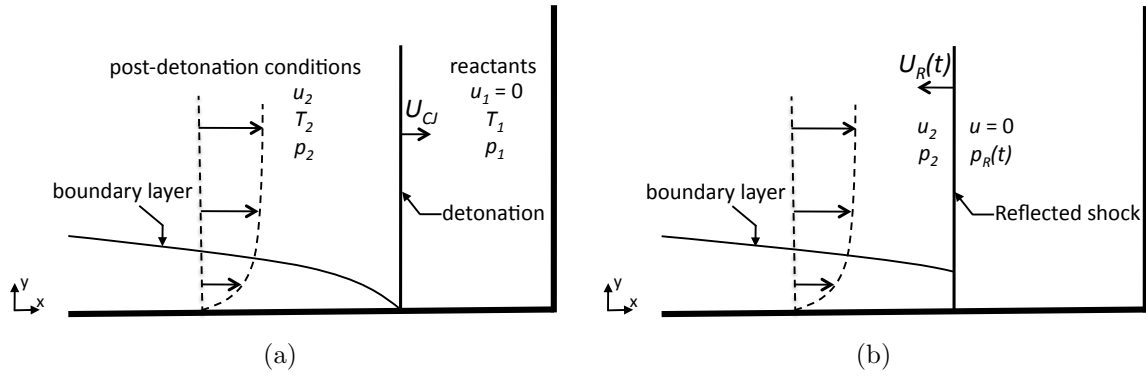


Figure 3. Relevant fluid dynamic and thermodynamic parameters involved in the detonation reflection process shown in the lab-fixed frame of reference used in all mathematical derivations presented herein sketched (a) before and (b) after detonation reflection occurs.

more accurate as the gradients in the TZ wave become smaller which occurs in long detonation tubes such as the 7.6 m long GALCIT Detonation Tube (GDT) discussed in Section III.

A. Boundary Layer Analysis

For the configuration shown in Figure 3, we can develop an approximate analytical laminar boundary layer solution to predict the boundary layer profile and heat transfer to the wall up until the arrival of the reflected shock wave. Let us suppose the detonation is initiated at $x = 0, t = 0$. In front of the detonation, $t > x/U_{CJ}$, the gas is stationary at initial pressure p_1 and temperature T_1 . Behind the detonation, $t < x/U_{CJ}$, the free-stream properties are the computed Chapman–Jouguet post-detonation properties p_2 and T_2 . The free-stream properties (written with a sub-script 2) are used to define laminar boundary layer solution parameters and are calculated with the shock and detonation toolbox.²³ Through the Levy–Lees transformation,²⁴ the two-dimensional compressible laminar boundary layer equations can be transformed with the similarity variable η where

$$\eta(x, y, t) = \frac{1}{\delta(x, t)} \int_0^y \frac{\rho(x, y', t)}{\rho_2} dy' \quad (1)$$

and δ is the boundary layer thickness written in the lab-fixed frame

$$\delta(x, t) = \sqrt{\nu_2 \left(t - \frac{x}{U_{CJ}} \right)}. \quad (2)$$

Assuming that the detonation products behave as a perfect gas, the analysis results in an ordinary differential equation in η which may be solved to yield the fluid velocity:

$$0 = f''' + \frac{1}{2} \left(\eta - \frac{u_2}{U_{CJ}} f \right) f'' \quad (3)$$

using

$$f(\eta) = \int_0^\eta \frac{u(\eta')}{u_2} d\eta' \quad (4)$$

and u_2 is the fluid velocity behind the detonation. Although Equation (3) does allow for varying density and viscosity through the boundary layer, we make the simplifying assumption that

$$\frac{\rho\mu}{\rho_2\mu_2} = C = 1 \quad (5)$$

where C is the Chapman–Rubesin parameter. The boundary conditions are that of zero flow velocity at the wall and uniform velocity u_2 as $\eta \rightarrow \infty$

$$f(0) = f'(0) = 0 \quad (6)$$

$$\lim_{\eta \rightarrow \infty} f'(\eta) = 1. \quad (7)$$

Applying the boundary layer analysis to the conservation of energy equation results in

$$0 = \frac{1}{Pr} g'' + \frac{u_2^2}{h_2} f''^2 + \frac{1}{2} \left(\eta - \frac{u_2}{U_{CJ}} f \right) g' \quad (8)$$

where Pr is the Prandtl number and is assumed to equal 0.7, h is enthalpy, and, for a perfect gas,

$$g(\eta) = \frac{h(\eta)}{h_2} = \frac{T(\eta)}{T_2}. \quad (9)$$

The boundary conditions are given by the wall temperature and free-stream enthalpy

$$h(0) = h_w = c_{p,2} T_w \quad (10)$$

$$\lim_{\eta \rightarrow \infty} h(\eta) = 1. \quad (11)$$

Equations (9) and (10) use $h = c_{p,2} T$ and assume that the specific heat is constant behind the detonation front and the effects of chemical reaction are negligible. In general, the flow within the boundary layer is reacting and non-equilibrium, which requires a numerical solution and the resulting flow field is not self-similar.

The solutions to Equations 3 and 8 were obtained using the Matlab function `ode45` combined with a shooting technique to implement the boundary conditions. Once the temperature profile was known, the heat flux to the wall was computed using

$$\dot{q} = k \left. \frac{dT}{dy} \right|_{y=0} \quad (12)$$

where k is the thermal conductivity in the fluid. This predicted heat flux is compared with the measured heat flux behind detonations in Section IV.

B. Detonation Reflection

A semi-empirical model has been developed^{4,25} in our laboratory that predicts the speed and strength of a reflected detonation. The relevant portion of the model is that the speed of the reflected detonation is given by

$$U_R(t) = -u(x, t) + c(x, t) \sqrt{1 + \frac{\gamma + 1}{2\gamma} \left[\frac{p_R(t)}{p(x, t)} - 1 \right]} \quad (13)$$

where theoretical values for post-detonation fluid velocity u , sound speed c , pressure p , and ratio of specific heats γ are calculated using Cantera 1.8²⁶ and the pressure behind the shock is given by

$$p_R(t) = (p_{CJ,ref} - p_3) \exp \left[-\frac{t - t_0}{\tau} \right] + p_3 \quad (14)$$

where t_0 is the time of reflection, τ is a time constant corresponding to the pressure decay caused by the TZ expansion, the final equilibrium pressure p_3 is calculated using Cantera and the theoretical peak reflected detonation pressure, $p_{CJ,ref}$ is calculated using the Shock and Detonation Toolbox.²³ For a very long detonation tube, such as considered here, $\tau \gg t - t_0$ implying that p_R may be approximated as

$$p_R(t) = p_{CJ,ref} \quad (15)$$

and

$$U_R = U_{R,CJ} \quad (16)$$

which is also computed using the shock and detonation toolbox,²³ values for the present experiments are given in Table 1.

III. Experimental Setup

Experiments were performed in the GALCIT Detonation Tube (GDT)²⁷ shown in Figure 4. The GDT is a 7.6 m long, inner diameter 280 mm detonation tube equipped with a test section of 150 mm wide square cross-section and two quartz windows to provide optical access. The tube was initially evacuated and then filled via the method of partial pressures to the desired composition. The experimental work presented herein is a stoichiometric hydrogen–oxygen mixture diluted with varying amounts of argon at varying initial pressure as given in Table 1. These run conditions were chosen to give a range of cell sizes and post-detonation temperatures allowing us to examine these effects on the wave reflection process. Increasing the initial pressure decreases the cell size from approximately 14 mm²⁸ for an initial pressure of 10 kPa to 3 mm for an initial pressure of 40 kPa.²⁹ Argon dilution increases the cell size and decreases the post-detonation temperature.

The experiment was initiated by injecting a mixture of acetylene–oxygen into the ignition end of the GDT for a duration of 4.5 s. This injection was followed by a 1 s settling period before a 2 μ F capacitor charged to 9 kV discharged through an 80 μ m diameter copper wire located in the ignition end of the GDT. This vaporized the copper wire and created a blast wave in the acetylene–oxygen, thereby initiating a detonation. This wave propagated into the H₂–O₂ mixture where it decayed in speed to the Chapman-Jouguet speed.

After ignition, a detonation enters the test section shown in Figure 5(a).³⁰ A splitter plate was constructed (see Figure 5(b)) that raised the location of the boundary layer into the center of the windows. This splitter plate was instrumented with 12 PCB 113B26 pressure transducers and 12 surface junction thermocouples identical to those employed by Sanderson and Sturtevant³¹ for measuring heat flux inside the test section. The thermocouples are connected to a TriTek Model 205B instrumentation amplifier with a response time of 7.5 μ s to a unit step input. In comparing this response time to the signal response, it seems that the gauge response time is sufficiently small so that the amplifiers dominate the overall response time. The gauges themselves are hand made and may have considerable differences in response. Calibration efforts along the lines of Mohammed et al.^{32,33} would be necessary to better deduce the gauge response. The spectral method employed by Sanderson and Sturtevant³¹ for reducing the heat flux data is also employed here. The locations of all gauges are given on the all relevant plots.

A Z-type schlieren system is used to visualize the incident detonation and shock wave reflection. The schlieren system consists of a pulsed EverGreen 70 PIV laser with a pulse width duration less than or equal to 10 ns and a Cooke PCO.2000 digital 14 bit CCD camera system. This allows two images to be taken in quick succession and was used to visualize the incoming detonation and the reflected shock wave for each test.

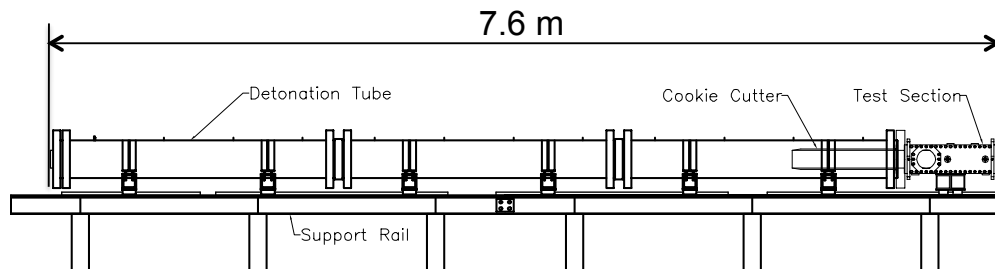


Figure 4. Schematic of the GALCIT Detonation Tube in which detonation experiments were performed (for more information, see Akbar 1997²⁷).

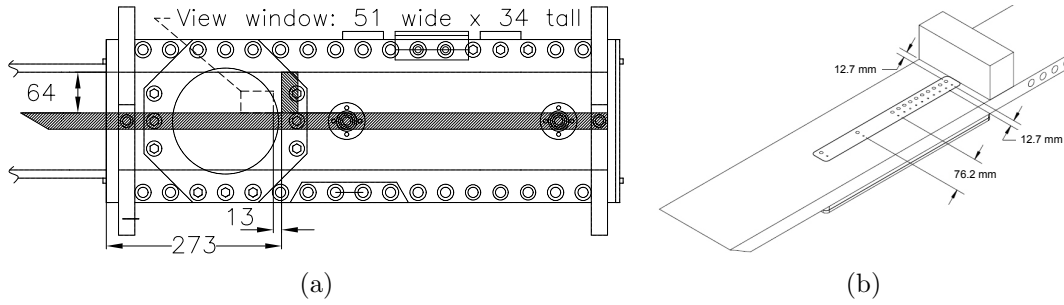


Figure 5. Detail views of the test section for the GDT; dimensions in mm. (a) Location of viewing window relative to end-wall. (b) Pressure and thermocouple gauge locations relative to end-wall.

Table 1. Run conditions with measured incident shock speed U_I , theoretical CJ detonation speed U_{CJ} , fluid velocity u_2 , temperature behind the incident wave T_2 , equilibrium ratio of specific heats $\gamma_{e,2}$ behind the incident wave,³⁴ unit Reynolds number, mean measured reflected shock speed over the first 127 mm St of reflected wave propagation, and computed reflected shock speed.

Initial Pressure (kPa)	Argon dilution	U_I ^a (m/s)	U_{CJ} ^b (m/s)	u_2 ^b (m/s)	T_2 ^b (K)	$\gamma_{e,2}$ ^b	Re_1 ^c	$\bar{U}_{R,meas}$ ^a (m/s)	$U_{R,comp}$ ^d (m/s)
10.0	0%	2702	2719	1239	3272	1.12	$0.49 \cdot 10^6$	1005	1026
	50.0%	1838	1854	827	3055	1.15	$0.64 \cdot 10^6$	699	717
	66.7%	1681	1664	737	2892	1.18	$0.66 \cdot 10^6$	688	668
25.0	0%	2763	2760	1260	3425	1.12	$1.20 \cdot 10^6$	1038	1049
	50.0%	1865	1872	840	3179	1.15	$1.56 \cdot 10^6$	709	736
	66.7%	1684	1691	745	2992	1.19	$1.62 \cdot 10^6$	686	686
	83.3%	1435	1457	589	2474	1.35	$1.43 \cdot 10^6$	720	661
40.0	0%	2792	2786	1270	3508	1.12	$1.90 \cdot 10^6$	1033	1061
	50.0%	1888	1889	846	3245	1.16	$2.47 \cdot 10^6$	728	746
	66.7%	1699	1705	750	3045	1.20	$2.57 \cdot 10^6$	701	696
	83.3%	1445	1462	588	2489	1.37	$2.25 \cdot 10^6$	720	670

^a Measured using time of arrival from PCB pressure transducers.

^b Computed using Cantera 1.8²⁶ and the Shock and Detonation Toolbox.²³

^c Computed using Equation (17) at time $t - t_a = 1 \text{ m}/U_{CJ}$ corresponding to a location 1 m behind the detonation.

^d Computed using the ideal reflection model described in the shock and detonation toolbox.²³

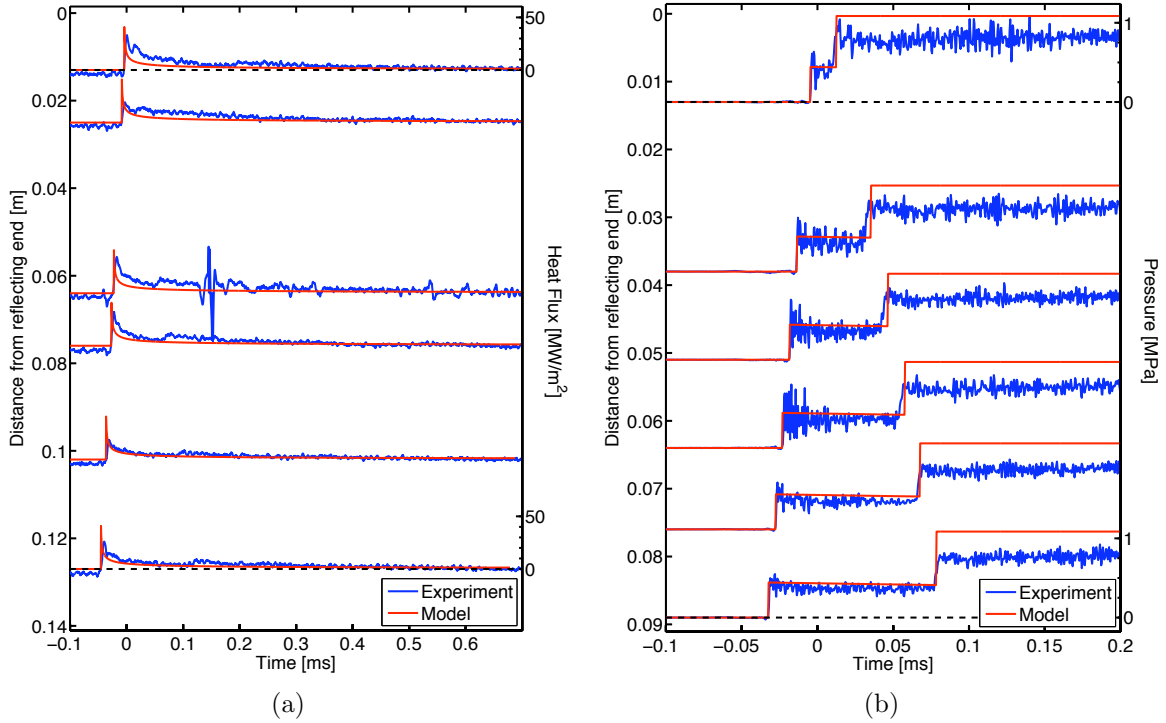


Figure 6. Results for a stoichiometric hydrogen–oxygen detonation of initial pressure 25 kPa with 0% argon dilution. Experimental measurements (blue) are compared to (a) the laminar boundary layer heat flux model discussed in Section II A and (b) the one-dimensional pressure model discussed in Section II B and

IV. Discussion

Figure 6 portrays results for 0% argon dilution; this case has the largest discrepancy between observed and computed reflected shock pressures of the cases examined in this paper. The heat flux plot in Figure 6(a) shows the heat transfer measurements compared to the laminar boundary layer theory described in Section II A. The incident detonation is clearly marked by a spike in both measured and predicted heat transfer. The reflected detonation is much less clear and plays only a lesser role in the heat flux measurements. The heat-flux model is only valid for times before the arrival of the reflected shock. Figure 7 plots the heat-flux data in a $St-Re$ plot where the Stanton and Reynolds³⁵ numbers are computed from

$$Re = \frac{\rho_2 u_2^2 (t - t_a)}{\mu_2} \quad (17)$$

$$St = \frac{\dot{q}}{(h_2 - h_w) \rho_2 u_2} \quad (18)$$

where t_a is the arrival time of the detonation. We observe that for times after the response time of the gauge and before the arrival of the reflected shock, the laminar theory does an adequate job of predicting the measured heat transfer. This suggests that the boundary layer is in fact laminar for this duration. Using a turbulent transition Reynolds number of³⁵ $Re_T \approx 6 \cdot 10^5$ it is perhaps no surprise that transition does not occur before the arrival of the reflected shock (which corresponds to $Re_{ref} = 5.5 \cdot 10^5$ for the undiluted initial pressure 25 kPa detonation). However a substantial difference between shock and detonation waves is the presence of transverse waves behind detonations. This work indicates that the transverse waves do not significantly effect turbulent transition for the mixtures tested. This agrees with the work of Liu et al.¹⁶ who found reasonable qualitative agreement with the experimental work of Laderman et al.³⁶ with a laminar boundary layer model applied to hydrogen–oxygen mixtures of initial pressure 1 atm.

The trend of agreement with the laminar boundary layer theory is seen for all initial pressures tested as observed in Figures 7(b), 7(c), and 8 with the largest differences occurring in the 10 kPa initial pressure case where the Reynolds number is smaller and the cell size larger than the other considered cases. We also see

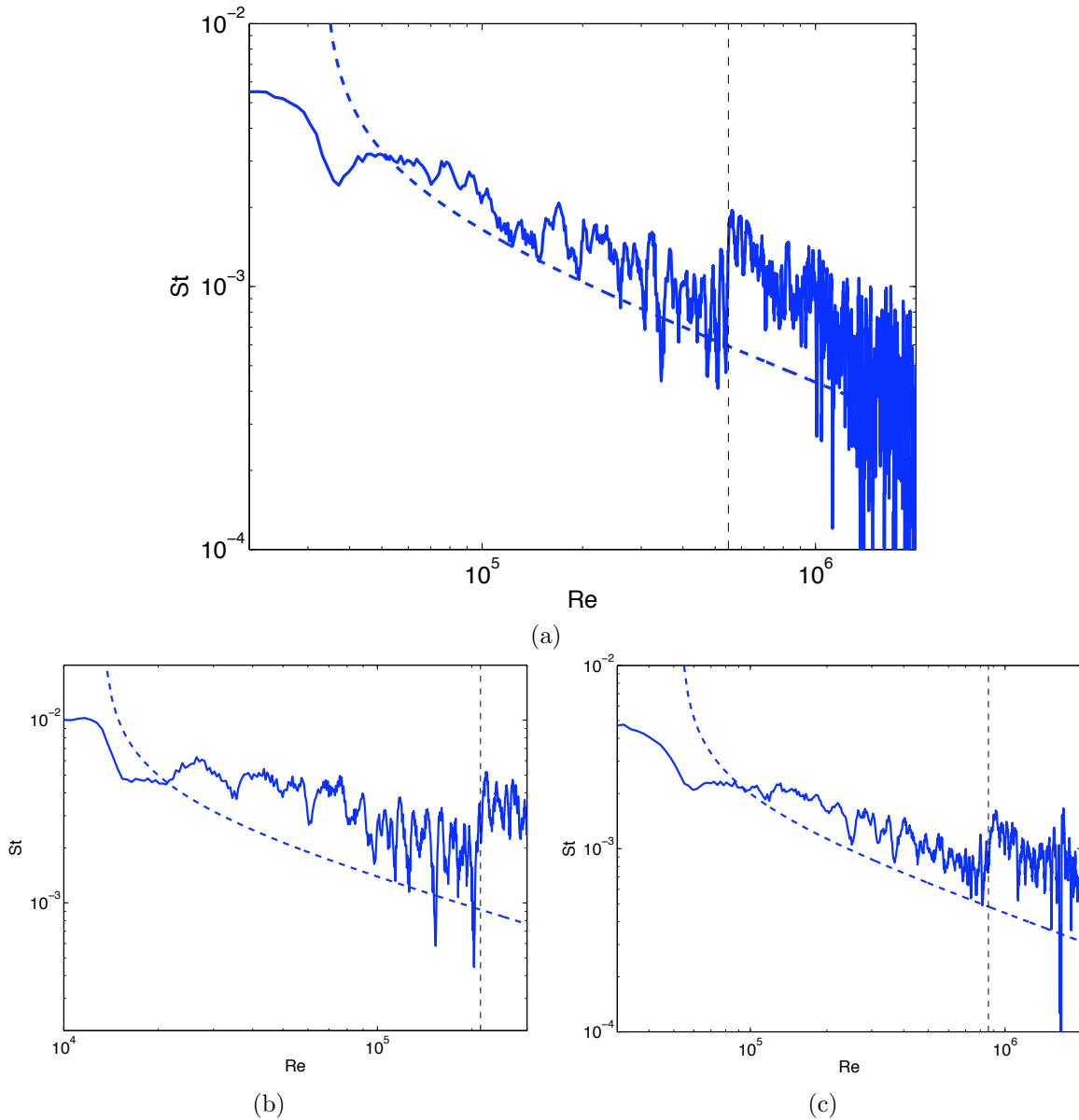


Figure 7. Stanton–Reynolds plot comparing measured and computed heat flux for a stoichiometric hydrogen–oxygen detonation with 0% argon dilution at a distance of 127 mm from the reflecting end wall; initial pressure (a) 25 kPa, (b) 10 kPa, and (c) 40 kPa. The dashed black line indicates the arrival of the reflected wave.

on each heat flux graph that the heat transfer is under-predicted near the location of detonation reflection indicating the wave reflection process and resulting fluid dynamics are more complicated than incorporated into the simple two-dimensional laminar boundary layer theory.

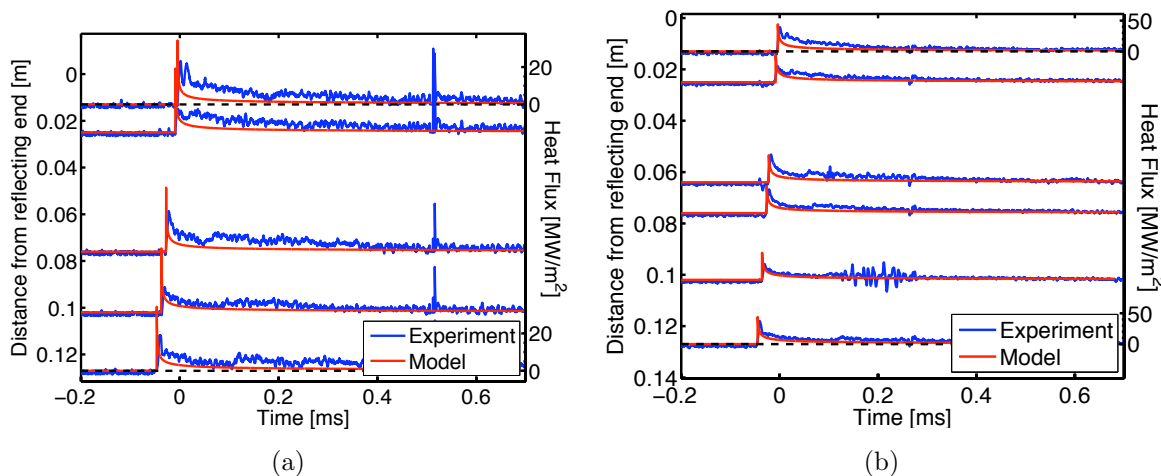


Figure 8. Heat flux measurements for detonations of stoichiometric hydrogen–oxygen with 0% argon dilution at initial pressure (a) 10 kPa and (b) 40 kPa.

Examining the corresponding pressure plot, Figure 6(b), we observe two sharp increases in pressure for each measurement location. The first increase is due to the incident detonation; following this rise are high-frequency pressure oscillations corresponding to the transverse waves associated with gaseous detonations. The second increase occurs from the reflected shock wave propagating back towards the location of ignition. Plotted with the experimental data are the predictions of the model introduced in Section II B. We see that the arrival time and resulting pressure of the incident detonation is well-predicted by the one-dimensional Chapman–Jouguet theory. The reflected shock wave, however, is not adequately described by the pressure model. The reflected shock speed is within 8% of the predicted value in the highest dilution case and 3% for the undiluted case. However the reflected shock pressure is under predicted by up to 40% in the undiluted cases and up to 6% in the argon dilution cases. This trend of accurate arrival time, but inaccurate pressures is the same as observed in earlier work⁴ and initially suggested the possibility of shock wave–boundary layer interaction. Figure 9 shows the schlieren image corresponding to the graphs plotted in Figure 6 with Figure 9(a) showing the incident detonation propagating to the right and Figure 9(b) showing the reflected shock wave propagating back to the left. As is observed in the schlieren photographs, there is no significant shock wave–boundary layer interaction.

Another feature of note in the pressure signals is that the rise time of the pressure signals through the reflected shock wave occurs over several microseconds—slower than would be expected from a shock. This corresponds to the reflected shock wave being apparently composed of multiple shocks as observed in Figures 9 and 10. The source of these shocks is not fully understood. The spacing does not seem to be a strong function of cell size as observed by essentially no change in the wave thickness for initial pressures of 10 kPa (approximately 14 mm cell width²⁸) and 40 kPa (approximately 3 mm cell width²⁹) as seen in Figure 10.

We next examine the effects of argon dilution. Pressure traces for detonations in hydrogen–oxygen–argon at 25 kPa and argon dilutions of 50, 66.7, and 83.3% is given in Figure 11. We observe that the pressure signals are much better predicted by the analytical pressure model. This result is still under investigation; one significant point is that the effect of adding argon is to decrease the post-detonation temperature. The effect of the transverse waves on the wall pressure are clearly observed in the 83% argon dilution case shown in Figure 11(c) as additional pressure waves behind the incident detonation and in a decrease in the frequency of the pressure signals after the arrival of the detonation.

The schlieren images corresponding to the pressure measurements of Figure 11 are shown in Figure 12. Here we observe the general trend of the reflected shock wave becoming gradually thicker from 1.9 mm at 0% argon dilution to 2.6 mm at 83.3% argon dilution. We also observe a small amount of shock wave–boundary layer interaction for the 50 and 66.7% argon dilution cases as marked by the shock wave angling to the left near the floor of the detonation tube. This effect was unexpected due to the fact that argon is known⁹

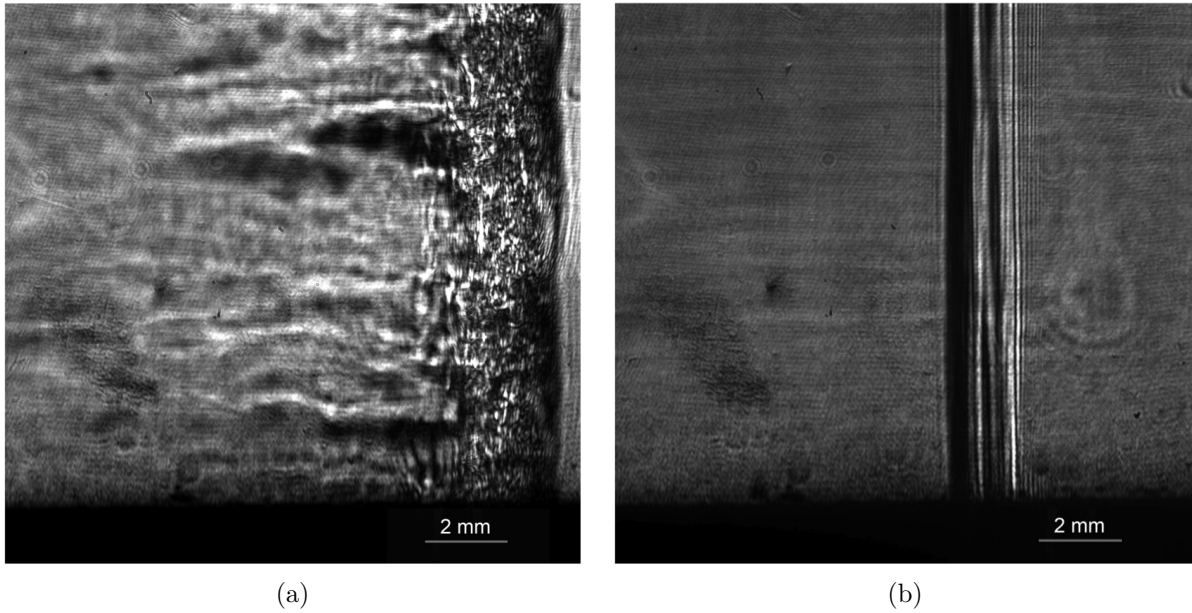


Figure 9. Schlieren images showing (a) incident detonation and (b) reflected shock wave for a stoichiometric hydrogen–oxygen detonation with no argon dilution at initial pressure 25 kPa.

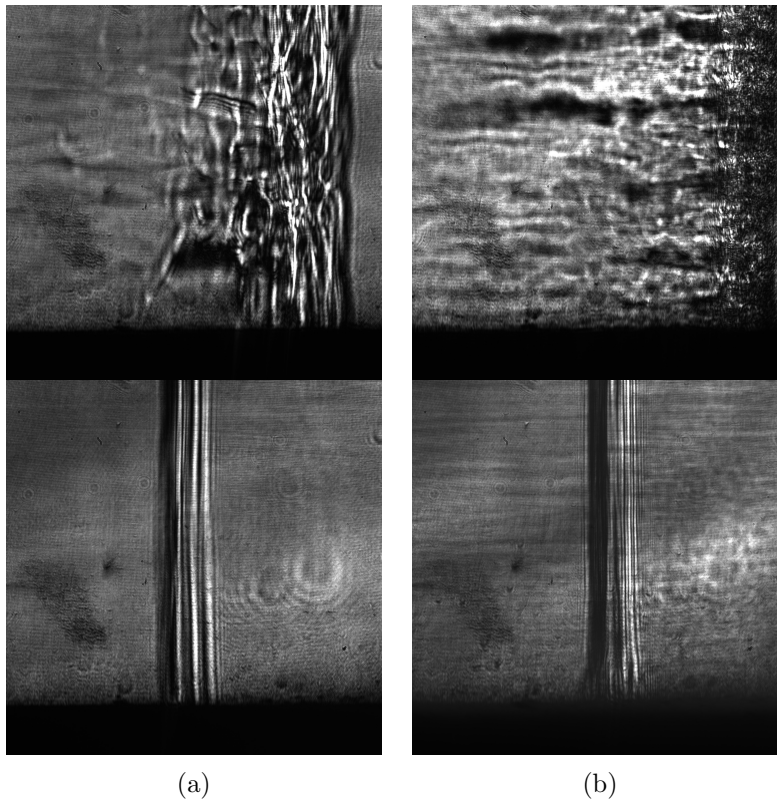
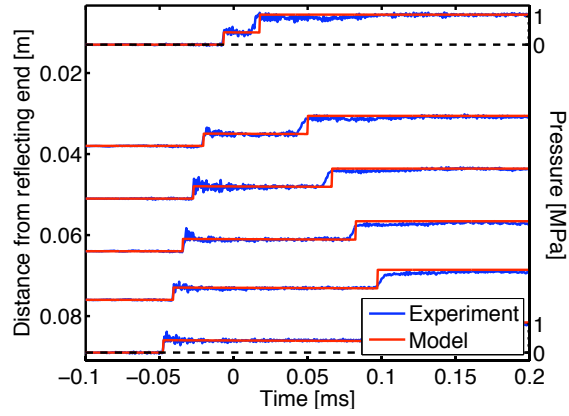
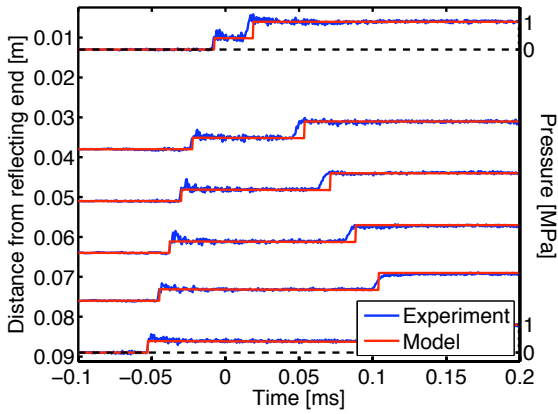


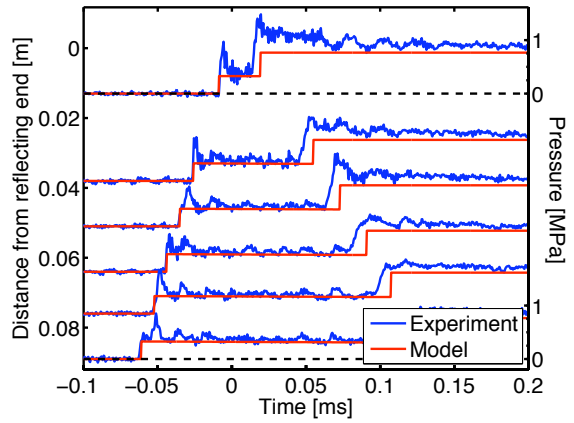
Figure 10. Schlieren images for stoichiometric hydrogen–oxygen detonations with no argon dilution at initial pressure (a) 10 kPa and (b) 40 kPa.



(a)



(b)



(c)

Figure 11. Pressure measurements for detonations of stoichiometric hydrogen–oxygen at initial pressure 25 kPa with (a) 50%, (b) 66.7%, and (c) 83.3% argon dilution.

to inhibit boundary layer interaction in shock tubes due to the increase in γ ; however there is no visible boundary layer interaction in the 83.3% argon dilution case.

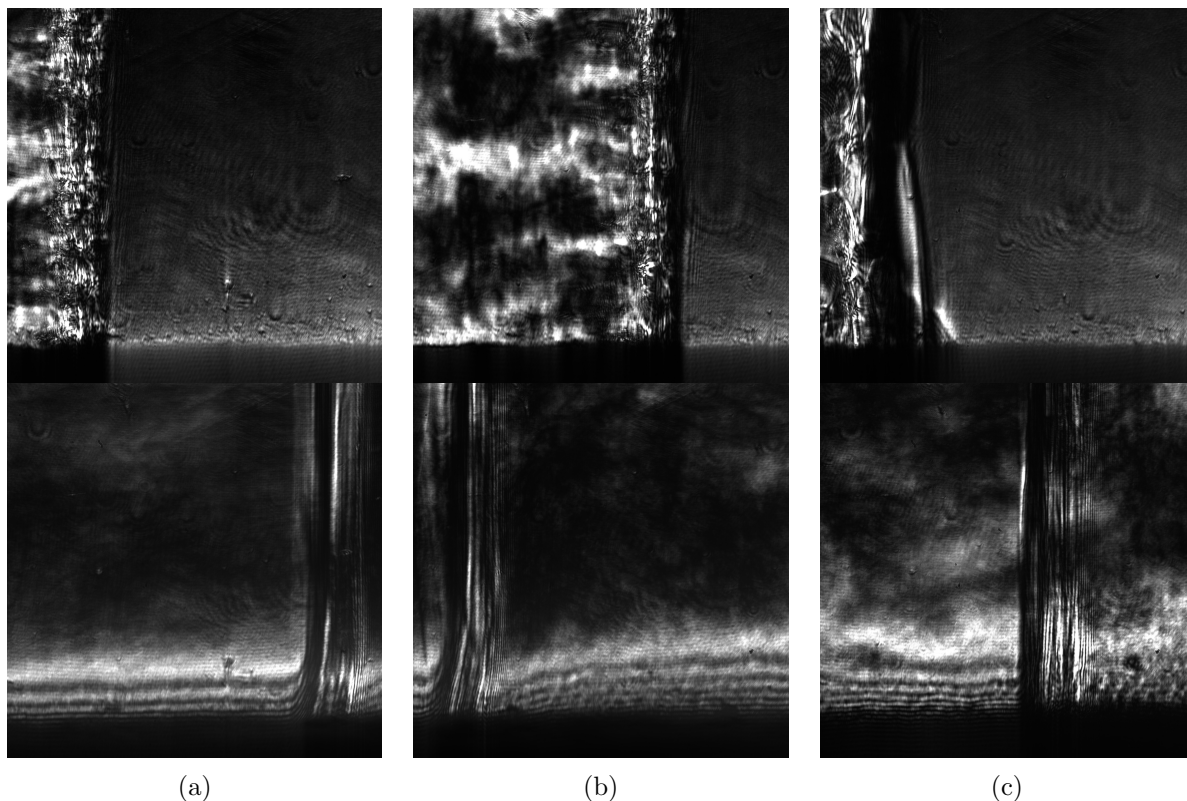


Figure 12. Schlieren images of stoichiometric hydrogen–oxygen detonations of initial pressure 25 kPa with (a) 50%, (b) 66.7%, and (c) 83.3% argon dilution.

Although the measurements and schlieren images were not shown for the remaining test cases, similar qualitative trends were observed in both pressure measurements and schlieren images. The largest difference in the remaining data is that the heat flux measurements became less useful at higher dilutions and lower pressures due to the decreased signal amplitude resulting in an unfavorable signal-to-noise ratio.

V. Conclusions

The heat flux to the tube wall and wall pressure are investigated behind stoichiometric hydrogen–oxygen detonations. Laminar boundary layer theory well-predicts the heat transfer observed behind gaseous detonations for the 25 kPa and 40 kPa initial pressure cases. This suggests that the boundary layer for these cases is laminar. The laminar theory is less accurate for the 10 kPa initial pressure case; the source of this discrepancy is still under investigation.

The behavior of the reflected shock wave created when a detonation normally impinges upon an end wall is investigated. The ideal model of detonation reflection predicts the speed of the reflected wave within 3–8%. The pressure behind the reflected waves is substantially under predicted (up to 40%) for the undiluted cases, but the agreement is much better (within 6%) for the diluted cases. This trend was previously observed in the work of Karnesky et al.⁴ and was thought to be caused by shock wave–boundary layer interaction. The present work, however, discounts such interaction as the source of the discrepancy through schlieren photographs taken of the reflected shock wave. Paradoxically, some degree of interaction is observed for argon dilutions of 50 and 67% although the ideal model more accurately predicts the pressure behind the reflected wave. These findings are puzzling and still under investigation.

Acknowledgments

This research is sponsored by the DHS through the University of Rhode Island, Center of Excellence for Explosives Detection. The authors would also like to thank Bahram Valiferdowski for his help in designing the splitter plate as well as the Caltech SURF program for sponsoring Jeff Odell.

References

- ¹Shepherd, J. E., "Structural Response of Piping to Internal Gas Detonation," *Journal of Pressure Vessel Technology*, Vol. 131, No. 3, June 2009, pp. 87–115.
- ²Lee, J. H. S., *The Detonation Phenomenon*, Cambridge University Press, 2008.
- ³Fickett, W. and Davis, W. C., *Detonation*, University of California Press, Berkeley, CA, 1979.
- ⁴Karnesky, J., Damazo, J., Shepherd, J. E., and Rusinek, A., "Plastic response of thin-walled tubes to detonation," *ASME 2010 Pressure Vessels and Piping Conference*, ASME, 2010.
- ⁵Shepherd, J., Teodorczyk, A., Knystautas, R., and Lee, J., "Shock Waves Produced by Reflected Detonations," *Progress in Astronautics and Aeronautics*, Vol. 134, 1991, pp. 244–264.
- ⁶Taylor, G. I., "The Dynamics of the Combustion Products behind Plane and Spherical Detonation Fronts in Explosives," *Proc. Roy. Soc.*, Vol. A200, 1950, pp. 235–247.
- ⁷Zel'dovich, Y. B., "On the Theory of the Propagation of Detonations in Gaseous Systems," *JETP*, Vol. 10, 1940, pp. 542–568, Available in translation as NACA TM 1261 (1950).
- ⁸Damazo, J., Ziegler, J., Karnesky, J., and Shepherd, J. E., "Investigating Shock Wave–Boundary Layer Interaction Caused by Reflecting Detonations," *Proceedings of the 8th ISPHMIE Conference*, Yokohama, Japan, September 5–10 2010.
- ⁹Mark, H., "The Interaction of a Reflected Shock Wave with the Boundary Layer in a Shock Tube," Tech. Rep. TM1418, National Advisory Committee for Aeronautics, March 1958.
- ¹⁰Strehlow, R. A. and Cohen, A., "Limitations of the Reflected Shock Technique for Studying Fast Chemical Reactions and Its Application to the Observation of Relaxation in Nitrogen and Oxygen," *Journal of Chemical Physics*, Vol. 30, No. 1, 1959, pp. 257–265.
- ¹¹Taylor, J. R. and Hornung, H. G., "Real Gas and Wall Roughness Effects on the Bifurcation of the Shock Reflected from the End Wall of a Tube," *Proceedings of the 13th International Symposium on Shock Tubes and Waves*, Niagara Falls, USA, July 6–9 1981.
- ¹²Petersen, E. L. and Hanson, R. K., "Improved Turbulent Boundary-Layer Model for Shock Tubes," *AIAA Journal*, Vol. 41, No. 7, 2003, pp. 1314–1322.
- ¹³Mirels, H., "Boundary Layer Behind Shock or Thin Expansion Wave Moving Into Stationary Fluid," NACA TN 3712, Lewis Flight Propulsion Laboratory, Cleveland, Ohio, 1956.
- ¹⁴Mirels, H., "Laminar Boundary Layer Behind a Strong Shock Moving Into Air," NACA TN D-291, Lewis Flight Propulsion Laboratory, Cleveland, Ohio, 1961.
- ¹⁵Sturtevant, B. and Okamura, T. T., "Dependence of Shock-Tube Boundary Layers on Shock Strength," *The Physics of Fluids*, Vol. 12, No. 8, 1969, pp. 1723–1725.
- ¹⁶Liu, W. S., Du, X. X., and Glass, I. I., "Laminar Boundary Layers Behind Detonation Waves," *Proceedings of the Royal Society of London Series A, Mathematical and Physical Sciences*, Vol. 387, No. 1793, June 1983, pp. 331–349.
- ¹⁷Ziegler, J., *Simulations of Compressible, Diffusive, Reactive Flows with Detailed Chemistry Using a High-Order Hybrid WENO-CD Scheme*, Ph.D. thesis, California Institute of Technology, 2011.
- ¹⁸Gamezo, V. N., Khokhlov, A. M., and Oran, E. S., "The Influence of Shock Bifurcations on Shock-Flame Interactions and DDT," *Combustion and Flame*, Vol. 126, 2001, pp. 1810–1826.
- ¹⁹Weber, J., Oran, E., Boris, J., and Anderson, J., "The numerical simulation of shock bifurcation near the end wall of a shock tube," *Physics of Fluids*, Vol. 7, No. 10, 2006, pp. 2475–2488.
- ²⁰Kessler, D., Gamezo, V., and Oran, E., "Three-dimensional reactive shock bifurcations," *Proceedings of the Combustion Institute*, Vol. 30, 2005, pp. 1841–1847.
- ²¹Davies, L. and Wilson, J. L., "Influence of Reflected Shock and Boundary-Layer Interaction on Shock-Tube Flows," *Shock Tube Symposium*, 1969.
- ²²Nettleton, M. A., *Gaseous Detonations*, Chapman and Hall, NY, 1987.
- ²³Browne, S., Zeigler, J., and Shepherd, J., "Numerical Solution Methods for Shock and Detonation Jump Conditions," Tech. Rep. FM2006-006, Graduate Aeronautical Laboratories California Institute of Technology, February 2008.
- ²⁴Schlichting, H. and Gersten, K., *Boundary-layer Theory*, Springer, Berlin, 1965.
- ²⁵Karnesky, J., *Detonation Induced Strain in Tubes*, PhD dissertation, California Institute of Technology, 2010.
- ²⁶Goodwin, D. G., "Cantera – An open-source, extensible software suite for CVD process simulations," *Electrochemical Society*, 2003, pp. 155–162.
- ²⁷Akbar, R., *Mach Reflection of Gaseous Detonations*, Ph.D. thesis, Rensselaer Polytechnic Institute, 1997.
- ²⁸Strehlow, R., "Transverse waves in detonations: II. structure and spacing in H₂-O₂, C₂H₂-O₂, C₂H₄-O₂ and CH₄-O₂ systems," *AIAA J*, Vol. 7, 1969, pp. 492–496.
- ²⁹Desbordes, D., *Aspects stationnaires et transitoires de la detonation dans les gaz: relation avec la structure cellulaire du front*, PhD dissertation, Universite de Poitiers, 1990.
- ³⁰Kaneshige, M. J., *Gaseous Detonation Initiation and Stabilization by Hypervelocity Projectiles*, PhD dissertation, California Institute of Technology, 1999.

³¹Sanderson, S. R. and Sturtevant, B., “Transient Heat Flux Measurement Using a Surface Junction Thermocouple,” *Review of Scientific Instruments*, Vol. 73, No. 7, 2002, pp. 2781–7.

³²Mohammed, H., Salleh, H., and Yusoff, M., “Determination of the Effusivity of Different Scratched Coaxial Temperature Sensors Under Hypersonic Flow,” *International Journal of Thermophysics*, Vol. 31, 2010, pp. 2305–2322.

³³Mohammed, H., Salleh, H., and Yusoff, M., “The Effect of Scratch Technique on the Thermal-Product Value of Temperature Sensors,” *Thermophysics and Aeromechanics*, Vol. 18, No. 1, 2011, pp. 51–64.

³⁴Radulescu, M. I. and Hanson, R. K., “Effect of heat loss on pulse-detonation-engine flow fields and performance,” *Journal Of Propulsion And Power*, Vol. 21, No. 2, Mar-Apr 2005, pp. 274–285.

³⁵Petersen, E. L. and Hanson, R. K., “Measurement of reflected-shock bifurcation over a wide range of gas composition and pressure,” *Shock Waves*, Vol. 15, 2006, pp. 333–340.

³⁶Laderman, A., Hecht, G., and Oppenheim, A., *Temperature – its measurement and control in science and industry*, Reinhold Publishing Corporation, New York, 1962.

APPENDIX: EXPERIMENTS AND ANALYSIS OF WATER-SHEET BREAKUP AND MITIGATING POTENTIAL UNDER BLAST LOADING

A. J. Zakrajsek¹, D. R. Guildenbecher^{1,2}, and S. F. Son¹

¹*School of Mechanical Engineering, Purdue University, West Lafayette IN 47907*

²*Present Address: Sandia National Laboratories, Albuquerque NM 87123*

Abstract An explosion yielding a blast wave can cause catastrophic damage to people and property. To mitigate damage from such an event, a number of investigators have proposed the use of water in various configurations. In this investigation, an unconfined free-flowing water-sheet, with an approximate thickness of 0.3 cm, is experimentally examined using an explosively driven shock tube at three different standoff distances. The results show that the water-sheet mitigates the initial peak overpressure and impulse of the blast. Further insights into the underlying physics are revealed by a numerical simulation using Sandia's CTH hydrocode. In simulations and experiments, the air behind the water sheet experiences two distinct pressure peaks. An initial pressure rise results from the passage of a low pressure shock wave ($M \approx 1$) through the intact sheet and into the air downstream of the water sheet. Following this, the water sheet breaks apart due to an increase in pressure on the forward surface caused by the buildup of the subsonic detonation products. Passage of the detonation products after breakup results in a second rise in pressure behind the water-sheet. In simulations, an initial perturbation of the water sheet is shown to affect the breakup time significantly. Additional simulations show that increasing the sheet thickness tends to increase the shock wave mitigation. These results indicate that it may be possible to optimize the thickness and surface morphology of a water-sheet to effectively mitigate damage due to explosive blast waves.

Keywords: *Water blast mitigation, water-sheet, explosively driven shock tube, protective water barrier.*

Corresponding Author: Steven F. Son

Zucrow Laboratories - Chaffee Hall 130
500 Allison Rd. West Lafayette, IN 47907
sson@purdue.edu
Office Number: 765-494-8208
Fax Number: 765-494-0530

1 Introduction

Since 1968, bombings have accounted for nearly half of international terrorist attacks [1]. To counter these threats, defensive mechanisms, such as blast mitigants, are needed to protect structures and individuals from blast waves. Because it is often readily available, water is an attractive material for use as a blast mitigant [2]. Previous investigations have focused on blast mitigation by water sprays or confined masses of water [2, 3] with mixed success as quantified by the peak overpressure and impulse mitigation. An alternative geometry is that of a free-flowing water-sheet forming a shield around the object to be protected. A few numerical models have considered this geometry [4, 5], and their results indicate that water-sheets may effectively limit the peak overpressure of the blast. However, there are limited experimental data to validate these findings. Meekunnasombat *et al.* [6] considered liquid layers in a confined vertical shock tube, and their experiments highlighted the advantageous behavior of multiple layers of water. However, it is unclear if their results can be extended to the case of the unconfined water-sheet, which is the likely geometry for practical blast mitigation. In addition, Bremond and Villiermaux [7] considered the breakup of a thin soap film under normally incident shock loading. However, it is unclear if the physical breakup mechanisms revealed in their investigation can be extended to the thicker water-sheets considered here.

The aim of this work is to study the blast mitigating potential associated with a sheet of water. To elucidate the fundamental physics, an experimental investigation is coupled with a numerical model. Sections 2 and 3 focus on the experimental configuration and results, respectively. Numerical results are presented in Section 4. The results presented here form an initial starting point to determine the feasibility of water-sheets as a possible blast mitigant.

2 Experimental configuration

2.1 Explosively driven shock tube

Experiments are conducted in an open field, with an explosively driven shock tube, and a custom fabricated water-sheet generator. A schematic of the experimental configuration is shown in Fig. 1. The explosively driven shock tube is used to produce a relevant laboratory size blast wave. Previous work has shown that this configuration yields a blast profile similar to open field explosive tests, and the shock tube directs the energy from the blast in one direction allowing for the use of less explosive as compared to a conventional open field explosive test [8, 9].

In an experiment, the explosively driven shock tube is loaded with 3 grams of Primasheet 1000. Primasheet 1000 is a pentaerythritol tetranitrate (PETN) based plastic explosive consisting of approximately 63% PETN powder [9]. Initiation of the PETN plastic sheet explosive is achieved by a combination of detonation cord (PETN powder) and an explosive bridge wire (EBW) detonator (RP-502 EBW) charged by a firing set.

The shock tube consists of a detonation chamber and a high explosive chamber. The two chambers are bolted together to protect the cables, test apparatus, and other equipment from the fragments produced by the aluminum detonator cap. A small hole links the two chambers and allows for passage of detonation cord. By changing the distance of the shock tube from the water-sheet (defined as the *standoff distance*), the characteristics of the incident shock wave are altered. Decreasing the standoff distance increases the overpressure at the water-sheet.

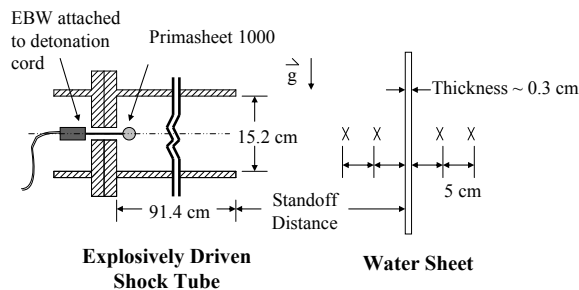


Fig. 1 Experimental configuration for investigation of blast loading of an unconfined water-sheet. The out of plane water-sheet dimension is roughly 70 cm, while the in plane height is 30 cm. The “X’s” indicate the location of the static pressure gauges which are positioned along the centerline of the shock tube.

2.2 Water-sheet generator and pressure gauges

A water-sheet is generated with a custom fabricated water-sheet generator, operating at a constant flow rate of approximately 56 L/min, producing a sheet approximately 0.3 cm thick. In the absence of blast loading, the water-sheet is continuous and displays surface perturbations, which likely arise from turbulent or capillary instabilities. In an experiment, the incoming blast wave is approximately normal to the water-sheet.

Due to space constraints near the water-sheet, typical pencil gauges cannot be placed at the locations marked in Fig. 1 without disrupting the water flow. Instead, PCB 113A22/113B22 piezoelectric dynamic pressure sensors are threaded into custom fabricated plates orientated to measure the static pressure of the blast. The experimental configuration includes two pressure gauges placed in front and two behind the water-sheet, as shown in Fig 1. As the water-sheet standoff distance is varied from one experiment to the next, the pressure gauges are repositioned to maintain the distances with respect to the water-sheet shown in Fig. 1.

2.3 Shadowgraphy visualization

In select experiments, the shock wave is visualized using the high-speed shadowgraphy technique described in [10]. Videos are recorded at 11,494 fps and an exposure of 26 μ s using a Vision Research Phantom v7.3 digital high-speed camera and an Oriel 1000 W xenon arc lamp. The field of view is approximately 53 by 53 cm and is recorded on a 171 by 171 pixel region of the CCD.

3 Experimental results

Experiments were performed at three different standoff distances: 20 cm, 31 cm, and 41 cm (distance from exit of shock tube to water sheet). To verify repeatability, all experiments were performed three times.

3.1 Pressure measurements

Figure 2 shows the free field pressure traces taken without the water sheet. Additionally, tabulated values for all free field distances measured are shown in Table 1. Figure 3 displays the pressure traces from an experiment with a water-sheet at a 31 cm standoff distance. Note the significantly lower peak pressures at distances behind the water sheet (36 and 41 cm). Other standoff distances produce similar results. Table 2 summarizes the pressure measurements after

the water sheets, for all three standoff distances considered. In this table, the peak overpressure is taken as the highest recorded static pressure during the transient experiment. The standard error is calculated between the three experiments performed at each condition.

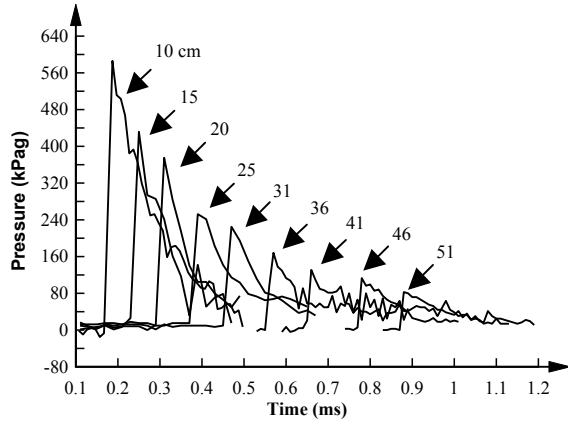


Fig. 2 Free field experimental pressure traces. Numbers indicate the distances in cm between the exit of the shock tube and the pressure gauge.

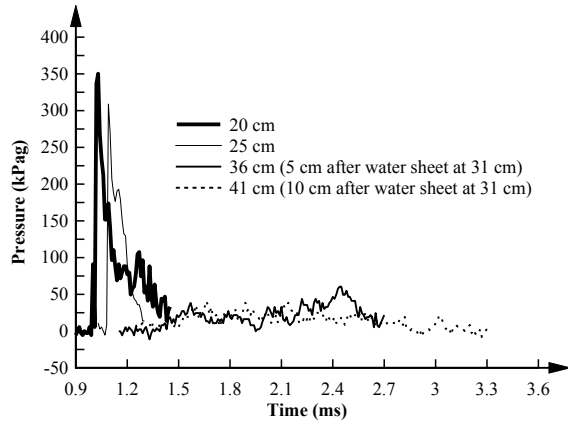


Fig. 3 Pressure trace of a blast test with a water-sheet at a 31 cm standoff distance. Numbers indicate the distances in cm between the exit of the shock tube and the pressure gauge.

Table 1 Free field experimental shock wave parameters. Uncertainties indicate the standard error.

Pressure Gauge Standoff Distance (cm)	Peak Overpressure (kPa)	Impulse (kPa-ms)	Positive Pulse (ms)
10	586 ± 29	60 ± 9	0.2 ± 0.1
15	436 ± 18	35 ± 8	0.2 ± 0.1
20	389 ± 15	32 ± 5	0.3 ± 0.1
25	253 ± 21	32 ± 3	0.3 ± 0.1
31	203 ± 19	19 ± 5	0.2 ± 0.1
36	169 ± 3	19 ± 4	0.3 ± 0.1
41	130 ± 1	18 ± 2	0.3 ± 0.1
46	117 ± 4	18 ± 1	0.4 ± 0.1
51	88 ± 6	12 ± 1	0.3 ± 0.1

Table 2 Initial experimental shock wave parameters 5 and 10 cm after the water sheets. Uncertainties indicate the standard error.

Water Sheet Standoff Distance (cm)	5 cm after Water Sheet		
	Peak Overpressure (kPa)	Impulse (kPa-ms)	Positive Pulse (ms)
20	60 ± 8	18 ± 3	0.3 ± 0.1
31	31 ± 4	5 ± 2	0.3 ± 0.1
41	26 ± 5	6 ± 2	0.4 ± 0.1
Water Sheet Standoff Distance (cm)	10 cm after Water Sheet		
	Peak Overpressure (kPa)	Impulse (kPa-ms)	Positive Pulse (ms)
20	53 ± 6	12 ± 3	0.3 ± 0.1
31	27 ± 8	4 ± 0.3	0.3 ± 0.1
41	23 ± 3	6 ± 0.4	0.4 ± 0.1

3.2 Pressure trace after water sheet

The experimental results show that the unconstrained free flowing water-sheet significantly reduces the initial overpressure and impulse of the blast. This is best illustrated in Fig. 3. At the 31 cm water-sheet standoff distance the peak overpressure is reduced by 82% and the impulse is reduced by nearly 75% as measured by the pressure gage placed 5 cm behind the water sheet. These results show qualitative agreement with previous work with water shields [4, 5].

The pressures measured downstream of the water-sheet also show a somewhat unexpected increase in the pressure at a finite time following the passage of the initial shock wave. Some pressure traces showed this rise in the pressure more distinctly. Figure 4 highlights the pressures measured downstream of the water-sheet at 31 cm. Based on the distances between the measurement points and the delay time between the initial pressure rise, it is found that the initial transmitted wave propagates at approximately sonic conditions. The second pressure increase, which occurs sometime after the passage of the sonic wave, is a subsonic pressure wave and is likely result of the detonation products which reach the downstream pressure gauges after the water-sheet breaks apart.

The breakup time of the water-sheet is estimated from the pressure recordings and is defined as the elapsed time between the instant when the shock wave reaches the water-sheet and the second rise in pressure, which is assumed to be due to passage of the detonation products. The experimental breakup times are shown in Fig. 5, which indicates that the water-sheet breakup time decreases with increasing incident shock pressure.

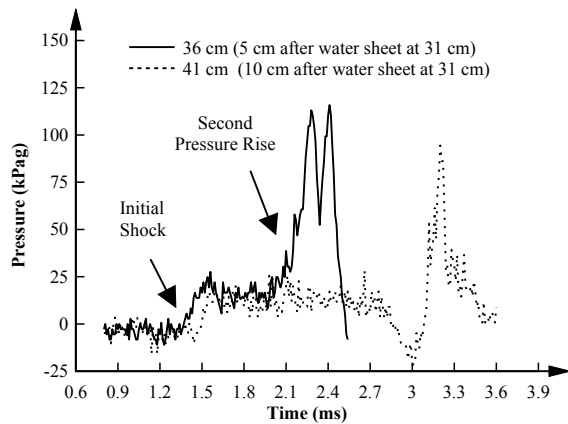


Fig. 4 Pressure trace of gauges 5 and 10 cm behind the water-sheet at a 31 cm standoff distance.

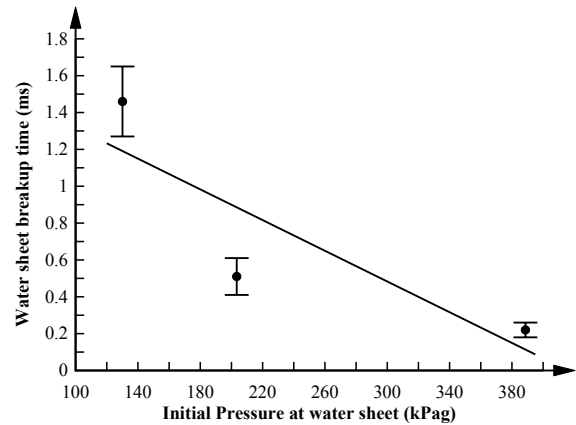


Fig. 5 Experimental breakup times of the water-sheet. The error bars represent the standard error between the three tests conducted. The solid line highlights the general trend of the data.

3.3 Role of the standoff distance

Three different standoff distances are considered, such that as the standoff distance increases the water-sheet is loaded by a comparatively weaker blast wave. Regardless, the velocity of the transmitted wave is approximately sonic in all cases, and it is found that the initial peak overpressure is approximately the same. Based on this observation alone, one could conclude that the standoff distance has a minimal effect on the transmitted wave. However, as discussed in the previous section for the conditions considered here, the transmitted sonic wave is followed by a large second rise in pressure caused by passage of the reaction products. To determine if this second rise in pressure can be minimized, the physical mechanisms are analyzed in more detail.

3.4 Shadowgraphy visualization

The shock wave interaction with the water-sheet is visualized using shadowgraphy. Select images from a high-speed shadowgraphy video are shown in Fig. 6, where the flow is right to left. The video is taken without pressure gauges which tend to obstruct the observation of the incident, reflected, and transmitted shock waves. The reflected wave seen in the third image is due to the impedance differences between the air and water [11]. In the fourth image a weak transmitted shock wave is observed.

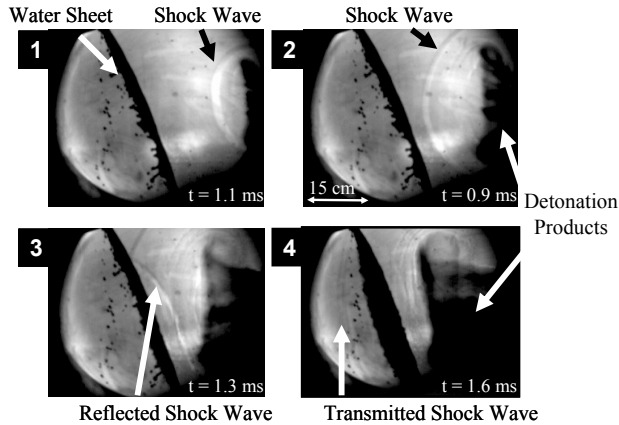


Fig. 6 High speed shadowgraphy of a blast loaded water-sheet at a 31 cm standoff distance.

The shadowgraphy images were compared to the pressure traces and were found to be in agreement. The last image in Fig. 6 shows the initial transition of a shock wave and change in water-sheet geometry. In agreement with the pressure readings, velocity estimates from the high speed videos indicate that the large cloud of detonation products travels at speeds below sonic conditions.

4 Numerical simulation using CTH

Numerical simulations were completed utilizing Sandia's hydrocode, CTH. CTH is a multi-material, large deformation, strong shock wave, solid mechanics code developed at Sandia National Laboratories [12]. In what follows, the CTH model is first validated using the free field conditions and is then used to qualitatively study the interaction of the shock wave and water-sheet.

4.1 Model geometry and boundary conditions

An axisymmetric model of a shock tube with a 3 gram charge of Primasheet 1000, similar to the experimental configuration, was first attempted. Results demonstrated a direct dependence between the shape and placement of the explosive charge and the simulated pressure at the exit of the shock tube. In addition, CTH did not demonstrate the pulse width increasing effect observed in previous shock tube experiments [8, 9]. This led to the development and use of an open field charge model.

The model developed and compared to the experimental results is shown in Fig. 7. The model is axisymmetric with a spherical open field charge of PETN. The bottom boundary condition is set to allow

the pressure to be zero in the ghost cells and to later remove all material from that ghost cell. This boundary condition ensures that mass does not enter the mesh but is allowed to leave. The remaining three boundary conditions use a sound speed based absorbing/transmitting condition to approximate an infinite or semi-infinite medium. Here mass can flow into and out of the mesh.

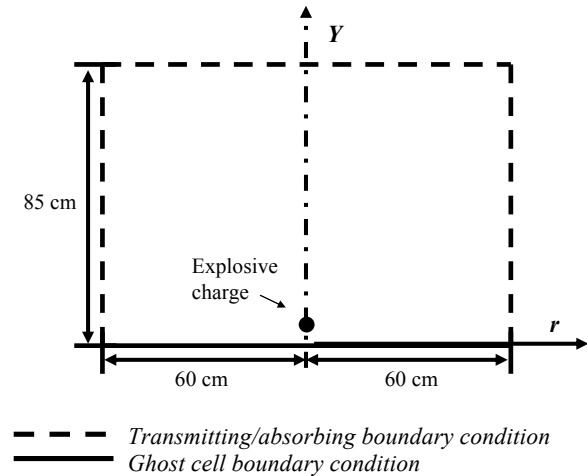


Fig. 7 CTH simulation geometry and boundary conditions.

4.2 Material equations-of-state

The explosive charge is assumed to follow the Jones–Wilkins–Lee (JWL) equation-of-state (EOS) for PETN. Since the experimental explosive is comprised of 63% PETN, the model mass is scaled to allow the use of the JWL EOS. The explosive charge is detonated using a history variable reactive burn (HVRB) model. The HVRB is a pressure-based model used to treat shock induced initiation that grows to a detonation for heterogeneous explosive material [13]. When the HVRB is used, the equations of state for the un-reacted and reacted phases are usually the Mie–Grüneisen and JWL equations of state [13]. Atmospheric air was modeled at an initial absolute pressure of 100 kPa using a tabulated SESAME EOS. The SESAME EOS Library is a standardized, computer-based library of thermodynamic properties developed by Los Alamos [14].

4.3 Comparison to free field experiments (without water-sheet)

Fixed nodes are included in the CTH model to match the experimental free field pressure gauge locations. The mass of PETN used in the model (48.4 grams) was determined by comparing the predicted pressure

to the experimental pressures and adjusting the mass until reasonable agreement was obtained. It should be noted that the mass of the PETN used in the model is an order of magnitude larger than the experiment value. This difference can be attributed to the fact that a shock tubes is used in the experiment to focus the blast in one direction. Figure 8 compares the free field pressure traces between the final CTH model and the experimental results. The average percent difference between the peak overpressure is 7.8% and the average percent difference between the impulses is around 20%.

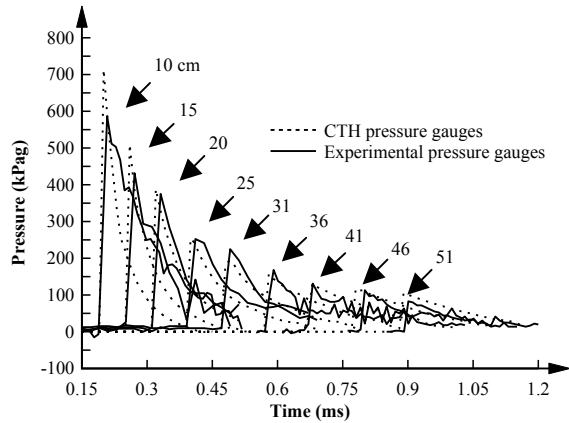


Fig. 8 Comparison of CTH pressure traces vs. experimental pressure traces. Numbers indicate the distances in cm between the exit of the shock tube and the pressure gauge.

4.4 Modeling the water-sheet in CTH

Modeling the 0.3 cm thick water-sheet requires a fine mesh. The meshing style is a fixed Eulerian mesh, where the materials flow through the fixed mesh. The mesh consisted of 24,000 and 17,000 nodes in the x- and y-direction, respectively. This resulted in a structured mesh, with meshing cells being $\frac{1}{2}$ mm by $\frac{1}{2}$ mm. A convergence study was performed to show that the solution was not dependent on mesh refinement.

Liquid water is modeled with the Mie-Grüneisen EOS. In simulations where the surface of the water-sheet is assumed to be initially smooth, sheet breakup and the transmission of a second pressure rise is not observed. However, as mentioned in the experimental section, the actual water-sheet displays visible surface roughness. Therefore, it is desired to determine what effect this roughness has on the fragmentation process. To do so, several test cases are considered in which the surface of the water sheet is modeled using a sine wave with different spatial frequencies. Comparisons of the water-sheet geometries are shown in Fig. 9. In all cases, the thickness of the water sheet

varies between 0.3 cm and 0.1 cm, and all geometries contain the same total mass (cross-sectional area). The water-sheets are also assumed to be infinite (stretching across CTH domain) to eliminate effects caused by diffraction of the shock wave around the water-sheet, and to better isolate the interaction of the shock wave and water-sheet. In addition, it should be noted that the CTH models do not include surface tension effects which may play a significant role in the physical breakup process. Because of these simplifications, the simulation results are considered for qualitative insight into the physical phenomena, rather than quantitative predictions.

As expected, varying these perturbations affects the breakup time and the magnitude of the transmitted shock wave. Results presented in the remainder of this work are calculated assuming an initial perturbation given by case (D) in Fig. 9, as this case shows the best qualitative agreement with the experimental results.

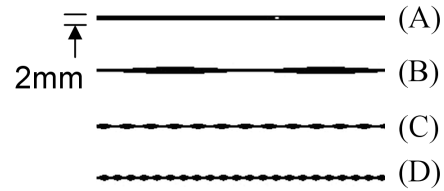


Fig. 9 (A) Straight 2 mm thick water-sheet, (B) water sheet with a wavelength of 50 mm, (C) water sheet with a wavelength of 8.3 mm, and (D) water sheet with a wavelength of 4.2 mm. *NOTE: All the water sheets with perturbations are between 0.3 cm and 0.1 cm thick.*

4.5 Water sheet simulation results and comparisons

Figure 10 shows a comparison of the CTH model and experimental results at 5 and 10 cm after the water-sheet at a 20 cm standoff distance. Both the experimental and numerical results show an initially transmitted pressure wave and a later second pressure rise. To highlight the physical processes, Fig. 11 shows predicted contours of pressure at select time intervals. Due to the impedance mismatch at the air-water interface, a significant portion of the initial shock reflects off the water-sheet and only a weak shock wave is initially transmitted. However, as observed in experiments, the water-sheet eventually fragments, and consequently the high pressure detonation products are released, causing the observed second rise in pressure.

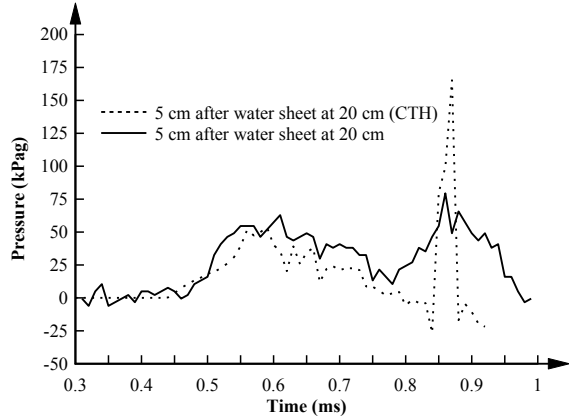


Fig. 10 Comparison between CTH and experimental pressure traces 5 cm after the water-sheet at a 20 cm standoff distance.

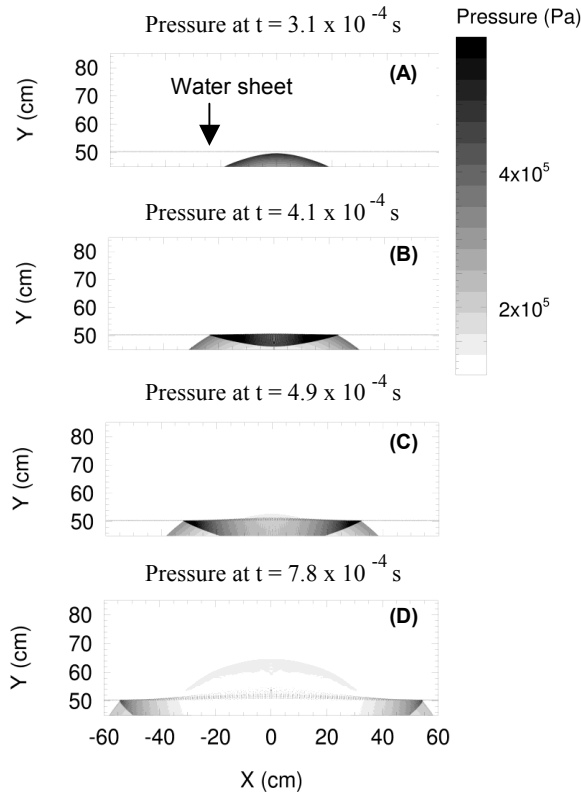


Fig. 11 Simulation results showing absolute pressure for shock wave interaction with the water-sheet at the 20 cm standoff distance. (A) initial shock wave reaches the water-sheet, (B) reflection of a shock wave off the surface of the water-sheet, (C) development of weak transmitted shock wave behind the intact water-sheet, and (D) water-sheet breakup and transition of pressure wave.

5 Discussion

Figure 12 highlights the general form of the transient overpressure observed in experiments and simulations. As discussed by Henderson et al. [11], when a blast wave first contacts a water-sheet, a large portion of the incident energy is reflected back towards the source due to the impedance mismatch at the air-water interface. The remaining energy, which is transmitted through the water-sheet, forms the observed weak shock wave and the resulting initial pressure rise. For the experimental conditions considered here, the initial blast peak overpressure is mitigated by as much as 80%. However, a second rise in pressure is observed, resulting in a much greater overpressure behind the water-sheet. If a mechanism is available to prevent this second pressure rise, a water-sheet may be an effective emergency blast mitigant.

High speed shadowgraphy (Fig. 6) and simulations (Fig. 11) confirm that the second rise in pressure is due to the breakup of the water-sheet and the passage of the detonation products. When the blast wave initially reflects off the water-sheet, a large pressure differential exists between forward and back surfaces of the water-sheet (see Fig. 11). It is well known that pressure differentials of this nature give rise to surface instabilities which grow and eventually lead to fragmentation. This process takes a finite time, referred to as the breakup time (Fig. 5). It should also be noted that the pressure differential across the water-sheet decreases with time due to the propagation of the reflected shock wave away from the water-sheet. Therefore, water-sheet fragmentation may be prevented if the characteristic breakup-time is sufficiently longer than the time required for dissipation of the pressure differential across the water-sheet.

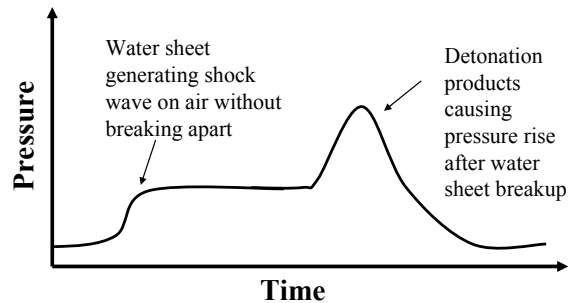


Fig. 12 Typical pressure trace of water-sheet breakup under shock loading.

A few methods are available to increase the effective breakup time of a water-sheet. (1) To the extent possible, the surface of the water-sheet should be free from initial perturbations; (2) the thickness of the water-sheet can be increased; and/or (3) multiple water-sheets can be utilized. The effectiveness of method (1) is confirmed by the simulation results presented in the previous section. However, this method may be difficult to implement due to the capillary instability and water-sheet turbulence. Methods (2) and (3) have been shown to increase blast mitigation in previous investigations [4-6] and were also qualitatively investigated using the CTH model discussed in the previous section. The details of those simulations are omitted for conciseness. However, the conclusions are consistent with the previously published work. Further quantitative experiments and simulations are needed to confirm these results.

5 Conclusions

An experimental investigation of blast mitigation using a 0.3 cm thick water-sheet is presented. Results show an initially decreased peak overpressure and impulse regardless of water-sheet standoff distance. This initial mitigating potential agrees qualitatively with previous literature.

A numerical model using CTH is developed and validated with the free-field experimental data. In simulations with a water-sheet, an initial pressure rise results from the passage of a low pressure shock wave ($M \approx 1$) through the intact sheet and into the air behind it. Following this, the water-sheet breaks apart due to an increase in pressure on the forward surface caused by the buildup of the subsonic detonation products. Passage of the detonation products after breakup results in a large second rise in pressure behind the water-sheet. Additionally, the numerical model along with experimental shadowgraphy reveal that water sheet breakup follows a multi-step process. The water sheet breakup time was found to be a function of the perturbation in the water sheet. In addition, from experimental and numerical results the water-sheet breakup time decreases with increasing strength of the incident shock wave.

The water-sheet is shown to be advantageous for mitigating an incident blast wave if sheet breakup can be prevented or delayed. A few possible methods are proposed and further experimental and numerical investigations are needed to confirm their validity.

Acknowledgements We would like to thank the Department of Homeland Security and the Center of

Excellence for Explosive Detection, Mitigation and Response, Sponsor Award No. 080409/0002251. We would also like to thank Justin Wagner for his technical review of this paper. Additionally, special thanks to Eric Miklaszewski, Matthew Massaro, and Jesus Mares who assisted with experiments.

Sandia National Laboratories is a multi-program laboratory managed and operated by Sandia Corporation, a wholly owned subsidiary of Lockheed Martin Corporation, for the U.S. Department of Energy's National Nuclear Security Administration under contract DE-AC04-94AL85000.

References

1. National Research Council: Protecting buildings from bomb damage: Transfer of blast-effects mitigation technologies from military to civilian applications. National Academy, Washington, DC (1995)
2. Kailasanath, K., Tatem, P. A., Williams, F. W., and Mawhinney, J.: Blast mitigation using water – A status report. NRL Memorandum Report, 6410-02-8606 (2002)
3. Schwer, D., Kailasanath, K.: Blast Mitigation by Water Mist (3) Mitigation of Confined and Unconfined Blasts. NRL Memorandum Report, 6410-06-8976, (2006)
4. Cheng, M., Hung, K. C., and Chong, O. Y.: Numerical Study of Water Mitigation Effects on Blast Waves. Shock Waves 14, 217-223 (2005)
5. Shin, Y. S., Lee, M., Lam, K. Y., Yeo, K. S.: Modeling mitigation effects of water shield on shock waves. Shock Vib. 5, 225-234 (1998)
6. Meekunnasombat, P., Oakley, J.G., Anderson, M.H., Bonazza, R.: Experimental study of a shock-accelerated liquid layer. Shock Waves 15, 383-397 (2006)
7. Bremond, N., Villermaux, E.: Bursting thin liquid films. J. Fluid Mech. 524:121-30 (2005)
8. Freiwald, D. A.: Approximate blast wave theory and experimental data for Shock trajectories in linear explosive driven shock tubes. Jpn. J. Appl. Phys. 43, 2224-2226 (1972)
9. Alley, M. D.: Explosive Blast Loading Experiments for TBI Scenarios: Characterization and Mitigation. Thesis. West Lafayette, IN / Purdue University, (2009)
10. Settles, G.: High-speed imaging of shock waves, explosives, and gunshots. Am. Sci. 94, 22-31 (2006)
11. Henderson, L. F., Ma, J. H., Sakurai, A., Takayama, K.: Refraction of a shock wave at an air-water interface. Fluid Dynamics Res 5, 337-350 (1990b)
12. Crawford, D.: CTH Shock Physics. Sandia National Laboratories. <http://www.sandia.gov/CTH/> (2012). Accessed 14 Dec. 2011
13. Todd, S. N., Anderson, M. U., Caipen, T. L.: Modeling for non shock initiation. Dynamic Behav. of Mater. 1, 179-186 (2011)
14. Lyon, S. P., Johnson, J. D.: SESAME." The Los Alamos National Laboratory Equation of State

Database. Equation of State and Mechanics of
Materials (T-1), LANL.
http://t1web.lanl.gov/doc/SESAME_3Ddatabase_1992.html (1992). Accessed 10 Nov. 2011